

Middle Atmosphere Program

(NASA-CR-184979) MIDDLE ATMOSPHERE PROGRAM.
HANDBOOK FOR MAP, VOLUME 27 (International
Council of Scientific Unions) 571 pCSCL 04A

N89-29853
--THRU--
N89-29930
Unclas
0210823

G3/46

ICSU

International Council of Scientific Unions

SCOSTEP

Scientific Committee on Solar-Terrestrial Physics

J. G. Roederer, President

W. I. Axford, Vice President

C. H. Liu, Scientific Secretary

MAP ORGANIZATION

MIDDLE ATMOSPHERE PROGRAM STEERING COMMITTEE

S. A. Bowhill, SCOSTEP, Chairman

K. Labitzke, COSPAR, Vice Chairman

C. H. Liu, SCOSTEP, Secretary

H. S. Ahluwalia, IUPAP
R. D. Bojkov, WMO
A. D. Danilov, COSPAR
J. C. Gille, COSPAR
I. Hirota, IUGG/IAMAP
A. H. Manson, SCOSTEP

T. Nagata, SCAR
R. G. Roper, IUGG/IAMAP
P. C. Simon, IAU
J. Taubenheim, IUGG/IAGA
T. E. VanZandt, URSI
R. A. Vincent, URSI

MAP STANDING COMMITTEES

Data Management -- G. Hartmann and I. Hirota, Co-Chairmen
Publications -- Belva Edwards, Chairman

MAP STUDY GROUPS

MSG-5 Ions and Aerosols, F. Arnold and M. P. McCormick, Co-Chairmen
MSG-8 Atmospheric Chemistry, G. Witt, Chairman
MSG-9 Measurement of Middle Atmosphere Parameters by Long Duration
Balloon Flights, J. E. Blamont, Chairman

MAP PROJECTS

	Coordinator
AMA:	T. Hirasawa
ATMAP:	J. M. Forbes
DYNAMICS:	K. Labitzke
GLOBMET:	R. G. Roper
GLOBUS:	J. P. Pommereau
GOSSA:	M. P. McCormick
GRATMAP:	D. C. Fritts
MAC-EPSILON:	E. V. Thrane

	Coordinator
MAC-SINE:	E. V. Thrane
MAE:	R. A. Goldberg
MASH:	A. O'Neill
NIEO:	S. Kato
OZMAP:	D. F. Heath
SSIM:	P. C. Simon
SUPER CAMP:	E. Kopp
WINE	U. von Zahn

MAP REGIONAL CONSULTATIVE GROUP

Europe: M. L. Chanin, Chairman

**MIDDLE
ATMOSPHERE
PROGRAM
HANDBOOK
FOR MAP**

Volume 27

**Extended Abstracts Papers presented at
COSPAR Symposium 6, The Middle
Atmosphere After MAP, Espoo, Finland,
July 18-23, 1988
Minutes MAP Steering Committee Meeting
Espoo, Finland, July 18, 1988
International Workshop on Noctilucent Clouds,
Tallinn, Estonia, USSR, July 17-31, 1988**

**Edited by
Belva Edwards**

April 1989

**Published for the ICSU Scientific Committee on Solar-Terrestrial
Physics (SCOSTEP) with financial assistance from the National
Aeronautics and Space Administration under the 1987 Middle
Atmosphere Program Management Contract and Unesco Subvention
1988-1989.**

**Copies available from SCOSTEP Secretariat, University of Illinois,
1406 W. Green Street, Urbana, Illinois 61801.**

Editor's Note

Part 1 of this volume contains abstracts and extended figure captions of most of the papers presented at COSPAR Symposium 6, The Middle Atmosphere After MAP, held at Espoo, Finland, July 18-23, 1988. It is intended to be a "quick" synopsis of the Symposium and not a complete record; therefore, some of the figures, reproduced from transparencies presented at the Symposium, are of secondary quality and some citations are made for which the full reference is not given. I regret the inconvenience to readers caused by the omissions and apologize to the authors concerned.

Part 2 contains the Draft Minutes and related documents of the MAP Steering Committee Meeting held at Espoo. Part 3 is a report of the International Workshop on Noctilucent Clouds held at Tallinn, Estonia, USSR, July 27-31, 1988, which was kindly furnished by G. E. Thomas.

CONTENTS

PART 1

1. INTRODUCTION AND NEW INTERNATIONAL EQUATORIAL OBSERVATORY (NIEO)	1
1.1 The Middle Atmosphere Program: An Overview, <i>S. A. Bowhill</i>	1
1.2 Japanese Contributions to MAP, <i>S. Kato</i>	4
1.3 Progress in D-Region Studies during MAP, <i>A. D. Danilov</i>	10
1.4 Equatorial Radar System, <i>S. Fukao, T. Tsuda, T. Sato, and S. Kato</i>	13
1.5 A Perspective of Middle-Atmosphere Dynamics (MAD) Studies at the New Equatorial Observatory (NIEO), <i>M. D. Yamanaka and S. Fukao</i>	16
2. DYNAMICS OF THE MIDDLE ATMOSPHERE IN WINTER (DYNAMICS)	18
2.1 Interrelation Between the Different Variations of Turbulent Diffusion and Ionospheric Absorption Originating in the Middle Atmosphere, <i>P. Bencze</i>	18
2.2 Variability of Quasi-Stationary Planetary Waves, <i>A. A. Krivolutsky, N. D. Petushkov, and D. A. Tarasenko</i>	20
2.3 Wave Propagation into the Middle Atmosphere, <i>I. Hirota</i>	22
2.4 Effects from the "Coupling from Below" on the Lower Thermosphere Dynamics, <i>E. S. Kazimirovsky</i>	27
2.5 Transport Processes in the Middle Atmosphere: Reflections After MAP, <i>W. L. Grose</i>	30
3. GLOBAL BUDGET OF STRATOSPHERIC TRACE CONSTITUENTS (GLOBUS)	45
3.1 MAP/GLOBUS 1983: A Review, <i>D. Offermann</i>	45
3.2 An Overview of MAP/GLOBUS NO _x , <i>J. P. Pommereau</i>	54
3.3 Measurements of Nitric Oxide in the Stratosphere at 44°N in Autumn, <i>Y. Kondo, W. A. Matthews, P. Amedieu, and D. E. Robbins</i>	62
3.4 Seasonal Variation of the Temporal Variance of Long-Lived Trace Gases Measured during MAP, <i>E. P. Röth and U. Schmidt</i>	66
3.5 Evidence of CO ₂ -Induced Progressive Cooling of the Middle Atmosphere Derived from Radio Observations, <i>J. Taubenheim, G. v. Cossart, and G. Entzian</i>	70
4. GRAVITY WAVES AND TURBULENCE IN THE MIDDLE ATMOSPHERE PROGRAM (GRATMAP)	72
4.1 An Overview of Gravity Wave Studies during MAP/MAC, <i>D. C. Fritts</i>	72
4.2 Observations of Gravity Wave Scales, Fluxes, and Saturation during MAP, <i>I. M. Reid</i>	87
4.3 Measurements of Turbulence and its Evolution and Variability during MAP, <i>W. K. Hocking</i>	104
4.4 Advances in Understanding the Gravity Wave Spectrum during MAP, <i>T. E. VanZandt</i>	123
5. MIDDLE ATMOSPHERE OF THE SOUTHERN HEMISPHERE (MASH) GLOBAL METEOR OBSERVATIONS SYSTEM (GLOBMET) SOLAR SPECTRAL IRRADIANCE MEASUREMENTS (SSIM) GLOBAL OBSERVATIONS AND STUDIES OF STRATOSPHERIC AEROSOLS (GOSSA)	132
5.1 Progress with the MASH Project, <i>A. O'Neill</i>	132

5.2 Why do Planetary Wave Number One and the Ozone Transport Vary Annually in the Northern Hemisphere and Semiannually in the Southern Hemisphere?, <i>M. A. Geller, M. F. Wu, and E. R. Nash</i>	141
5.3 An Overview of GLOBMET during MAP and MAC, <i>R. G. Roper</i>	159
5.4 The Meteor Radar as a Tool for Upper Atmosphere Research, <i>S. K. Avery</i>	160
5.5 Remote Sensing of the Atmospheric Aerosols and Noctilucent Clouds from Space, <i>O. Avaste, M. Gadsden, R. Røom</i>	173
5.6 Lower Stratospheric Aerosols at a Tropical Latitude Station, <i>B. V. Krishnamurthy, K. Parameswaran, K. O. Rose, and M. Satyanarayana</i> ...	174
5.7 Some New Results in the Investigation of the Middle Atmosphere from Space Using the Daytime Horizon Scanning Method, <i>R. Røom, K. Eerme, and U. Veismann</i>	176
6. MIDDLE ATMOSPHERE ELECTRODYNAMICS (MAE)	178
6.1 Middle Atmosphere Electrodynamics During MAP, <i>R. A. Goldberg</i>	178
6.2 Middle Atmosphere Electrical Energy Coupling, <i>L. C. Hale</i>	186
6.3 Electric Field Measurements with Stratospheric Balloons, <i>I. B. Iversen</i>	194
6.4 The use of DC-Probe Measurements in the Middle Atmosphere Program, <i>E. V. Thrane</i>	201
6.5 Results of Rocket Measurements of D-Region Ionization over Thumba in MAP, <i>D. K. Chakrabarty, G. Beig, S. C. Garg, P. Subrahmanyam, K. S. Zalpuri, Y. V. Somayajulu, M. N. M. Rao, C. B. Tandel, and T. R. Murlikrishna</i>	209
6.6 Model Representation of the Ambient Electron Density Distribution in the Middle Atmosphere, <i>Y. V. Ramanamurthy</i>	212
6.7 Effect of Volcanic Debris on Stratospheric Ion Conductivity, <i>Y. V. Somayajulu, S. C. Garg, T. John, and K. S. Zalpuri</i>	216
6.8 Relativistic Magnetospheric Electrons: Lower Ionospheric Conductivity and Long- Term Atmospheric Variability, <i>D. N. Baker, J. B. Blake, R. Klebesadel, D. D. Sentman, D. J. Gorney, and P. R. Higbie</i>	217
7. WINTER IN NORTHERN EUROPE (WINE)	220
7.1 The Project "Winter in Northern Europe" (MAP/WINE): Introduction and Outlook, <i>U. von Zahn</i>	220
7.2 Small-Scale Structure and Turbulence Observed in MAP/WINE, <i>T. A. Blix</i>	226
7.3 Middle Atmosphere Thermal Structure During MAP/WINE, <i>D. Offermann</i>	237
7.4 The Soviet Contributions Towards MAP/WINE, <i>Z. Ta. Rapoport and E. S. Kazimirovsky</i>	245
7.5 Mean, Zonal and Fluctuating Winds in the Middle Atmosphere and Lower Thermosphere Observed During MAP/WINE in Northern Scandinavia, <i>J. Röttger</i>	251
7.6 Large-Scale Dynamics of the Stratosphere and Mesosphere During the MAP/WINE Campaign Winter 1983/84 in Comparison with Other Winters, <i>K. Petzoldt</i>	271
7.7. Plasma Phenomena Observed in the MAP/WINE Campaign, <i>M. Friedrich</i>	277
8. ATMOSPHERIC TIDES MIDDLE ATMOSPHERE PROGRAM (ATMAP)	280
8.1 The Atmospheric Tides Middle Atmosphere Program, <i>J. M. Forbes</i>	280
8.2 Asymmetries in Tidal Structure Between Adelaide and Kyoto, <i>R. A. Vincent</i>	283
8.3 Nonmigrating Tides, <i>S. Kato</i>	293
8.4 Global Behavior of the Height/Seasonal Structure of Tides Between 40° and 60° Latitude, <i>A. H. Manson, C. E. Meek, H. Teitelbaum, G. J. Fraser, M. J. Smith, R. R. Clark, R. Schminder, and D. Kürschner</i>	303
8.5 Recent Progress in Tidal Modeling, <i>F. Vial and J. M. Forbes</i>	317
8.6 Long-Term Variations in Midlatitude Southern Hemisphere Mesospheric Winds, <i>G. J. Fraser</i>	321

8.7 The Geomagnetic Control of the Lower Thermosphere Wind System Over East Siberia, <i>E. S. Kazimirovsky, G. V. Gergasova, E. I. Zhovty, and M. A. Chernigovskaya</i>	330
8.8 Midlatitude Seasonal Behavior of Tides Near the Mesopause Level, <i>E. S. Kazimirovsky and E. I. Zhovty</i>	334
8.9 Measurements of Vertical Motions by the Saskatoon MF Radar (1983-85): Relationships with Horizontal Winds and Gravity Waves, <i>A. H. Manson and C. E. Meek</i>	339
8.10 Nonlinear Interaction Between the Diurnal and Semidiurnal Tides: Terdiurnal and Diurnal Secondary Waves, <i>H. Teitelbaum, F. Vial, A. H. Manson, R. Giraldez, and M. Masseboeuf</i>	342
9. MIDDLE ATMOSPHERE COOPERATION/SUMMER IN NORTHERN EUROPE (MAC/SINE) AND MAC/EPSILON	347
9.1 The MAC/SINE and MAC/Epsilon Campaigns, <i>E. V. Thrane</i>	347
9.2 Dynamics of the Upper Middle Atmosphere (80 - 110 km) at Tromsø, June-December 1987, Using the Tromsø/Saskatoon M.F. Radar, <i>A. H. Manson and C. E. Meek</i>	354
9.3 VHF Radar Measurements in the Summer Polar Mesosphere, <i>R. Rüster, I. M. Reid, P. Czechowsky, and G. Schmidt</i>	359
9.4 VHF Radar Measurements Over Andoya (Northern Norway), <i>P. Czechowsky, I. M. Reid, R. Rüster, and G. Schmidt</i>	365
9.5 EISCAT Observations During MAC/SINE and MAC/Epsilon, <i>J. Röttger, U.-P. Hoppe, and C. Hall</i>	370
9.6 A Comparison of Results Obtained from Foil Chaff Clouds at 69° Northern Latitude During Winter, Summer and Autumn, <i>H. U. Widdel and U. von Zahn</i> ..	377
9.7 Rocket Measurements of Electron Density Irregularities During MAC/SINE, <i>J. C. Ulwick</i>	386
9.8 Turbulent Small-Scale Neutral and Ion Density Fluctuations as Measured During MAC/Epsilon, <i>F.-J. Lübken, W. Hillert, U. von Zahn, T. Blix, and E. Thrane</i> ..	390
9.9 Middle Atmosphere Measurements of Small-Scale Electron Density Irregularities and Ion Properties During the MAC/Epsilon Campaign, <i>S. P. Blood, J. D. Mitchell, and C. L. Croskey</i>	397
9.10 Preliminary Measurements of Auroral Energy Deposition and Middle Atmosphere Electrodynamics Response During MAC/Epsilon, <i>R. A. Goldberg</i>	400
9.11 Positive Ion Composition in the Polar D and E Regions Measured During Moderate Ionospheric Absorption, <i>P. Lämmerzahl and D. Krankowsky</i>	408
9.12 Case Study of Modeled and Measured D-Region Plasma Densities, <i>M. Friedrich</i>	411
10. OBSERVATIONS OF, AND SOURCES OF THE SPATIAL AND TEMPORAL VARIABILITY OF OZONE IN THE MIDDLE ATMOSPHERE ON CLIMATOLOGICAL TIME SCALES (OZMAP) AND EQUATORIAL DYNAMICS	413
10.1 Seasonal Variations of Ozone Trends, <i>G. Entzian, K. H. Grasnick, and J. Taubenheim</i>	413
10.2 Stratospheric Temperature - Ozone Relationships 1978 - 1986, <i>M. E. Gelman, R. M. Nagatani, A. J. Miller, and K. W. Johnson</i>	417
10.3 Subtropical Middle Atmosphere Dynamics Observed by the Chung Li Radar, <i>I. J. Fu, C. H. Liu, J. Röttger, and J. K. Chao</i>	423
POSTER SESSION	427
P.1 Wind and Waves in the Middle Atmosphere Observed with the MU Radar, <i>S. Fukao, T. Tsuda, T. Sato, M. Yamamoto, and S. Kato</i>	427
P.2 Seasonal Variation of Turbulence Intensities in the Upper Mesosphere and Lower	

Thermosphere Measured by Radar Techniques, <i>W. K. Hocking</i>	439
P.3 A Comparison of Radar Measurements of Atmospheric Turbulence Intensities by Both C_n^2 and Spectrum Width Methods, <i>W. K. Hocking, K. Lawry, and D. Neudegg</i>	443
P.4 MU Radar Observation of a Mesospheric Gravity Wave Breaking Caused by Convective Instability, <i>Y. Muraoka, T. Sugiyama, K. Kawahira, T. Sato, T. Tsuda, S. Fukao, and S. Sato</i>	447
P.5 A Numerical Study of Scalar Gradients in Kelvin-Helmholtz Billows, <i>J. W. Parker and S. A. Bowhill</i>	449
P.6 Estimations of Model Parameters for Gravity Wave Spectra Observed by MST Radar, <i>A. O. Scheffler, C. H. Liu, and S. J. Franke</i>	455
P.7 Spectral Analysis of Temperature and Brunt-Väisälä Frequency Fluctuations Observed by Radiosondes, <i>T. Tsuda, T. E. VanZandt, S. Kato, S. Fukao, and T. Sato</i>	461
P.8 Observations of Gravity Waves in the Mesosphere with the MU Radar, <i>T. Tsuda, S. Kato, T. Inoue, T. Yokoi, M. Yamamoto, S. Fukao, and T. Sato</i>	469
P.9 Measurement of Vertical Velocity Using Clear-Air Doppler Radars, <i>T. E. VanZandt, J. L. Green, G. D. Nastrom, K. S. Gage, W. L. Clark, and J. M. Warnock</i>	477
P.10 Picture of the Global Field of "Quasi-Monochromatic" Gravity Waves Observed by Stratospheric Balloons and MST Radars, <i>M. D. Yamanaka</i>	482
P.11 Higher Order Dispersion in the Propagation of a Gravity Wave Packet, <i>K. C. Yeh and B. Dong</i>	484
P.12 Gravity Wave Climatology at Midlatitude from Rayleigh Lidar Data, <i>R. Wilson, M. L. Chanin, and A. Hauchecorne</i>	488

PART 2

DRAFT MINUTES MAP STEERING COMMITTEE MEETING, July 18, 1988 499

Appendix 1. MAP Data Management Report	501
Appendix 2. Publications Report	501
Appendix 3. The Stratospheric Winter 1987/88	502
Appendix 4. GLOBMET	522
Appendix 5. The MAC/SINE and MAC/Epsilon Campaigns	523
Appendix 6. Middle Atmosphere Electrodynamics (MAE)	537
Appendix 7. Report on Progress with MASH Project	539
Appendix 8. New International Equatorial Observatory (NIEO)	540
Appendix 9. Super CAMP	541
Appendix 10. GLOBUS NO _x	542
Appendix 11. Publications with Results of the Project MAP/WINE	544
Appendix 12. MAP Activities - USSR	549
Appendix 13. MAP Activities 1981-1988 - Federal Republic of Germany	550
Appendix 14. MAP Activities - Brazil	551
Appendix 15. MAC Activities - Czechoslovakia	553
Appendix 16. MAP Activities - United Kingdom	554
Appendix 17. MAP Activities - Hungary	555
Appendix 18. List of Attendees at Meeting	556
Appendix 19. Agenda of Meeting	556

PART 3

INTERNATIONAL WORKSHOP ON NOCTILUCENT CLOUDS 557

1. INTRODUCTION AND NEW INTERNATIONAL EQUATORIAL OBSERVATORY (NIEO)

1.1 THE MIDDLE ATMOSPHERE PROGRAM: AN OVERVIEW

S. A. Bowhill

Department of Electrical Engineering
University of Lowell, Lowell, MA 01854

The Middle Atmosphere Program (MAP) took place from January 1, 1982 through December 31, 1986, and was followed by Middle Atmosphere Cooperation (MAC) through to the end of 1988. The inception and organization of the program are described, together with some of the salient features of its results.

REGIONS OF THE ATMOSPHERE

Troposphere 0-17 km

Stratosphere 17-50 km

Mesosphere 50-85 km

Thermosphere 85 km

Middle atmosphere consists of the stratosphere and mesosphere.

RELEVANCE OF THE STRATOSPHERE

Ozone layer effects

Chlorofluorocarbon effects

Clear air turbulence

Radioactivity residence times

Scatter communication

RELEVANCE OF THE MESOSPHERE

Modeling for aerospace applications

Communication by meteors, etc.

Radio absorption effects

AIMS OF MAP

"Under the aegis of MAP, scientists will collaborate internationally

1. To determine the structure and composition of the atmosphere in the regions of the stratosphere and mesosphere, i.e., in the approximate altitude range 15 to 85 km; especially in regard to important minor species.

2. To determine the interaction of radiation from the sun, the earth and the atmosphere with the middle atmosphere.

3. To investigate the motions of the middle atmosphere on all scales, including the interactions with the troposphere and magnetosphere, and to monitor these motions on a continuing basis."

SOURCES OF ENERGY IN THE SOLAR-TERRESTRIAL SYSTEM

Tides, gravity waves, planetary waves, solar ultraviolet radiation, solar X-radiation, cosmic rays, magnetospheric electric fields, energetic particle precipitation, global electrical circuit.

MAP STEERING COMMITTEE

S. A. Bowhill, SCOSTEP, Chairman
K. Labitzke, COSPAR, Vice Chairman
C. H. Liu, SCOSTEP, Secretary

H. S. Ahluwalia, IUPAP
R. D. Bojkov, WMO
A. D. Danilov, COSPAR
J. C. Gille, COSPAR
I. Hirota, IAMAP
A. H. Manson, SCOSTEP

T. Nagata, SCAR
R. G. Roper, IAMAP
P. C. Simon, IAU
J. Taubenheim, IUGG
T. E. VanZandt, URSI
R. A. Vincent, URSI

MAP STUDY GROUPS AND CHAIRMEN

MSG-1: Tropospheric-Stratospheric Coupling, Chemical and Dynamical, J. R. Holton
MSG-2: Transport of Trace Constituents, J. D. Mahlman
MSG-3: Tides, Gravity Waves and Turbulence, M. A. Geller
MSG-4: Electrodynamics of the Middle Atmosphere, H. Volland
MSG-5: Ions and Aerosols, F. Arnold and M. P. McCormick
MSG-6: Scientific Aspects of an International Equatorial Observatory, S. Kato
MSG-7: Penetration of Solar Radiation into the Atmosphere, J. E. Frederick
MSG-8: Atmospheric Chemistry, G. Witt
MSG-9: Measurement of Middle Atmosphere Parameters by Long Duration Balloon Flights, J. E. Blamont

PRE-MAP PROJECTS AND CHAIRMEN

PMP-1: Coordinated Study of the Middle Atmosphere in Winter, K. Labitzke
PMP-2: Equatorial Wave Dynamics, I. Hirota
PMP-3: Study of Photochemical Processes in the Upper Stratosphere and Mesosphere by Complementary Spacecraft, *in situ*, and Ground Measurements, J. Gille
PMP-4: Presentation of Meteorological and Chemical Variables in the Format of Monthly Mean Zonal Cross Sections, J. Barnett
PMP-5: Solar Spectrum Irradiance Measurements, P. C. Simon

MAP PROJECTS AND COORDINATORS

AMA: Antarctic Middle Atmosphere Program, T. Hirasawa
ATMAP: Atmospheric Tides in the Middle Atmosphere Program, J. M. Forbes
DYNAMICS: Dynamics of the Middle Atmosphere in Winter, K. Labitzke
GLOBMET: Global Meteor Observation System, R. G. Roper
GLOBUS: Global Budget of Stratospheric Trace Constituents, D. Offermann
GOSSA: Global Observations and Studies of Stratospheric Aerosols, M. P. McCormick
GRATMAP: Gravity Waves and Turbulence in the Middle Atmosphere Program, D. C. Fritts
MAC-EPSILON: The project is planned as a case study of middle atmosphere turbulence by measure of instrumented sounding rockets, meteorological rockets and ground-based observations, E. V. Thrane
MAC-SINE: Middle Atmosphere Cooperation - Summer in Northern Europe, E. V. Thrane
MAE: Middle Atmosphere Electrodynamics, R. A. Goldberg
MASH: Middle Atmosphere of the Southern Hemisphere, A. O'Neill
NIEO: New International Equatorial Observatory, S. Kato
OZMAP: Observations of, and Sources of the Spatial and Temporal Variability of Ozone in the Middle Atmosphere on Climatological Time Scales, D. F. Heath
SSIM: Solar Spectral Irradiance Measurements, P. C. Simon
SUPER CAMP: This project is a follow-on of CAMP (Cold Arctic Mesopause Project) and will focus on a study of the middle atmosphere above the northern polar region from 50° to 80° during the summer, in the effort to understand latitudinal variability of vertical transport, wave dissipation, and its implications on densities of minor constituents, E. Kopp
WINE: Winter in Northern Europe, U von Zahn

MAP HANDBOOK TOPICS AND VOLUME NUMBERS

Study Group Reports: 1, 3, 8, 11, 17, 21
 Technique Handbooks: 13, 15, 19
 Project Reports: 1, 3, 4, 8, 11, 12, 17, 21
 National Plans and Reports: 1, 4, 8, 9, 11, 17, 21
 Steering Committee Minutes: 3, 4, 8, 11, 17, 21, 26
 MAP Assembly Proceedings: 4, 17
 Directories: 6, 24
 Regional Definition Group Reports: 4
 Symposium Papers: 2, 10, 18, 25
 Workshop Reports: 8, 9, 11, 12, 14, 17, 20, 21
 Data Presentation Handbooks: 5, 12, 16, 22

SCIENTIFIC DESIDERATA

For winds studies; for tidal studies; for gravity waves; for turbulence studies; for studies of mesoscale effects and for studies of chemistry.

PROBLEMS WITH CURRENT TECHNIQUES

Height coverage; height resolution; time resolution; measurement of spectral parameters; monostaticity; and poor geographical distribution.

FUTURE PROGRAMS OF OBSERVATION

MAP/MAC now concluding
 MAC-EPSILON
 Definition and purpose of MAS
 Relationship to GIS and STEP
 New equatorial observatory
 Upgrading of existing facilities
 Data analysis phase

DIVIDENDS FROM MAP

- More groups working
- Greater international communication
- Prototype for small international programs
- Increased funding agency awareness
- Scientific interest in stratosphere added to operational interest
- Increased awareness of interdisciplinary aspects
- Satellite groups now driven by user pressure

LESSONS FROM MAP

- Clear definition of area
- Early preparations for national participation
- Study groups to define needs
- Pre-projects to exercise cooperative efforts
- Project structure not imposed from above
- Workshops actively encouraged
- Publications must be uniform and timely
- Alertness for new techniques
- Unite techniques in campaigns
- Take advantage of all symposium opportunities
- MAP area now fully defined and flourishing

1.2 JAPANESE CONTRIBUTIONS TO MAP

S. Kato

Radio Atmospheric Science Center
Kyoto University, Kyoto 611, Japan

Japan contributed much to MAP in many branches. The MU radar, in operation during the MAP period, produced various novel possibilities in observations of middle atmosphere dynamics; possibilities which have been fairly well realized. Gravity wave saturation and its spectrum in the mesosphere have been observed successfully. Campaign observations by radars between Kyoto and Adelaide have been especially significant in tidal and planetary wave observations. In Antarctica, middle atmosphere observation of the dramatic behavior of aerosols in winter is well elucidated together with the ozone hole. Theoretical and numerical studies have been progressing actively since a time much earlier than MAP. Now it is pointed out that gravity waves play an important role in producing the weak-wind region in the stratosphere as well as the mesosphere.

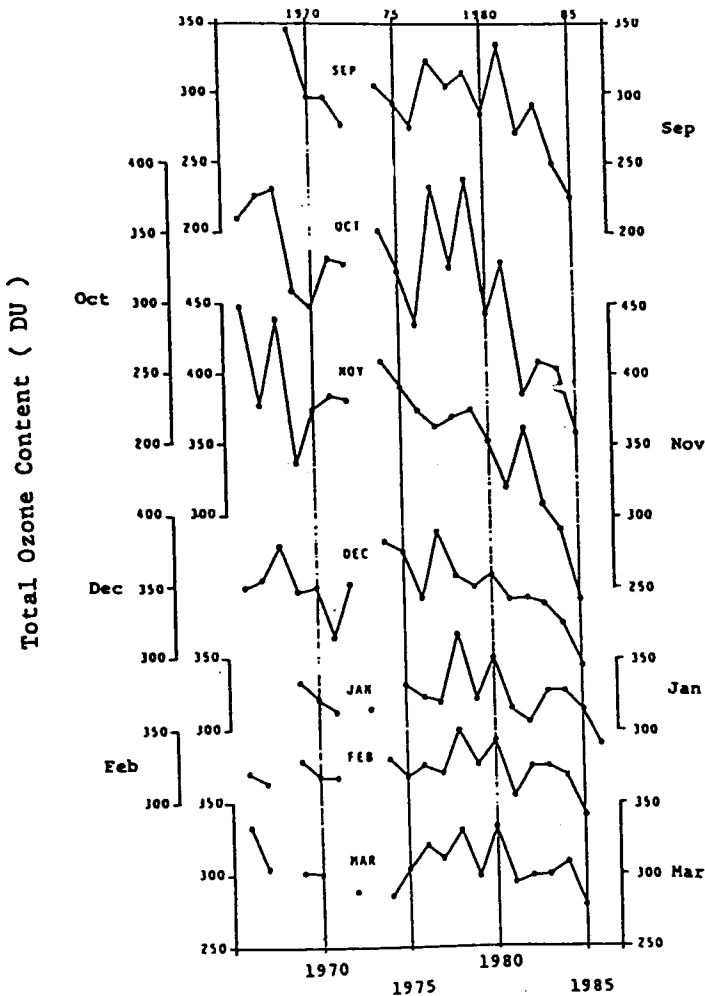


Figure 1. Ozone depletion at Antarctica [Iwasaka and Kondoh, *Geophys. Res. Lett.*, 14, 87, 1987].

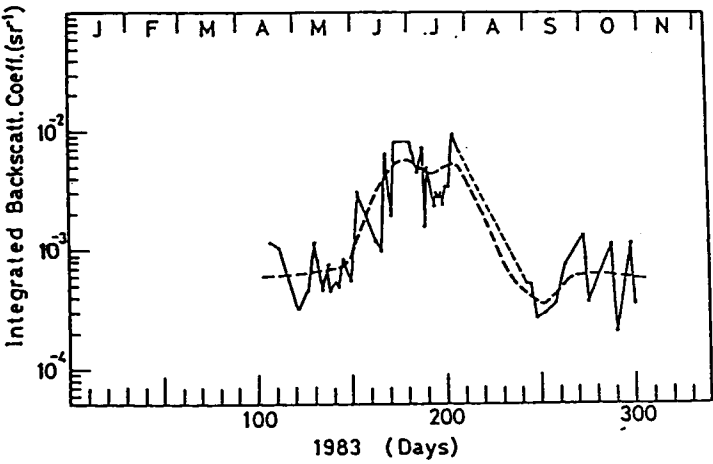


Figure 3. Aerosol is increased tremendously in winter [Iwasaka, *J.G.G.*, 38, 99, 1986].

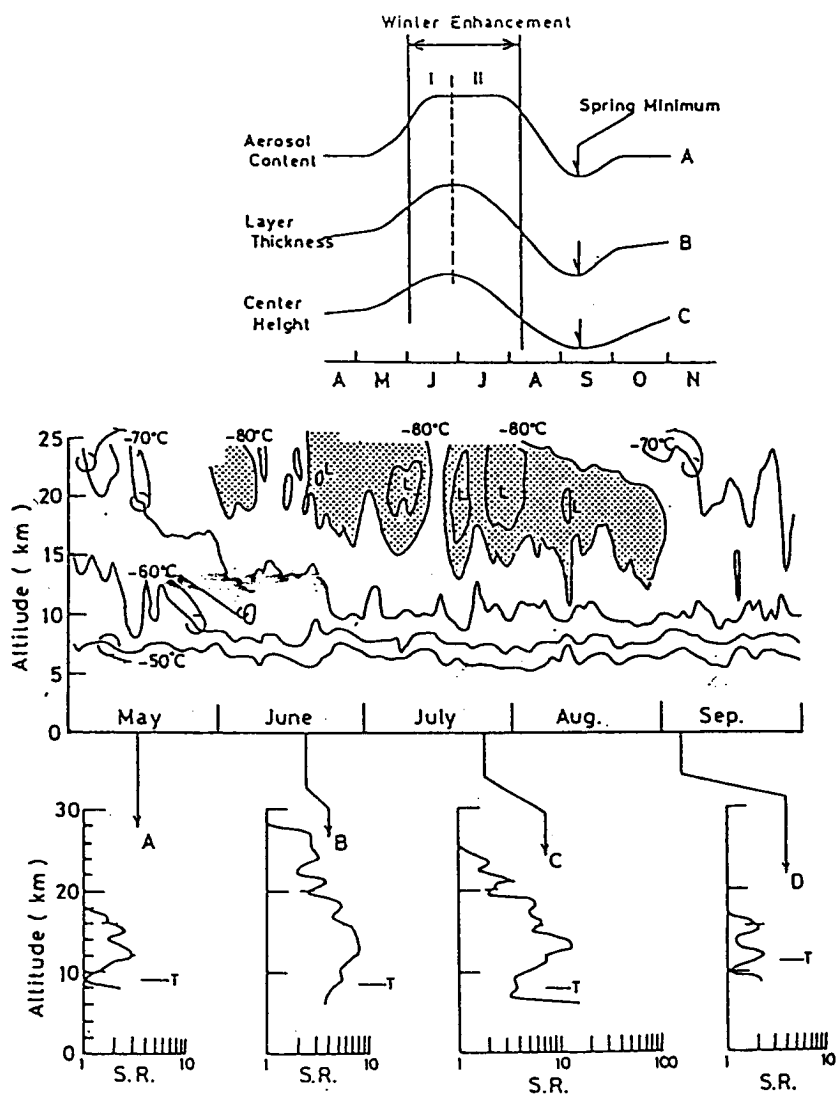


Figure 4. Note that the low temperature as (-80°) may cause the aerosol behavior as shown in the upper figure [Iwasaka, *J.G.G.*, 38, 99, 1986]

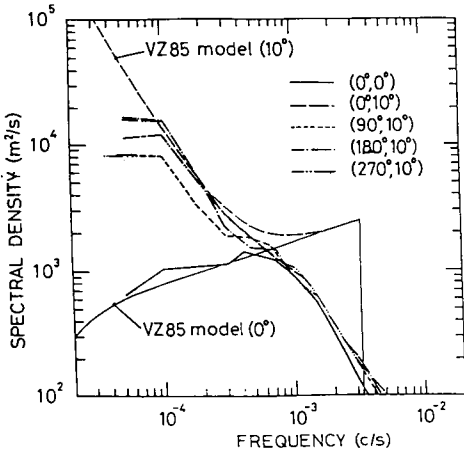


Figure 5. The frequency spectrum of line-of-sight velocity fluctuation for various radar beam directions: The VZ 85 model by VanZandt is also shown. No saturation is found in the spectrum shape [Tsuda *et al.*, 1988].

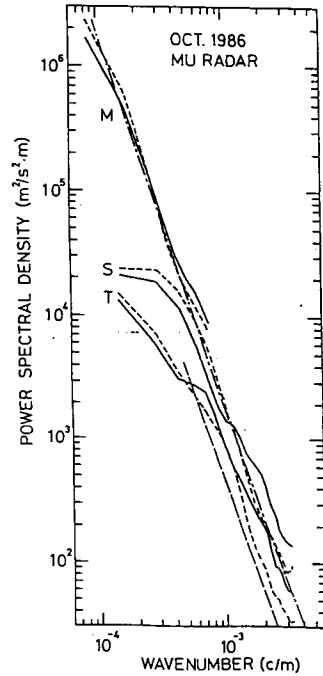


Figure 6. Saturated gravity wave vertical wave number spectrum observed by the MU radar: M, S, T, stand for the mesosphere, stratosphere and troposphere, respectively. The result is consistent with the saturated gravity wave spectrum with the dominant vertical scale 3.2 – 2.2 km, 10 km to the stratosphere and mesosphere. Similar experiment in 1987 gives the scale of the troposphere available in another experiment, as 5 km [Tsuda *et al.*, 1988].

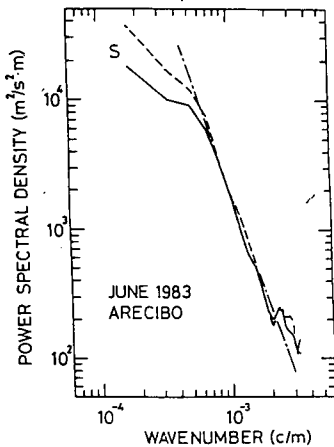


Figure 7. Similar to Figure 6 except at Arecibo only for the stratosphere which has the dominant vertical scale as 2 km [Tsuda *et al.*, 1988].

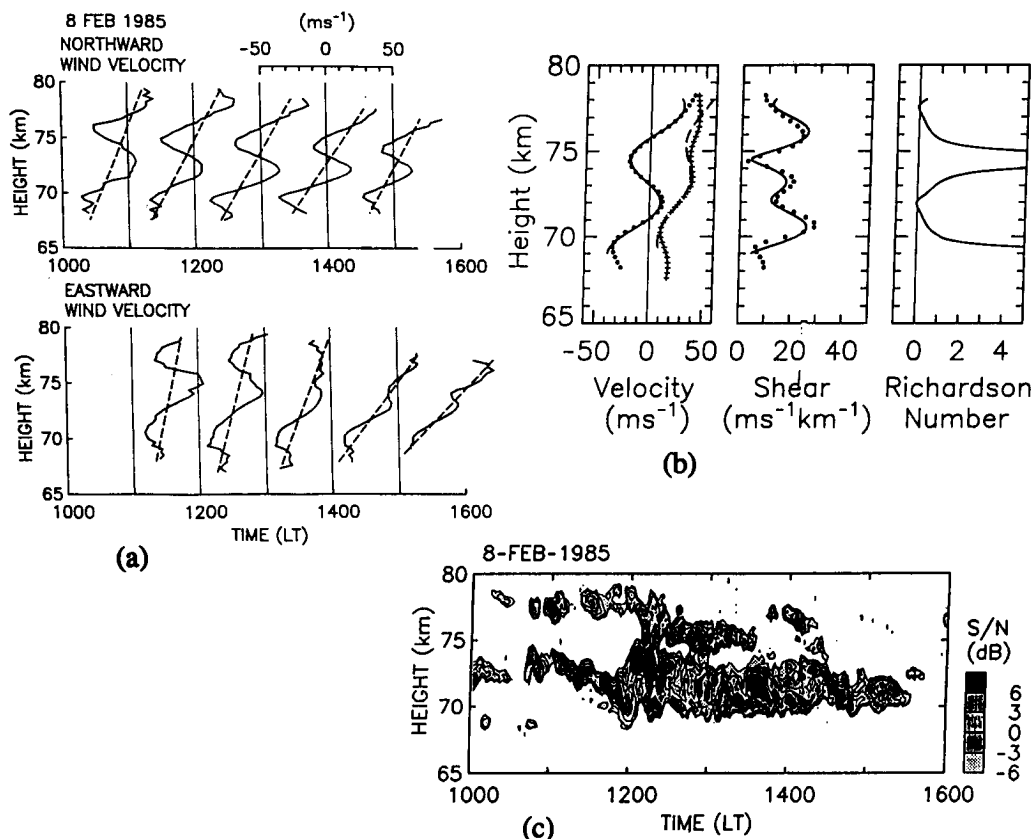


Figure 8. Observed quasi-monochromatic gravity wave which is saturated as noted by Richardson number etc. [Yamamoto et al., *J. Geophys. Res.*, 92, 11993, 1987]. Note that the observed period is around 20 h (a) wind (b) shear and Richardson number (c) the MU radar echo.

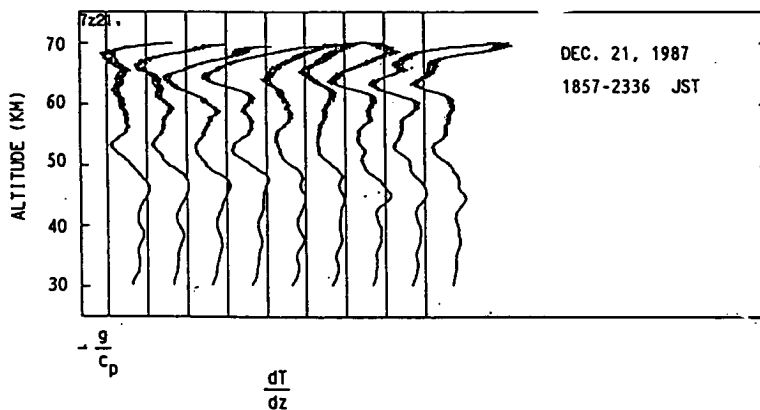


Figure 9. Lidar observation by Shibata [1988]. Temperature gradient, shown together with the adiabatic lapse rate, suggests a convective instability around 65 km height.

1.3 PROGRESS IN D-REGION STUDIES DURING MAP

A. D. Danilov

USSR State Committee for Hydrometeorology and Control of Natural Environment,
Pavlik Morozov St., 12 Moscow 123376, USSR

During MAP, active studies of the ionospheric D region were performed. The most interesting and fruitful were those in which variations of D-region parameters and of the dynamical regime of the middle atmosphere were intercompared.

As a result, the general picture of the D-region behavior became much clearer than before. It appears that the D region is strongly influenced by dissipation of internal gravity waves which come from below and are destroyed at altitudes 80-100 km. This influence is much stronger in winter than in summer due to the filtering effect of the stratospheric circulation on these waves. As a result, strong day-to-day variability of the D region in winter and relative stability in summer, is now clear.

Joint consideration of simultaneous data on the D region and dynamics of the middle atmosphere allowed to formulate three main features of winter anomaly (WA) and to understand its sources. The most pronounced manifestation of WA is the existence of the so-called anomalous days which is due to two factors: enhancement of NO because of the increased turbulence, and increase of the atmospheric temperature. Both factors lead to the same result increasing the ionization rate and decreasing the effective recombination coefficient. The net change of the electron concentration may in some cases amount to two orders of magnitude.

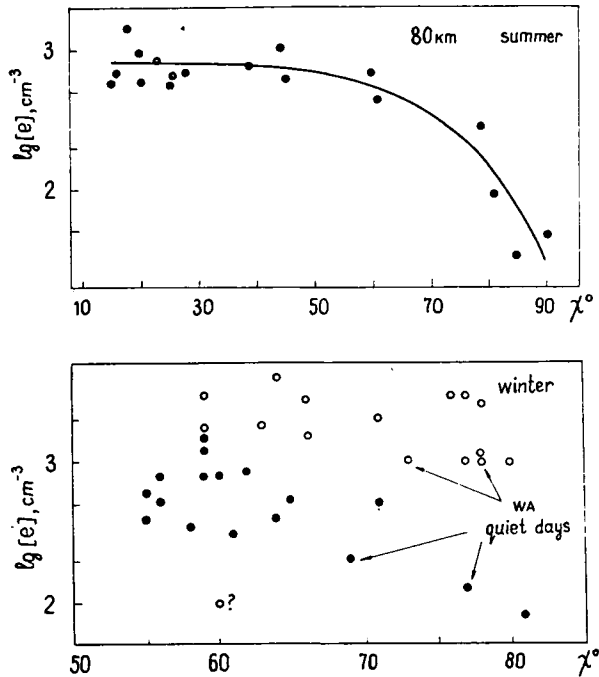


Figure 1. Electron concentrations as a function of solar zenith angle χ according to Danilov et al. [in *Spatial and Temporal Structure of the Lower Ionosphere*, 1982]. The dark points are normal days, the open ones are winter anomaly days.

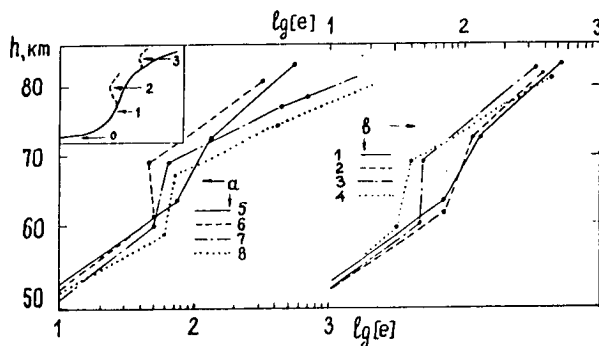


Figure 2. D-region electron profiles obtained by Pakhomov and Korneeva, [*Geomagnetism i aeronomia*, 28, No. 4, 1988] for various seasons as a result of an averaging of rocket measurements: 1 – summer; 2 – fall; 3 – spring, average; 4 – spring 1979; 5 – winter, low ionization; 6 – winter, moderate ionization; 7 – winter, high ionization.

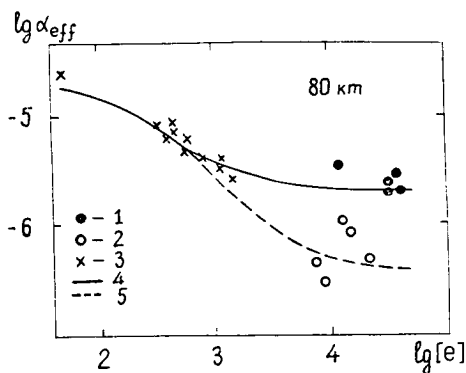


Figure 3. The effective recombination coefficient α_{eff} versus the electron concentration $[e]$ at 80 km according to Danilov and Simonov [in *Ionosfernye issledovaniya*, N 34, 54, 1981]: 1 – PCA, summer 1972; 2 – PCA, winter 1969; 3 – solar eclipses 1969 and 1970; 4 and 5 – theoretical curves (taking into account the dependences of α_{eff} on f^+ and f^+ on $[e]$ and the season) for summer and winter, respectively.

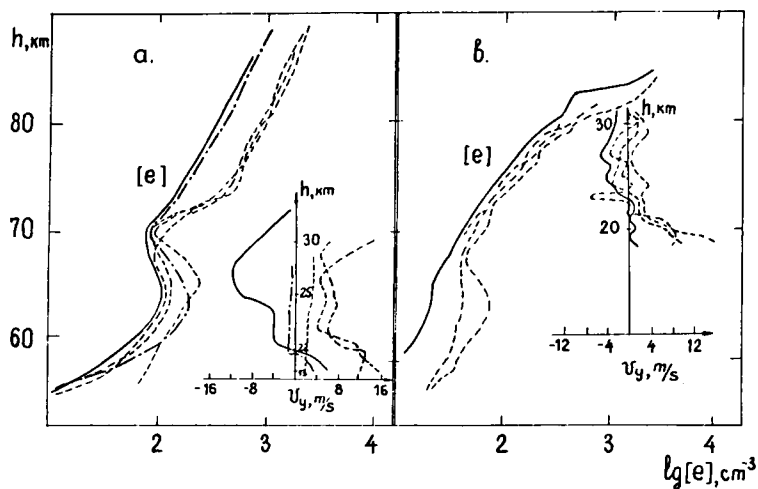


Figure 4. Profiles of the electron concentration $[e]$ and the zonal component of the stratospheric wind V_y measured in Pittsburgh (a) and Volgograd (b) [Danilov et al., *Geomagnetism i aeronomia*, 26, 710, 1986]. The same kind of line represents the same rocket flight at which both $[e]$ and V_y were measured.

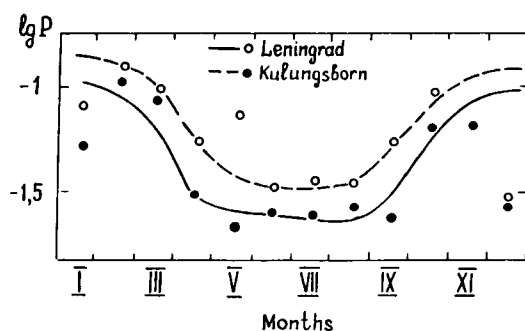


Figure 5. Seasonal variations of the fraction of time when SPA were observed [Danilov et al., *Geomagnetism i aeronomia*, 27, 536, 1987].

1.4 EQUATORIAL RADAR SYSTEM

S. Fukao, T. Tsuda, T. Sato, and S. Kato

Radio Atmospheric Science Center
Kyoto University Uji, Kyoto611, Japan

A large clear air radar with the sensitivity of an incoherent-scatter radar for observing the whole equatorial atmosphere up to 1000 km altitude is now being designed in Japan. The radar, called the Equatorial Radar, will be built in Pontianak, Kalimantan Island, Indonesia (0.03 deg north, 109.3 deg east). The system is a 47-MHz monostatic Doppler radar with an active phased array configuration similar to that of the MU radar in Japan, which has been in successful operation since 1983. It will have a PA product of more than $5 \times 10^9 \text{ Wm}^2$ (P = average transmitter power, A = effective antenna aperture) with sensitivity more than 10 times that of the MU radar. This system configuration enables pulse-to-pulse beam steering within 25 deg from the zenith. As is the case of the MU radar, a variety of sophisticated operations will be made feasible under the supervision of the radar controller. A brief description of the system configuration will be presented.

TABLE 1. Basic Parameters of the International Equatorial Radar.

Parameter	Value
Location	Pontianak, West Kalimantan, Indonesia (0.03°N, 109.29°E)
Radar system	Monostatic pulse radar; active phased array system
Operation frequency	47 MHz
Antenna	Circular array of ~ 2,500 crossed Yagis
aperture	~ 60,000 m ² (~280 m in diameter)
beam width	1.2° (one way; half power for full array)
steerability	Steering is completed in each IPP
beam directions	~ 2,000: 0°–20° off zenith angle
polarizations	Circular
Transmitter	~ 2,500 solid-state amplifiers (TR modules; each with output power of ~ 500 W peak and ~ 25 W average)
peak power	~ 1.1 MW (maximum)
average power	~ 55 kW (duty ratio 5%)(maximum)
bandwidth	~ 2 MHz (maximum) (pulse width: 1–512 μs variable)
IPP	200 μs to 65 ms (variable)
Receiver	
bandwidth	~ 2 MHz (maximum)
IF	5 MHz
A/D converter	12–16 (not fixed) bits x 8 channels
Pulse compression	binary phase coding up to 32 elements; Barker and complementary codes presently in use

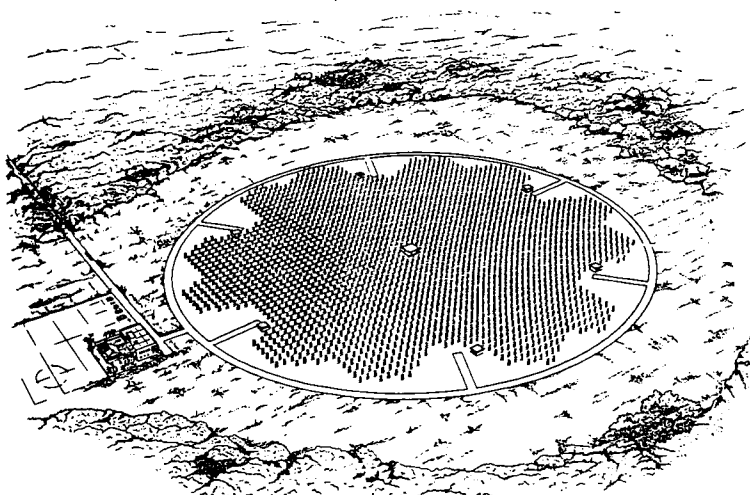


Figure 1. Artist's conception of the equatorial radar.

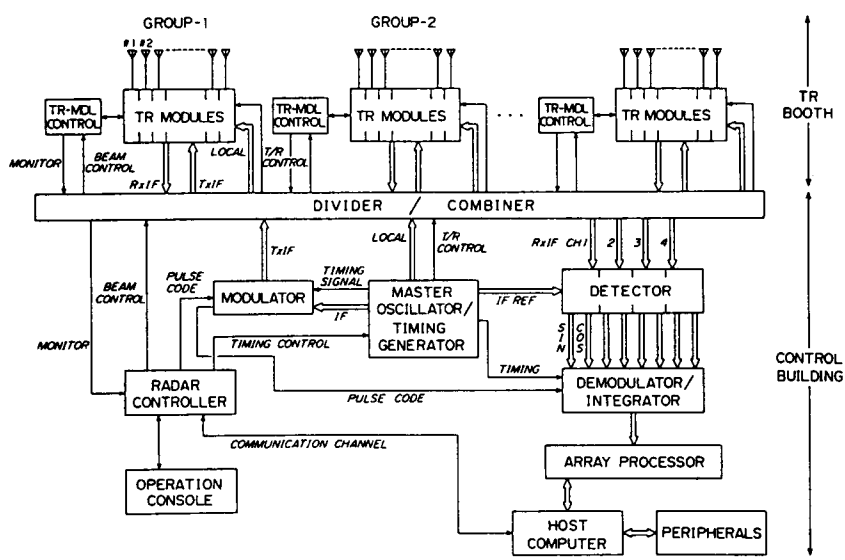


Figure 2. General block diagram of the equatorial radar.

OFFICE
OF THE DIRECTOR

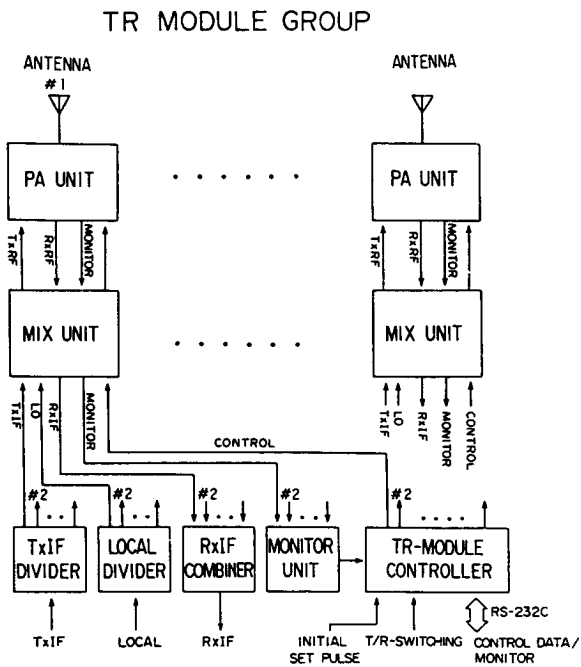


Figure 3. Block diagram of one group of TR modules.

1.5 A PERSPECTIVE OF MIDDLE-ATMOSPHERE DYNAMICS (MAD) STUDIES AT THE NEW INTERNATIONAL EQUATOIRAL OBSERVATORY (NIEO)

M. D. Yamanaka

Faculty of Education, Yamaguchi University
Yamaguchi 753, Japan

S. Fukao

Radio Atmospheric Science Center
Kyoto University, Kyoto 611, Japan

The equatorial region has attracted many MAD studies mainly based on data of limited locations and resolutions. At NIEO we can establish (i) Climatology of the equatorial middle atmosphere; all of the mean zonal flow, the meridional/east-west circulations and the planetary/gravity waves will be described based on massive, reliable data statistics. Indeed, MAD is a transition field between the meteorology and the aeronomy. We emphasize also the following two aspects of studies at NIEO; (ii) Troposphere-stratosphere coupling at the equator; the candidate location of NIEO is just at the "stratospheric fountain" area where the tracers and waves are pumped up into the middle atmosphere. (iii) Mesosphere-thermosphere coupling at the equator; thermospheric superrotation, which may be caused either by ion drag or by tidal breaking, will be examined in detail by observations covering a wide altitude range from the mesosphere through the thermosphere.

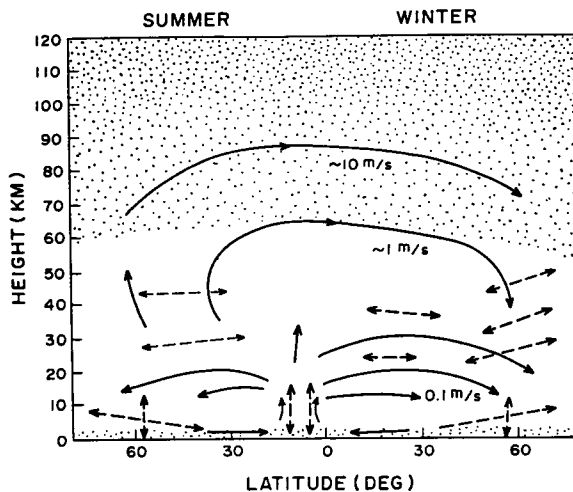


Figure 1. Schematic picture of the meridional circulations in a Lagrangian viewpoint [after Kida]

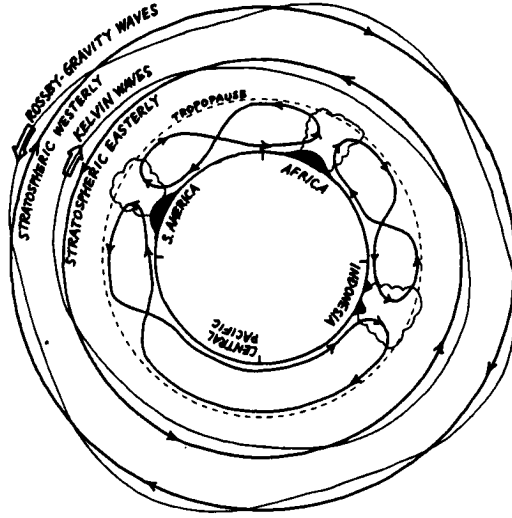


Figure 2. Schematic picture of the zonal structure of the equatorial atmosphere.

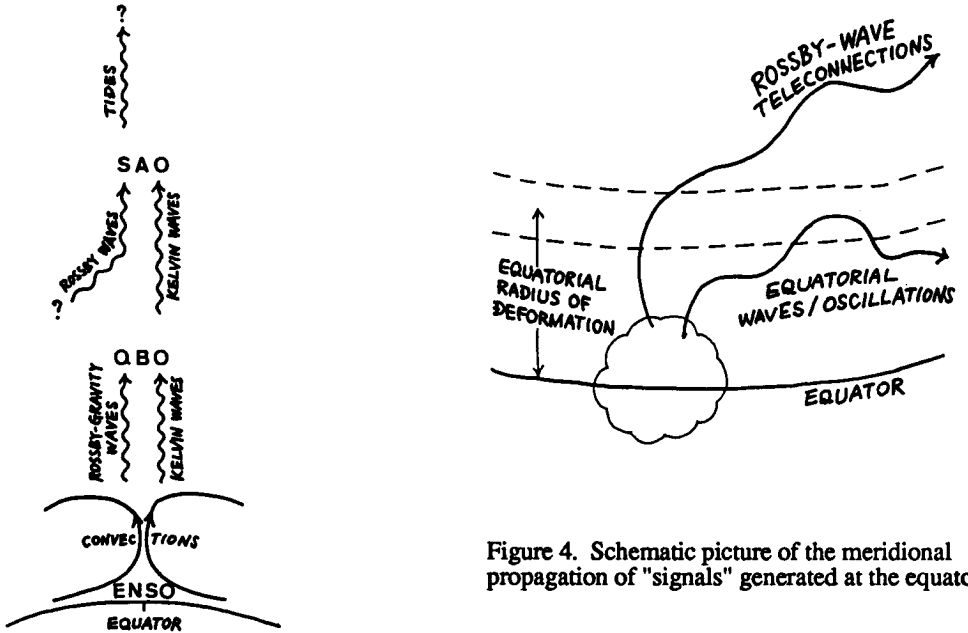


Figure 3. Schematic picture of the vertical propagation of equatorial waves.

Figure 4. Schematic picture of the meridional propagation of "signals" generated at the equator.

2. DYNAMICS OF THE MIDDLE ATMOSPHERE IN WINTER (DYNAMICS)

2.1 INTERRELATION BETWEEN THE DIFFERENT VARIATIONS OF TURBULENT DIFFUSION AND IONOSPHERIC ABSORPTION ORIGINATING IN THE MIDDLE ATMOSPHERE

P. Bencze

Geodetic and Geophysical Research Institute
Hungarian Academy of Sciences, H-9401 Sopron, Box 5, Hungary

The turbulent diffusion coefficient has been computed from the parameters of sporadic E layers using the wind shear theory of midlatitude sporadic E and models of the ionosphere as well as that of the neutral upper atmosphere. The turbulent diffusion coefficient obtained for the period of circulation disturbances associated with stratospheric warmings and for the intervals of the winter anomaly indicate changes similar to the ionospheric absorption of radio waves, in the former case decreased, in the latter case increased values. This may hit at the role of turbulent transport in the formation of these anomalies. On the basis of these findings, a seasonal variation of the turbulent diffusion coefficient having minimum in summer and an increase of this parameter with increasing geomagnetic activity are anticipated.

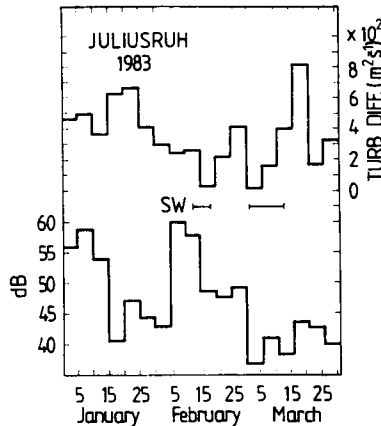


Figure 1. Daytime values of the turbulent diffusion coefficient determined by means of sporadic E parameters in the height range 100–135 km and noon values of the ionospheric absorption measured by the A1 method in Juliusruh (54°38'N; 13°23'E) in the first months of 1983. For the reduction of the scattering 5 day averages are shown. Both parameters indicate decreased values related to stratospheric warmings (SW). As the turbulent diffusion coefficient is proportional to the momentum deposition, the decrease of the turbulent diffusion coefficient might indicate reduced mean zonal momentum deposition in the mesosphere/lower thermosphere connected with stratospheric warmings (decrease of the eastward mean wind). (Another explanation can be the conditions that the turbulent diffusion coefficient indicates turbulence due to shear instability. Its decrease is connected with the increase of the vertical wavelength of gravity waves and these waves saturate at higher altitudes.)

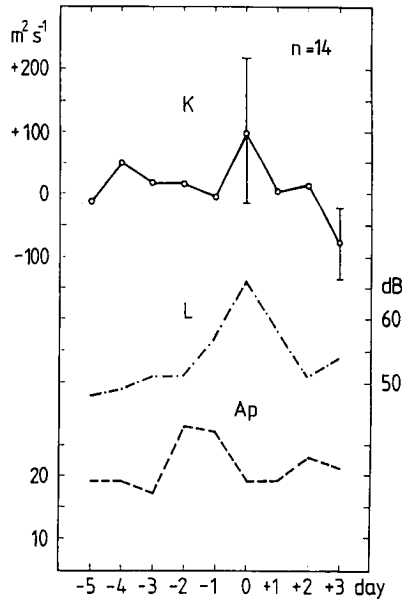


Figure 2. Departures of the daytime turbulent diffusion coefficient K , determined by means of sporadic E parameters, from the monthly hourly mean in the height range 100–115 km before and after days of excessive ionospheric absorption L , measured by the A1 at noon in Juliusruh ($54^{\circ}38'N$; $13^{\circ}23'E$) in the winters 1980-81, 1981-82, and 1982-83, as well as the variation of the geomagnetic activity index A_p . Both K and L indicate increased values during these events. Considering that the turbulent diffusion coefficient is related to the momentum deposition in a simple way, the increase of the turbulent diffusion coefficient might be an indication of the increased mean zonal momentum deposition in the mesosphere/lower thermosphere related to winter anomaly events (increase of the eastward mean wind.)

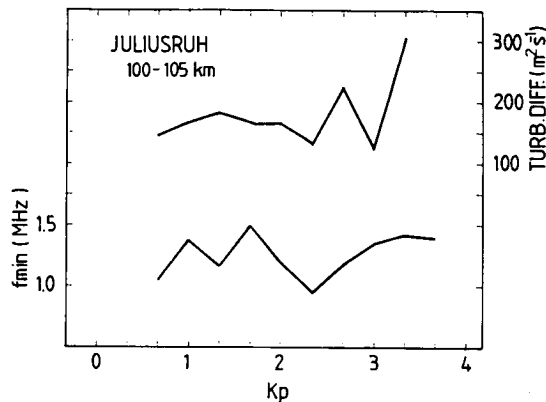


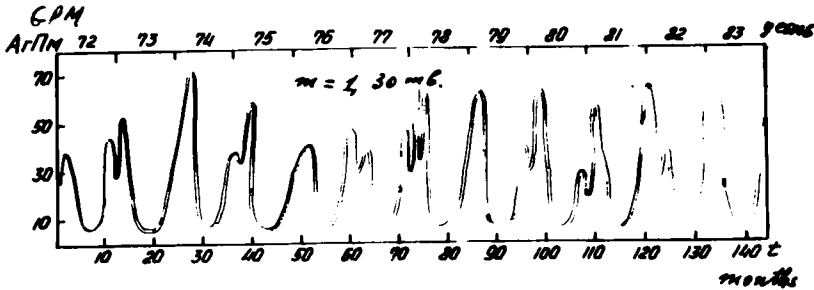
Figure 3. Daytime values of the turbulent diffusion coefficient determined by means of sporadic E parameters in the height range 100–105 km and the ionospheric absorption at noon characterized by f_{min} in Juliusruh ($54^{\circ}38'N$; $13^{\circ}23'E$) as a function of the geomagnetic activity. Both parameters indicate increased values at small K_p values, which can be connected with the storm after-effect, and rising values toward increasing K_p . Considering the turbulent diffusion coefficient as an indicator of the momentum deposition, the increase of it might be due to the increased mean zonal momentum deposition in the mesosphere/lower thermosphere connected with the geomagnetic activity (increase of the westward mean wind in summer.)

2.2 VARIABILITY OF QUASI-STATIONARY PLANETARY WAVES

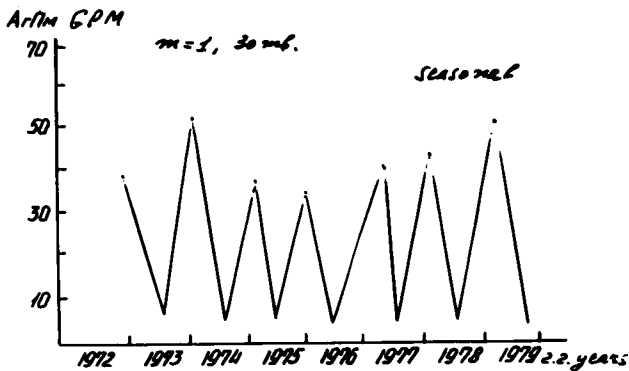
A. A. Krivolutsky, N. D. Petushkov, and D. A. Tarasenko

Central Aerological Observatory
 USSR State Committee for Hydrometeorology and Control of Natural Environment
 GAO GOSCOMGYDROMET Moscow, USSR

The results of the analysis of nonzonal perturbations ($m = 1, 2, 3$) of the geopotential field at a 30-mb level are presented. A long-period modulation of the harmonics' amplitude is discovered. Calculations of eigenfunctions and eigennumbers of the Laplace tidal equation ($\sigma = 0$, $m = 1$) are carried out for a real latitudinal wind profile. The observed first zonal harmonic in different years is caused by the same mode ($m = 1$, $n = 2$). Thus, the difference in the wave amplitudes could not be accounted for by the difference in stratospheric zonal circulation in different years and should be related to tropospheric processes.



(a)



(b)

Figure 1. Monthly (a) and seasonal (b) mean amplitude of the zonal harmonic for $m = 1$ (30 mb).

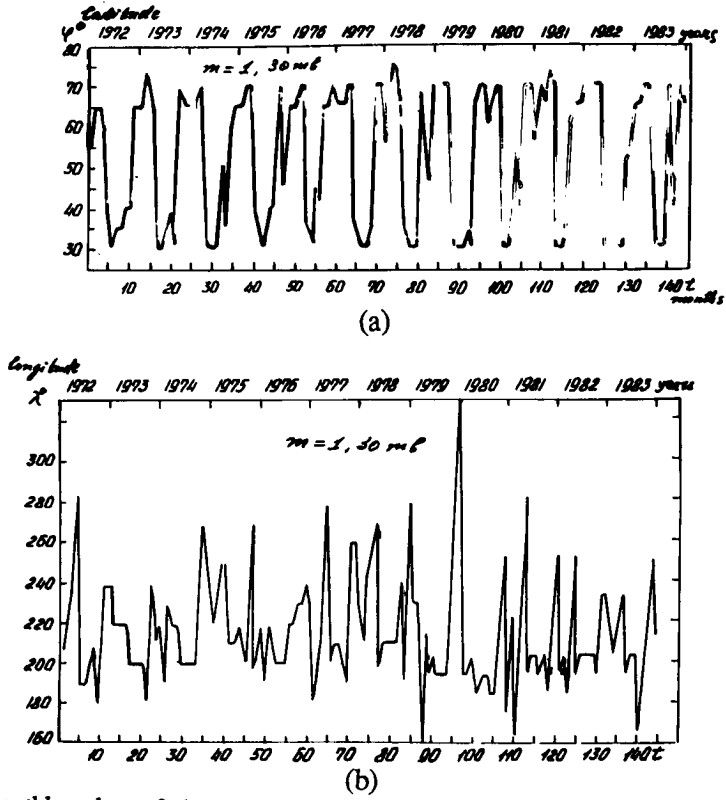


Figure 2. Monthly values of phase coordinates: latitude (a); longitude (b), for $m=1$ (30 mb).

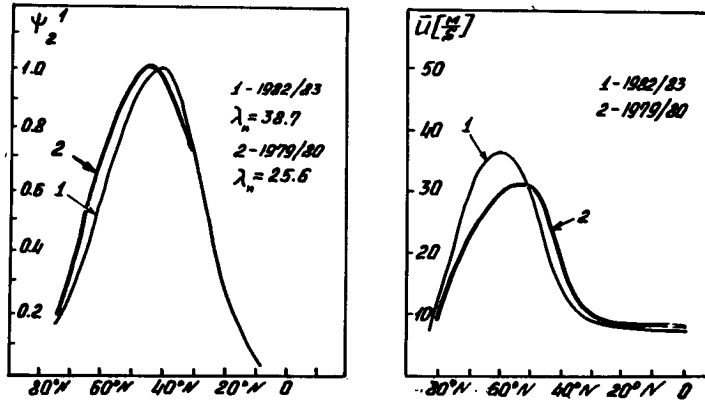


Figure 3. The eigenfunction $\psi_n^m(\lambda_n > 12.5)$ and profiles of geostrophic wind for two winter seasons, 1979/80 and 1982/83.

2.3 WAVE PROPAGATION INTO THE MIDDLE ATMOSPHERE

I. Hirota

Geophysical Institute
Kyoto University, Sakyo, Kyoto 606, Japan

Recent observations of various types of waves propagating into the middle atmosphere are reviewed. Emphasis is made on the excitation processes in the lower atmosphere and their vertical propagation through the background flow as a function of the latitude, height and season. The following subjects are discussed: 1. Vertical propagation of quasi-stationary forced Rossby waves into the winter stratosphere in connection with the sudden warming. 2. Spectral distribution and seasonal characteristics of normal mode (free) Rossby waves and the asymmetry of the Northern and Southern Hemispheres. 3. Seasonal variation of internal gravity waves in the middle atmosphere. Further discussions will be presented for future studies based on accumulated observational data during the MAP period.

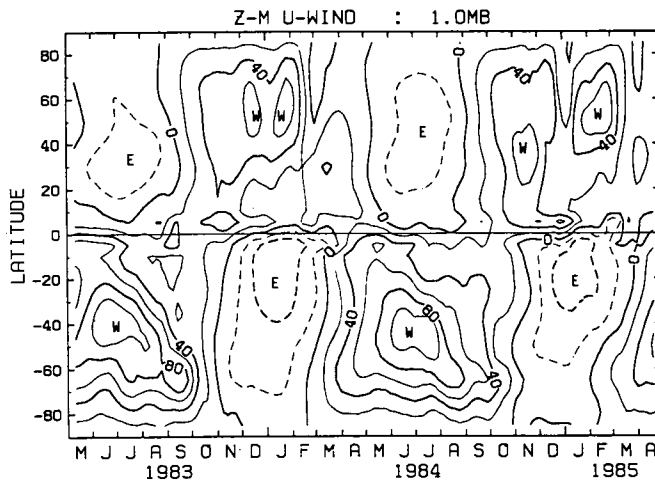


Figure 1. Latitude-time section of the zonal mean geostrophic wind at the 1 mb level estimated from the 20-day average height field. Units are m/s. Positive values denote westerly winds.

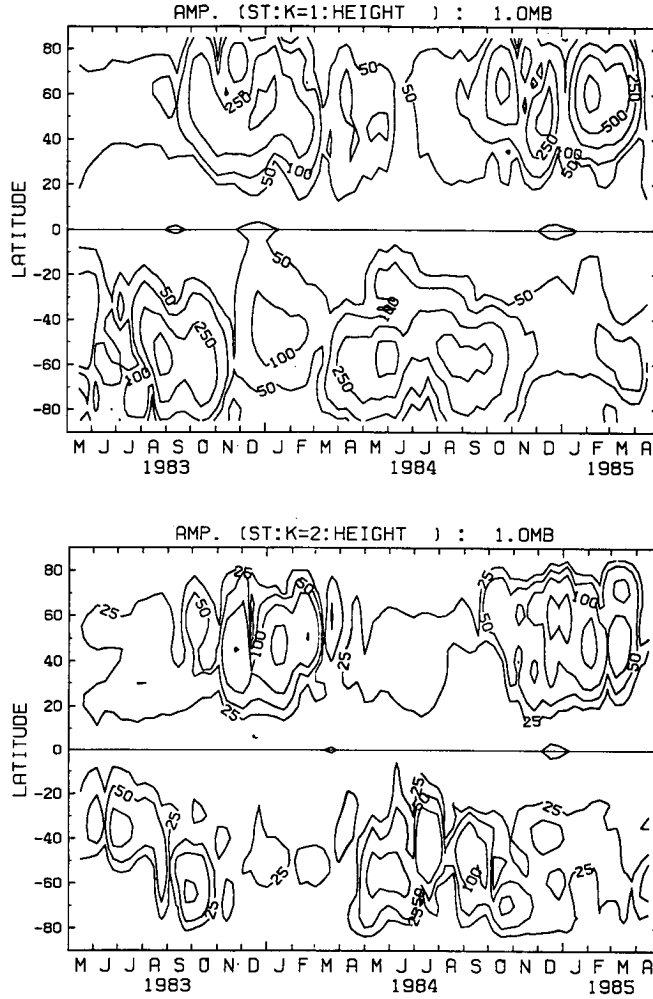


Figure 2. Latitude-time section of the quasi-steady wave amplitude of wave number 1 (upper) and wave number 2 (lower) at the 1 mb level. Units are meters.

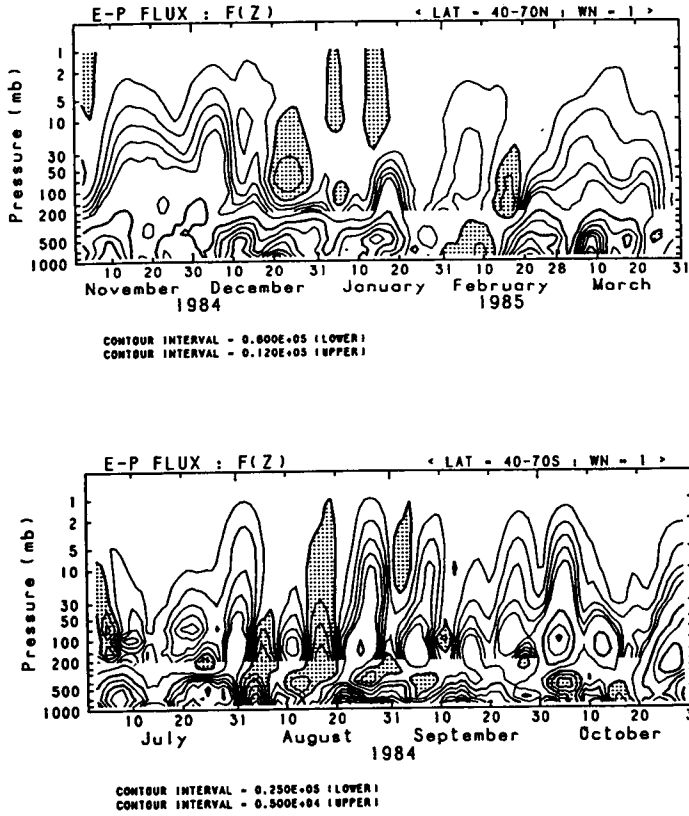


Figure 3. Time-height section of vertical component of the E-P flux, $F(z)$, averaged over 40°N to 70°N (upper) and 40°S to 70°S (lower) for wave number 1.

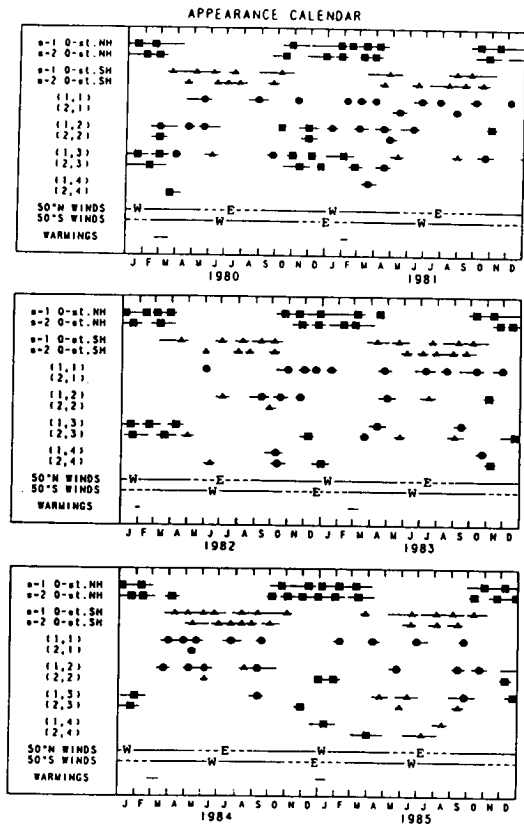


Figure 4. Appearance calendar of various normal mode Rossby waves and quasi-stationary waves at 1 mb, along with the change of the 1 mb zonal mean wind regime at 50°N and 50°S. See Hirooka and Hirota [1988, to be published in PAGEOPH] for more detail.

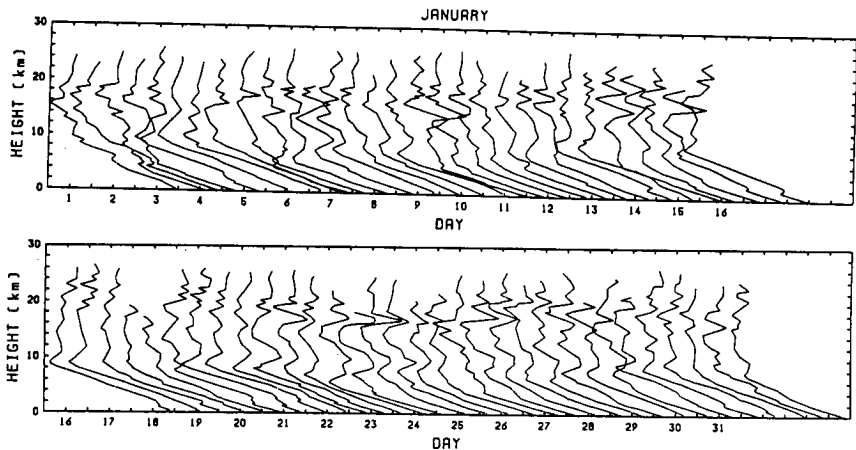


Figure 5. Vertical distribution of temperature by daily balloon observations at Akita (40°N) for January 1986. Note that small-scale fluctuations are observed mainly above the tropopause level.

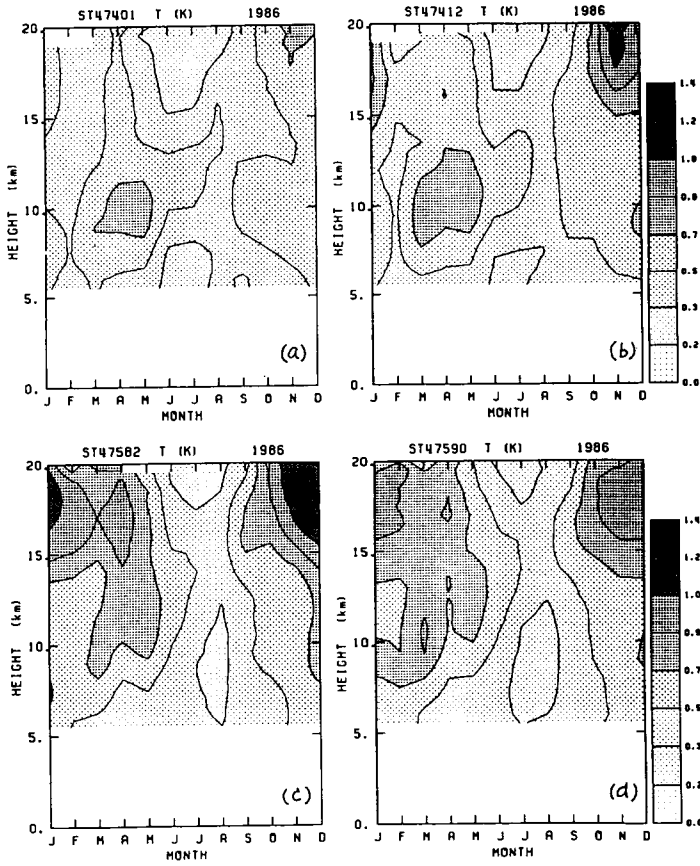


Figure 6. Seasonal variation of gravity wave amplitudes in temperature observed by balloon at four stations: (a) Wakkanai, 45°N, (b) Sapporo, 43°N, (c) Akita, 40°N, (d) Sendai, 38°N.

ORIGINAL PAGE IS
OF POOR QUALITY

2.4 EFFECTS FROM THE "COUPLING FROM BELOW" ON THE LOWER THERMOSPHERE DYNAMICS

E. S. Kazimirovsky

Siberian Institute of Terrestrial Magnetism,
Ionosphere and Radio Wave Propagation (SibIZMIR)
Irkutsk 33, Box 4, 664033 USSR

Results of wind measurements at the midlatitude ionospheric D region are presented. The wind regime of the lower thermosphere is rather sensitive to stratospheric temperature variations, especially to sudden stratospheric warmings. The longitudinal effect in D-region dynamics was revealed on the basis of simultaneous wind measurements at some points located practically at the same latitude but in different climatic regions. The distance differences are observed in the statistical distributions of wind parameters, during winter the average zonal wind speed over East Siberia was about twice that over Central Europe, and the semidiurnal zonal tide is weaker over East Siberia. The data on the seasonal reconstruction of circulation and the response of the D-region wind field to the stratospheric warmings depend on the intensity and locations of stratospheric disturbances in relation to the observatory. We interpret these experimental facts as a meteorological control of the D region and as a dependence of the lower thermosphere dynamics on the conditions of dissipation of internal waves propagating from the troposphere and stratosphere.

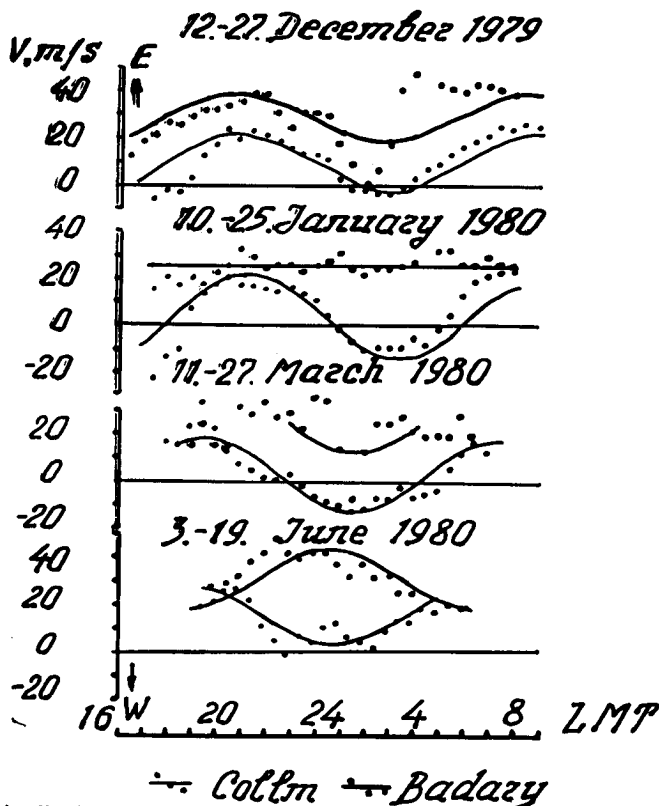


Figure 1. Longitudinal effects in the results of high atmosphere wind measurements (DI, 85-95 km) obtained over Central Europe and East Siberia: mean nighttime variations of the measured wind, zonal component.

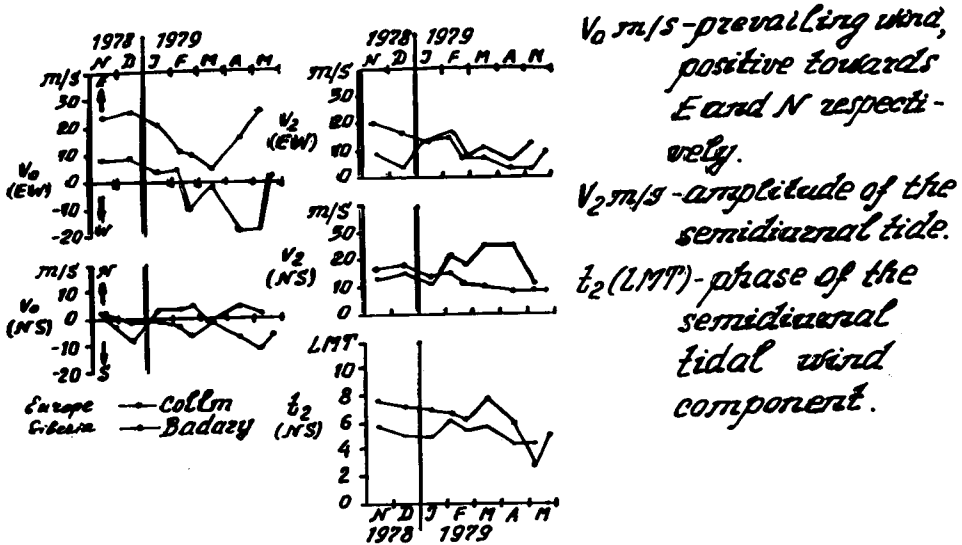


Figure 2. Longitudinal effects in the results of high atmosphere wind measurements (DI, 85 km) obtained over Central Europe and East Siberia: seasonal variations (November 1978 - May 1979) of the wind find parameters in the upper mesopause region.

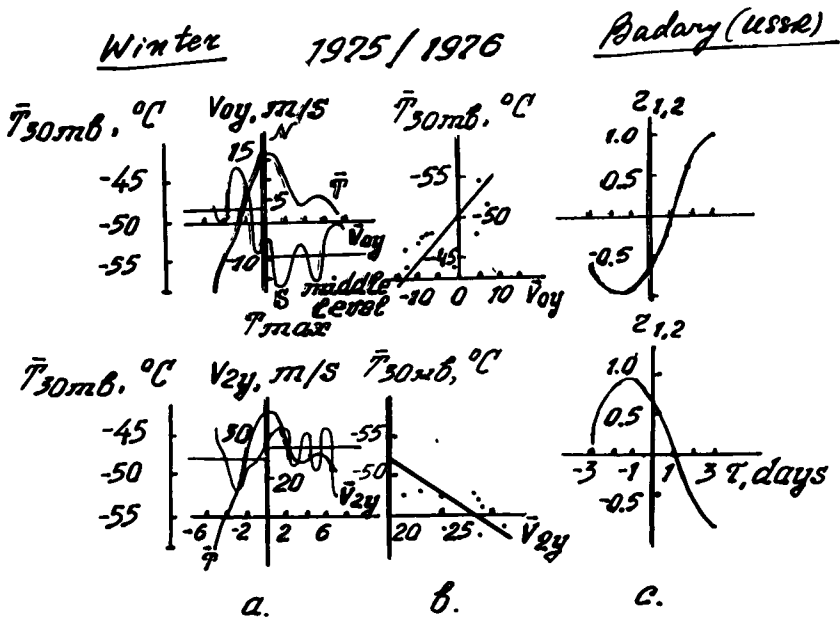


Figure 3. Comparison of T_{30mb} (°C) with meridional wind parameters (prevailing and tidal wind) in the ionospheric D region. (a) Superposed epoch method; (b) Correlograms; (c) Cross-correlation function.

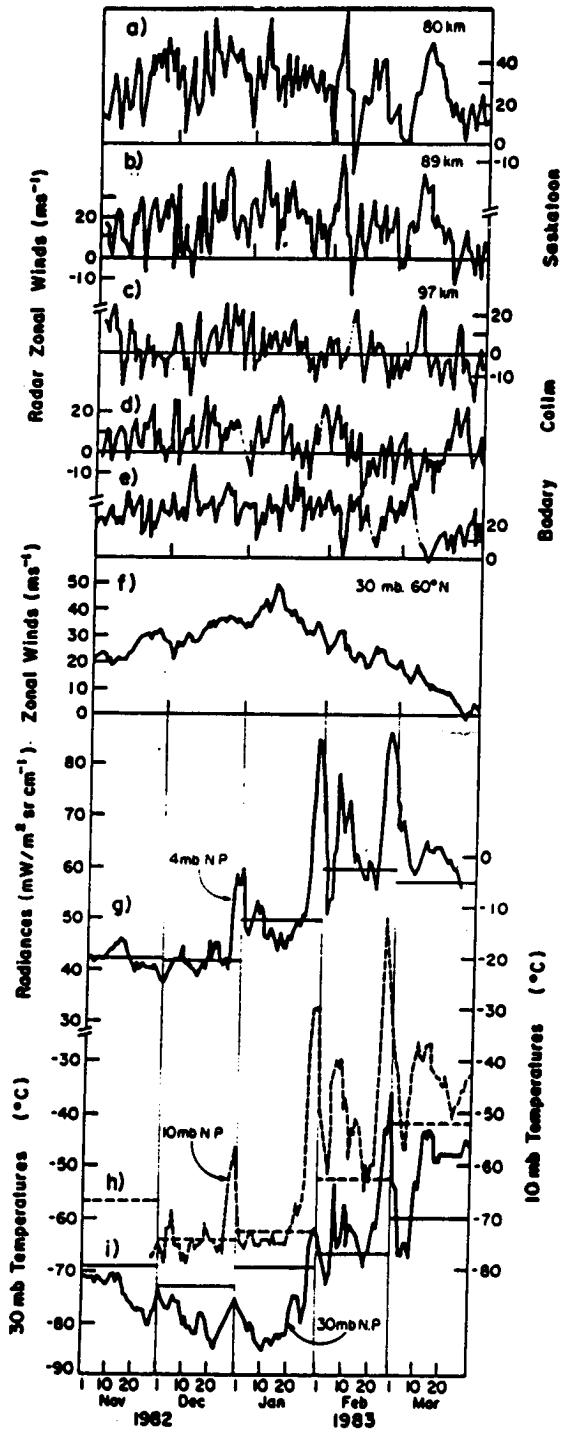


Figure 4. Stratospheric and mesospheric data during the winter 1982-83: (a),(b),(c) Saskatoon; (d) Collm; (e) Bodary; (f) 60°N winds; (g),(h), (i) North Pole data.

2.5 TRANSPORT PROCESSES IN THE MIDDLE ATMOSPHERE: REFLECTIONS AFTER MAP

W. L. Grose

NASA Langley Research Center
Mail Stop 401B, Hampton, VA 23665-5225

The Middle Atmosphere Program (MAP) has provided a focus for considerable research on atmospheric radiative, chemical, and dynamical processes and the mutual coupling among these processes. In particular, major advances have occurred in our understanding of constituent transport as a result of near-global measurements obtained during MAP from several satellite-based instruments (e.g., LIMS, SAMS, SAGE, and SSU among others). Using selected portions of these data, we will review the development of progress in understanding transport processes with special emphasis on dynamically active periods. Examples will be presented which demonstrate coupling between chemistry and dynamics. In addition to the constituent data, we will review the use of Ertel's potential vorticity, inferred from satellite temperature data, as a diagnostic for interpreting transport phenomena. Finally, we will briefly illustrate the use of 3-D model simulations, in conjunction with the satellite data, for providing additional insight into fundamental transport mechanisms.

TABLE 1: Tracers and Their Domain for Transport Studies

<u>Parameter</u>	<u>Comment</u>
A. Middle and Upper Stratosphere	
N ₂ O, CH ₄ (SAMS)	zonal mean only
O ₃ (SBUV, LIMS, SAGE)	higher latitudes mainly
H ₂ O, nighttime NO ₂ (LIMS)	four longitudinal waves for NO ₂
Potential vorticity, PV (LIMS, SSU)	derived quantity
B. Lower Stratosphere	
N ₂ O, HNO ₃ , O ₃ (LIMS)	six longitudinal waves
O ₃ and aerosols (SAGE)	limited coverage per day
Aerosols (SME)	El Chichon dispersion
PV (LIMS and SSU)	derived quantity
NO _y = HNO ₃ + NO ₂ (LIMS)	appropriate for nighttime data only; four longitudinal waves
C. Total Column	
Ozone (TOMS, SBUV)	85 to 90% in stratosphere

E. E. Remsberg, 1987

TABLE 2. Uncertainties in Derived Quantities

- Instrument
- Sampling
- Inversion
- Synoptic Mapping
- Tie-on Level
- Geostrophic Approximation
- Numerical Differentiation

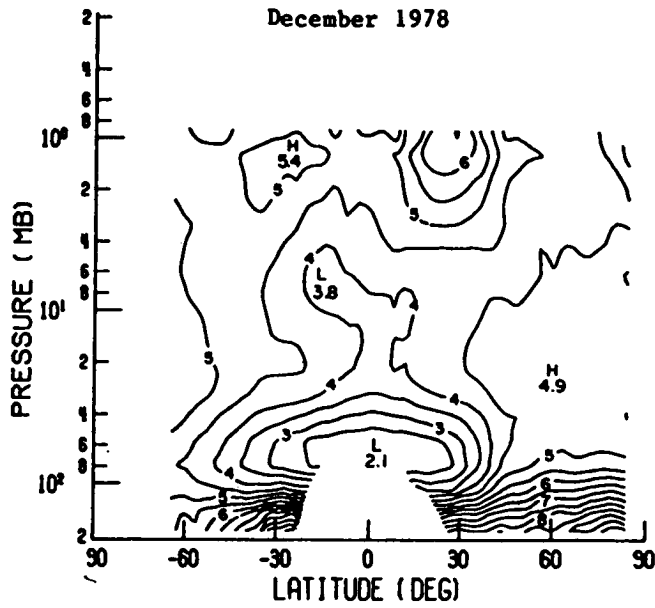


Figure 1. Zonal mean water vapor mixing ratio (ppmv) Nimbus 7 LIMS [Remsberg et al., 1984].

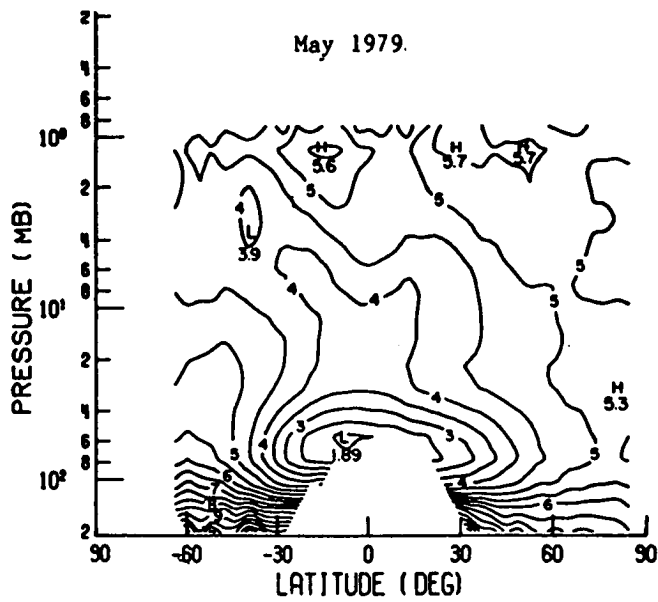
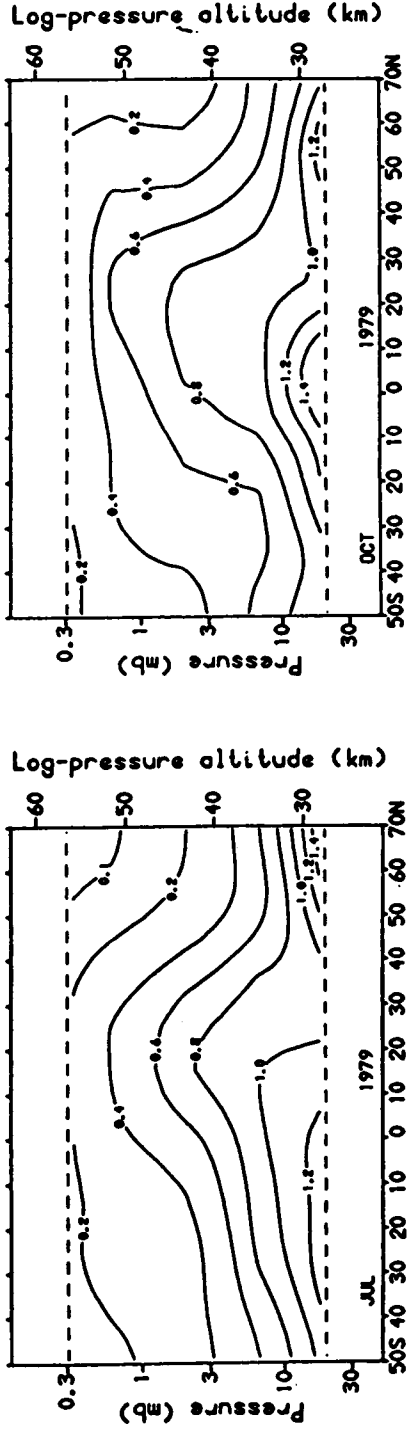
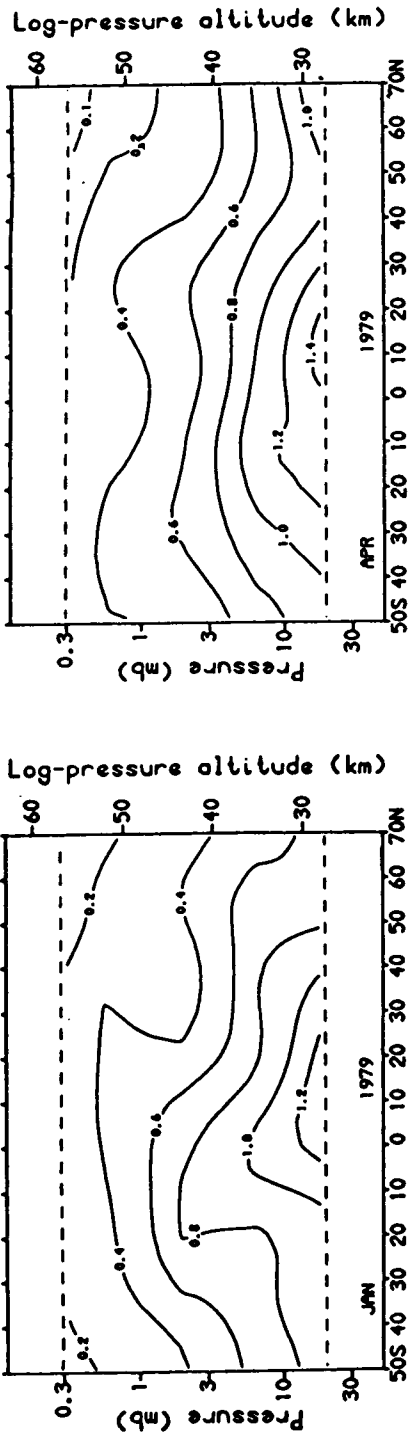


Figure 2. Zonal mean water vapor mixing ratio (ppmv) Nimbus 7 LIMS.

Nimbus 7 SAMS



CH_4 (ppmv)

Figure 3. After Jones and Pyle [1984].

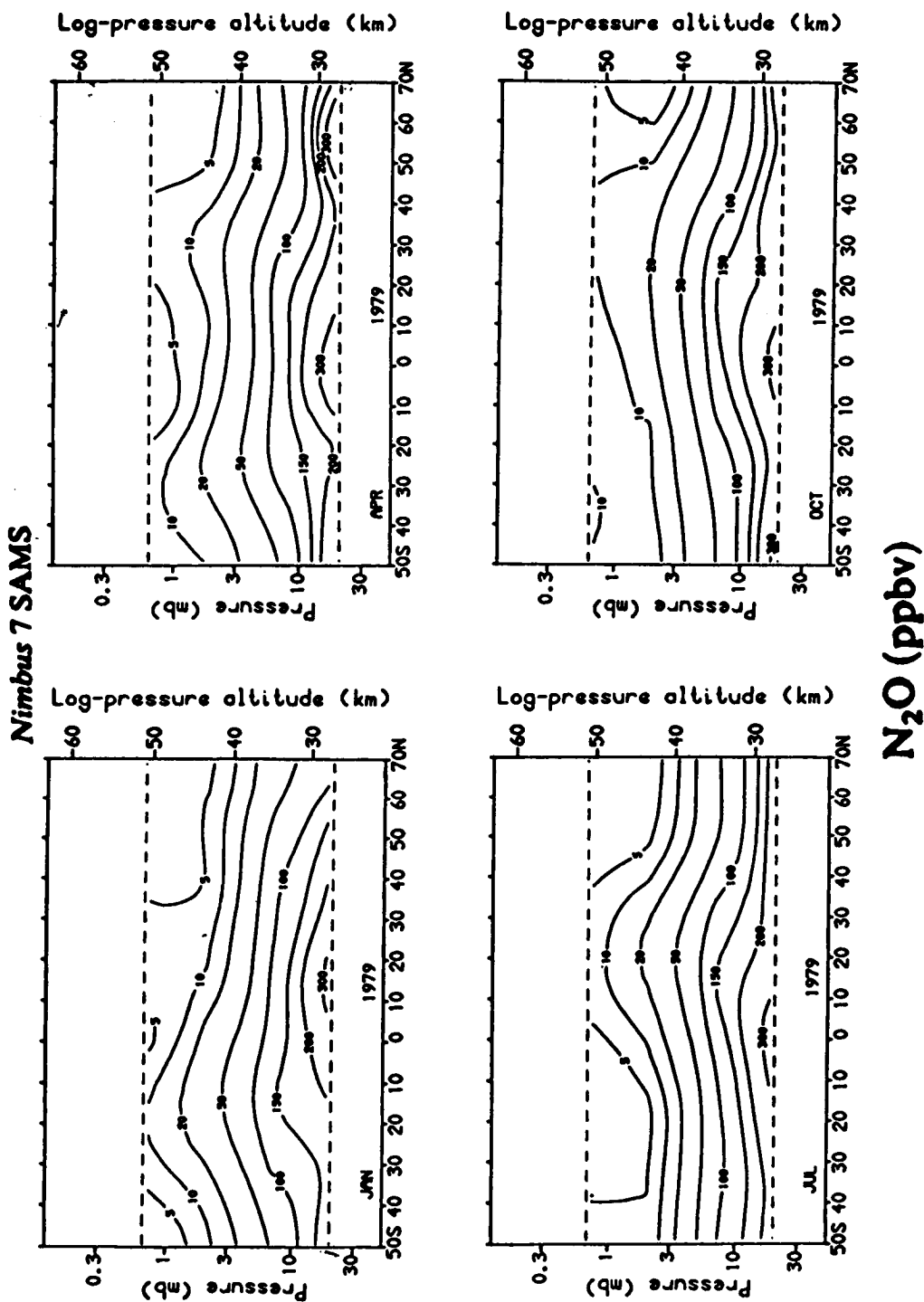


Figure 4. After Jones and Pyle [1984].

Diabatic Circulation Deduced from Satellite Observations

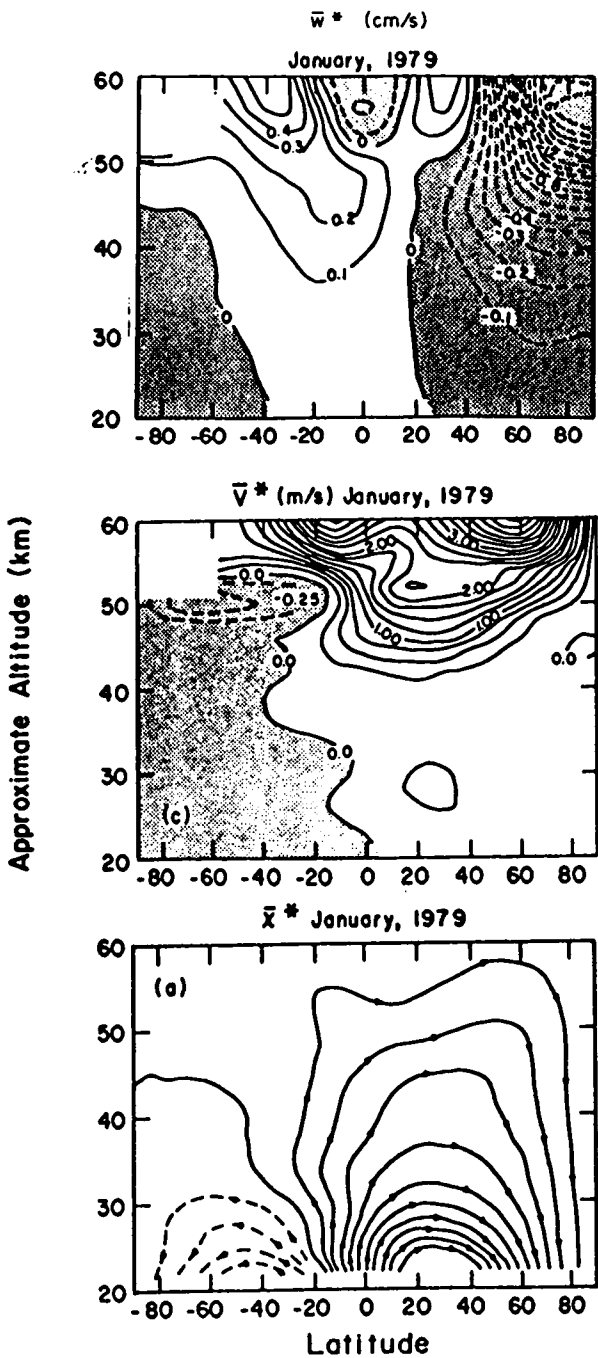


Figure 5. After Solomon et al. [*J. Atmos. Sci.*, 43, 1986].

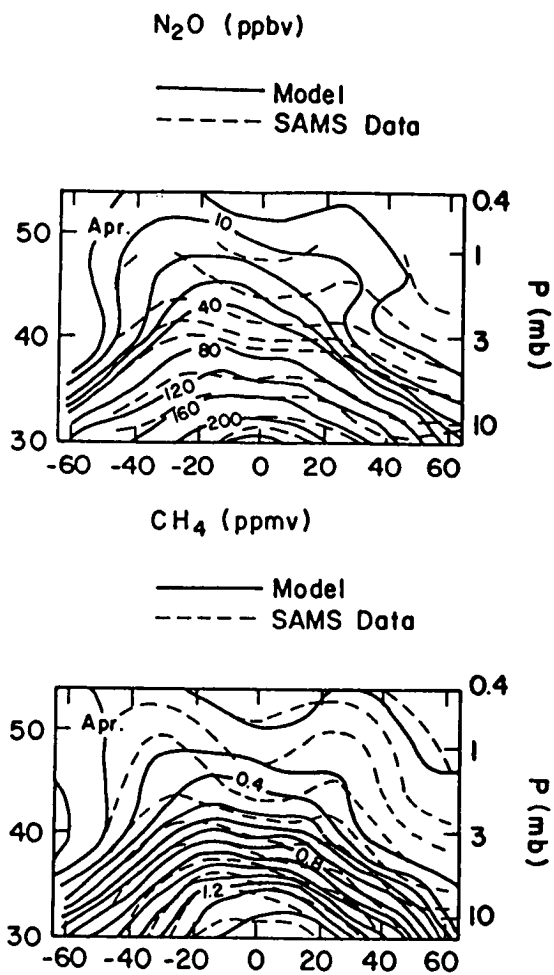


Figure 6. After Solomon et al. [*J. Atmos. Sci.*, 43, 1986].

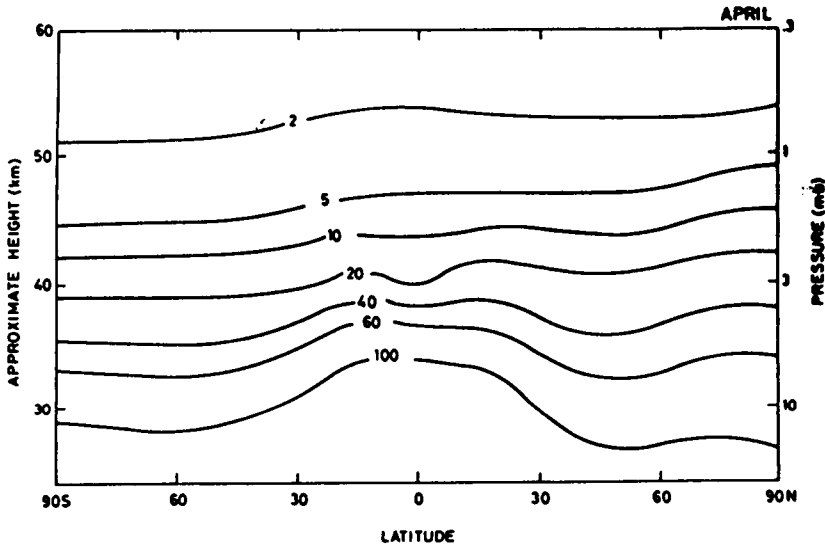


Figure 7. Monthly-averaged latitude-height cross section of N_2O volume mixing ratio (ppbv) for April from run B [Gray and Pyle, *Q. J. R. Met Soc.*, 1986].

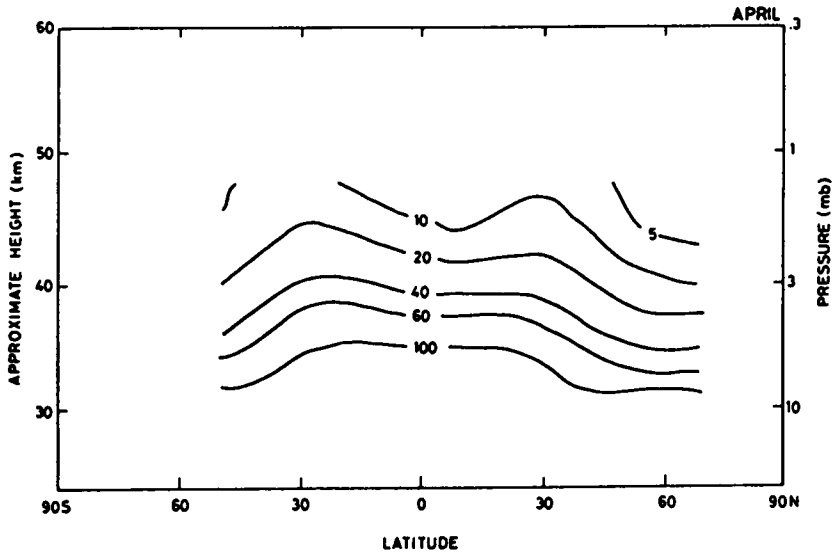


Figure 8. Monthly-averaged latitude-height cross section of N_2O volume mixing ratio (ppbv) for April 1979 from the SAMS satellite measurements [Gray and Pyle, *Q. J. R. Met Soc.*, 1986].

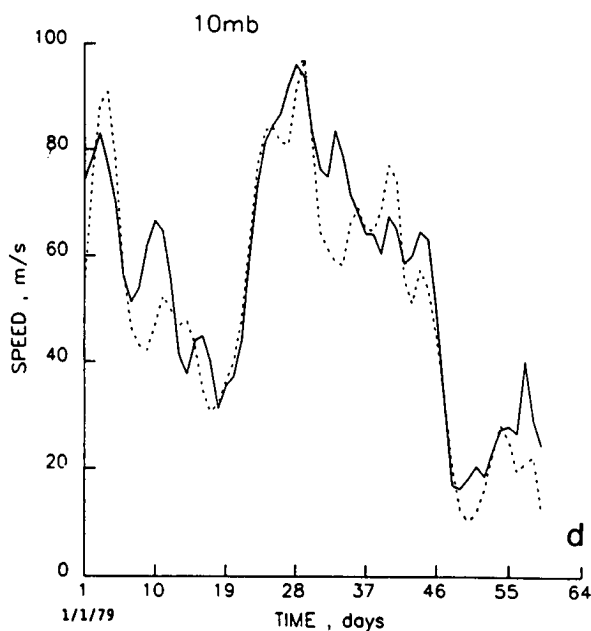


Figure 9. Time series comparison of horizontal wind speed (m/s) over Berlin between radiosonde 12 GMT measurements (dashed) and LIMS geostrophic values (solid) derived from the 12 GMT geopotential height map sequence. Analysis is for January 1 (day 1) to February 28 (day 59), 1979. Note that 50 mb values are derived from NMC heights.

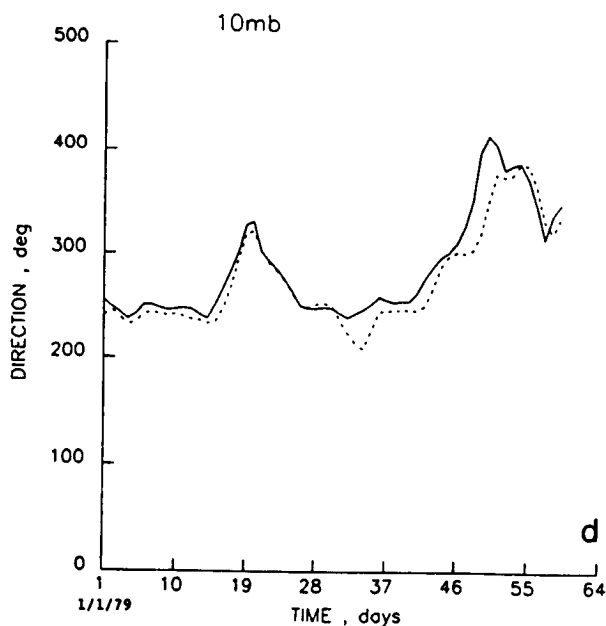


Figure 10. As in Figure 9, but for horizontal wind direction (deg). Values denote the phase of the wind vector over Berlin relative to true north ($0^\circ/360^\circ$), e.g., 270 deg = west to east airflow.

TRANSFORMED EULERIAN FORMULATION

$$\frac{\partial \bar{u}}{\partial t} - f \bar{v} + \frac{1}{r_0 \cos^2 \phi} \frac{\partial}{\partial \phi} (\cos^2 \phi \bar{u}' v') = 0 \quad \text{Momentum Equation}$$

$$\frac{\partial \bar{\theta}}{\partial t} + \bar{\theta}_p \bar{\omega} + \frac{1}{r_0 \cos \phi} \frac{\partial}{\partial \phi} (\cos \phi \bar{v}' \theta') = \bar{Q} \quad \text{Thermodynamic Equation}$$

$$\tilde{F} = (F_\phi, F_p)$$

$$F_\phi = -r_0 \cos \phi \bar{u}' v' \quad F_p = f r_0 \cos \phi \frac{\bar{v}' \theta'}{\bar{\theta}_p} \quad \text{Eliassen-Palm Flux}$$

$$\bar{\omega}^* = \bar{\omega} + \frac{1}{r_0 \cos \phi} \frac{\partial}{\partial \phi} \left(\frac{\bar{v}' \theta' \cos \phi}{\bar{\theta}_p} \right) \quad \bar{v}^* = \bar{v} - \frac{\partial}{\partial p} \left(\frac{\bar{v}' \theta'}{\bar{\theta}_p} \right)$$

$$\frac{\partial \bar{u}}{\partial t} - f \bar{v}^* = \frac{1}{r_0 \cos \phi} \nabla \cdot \tilde{F} \quad \text{Transformed Equations}$$

$$\frac{\partial \bar{\theta}}{\partial t} + \bar{\theta}_p \bar{\omega}^* = \bar{Q}$$

——— THERMAL EQUATION
 - - - MOMENTUM EQUATION

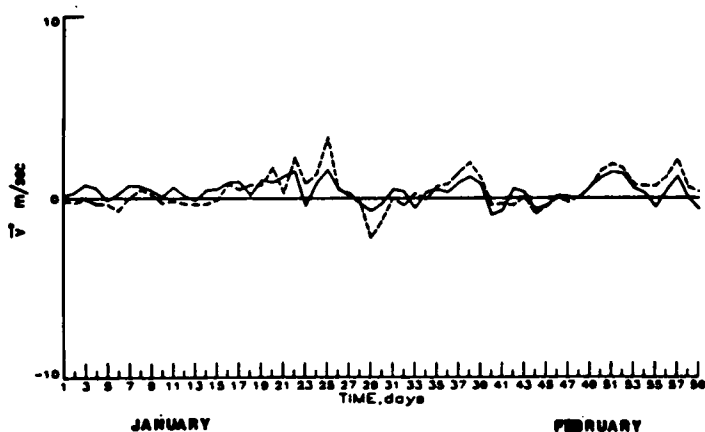


Figure 11. Residual meridional velocity (in units of ms^{-1}) inferred from the momentum equation and from the thermodynamic equation for January-February 1979 at 68°N latitude and 10 mb pressure (LIMS data).

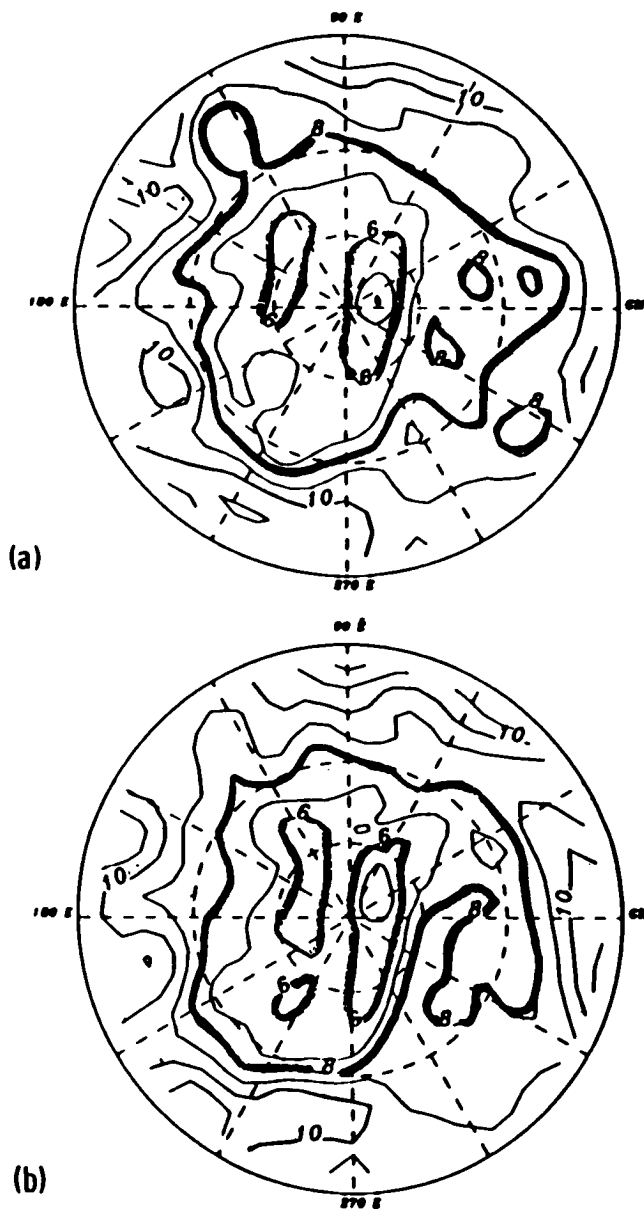


Figure 12. Ozone mixing ratio (ppmv) on the 10 mb pressure level of the Northern Hemisphere for the LaRC model simulation: (a) February 1, (b) February 3, (c) February 5, (d) February 7, and (e) February 9.

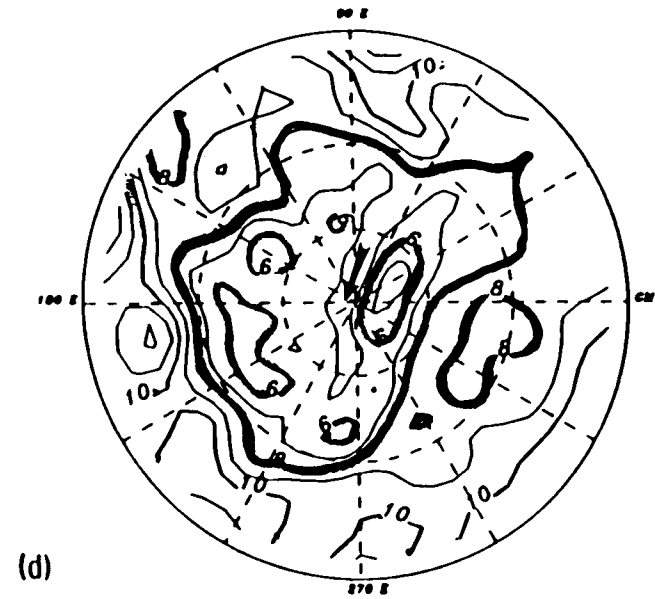
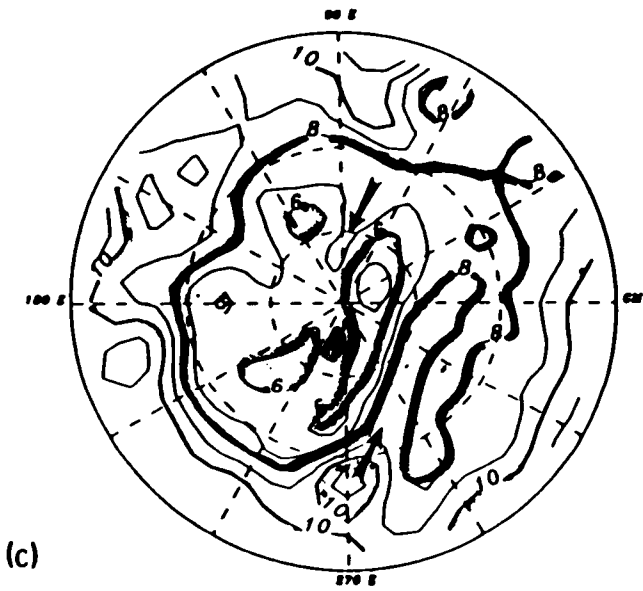


Figure 12 continued.

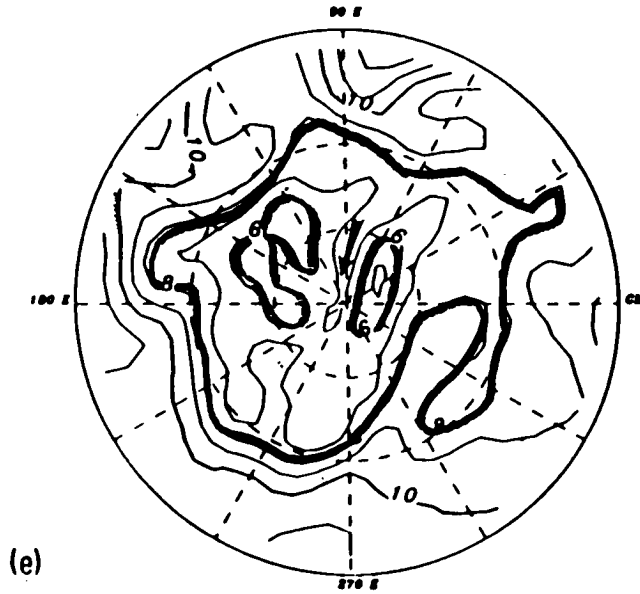


Figure 12 continued.

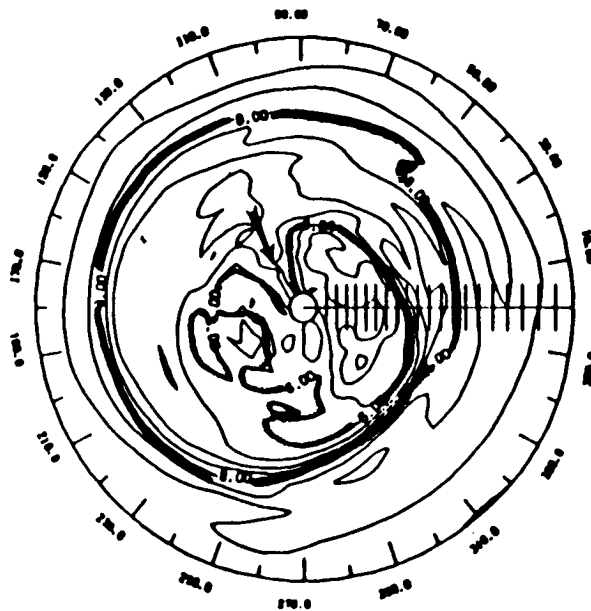


Figure 13. Ozone mixing ratio (ppmv) on the 10 mb pressure level of the Northern Hemisphere from the LIMS experiment, January 26, 1979.

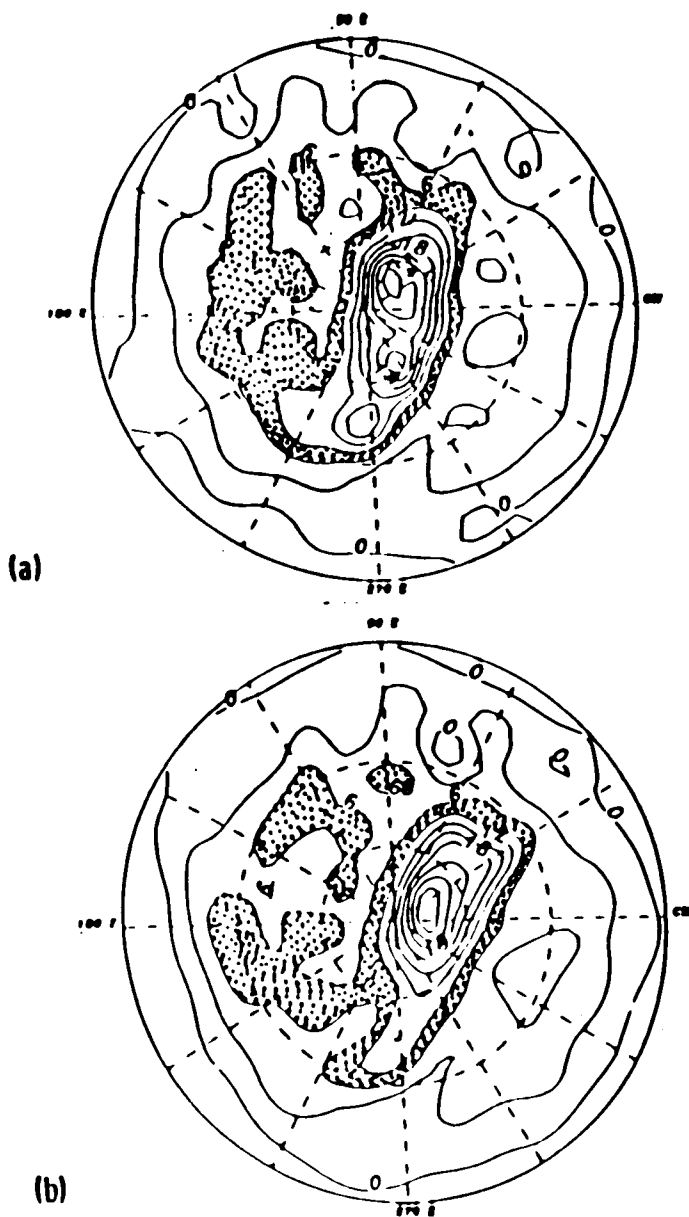


Figure 14. Ertel's potential vorticity 850 K N.H. LaRc 3-D model. (a) February 1; (b) February 7.

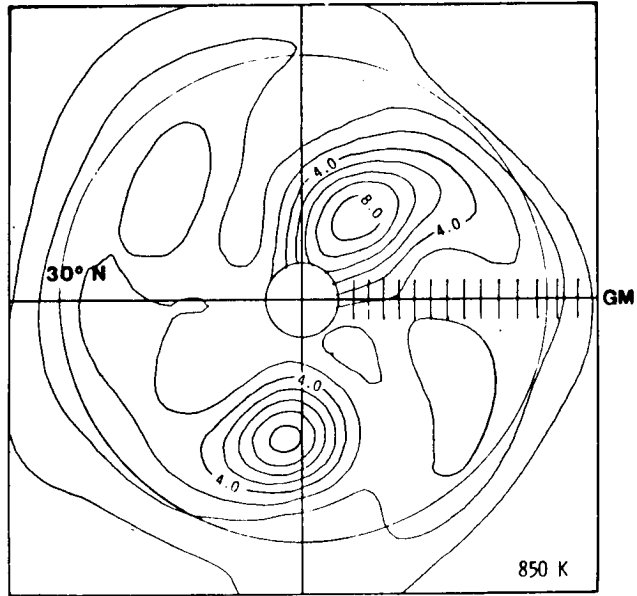


Figure 15. Ertel's potential vorticity $((K \times M \times M / (KG \times S)) \times 1.E-4)$ LIMS N.H. 25 February 1979.

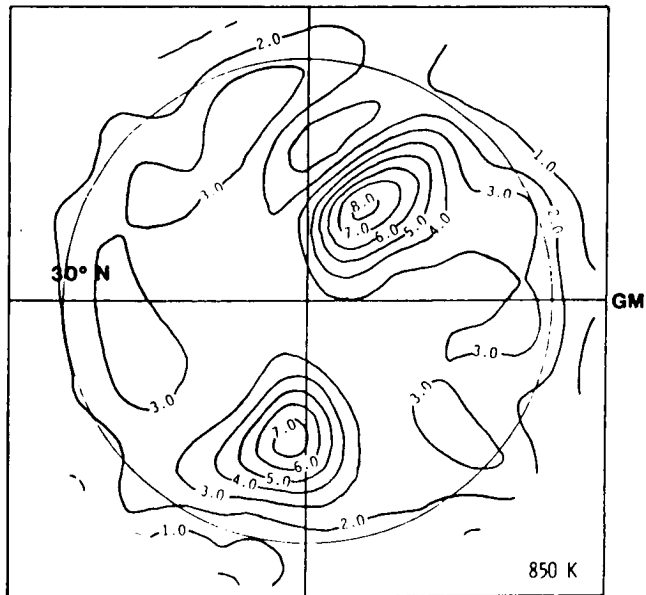


Figure 16. Ertel's potential vorticity $((K \times M \times M / (KG \times S)) \times 1.E-4)$ SSU N.H. 25 February 1979.

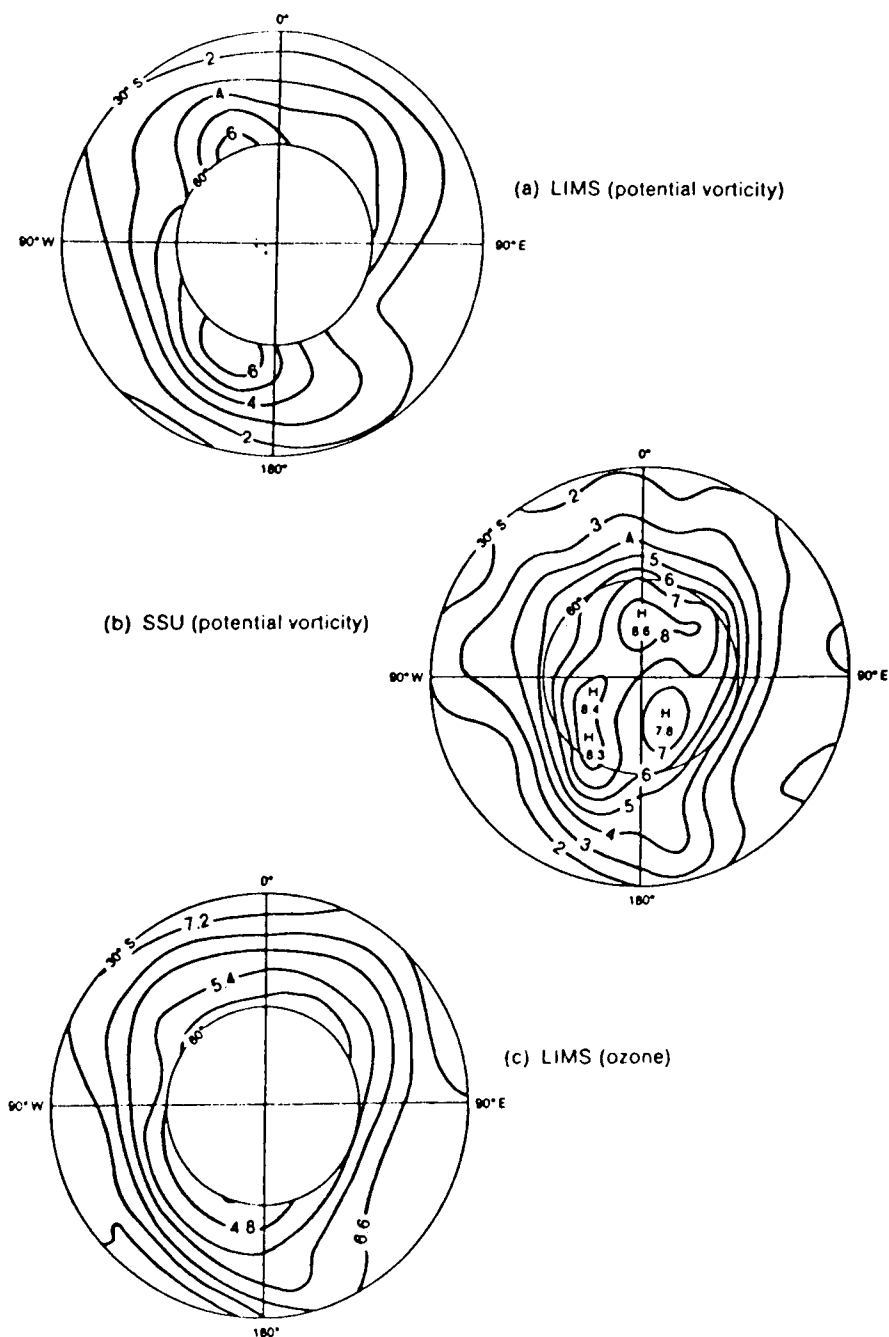


Figure 17. (a) LIMS and (b) SSU maps of modulus of Ertel's potential vorticity on the 850 K isentropic surface for the Southern Hemisphere on May 24, 1979. Units: $10^{-4} \text{ K m}^2 \text{ kg}^{-1} \text{ s}^{-1}$. (c) Ozone mixing ratio (ppmv) from LIMS on the 850 K surface on the same day.

3. GLOBAL BUDGET OF STRATOSPHERIC TRACE CONSTITUENTS (GLOBUS)

3.1 MAP/GLOBUS 1983: A REVIEW

D. Offermann

Physics Department, University of Wuppertal
5600 Wuppertal 1, Federal Republic of Germany

MAP/GLOBUS 1983 was a project for the study of stratospheric trace gases and dynamics. A respective field campaign was performed in September/October 1983 in Western Europe. A large number of measurements were taken by instruments based on the ground, on airplane, balloons, and satellite. The structure of the campaign will be described, and a survey of the results will be given.

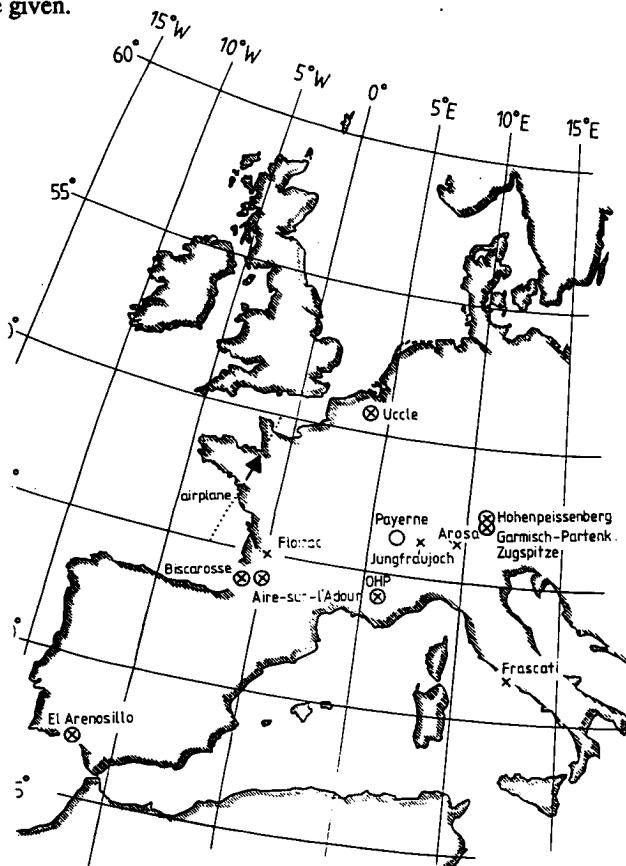


Figure 1. Stations involved in the MAP/GLOBUS 1983 campaign, September 1983: 13 large balloon payloads were launched from Aire-sur-l'Adour. Eleven ground-based experiments were operated almost continuously in Western Europe (crosses). One-hundred-thirty ozone sondes were released from the stations indicated by circles. Six meteorological rockets were launched from El Arenosillo. Dotted line is the trajectory of a research airplane. In total 35 scientific groups participated in the campaign.

Campaign Results

<u>Objective</u>	<u>References</u>
O ₃ : measurements and intercomparisons	Muller and Krueger, Planet. Space Sci. 35, 539, 1987 De LaNoë et al., PSS 35, 547, 1987 Aimedieu et al., PSS 35, 563, 1987 Robbins, PSS 35, 587, 1987 Simon et al., PSS 35, 595, 1987 Matthews et al., PSS 35, 603, 1987 Attmannspacher et al., BPT-Rep.5/87 GSF, Munich, 1987
NO _x : measurements and intercomparisons	Fabian et al., PSS 35, 609, 1987 Pommereau et al., PSS 35, 615, 1987 Naudet et al., PSS 35, 631, 1987
Source and sink gases: measurements and intercomparisons	Schmidt et al., PSS 35, 647, 1987 Borchers et al., PSS 35, 657, 1987 Zander et al., PSS 35, 665, 1987
Ion measurements	Ingels et al., PSS 35, 685, 1987 Schlager and Arnold, PSS 35, 693, 1987
Stratospheric dynamics	Langematz et al., PSS 35, 525, 1987 Offermann et al., PSS 35, 673, 1987
Interpretation	Brasseur et al., PSS 35, 637, 1987 Offermann, Ann. Geophys. 5A, 187, 1987

Figure 2. Publications of campaign data and results, grouped by scientific objectives. Instrumental papers are not included.

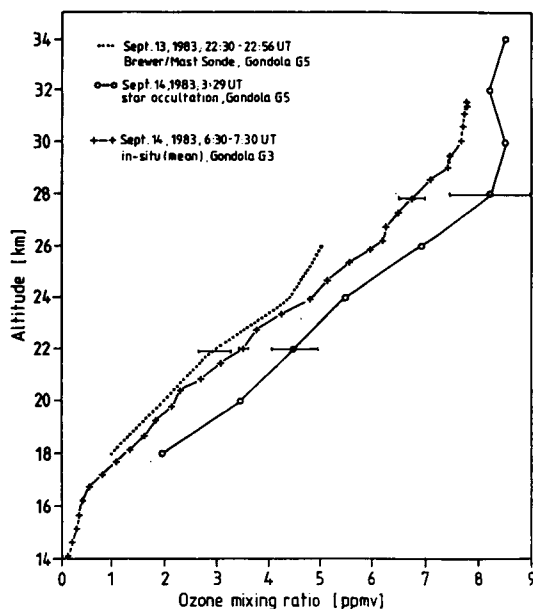


Figure 3. Example for ozone intercomparison. The crosses are weighted mean values of 7 simultaneous *in situ* measurements on one gondola [Aimedieu et al., 1987]. Accuracy is $\pm 3\%$. Circles denote a remote sensing experiment. Accuracy is $\pm 10\%$ [Simon et al., 1987]. There is indication for a systematic difference between *in situ* and remote sensing results, the latter being higher by about 20%.

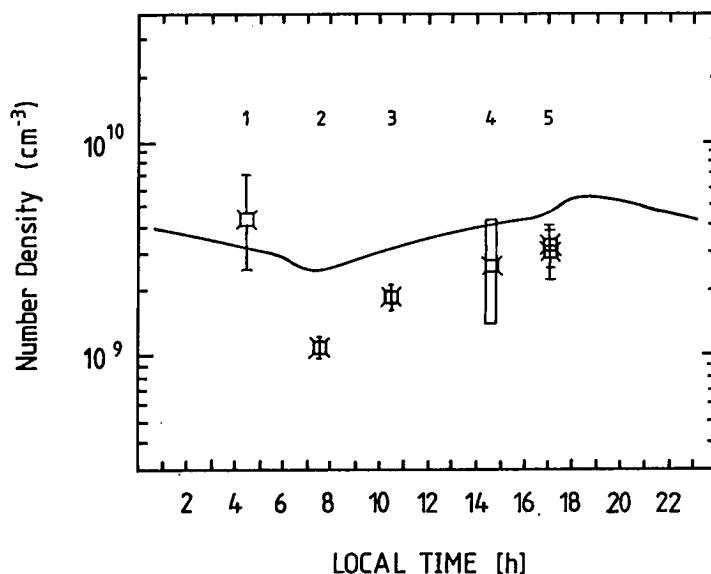


Figure 4. Diurnal variation of NO_2 . Squares are data measured by the following techniques: 1) infrared emission; 2,3) matrix isolation; 4) SME; 5) visible absorption (two measurements). Solid line is from a 1-D model calculation by Wuebbles (extrapolated to 44°N). For details see Pommereau et al.[1987], Brasseur et al.[1987], Riese [1988].

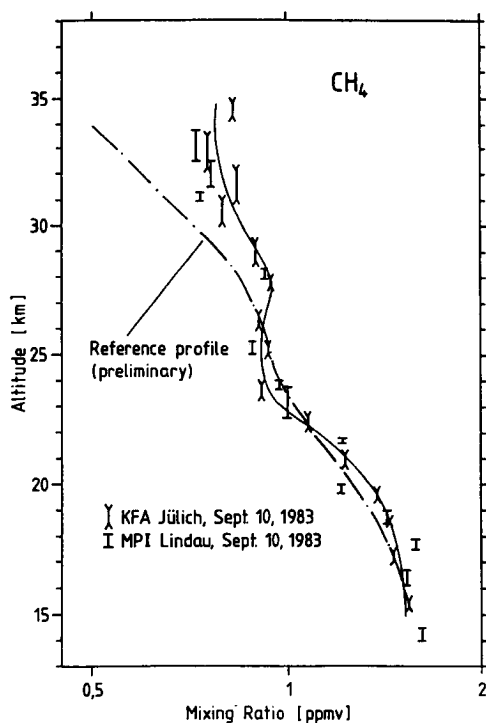


Figure 5. Cryo sampler intercomparison. Accuracy of data points is $\pm 5\%$. Measured data points show wave-like structures when compared to the reference profile. For details see Schmidt et al. [1987]; Offermann et al. [1987].

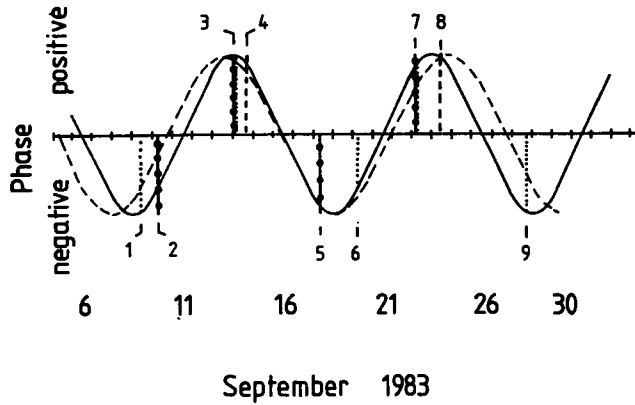


Figure 6. Wave action on trace gas mixing ratio results in positive or negative deviations (phases) from reference values. These are shown for various measurements: 1,6) matrix isolation; 2) cryo sampler; 3) star occultation; 4,8) UV photometer (*in situ*); 5) ion spectrometer; 7) infrared emission; 9) visible absorption spectrometers. Solid curve was adjusted to the data in a preliminary analysis. It has a period of 10 days [Offermann, 1987]. Dashed curve is from an independent wave analysis performed recently.

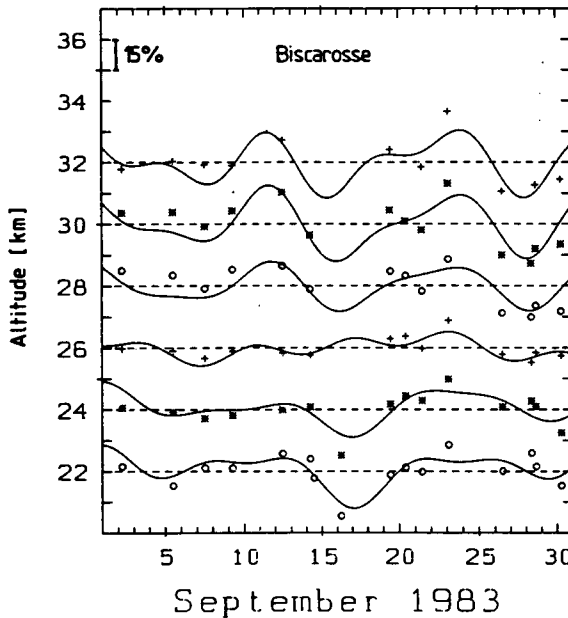


Figure 7. Relative variations of ozone densities during September 1983 as measured by ozone sondes above Biscarosse (symbols). Similar measurements were taken at six other stations (see Figure 1). Solid curves are the result of a least square fit using three superimposed harmonic functions. The three functions are required to have the same periods at all seven stations. Amplitudes and phases, however, are free fit parameters at all stations and altitudes (at altitude steps of 1 km).

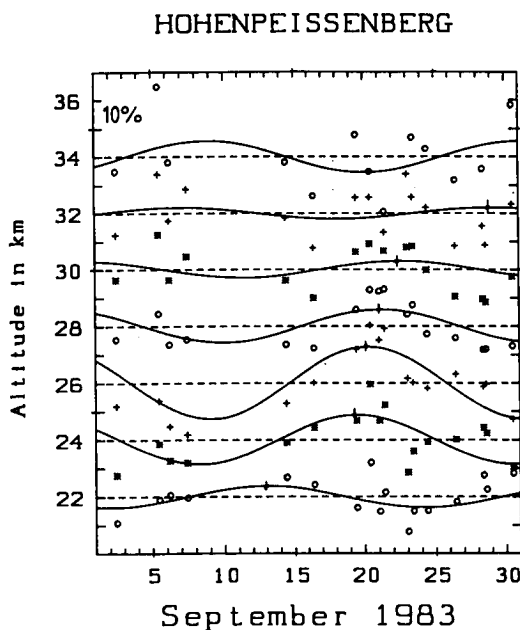


Figure 8. Relative variations of ozone densities above Hohenpiessenberg. Solid curves show one (#2) of the three harmonic fit functions. They indicate a vertical phase progression. Combination of these data with those of the six other stations yields the horizontal and vertical wavelengths for the harmonic function #2. Similar analyses can be performed for the other two fit functions.

Results of the Harmonic Analysis

<u>Parameter derived</u>	<u>Fit Functions</u>		
	<u>#1</u>	<u>#2</u>	<u>#3</u>
Period	22.3 days	11.1 days	6.5 days
Horizontal wavelength	1630 km	1300 km	1630 km
Horizontal phase speed	0.85 m/s	1.4 m/s	2.9 m/s
Vertical wavelength	35 km	26 km	26 km
Vertical phase speed	1.8 cm/s	2.7 cm/s	-4.6 cm/s
Polarization angle	tbd		

Figure 9. The harmonic analysis allows determination of horizontal and vertical phase speeds. Horizontal wave propagation is almost entire from west to east. Vertical propagation is upward for waves #1 and #2, and downward for wave #3. Vertical wavelengths (and phase speeds) are estimates only, as the altitude range covered by the measurements is only a fraction of the wavelengths obtained.

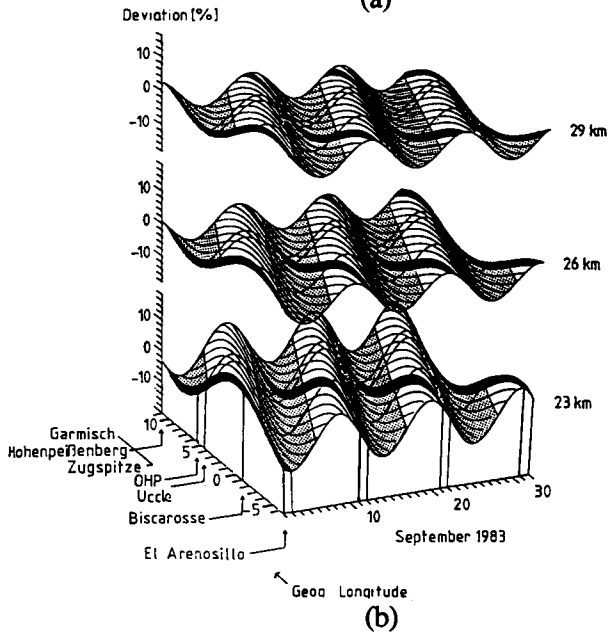
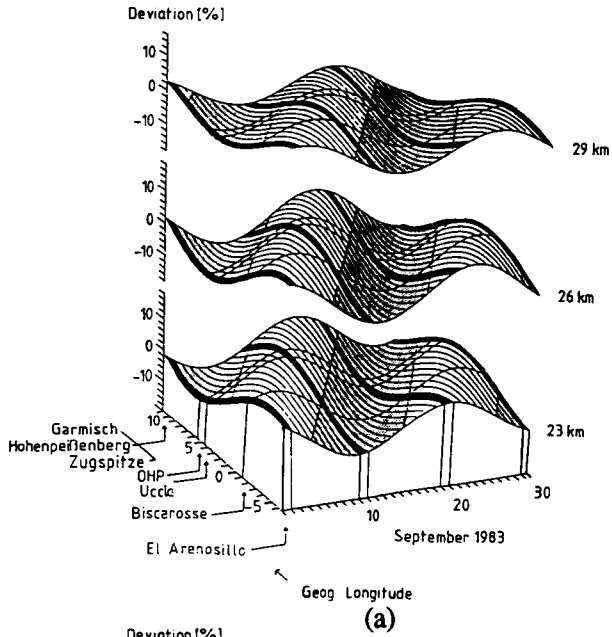


Figure 10. a-c Three-dimensional space/time plots of a) wave #1; b) wave #2; and c) superposition of waves #1, #2, and #3 from Figure 9. Three selected altitudes are given.

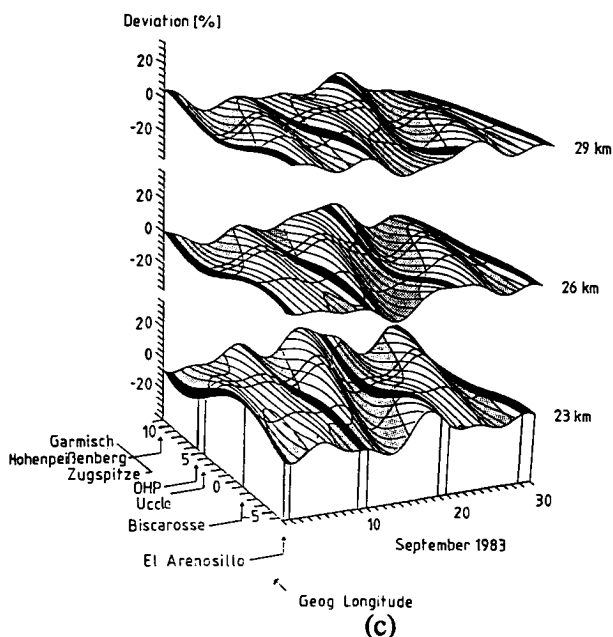
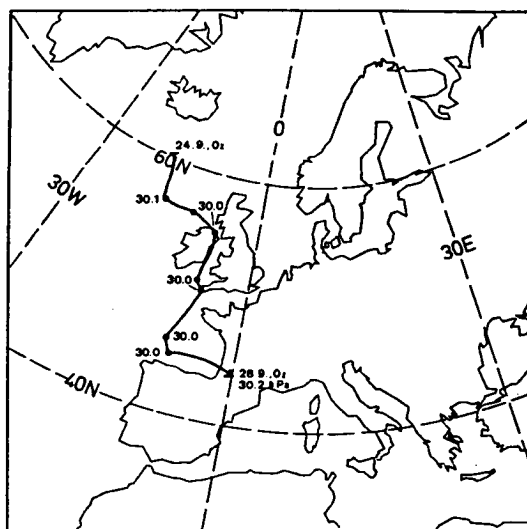


Figure 10 continued.



Trajectory on 600 K ending at Aire-sur-l'Adour on 28. September 1983, 00 UT and calculated backwards till 24. September 1983, 00 UT. Along the trajectory pressure is indicated.

Figure 11. Trajectory (4 days) of an air parcel arriving at Aire-sur-l'Adour on September 28, 1983. Altitude level is 600 K, i.e., about 30 hPa. (For details see Langematz et al., 1987). The last two days of the trajectory are used for the subsequent analysis in Figure 12.

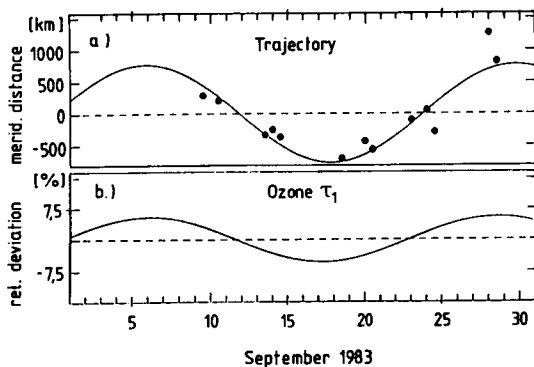


Figure 12. a) Meridional component of two-day-trajectories (30 hPa) versus time. b) Ozone wave #1 from Figures 9 and 10a for the altitude of 30 hPa at Aire-sur-l'Adour. The similarity of the two oscillations suggests that wave #1 observed in the ozone densities results mostly from horizontal transport.

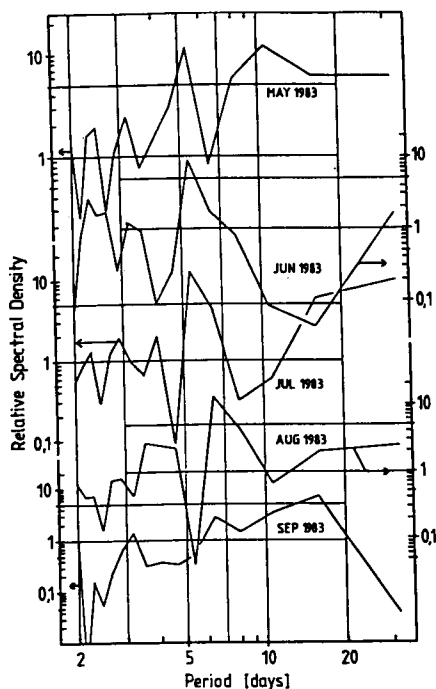


Figure 13. Spectral analysis (FFT) of upper mesosphere temperatures at 86 km. Temperatures were measured before and during the MAP/GLOBUS campaign by an OH^+ spectrometer at Wuppertal and Belfast. A strong mesospheric oscillation at 5.3 days is found during all of the summer, which shifts to 6.4 days in the beginning autumn. These measurements as well as their evaluation were made independently from the GLOBUS campaign.

Wave results

1. Waves consistently found in:
 - a.) ozone densities (3D)
 - b.) various trace constituents
 - c.) trajectories
 - d.) mesospheric temperatures
2. Compatible with planetary waves
3. Horizontal wavelengths extremely short
4. Wave #2: first harmonic of wave #1?
5. Strong influence on trace gas mixing ratios.
 - => Polarization angle between
horizontal and vertical motion (?)

Figure 14. Summary of results obtained for the stratospheric waves.

3.2 AN OVERVIEW OF MAP/GLOBUS NO_x

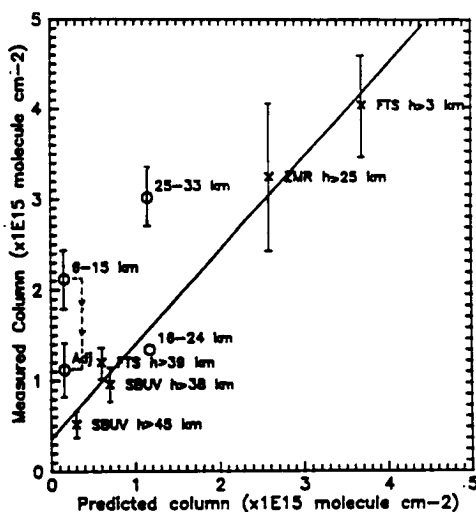
J. P. Pommereau

Service d'Aeronomie, CNRS, BP 3
91371 Verrieres-le-Buisson, France

GLOBUS NO_x is a combined observation of nitrogen compounds by more than 20 experiments, from satellites, remote and in situ instruments on board balloons and ground observatories, within a short time period. Held in September 1985 above Southern France, the field campaign has been a technical success. Most of the observations have been achieved as anticipated. NO, NO₂ and relevant species and physical parameters involved in their photochemistry, were measured between 5 km and 40 km at several periods of the day. A first step of data interpretation which consists of instrumental intercomparisons, is now achieved. Several systematic biases between data of various origins which have appeared in the past, are now understood and reduced. A second step which deals with atmospheric photochemistry issues like diurnal cycles and budget, is now on its way. It will be the object of a close exchange between experimenters involved in the campaign and modelers.

TABLE 1. Measurements Achieved During GLOBUS NO_x

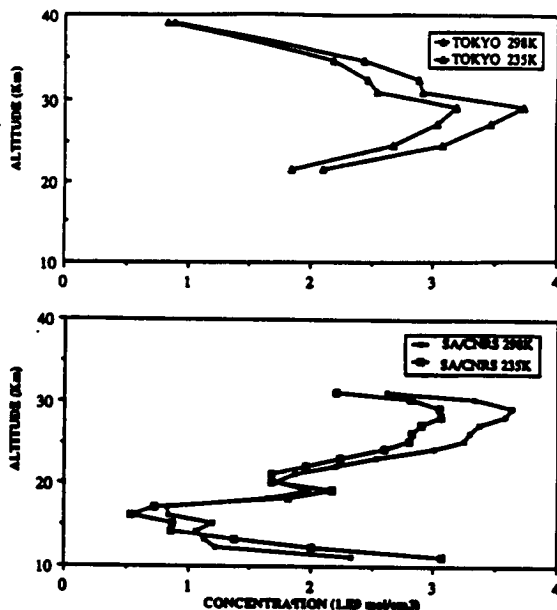
	Balloon	Satellite	Ground	Total
NO _x	11	3	6	20
Other	11	3	5	19
Total	22	6	11	39



Comparison of NO Measurements

- Ground-based ZMR, FT spectrometer
- Balloon-borne IR interferometer
- SBUV
- In situ chemiluminescence.

Figure 1. Intercomparison of NO column measurements during MAP/GLOBUS 1985, R. L. McKenzie, W. A. Matthews, Y. Kondo, R. Zander, P. Demoulin, P. Fabian, D. G. Murcray, F. J. Murcray, O. Lado-Bordowsky, C. Camy-Peyret, H. K. Roscoe, J. A. Pyle, R. D. McPeters, submitted to *J. Atmos. Chem.*, 1988.



NO₂ Remote Sensing Comparison: Solar Visible Occultation from Balloon

- Three instruments on a common balloon gondola (Tokyo, IASB, CNRS)
- Method overestimates NO₂ concentration because of temperature dependence of the absorption cross sections of the gas. Correcting factor between 12% and 18% in the stratosphere
- Total uncertainty: 15% in the stratosphere, 30% in the troposphere

Figure 2. Balloon observations of nitrogen dioxide by visible occultation during GLOBUS NO_x, J. P. Pommereau, F. Goutail, N. Iwagami, K. Shibasaki, P. C. Simon, W. Peetermans, J. P. Naudet, P. Rigaud, D. Huguenin, submitted to *J. Atmos. Chem.*, 1988.

**NO₂ Remote Sensing Comparison:
SAGE 2 and Balloon Occultation**
 -Differences much smaller than Instruments
 Uncertainties
 -Average systematic difference < 4%

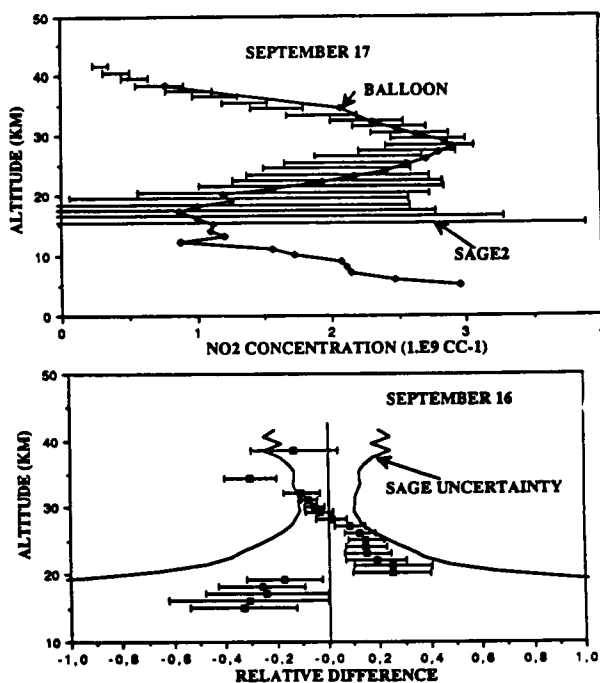
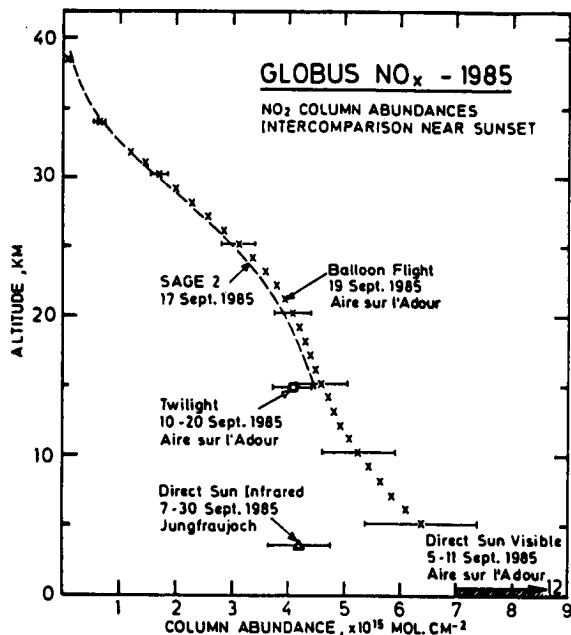


Figure 3. Nitrogen dioxide data comparison with infrared and visible balloon remote sensing measurements during GLOBUS NO_x, J. Lenoble, W. P. Chu, D. G. Murcray, O. Lado-Bordowski, C. Camy-Perret, A. Perrin, J. P. Pommereau, F. Goutail, K. Shibasaki, N. Iwagami, and P. C. Simon, submitted to Quad. Ozone Symp., 1988.



Comparison of Ground-Based, Balloon and Satellite NO₂ Measurements

- Data generally consistent when local NO₂ contamination inside the boundary layer absent
- Further simultaneous direct sun IR and visible observations needed

Figure 4. Measurements of column abundances of nitrogen dioxide, NO₂, from the ground during the GLOBUS NO_x campaign, R. Zander, P. Demoulin, G. Roland, W. A. Matthews, P. V. Johnston, J. P. Pommereau, N. Iwagami, K. Shibasaki, submitted to Quad Ozone Symp., 1988.

Ozone Measurements 30-55 km

- Microwave at Bordeaux Observatory
- Umkehr at Haute-Provence Observatory
- Satellite EXOS-C BUVa

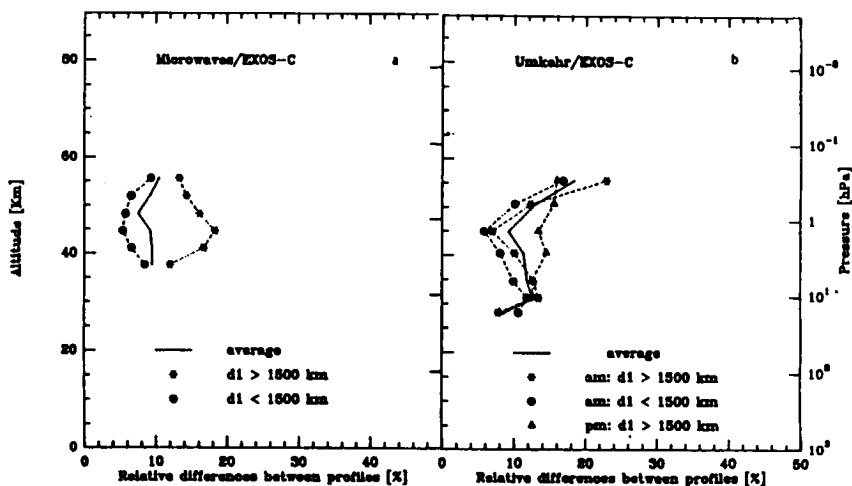


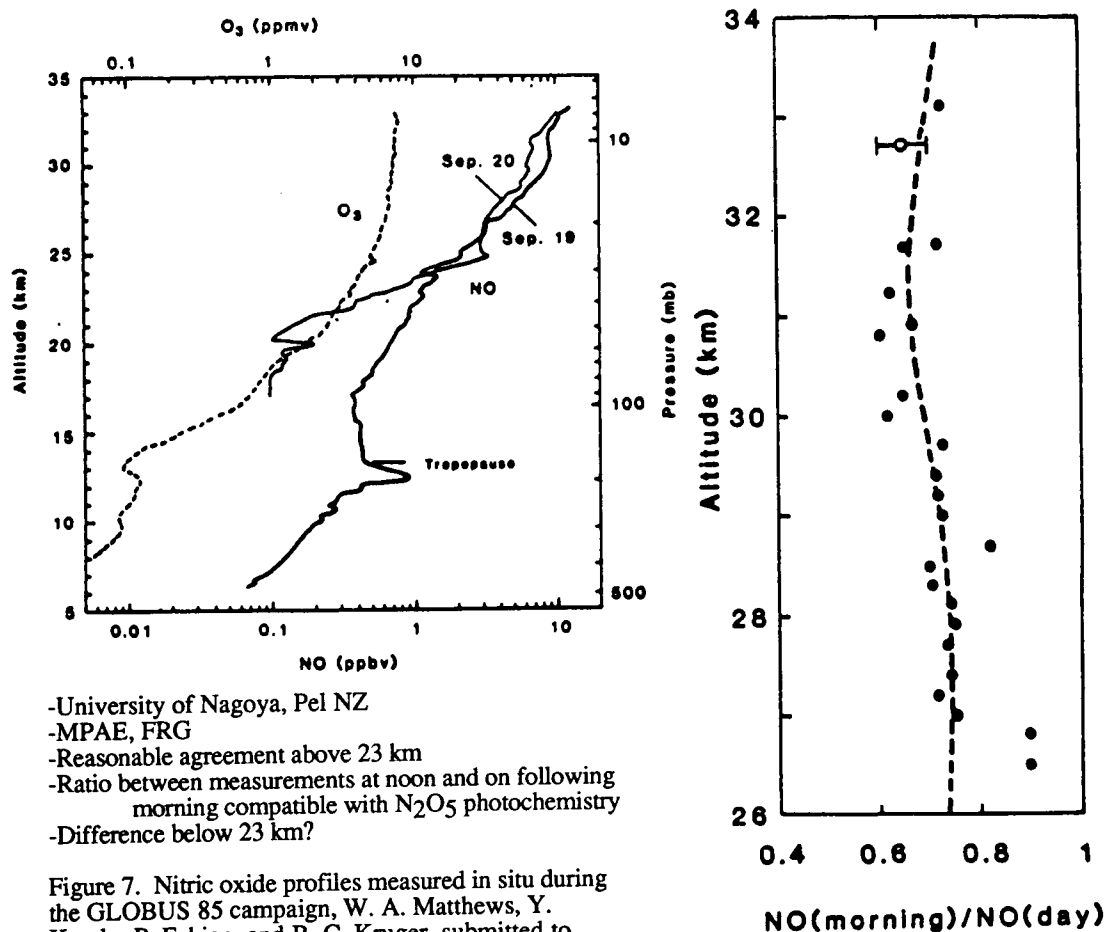
Figure 5. Comparison of stratospheric and mesospheric ozone profiles obtained by ground-based and satellite observations, J. de La Noe, M. Koike, T. Ogawa, P. Marché, submitted to Quad Ozone Symp., 1988.

Ozone Instruments Total Accuracy

- In situ UV Photometer: 3% Total Uncertainty
- Remote Visible Occultation: 5-10%
- SAGE II: 10%
- In situ Gas Phase Chemiluminescence: 10%
- Umkehr: Layers 4 and 5, 10%; Layer 6, 15%
- SBUV: 10% Average, Peak Systematically Lower
- EXOS-C BUV: 10-15%
- Brewer-Mast Sondes: 5-10% between 18 and 25 km, 15-20% above
- Solar UV Occultation: Systematic Underestimation by 30-35%

Figure 6. Measurements of stratospheric ozone during the MAP/GLOBUS NO_x campaign, D. Robbins, P. Amedieu, J. Pelon, J. P. Pommereau, F. Goutail, N. Iwagami, K. Shibasaki, T. Ogawa, M. Koike, P. Marché, J. P. Naudet, P. Rigaud, D. Huguenin, J. Lenoble, G. Maddrea Jr., submitted to *J. Geophys. Res.*, 1988.

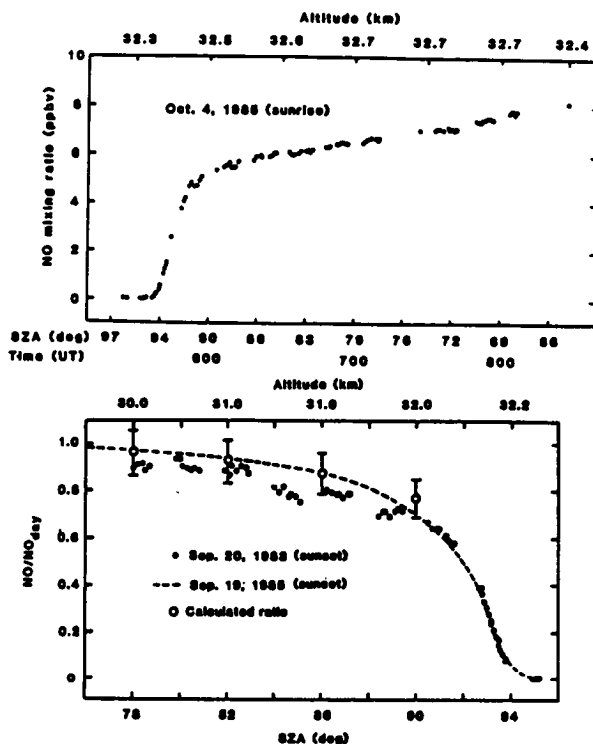
NO Vertical Profiles by In situ Chemiluminescence



- University of Nagoya, Pel NZ
- MPAE, FRG
- Reasonable agreement above 23 km
- Ratio between measurements at noon and on following morning compatible with N₂O₅ photochemistry
- Difference below 23 km?

Figure 7. Nitric oxide profiles measured in situ during the GLOBUS 85 campaign, W. A. Matthews, Y. Kondo, P. Fabian, and B. C. Kruger, submitted to *J. Atmos. Chem.*, 1988.

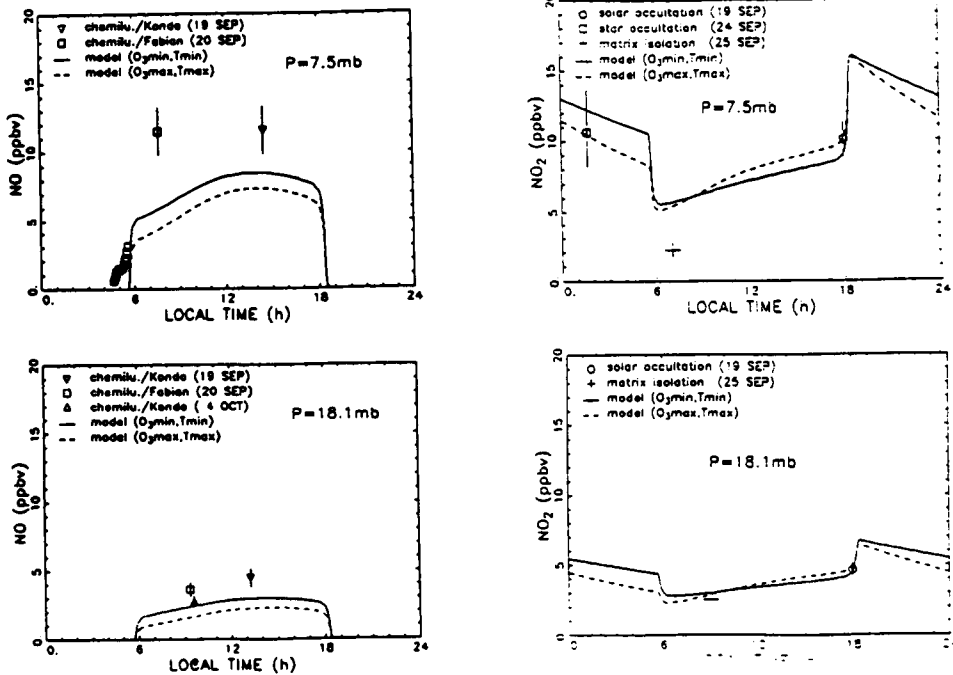
NO Diurnal Variation



- Variation observed in situ from sunrise until sunset around 32 km with two balloon flights
- From rate of increase of NO during morning: $[N_2O_5]$ at the end of the night = 3.9 ± 1.5 ppbv
- NO decrease at the end of afternoon at $SZA > 80^\circ$, requires decrease of JNO_2

Figure 8. Diurnal variation of nitric oxide at 32 km: measurements and interpretation, Y. Kondo, W. A. Matthews, P. Amedieu, D. E. Robbins, *J. Geophys. Res.*, in press, 1988.

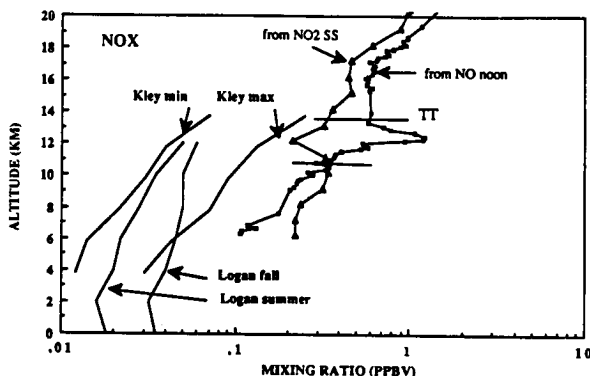
NO/NO₂ Diurnal Variation. Model Comparisons



- Agreement between NO₂ Predicted and Measured (Night, Morning, Evening)
- Much More NO than Predicted, Partitioning between NO and NO₂ differs from that Observed, Difference Increases at High Altitude
- NO decay in the Afternoon at SZA > 80°. JNO₂ Reduced by Multiple Scattering?

Figure 9. Diurnal variation of stratospheric NO and NO₂ from MAP/GLOBUS 1985, J. P. Naudet, M. Pirre, R. Ramaroson, P. Rigaud, P. Fabian, M. Helten, N. Iwagami, K. Shibasaki, T. Ogawa, Y. Kondo, W. A. Matthews, J. P. Pommereau, F. Goutain, P. C. Simon, W. Peetermans, submitted to Quad. Ozone Symp., 1988.

A NO_x Source in the Upper Troposphere?



- NO_x Observed Larger than Predicted by Factor 3 to 10
- Models Include Mean Transport from Stratosphere
- Local Transport from 20 km at Least, Would Have Left Signature on Potential Temperature and Ozone
- Transport from Surface Level Would Require Much More than NO_x Lifetime [Kley et al., 1981]

Conclusion: Source present in Upper Troposphere

Figure 10. Observed and predicted NO_x below 20 km [Logan et al., 1981; Kley et al., 1981]. A NO_x source in the upper troposphere?, J. P. Pommereau, F. Goutail, Y. Kondo, W. A. Matthews, M. Helten, submitted to Quad. Ozone Symp., 1988.

CONCLUSIONS

Experimental

- Better evaluation of NO , NO_2 , O_3 experimental uncertainties
- Instruments improvements: Result of previous campaigns
- Systematic errors found and reduced
- Consistency of all NO data after correction of chemiluminescence data?
- Further comparison between IR and visible ground-based NO_2 instruments still required
- Interpretation of NO_x measurements by chemiluminescence and converter still to come

NO_x Photochemistry

- Excess of NO compared to NO_2 in the stratosphere. Significant? Mechanism?
- NO decrease in the afternoon after SZA 80° . J_{NO_2} decrease? Effect of multiple scattering?
- Source of NO_x in the upper troposphere. Aircraft emission? Lightning?
- Interpretation will follow on. Data base (NO_x constituents, related species and atmospheric parameters) available for further studies

3.3 MEASUREMENTS OF NITRIC OXIDE IN THE STRATOSPHERE AT 44°N IN AUTUMN

Y. Kondo

Research Institute of Atmospheric
Nagoya University, Toyokawa, Aichi 442, Japan

W. A. Matthews

DSIR Lauder, New Zealand

P. Aumedieu

CNRS, Service d'Aeronomie, France

D. E. Robbins

NASA Johnson Space Center, USA

Precision of the chemiluminescent instrument for balloon-borne NO measurement has been improved by precise determinations of the flow rates of the sample air and the calibration NO in N₂ gas. Based on the new calibration of these values, NO mixing ratio in the stratosphere has been reanalyzed. The revision of the NO data does not at all alter the form of the diurnal variation. The average of the four NO profiles between 15 and 32 km obtained at 44°N in autumn is given.

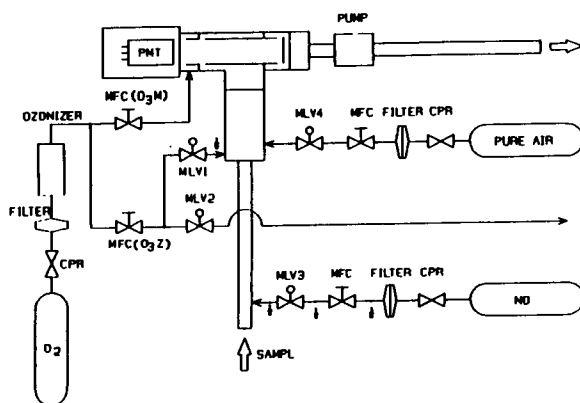


Figure 1. We have made some modifications to the NO chemiluminescent instrument described by Kondo et al. [1985]. Both the ozone/oxygen flow injected into the reaction chamber and the flow used for zeroing are regulated by mass flow controllers. The ozone/oxygen flow used for zeroing is exhausted directly outside the instrument. This reduces the mass flow rate during the measurement mode and thus reduces an uncertainty in estimating the net sample flow rate especially at high altitude. To measure the zero level of the instrument, purified air with an NO concentration of less than 5 pptv is injected into the system for 40 s every 10 minutes.

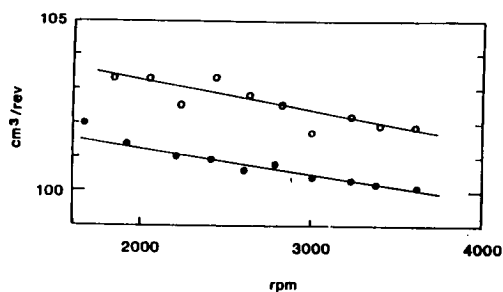


Figure 2. Calibration of the pumping rate at 1 atmosphere with no flow resistance. It can be seen that the pumping volume per 1 revolution of the rotor is almost constant of 100 cm^3 independent of the rotor frequency.

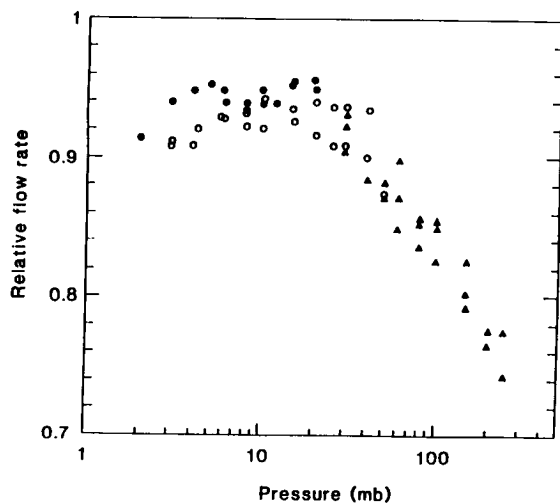


Figure 3. Change of the pumping rate with the pressure when the pump is connected to the reaction chamber and other parts of the instrument. The value given is relative to that measured when the pump is not connected to the reaction chamber.

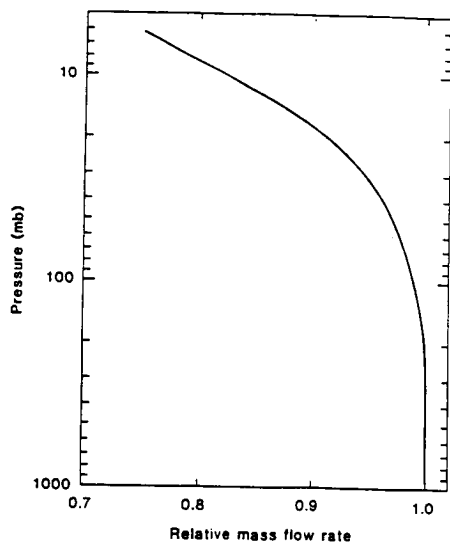


Figure 4. To regulate the flow of the calibration NO in N_2 , a mass flow controller is used. The sensitivity of the mass flow sensor increases with ambient pressure and thus results to a corresponding decrease of the net mass flow of the NO/N_2 gas. The change of the mass flow rate with the ambient pressure has been calibrated.

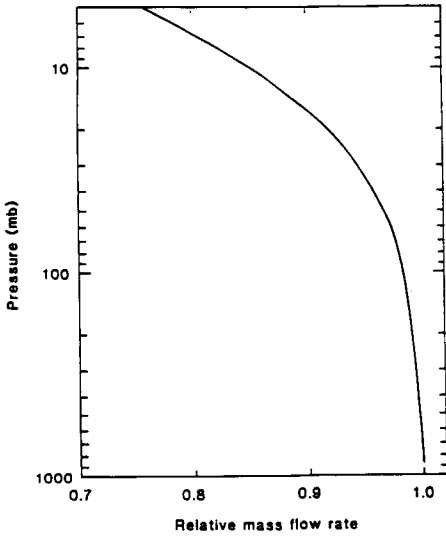


Figure 5. Same as Figure 4 but for ozone/oxygen flow. The effect of the change of this flow is not so significant in deriving the NO concentration.

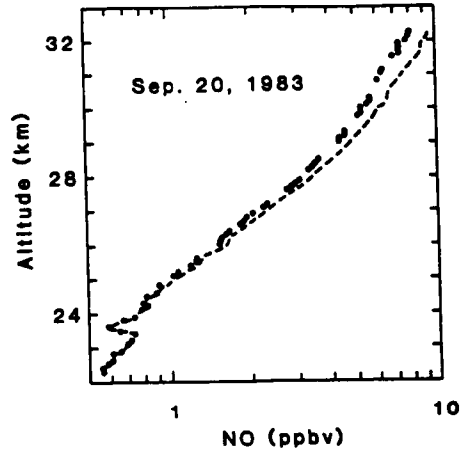


Figure 6. The NO mixing ratio has been calculated by taking into account the new calibration data of the pumping rate and the change in the sensitivity of the mass flow controllers with altitude. The dashed curve is the previous value given in Kondo et al. [1985] measured during the MAP/GLOBUS 1983 campaign. Closed circles are the new values revised this time.

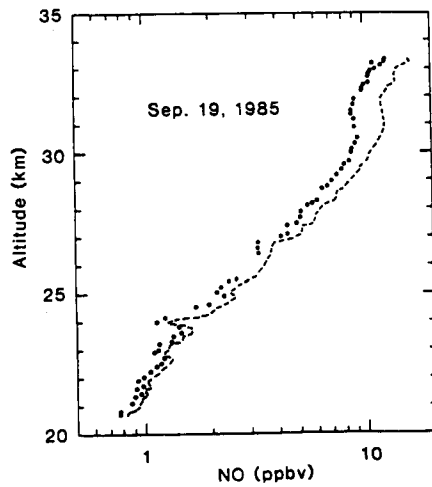


Figure 7. The same as Figure 6 but for the data on September 19, 1985.

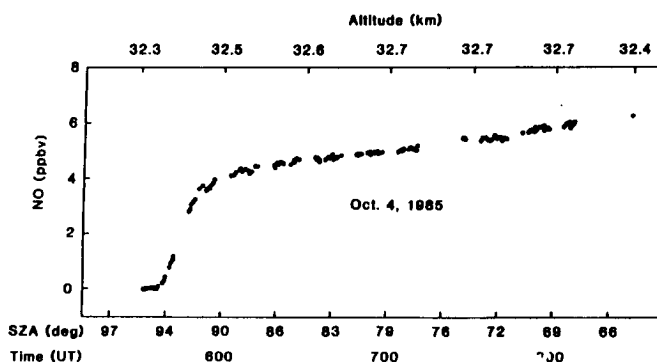


Figure 8. Temporal variation of NO measured near sunrise on October 4. NO concentration is about 77% of that given in Kondo et al. [1988]. The form of the diurnal variation relative to its daytime value is not changed at all. The N_2O_5 concentration derived from the analysis of the NO increase is also reduced to 3.0 ± 1.2 ppbv. This value is very close to the value derived by Evans [1986] from infrared emission measurements during the nighttime.

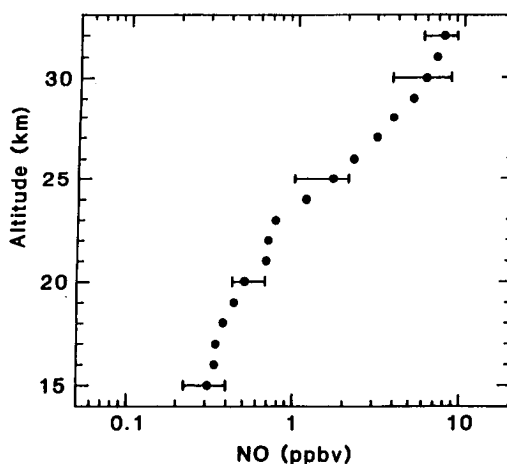


Figure 9. Thus far measurements of NO have been made four times from Aire-sur-l'Adour, France (44°N). Namely, on September 20, 1983; September 19, 1985; October 4, 1985; and September 17, 1987. NO was measured between 0830 and 1330 UT. The average of the four profiles is shown. The profile can be a reference of NO at midlatitude in autumn.

3.4 SEASONAL VARIATION OF THE TEMPORAL VARIANCE OF LONG-LIVED TRACE GASES MEASURED DURING MAP

E. P. Röth* and U. Schmidt

Institut für Atmosphärische Chemie
Kernforschungsanlage Jülich GmbH
D-5170 Jülich, Federal Republic of Germany

A series of balloon observations of long-lived trace gases has been performed in the midlatitude stratosphere during MAP. The temporal variance of the local mixing ratios of CH_4 , N_2O , CFCl_3 , and CF_2Cl_2 indicates a substantial annual variability. The concept of the equivalent displacement height (EDH) introduced by Ehhalt et al. [J. Atmos. Chem. 1, 27, 1983] is used to investigate some features of transport activity in the lower stratosphere. It appears that most of the temporal variance originates from strong transport effects during the periods of the spring and autumn turn-around of the stratospheric circulation. We found the dynamical process to be considerably reduced during October.

*Also at Institut für Physikalische Chemie, Universität Essen, D-4300 Essen 1, Federal Republic of Germany.

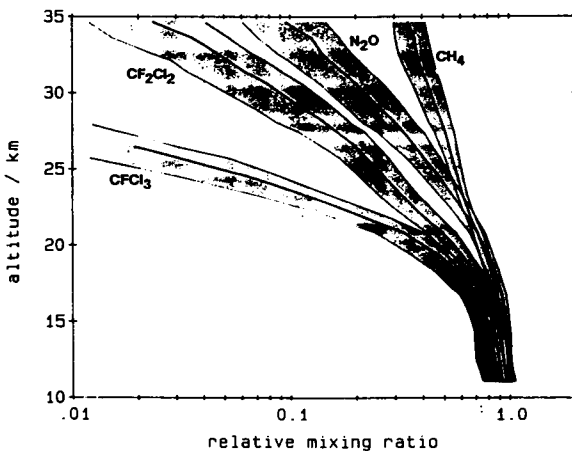


Figure 1. Vertical profiles of the volume mixing ratios of CH_4 , N_2O , CF_2Cl_2 , and CFCl_3 , averaged over 19 balloon flights in Southern France (44°N). The local mixing ratios are given relative to a tropospheric value of 1. The shaded areas indicate the mean standard deviations of the data points. [Volz et al. Ber. Kernforschungsanlage Jülich, JÜL-1742, 1981; and Schmidt et al., Ber. Kernforschungsanlage Jülich, JÜL-Spez-375, 1986]. Running means and standard deviations are deduced from a regression line within a window of 5 km height with a step width of 1 km.

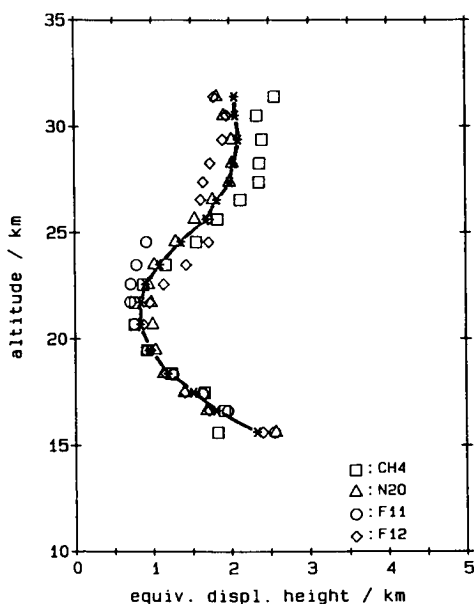


Figure 2. The vertical distribution of the equivalent displacement height for CH_4 , N_2O , CF_2Cl_2 , and CFCl_3 derived from the 19 balloon flights in Southern France displayed in Figure 1. The heavy line represents the EDH averaged at each level over the EDH of the individual source gases. The concentration of CFCl_3 becomes too low above 25 km for deducing a meaningful equivalent displacement height.

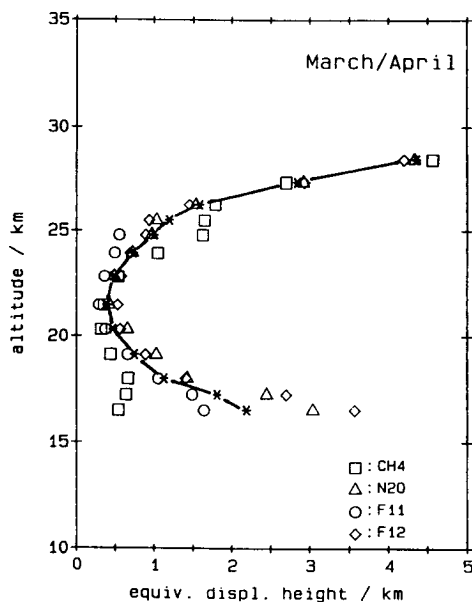


Figure 3. The vertical distribution of the equivalent displacement height, deduced from measurements of CH_4 , N_2O , and CFCl_3 , and CF_2Cl_2 . The balloons were launched in spring (March 1983 and April 1984). The heavy line runs through the averages of the individual EDH. Values for CFCl_3 above 25 km were omitted.

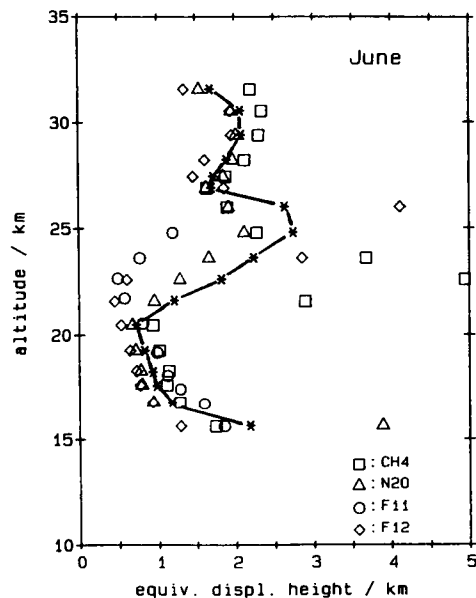


Figure 4. The vertical distribution of the equivalent displacement height, deduced from measurements of CH₄, N₂O, and CFCl₃, and CF₂Cl₂. The balloons were launched during June (1977-1979). The heavy line runs through averages of the individual EDH. Values for CFCl₃ above 25 km were omitted.

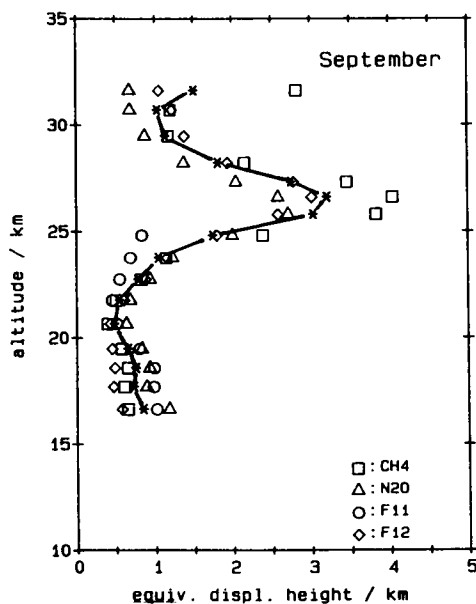


Figure 5. The vertical distribution of the equivalent displacement height, deduced from measurements of CH₄, N₂O, and CFCl₃, and CF₂Cl₂. The balloons were launched during the autumn turn-around period (September 1983-1987). The heavy line runs through the averages of the individual EDH. Values for CFCl₃ above 25 km were omitted.

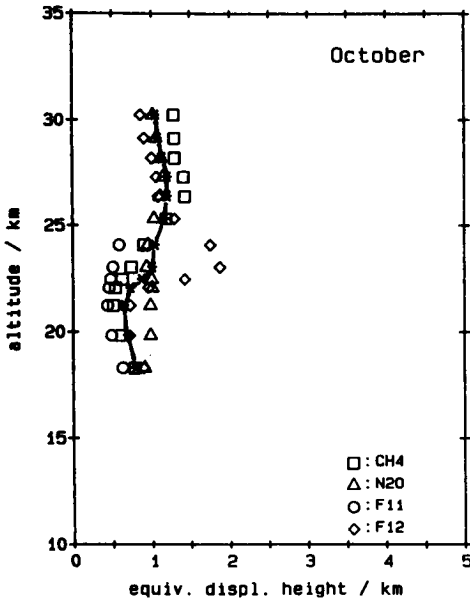


Figure 6. The vertical distribution of the equivalent displacement height, deduced from measurements of CH₄, N₂O, and CFCl₃, and CF₂Cl₂. The balloons were launched after the autumn turn-around period (October 1982-1986). The heavy line runs through the averages of the individual EDH. Values for CFCl₃ above 25 km were omitted.

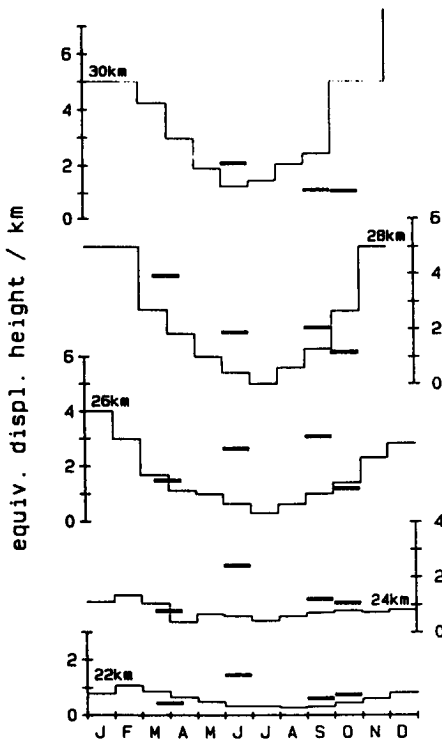


Figure 7. Comparison of the seasonal variation of the equivalent displacement height derived from long-lived tracer observations (heavy bars) and from balloon-borne ozone measurements (light line). The EDH of the long-lived tracers are the means shown in Figures 3 to 6, while the O₃ concentration profiles were published by Attmannspacher [Sonderbeobachtungen des Meteorol. Observatoriums Hohenpeisenberg, 1966-1985] and analyzed by Roth and Ehhalt (in Visconti and Garcia, editors, Transport Processes in the Middle Atmosphere, Reidel 1987, pp 137-152).

3.5 EVIDENCE OF CO₂-INDUCED PROGRESSIVE COOLING OF THE MIDDLE ATMOSPHERE DERIVED FROM RADIO OBSERVATIONS

J. Taubenheim, G. v. Cossart, and G. Entzian
Academy of Sciences of the German Democratic Republic
Heinrich-Hertz-Institut für Atmosphärenforschung und Geomagnetismus
Berlin 1199, G. D. R.

Reflection heights of low-frequency radio waves in midlatitude summer, which are closely associated with the neutral atmosphere isobaric level of 0.0052 hPa, exhibit a statistically significant downgoing trend from 1962 through 1987. This indicates a systematic decrease of air pressure at 80 km height by $10.3 \pm 4.9\%$ over this period, to be regarded as a sufficient evidence of a true signal of progressive cooling of the middle atmosphere, expected with the growing content of CO₂ and other "greenhouse" gases in the atmosphere. It is quantitatively consistent with a temperature decrease at the stratopause by about 4 K, as predicted by the recent model of interactive greenhouse and ozone processes of Brasseur and de Rudder [1987].

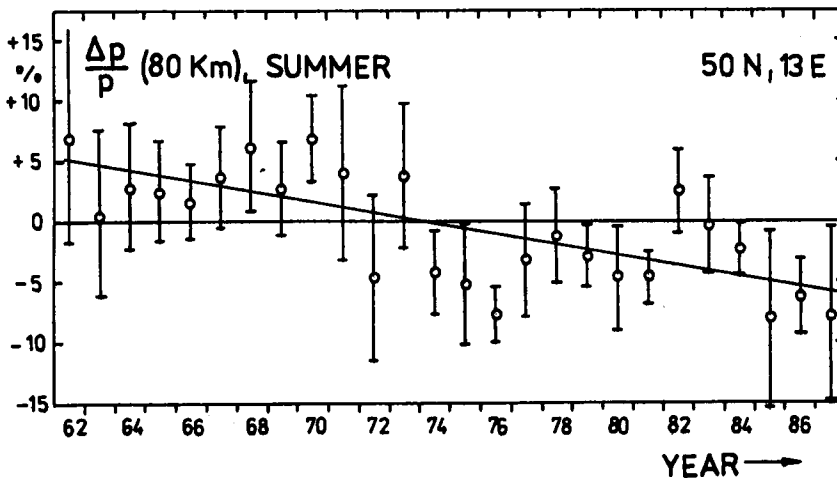


Figure 1. Mean values of air pressure at 80 km altitude in summer half-years (April-September) 1962 through 1987, determined from low-frequency radio wave reflection height measurements for the geographic location 51°N, 13°E, after eliminating the solar-cycle variation. Values are expressed as percentage deviations from the long-term average. Error bars indicate the 95% confidence limits. Analysis uses the straightforward connection of radio wave reflection heights with an isobaric surface, if nitric oxide content is sufficiently constant. Winter variability of NO near the mesopause is avoided by taking summer months only, a possible long-term NO trend causes only minor modification of the results.

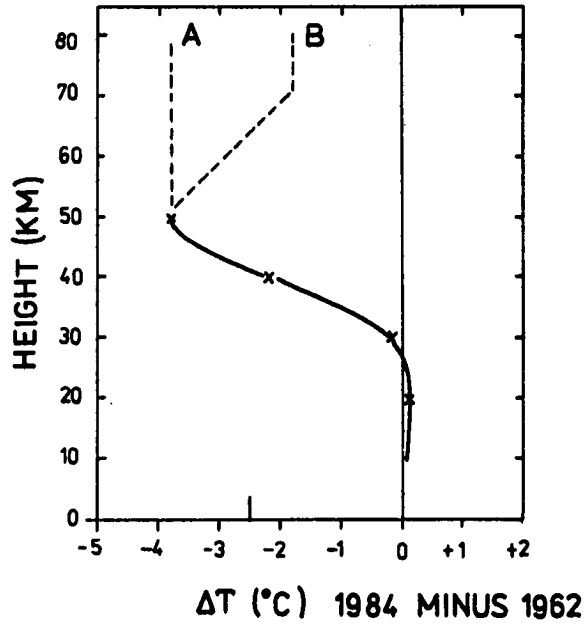


Figure 2. Temperature change in the middle atmosphere between 1962 and 1984 as predicted by the model of Brasseur and de Rudder (crosses), with two optional arbitrary extensions up to 80 km. The one-dimensional Brasseur-de Rudder model (its scenario No. 5c being adopted here) takes into account CO_2 greenhouse processes together with stratospheric ozone decrease. Using the barometric formula, options A and B produce pressure decrease at 80 km by 9.6 and 6.7%, respectively, in good agreement with the observations shown in Figure 1.

4. GRAVITY WAVES AND TURBULENCE IN THE MIDDLE ATMOSPHERE PROGRAM (GRATMAP)

4.1 AN OVERVIEW OF GRAVITY WAVE STUDIES DURING MAP/MAC

D. C. Fritts

Geophysical Institute
University of Alaska, Fairbanks, AK 99775-0800

Considerable progress has been made in understanding gravity waves and their effects in the middle atmosphere during the MAP and MAC periods. During this time, gravity waves have been recognized to play a central role in controlling the large-scale circulation and the thermal and constituent structure of this region through wave transports of energy and momentum, a significant induced meridional circulation, and through the action of wave-induced turbulence. Both theoretical and observational studies also have contributed to our understanding of the gravity wave spectrum, its temporal and spatial variability, and the processes responsible for wave saturation. As a result, we are beginning to understand the propagation, interactions, and detailed effects of such motions in the middle atmosphere. This talk will provide an overview of this work and a lead-in to the review talks that follow.

Gravity Wave Overview

- Advances in observational capabilities
- Understanding of gravity wave propagation, saturation, and effects
- Large-scale middle atmosphere effects of gravity waves and turbulence
 - Gravity wave variability
 - Future directions

Gravity wave scales, fluxes and saturation

I. M. Reid

Turbulence, evolution and variability

W. K. Hocking

Gravity wave spectral understanding

T. E. VanZandt

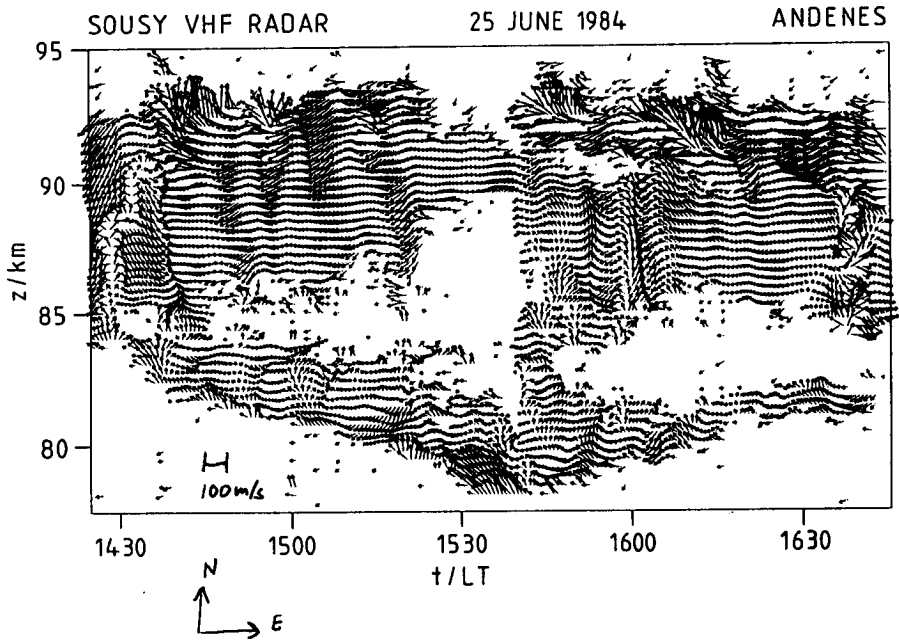


Figure 1. Time-height cross section of horizontal wind observed with the SOUSY radar during June 1984 exhibiting MAP/MAC remote sensing capabilities [Reid et al., submitted 1988].

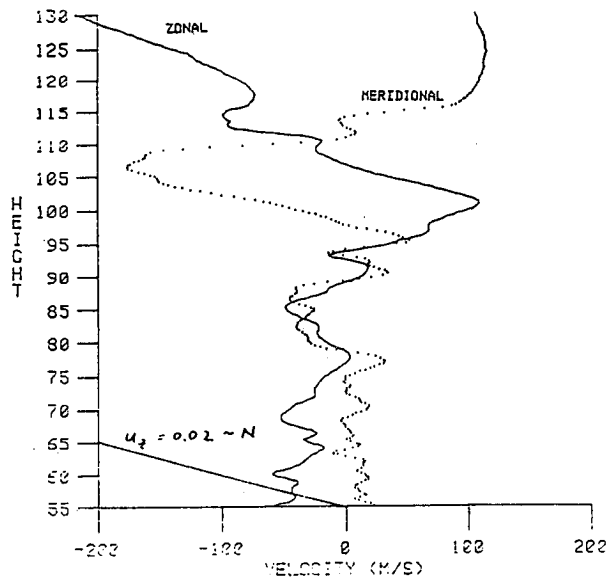


Figure 2. Vertical profiles of zonal and meridional winds from active falling sphere obtained during the STATE experiment [Fritts et al., *J. Geophys. Res.*, 1988].

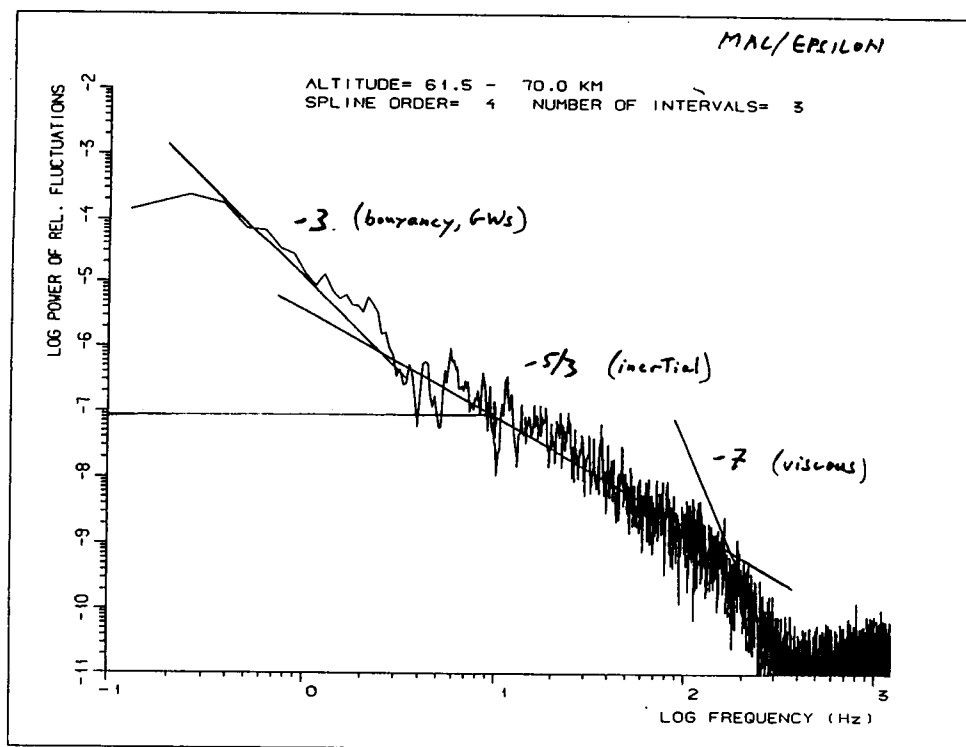


Figure 3. Frequency spectrum of ion fluctuations obtained by positive ion probe during MAC/Epsilon experiment showing in situ small-scale measurement capabilities [Thrane et al., 1988, in preparation].

Gravity Wave Saturation

Structure
 $u' \sim m^{1/2} e^{z/2H} e^{i\phi}$

$$\theta'_z/\theta = -u'/(c-\bar{u})$$

Linear saturation theory

m or z increasing \Rightarrow wave growth and instability

1. Dynamical (KH or shear) instability

$$Ri = \frac{\frac{g}{\theta} \frac{\partial \theta}{\partial z}}{(u_z'^2 + v_z'^2)} < 1/4$$

2. Convective instability

$$\frac{\partial \theta}{\partial z} < 0, \frac{u'}{(c - \bar{u})} > 1 \quad - \text{vertical}$$

$$\frac{\partial \theta}{\partial z} < 0 \quad - \text{slantwise}$$

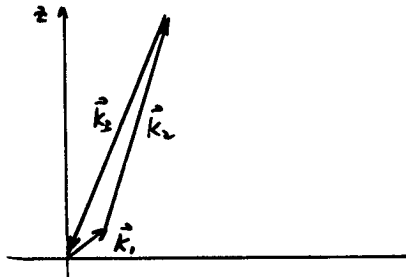
\Rightarrow amplitude limits $u' \sim c - \bar{u} \sim N/m$ or $u'_z \sim N$

Nonlinear theory

3. Wave-wave interactions -- resonant and nonresonant

- Parametric subharmonic instability (PSI)

McComas and Bretherton [1977], Yeh and Liu [1981], Dunkerton [1987].



4. Wave-vortical mode interactions -- nonresonant - Dong and Yeh [1987]

$$\frac{u'}{(c - \bar{u})} > \sqrt{2} \quad - \text{less restrictive than linear instabilities}$$

Figure 4. Illustration of linear gravity wave structure and conditions from "linear" saturation; Schematic of nonlinear wave-wave interactions (PSI) and wave-vortical mode threshold for nonlinear wave saturation.

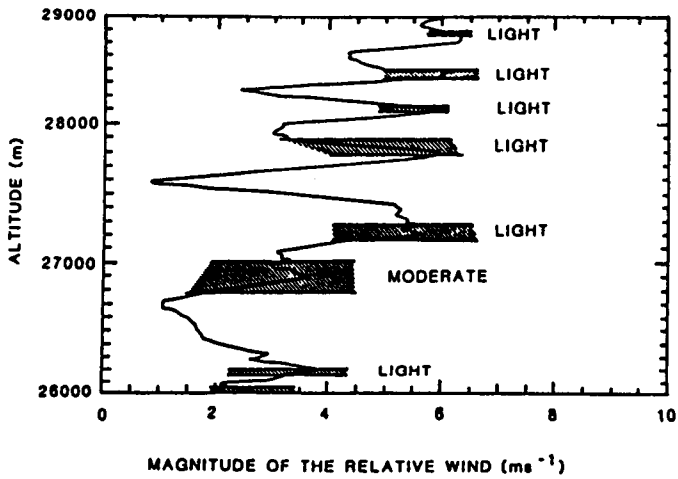


Figure 5. Correlation of turbulence occurrence with preferred sites within wave field suggesting linear rather than nonlinear saturation processes [Sidi and Barat, *J. Geophys. Res.*, 1986].

Gravity Wave Fluxes

Momentum flux: $\overline{u'w'} \sim \frac{\omega}{N} \overline{u'^2}$

Energy flux: $c_{gz} E \sim \frac{\omega}{N} (c - \bar{u}) \overline{u'^2}$

⇒ dominant fluxes by gravity waves with large u' or λ_z .

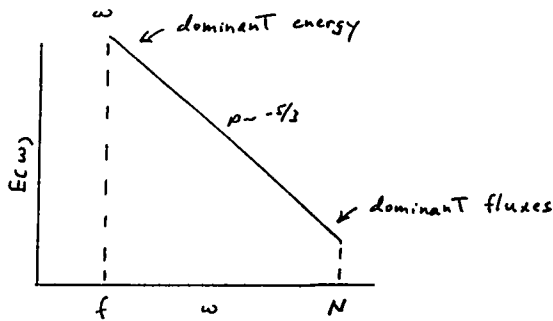


Figure 6. Schematic of gravity wave fluxes and their dominance by high frequency motions.

A Saturated Gravity Wave Spectrum: Saturation Conditions

Monochromatic wave: $\theta_z = 0 \Rightarrow \bar{\theta}^2/2 = \overline{\theta_z'^2}$

Gravity wave spectrum: $\bar{\theta}_z^2/2 = \int F_{\theta_z}(m) dm = \int \frac{m^2 \bar{\theta}^2}{p N^2} F_u(m) dm$

\Rightarrow saturated PSDs are

$$F_{\theta'/\theta}^s(m) \approx \frac{1}{10} \frac{N^4}{g^2 m^2} \quad \text{for} \quad \frac{\theta'}{\bar{\theta}}, \frac{T'}{\bar{T}}, \frac{e'}{\bar{e}}$$

$$F_u^s(m) \approx \frac{p}{10} \frac{N^2}{m^3} \quad \text{for} \quad u', v'$$

Variation of Wave Spectrum with $N(z)$

WKB scaling: $c_{gz} E \approx \frac{\omega}{m} E \sim \text{constant}$ (conservative, $\omega \sim \text{constant}$)

$$m_{GW} \sim N$$

$$\Rightarrow E_{GW} \sim m$$

$$\text{Thus } E_{WKB}(m > m_*) \sim N^3$$

$$E_{SAT}(m > m_*) \sim N^2$$

\Rightarrow Increase in $N(z)$ causes:

- enhanced wave dissipation and drag
- adjustment to new saturation spectrum

Consequences of a Saturated Gravity Wave Spectrum

Wave saturation and turbulence throughout atmosphere:

$$u'_z, \theta'_z \sim \text{bounded}, \quad E(z) \sim e^{z/H_E}, \quad H_E \sim 12 - 15 \text{ km}$$

No physical "breaking" level; smooth increase in drag and diffusion

Increases of $N^2(z) \Rightarrow$ enhanced saturation and enhanced drag and diffusion

Figure 7. Derivation of saturated spectrum amplitude following arguments of monochromatic theory [Smith et al., *J. Atmos. Sci.*, 1987] and scaling of wave energy due to changes in $N^2(z)$ showing tendency towards enhanced saturation.

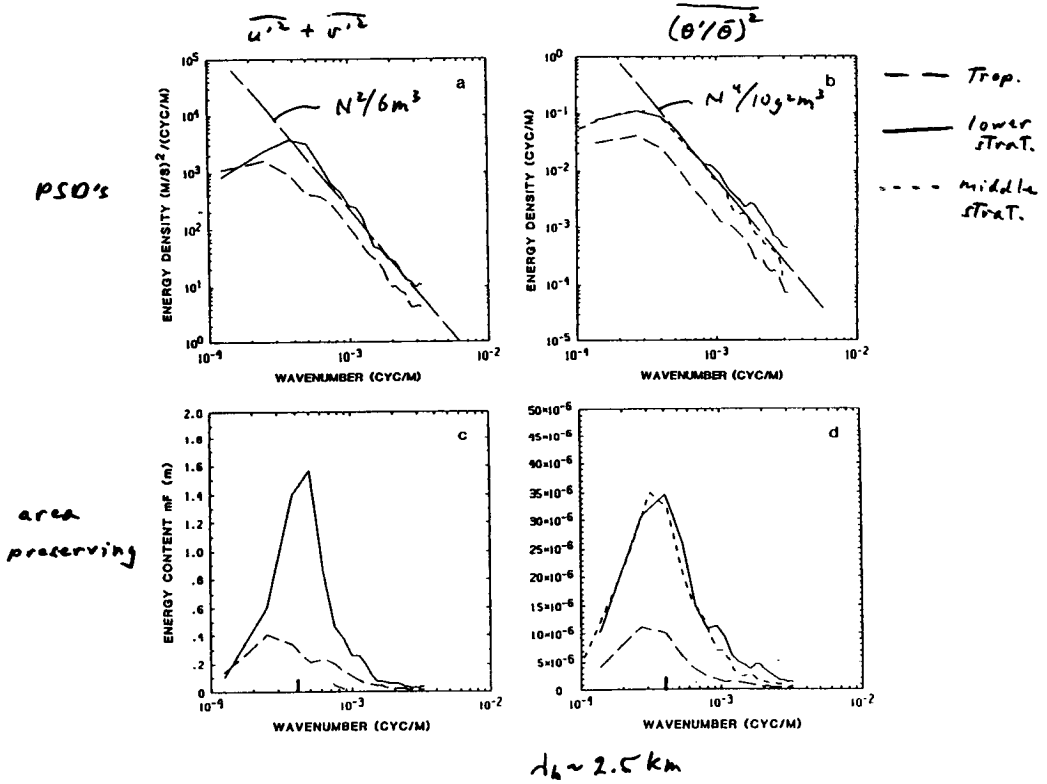


Figure 8. Predicted and observed saturated spectra of velocity and temperature using MU radar and balloon data [Fritts et al., *J. Atmos. Sci.*, 1988].

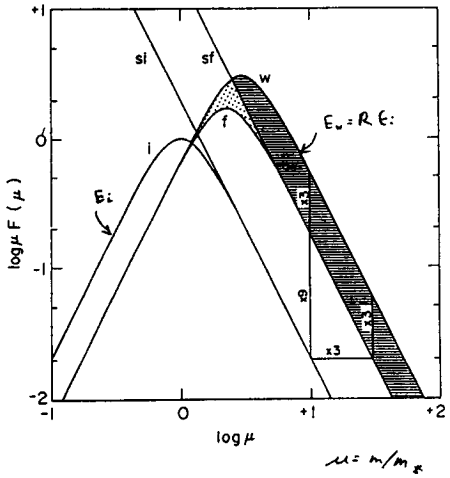
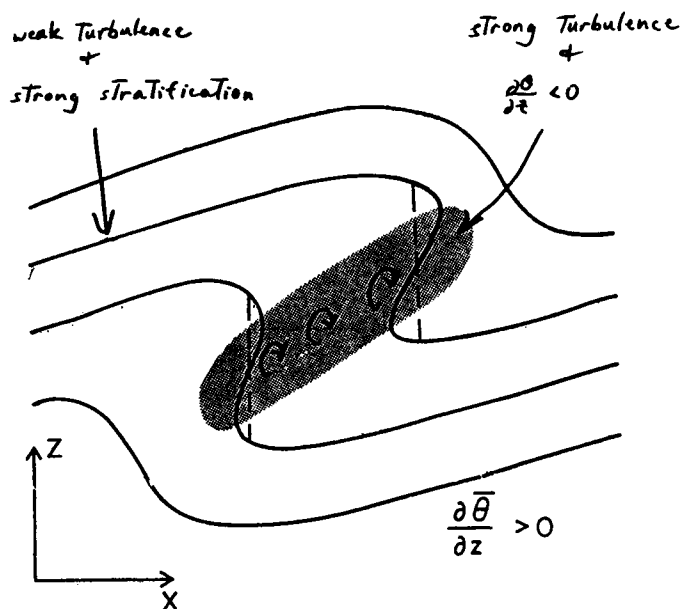


Figure 9. Illustration of the spectral change due to a change of 3 in $N(z)$ and the portion lost (shaded) due to enhanced saturation.



\Rightarrow reduction in effective diffusion
 observed $\sim 100 \text{ m}^2 \text{ s}^{-1}$
 required $\leq 20 \text{ m}^2 \text{ s}^{-1}$

$$\Rightarrow Pr \gg 1$$

Figure 10. Schematic of localized turbulence leading to an effective Prandtl number greater than 1.

Influences on the Large-Scale Circulation and Structure Gravity Wave Saturation/Dissipation

a. Momentum flux divergence and mean flow acceleration:

$$\frac{\partial}{\partial t} \bar{u} = -\frac{1}{\rho_0} \frac{\partial}{\partial z} (\rho_0 \overline{u'w'} \delta_-), \delta_- = 1 - f^2/\omega^2$$

$$\overline{u'w'}, \overline{v'w'} \sim 1 - 5 \text{ m}^2/\text{s}^2$$

$$\bar{u}_t, \bar{v}_t \sim 10 - 100 \text{ m/s/day}$$

b. Turbulent diffusion:

$$K \leq 20 \text{ m}^2/\text{s}, \text{ seasonally varying}$$

-plays some role, but appears less important now than thought previously.

Gravity Wave Variability

Geographic: Land/sea differences; Latitudinal source differences; Filtering by mean winds

Temporal: Seasonal and planetary wave modulation of sources and filtering; LF modulation of gravity wave energies and fluxes

Figure 11. Effects of wave saturation on the mean structure through momentum flux divergence and turbulent diffusion; Introduction to gravity wave variability.

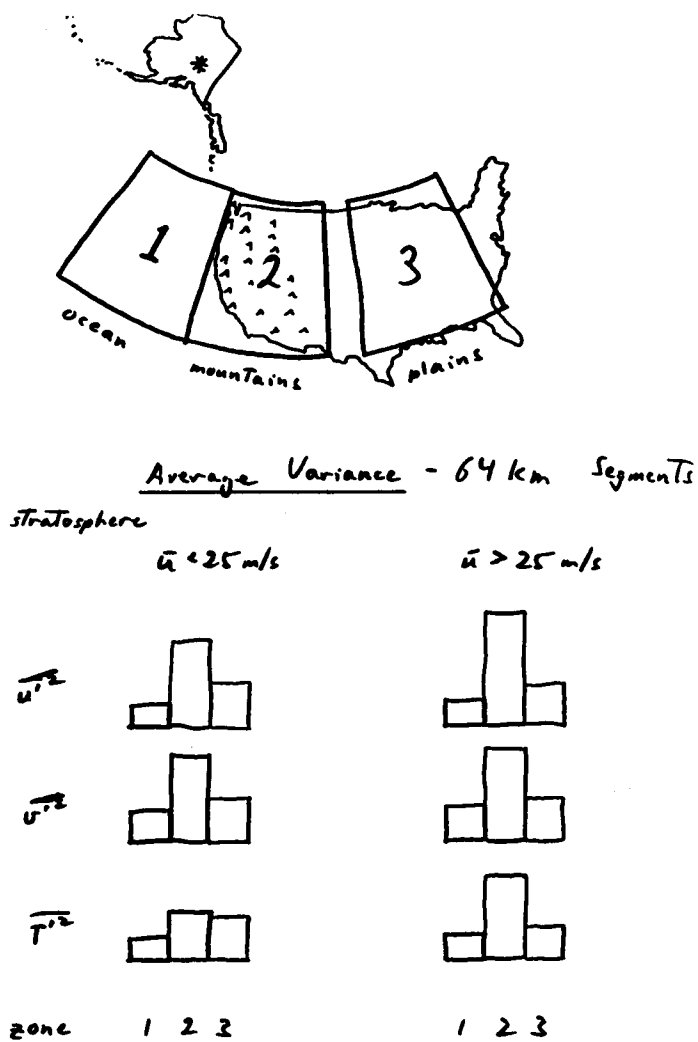


Figure 12. Geographic distribution of horizontal wind and temperature variance obtained with GASP data and suggesting strong topographic forcing [Nastrom et al., *J. Atmos. Sci.*, 1987].

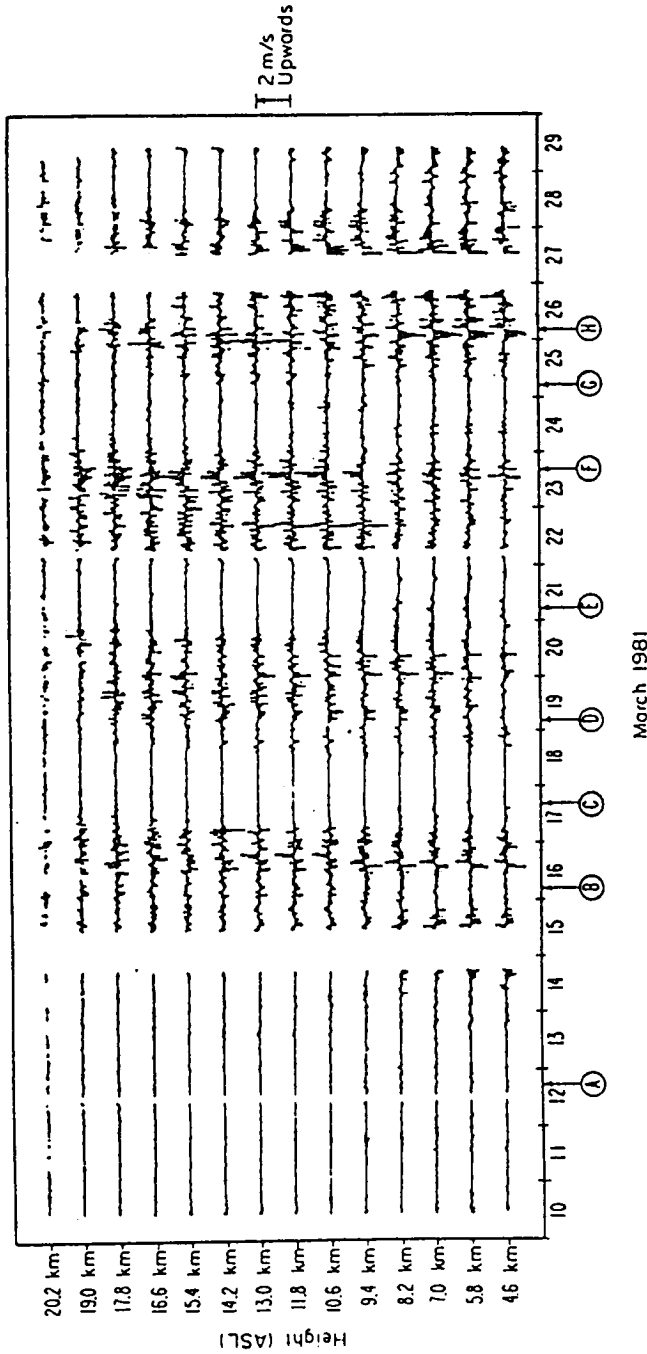


Figure 13. Vertical velocity variability from Platteville radar showing periods of enhanced activity correlating with strong topographic forcing [Ecklund et al, *Mon. Weather Rev.*, 1981].

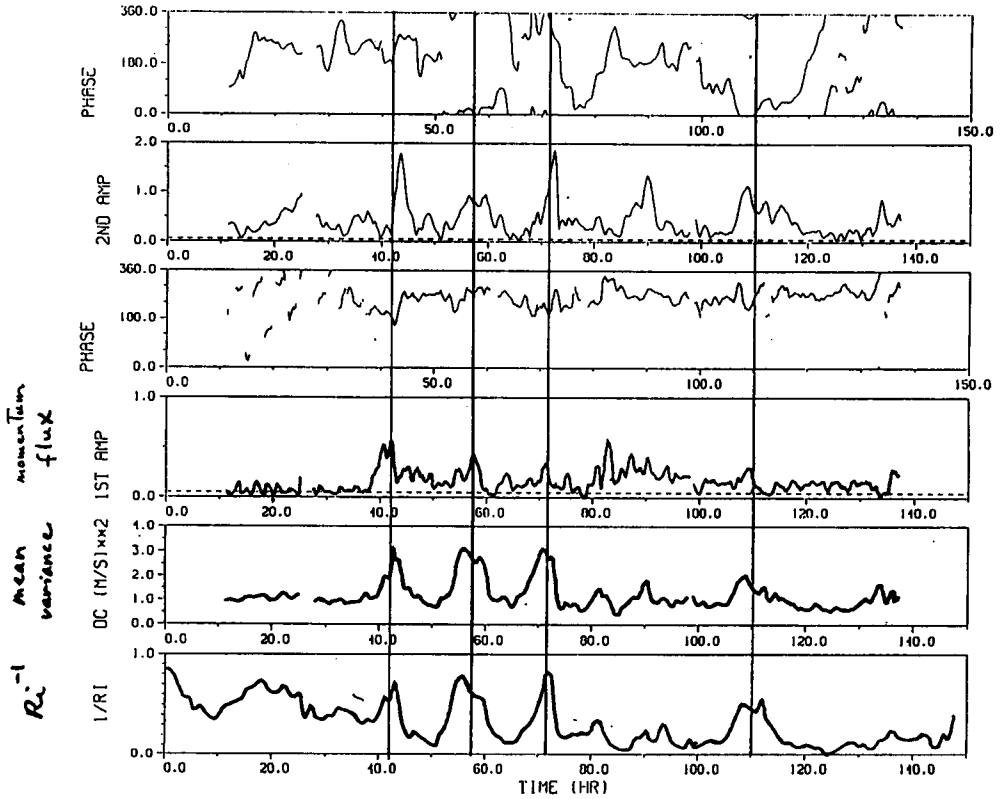


Figure 14. Correlation of inverse Richardson number Ri^{-1} , with mean variance and momentum flux suggesting shear-excited gravity waves [VanZandt et al., *J. Atmos. Sci.*, submitted, 1988].

ORIGINAL PAGE IS
OF POOR QUALITY

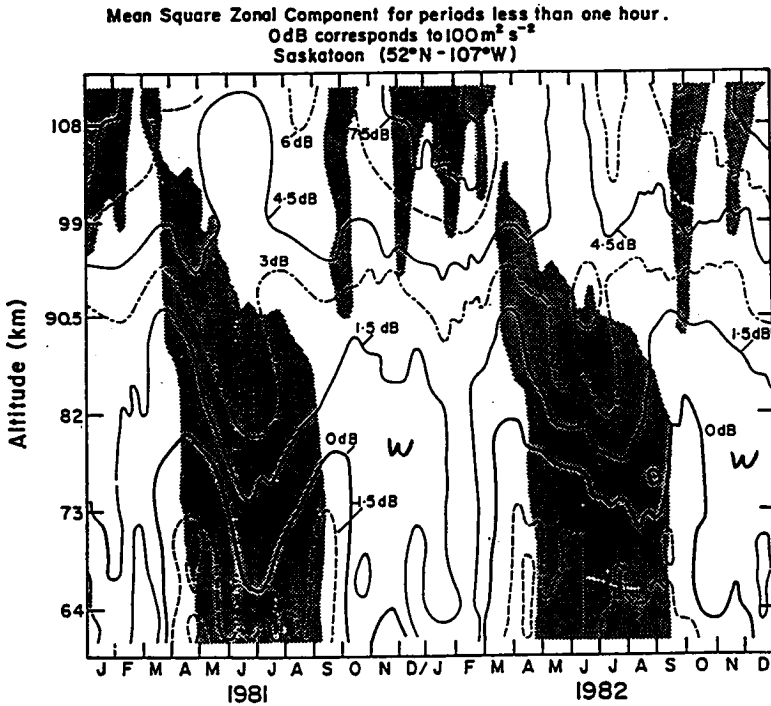


Figure 15. Time-height cross section of high frequency gravity wave zonal variance showing strong seasonal modulation and pronounced minima near equinoctial transitions [Meek et al., *Radio Sci.*, 1985].

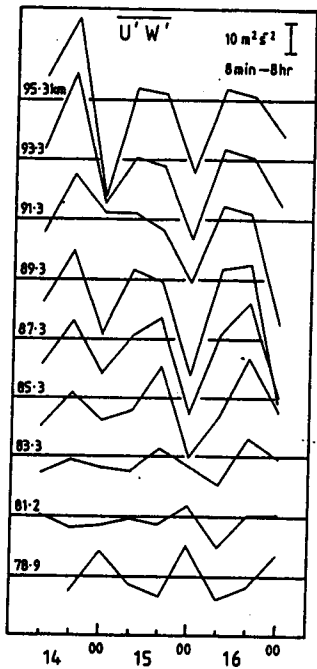


Figure 16. Eight-hour estimates of the momentum flux using the Adelaide HF radar which reveals a strong 24-h modulation and provides evidence of a strong modulation by the diurnal tides [Fritts and Vincent, *J. Atmos. Sci.*, 1987].

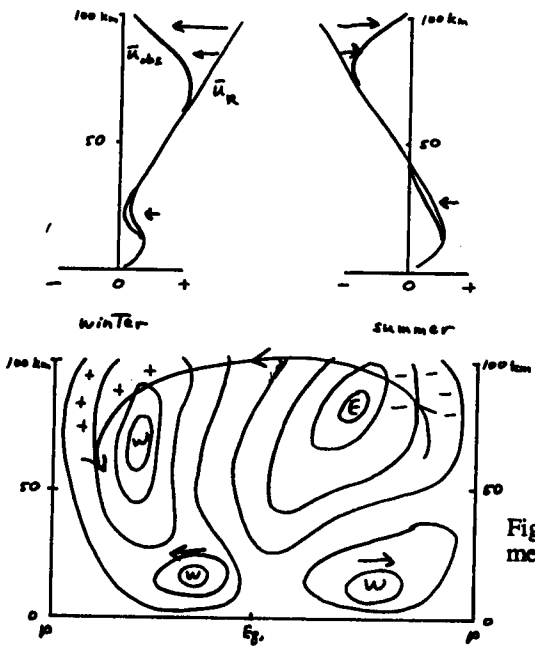


Figure 17. Schematic of gravity wave effects on mean wind profiles and the meridional circulation.

Unknowns and Future Needs

Causes and effects of gravity wave variability

- variable sources, source distributions and spectra
- filtering by/interactions with other motions
- forcing, wave excitation in middle atmosphere

Evolution of gravity wave/turbulence spectrum

- wave saturation
- effects of stratification

More complete, distributed gravity wave/turbulence climatology

- gravity wave sources
- wave parameters, amplitudes, fluxes
- wave drag and effective diffusion
- meridional propagation, fluxes

Parameterizations of

- wave and turbulence effects
- mechanisms of large-scale variability

Figure 18. Statement of unknowns and future needs for gravity wave and turbulence studies in the middle atmosphere.

4.2 OBSERVATIONS OF GRAVITY WAVE SCALES, FLUXES, AND SATURATION DURING MAP

I. M. Reid

Max-Planck-Institut für Aeronomie
Postfach 20, D-3411 Katlenburg-Lindau
Federal Republic of Germany

During the MAP/MAC period, considerable improvements in instrumentation and experimental technique have occurred, and many hitherto unavailable parameters relating to gravity waves have become available. Studies of individual wave events and simultaneous observations made with a variety of techniques have provided insight into wave saturation mechanisms. In addition, long data sets of upper middle atmosphere winds have been collected at a number of widely spaced sites, allowing climatological investigations of gravity wave amplitudes, wave number spectra, polarization, mean flow acceleration, and other saturation effects to be undertaken. In this paper, observations of gravity wave scales, momentum fluxes, saturation and saturation effects obtained during MAP/MAC, made on both a statistical and case study basis are reviewed.

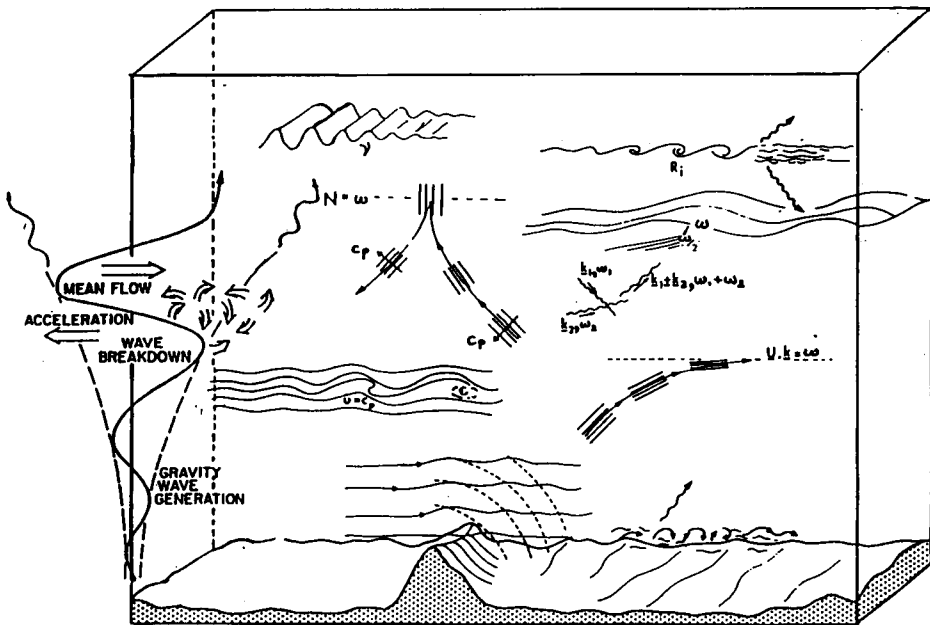


Figure 1. Schematic diagram showing processes whereby gravity waves interact with each other and with the background wind. (Adapted from a diagram by S. A. Thorpe).

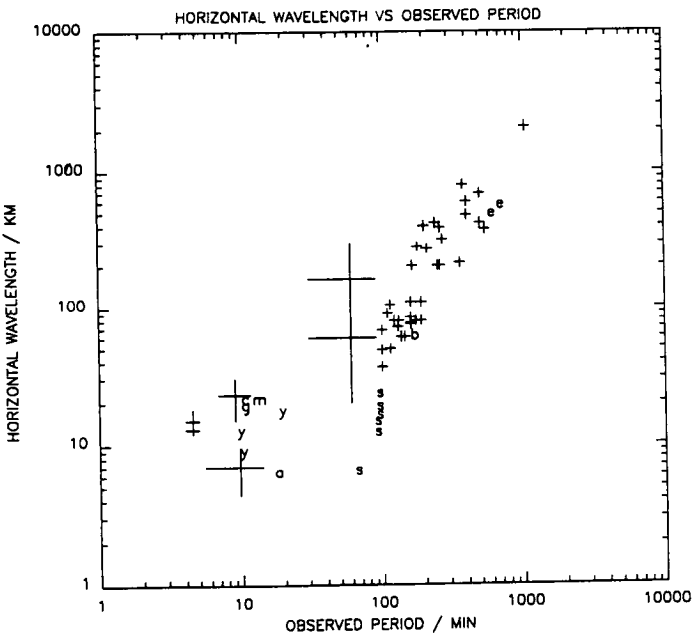


Figure 2. Collation of tropospheric and stratospheric observations of horizontal scale shown as a function of observed period.

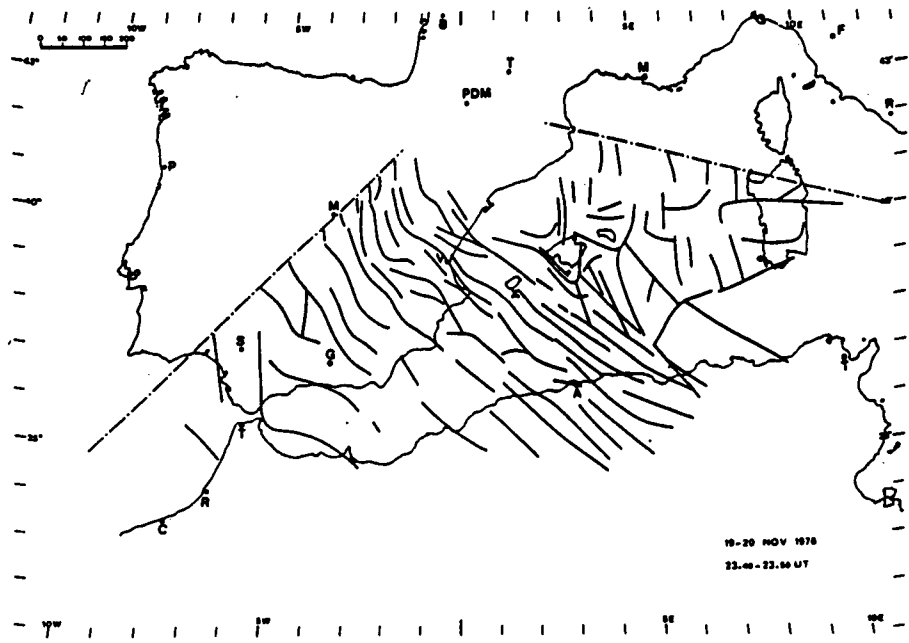


Figure 3. Bright crests evident in 558 nm airglow generally believed to be associated with the passage of gravity waves. [After Herse et al., *Appl Opt.*, 19, 355, 1980].

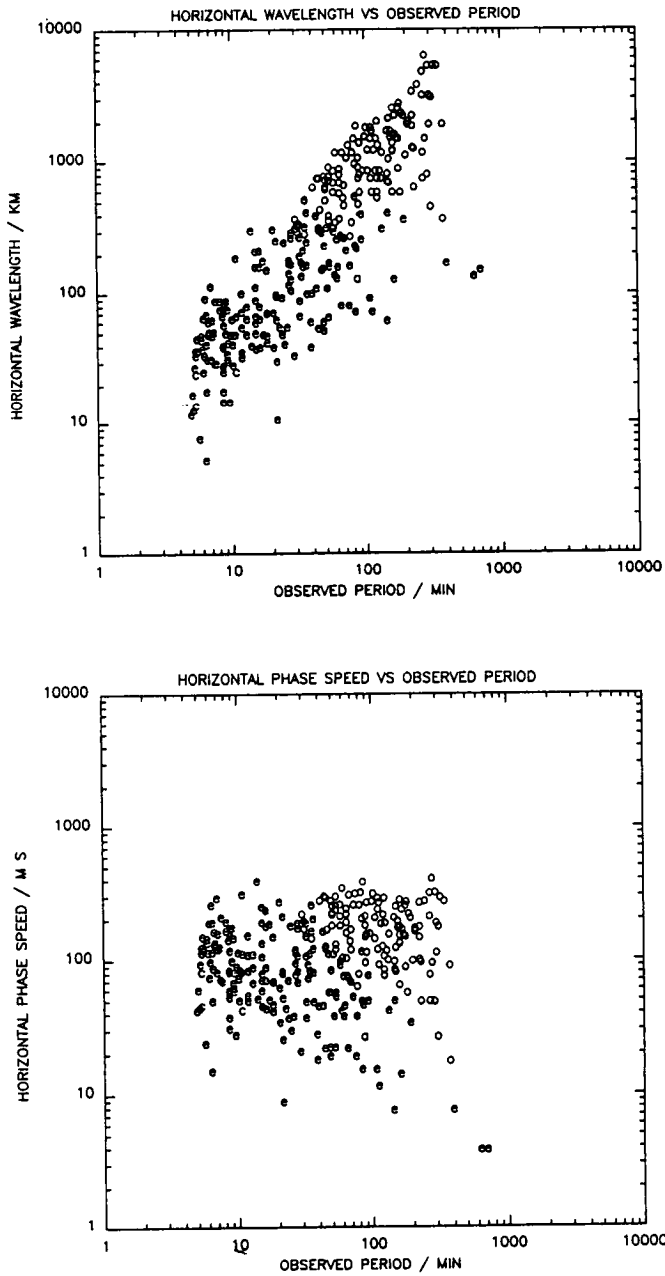


Figure 4. (a) Collation of 558 nm (~ 95 km) measurements of gravity wave horizontal scale shown as a function of observed period. (b) As for Figure 4(a) but for horizontal phase speed.

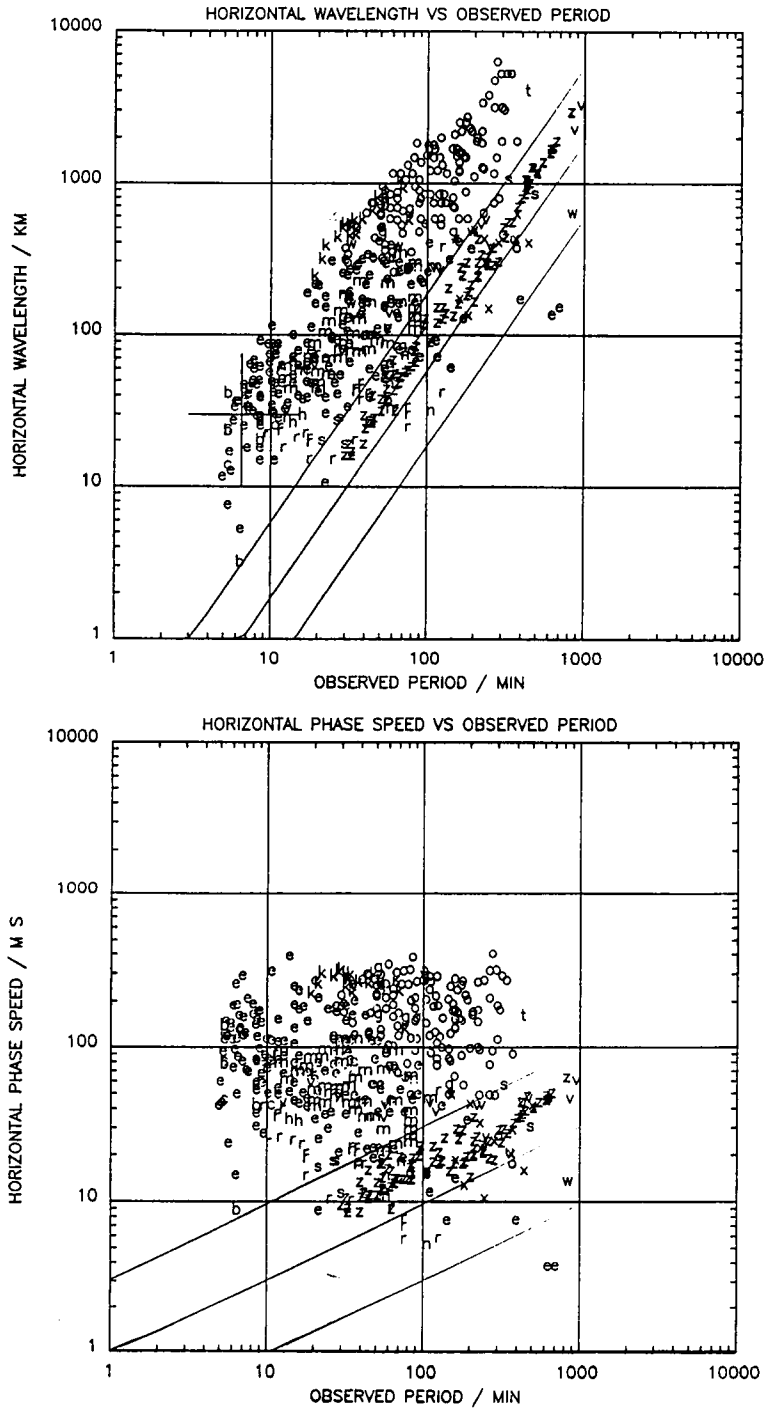


Figure 5. (a) Collation of radar and optical observations of mesospheric and lower thermospheric gravity wave horizontal scales. (b) As for Figure 5(a) but for horizontal phase speed.

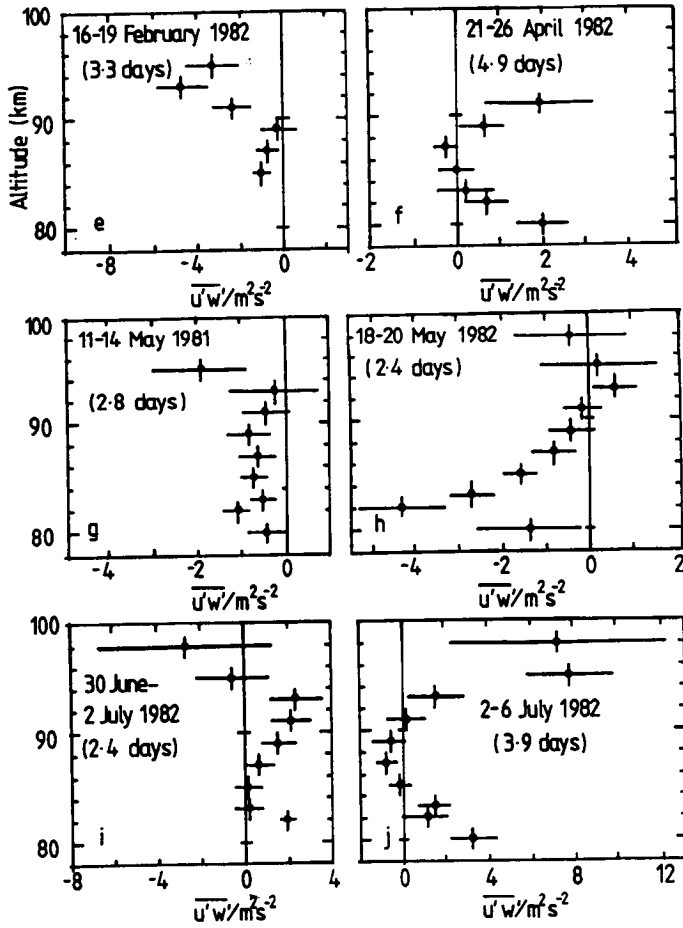


Figure 6. Measurements of the upward flux of zonal momentum obtained at Adelaide (35°S) in six different observational periods. [After Reid and Vincent, *J. Atmos. Terr. Phys.*, 49, 1987].

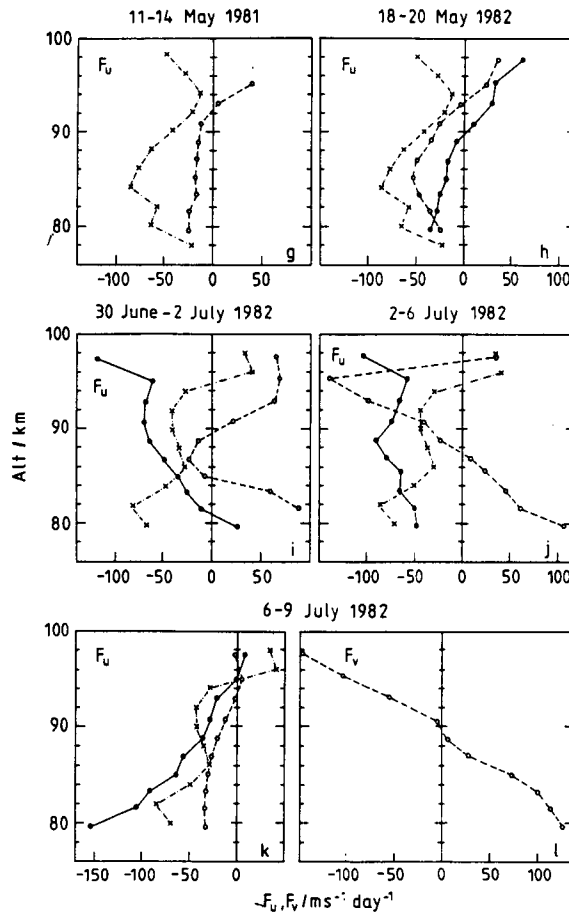


Figure 7. Zonal (F_u) and meridional (F_v) mean flow accelerations measured at Adelaide (open circles), the Coriolis torque due to the mean meridional wind component for the same period reversed in sign (solid circles), and for the monthly mean values measured at Adelaide between 1978-1983 (crosses). [After Reid and Vincent, *J. Atmos. Terr. Phys.*, 49, 1987].

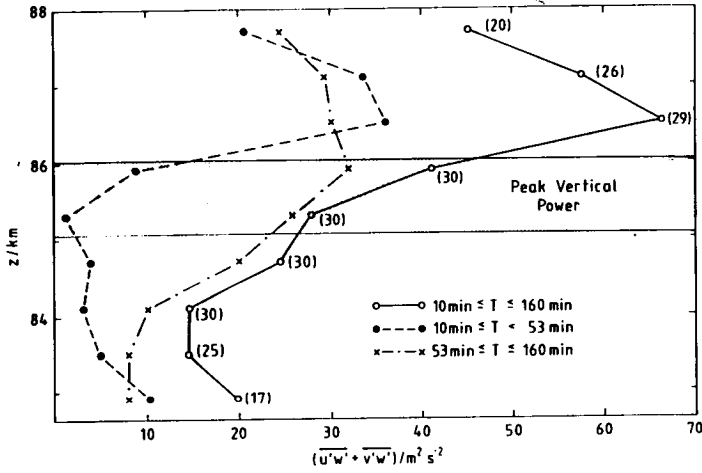


Figure 8. Total upward flux of horizontal momentum measured in a three hour period over Andoya, Norway, using the mobile SOUSY VHF (53.5 MHz) radar. The shaded area indicates the 3 dB of the radar echo. [After Reid et al., *Geophys. Res. Lett.*, 1988, in press].

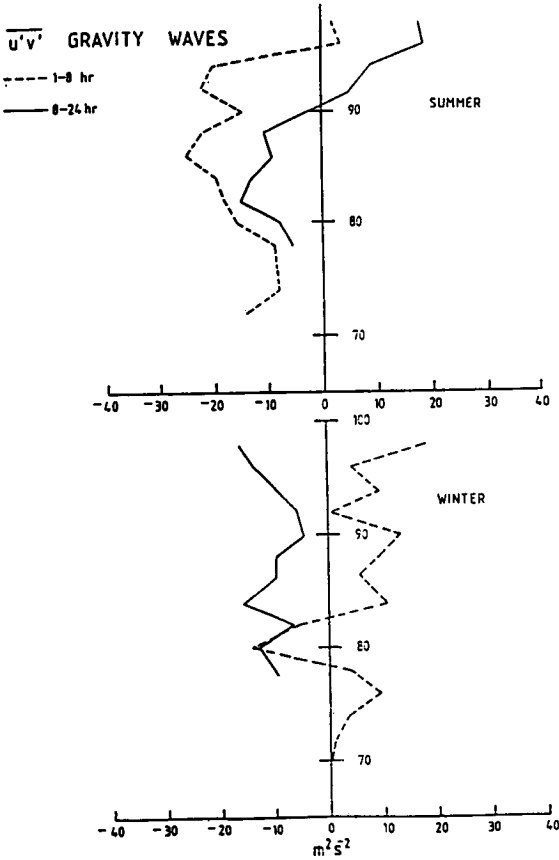


Figure 9. Horizontal transport of horizontal momentum measured at Adelaide. [After Vincent and Fritts, *J. Atmos. Sci.*, 44, 1987].

Vertical Energy Flux		
Gossard	leaving troposphere	100 mW m ⁻²
Chemin and Hauchecorne	50 km	30 mW m ⁻²
Vincent	85 km	12-13 mW m ⁻² (mid and low latitudes) 29 mW m ⁻² (high latitude)
Gavrilov and Kalov	90 km	1-6 mW m ⁻²
Gavrilov and Shved	95 km	1-8 mW m ⁻²
Jacobs and Tacka	95 km	15 mW m ⁻²
Maximize in Winter		
Maximize at high frequencies (periods less than ~1h)		

Figure 10. Measurements of the gravity wave vertical energy flux at various heights through the atmosphere.

Parameter	Range of values	Parameter	Range of values
τ	0.5-6 hrs	F_{xz}	1-4 m ² s ⁻²
V	6-20 m s ⁻¹	F_{yz}	1-10 m ² s ⁻²
λ_{11}	100-800 km	F_{xy}	2-20 m ² s ⁻²
λ_z	10-30 km	F_{Tx}	1-20 erg cm ⁻² s ⁻¹
C	20-160 m s ⁻¹	F_{Ty}	1-200 erg cm ⁻² s ⁻¹
F_z	1-6 erg cm ⁻² s ⁻¹	F_{Tz}	1-6 erg cm ⁻² s ⁻¹
F_x	1-20 erg cm ⁻² s ⁻¹	F_{mx}	2-10 10 ⁻⁸ kg m ⁻² s ⁻¹
F_y	1-10 erg cm ⁻² s ⁻¹	F_{my}	1-4 10 ⁻⁶ kg m ⁻² s ⁻¹
		F_{mz}	1-3 10 ⁻⁸ kg m ⁻² s ⁻¹

Figure 11. Summary of gravity wave characteristics obtained using meteor radars. Note that erg cm⁻² s⁻¹ = mW m⁻². [After Gavrilov, *Handbook for MAP*, 25, 1988].

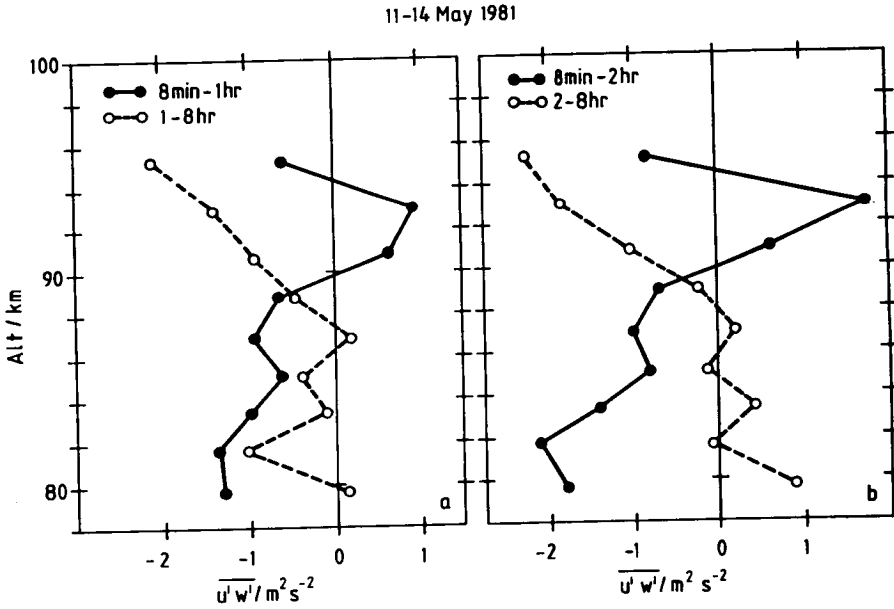


Figure 12. Contributions to the upward flux of horizontal momentum for different period ranges for observations made at Adelaide. Short period motions (≤ 1 h) contribute approximately 70% of the total flux. [After Reid and Vincent, *J. Atmos. Terr. Phys.*, 49, 1987].

FOR SHORT (OBSERVED) PERIOD GRAVITY WAVES (≤ 1 h)

- SCALE FOUND TO INCREASE FROM ABOUT 30 KM AT 10 MIN TO ABOUT 80 KM AT 100 MIN (SUGGESTS 20 AND 55 KM RESP. FOR ISOTROPIC WAVEFIELD)
- VALUES OF $\overline{w'w'}$ UP TO $3\text{m}^2\text{s}^{-1}$ FOUND TO BE ASSOCIATED WITH THESE WAVES, BUT MORE TYPICAL VALUES ARE ABOUT $1\text{m}^2\text{s}^{-1}$
- FLUX CONVERGENCE ASSOCIATED WITH INDIVIDUAL SHORT PERIOD GRAVITY WAVE EVENTS APPEARS EASILY ABLE TO PROVIDE SUBSTANTIAL ($\sim 50\text{ms}^{-1}\text{day}^{-1}$) MEAN FLOW ACCELERATION
- 89% OF VALUES OF ZONAL SCALE LESS THAN 80 KM
- 87% OF ZONAL PHASE VELOCITIES WITHIN 60ms^{-1} OF ZERO
- MOST LIKELY ZONAL PHASE SPEED (44%) LAY IN $20\text{--}30\text{ms}^{-1}$ INTERVAL

FOR 8 MIN-8H PERIOD BAND

- WHEN AVERAGED OVER PERIODS OF 2-5 DAYS, MAGNITUDE OF $\overline{w'w'}$ TYPICALLY LESS THAN $3\text{m}^2\text{s}^{-1}$
- LARGEST VALUES OBSERVED IN WINTER AND SUMMER
- ABOUT 70% OF $\overline{w'w'}$ DUE TO PERIODS LESS THAN 1H AND CONTRIBUTION TO F_z IS COMPARABLE
- ZONAL MEAN FLOW ACCELERATION OFTEN IN CORRECT SENSE AND OF SUFFICIENT MAGNITUDE TO DECELERATE THE ZONAL WIND COMPONENT AND TO BALANCE THE CORIOLIS TORQUE DUE TO THE MEAN MERIDIONAL WIND
- WHEN AVERAGED OVER PERIODS OF AROUND 3 DAYS, VALUES OF F_z UP TO $190\text{ms}^{-1}\text{day}^{-1}$ WERE CALCULATED, BUT MORE TYPICAL VALUES $\sim 50\text{--}80\text{ms}^{-1}\text{day}^{-1}$
- VALUES OF $\overline{u'w'}$ AND $\overline{v'w'}$ FOUND TO BE SIMILAR

Figure 13. Summary of characteristics of individual short period (≤ 1 h) gravity waves (top), and of motions in the 8 min - 8 h period band (bottom) measured at Adelaide by Reid and Vincent [*J. Atmos. Terr. Phys.*, 49, 1987].

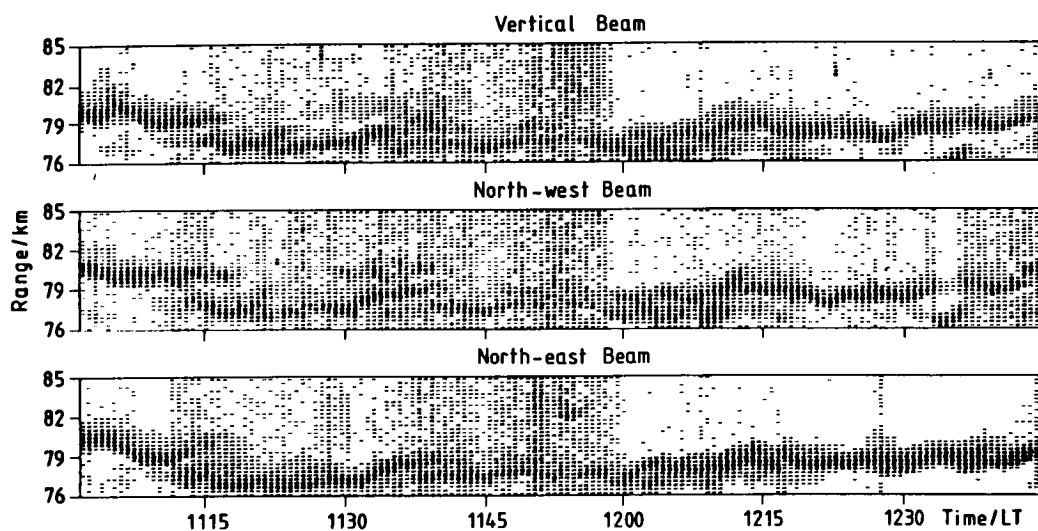


Figure 14. Cat's-eye-like structures consistent with dynamical instability observed at Andoya with the mobile SOUSY radar on 1 February 1984 in three different beam directions. [After Reid et al., *Nature*, 327, 1987].

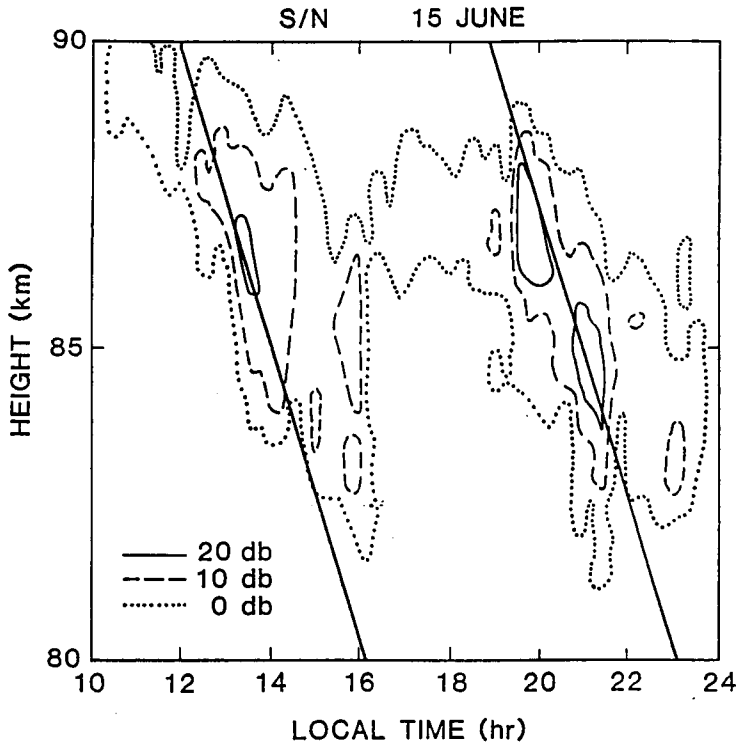


Figure 15. Power measured during the STATE campaign with the Poker Flat VHF (50 MHz) radar. The diagonal lines indicate the region of maximum instability induced by a long period gravity wave. [After Fritts et al., *J. Geophys. Res.*, 1988, in press].

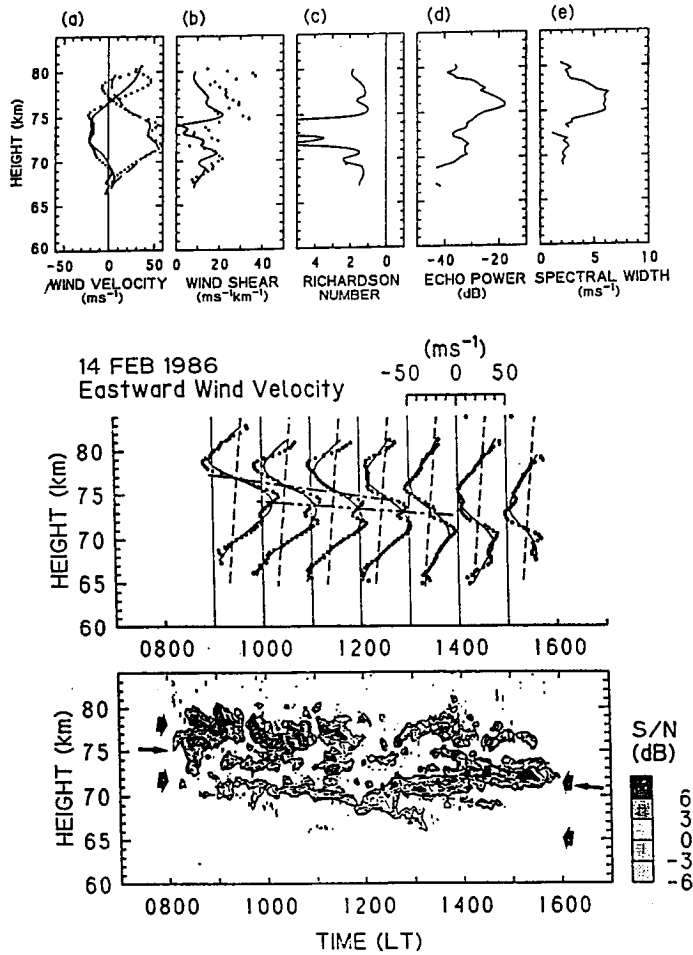


Figure 16. (top) Wind velocity, shear, wave modified Richardson number, echo power and spectral width, (center) Vertical wind profiles of the corresponding inertia period gravity wave, and (bottom) The echo power as a function of height and time measured using the MU VHF radar [After Yamamoto et al., *Physica Scr.*, 1988, in press].

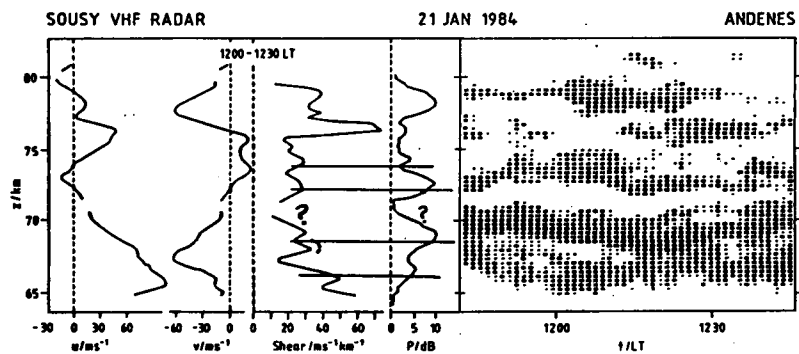


Figure 17. (left) Horizontal wind components, the shear and mean power measured between 1200-1230 LT at Andoya on 21 January 1984, and (right) A height-time intensity plot of the backscattered power for approximately the same interval. [After Czechowsky et al., submitted to *Geophys. Res.*, 1988].

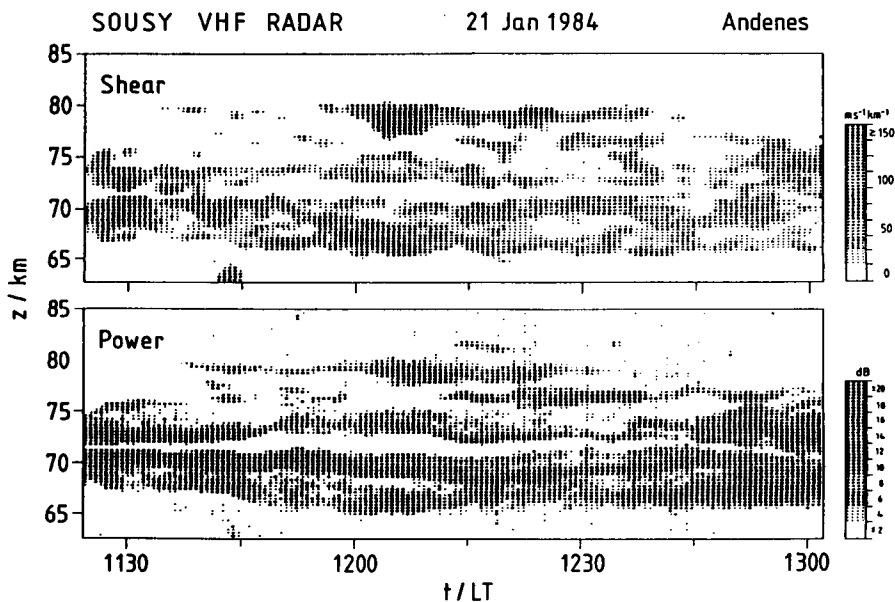


Figure 18. Height-time intensity plot of shear (top) and backscattered power (bottom) on 21 January 1984 at Andoya. [After Czechowsky et al., submitted to *Geophys. Res.*, 1988].

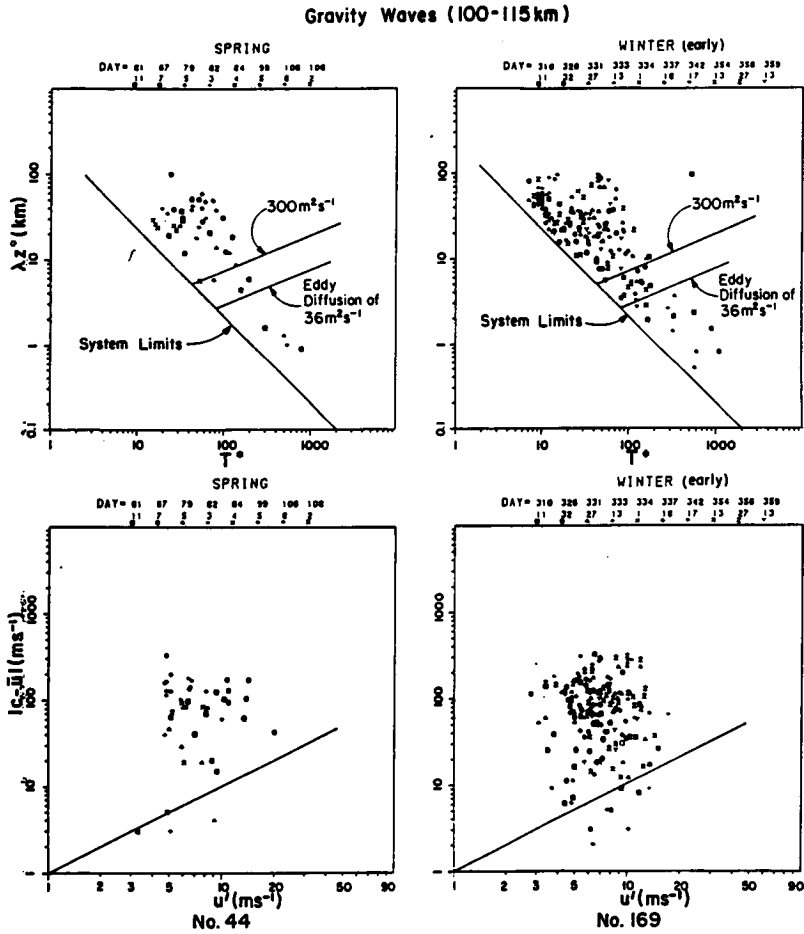
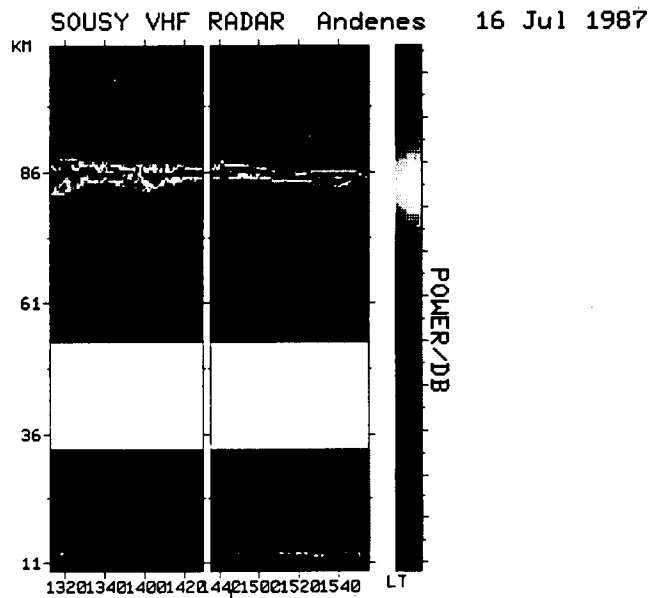


Figure 19. Gravity wave characteristics measured at Saskatoon, Canada. The condition for convective instability of monochromatic gravity waves $|c - \bar{u}| > u'$ is rarely met. [After Manson and Meek, *J. Atmos. Sci.*, 1988].

GRAVITY WAVES IN THE UPPER MIDDLE ATMOSPHERE PRODUCE

- ZONAL MEAN FLOW ACCELERATION AND BALANCE CORIOLIS TORQUE DUE TO MEAN MERIDIONAL WIND
- TURBULENCE → SCATTERING IRREG.
- HEATING/COOLING
- SOME FORMS OF SCATTERING STRUCTURES
- VARIATIONS IN EDDY DIFFUSIVITY/ADVECTION AND HENCE MINOR CONSISTUENT CONCENTRATIONS
- SOME VARIATIONS IN AIRGLOW INTENSITY IN TIME/SPATIALLY PERHAPS SEASONALLY/LATITUDINALLY



THEY ARE

- UBIQUITOUS (High Frequency)
- ENERGETICALLY MOST IMPORTANT AT LOW FREQUENCIES
- MOST IMPORTANT FOR VERTICAL TRANSPORT OF MOMENTUM AT HIGH FREQUENCIES
- DIFFICULT TO OBSERVE - OFTEN SUPERIMPOSED
- SUBJECT TO DISSIPATION/DIFFUSION SATURATION/BREAKING
- GENERATED IN TROPOSPHERE ($\geq 65\%$ long period)
- TRANSIENT IN SENSE THAT MEAN FLOW ACCELERATIONS OCCUR SPORADICALLY

Figure 20. Summary of some gravity wave characteristics in the upper middle atmosphere.

4.3 MEASUREMENTS OF TURBULENCE AND ITS EVOLUTION AND VARIABILITY DURING MAP

W. K. Hocking

Department of Physics and Mathematical Physics
University of Adelaide, GPO Box 498
Adelaide, S. A. 5001, Australia

The understanding of turbulence in the middle atmosphere has improved considerably during the MAP period. For a theoretical viewpoint, several advances have been made including understanding the ways in which turbulence is generated, and the differences between the rates of diffusion of momentum and heat. Experimentally, a proper understanding of how radars can be used to measure turbulence has emerged, and turbulent energy dissipation rates in the middle atmosphere have been measured with MF, HF, and VHF radars. New rocket techniques have been developed which have enabled detailed studies of the fine structure of turbulence to be made. Whilst some discrepancies between techniques still exist, these will undoubtedly be resolved soon, and these different techniques are already providing a great improvement in the understanding of turbulence on a global scale. It is to be hoped that the years following MAP will be as productive as the years of MAP, and that these improvements can be built on to provide even greater understanding.

1. Visualization of Turbulence

Although turbulence is in general associated with some sort of chaotic behavior, its visualization differs from scientist to scientist. To some, the details of the fine scale structure are completely unimportant, and turbulence is represented by a simple "K" term in the fluid dynamical equations, viz.

$$K \frac{\partial^2 u}{\partial z^2} \quad (1)$$

and similar terms (Figure 1). These "K" coefficients hide a multitude of sins, and represent perhaps the coarsest visualization of turbulence. No heed is paid to the time scales involved in mixing processes, and K represents simply a coefficient which determines how "well" the fluid mixes. Nevertheless, for many workers this simple visualization seems adequate. An only slightly more sophisticated approach involves comparing the mixing of a turbulent field with the mixing which occurs at a molecular level in a gas, and a "diffusion coefficient" D is defined through the relations like

$$\sigma_z^2 = 2 D t \quad (2)$$

Here, σ_z^2 represents the mean square vertical displacement of an originally compact array of parcels which spreads out over time t. The analogy with molecular processes is quite poor, however, and if indeed σ_z^2 does vary proportionally to t it is more fortuitous than rigorous. Nevertheless, this representation does at least attempt to consider the time scales associated with the turbulent mixing, something that (1) does not.

More refined consideration of the temporal variation of σ_z^2 with respect to time shows that (2) is incorrect, because as the particles diffuse apart, larger scale motions become effective, hastening the process. In fact

$$\sigma_z^2 \approx \beta \epsilon t^3 \quad (3)$$

more accurately describes the diffusive process, although the power of t depends largely on the spectrum of scales within the turbulent area.

Approaches to Turbulence

1. K-theory

$$K \frac{\partial^2 u}{\partial z^2} \quad \text{etc.}$$

$$(\rho \overline{u'w'}) = -\rho K_m \frac{\partial u}{\partial z}$$

2. Molecular "analogy"

$$\sigma_z^2 = 2Dt$$

3. More refined

$$\sigma_z^2 \approx \beta \epsilon t^3$$

4. Examination of fine detail

- intermittency
- structure of "eddies", etc.

5. New perspectives on turbulence and turbulent diffusion

- Stokes diffusion
- Deterministic chaos

Figure 1. Measurements of turbulence and its evolution and variability during MAP.

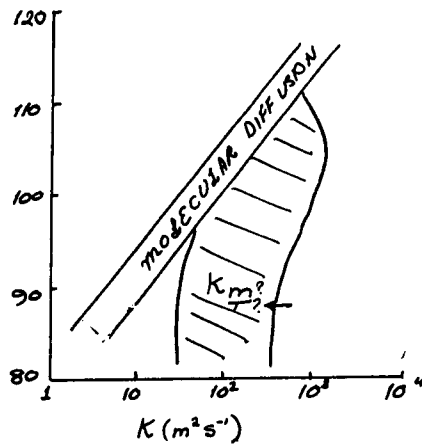


Figure 2. From Hocking [1987].

2. The "Gross" Approach

These types of "gross overview" descriptions, in which only the consequences of turbulence are important, and its detail is not, shall be referred to as "gross" views.

Many attempts have been made to make estimates of "K" in the middle atmosphere, largely by utilizing equations like (1). For example, one can generate equations which describe momentum and fluid motions in the atmosphere, leaving "K" as an "unknown" variable, and then proceed to use measurements of other known quantities like wind speeds, temperature distribution, and gravity wave fluxes to infer values for K. One of the most recent and best-known attempts at this is the model due to Garcia and Solomon [1985].

It is also possible to include chemistry in these models, and use measurements of concentration of atomic and molecular species to infer values for K. Early attempts at this include papers by Johnson and Wilkins [1965], Colegrove et al. [1965] and others. These authors looked in particular at the relative concentration of atomic oxygen and molecular oxygen at 90 and 120 km to infer information about K. More recently Groves [1986] has done similar things. When this type of approach is adopted, profiles of K as a function of height can be deduced. Figure 2 shows the range of values within which most measurements lie.

When one begins to consider these "diffusion" coefficients a little more carefully, however, it becomes clear that it is necessary to distinguish different types of K values. The diffusion coefficient for momentum is different from that for temperature, for example, and one needs to define K_T and K_m as separate entities. The rates between them, $P_T = K_m/K_p$, is called the Prandtl number. The estimates made by Garcia and Solomon, for example, represent estimates of K_m . The measurements in Figure 2 represent K_T . Values of K_m estimated by Garcia and Solomon agree with the profile for K_T in Figure 2. However, recently Strobel et al. [1987] have carefully constructed a computer model involving as much atmospheric chemistry as possible. They assumed a variety of forms for K_T and compared resultant profiles of minor species to measured values. An example is shown in Figure 3, for four different model K_T profiles. As a conclusion of their results, Figure 4 shows the acceptable range of K_T values which they deduced. The values are clearly less, by an order of magnitude, than those indicated earlier, and also less than the values for K_m inferred by Garcia and Solomon. Strobel et al. have taken this to infer that the Prandtl number in the middle atmosphere is about 10, a significant result. But before one accepts this argument, several issues need to be answered.

First, early estimates of the K_T by Johnson and Wilkins [1965] give much larger values for K_T , as do more recent estimates by Groves [1988]. It is certainly easy to dismiss the early results as being incorrect, due to the lack of sophistication of their models. However, Strobel's results show K_T to be much less than the molecular diffusion coefficient ν , so $(K_T + \nu)$ is $\sim \nu$. The results are very insensitive above 85 km, so we can only make use of these data below that height.

3. A Closer Look

Often this gross view is inadequate however. Even for workers who only need to know an estimate of K, it is useful to look closer at the turbulence causing the diffusion. To some, turbulence is visualized as a homogeneous process acting everywhere, something like the process in the atmospheric boundary layer, and that diffusion occurs simply because of this. Inertial range turbulence theory is adequate for such a model. In such a turbulent patch, it is possible to show that an individual cloud of particles which are initially close together diffuse apart in a manner

$$\sigma^2 = \beta \epsilon t^3 \quad (4)$$

as already discussed. One can then develop models around such a visualization.

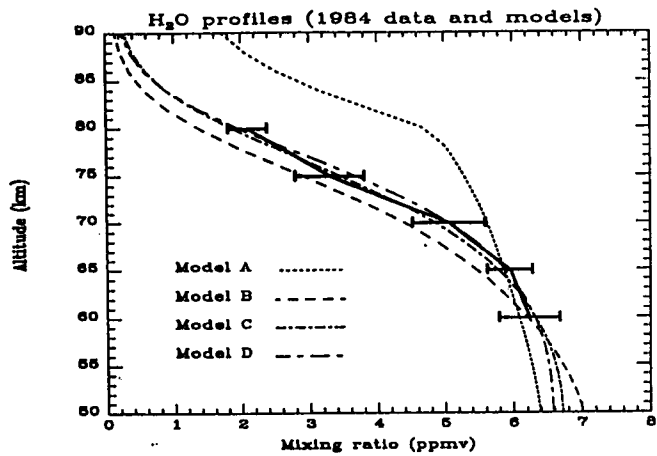


Figure 3. From Strobel et al., [1987].

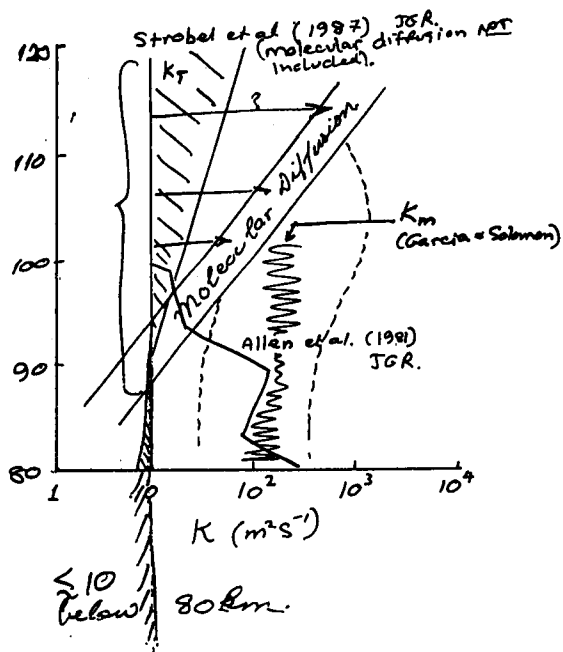


Figure 4.

Unfortunately, however, the middle atmosphere is not so simple! (In fact, turbulence generally is not.) Rather than being a homogeneous process acting uniformly throughout the region, it has been clearly shown through the MAP period that turbulence is both temporally and spatially intermittent. It occurs only for short periods of time at varying spatial locations. This is shown particularly well by Figures 5, 6, and 7 which show the occurrence of turbulent events in the upper troposphere and lower stratosphere. Clearly, events occur intermittently and last for varying lengths of time. Turbulent layers also have varying depths and spatial extents.

It appears that most of the turbulence is due to gravity waves and tides, and especially due to the superposition of gravity waves. The waves add up in such a way that R_i drops below 0.25, and even 0.0, producing instability. Fritts and Rastogi [1985] have shown that convective breakdown seems to be the major cause especially at high ω . Desaubies and Smith [1982] have modeled the results of an ensemble of gravity waves adding together, and do indeed find that a random distribution of breaking heights, times, and layer depths result. Figures 8 and 9 are for oceans, but similar concepts apply in the atmosphere.

The consequences of this intermittency are important. They mean, for example, that we must revisualize how large-scale turbulent diffusion takes place. An important proposal due to Dewan [1981], VanZandt and later Woodman and Rastogi [1984] suggested that the random occurrence of layers acts like a Monte Carlo process gradually causing diffusion, as first one layer forms, causing diffusion, and later another forms to cause transport over the depth of that layer. Thus the factors which control the large-scale diffusion are not the rates of diffusion across individual layers, but the frequency of occurrence and depth of individual layers (Figure 10).

Other consequences of the intermittency of turbulence include the possibility that the average rates of diffusivity of momentum and heat may be different, and that the Prandtl number may exceed 1, and perhaps be in the range 1 to 3 [Fritts and Dunkerton, 1985]. This is to say that if one parameterizes the rate of heat transport as $\alpha K_t (\partial\theta/\partial z)$, where $\partial\theta/\partial z$ is the mean temperature gradient, ignoring the effects of the wave on the mean, then the effective diffusive coefficient which must be used to describe the rate of diffusion is less than it would be if we properly included the effect of the wave in $\partial\theta/\partial z$. This is not so for momentum diffusion, because $\bar{u'w'}$ are not in phase quadrature.

4. Measurements of Turbulence

At this level of understanding, we have sufficient knowledge to make useful measurements of turbulence intensities. The three most direct techniques for measurements of turbulent energy dissipation rates used during the MAP period were based on balloons (stratosphere), rockets and radar experiments. There are many many subtleties associated with these techniques which I do not wish to dwell on here. They include such aspects as radar beam-broadening, layer thickness, and ion-neutral density mixing ratios. Other effects are also important as balloons can only be launched in quiet conditions, etc. Nevertheless, useful measurements have been made. For example, Barat [1982] and colleagues measured detailed temperature and velocity fluctuation in the stratosphere with balloon-borne anemometers (Figure 11). They found that the resultant structure function showed at least some ranges which an $r^{2/3}$ law held (Figure 12) and used their data to infer turbulent energy dissipation rate in the stratosphere. Rocket measurements have been able to produce detailed spectra of ion density fluctuations, (Figures 13 and 14) [Royrvik and Smith, 1984; Thrane et al. 1987], neutral species fluctuations, and mass spectrometer measurements [Luebken et al., 1987] Whilst not always showing the classic $k^{-5/3}$ Kolmogoroff law, most spectra hovered around the mark, and inferences about turbulent energy dissipation rate were possible. Large variability was found, and values were generally in the range 10^{-4} to 10^{-1} Wkg^{-1} above 80 km. Mesospheric radar measurements have also been made, particularly at Adelaide. This

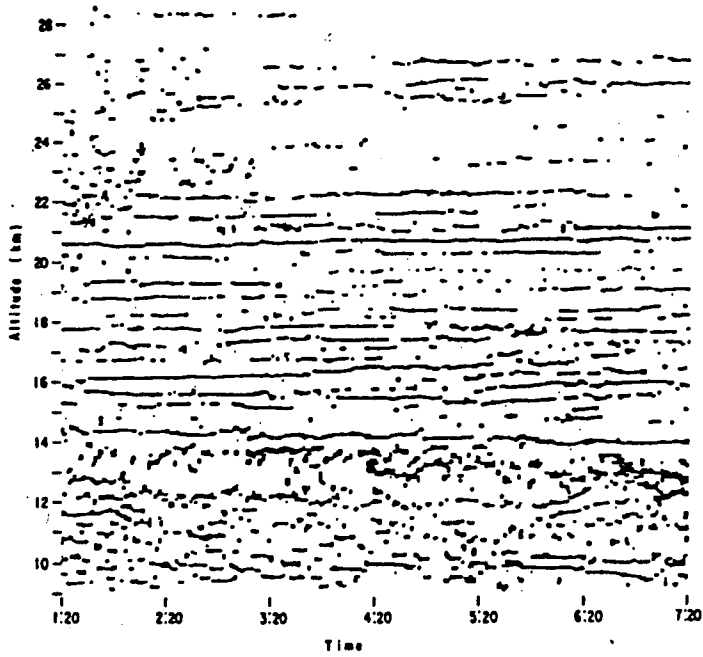


Figure 5. A map showing the evolution of thin turbulent layers over 9 - 28 km from radar observations at Arecibo. [Woodman and Rastogi, 1984].

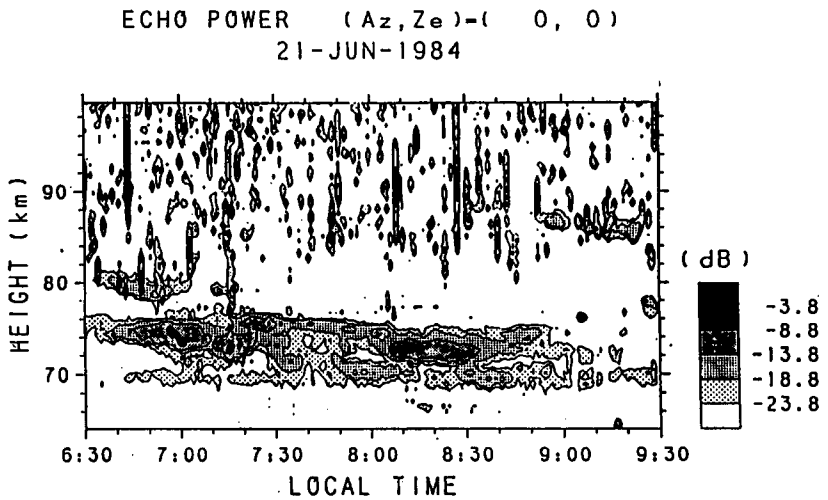


Figure 6. Time-height contour of thermospheric echo power in the vertical beam direction [Sato et al., 1985].

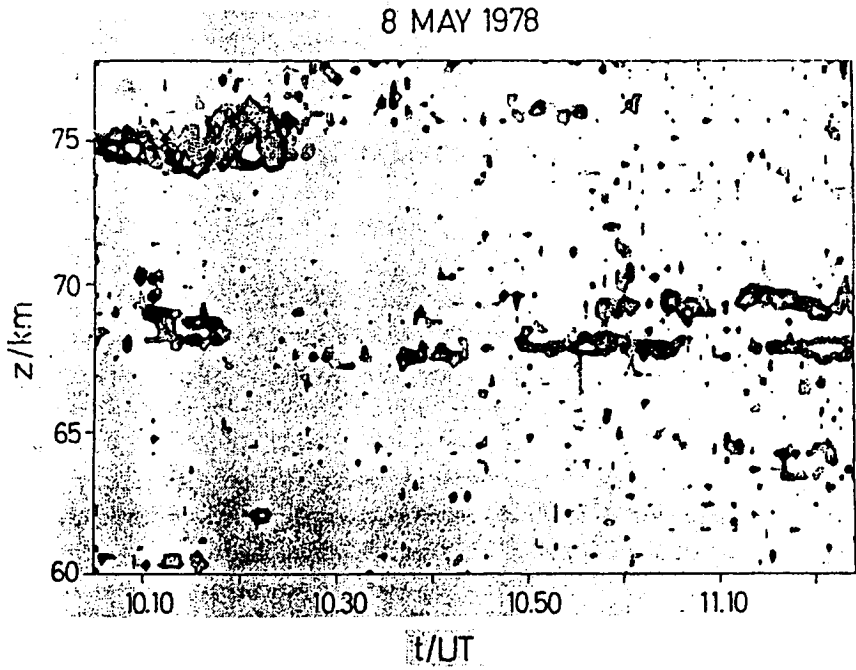


Figure 7.

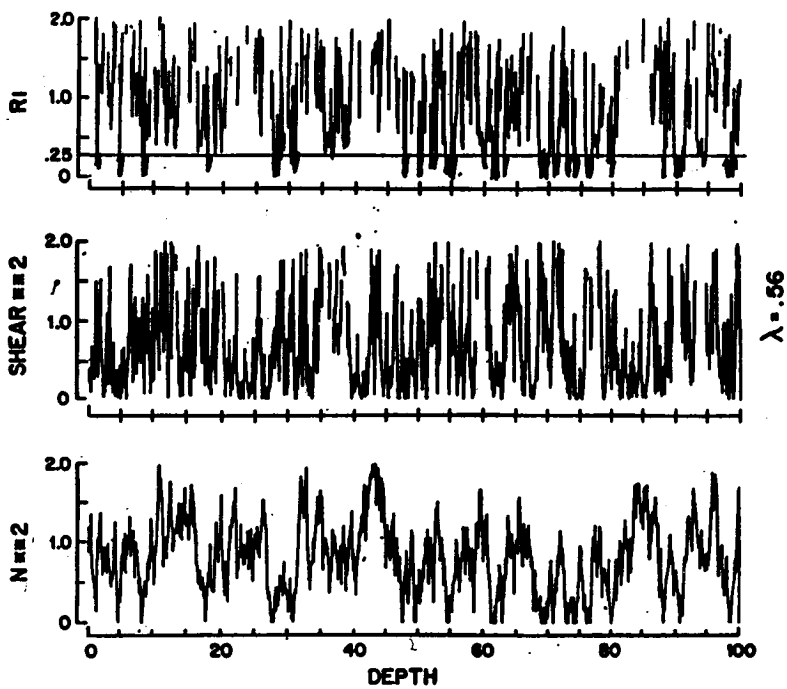


Figure 8. From Desaubies and Smith [1982].

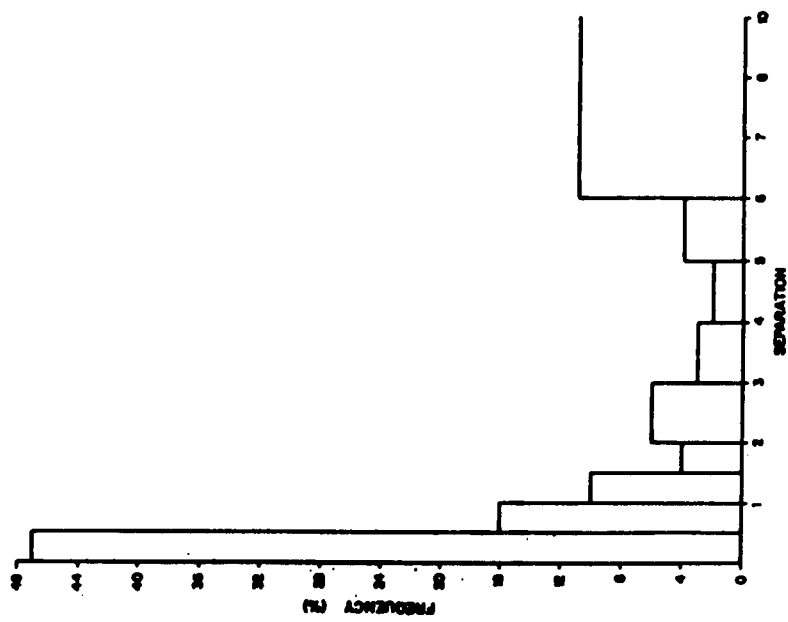


Figure 9. (b) Histogram of separation between events [Desaubies and Smith, 1982].

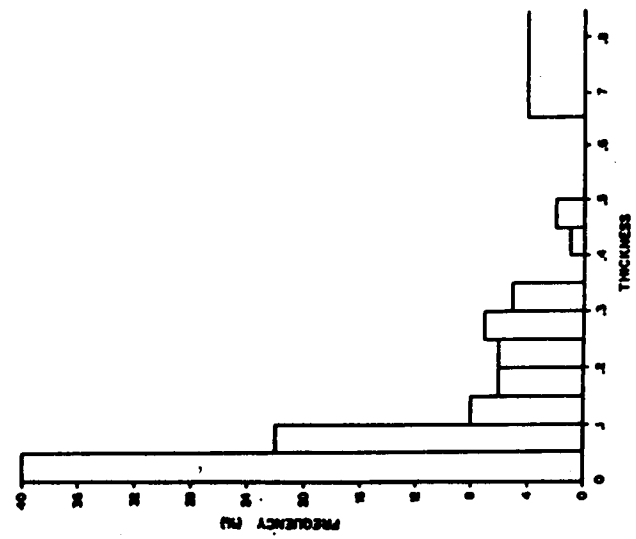
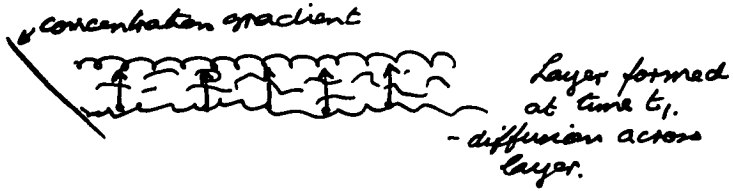


Figure 9. (a) Layer thicknesses. Histogram of the thickness of individual events. Events thicker than 0.65 are in the last bin. Most events are thin and do not contribute to the total energy [Desaubies and Smith, 1982].

$$t = t_1$$



$$t = t_2 > t_1$$

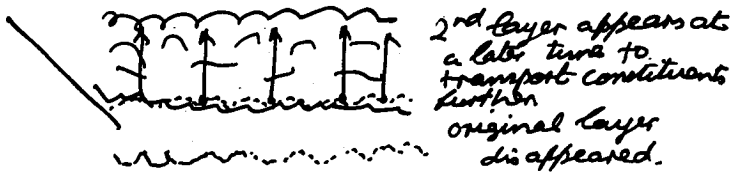


Figure 10.

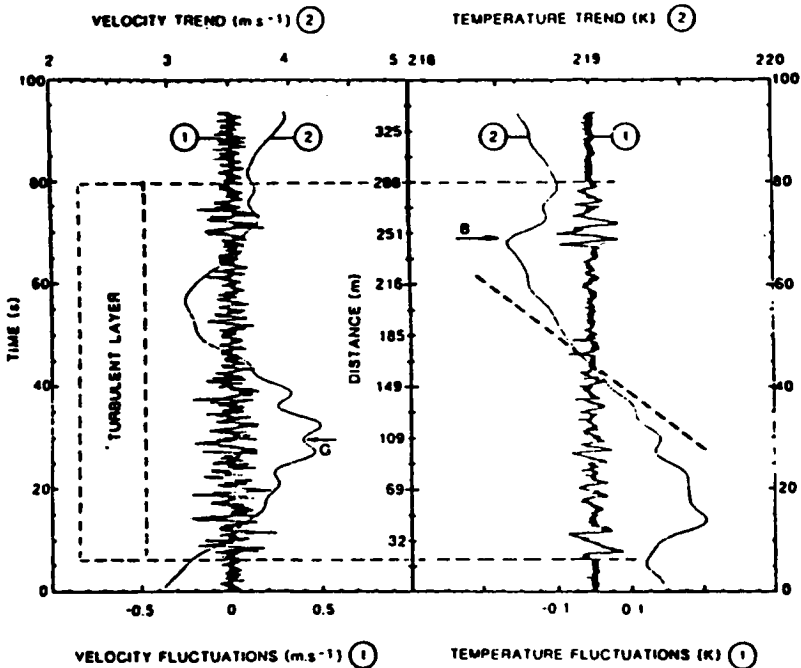


Figure 11. Detailed study of the layer No. 5 both velocity (a) and temperature (b) signals are separated in a fluctuating part (curve 1) and a low frequency part (smooth curve 2). The temperature gradient is near the adiabatic lapse rate (dashed straight line) in the core of the turbulent layer.

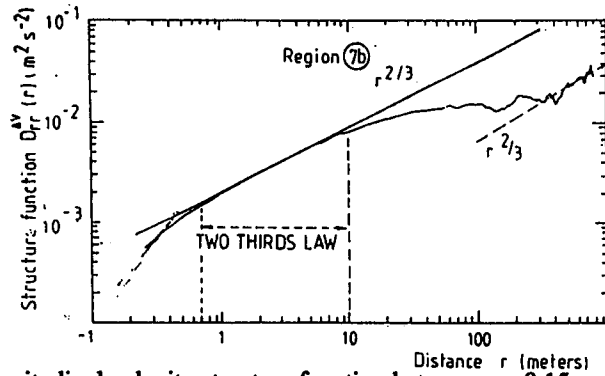


Figure 12. The longitudinal velocity structure function between $r = 0.15$ and 800 m. A gap occurs around $r = 100$ m. Measurement is made in a 35 m thick layer while the total turbulent layer 7 is 240 m thick.

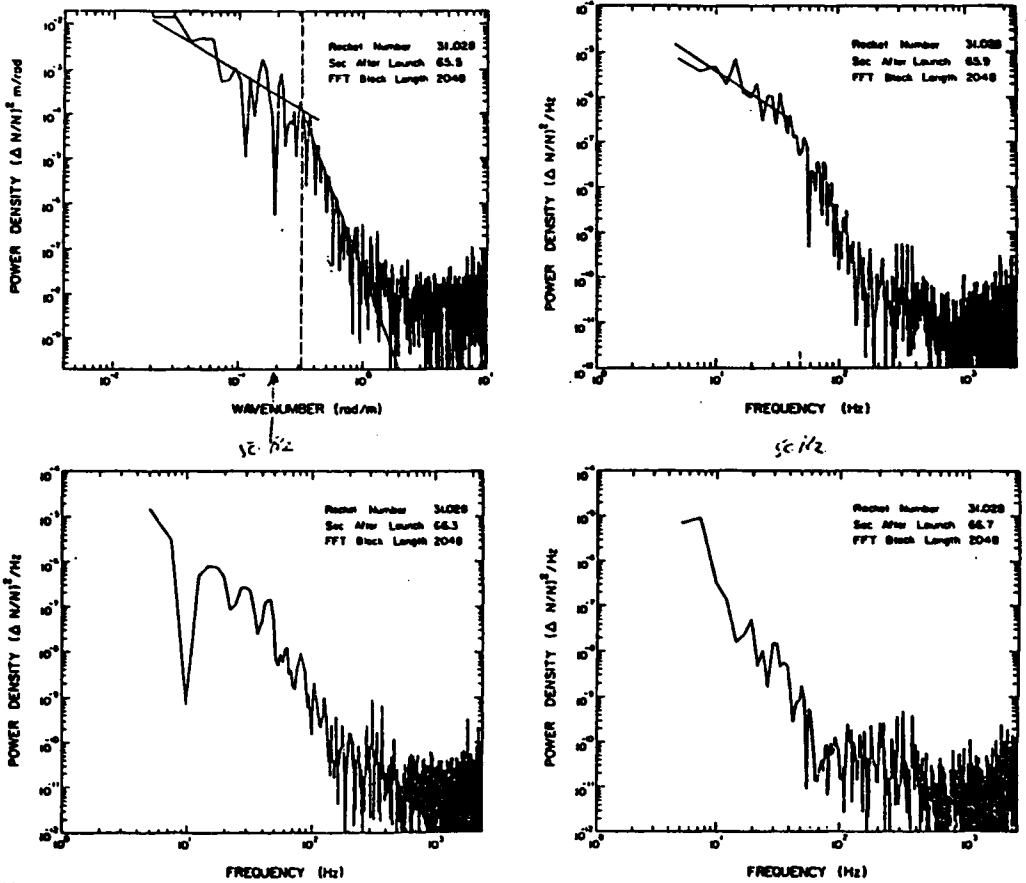


Figure 13. Spectra of relative electron density variations ($\Delta N/N$) in the scattering layer observed by the probe experiment on February 27, 1983 between 85.2 and 86.6 km altitude. The first spectrum has been shown in units of wavelength assuming a rocket velocity of 1.5 km. The three remaining spectra are in units of hertz. The last spectrum is from a region of no detectable turbulence. [Royrvik and Smith, 1984].

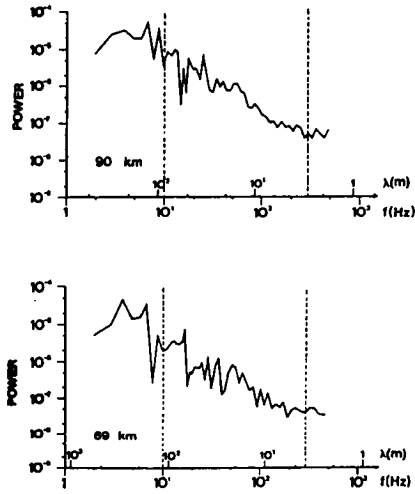


Figure 14. Power spectra $P(f)$ of the ion density fluctuations $\delta N_i/(N_i)$ for four different height intervals centered at 69, 90, 105, and 109 km. The broken lines indicate the estimated limits of useful observations. The upper abscissa scale indicates possible length scales of the fluctuations [Thrane et al., 1985].

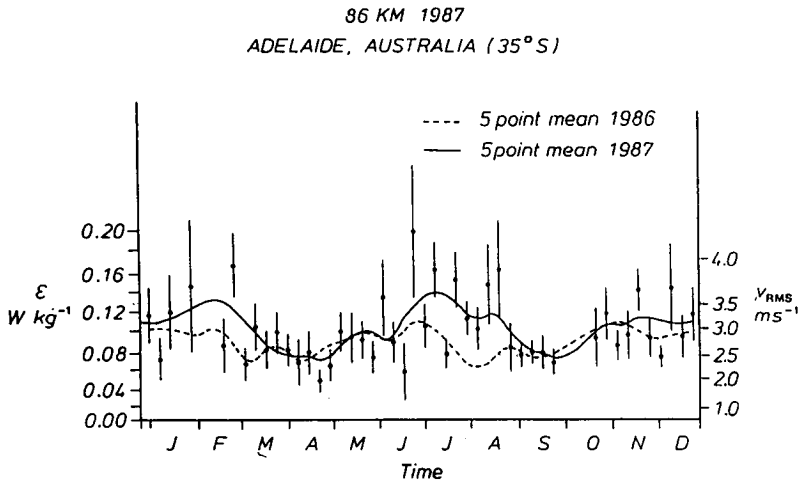


Figure 15.

represents the largest data set at any one site, with data being recorded between 80 and 95 km continuously at 2-h intervals for 3 years (Figure 15).

Figure 16 shows a diagram of the distributions of turbulent energy dissipation rates in the 80 – 120 km altitude region, using data up to about 1983. Subsequent measurements suggest that the shaded region would probably better indicate typical values. A region of very small values around the mesopause has also been noted in a variety of measurements.

The boundary of transition between regions where diffusion is turbulently controlled, and where it is viscously controlled (the turbopause) has also been investigated during MAP, particularly by Russian workers (e.g., Danilov [1984] Figure 17), but its detailed seasonal variation is still poorly understood.

Radar measurements of energy dissipation rates have also been made in the troposphere, by utilizing both absolute backscatter techniques [VanZandt et al., Gage et al., 1980; Weinstock, 1978a,b] (Figure 18), and also using spectral width methods (Figure 19) e.g., Sato and Woodman [1982]; Hocking [1983].

At this view-level, several other advances have been made. Theoretical studies by Weinstock [1981], Dalaudier and Sidi [1987], and Hill and Clifford [1978], etc. have also helped in understanding the energetics and spectral appearance of the turbulent regions. They have helped delineate boundaries between the inertial and buoyancy range of turbulence, for example, and clarified understanding of the energy transfer processes between these ranges.

5. Fine Structure

To really understand turbulence properly, however, requires better knowledge of the fine-scale structure. Although we call it isotropic, individual density structures are far from isotropic. In a stably stratified environment, intense mixing produces a mixture of irregular shapes, and as the driving source of the turbulence becomes less effective, the density inhomogeneities tend to settle out into a horizontally layered structure of interleaved fine scales. Figure 20 shows an example of decaying turbulence in a salt-stratified solution, and Figure 21 shows recent results due to McEwan [1983a,b]. Both show the tendency for the turbulence to stretch out horizontally and "laminarize" as the turbulence dies. It seems that the turbulence does not normally force the background state to alter substantially, although some modification takes place. The energetics are such that turbulence must act for some time to be able to drive a layer towards adiabatic.

Theoretical modeling also shows a tendency for the generation of horizontal interleaved structures. For example, a closure model employed by Sykes and Llewellyn [1982] has shown the tendency for stratified structures to develop (Figure 22). Simulations of K-H vortices by Klaassen and Peltier [1985a,b] also have shown a tendency for interleaved structures in temperature to develop as a result of the turbulence (Figure 23).

That stratification and turbulence do coexist has been shown by radar measurements. In 1980 Woodman et al. [1981] presented evidence for this at the URSI meetings in Washington, and more recently Hocking [1987] has shown that this can occur using the Adelaide 2 MHz radar (Figure 24).

6. New Perspectives

There are always new ways of visualizing turbulence, and new aspects to its interpretation. One recent advance concerns the process of large-scale diffusion in the atmosphere. We have already seen earlier proposals to explain how large-scale diffusion occurs in the atmosphere, but an important new model has also been developed. A gravity wave carries parcels of air in an elliptical orbit and returns it (almost) to its start position after one cycle. But detailed analysis shows that this is not actually true. In fact the particle drifts

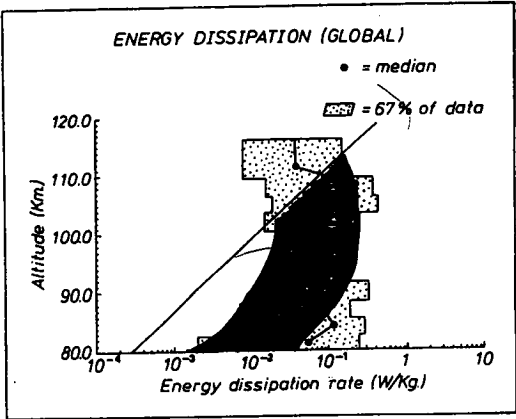


Figure 16. From Hocking [1987].

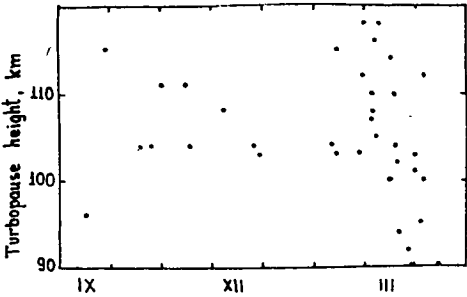


Figure 17. Turbopause height measured at Heiss Island versus season [Danilov, 1984].

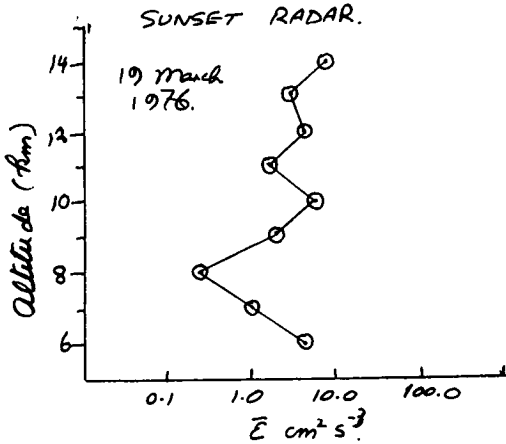


Figure 18. From Gage et al. [1980].

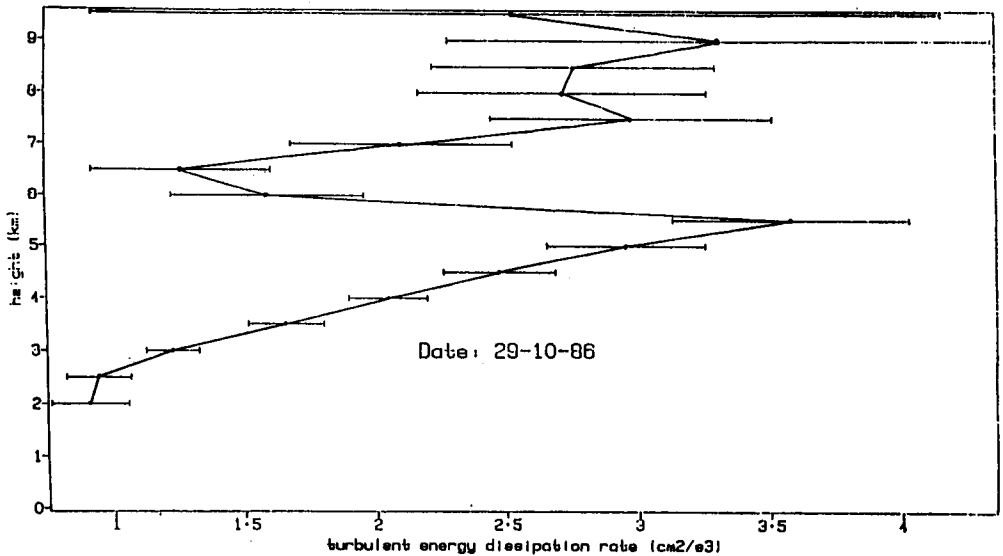


Figure 19. Adelaide.

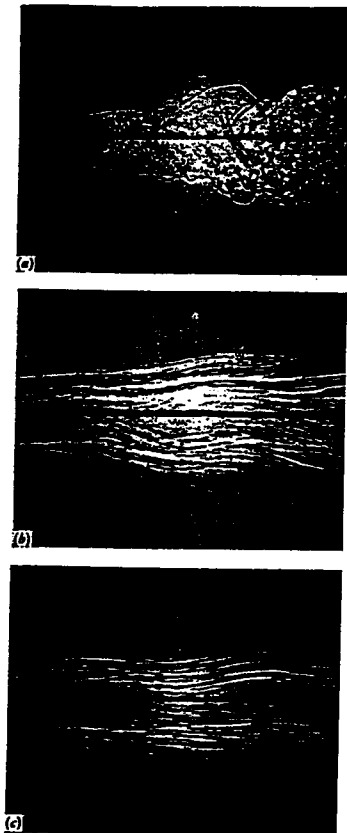


Figure 20. Shadowgraph pictures of a turbulent wake behind a circular cylinder in a stratified fluid (a) near the body: the wake resembles that in a homogeneous fluid. (b) 50 diameters behind the body: the large scale motions have been damped. (c) 100 diameters behind the body: the fine structure has also decayed leaving horizontal striations of concentrations (From Pao [1968] Boeing Scientific Labs., Document DI-82-0959, presented at Symposium on Clear Air Turbulence and its Detection, Seattle, WA, 1968).

ORIGINAL PAGE
BLACK AND WHITE PHOTOGRAPH

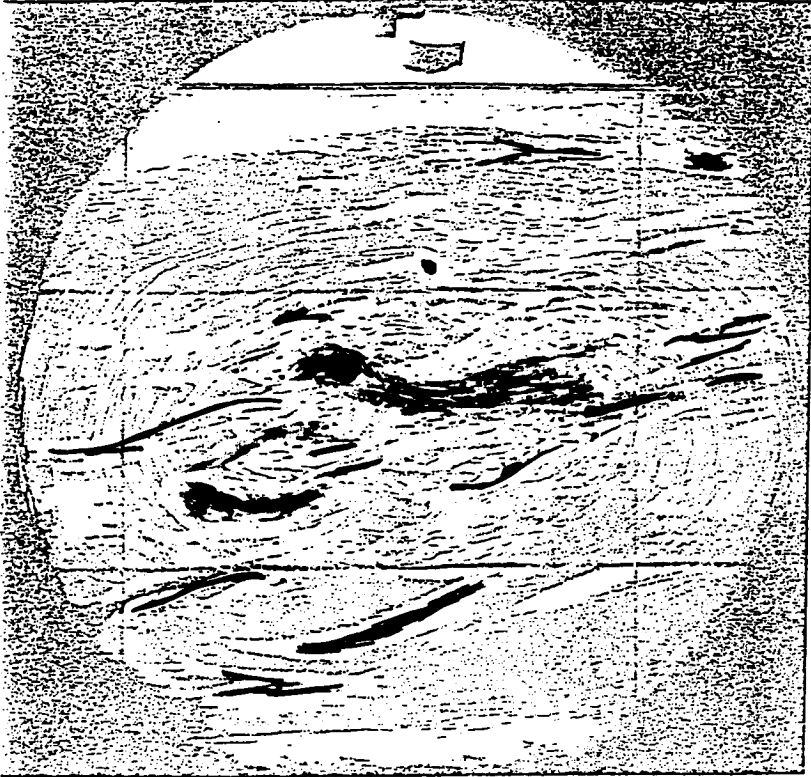


Figure 21. From McEwan [1983].

ORIGINAL FIGURE
OF POOR QUALITY

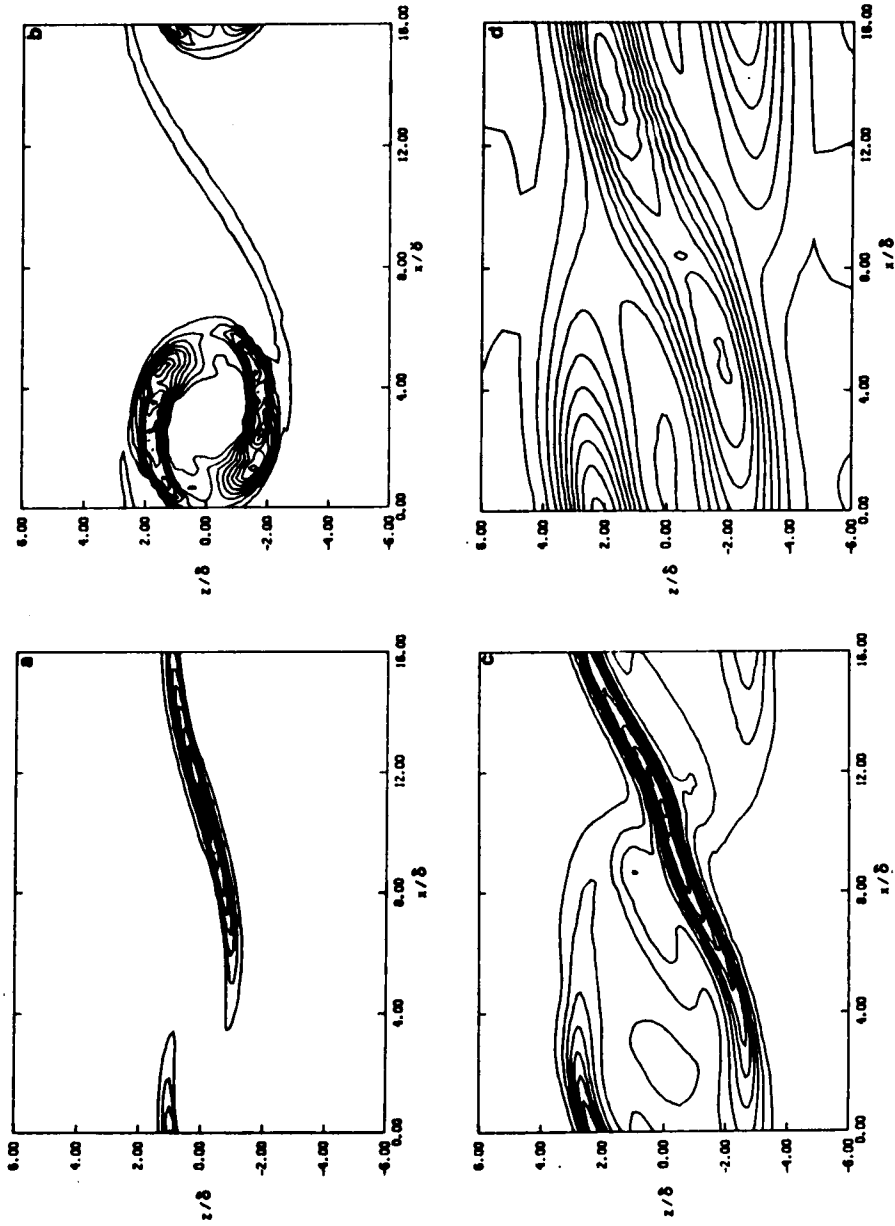


Figure 22. Isopleths of dimensionless temperature variance $\theta^2/\Delta T^2$ for the case with $Ri = 0.1$; (a) $r = 3.0$, (b) $4 = 4.9$, (c) $r = 6.9$, (d) $r = 9.7$. Contour intervals are (a) 0.0005, (b) 0.03, (c) 0.02, (d) 0.004 [Sykes and Lewellen, 1982].

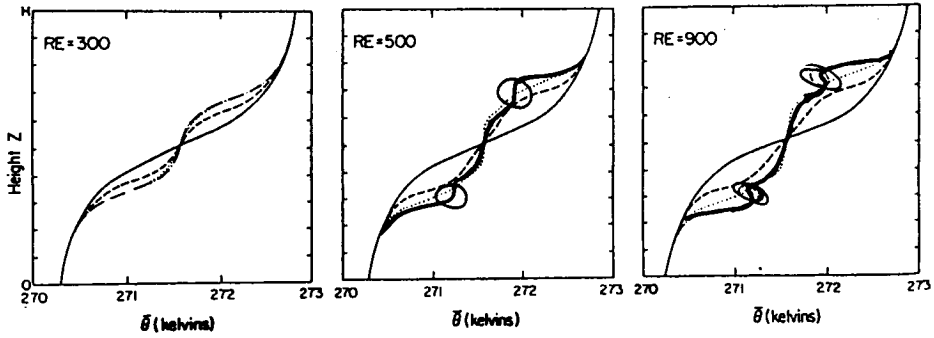


Figure 23. Evolution of the mean velocity defect profile $\bar{u}(z, t) - u'(z)$ for Re = 300, 500, and 900 KH waves. The profiles are shown at the key times (1) solid, (3) dashed, (5) dot-dashed, and (7) dotted. For Re = 300, key times (5a) and (7b) were used [Klaassen and Peltier, 1985].

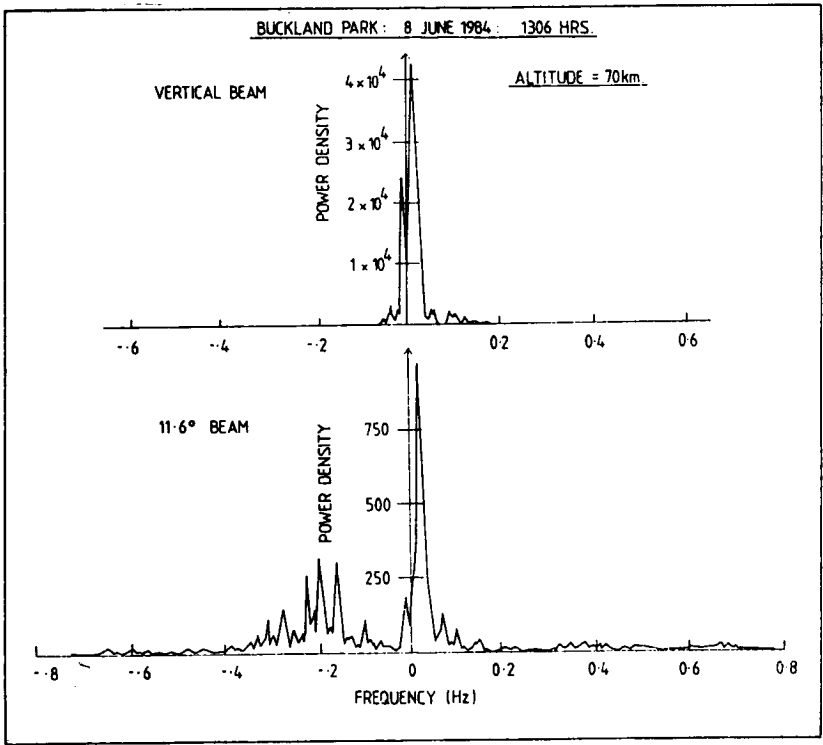


Figure 24. From Hocking [1987].

slightly from its start position, and this constitutes a so-called "Stokes drift". This is true even for nondissipating waves, but more so for dissipating ones.. Figure 25 shows a typical particle "orbit" due to the influence of several waves. When one has a spectrum of waves, the "Stokes drifts" of the waves add in a random-like manner to produce a sort of random walk. The result is a dispersion of an initially compact cloud of particles (Figure 26). This process gives effective diffusion coefficients (for whatever defining such a parameter is worth!) of $\sim 100 - 200 \text{ m}^2\text{s}^{-1}$. This process may be a major means of large-scale diffusion in the middle atmosphere. Other recent advances include studies by Kelley et al. [1987, 1988] which have shown that the electron density inertial range extends to scales much smaller than those for neutral fluctuations, at least in the case of high Schmidt number. This is another important area of study to be continued.

REFERENCES

- Barat, J., *J. Atmos. Sci.*, **39**, 2553-2564, 1982.
 Colegrove, F. D., W. B. Hanson, and F. S. Johnson, *J. Geophys. Res.*, **70**, 4931-4941, 1965.
 Dalaudier, F., and C. Sidi, *J. Atmos. Sci.*, **44**, 3121-3126, 1987.
 Danilov, A. D., *Adv. Space Res.*, **4**, 67-78, 1984.
 Desaubies, Y., and W. K. Smith, *J. Phys. Oceanography*, 1245, 1982.
 Dewan, E.M., *Science*, **211**, 1041-1042, 1981.
 Fritts, D. C., and T. J. Dunkerton, *J. Atmos. Sci.*, **42**, 549-556, 1985.
 Fritts, D. C., and P. K. Rastogi, *Radio Sci.*, **16**, 1401-1406, 1985.
 Gage, K. S., J. L. Green, and T. E. VanZandt, *Radio Sci.*, **15**, 407-416, 1980.
 Garcia, R. R., and S. Solomon, *J. Geophys. Res.*, **90**, 3850-3868, 1985.
 Groves, G. V., *J. Atmos. Terr. Phys.*, **48**, 563-571, 1986.
 Hill, R. J., and S. F. Clifford, *J. Opt. Soc. Am.*, **68**, 892-899, 1978.
 Hocking, W. K., *J. Atmos. Terr. Phys.*, **45**, 89-102, 1983a.
 Hocking, W. K., *J. Atmos. Terr. Phys.*, **45**, 103-114, 1983b.
 Hocking, W. K., *Adv. Space Res.*, **7**, 171-181, 1987.
 Johnson, F. S., and E. M. Wilkins, *J. Geophys. Res.*, **70**, 1281-1284, 1965.
 Kelley, M. C., D. T. Farley, and J. Rottger, *Geophys. Res., Lett.*, **14**, 1031-1034, 1987.
 Klaassen, G. P., and W. R. Peltier, *J. Fluid Mech.*, **155**, 1-35, 1985a.
 Klaassen, G. P., and W. R. Peltier, *J. Atmos. Sci.*, 1321-1339, 1985b.
 Luebken, F. J., U. von Zahn, E. V. Thrane, T. Blix, G. A. Kokin, and S. V. Pachomov, *J. Atmos. Terr. Phys.*, **49**, 863-869, 1987.
 McEwan, A. D., *J. Fluid Mech.*, **128**, 47-57, 1983a.
 McEwan, A. D., *J. Fluid Mech.*, **128**, 59-80, 1983b.
 Royrvik, O., and L. G. Smith, *J. Geophys. Res.*, **89**, 9014-9022, 1984.
 Sato, T., and R. F. Woodman, *J. Atmos. Sci.*, **39**, 2656-2552, 1982.
 Strobel, D. F., M. E. Summers, R. M. Bevilacqua, M. T. Deland, and M. Allen, *J. Geophys. Res.*, **92**, 6691-6698, 1987.
 Sykes, R. I., and W. S. Lewellen, *J. Atmos. Sci.*, **39**, 1506-1520, 1982.
 Thrane, E. V., O. Andreassen, T. Blix, B. Grandal, A. Brekke, C. R. Philbrick, F. J. Schmidlin, H. U. Widdel, U. von Zahn, and F. J. Luebken, *J. Atmos. Terr. Phys.*, **47**, 243-250-1985.
 Weinstock, J., *J. Atmos. Sci.*, **35**, 1022-1027, 1987a.
 Weinstock, J., *J. Atmos. Sci.*, **35**, 634-49, 1978b.
 Weinstock, J., *Radio Sci.*, **16**, 1401-1406, 1981.
 Woodman, R. F., J. Rottger, T. Sato, P. Czechowsky, and G. Schmidt, paper presented at URSI Conf., Washington, August, 1981.

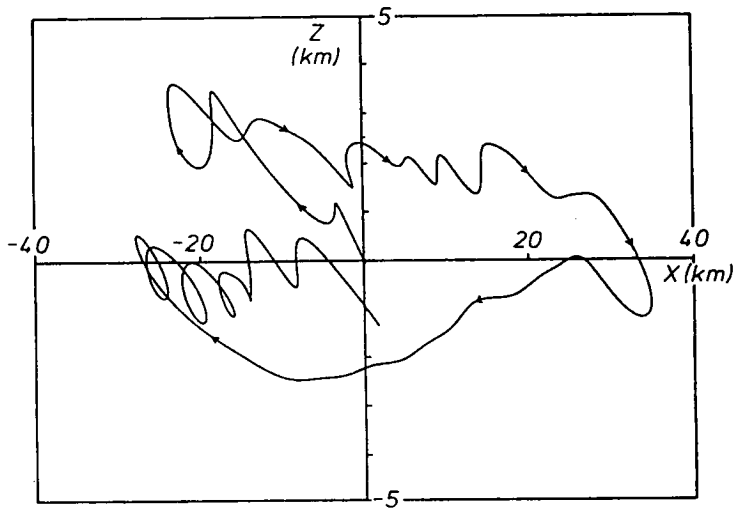
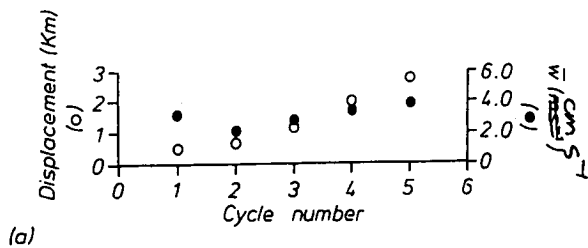
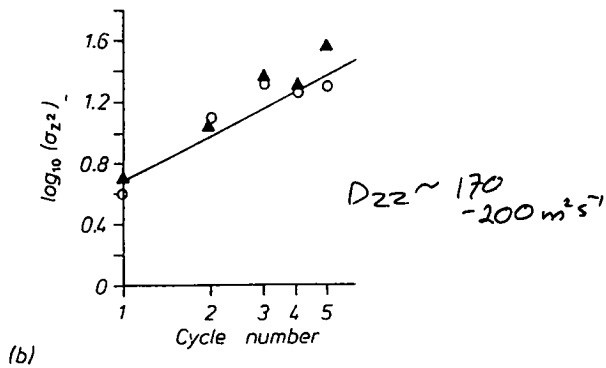


Figure 25.



(a)



(b)

Figure 26.

4.4 ADVANCES IN UNDERSTANDING THE GRAVITY WAVE SPECTRUM DURING MAP

T. E. VanZandt

NOAA, Aeronomy Laboratory
R/E/AL3, 325 Broadway, Boulder, CO 80303

1. Introduction

Prior to MAP, virtually nothing was known about gravity wave spectra in the atmosphere. Fluctuations of atmospheric variables had been extensively observed during the 60s and 70s, but they had not been interpreted as being due to gravity waves. Weinstein et al. [1966] considered three processes that might cause the observed fluctuations: inertial oscillations, gravity waves, and paired vortices. They favored inertial oscillations and rejected gravity waves and paired vortices. Their analysis appears to have been tacitly accepted, since there was very little further discussion of the causes of the fluctuations until 1979.

In 1979 new or renewed interpretations were advanced. Dewan [1979] suggested that the observed fluctuations were due to a random superposition of gravity waves. Alternatively, Gage [1979] suggested that they were due to two-dimensional turbulence. The tension between these conflicting interpretations, the important new data generated during MAP, and the recognition that gravity waves play a critical role in the large-scale dynamics of the atmosphere have stimulated a great deal of work devoted to describing the fluctuations, usually in terms of power spectra, and to understanding their causes and effects.

The development of observational techniques has played a major role in these studies. Radar and lidar have been particularly important since they can measure atmospheric parameters continuously over large height ranges. Thus they permit the calculation of power spectra versus frequency from time series for the first time and the calculation of spectra versus vertical wave number, which previously could be obtained only from infrequent balloon or smoke trail data. The MST radar technique also has the unique capability of measuring the vertical velocity.

2. The Garrett and Munk Model Gravity Wave Spectrum

Oceanic internal fluctuations had been shown by Garrett and Munk [1972, 1975] to be due to a random superposition of gravity waves. Following Dewan's suggestion, VanZandt [1982] showed that the GM (1975) model also fits the atmospheric spectra. Their model for the energy spectrum can be written

$$F(\omega, m) + CE\omega^{-p}/(1 + m/m_*)^t \quad (1)$$

where ω is the frequency, m is the vertical wave number, C is a normalization constant, E is the energy per unit mass, and m_* is the characteristic vertical wave number or wave number bandwidth. Model spectra for horizontal velocity u , vertical velocity w , potential temperature θ , pressure, density, etc. versus ω , m , and horizontal wave number k can be obtained by use of the gravity wave dispersion and polarization relations in suitable integrals of (1).

The spectrum is defined by only for parameters: E , m_* , p , and t , which can be determined by fitting the model to two spectra, one versus ω and one versus k or m . VanZandt [1982] estimated these parameters by the fittings shown in Figures 1 and 2. Determination of the parameters using nonsimultaneous spectra was possible only because the parameters do not vary a great deal from place to place and time to time. The standard deviation of E over many observed spectra is found to be a factor of 2 or 3; m_* , which is the least well-determined parameter, appears to be constant within a factor $2^{1/2}$ at a given height, but it increases slowly

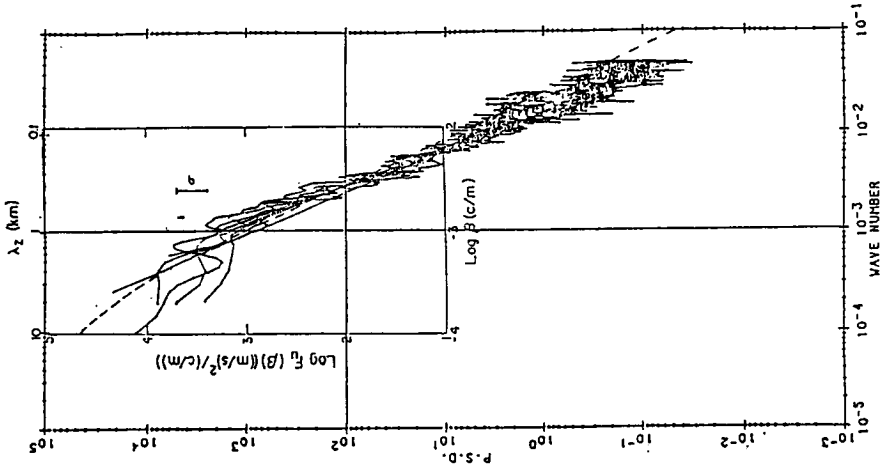


Figure 2. The GW model F_u spectrum (dashed line) superimposed on observed spectra: solid straight line, Daniels [1971]; raw spectra, Dewan et al. [1984].

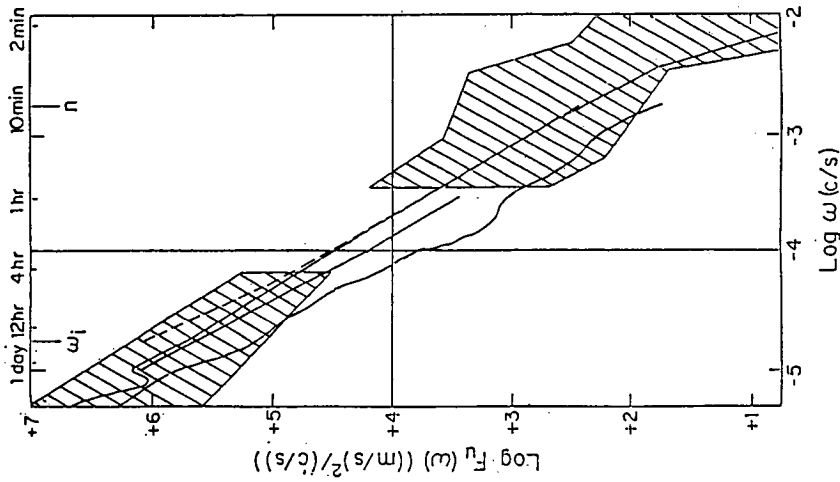


Figure 1. The GE model $F_u(w)$ spectrum (dashed line) superimposed on observed spectra: upper, Vinnichenko [1970]; middle Balsley and Garello [1985]; lower, Balsley and Carter [1982].

with height; $p \approx 5/3 \pm 1/6$; and m_* lies between 2.5 and 3, with theory (discussed later) suggesting a value closer to 3.

In each figure the model spectrum is the dashed curve. In Figure 1 the parameters were determined by fitting to the line that runs through the hatched areas. The model vertical wave number spectrum in Figure 2 was fitted to the observed spectrum indicated by the solid straight line in the inner box, which was derived from balloon data in the troposphere. It also fits the spectra reported by Dewan et al. [1984] from smoke-trail data in the middle stratosphere. The similarity of the five smoke-trail spectra, which were taken at three quite different locations, illustrates the constancy of vertical wave number spectra.

Once the four parameters have been determined, the model predicts all of the other spectra, so that the model can be tested by comparing the predicted spectra with observations. Two examples of such tests are shown in Figures 3 and 4, which compare predicted model spectra with observed spectra of temperature versus vertical wave number (Figure 3) and of horizontal velocity and potential temperature versus horizontal wave number (Figure 4). In Figure 4 the model fits the observed spectra extraordinarily well for wavelengths shorter than about 200 km, even following the curvature at wavelengths shorter than about 10 km. It must be emphasized that the model spectra are defined solely by the parameters determined in Figures 1 and 2; they are not adjusted at all to fit the observed spectra. Comparisons such as these strongly support the concept that the observed fluctuations are due to a random superposition of gravity waves.

The GM model has been extended to apply to radial velocities such as those measured by an oblique radar or lidar [Scheffler and Liu, 1985; VanZandt, 1985] and to take into account Doppler shifting of frequency spectra by the background wind [Scheffler and Liu, 1986; Fritts and VanZandt, 1987].

The GM model is thus a good description of the spectrum of the mean gravity wave field. While description of the mean state is important, departures from the mean are in some respects more critical. In particular, the mean state provides little or no information about the sources, propagation, and sinks of gravity wave energy. Moreover, the model does not explain the values of the parameters that are observed, or why the range of each parameter is limited. Publication of the GM model in 1972 stimulated research to try to explain the observed spectral shapes and amplitudes in terms of nonlinear interactions in the wave field. In spite of a great deal of work, reviewed by Müller et al. [1986], the problem is still not solved satisfactorily.

Saturated Vertical Wave Number Spectra

In the atmosphere, however, there has been some progress toward explaining the value of t and the variation of m_* with altitude in terms of saturation of the gravity wave spectrum. Dewan and Good [1986] and Smith et al. [1987] argued that because the amplitude of the spectrum increases with altitude, the large wave number part of the spectrum should be saturated. This process is quite important because in regions where gravity waves are saturated and dissipate, horizontal momentum is transferred from the gravity wave field to the mean flow. This acceleration has important effects on the global dynamics of the atmosphere [Houghton, 1978; Lindzen, 1981].

According to Smith et al. [1987] and Fritts et al. [1988], the saturated velocity and temperature spectrum are approximately

$$F_u^s(m) = N^2/6m^3 \text{ and } F_T^s(m) = N^4/10m^3 \quad (2)$$

In Figure 5 these spectra are plotted as dashed lines with a value of N appropriate to the lower stratosphere. They agree very well with observed lower stratospheric spectra, shown as solid

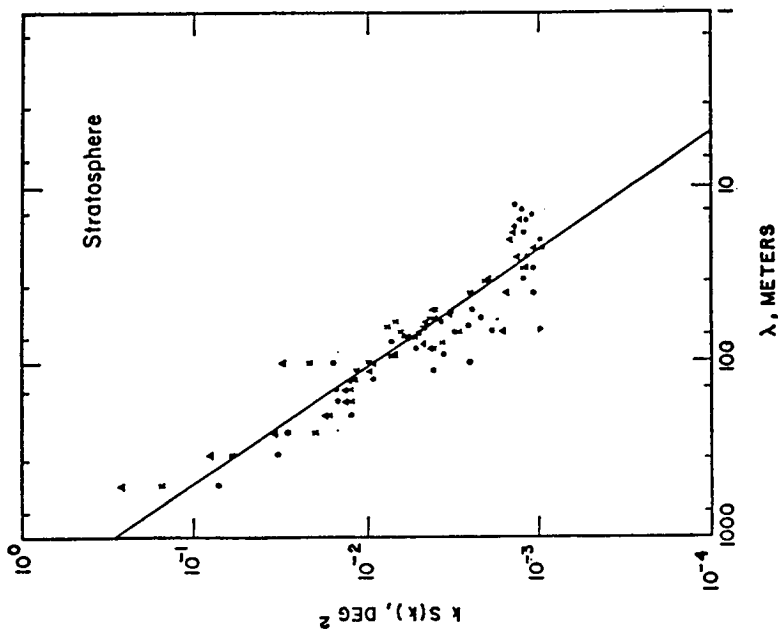


Figure 3. The GW model $F_0(m)$ spectrum superimposed on spectra observed by Mantis [1972].

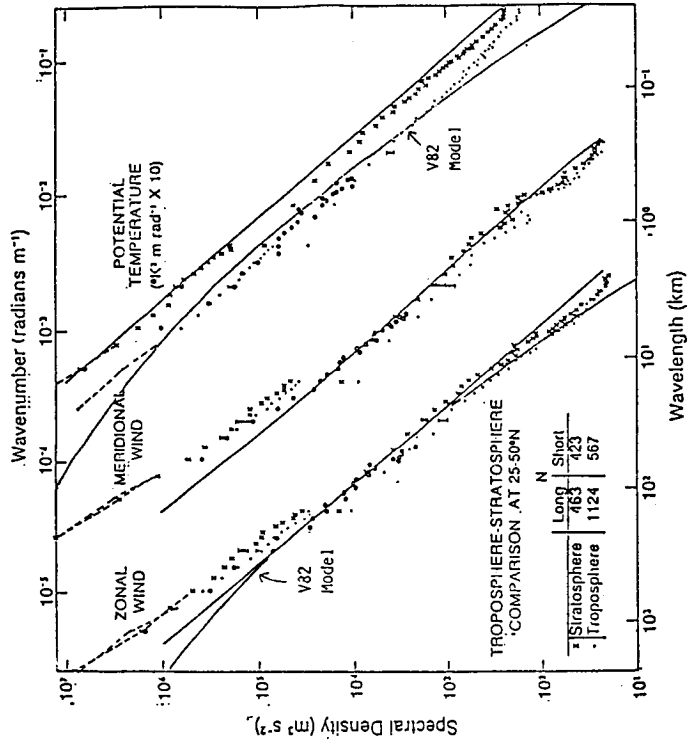


Figure 4. Comparison between observed spectra of horizontal wind and potential temperature versus k [from Nastrom and Gage, 1985] and the GM model [from VanZandt, 1982].

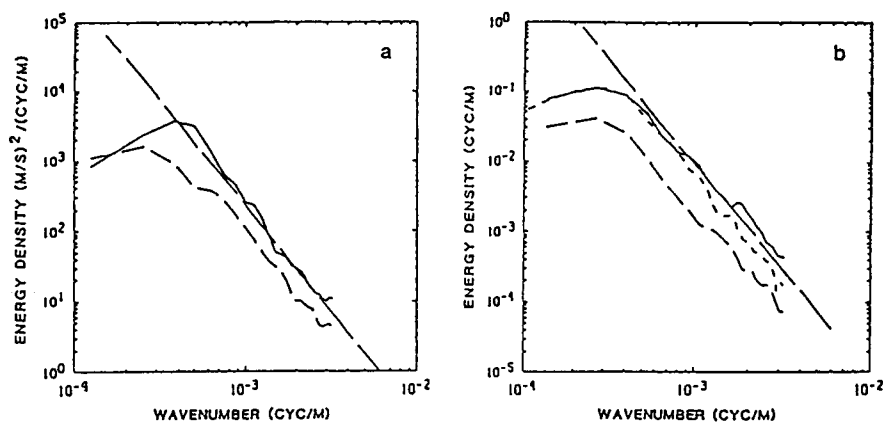


Figure 5. Comparison of the model saturated spectra (dashed lines) with observed spectra of (a) horizontal velocity and (b) normalized temperature. The observed spectra are (---) 5-12.5 km, (—) 12.5-20.5 km, and (- - -) 20.5-30 km. [After Fritts et al., 1988].

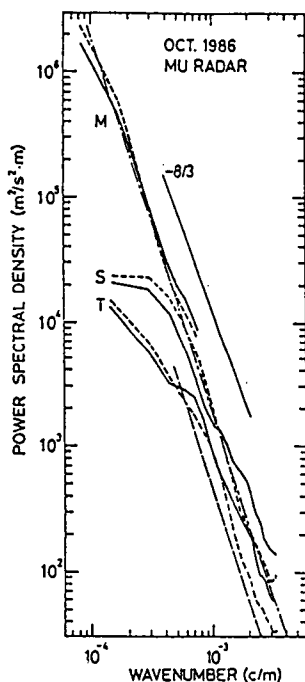


Figure 6. Comparison of the model saturated spectrum of horizontal velocity with spectra in the troposphere (T), stratosphere (S), and mesosphere (M) observed essentially simultaneously by the MU radar. The zonal spectra are indicated by solid curves and the meridional spectra (which are freer from contamination) by dashed curves. [After Tsuda et al., 1989].

curves. The saturated spectra for the troposphere are smaller because the tropospheric value of N is smaller.

In Figure 6, $F_u^s(m)$ is compared with spectra from the troposphere (T), stratosphere (S), and mesosphere (M) observed essentially simultaneously by the MU radar. The zonal spectra are indicated by solid curves and the meridional, by dashed curves. The tropospheric and stratospheric models are the dashed and dot-dashed lines, respectively. Again, the agreement is very good, particularly with the meridional spectra. The zonal spectra are contaminated by an instrumental effect at large wave number. The decrease of m^* with increasing altitude is discussed by Smith et al.

Vertical Velocity

Several studies of the spectra of vertical velocity have been made, taking advantage of the unique capability of the MST radar technique. Under light wind conditions (<5 m/s) the frequency spectra are rather flat, as shown by the curves labeled "QUIET" in Figure 7. The thin spectra are from the ALPEX radars in the delta of the Rhone river in southern France and the thick spectra are from the Flatland radar in Illinois. These spectra are reasonably consistent with the GM model, which predicts a slope of $-p + 2\bar{z} + 1/3$. But under high wind conditions (> 20 m/s), labeled "ACTIVE", the ALPEX spectra increase in amplitude and become much steeper, approaching a slope of $-5/3$, while the Flatland spectra increase only slightly and become slightly flatter. We attribute the drastic change in the ALPEX spectra, and at other spectra taken near rough terrain, to contamination of the vertical velocities by mountain waves.

Figure 8 compares the Flatland spectra, stratified by wind speed, with model Doppler-shifted spectra. The agreement between the observed and model spectra as the mean wind changes strongly suggests that the observed spectra are almost entirely due to gravity waves.

The following graphs show that it may be possible to measure synoptic-scale vertical velocities using the MST radar technique with a radar located in very flat terrain. This is very important since, although synoptic-scale vertical velocities play a critical role in atmospheric dynamics, it has not been possible to measure them directly.

Figure 9 is a mean spectrum extending out to a period of 45 h plotted on an area-preserving graph. In the lower left-hand corner is plotted an estimate of the mean spectral density due to synoptic-scale motions, assuming that the synoptic-scale variance is about 12 (cm/s)^2 and that the spectral density per unit of log frequency is uniform between 7 days and 5 hours. The fact that the Flatland spectrum lies at or below the estimated synoptic-scale spectrum suggests that a radar in very flat terrain may be able to measure the synoptic-scale velocity. Of course, such a measurement would be quite impossible at ALPEX or at any other station near rough terrain.

Two-Dimensional Turbulence

It was mentioned earlier that Gage [1979] suggested that the observed fluctuations are primarily due to 2 DT. But it is impossible to assess how much of the fluctuations are due to 2 DT because the theory makes only very few predictions, and the observations that can be compared with these predictions are also consistent with the gravity wave interpretation as shown above.

Because the role of 2 DT cannot be assessed by comparison with observations, almost all of the studies attempting to show the importance of 2 DT have proceeded by first assuming that the motions must be either 2 DT or gravity waves and they trying to show that the fluctuations cannot be due to gravity waves. These arguments have been flawed by the use of inappropriate data or questionable assumptions.

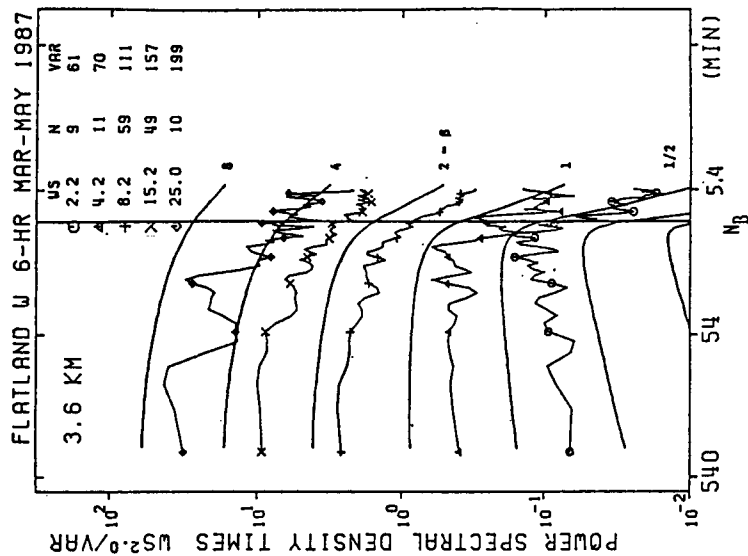


Figure 8. Comparison between frequency spectra of vertical velocity fluctuations at Flatland, stratified by background wind speed WS , with model Doppler-shifted spectra. $\beta = WS/C_*$ where C_* is the characteristic horizontal phase speed.

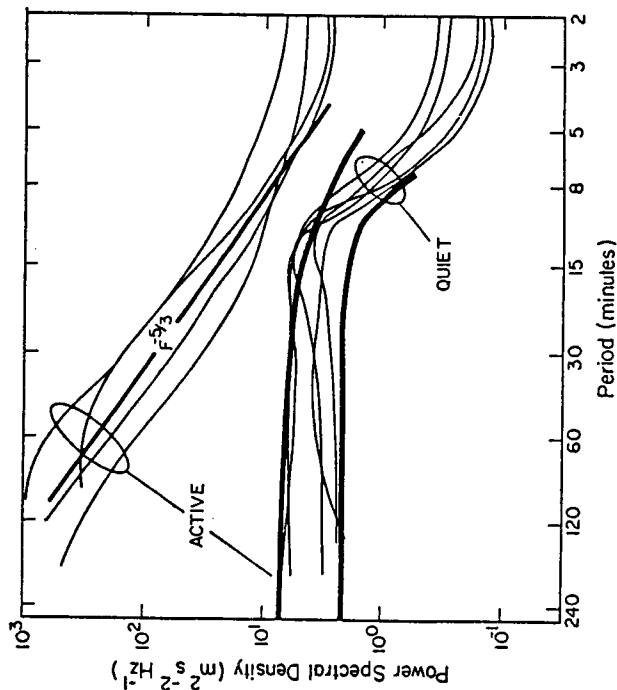


Figure 7. Frequency spectra of vertical velocity fluctuations. The ALPEX spectra from Ecklund et al. [1985] are the average of four 750 km range gates centered from 3.85 to 6.10 km and the Flatland spectra are from the 5.2 km range gate.

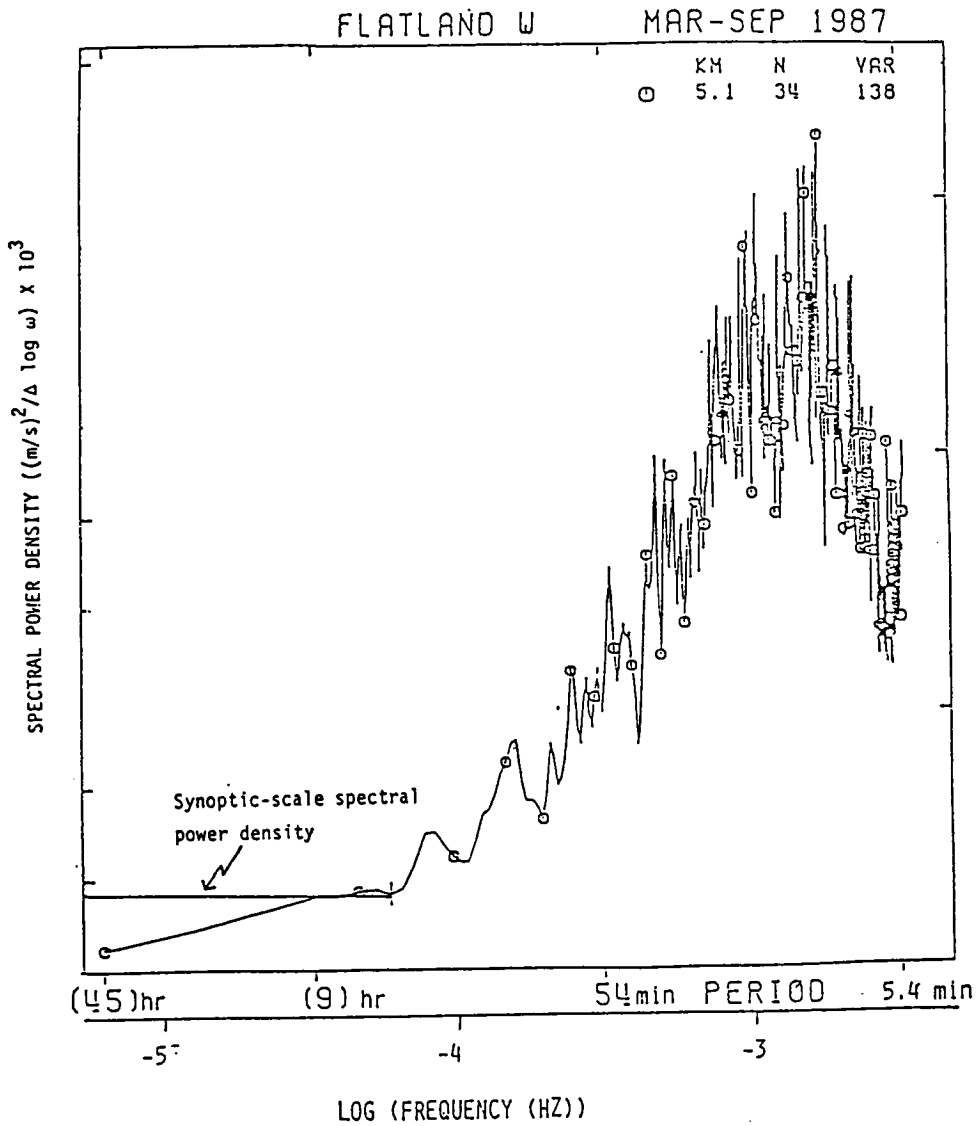


Figure 9. Mean frequency spectrum of vertical velocity at Flatland extending to 45 h compared with an estimate of the mean spectral density due to synoptic-scale vertical motions.

Conclusions

1. The observed fluctuations and power spectra in the free atmosphere are mostly if not entirely due to a superposition of gravity waves, which can be modeled by the GM model.
2. There is no evidence that 2 DT makes a significant contribution to the observed fluctuations. In any case, the agreement between observations and the GM model shows that the 2 DT contribution must be relatively small.
3. Spectra versus vertical wave number are saturated at large wave number, with theory and observations indicating that $t \approx 3$.
4. Vertical velocity fluctuations and spectra measured near rough terrain are strongly contaminated by mountain waves. But over very flat terrain the spectra are dominated by gravity waves at periods shorter than about 6 hours and apparently by synoptic-scale velocities at periods longer than 6 hours. Thus it may be possible to study synoptic-scale vertical velocities using radars located in very flat terrain.

REFERENCES

- Balsley, B. B., and D. A. Carter, *Geophys. Res. Lett.*, **9**, 465-468, 1982.
- Balsley, B. B., and R. Garelo, *Radio Sci.*, **20**, 1355-1361, 1985.
- Daniels, G. E., Terrestrial environment (climatic) criteria guidelines for use in space vehicle development, 1971 revision, *NASA TM X-64589*, 5.98-5.102, 1971.
- Dewan, E. M., *Science*, **204**, 832-835, 1979.
- Dewan, E. M., and R. E. Good, *J. Geophys. Res.*, **91**, 2742-2748, 1986.
- Dewan, E. M., N. Grossbard, A. F. Quesada, and R. E. Good, *Geophys. Res. Lett.*, **11**, 80-83, and correction, 624, 1984.
- Ecklund, W. L., B. B. Balsley, D. A. Carter, A. C. Riddle, M. Crochet, and R. Garelo, *Radio Sci.*, **20**, 1190-1206, 1985.
- Fritts, D. C., T. Tsuda, T. Sato, S. Fukao, and S. Kato, *Radio Sci.*, in press, 1988.
- Fritts, D. C., and T. E. VanZandt, *J. Geophys. Res.*, **92**, 9723-9732, 1987.
- Gage, K. S., *J. Atmos. Sci.*, **36**, 1950-1954, 1979.
- Garrett, C., and W. Munk, *Deep-Sea Res.*, **19**, 823-832, 1972.
- Garrett, C., and W. Munk, *J. Geophys. Res.*, **80**, 291-297, 1975.
- Houghton, J. R., *J. Roy. Meteorol. Soc.*, **104**, 1-29, 1978.
- Lindzen, R. S., *J. Geophys. Res.*, **86**, 9707-9714, 1981.
- Mantis, H. T., *J. Geophys. Res.*, **77**, 4539-4544, 1972.
- Müller, P., G. Holloway, F. Henyey, and N. Pomphrey, *Rev. Geophys.*, **24**, 493-563, 1986.
- Nastrom, G. D., and K. S. Gage, *J. Atmos. Sci.*, **42**, 950-960, 1985.
- Scheffler, A. O., and C. H. Liu, *Radio Sci.*, **20**, 1309-1322, 1985.
- Scheffler, A. O., and C. H. Liu, *J. Atmos. Terr. Phys.*, **48**, 1225-1231, 1986.
- Smith, S. A., D. C. Fritts, and T. E. VanZandt, *J. Atmos. Sci.*, **44**, 1404-1410, 1987.
- Tsuda, T., T. Inoue, D. C. Fritts, T. E. VanZandt, S. Kato, T. Sato, and S. Fukao, 1988, in preparation.
- VanZandt, T. E., *Geophys. Res. Lett.*, **9**, 575-578, 1982.
- VanZandt, T. E., *Radio Sci.*, **20**, 1323-1330, 1985.
- Vinnichenko, N. K., *Tellus*, **12**, 158-166, 1970.
- Weinstein, A. I., E. R. Reiter, and J. R. Scroggins, *J. Appl. Meteorol.*, **5**, 49-57, 1966.

**5. MIDDLE ATMOSPHERE OF THE SOUTHERN HEMISPHERE (MASH)
GLOBAL METEOR OBSERVATIONS SYSTEM (GLOBMET)
SOLAR SPECTRAL IRRADIANCE MEASUREMENTS (SSIM)
GLOBAL OBSERVATIONS AND STUDIES OF STRATOSPHERIC AEROSOLS
(GOSSA)**

5.1 PROGRESS WITH THE MASH PROJECT

A. O'Neill

Meteorological Office
Bracknell, Berkshire RG12 2S, United Kingdom

The aim of the MASH project is to study the dynamics of the middle atmosphere in the Southern Hemisphere, emphasizing inter-hemispheric differences. Both observational data and data from simulations with numerical models are being used. It is intended that MASH will be complemented by parallel studies on the transport and photochemistry of trace species in the Southern Hemisphere. Impetus for such studies has come from the unexpected finding of a springtime "ozone hole" over Antarctica.

A summary of recent progress with the MASH project is given. Data from polar-orbiting satellites are used to discuss the large-scale circulation found in the Southern Hemisphere at extratropical latitudes. Comparisons are made with that of the Northern Hemisphere. Particular attention is paid to the springtime final warming, the most spectacular large-scale phenomenon in the stratosphere of the Southern Hemisphere. The circulation before and after this event has to be taken into account in theories for the formation and subsequent disappearance of the ozone hole.

Aim of MASH: Concerted study of large-scale dynamics and transport processes, emphasizing inter-hemispheric differences and tropospheric coupling.

Events: Workshop in Williamsburg, 1986
MASH/GRATMAP Workshop in Adelaide, 1987
MASH Workshop in California, April 17-19, 1989

Data Sources (for large-scale circulation):

•Conventional	SCR (10-50 km)/PMR (40 - 80 km)	73 - 78
•Satellite	LIMS	End 78 - Mid 79
	SAMS	End 78 - Mid 83
This paper ⇒	SSU	End 78
•'Base Levels' (usually 100 mb)	UKMO ECMWF global NMC ANMRC hemispheric	

Outline of seasonal evolution of stratosphere in SH compared with NH

- Data: SSU, 3-channel pmr
- Phenomena: •Early winter SH vs NH Canadian warmings
 - Midwinter SH vs NH major midwinter warming
 - Final warming SH often drastic vs NH sometimes quiescent
 - Interannual variability SH

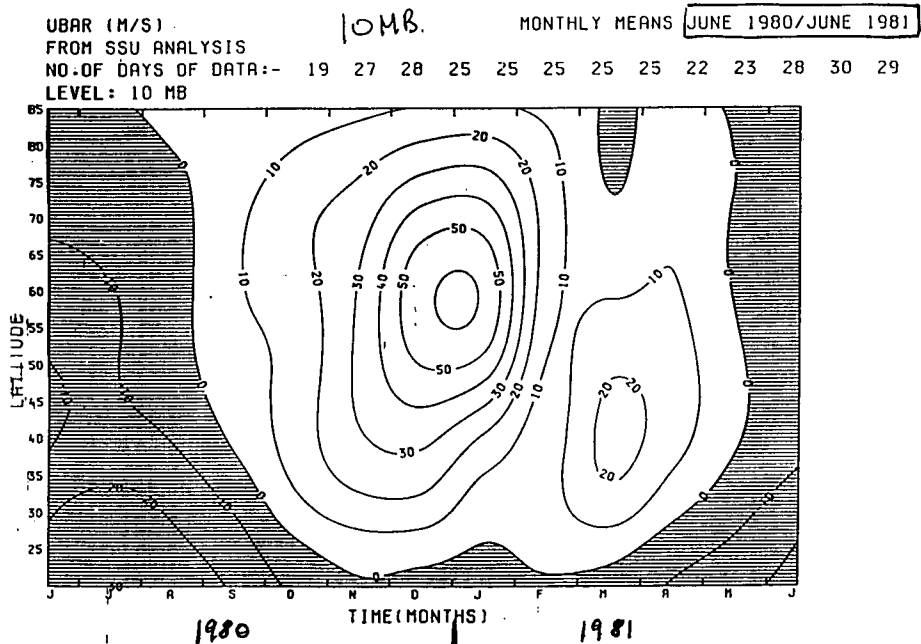


Figure 1.

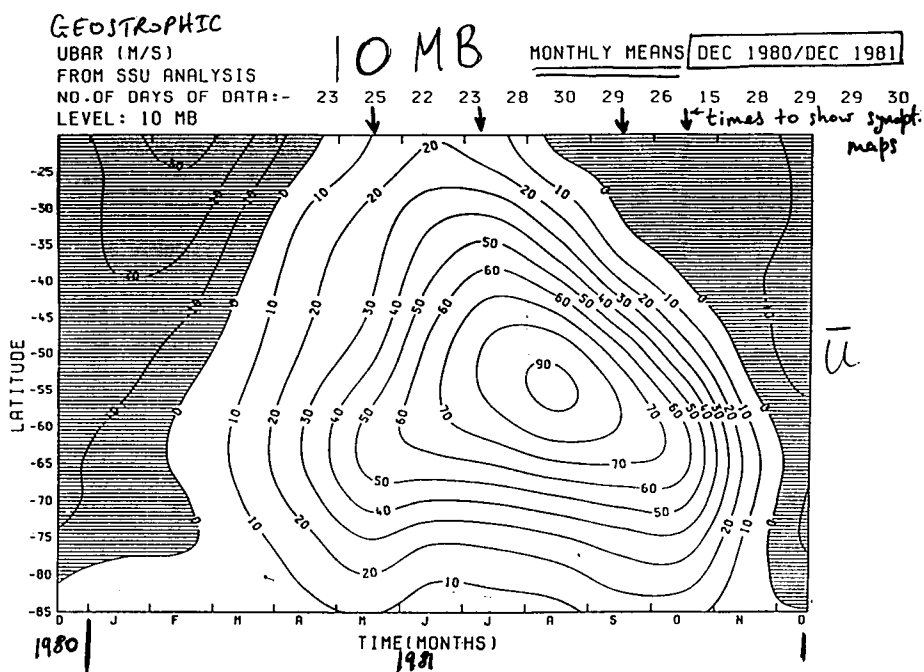


Figure 2.

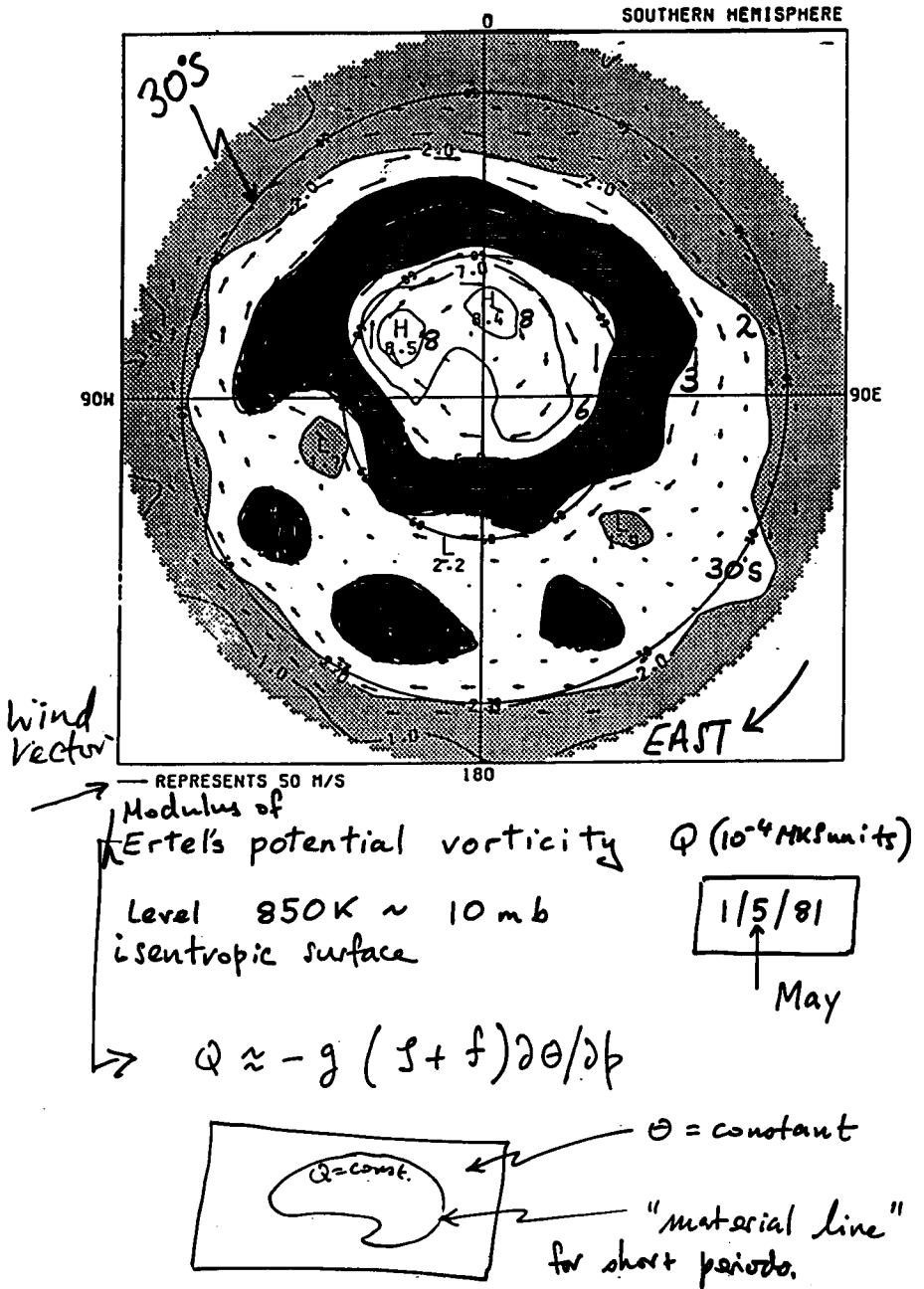


Figure 4.

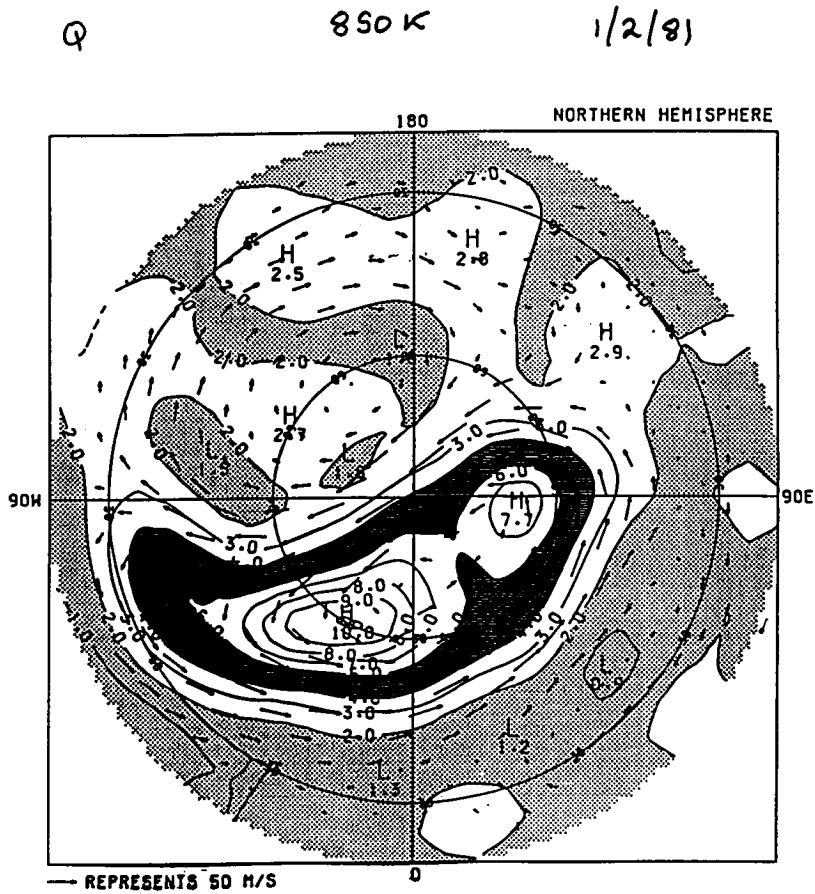


Figure 5.

ORIGINAL PAGE
BLACK AND WHITE PHOTOGRAPH

ORIGINAL PAGE
BLACK AND WHITE PHOTOGRAPH

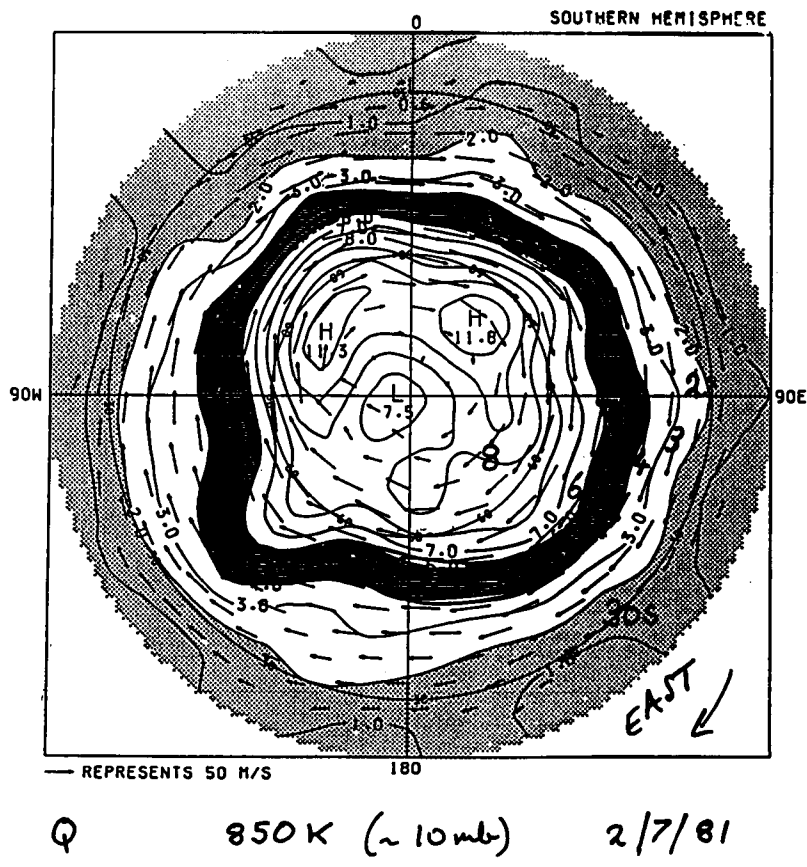


Figure 6.

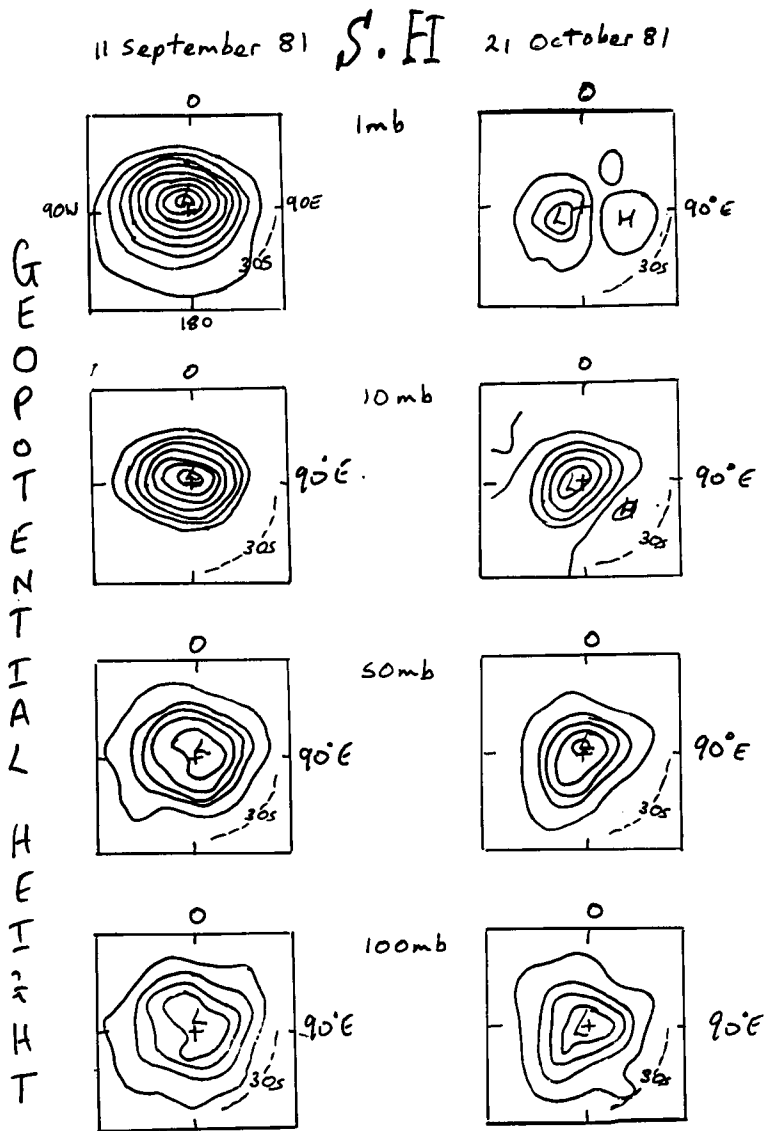


Figure 8.

Antarctic O₃ depletion

Two conditions required of all (current) chemical theories:

- (1) Liberation of ClO_x radicals from their reservoirs (e.g., ClONO_2)
- (2) Greatly reduced levels of NO_x .

- (1) requires heterogeneous chemistry on solid (ice) surfaces. PSCs.
- (2) requires 'denitrification' -- gravitational settling of ($\text{H}_2\text{O} - \text{HNO}_3$) ice \Rightarrow
i.e. $T \leq \text{frost point} \approx 193 \text{ K}$

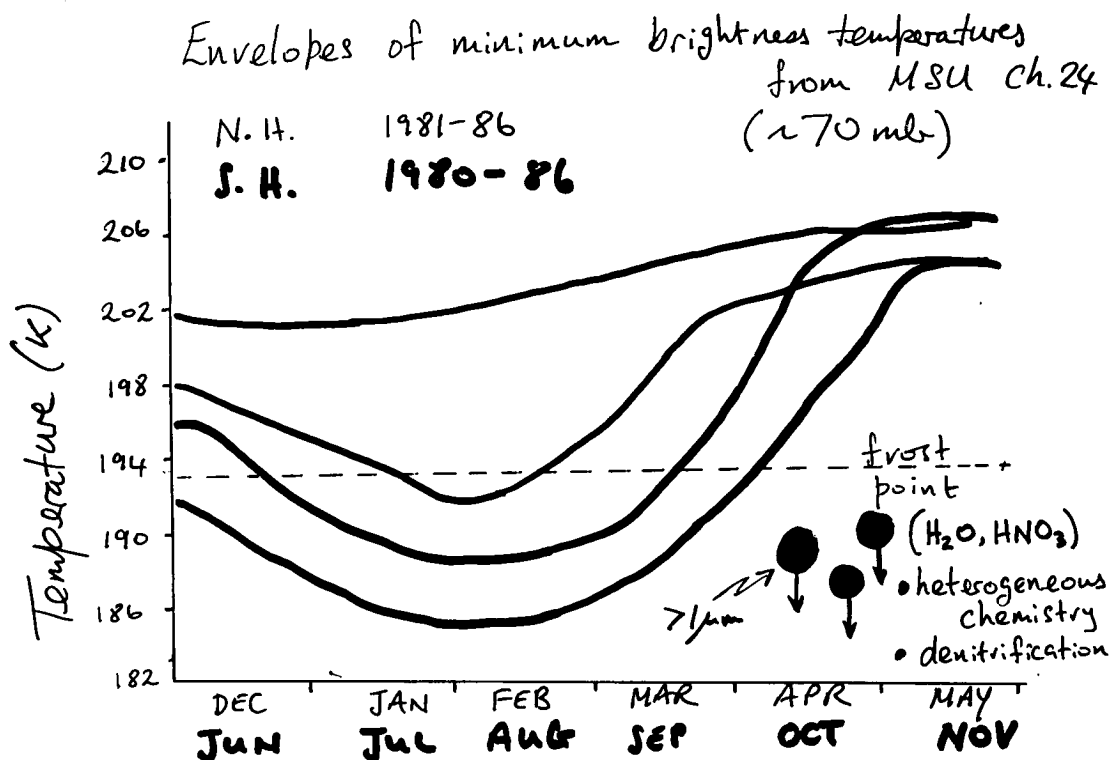


Figure 9.

General strategy for future work

- Exploit inter-hemispheric differences (e.g. in troposphere/stratosphere coupling)
- Sometimes difficult to infer causal relationships diagnostically, so we use hierarchy of models.
- Make best use of measurements of meteorological and trace fields by assimilation into numerical mode. (UARS, EOS)

5.2 WHY DO PLANETARY WAVE NUMBER ONE AND THE OZONE TRANSPORT VARY ANNUALLY IN THE NORTHERN HEMISPHERE AND SEMIANNUALLY IN THE SOUTHERN HEMISPHERE?

M. A. Geller, M. F. Wu

Code 610, NASA Goddard Space Flight Center
Greenbelt, MD 20771

E. R. Nash

Applied Research Corporation
Landover, MD 20785

Evidence is cited from our studies and those of others showing the different nature of the yearly variations of the middle atmospheres of the Northern and Southern Hemispheres. The Northern Hemisphere middle atmosphere is shown to be characterized by annual variations in planetary wave number one amplitude and the accompanying ozone transports. The Southern Hemisphere middle atmosphere is shown to be characterized by semiannual variations in the amplitude of planetary wave number one and the accompanying ozone transports. The amplitude of wave number two in both hemispheres appears to vary annually. Examination is made of the nature of the planetary wave forcing in both hemispheres as well as the planetary wave propagation characteristics in both hemispheres in an attempt to better understand this.

Storyline

- (1) Both the O_3 and planetary wave activity show different behavior in the Northern and Southern Hemispheres. These changes are plausibly consistent with each other.
- (2) Standing planetary wave number one shows an annual behavior in the Northern Hemisphere and a semiannual behavior in the Southern Hemisphere.
- (3) Standing wave number two shows an annual behavior in both hemispheres.
- (4) $\frac{dO_3}{dt}$ shows a semiannual behavior in the Southern Hemisphere and an annual behavior in the Northern Hemisphere. This indicates similar variations in the O_3 transports.
- (5) Wave number one dominates the ozone transports in both hemispheres (more in the SH).
- (6) The mean zonal wind in the lower troposphere displays an annual variation in the NH and a semiannual variation in the SH -- similar variations in the planetary wave forcings.
- (7) The EP flux vectors show most vertical propagation in the NH winter and in the SH Fall and Spring. This is consistent with the theory of Charney and Drazin and the observed mean zonal winds.
- (8) A recent model of Alan Plumb predicts that for small planetary wave forcing amplitudes (SH) the planetary waves behave linearly, consistent with the Charney-Drazin theory. For large forcing amplitudes (NH), the planetary waves decrease the mid-winter winds. This results in a semiannual planetary wave behavior in the SH and an annual behavior in the NH.
- (9) An annual behavior in planetary wave 2 occurs at a lower forcing amplitude than is the case for planetary wave 1.

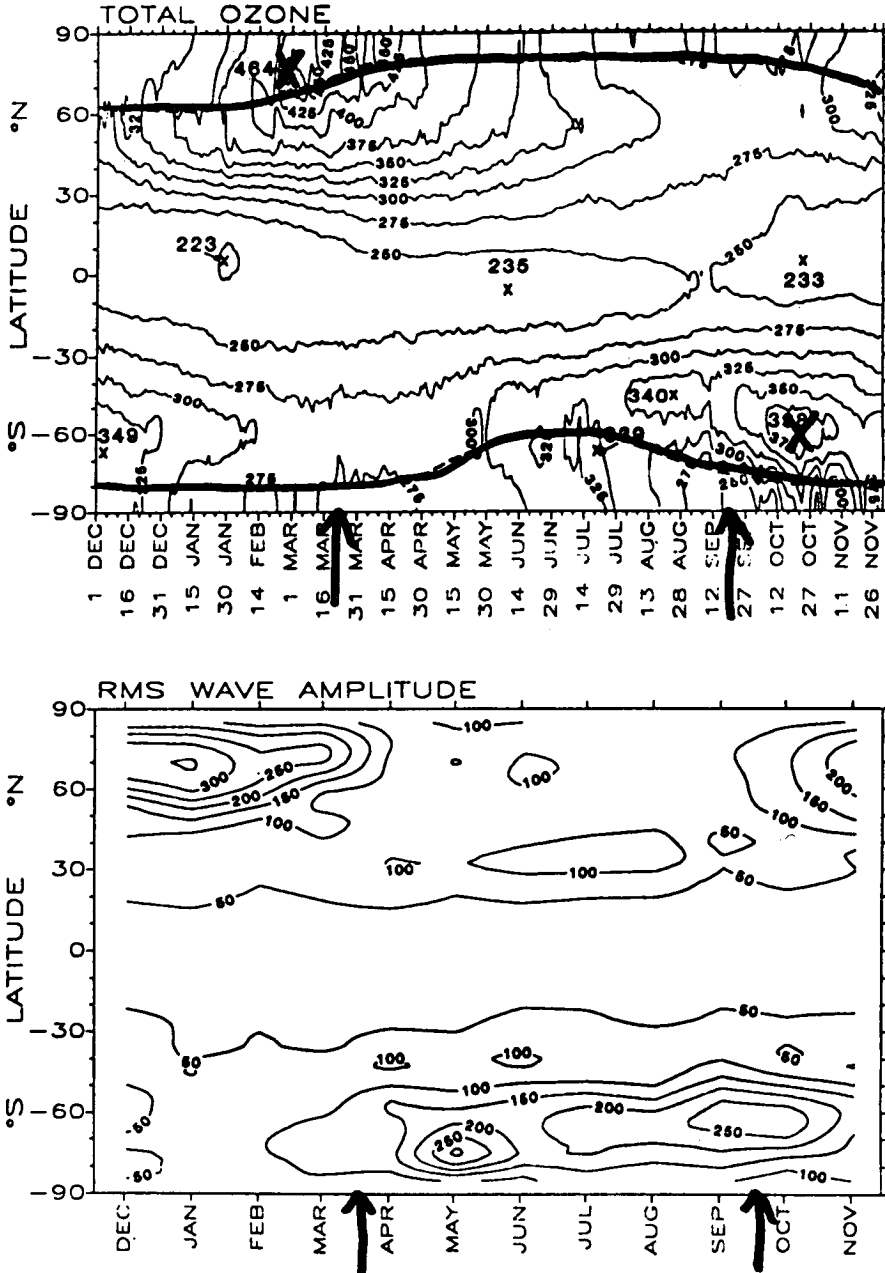


Figure 1. Top: Variation of SBUV-measured total ozone (in Dobson units) throughout the period December 1, 1978 to November 30, 1979. Bottom: Variation of the wave number one rms wave amplitude (in units of geopotential meters) at 100 mb for the period December to November [Geller and Wu, 1987].

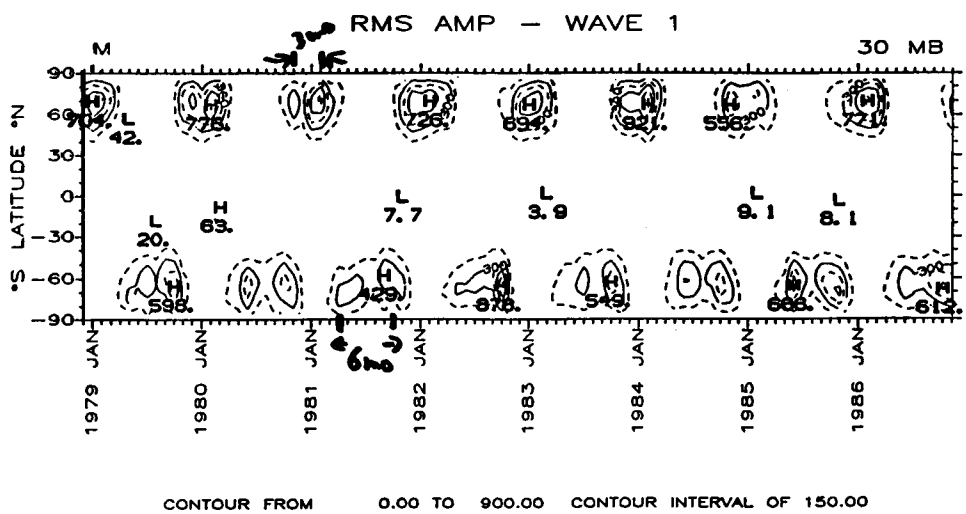


Figure 2. Variation of the wave number one rms wave amplitude (in units of geopotential meters) at 30 mb.

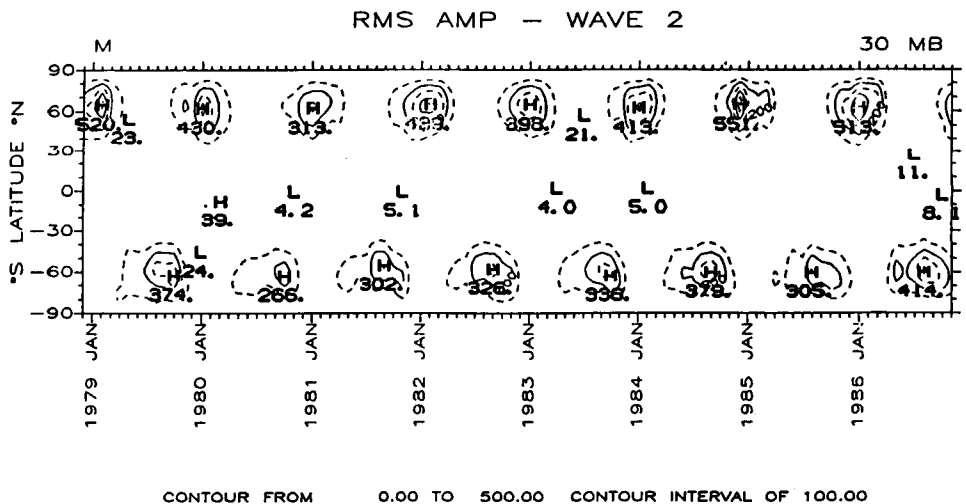


Figure 3. Variation of the wave number two rms wave amplitude (in units of geopotential meters) at 30 mb.

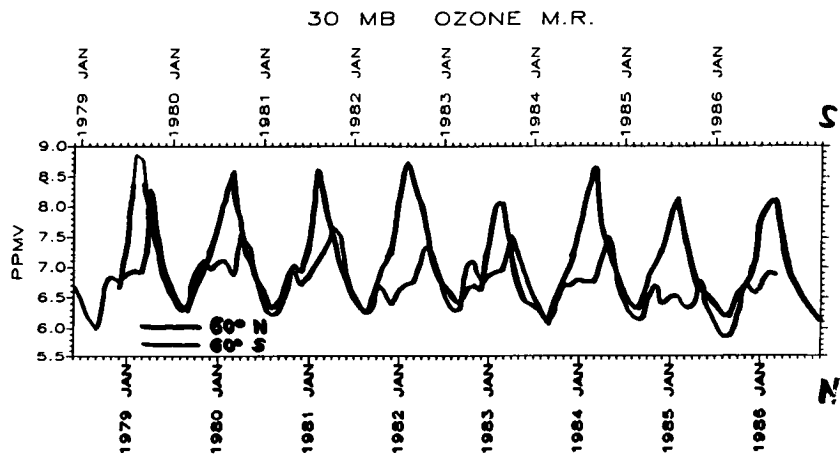


Figure 4. Variation of 30 mbar ozone mixing ratio (in ppmv) at 60°N and 60°S.

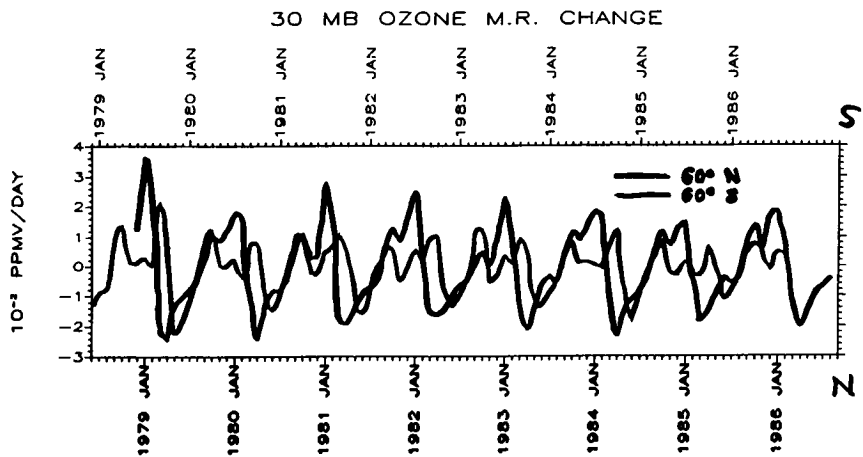


Figure 5. Variation of $\frac{dO_3}{dt}$ at 30 mbar in units of 10^{-2} ppmv/day at 60°N and 60°S.

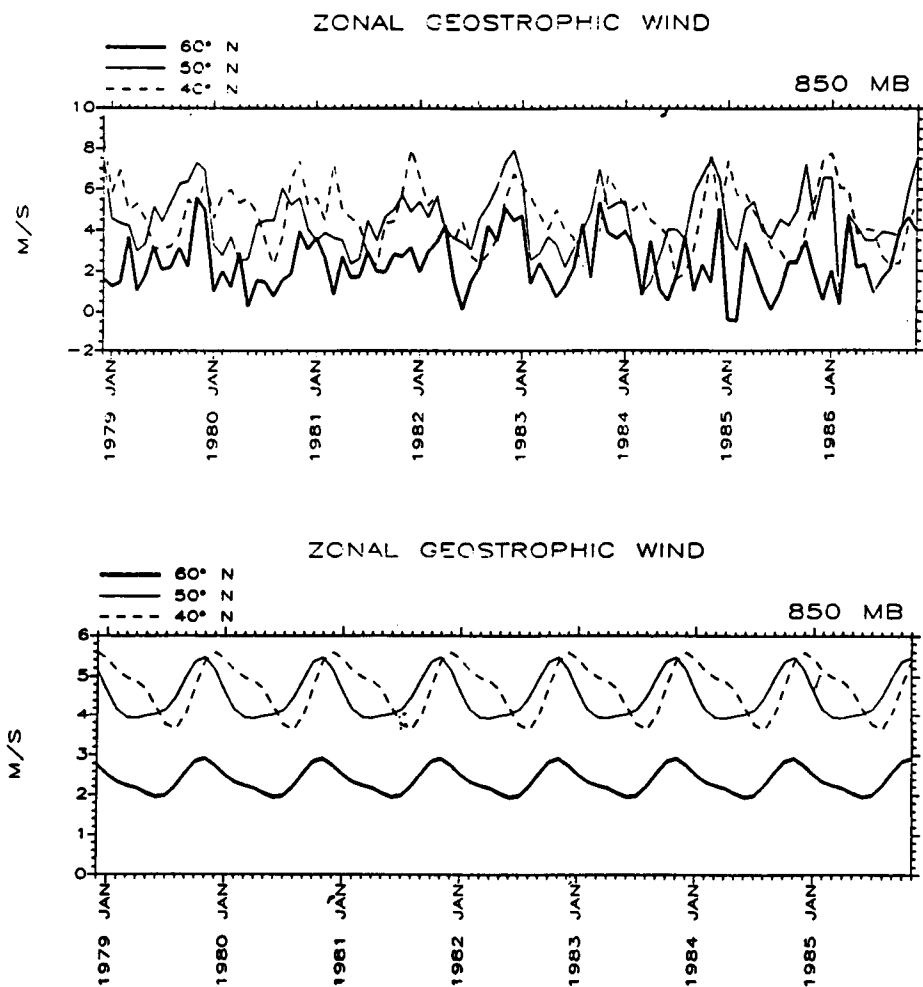


Figure 6. Mean zonal geospheric wind (in m s^{-1}) at 850 mb at 60°N, 50°N and 40°N. Top are monthly values and bottom is sum of annual and semiannual harmonics.

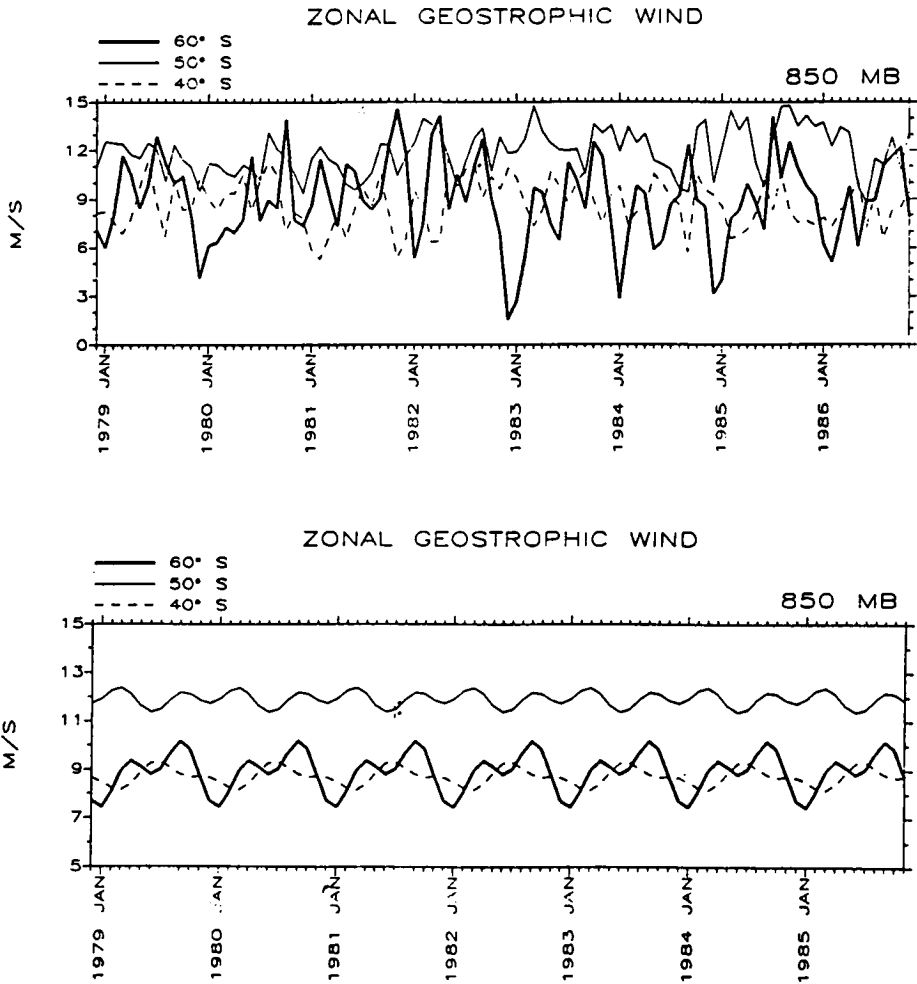


Figure 7. Mean zonal geospheric wind (in m s^{-1}) at 850 mb at 60°S, 50°S and 40°S. Top are monthly values and bottom is sum of annual and semiannual harmonics.

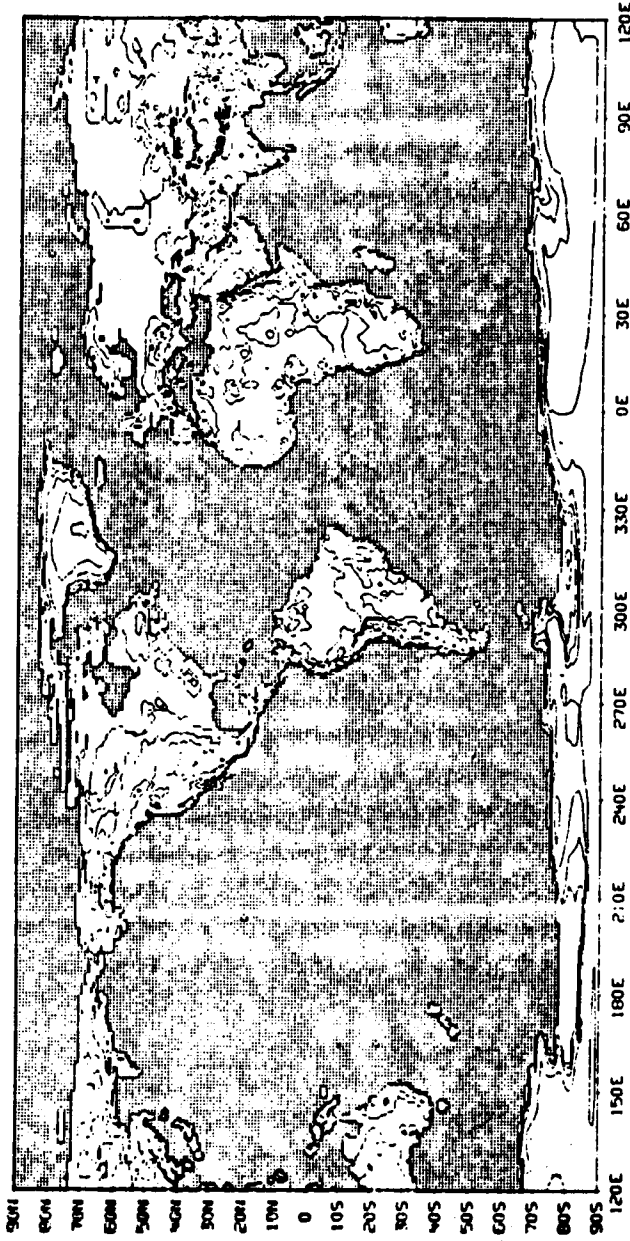


Figure 8. Analysis of the global terrain heights, with contours at 200, 500, 1000, 3000, 4000, 5000, 6000, 7000, 8000 m. The elevation of the coast is everywhere zero [Gates and Nelson, 1973].

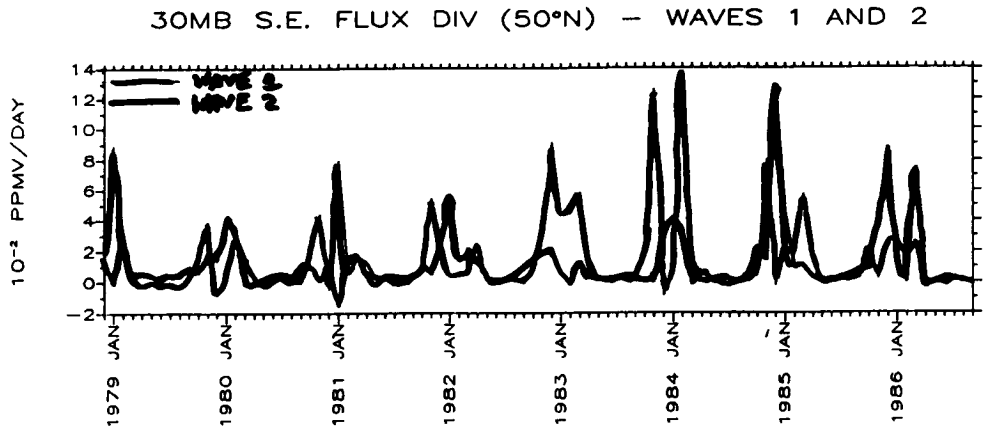


Figure 9. 30 mbar standing eddy divergence of O₃ flux at 50°N for wave numbers one and two.

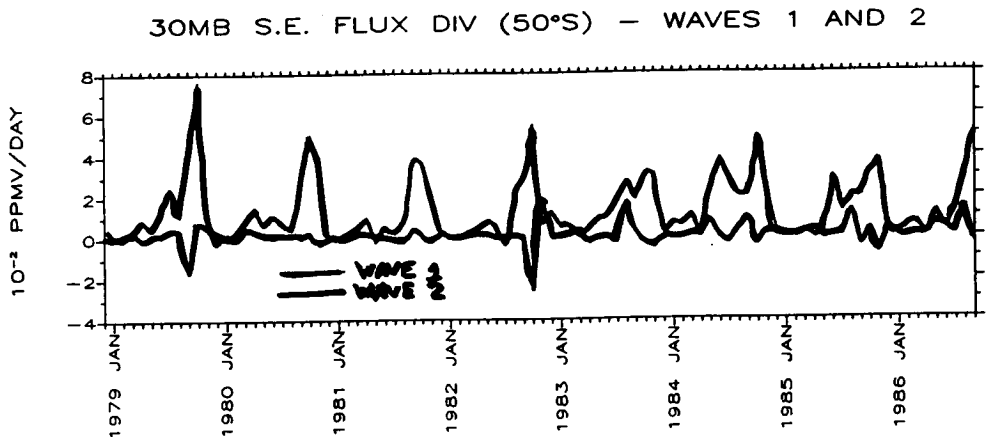


Figure 10. 30 mbar standing eddy divergence of O₃ flux at 50°S for wave numbers one and two.

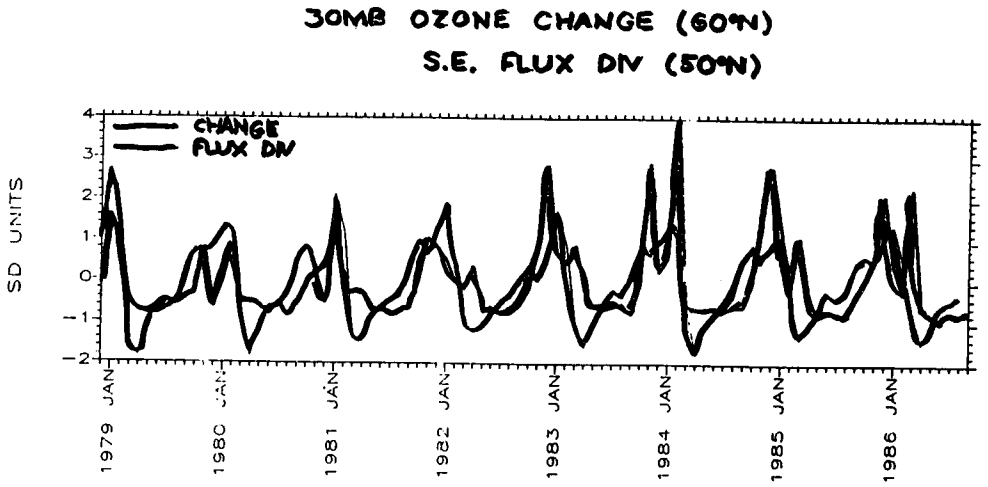


Figure 11. 30 mbar $\frac{dO_3}{dt}$ at 60°N and standing eddy ozone flux convergence at 50°N.

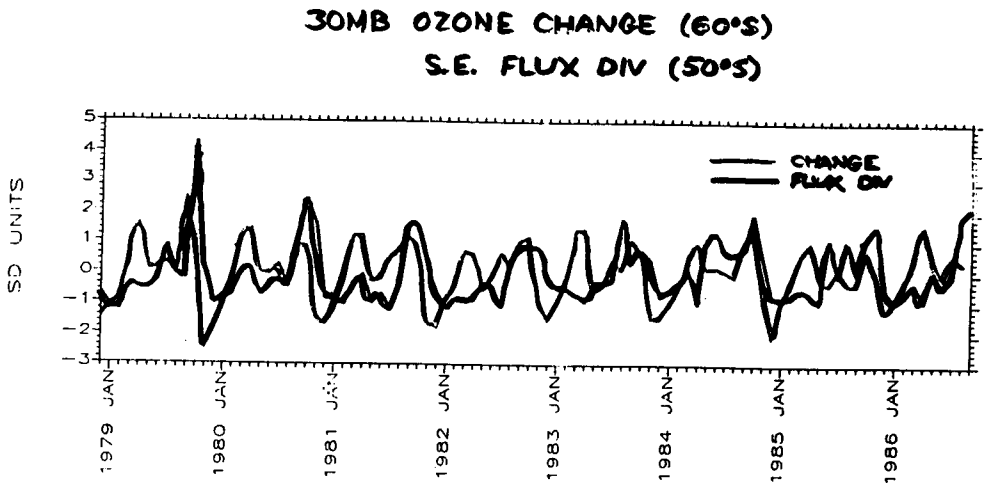


Figure 12. 30 mbar $\frac{dO_3}{dt}$ at 60°S and standing eddy ozone flux convergence at 50°S.

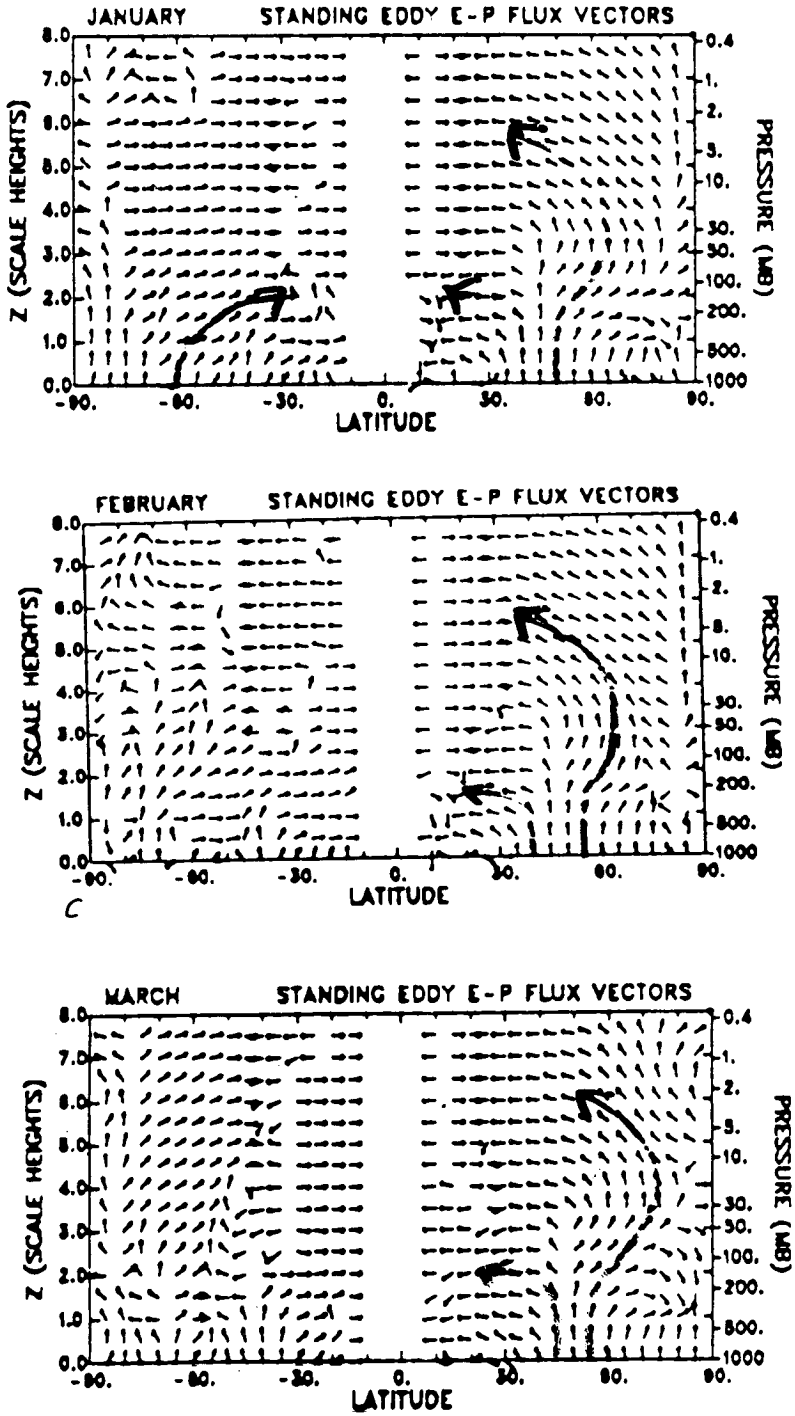


Figure 13. Monthly standing eddy Eliassen-Palm flux vectors (all the same length) for the 12 months.

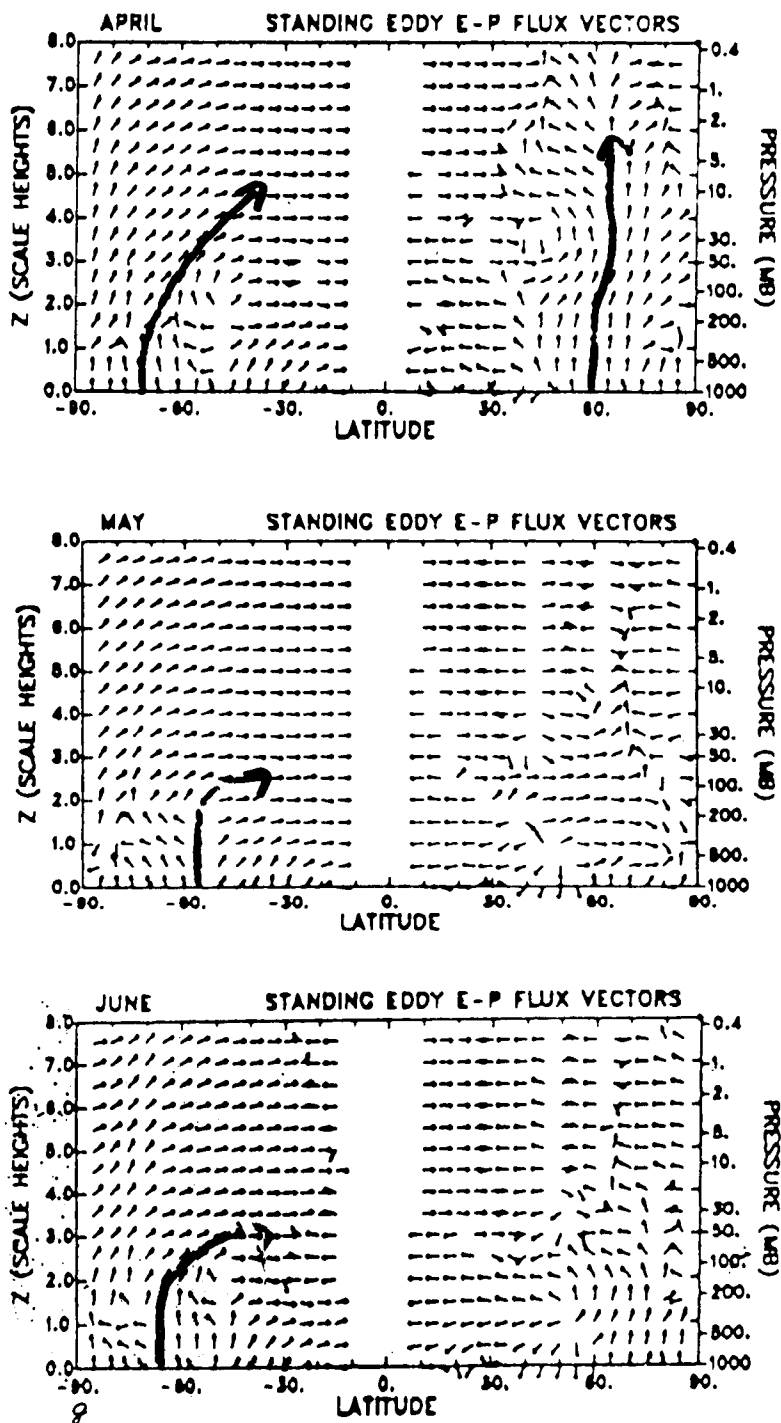


Figure 13 continued.

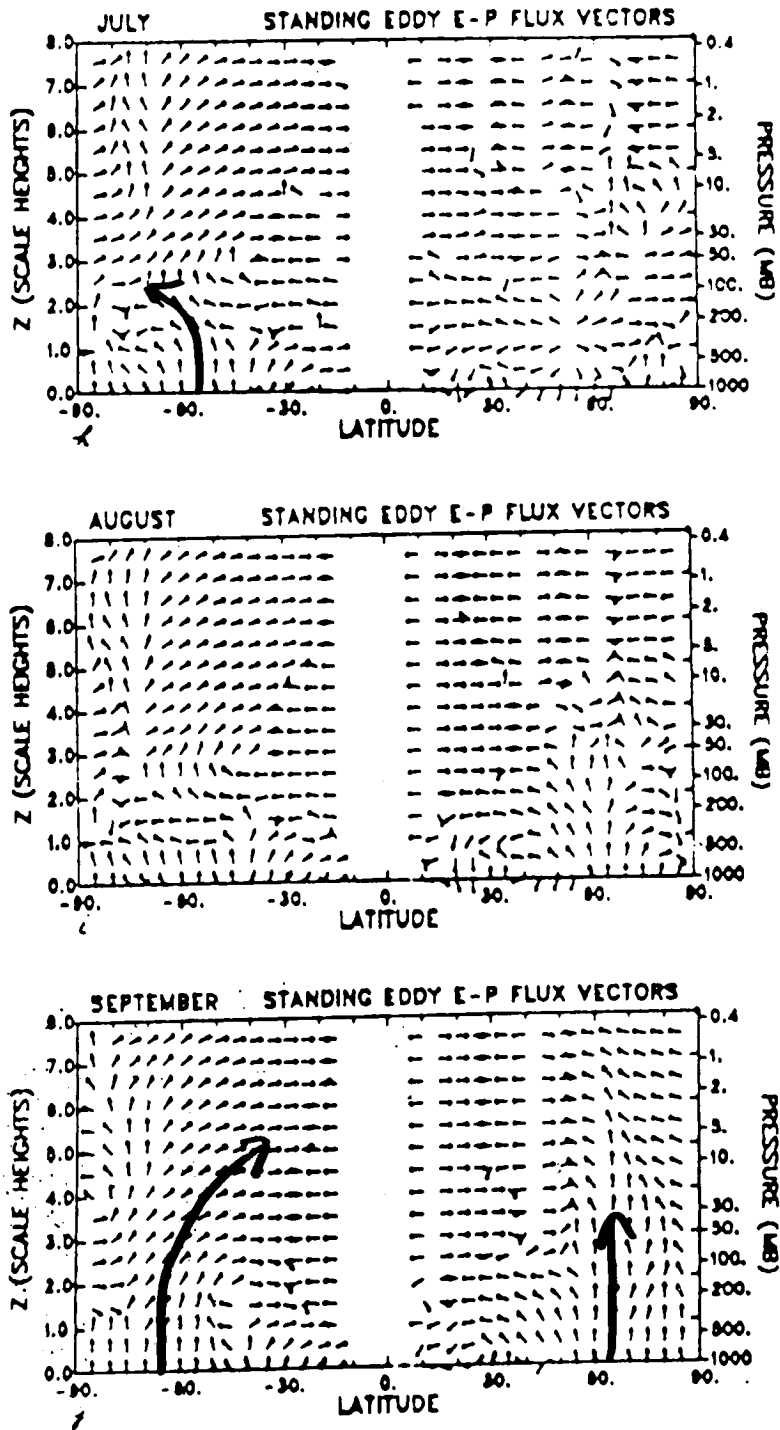


Figure 13 continued.

ORIGINAL FIGURE
OF POOR QUALITY

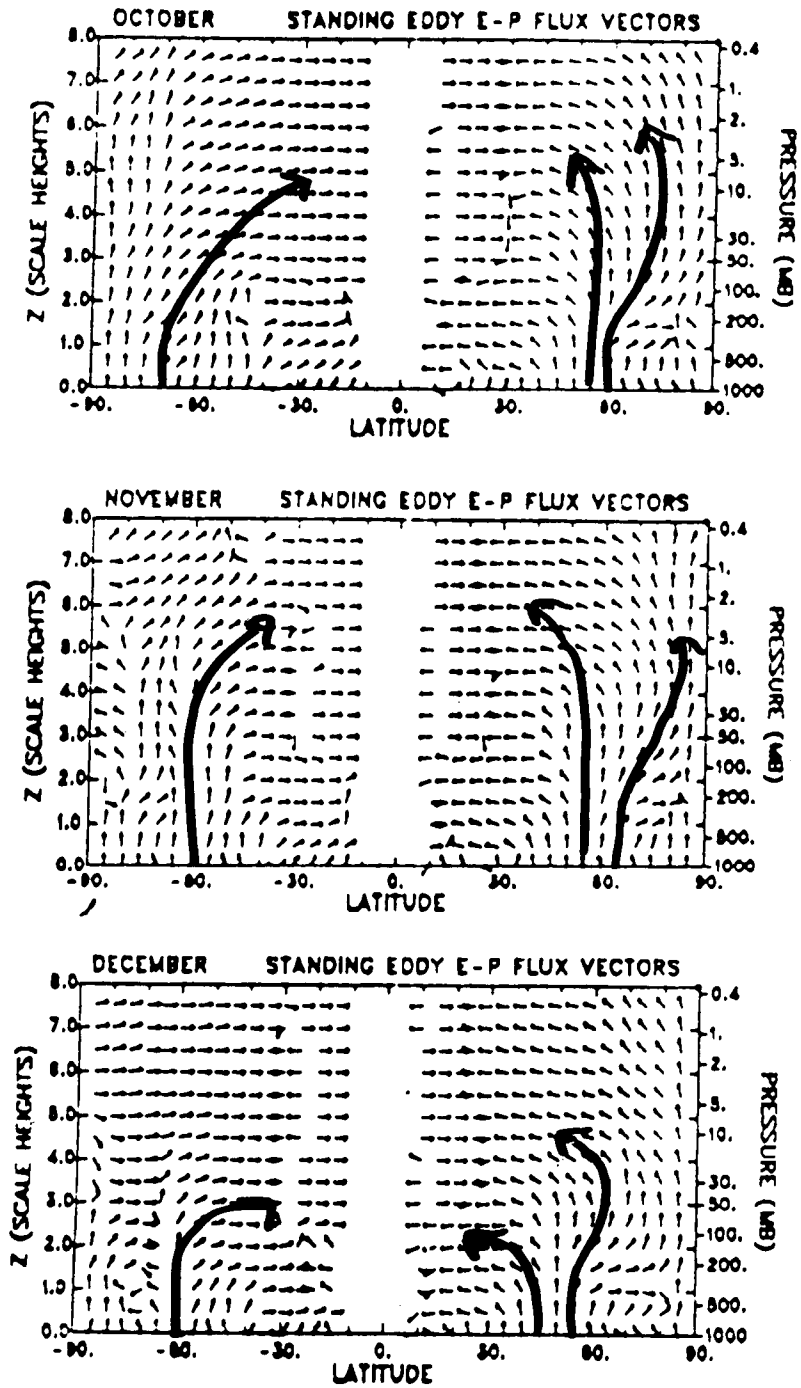


Figure 13 continued.

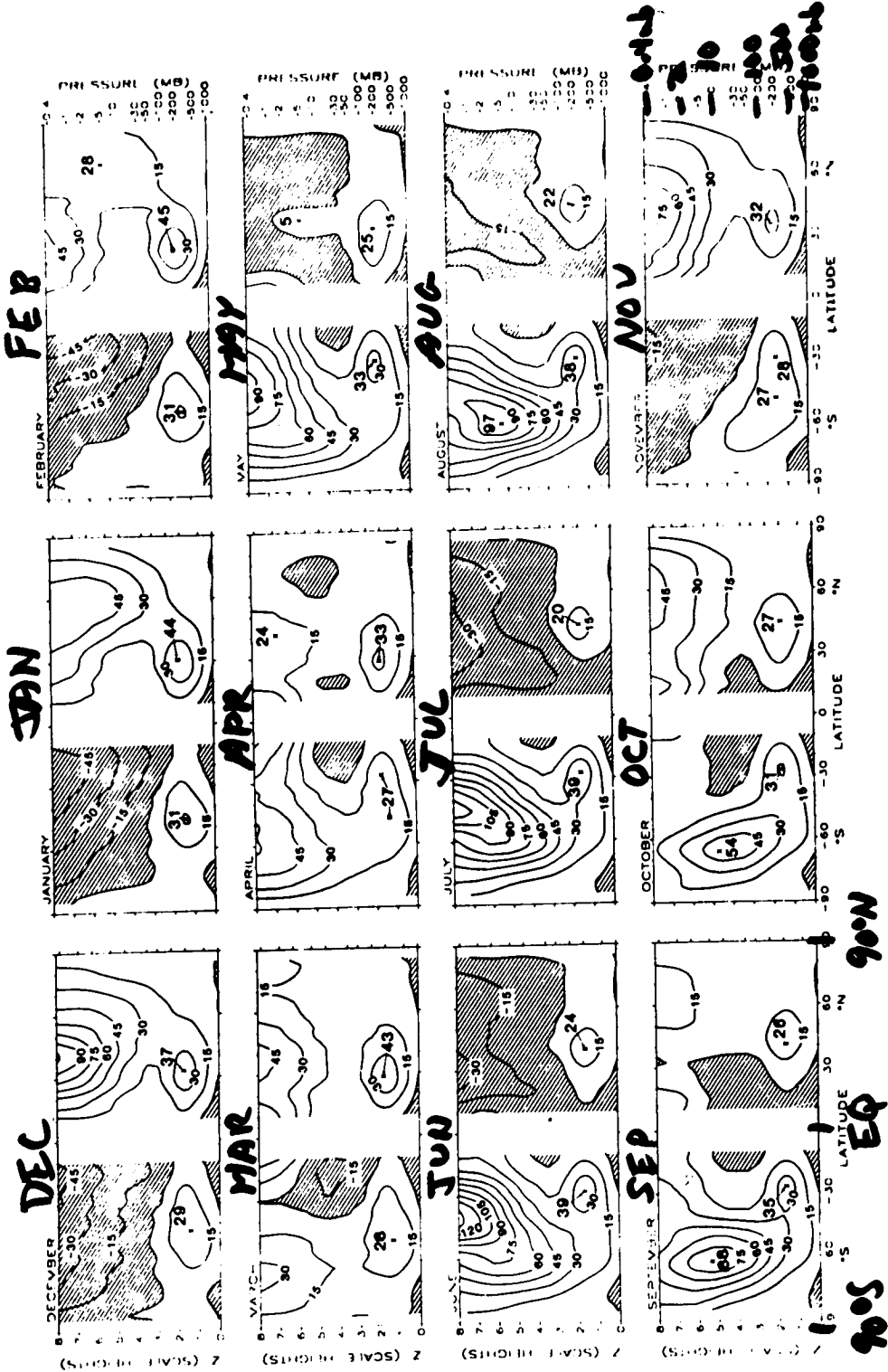
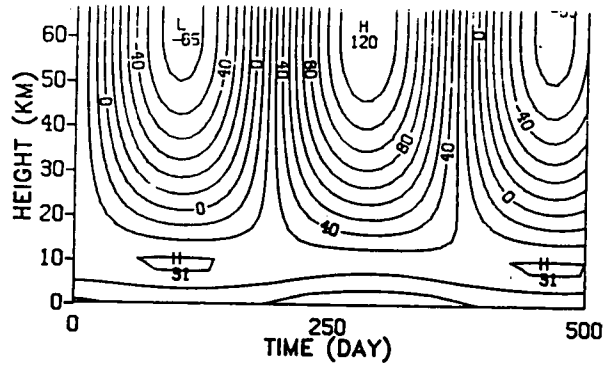
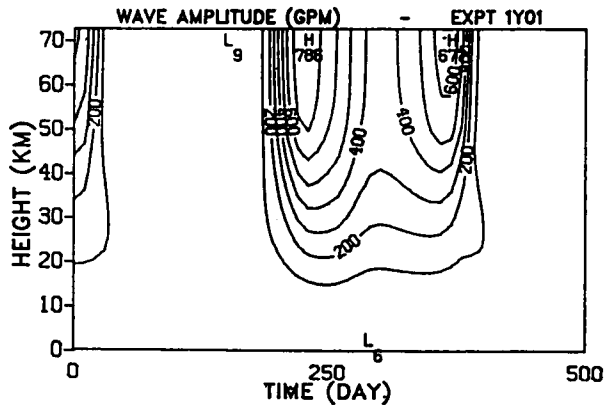


Figure 14. Monthly mean zonal winds (in m/s) for the 12 months of the year derived from a four-year data set.



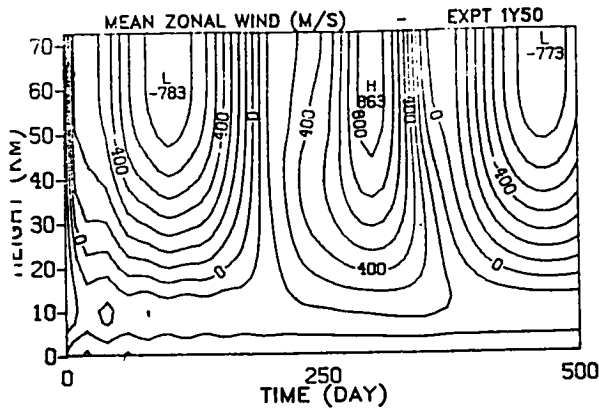
67 ms⁻¹



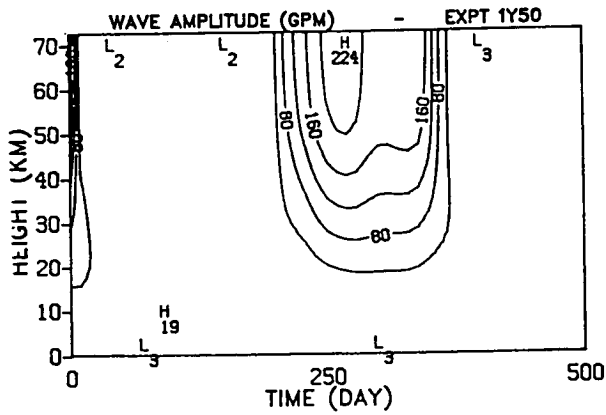
wn 1

Labels
x 0.1

Figure 15. Top: Modeled mean zonal wind variation. Bottom: Modeled planetary wave number one amplitude. Result from Plumb (unpublished, 1988) for a forcing amplitude of 1 m at zero.



$6 \text{ ms}^{-1} \times 1$



w_1

Figure 16. Top: Modeled mean zonal wind variation. Bottom: Modeled planetary wave number one amplitude. Result from Plumb (unpublished, 1988) for a forcing amplitude of 60 m at zero.

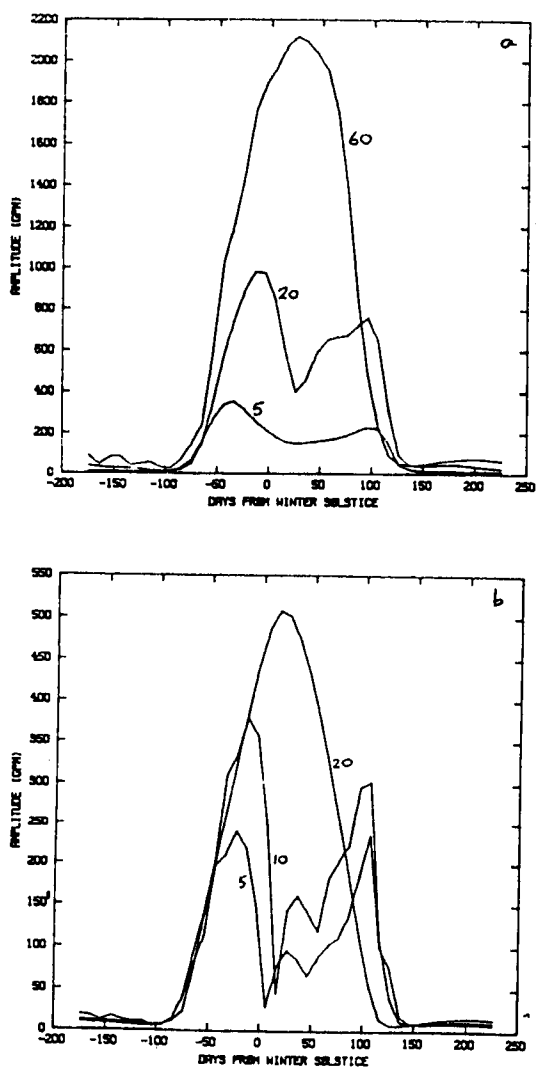


Figure 17. Response curves for wave number one (top) and wave number two (bottom) for different forcing amplitudes.

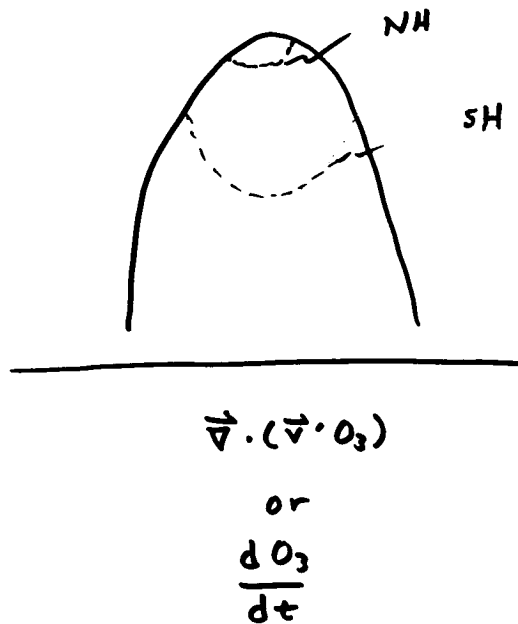


Figure 18. Schematic indicating large mid-winter notch out of ozone transport in the Southern Hemisphere and smaller one in the Northern Hemisphere.

Answer to our Original Question

It appears that the annual behavior of planetary wave one in the Northern Hemisphere and its semiannual behavior in the Southern Hemisphere are a result of the lower amplitude wave forcing in the Southern Hemisphere.

The annual cycle of the O_3 transports follow from this.

5.3 AN OVERVIEW OF GLOBMET DURING MAP AND MAC

R. G. Roper

School of Geophysical Sciences
Georgia Institute of Technology
Atlanta, GA 30332

Since its inception in 1982, GLOBMET (the Global Meteor Observations System) has contributed significantly to furthering our understanding of meteor astronomy, meteor physics and, by using the ionized trails as tracers, to the dynamics of the mesopause/lower thermosphere. An overview is given of the results of interest to MAP, as presented at the First GLOBMET Symposium held in Dushanbe, Tajicistan, USSR, in August 1985, and the Second Symposium held in Kazan, USSR in July 1988.

GLOBMET was proposed as a MAP Project by the Soviet Geophysical Committee in 1982. Papers presented at the First GLOBMET Symposium have been published in HANDBOOK FOR MAP, Volume 25; it is planned that papers from the Second Symposium will be published in a future volume of HANDBOOK FOR MAP.

5.4 THE METEOR RADAR AS A TOOL FOR UPPER ATMOSPHERE RESEARCH

S. K. Avery

Department of Electrical and Computer Engineering
Cooperative Institute for Research in Environmental Sciences
University of Colorado, Boulder, Colorado 80309-0425

Meteor radar provide measurements of the upper mesosphere-lower thermosphere neutral wind field by using the reflection of electromagnetic waves from meteor trails. These radars are relatively inexpensive and provide an excellent means of monitoring the mean winds and tides in the 80 - 100 km region. Recently new techniques have been developed to detect meteor echoes from other ground-based radar systems operating in the HF/VHF frequency range. The meteor echo information augments the data that are routinely collected by these radars. These new techniques will be discussed.

Brief History

- 1920s - Anomalous echoes from ionosphere
- World War II - Meteors identified as source of ionization
- 1950s - Atmospheric processes studies using meteor echoes
 - Established technique

Traditional meteor radar systems

- Roper (1984)
- CW or pulsed
- Low-powered Tx
- Wide antenna beams
- Coherent receivers - Doppler detection
 - Strong signal but short-lived
- Used for mesosphere dynamics studies

Meteor detection on ST/MST and IDI radars

- Present 24 hours day⁻¹
- Augments data routinely obtained by radar

Detection on IDI radar

- Adams et al. [1986] 2.66 MHz
- Frequency-domain interferometry
- Meteor echoes extracted using power threshold algorithm
 - Time-domain interferometry for location of echo

Detection ST/MST radars

- Avery [1987]; Fukao [1987]
 - Post-processing
- Real-time detection and collection

Problems

- Narrow antenna beams
- Coherent averaging/FFT
- Strong turbulence

MEDAC (Meteor echo detection collection)

- Operates in parallel with existing radars
 - Power threshold versus partial DFT
 - Inexpensive
- Field tested on ST radar at Platteville, CO
- Performance tested on Poker Flat MST radar
- Used in support of observation campaigns

Summary

- Meteor radars are a good measurement technique for studying mean winds, tides, planetary scale waves, long period gravity waves.
- ST/MST and IDI radars receive meteor echoes.
- With optimum detection, collection, and signal processing of these echoes, additional data can be obtained that augments the normal data taken by these radars.

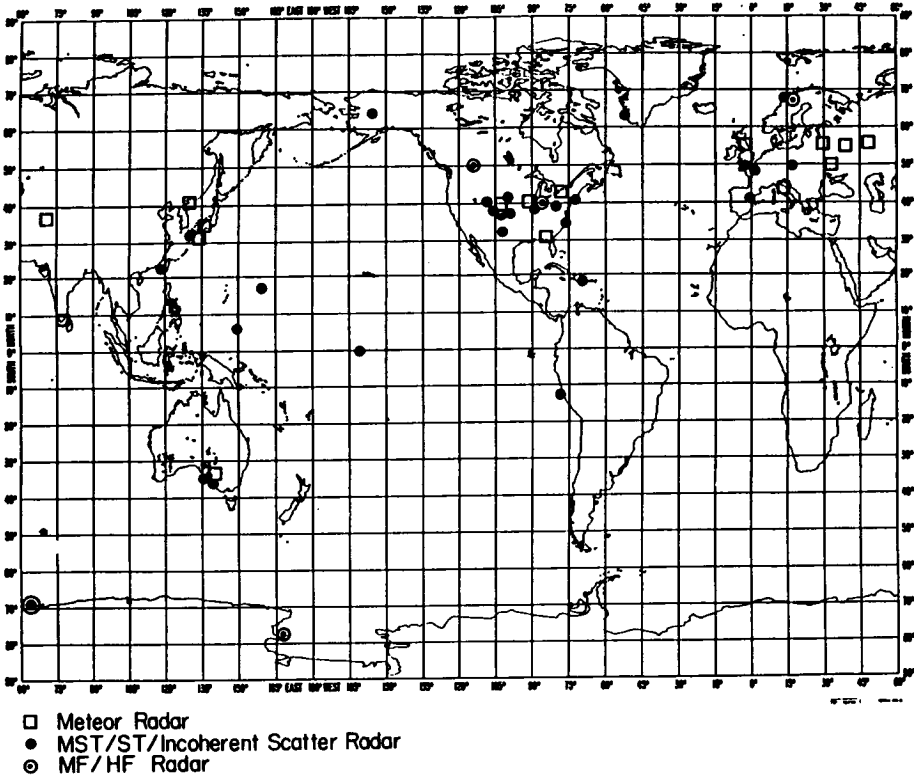


Figure 1. Geographic distribution of currently operating meteor radars, MST/ST/incoherent scatter radars, and MF/HF radars. Meteor radars are an established technique for studying the upper mesosphere/lower thermosphere.

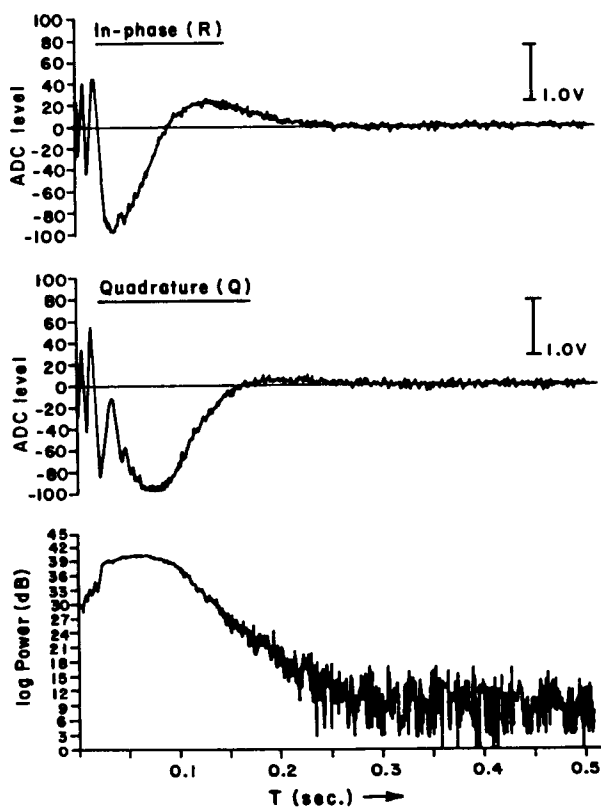


Figure 2. Output from the coherent receiver and power due from a meteor echo. The transmitted radar signal is scattered from free electrons associated with the ionized meteor trail. The fast rise time in the power is a function of the meteor velocity. The exponential decay in power is due to the diffusion of the trail. The high frequency in the voltage is due to the formation process of the first Fresnel zone of the diffraction pattern of the echo. The low frequency observed after the power has reached the peak is due to the neutral wind.

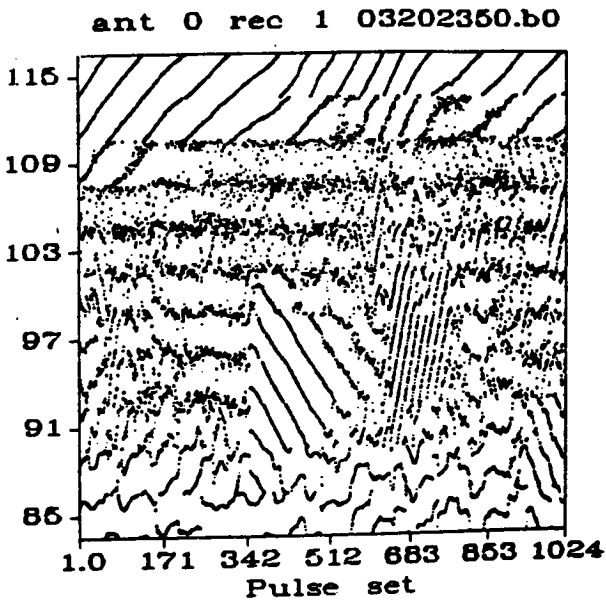
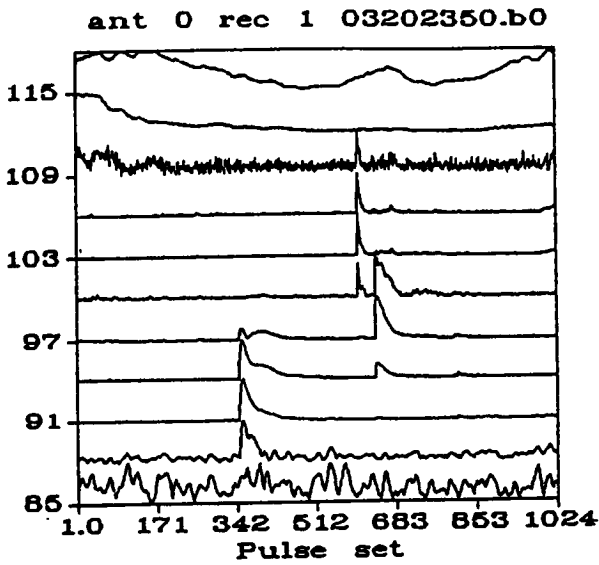


Figure 3. From Turek [1986]. Amplitude and phase of echo received on IDI radar. Meteor echoes are seen easily in the amplitude plot. For these echoes a clear phase progression is observed.

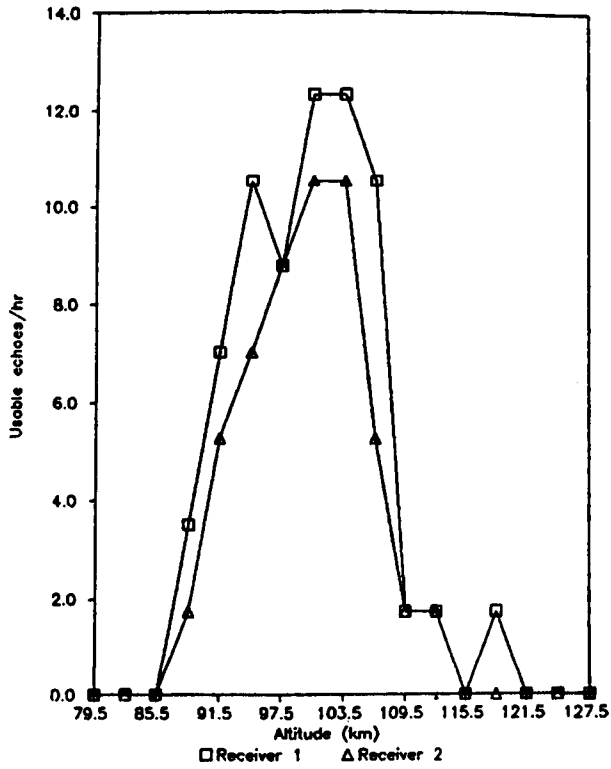


Figure 4. Meteor echo rate as a function of height for echoes observed on 2.66 MHz IDI radar [Turek, 1986]. Peak echo rate occurs at 103 km.

ORIGINAL PAGE IS
OF POOR QUALITY

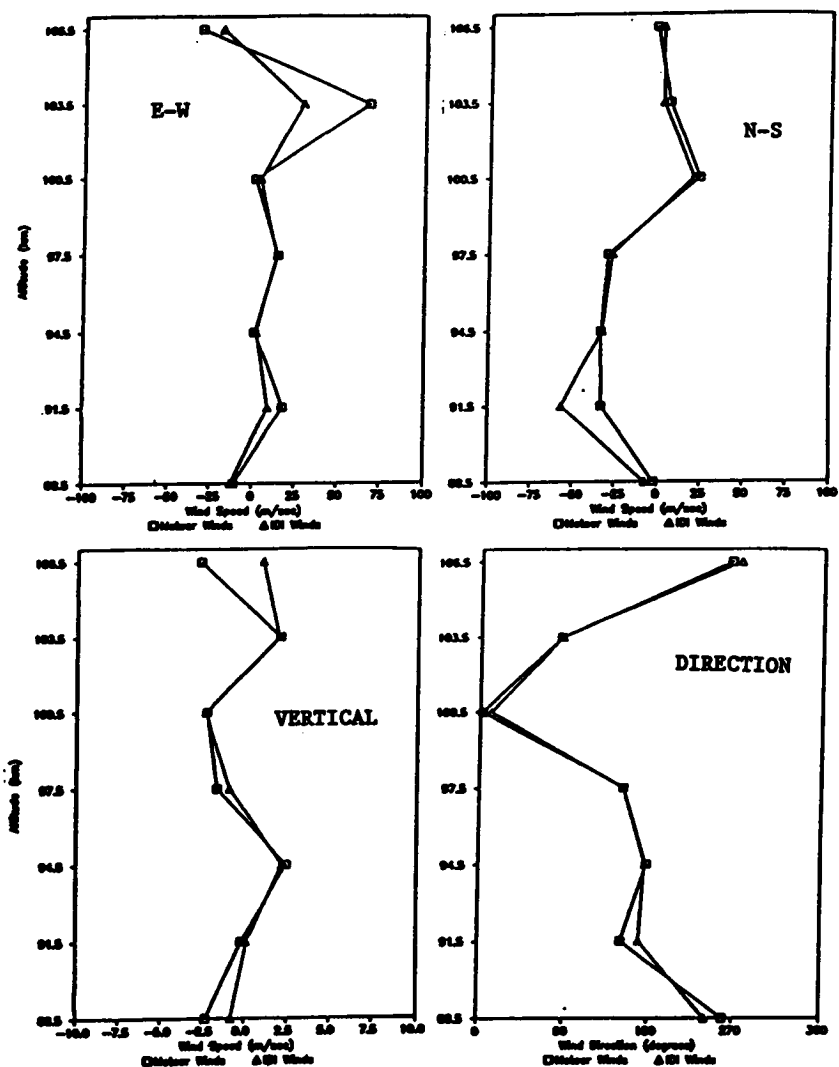


Figure 5. Comparison of winds derived from meteor echoes and those derived from regularly collected echoes on IDI radar.

ORIGINAL PAGE IS
OF POOR QUALITY

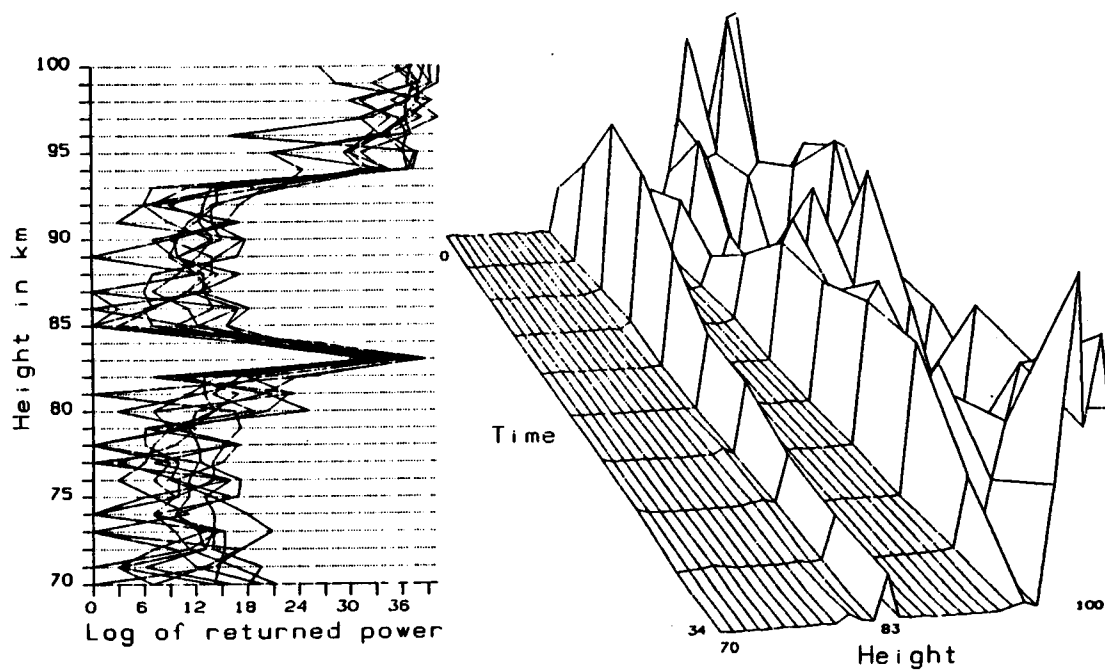


Figure 6. Profile of meteor echo observed at Jicamarca Radio Observatory. Power at the upper altitudes is due to the electrojet.

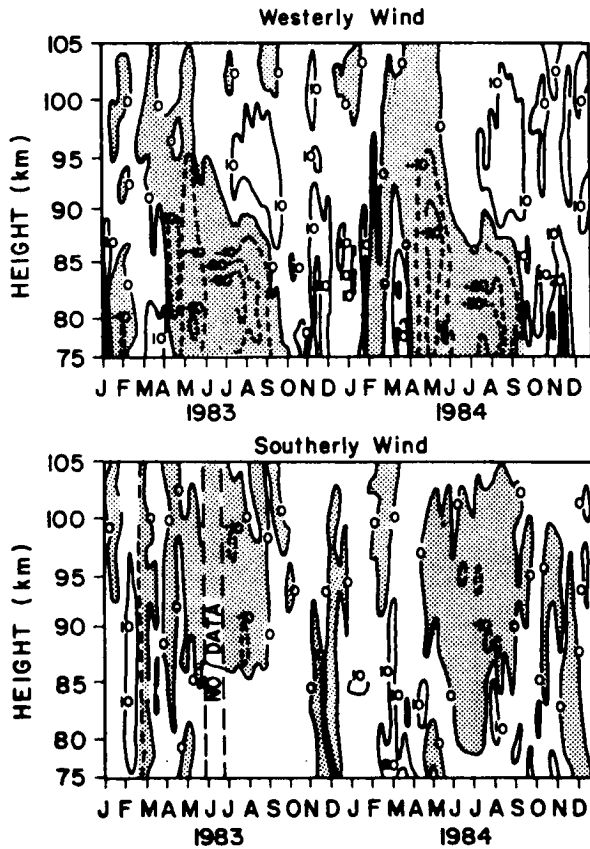


Figure 7. From Manson, et al. [1988]. Mean winds determined from meteor echoes observed on the Poker Flat, Alaska MST radar.

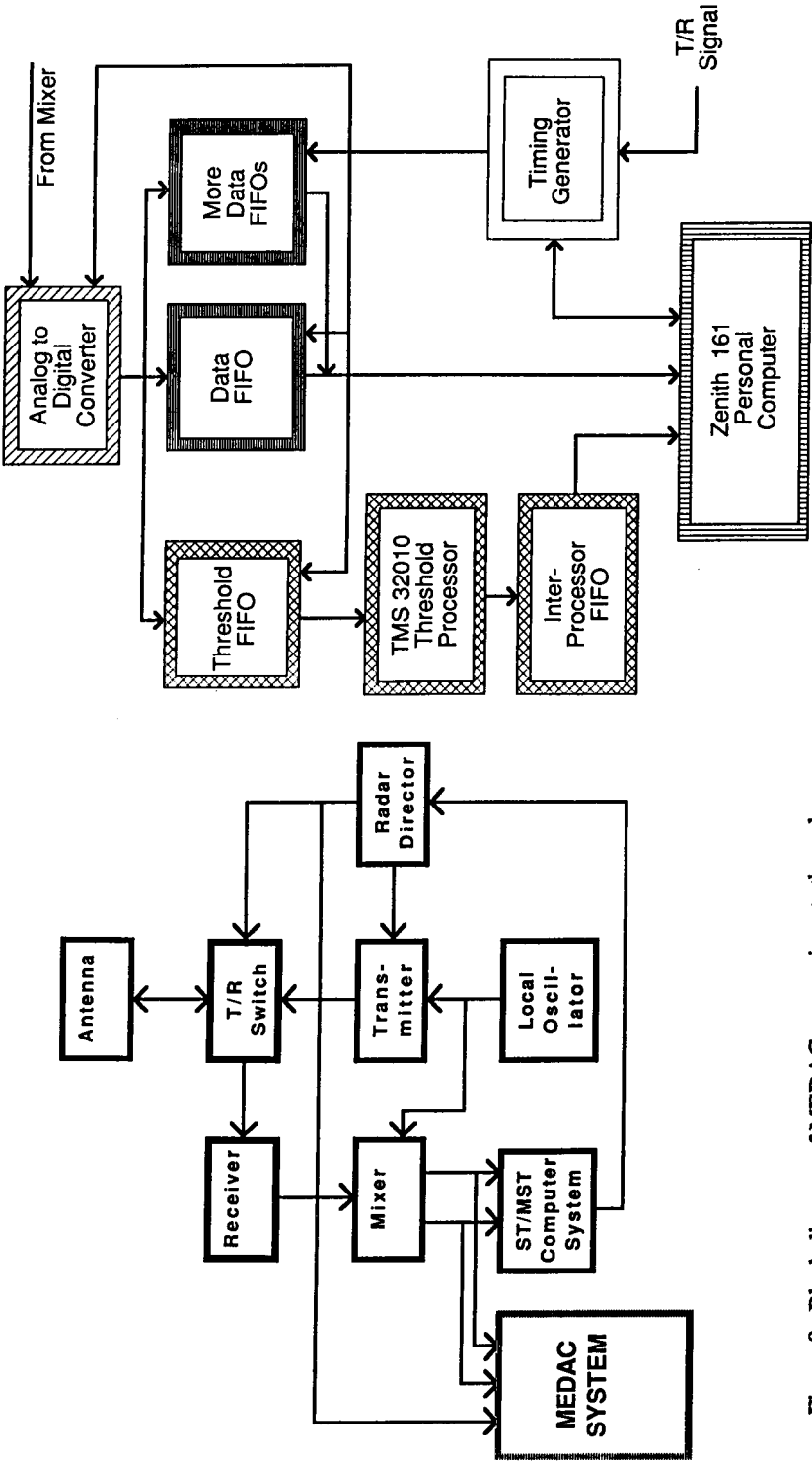


Figure 8. Block diagram of MEDAC connections to the radar.

Figure 9. Block diagram of MEDAC system.

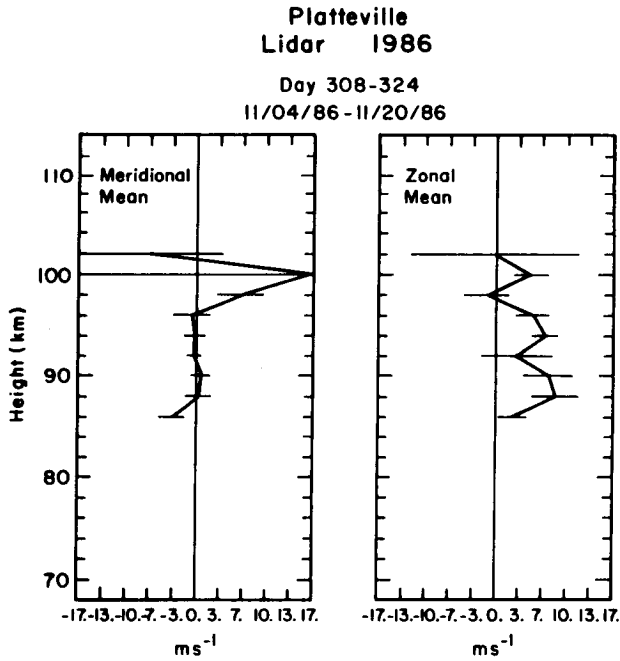


Figure 10. Mean winds from MEDAC system operating on Platteville, CO, ST radar. This observational campaign was carried out in coordination with the sodium lidar from the University of Illinois.

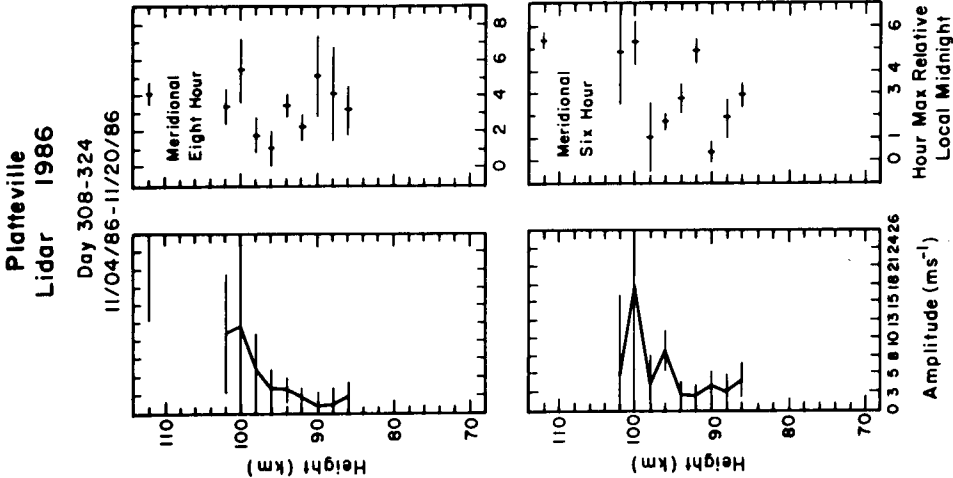


Figure 12. Eight- and six-hour components of wind field. The six-hour component was also observed with the sodium lidar.

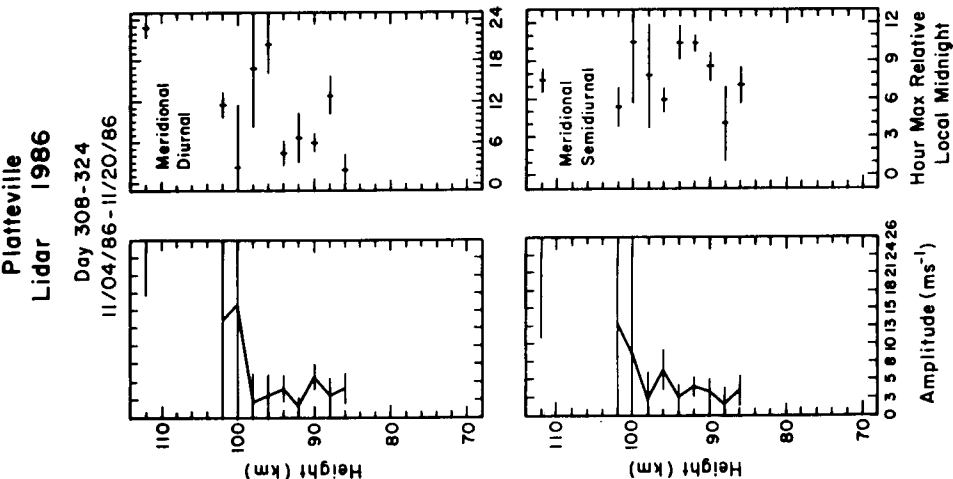


Figure 11. Amplitude and phase of the diurnal and semidiurnal tide during the same period as in Figure 10.

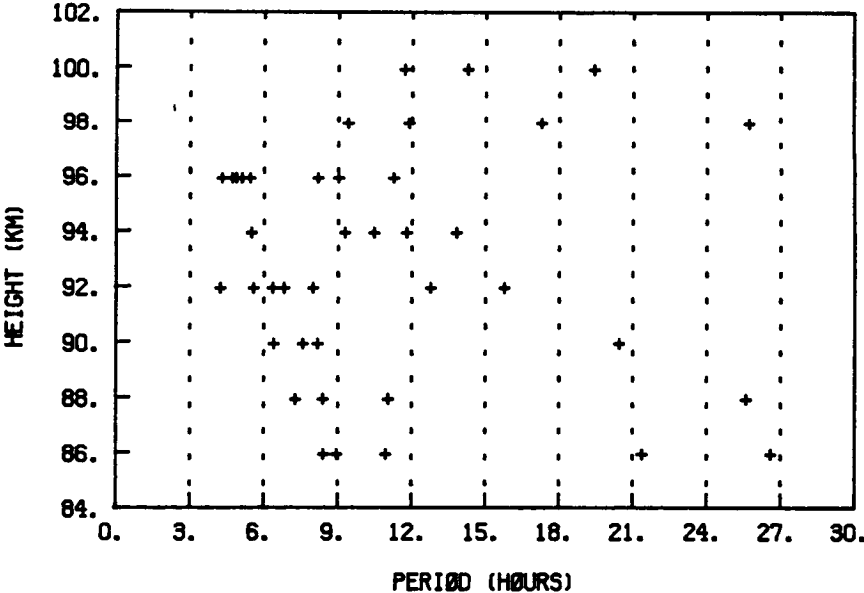


Figure 13. Period estimates of wave motions determined using a new algorithm for randomly sampled data, signal processing improvements can enhance the use of meteor radar data.

5.5 REMOTE SENSING OF THE ATMOSPHERIC AEROSOLS AND NOCTILUCENT CLOUDS FROM SPACE

O. Avaste

Tartu State University, USSR
202444 Tartu, Estonia, USSR

M. Gadsden

University of Aberdeen,
Aberdeen, AB9 2UE Scotland

R. Room

Laboratory of Space Radiometry, Institute of Astrophysics and Atmospheric Physics
202444 Tartu, Estonia, USSR

The method for the determination of the optical density of tropospheric and mesospheric aerosols and for the estimation of the scattering phase function in the forward directions ($0 - 30^\circ$) is proposed. The method is based on measurements of the brightness of the twilight horizon with the high-resolution limb-camera having five separated fields of view. In some detail the features of the camera are described and the mathematical aspects of remote sensing data-inversion are discussed.

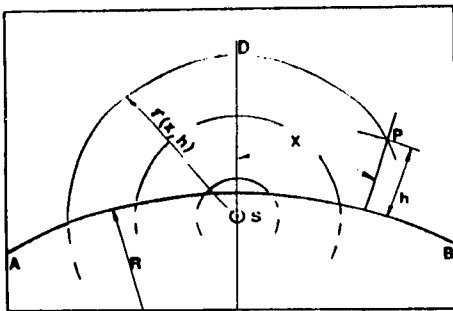


Figure 1. The coordinate system in the twilight horizon scanning equipment. AB - the limb of the Earth; S - the center of the Sun; P - the perigee point of the line-of-sight (line-of-sight is approximately perpendicular to the plane of figure).

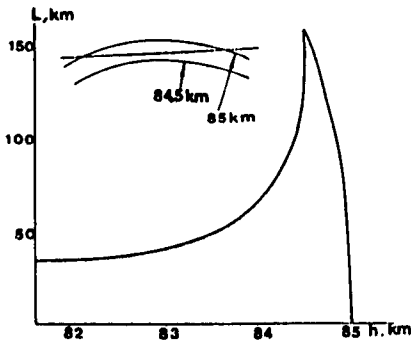


Figure 2. The optical path through the homogeneous layer as a function of height.

5.6 LOWER STRATOSPHERIC AEROSOLS AT A TROPICAL LATITUDE STATION

B. V. Krishnamurthy, K. Parameswaran, K. O. Rose, and M. Satyanarayana

Space Physics Laboratory, Vikram Sarabhai Space Centre
Trivandrum 695002, India

A pulsed ruby lidar has been in regular operation at the tropical station Trivandrum ($8^{\circ} 33' \text{ N}$, $76^{\circ} 57' \text{ E}$) since October 1986. The lidar data have been analyzed to obtain monthly mean aerosol extinction at lower stratospheric altitudes. The monthly mean variation of aerosol extinction shows a peak in March-April with a trough in the winter months. This behavior is compared with that of temperature at the same altitude, obtained from balloonsonde measurements at the same station. It is found that there is a negative correlation between the two with high extinction values corresponding to low temperature values and vice versa. This is attributed to the stratospheric aerosol microphysical processes. The association of stratospheric aerosol extinction with the tropopause altitude and temperature has been studied also and the implications of these results are discussed.

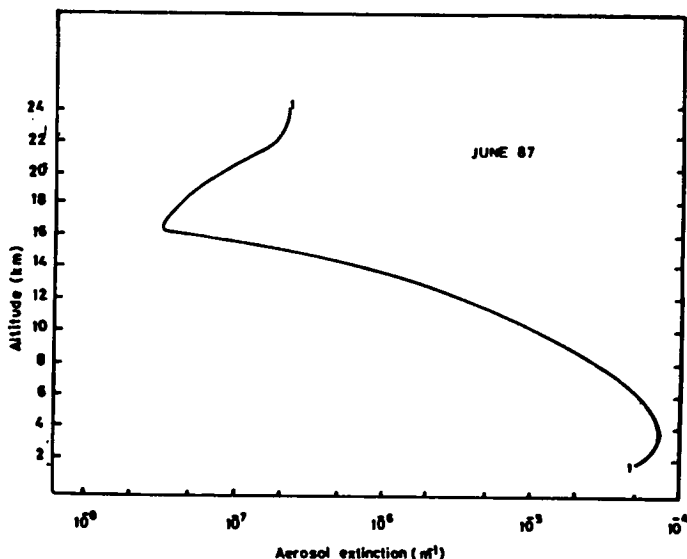


Figure 1. Monthly mean altitude profile of aerosol extinction for June 1987 at the tropical station Trivandrum ($8^{\circ} 33' \text{ N}$, $76^{\circ} 57' \text{ E}$). the profile is obtained using ruby lidar backscatter observations.

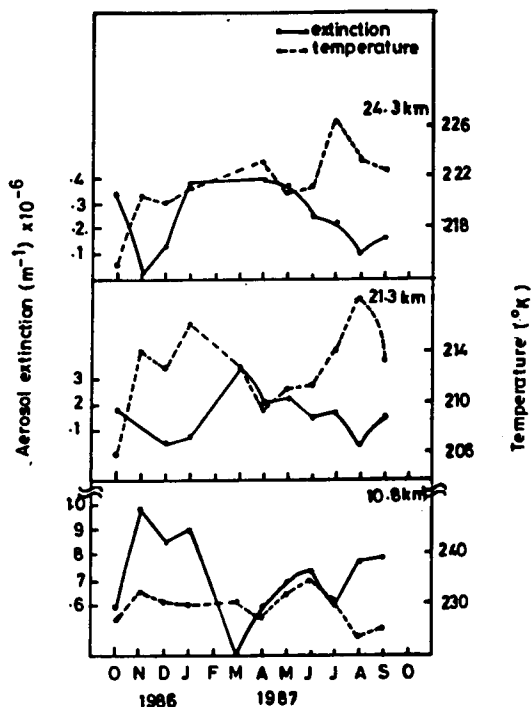


Figure 2. Variation of monthly mean aerosol extinction and temperature at 21.3 km and 24.3 km in the lower stratosphere and at 10.8 km in the troposphere. Aerosol extinction shows a negative correlation with temperature in the stratosphere whereas no such association is seen at 10.8 km. The negative correlation in the stratosphere is attributed to the *in situ* aerosol (sulfate) production processes of heterogeneous heteromolecular and homogeneous heteromolecular nucleation which are more efficient at lower temperatures.

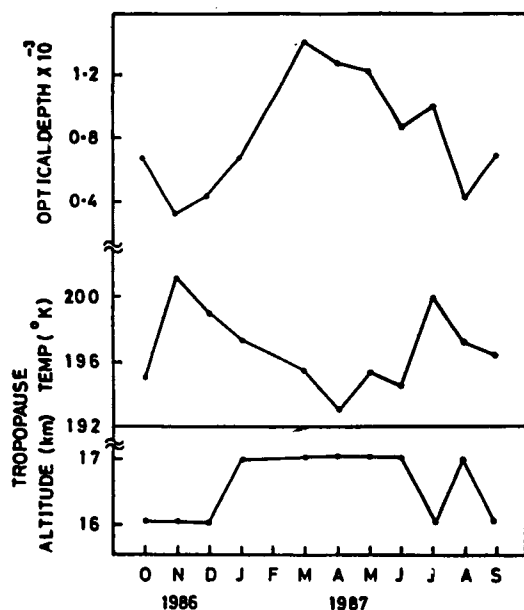


Figure 3. Variations of monthly mean stratospheric aerosol optical depth (from 18 km to 24 km) and tropopause altitude and temperature. The tropopause altitude is high during months of large optical depth. High tropopause altitude indicates increased convective activity. This would lead to an increase of convective transport of precursor gases (OCS and SO_2) from the troposphere into the stratosphere for *in situ* aerosol production.

5.7 SOME NEW RESULTS IN THE INVESTIGATION OF THE MIDDLE ATMOSPHERE FROM SPACE USING THE DAYTIME HORIZON SCANNING METHOD

R. Rõm, K. Eerme, and U. Veismann

Institute of Astrophysics and Atmospheric Physics
20244 Tartu, Estonia, USSR

The results of the restoration of the optical parameters of the El Chichon aerosol cloud at $\lambda 2.2 \mu\text{m}$ are presented. The eight-channel teleradiometer FAZA for visible and near-infrared spectral regions is described in some detail. Mathematical aspects of data processing for the ill-posed problems are discussed. The results of the restoration of the volume emission rate of the molecular oxygen on $\lambda 1.27 \mu\text{m}$ in the middle atmosphere and of the aerosol on $\lambda 0.84 \mu\text{m}$ are presented.

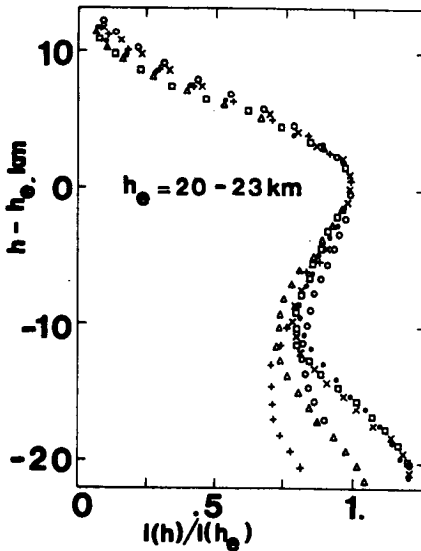


Figure 1. The daytime horizon radiance above the Sahara, 6 July 1982 at the wavelength $2.2 \mu\text{m}$ in relative units. h_0 - the height of the aerosol-caused radiance maximum in the stratosphere. The stratospheric aerosol layer at the wavelength $2.2 \mu\text{m}$ has the optical thickness 0.04.

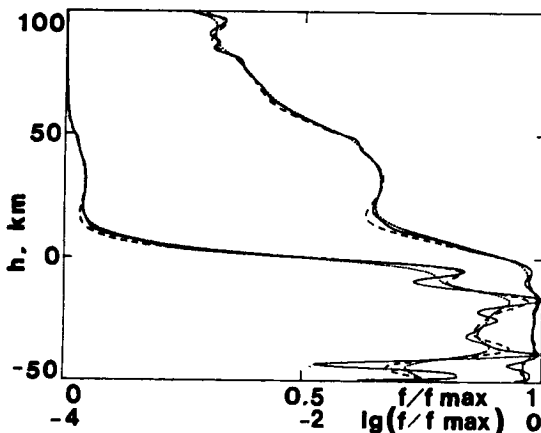


Figure 2. The modeling of the smooth and restoration processes. The standard deviation of the field response function of the teleradiometer is 3.0 km. The continuous line presents the nonsmoothed, the dotted line the smoothed and the dashed line the restored radiance of the daytime horizon. The left-hand curves are in the linear scale. The right-hand lines present the same curves, but in the logarithmic scale.

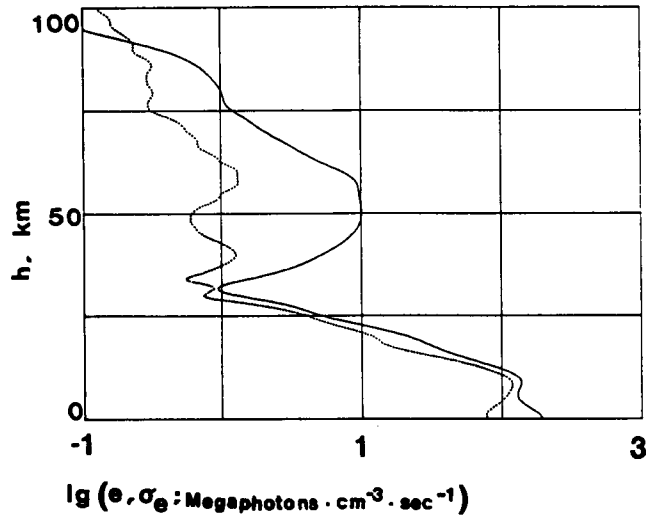


Figure 3. The mean volume emission rate e of the molecular oxygen at the wavelength $1.7 \mu\text{m}$ (continuous line) and its standard deviation σ_e (dotted line), as the functions of height h in the latitude interval $0 - 50^\circ \text{S}$ on 22 October 1985.

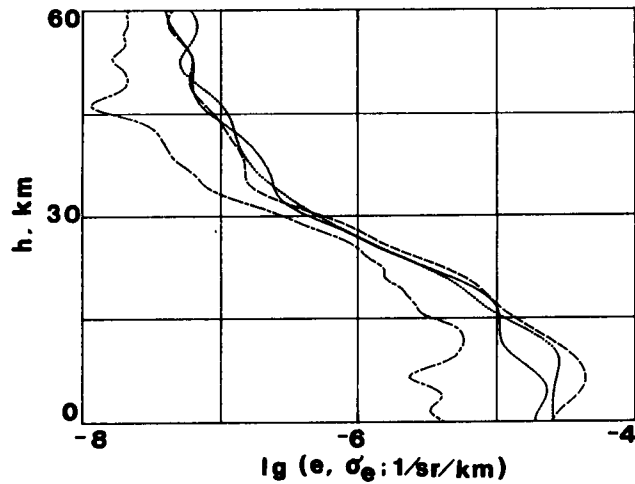


Figure 4. The relative volume emission rate $e_\lambda(h) = E_\lambda(h)/C_\lambda$ (E_λ is the volume emission coefficient, C_λ is the spectral solar constant) at the wavelength $0.84 \mu\text{m}$ on 22 October 1985. — - $0-5^\circ\text{S}$; - $10-15^\circ\text{S}$; - - - - - $20-25^\circ\text{S}$; - · - · - the standard deviation of the relative volume emission rate for $20-25^\circ\text{S}$.

6. MIDDLE ATMOSPHERE ELECTRODYNAMICS (MAE)

6.1 MIDDLE ATMOSPHERIC ELECTRODYNAMICS DURING MAP

R. A. Goldberg

NASA/Goddard Space Flight Center
Laboratory for Extraterrestrial Physics
Greenbelt, MD 20771 USA

The recent revival and strong motivation for research in middle atmospheric electrodynamicis can be attributed, in large part, to the discovery of large (V/m) electric fields within the lower mesosphere during the decade prior to MAP. Subsequent rocket soundings appeared to verify the preliminary findings. During the MAP era, more sophisticated techniques have been employed to obtain measurements which respond positively to criticisms of earlier results, and which provide more insight regarding the character of the fields. The occurrence of mesospheric V/m electric fields now seems to require the presence of aerosols, of local winds and related dynamics, and of an atmospheric electrical conductivity less than 10^{-10} S/m. Furthermore, new theoretical ideas describing the origin of the V/m fields are consistent with the measurements. The current status of results regarding V/m fields in the middle atmosphere is reviewed in light of the more widely accepted electric field structure for this region from rocket, balloon and modeling results.

WHAT IS MIDDLE ATMOSPHERE ELECTRODYNAMICS ?

- Study of the middle atmospheric electrical environment including :
 - Electric fields
 - Bulk ion properties
 - Charged aerosols
 - Free electrons
 - Current flow, etc.
- Recent problems under study include :
 - Existence and characteristics of large (V/m) E fields.
 - A.C. and D.C. E fields related to thunderstorms and lighting.
 - E field and plasma perturbations associated with waves and turbulence.
 - Modification of MAE parameters by high energy events such as REP's.

Figure 1. Middle atmospheric electrodynamicis (MAE) is concerned with the study of the middle atmospheric electrical environment including electric fields, bulk ion properties, charged aerosols, free electrons, current flow, etc. It is particularly concerned with the manner in which these parameters affect middle atmospheric coupling with other regions of the near earth environment and on how the region affects transmission of electromagnetic waves or other electrical signals traveling through it. Many of the recent topics receiving attention through dedicated rocket and balloon programs are listed in the figure and will be discussed in further detail in the four review papers which follow. This paper concentrates on the evolution of our knowledge regarding the apparent large (V/m) electric fields which are occasionally observed in the lower mesosphere.

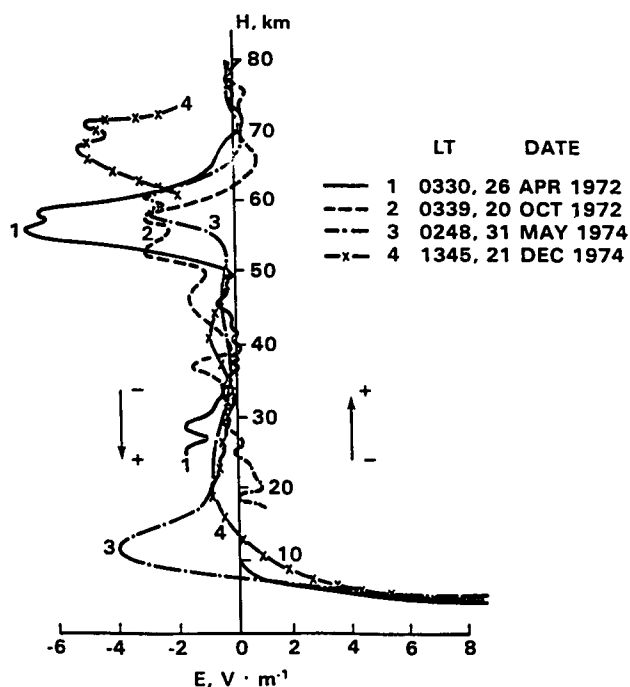


Figure 2. Discovery of the vertical V/m fields is attributed to Bragin et al. [1974] and Tyutin [1976], who reported four rocket measurements of them using field mills aboard the payloads. The figure displays three night and one day measurements, with the latter occurring at a higher altitude. The fact that all flights showed existence of the V/m field led the above authors to conclude that this was a permanent feature of the region, always contained within a region having a characteristic half width of about 10 km. Bragin, Yu. A., et al., *Cosmic Res.*, 12, 279, 1974; Tyutin, A. A., *Cosmic Res.*, 14, 132, 1976.

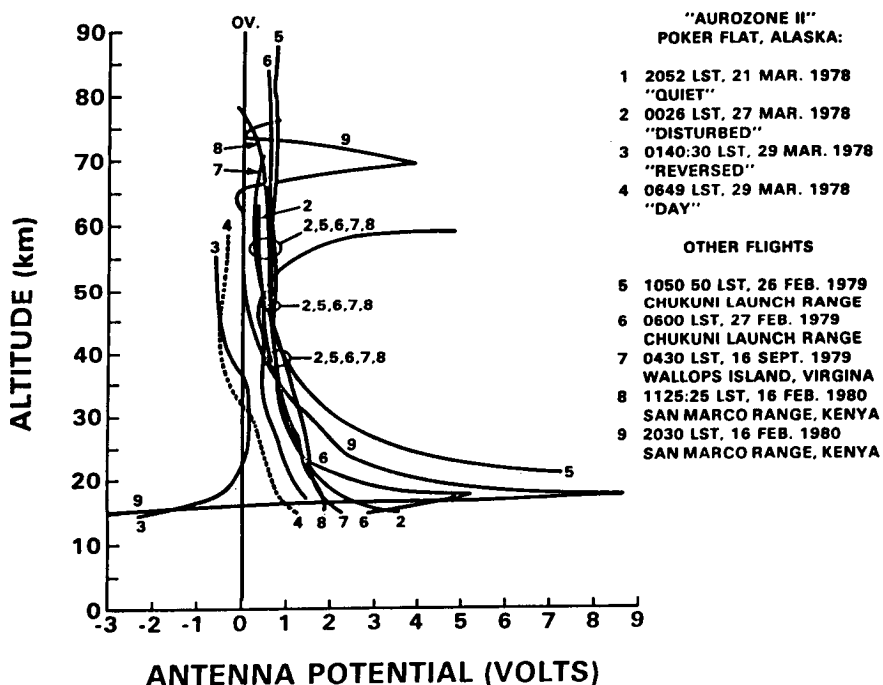


Figure 3. Hale et al. [1981] reported results of nine separate rocket flights carrying an asymmetric probe technique to measure vertical electric fields at several different locations, but could only detect V/m fields in two cases. They concluded that the fields were relatively infrequent, and certainly not a permanent feature of the region. Measurement of a vertical V/m field was also made by Maynard at Wallops Island, Virginia [Maynard et al., 1981] using a sophisticated three-dimensional boom-mounted probe array. Hale, L. C., et al., *Geophys. Res. Lett.*, 8, 927, 1981; Maynard, N. C., et al., *Geophys. Res. Lett.*, 8, 923, 1981.

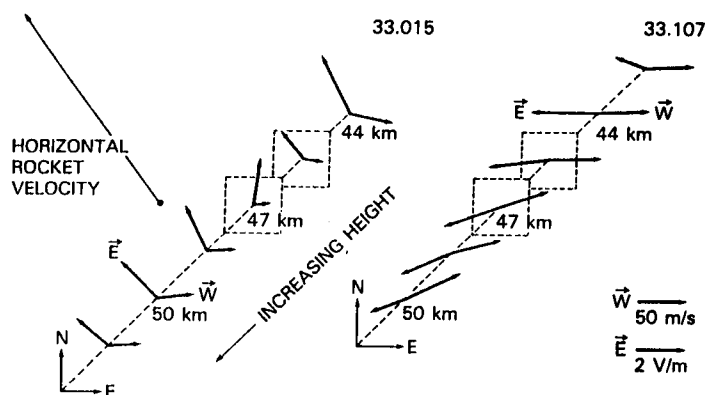


Figure 4. The first rocket measurements of large (V/m) horizontal electric fields were made on two separate nights at Andoya, Norway, in 1980 [Maynard et al., 1984]. The field directions (E) were found to anticorrelate with atmospheric wind directions (W) determined from simultaneous meteorological rockets. Furthermore, although energetic particle events were in progress during both measurements, the fields were observed to occur below those heights where significant ionizing radiations had penetrated, which helped contribute to the conclusion that electrical conductivities above 10^{-10} S/m would probably not support such fields. Maynard N. C., et al., *J. Atmos. Terr. Phys.*, 46, 807, 1984.

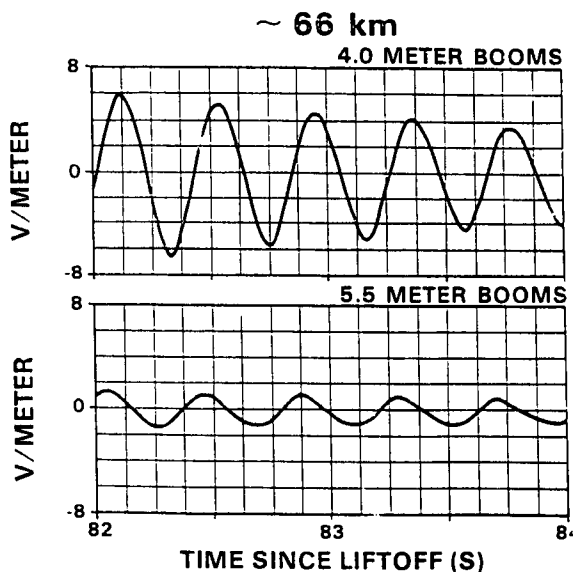


Figure 5. Kelley et al. [1983] also reported detection of an apparent V/m field near 66 km, using two sets of boom-mounted probes orthogonal to a rocket payload, each pair of different length. They found the field measured by the shorter booms to be of higher magnitude than that measured across the longer separation, leading them to conclude that the measurement was invalid, probably contaminated by wake effects and other sheath induced charge distributions. They also inferred that all previously reported measurements should be subject to closer scrutiny to establish their validity. Kelley, M. C., et al., *Geophys. Res. Lett.*, 10, 733, 1983.

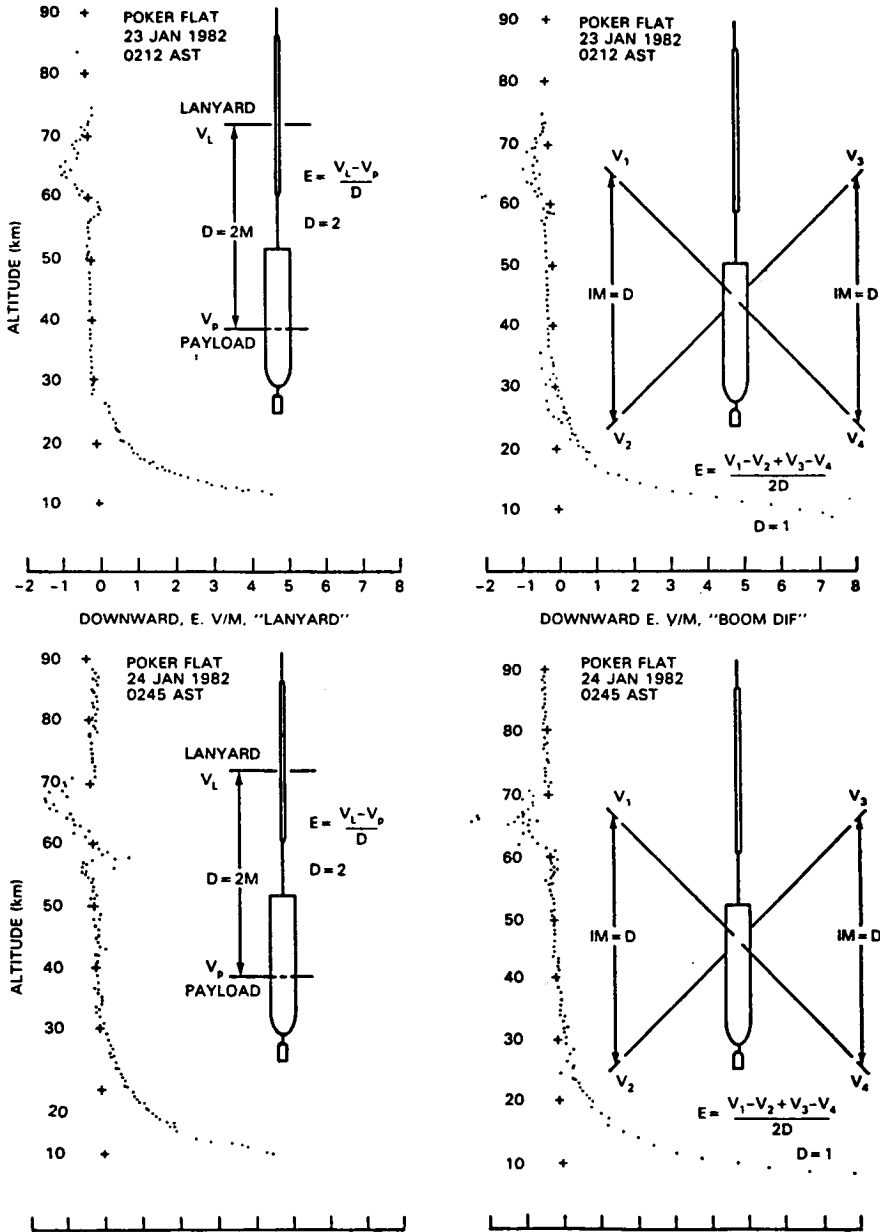


Figure 6. In defense of his earlier measurements, Hale [1984] showed two independent pairs of measurements made from Poker Flat, Alaska, in 1982. On each rocket, Hale measured vertical electric fields with both an asymmetric double probe and a symmetric boom-mounted probe technique. On both flights, each approach measured large vertical electric fields between 60 and 70 km of equivalent shape and magnitude, showing consistency between the two approaches. Later Maynard [1986] showed that an anomalously large electric field would be measured with his instrument prior to its detachment from the main rocket payload, but that once separated and in the normal operating mode, measurement values returned to anticipated levels. This implied that with proper care in design and applications, reliable measurements should be expected with his technique. Hale, L. C., *Adv. Space Res.*, 4, 175, 1984; Maynard, N.C., in *Rocket Techniques, Handbook for MAP, Vol. 19*, 1986.

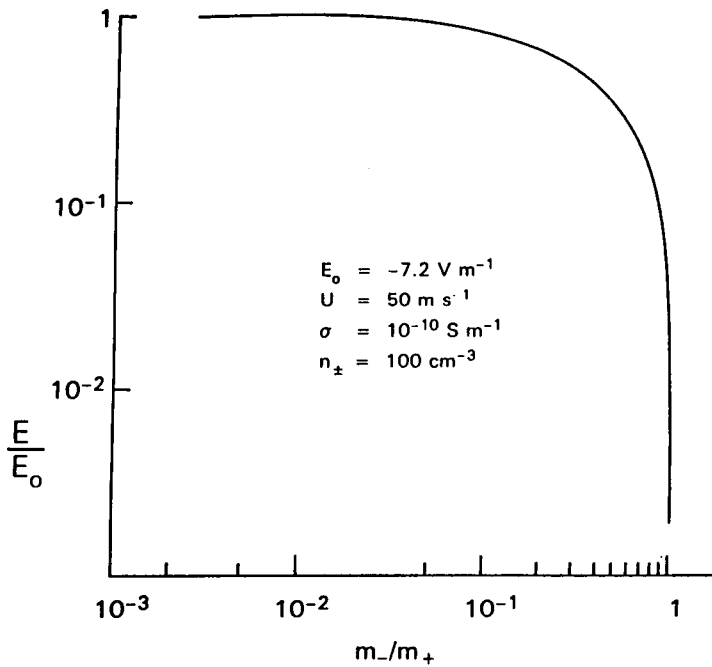


Figure 7. More recently, Curtis [1987] has produced a theory which can generate the large horizontal electric fields given the presence of horizontal winds, of charged aerosols for which the negative and positive species are of slightly different mass, and of an atmospheric electrical conductivity which is relatively low ($<10^{-10} \text{ S/m}$). The plot shows the derived relationship for changes in the electric field caused by variations in the negatively-to-positively charged aerosol mass ration, with the displayed values for number density, wind velocity, and conductivity, as boundary conditions. It is important to note that a very large electric field can be maintained until the mass ratio becomes very close to unity. If valid, this theory offers encouragement for the reality of the V/m horizontal electric field measurements. Curtis, S. A., IAGA Abstracts, CEDAR Symposium, IUGG 19th General Assembly, Vancouver, B.C., August 1987.

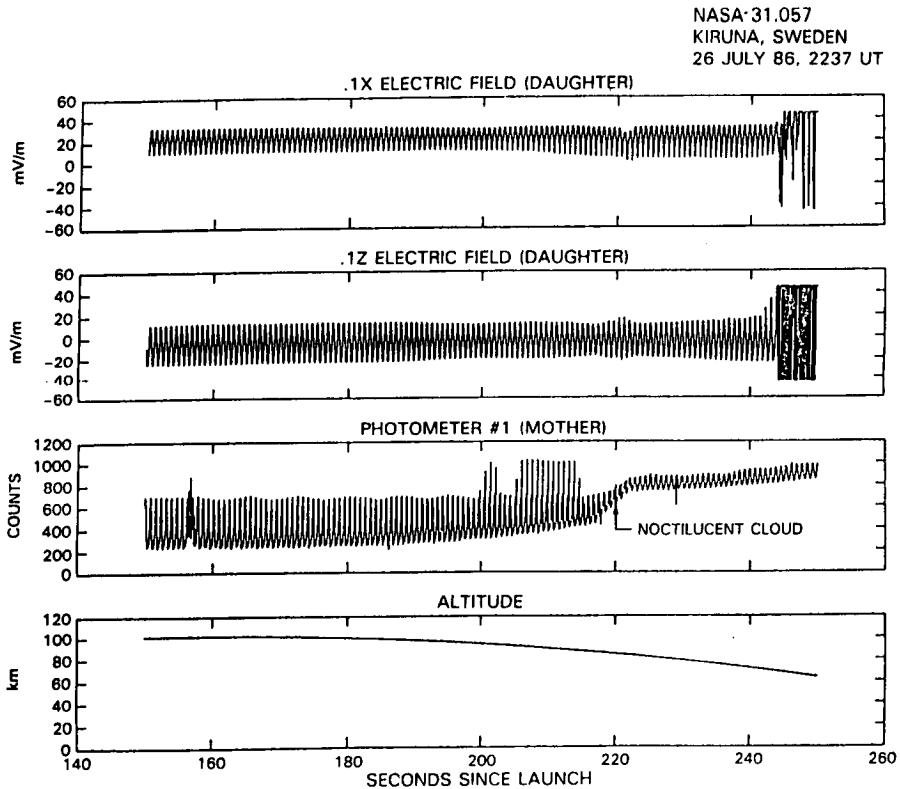


Figure 8. In July 1986, vector electric field measurements were made within a noctilucent cloud (NLC) [cf. Goldberg, 1987]. The Maynard technique was employed including deployment of the electric field array (daughter) from the main payload (mother). Displayed are two components of the electric field measured in the payload coordinate system, photometer measurements to demonstrate cloud passage [G. Witt, University of Stockholm, private communication] and altitude. The figure illustrates changes in both components of the electric field during passage through the NLC. Future measurements of this type in coordination with simultaneous measurements of winds and particulate size within NLCs should help validate the Curtis theory (Figure 7). Goldberg, R. A., Proceedings of the 8th ESA Symposium on European Rocket and Balloon Experiments and Related Research, p. 159, ESA SP-270, 1987.

WHERE ARE MAE E FIELD STUDIES GOING?

- Further experiments to validate the large (V/m) E fields are needed.
- Tests of the theoretical explanation will be attempted in a noctilucent cloud environment.
- Expansion of the studies is required to determine the frequency, extent, and importance of the large (V/m) E fields is required.

Figure 9. Further experiments are needed to validate the large V/m electric fields. If real, they offer an important mechanism for coupling electrodynamic effects down to tropospheric altitudes, by generating electrical currents which could significantly contribute to the global electric circuit. Such contributions would in turn be modulated by incoming radiations during high latitude disturbances, which would cause conductivity enhancements that might reduce or eliminate the electric fields altogether. The importance of such effects is dependent on the frequency and extent of such fields, which must still be determined. Finally, new theoretical ideas regarding the origin of V.m fields in the mesosphere can be checked through carefully planned experiments in NLC, which contain all the essential ingredients proposed by the theory.

6.2 MIDDLE ATMOSPHERE ELECTRICAL ENERGY COUPLING

L. C. Hale

Communications and Space Sciences Laboratory
 Department of Electrical Engineering
 The Pennsylvania State University
 University Park, PA 16802

The middle atmosphere (MA) has long been known as an absorber of radio waves, and as a region of nonlinear interactions among waves. The region of highest transverse conductivity near the top of the MA provides a common "return" for global thunderstorm, auroral "Birkeland", and ionospheric dynamo currents, with possibilities for coupling among them. Their associated fields and other transverse fields "map" to lower altitudes depending on scale size. Evidence now exists for motion-driven "aerosol" generators, and for charge trapped at the "base" of magnetic field lines, both capable of producing large MA electric fields. Ionospheric "Maxwell" currents (curl H) parallel to the magnetic field appear to map to lower altitudes, with rapidly time-varying components appearing as displacement currents in the stratosphere. Lightning couples a (primarily ELF and ULF) current transient to the ionosphere and magnetosphere whose wave shape is largely dependent on the MA conductivity profile. Electrical energy is of direct significance mainly in the upper MA, but electrodynamic transport of minor constituents such as "smoke" particles or CN may be important at other altitudes.

Electrical Energy in M.A.

From Inside: "Big Fields" [Bragin/Hale; Tyutin/Maynard/Croskey]
 Wind Driven Horizontal Aerosol [Curtis]
 Gravity Driven Vertical Aerosol [Maynard and Aikin]

From Below: "Classical" G.C. [C. T. R. Wilson]
 Lightning Radiation [J. R. Wait, Sentman]
 "Charge Perturbation" [Hale and Baginski; Kelley and Siefring]

These due to removal
 of "relaxation time"
 restriction

From Above: Perpendicular E-Fields [Park and D.]
 "Mapping" [Mozer Mafia; Hans Volland]
 "Trapped Charge" [Hale]
 Parallel J Maxwell [Hale]
 (curl H) Mapping [?]

Knowledge before MAP summarized in:

N. C. Maynard (Ed) Middle Atmosphere Electrodynamics, NASA CP 2090

Subsequent reviews:

R. A. Goldberg, JATP 46, 1984, ESA SP-270, 1987

M. C. Kelley, Rev. Geophys. SP SCI. 21, 1983

L. C. Hale, Adv. Space Res., 4, 1984

Energy to Middle Atmosphere from Below

"D.C." output of T-storm $\sim 10^8 \text{ W}$ but only $\sim 1\%$ above 20 km $\sim 10^6 \text{ W}$

~ 1000 storms = 10^{11} W , 10^9 W above 20 km

Locally $\sim 10^{-6} \text{ W/m}^3$ at 20 km (10^{-3} W/kg) but decreasing exponentially with altitude.

Lightning radiation (mainly VLF) is $\sim 1\%$ of flash energy [Krider and Guo] of about $10^9 \text{ J/flash} \times 100 - 1000 \text{ FL/s}$ mostly deposited in middle M.A. [Sentman], thus $\sim 3 \times 10^9 \text{ W}$ globally, $2 \times 10^{-10} \text{ W/m}^3$ average, perhaps $\sim 10^{-8} \text{ W/m}^3$ maximum at 60 km (10^{-2} W/kg).

However, in 1981 Penn State and Cornell (at NASA Wallops Facility) measured transients of orders of magnitude greater duration than predicted by conventional theory resulting in two Ph.D. theses: M. E. Baginski, Penn State, 1988 and C. L. Siefring, Cornell, 1988, and so far two accepted publication: L. C. Hale and M. E. Baginski, *Nature*, 329, 814, 1987 and M. E. Baginski, L. C. Hale, and J. J. Olivero, *Geophys. Res. Lett.*, in press.

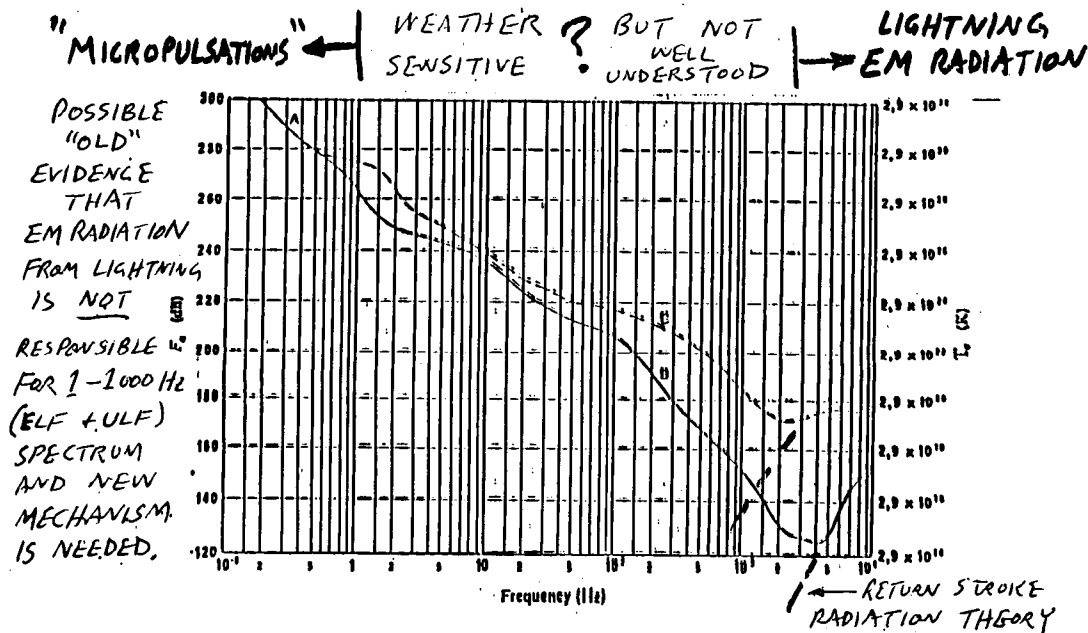


Figure 1. F minimum and maximum vs. frequency (0.1 to 10^4 Hz), A - micropulsations, B - minimum value expected of atmospheric noise, C - maximum value expected of atmospheric noise. Atmosphere noise spectrum after Spaulding in: *Handbook of Atmospheric*, H. Volland, Ed., CRC, Boca Raton, 1982.

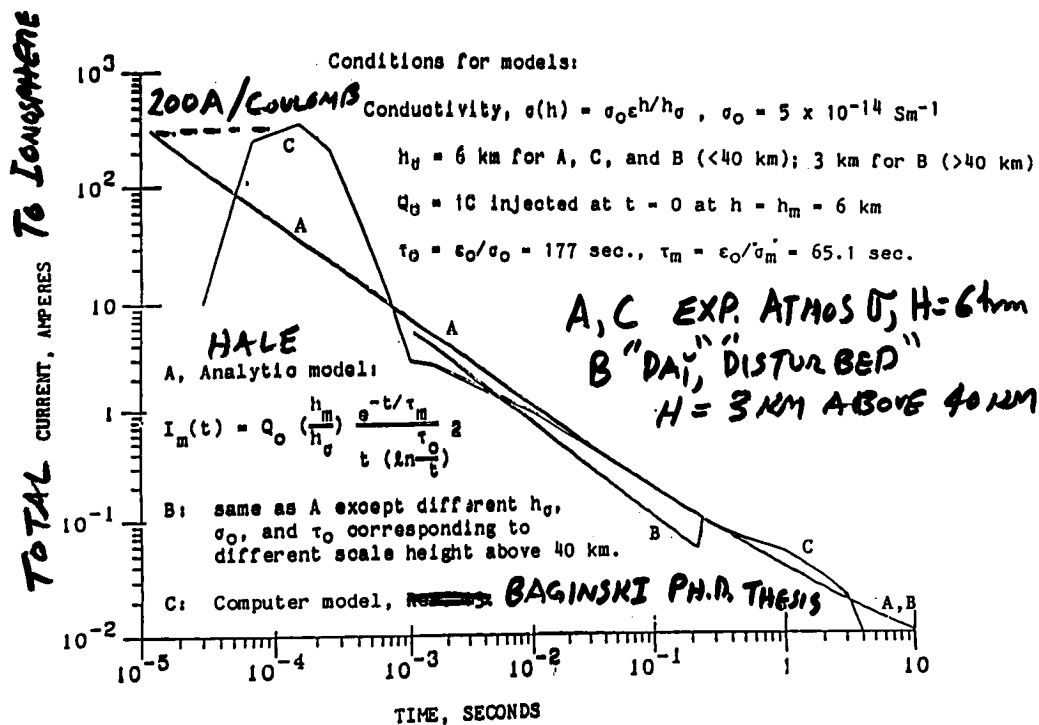


Figure 2. Comparison of computer model with analytic model of 'monopole decay'.

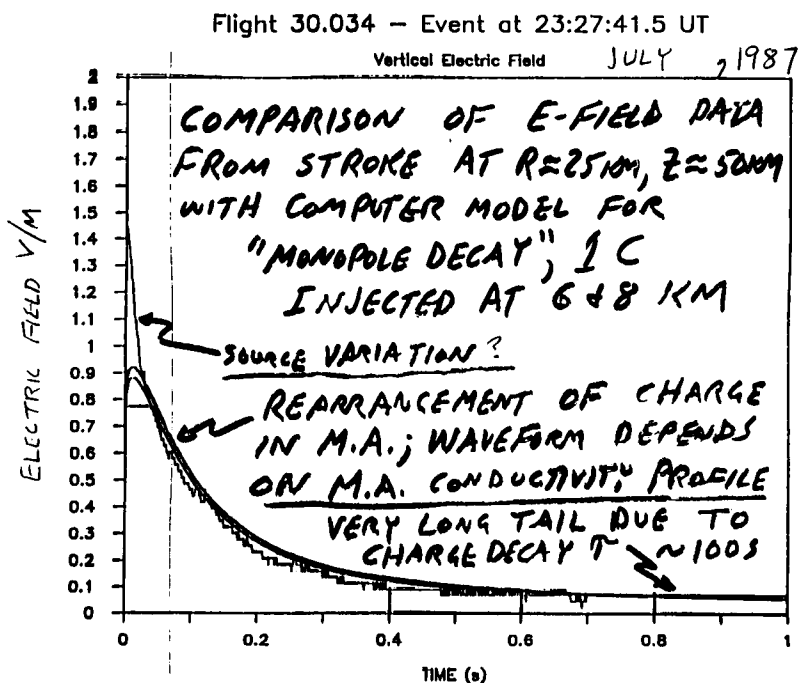


Figure 3. Experimental verification of theory on rocket over thunderstorm.

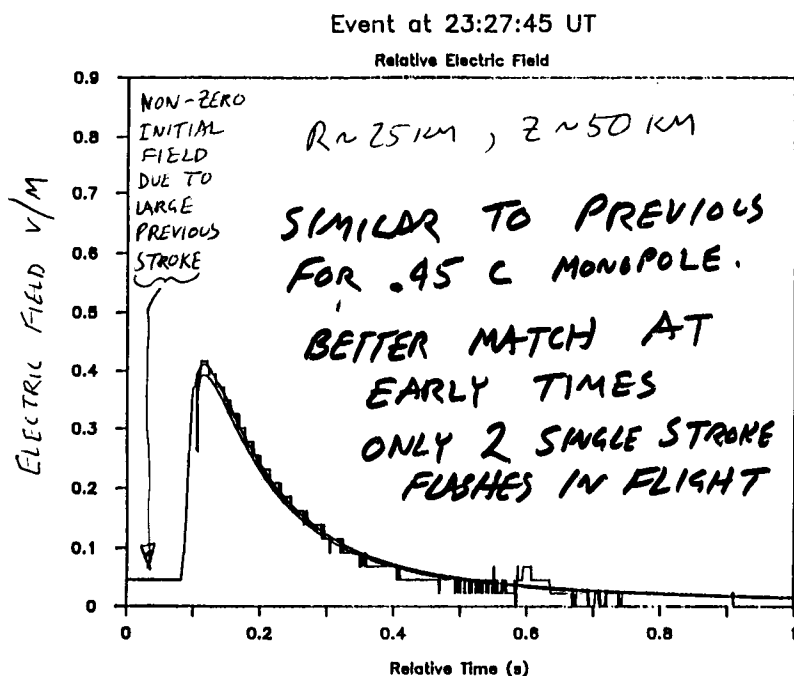


Figure 4. Experimental verification of theory on rocket over thunderstorm.

LIGHTNING LAUNCHED // CURRENTS
MOVE RIGHT UP FIELD LINES:

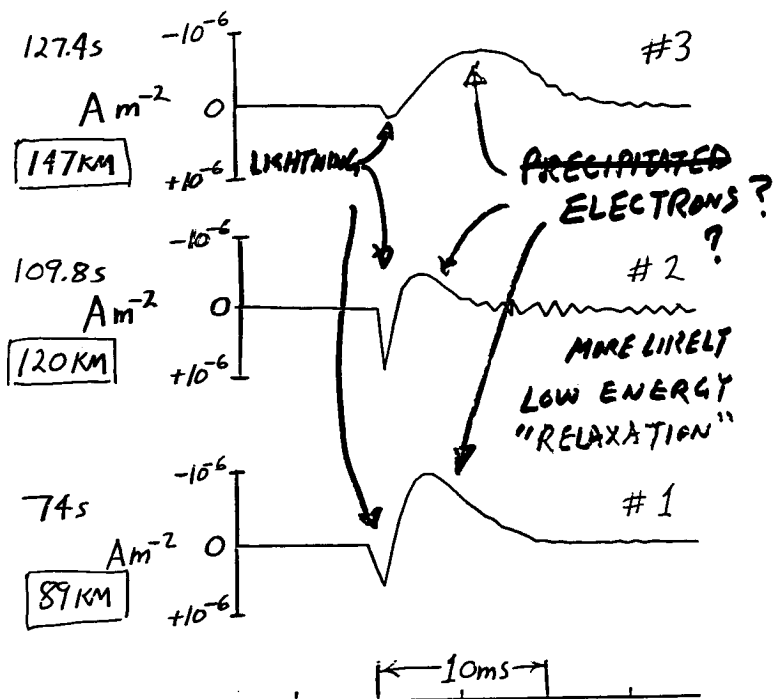


Figure 5. 33.052, 0155 UT, 15 July 1987: Three events related to Cornell E-field and "whistler" events. Not well correlated with lightning locator and initial direction indicates IC lightning or "positive" lightning.

Nongenerality of "Relaxation Time":
Maxwell's equations:

$$\nabla \cdot \mathbf{H} = \mathbf{J} + \frac{\partial \mathbf{D}}{\partial t}, \quad \nabla \cdot \mathbf{D} = \rho$$

Assume \mathbf{J} only conduction current and constant ϵ , $\mathbf{D} = \epsilon \mathbf{E}$

Isotropic scalar σ , $\tau_{\text{rel}} = \epsilon/\sigma$

Take divergence:

$$\nabla \cdot \nabla \times \mathbf{H} = \nabla \cdot (\sigma \mathbf{E}) + \nabla \cdot \frac{\partial \mathbf{D}}{\partial t}$$

$$0 = \mathbf{E} \cdot \nabla \sigma + \sigma \nabla \cdot \mathbf{E} + \epsilon \frac{\partial}{\partial t} \nabla \cdot \mathbf{E}$$

$$0 = \mathbf{E} \cdot \nabla \sigma + \sigma \nabla \cdot \mathbf{E} + \epsilon \frac{\partial \nabla \cdot \mathbf{E}}{\partial t}$$

$$\text{or} \quad 0 = \mathbf{E} \cdot \nabla \sigma + \left(\frac{\sigma}{\epsilon} \right) \rho + \frac{\partial \rho}{\partial t}$$

if and only if

$$\nabla \sigma \equiv 0$$

$$\mathbf{E} = \mathbf{E}_0 \epsilon^{1/\sigma_{\text{rel}}}$$

$$\rho = \rho_0 \epsilon^{1/\tau_{\text{rel}}}$$

singularity on boundary plays havoc with

Energy to Middle Atmosphere from Above

Fair weather return current $\sim 3 \times 10^{-12} \text{ A/M}^2 - 10^{-11} \text{ W/M}^3$ at 20 km ($\sim 10^{-6} \text{ W/KG}$) decreasing exponentially with altitude.

"Tangential" E-fields "map" downwards depending on scale size [Park and D.; Mozer and students, Volland] could produce substantial heating in upper middle atmosphere ($\sim 80 \text{ km}$) in PCA [Banks].

Low latitude balloon measurements show $\sim 30 \text{ mV/M}$ horiz field ($> 10 \times \text{expec.}$) carried over 1000s of km could perturb D.C. global circuit [Holzworth].

"Parallel" "D.C." fields do not map well but \mathbf{J}_{max} (curl \mathbf{H}) at ELF couples capacitively so AC magnetospheric fields appear as displacement currents in middle atmosphere.

Relaxation of "Relaxation Time" restrictions \rightarrow charge from REP electrons trapped at base of magnetic field lines -- could explain reversal of E-field during REP, lightning triggering [Hale, *Nature*, 327, p. 769].

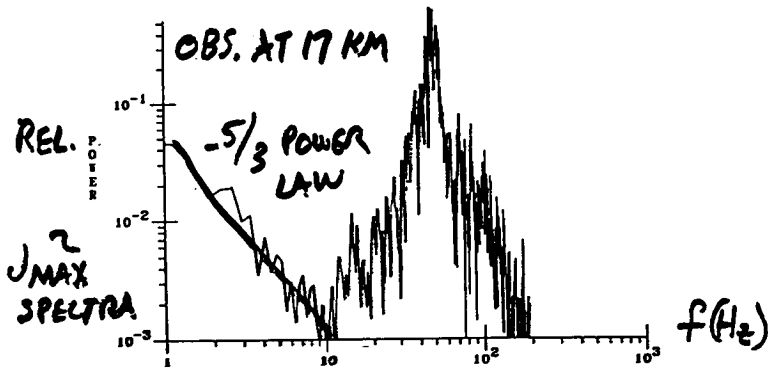


Figure 6. Conjunctive comparison with Viking satellite showed similar but featureless spectra [Lönquist]. Now believe "feature" originates in magnetosphere, J_{Maxwell} "maps" to middle atmosphere.

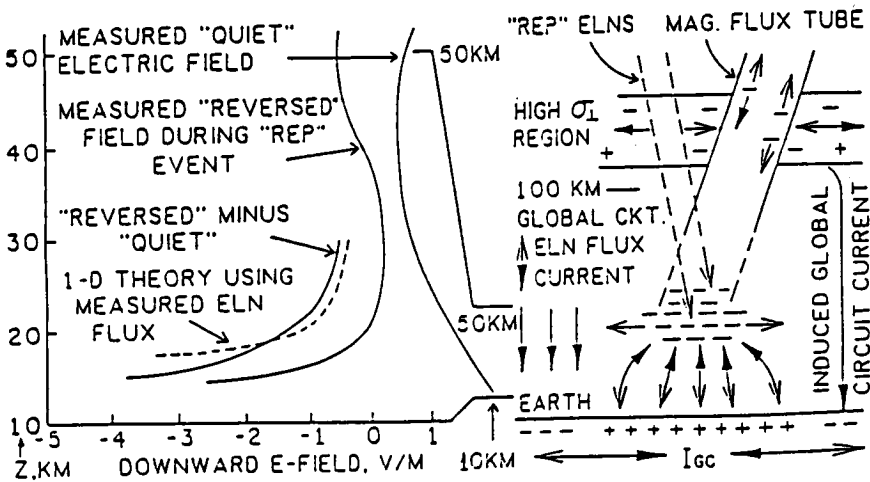


Figure 7. Removal of "relaxation time" restriction leads to possibility of excess charge due to high energy particles depositing at base of field lines and persisting for very long times, thus greatly enhancing coupling to lower altitudes.

DISTINGUISHING GENERATOR + LOAD

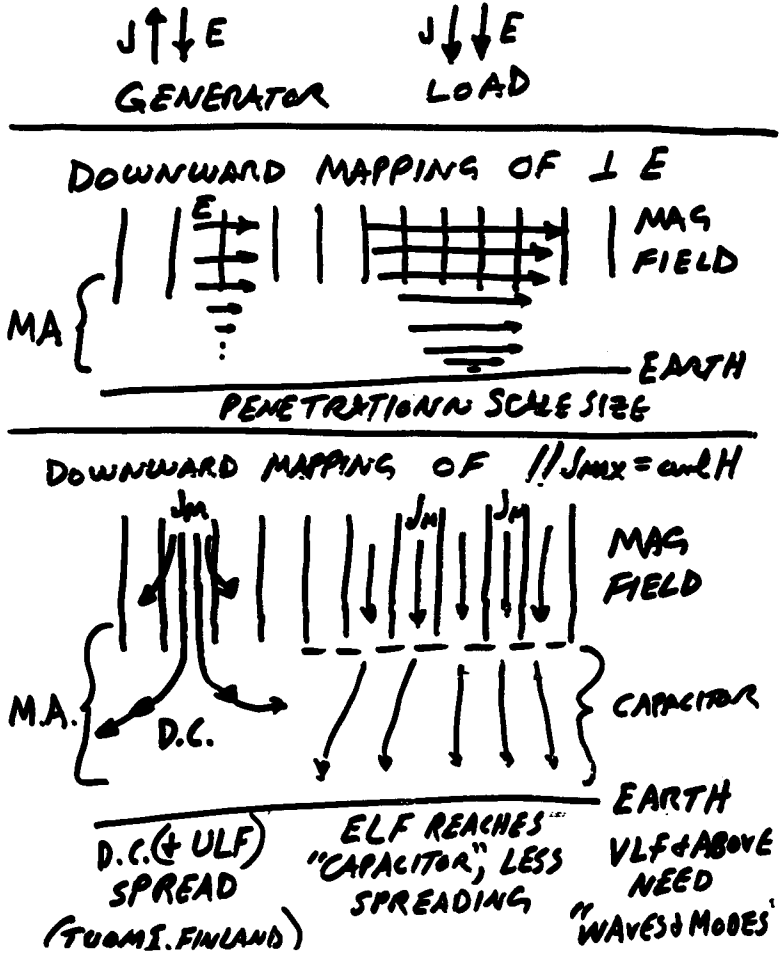


Figure 8.

6.3 ELECTRIC FIELD MEASUREMENTS WITH STRATOSPHERIC BALLOONS

I. B. Iversen

Danish Space Research Institute
Lundtoftevej 7
2800 Lyngby, Denmark

Electric fields and currents in the middle atmosphere are important elements of the modern picture of this region. Balloon instruments, reaching the level of the stratosphere, have been used extensively for the experimental work. The research has shown good progress, both in the MAP period and in the years before and after. Our knowledge has been increased about, e.g., the upper atmosphere potential, the electric properties of the medium itself and about the coupling with magnetospheric (ionospheric) fields and currents. Also various measurements have brought about a discussion of the possible existence of hitherto unknown sources. Throughout the MAP period the work on a possible definition of an electric index has continued.

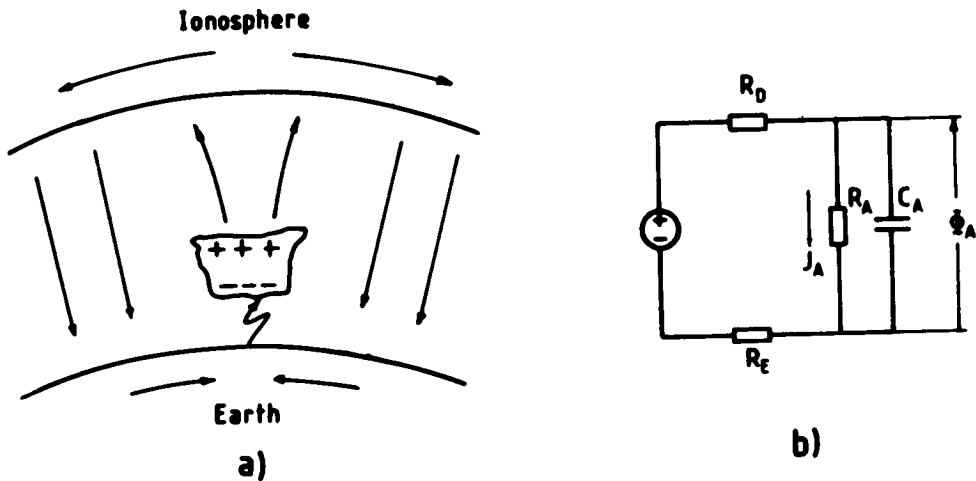


Figure 1. Schematic representation of the global electric circuit. In the classical picture thunderstorms are charging the upper atmosphere to a high potential (200-300 kV). A return current is, in fair-weather regions, flowing to the ground. a) illustrates the concept and b) is a simple equivalent electric diagram. From Volland [1984].

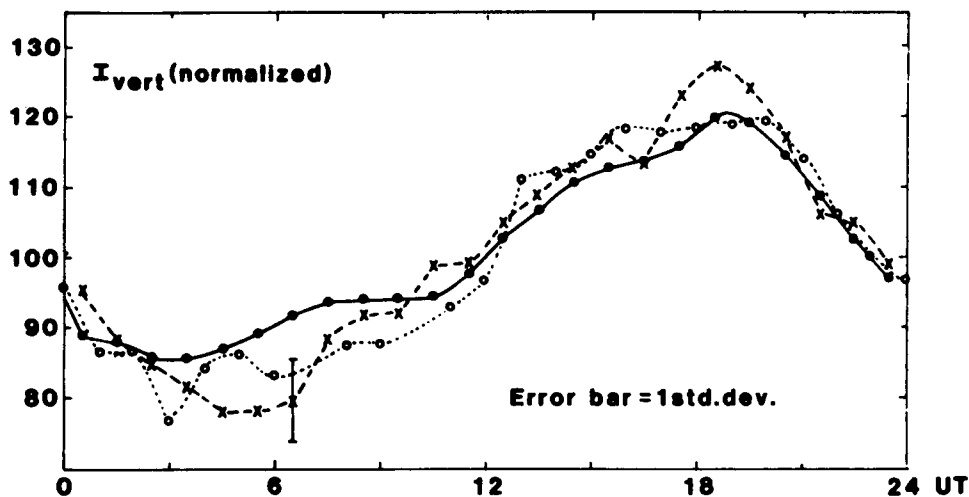


Figure 2. The upper atmosphere potential displays a "quiet day" curve, which is the average over many days. This typical variation is versus UT and is due to the uneven distribution of the continents. Three curves are shown: a) the original Carnegie curve marked —, b) airplane measurements marked o - - o, and c) balloon measurements marked x - - x. From D'Angelo et al. [1982].

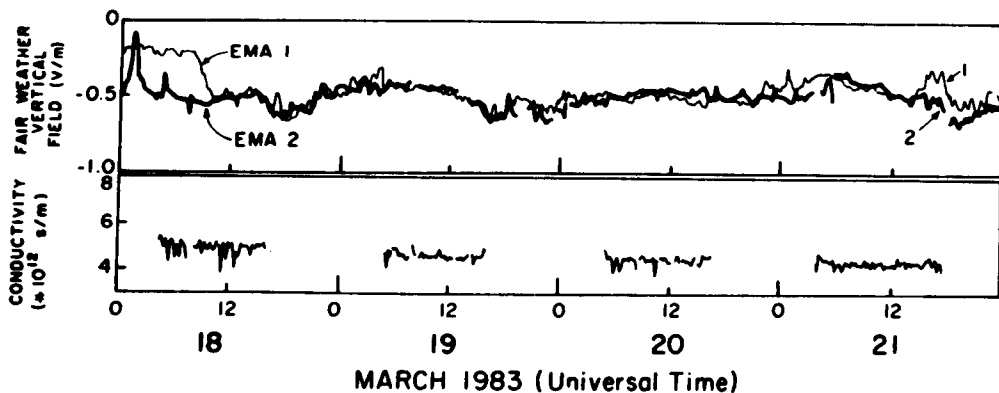


Figure 3. Two simultaneous measurements of the vertical electric field at 26 km altitude by two balloons separated by over 1500 km. These measurements have shown that also variations on a shorter time scale occur synchronized over a larger area supporting the concept of a uniform upper atmosphere potential. From Holzworth et al. [1984].

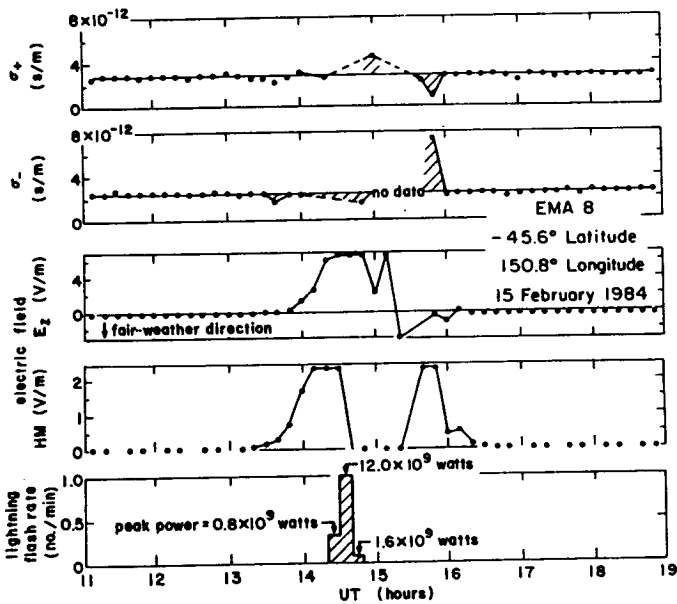


Figure 4. New observations related to the global circuit are still being reported. Fluctuations of both the positive and negative conductivity above a thunderstorm have been observed in several cases. The observations suggest a relationship between the battery and the resistor R_D in the equivalent diagram of Figure 1. From Holzworth et al. [1986].

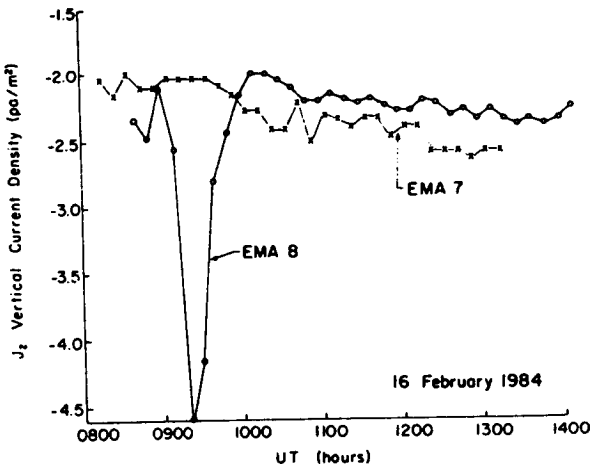


Figure 5. This is another example of measurements which cannot be explained by the simple circuit. A solar proton event has increased the conductivity of the upper polar atmosphere where a balloon experiment observed a clear increase in the vertical current (o-o-o-). A problem is, however, that a balloon measurement outside the polar region (x-x-x-) did not show a simultaneous decrease in vertical current which should be expected due to a worldwide decrease in the upper atmosphere potential (represented in Figure 1 by the voltage over the capacitor C_A). From Holzworth et al. [1987].

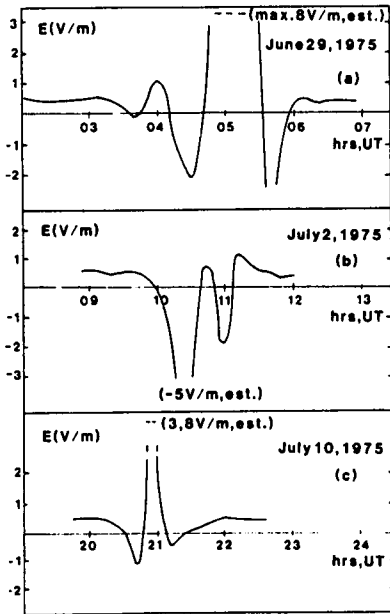


Figure 6. Also tropospheric structures of less magnitude than a full size thunderstorm can be electrified as observed with balloon instruments. Shown here are three examples of "dipole like" structures observed from a balloon passing by. The polarity of the central part is opposite to that of a typical thundercloud. From Madsen et al. [1983].

SONDRE STROMFJORD, GREENLAND
11 AUG 82

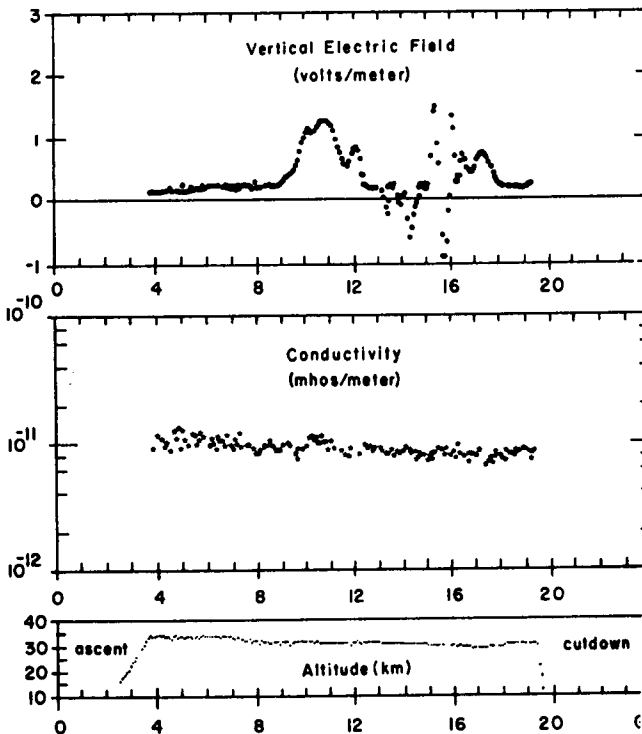


Figure 7. This is another example of the electric field over a non-thunder electrified cloud system, in this case a large storm over Greenland. Again, a major part shows the "fair region" field polarity. From Barcus et al. [1986].

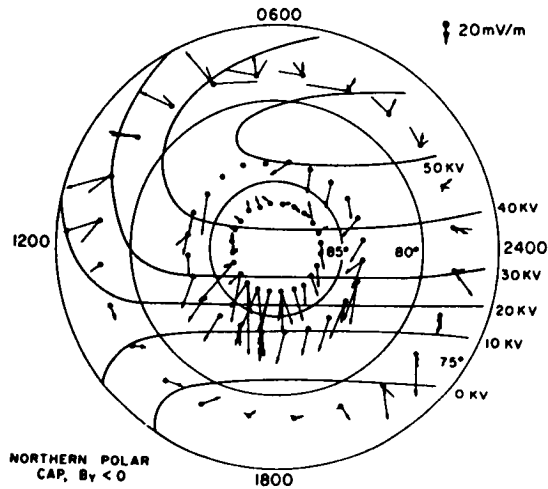


Figure 8. This is an example of ionospheric/magnetospheric electric fields mapping down through the middle atmosphere. In this case we see the polar cap plasma convection associated electric field. The classical "equalizing layer" in the upper atmosphere is obviously not a screen against external fields. From Mozer et al. [1974].

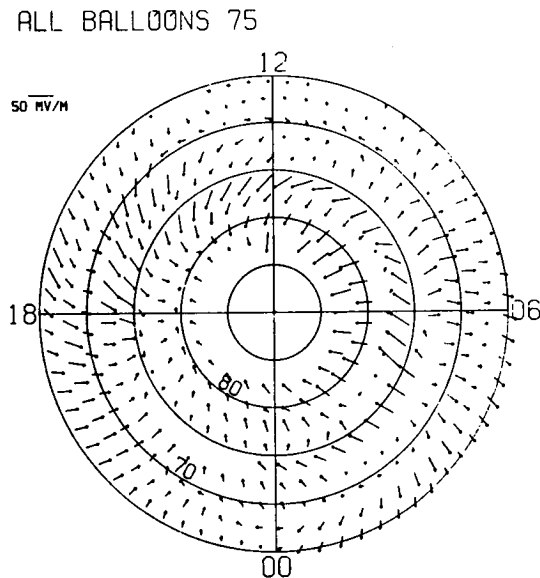


Figure 9. This example is equivalent to that seen in Figure 8. The convection pattern is shown over a wider latitude range based on a larger amount of data. From Iversen and Madsen [1978].

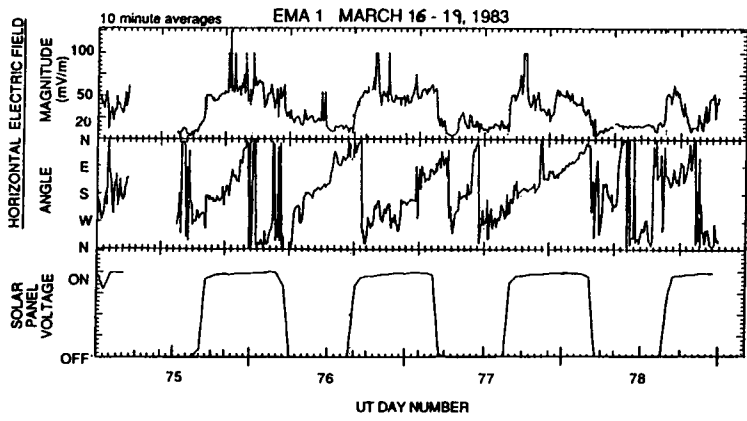


Figure 10. Many sources for the electric fields observed in the middle atmosphere are located below or above but also internal sources exist. The top and middle panels of this figure show the horizontal electric field magnitude and direction (relative to magnetic north) for four days of a superpressure balloon flight at 27 km altitude and 45° southern latitude. The point is that the observed rotational (counter clockwise) period of ~ 18 hours cannot be explained by any known ionospheric or tropospheric source. On the other hand, it is possible to relate the observation to an atmospheric inertial wave (Coriolis force driven) which for the actual latitude has this period. From Holzworth [1989].

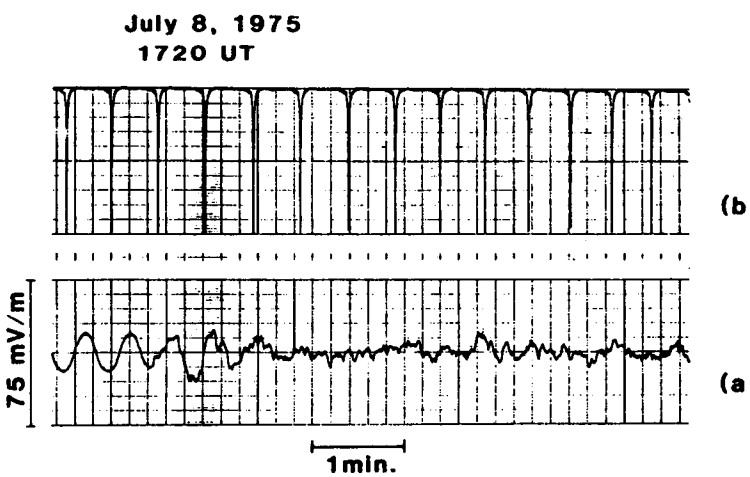


Figure 11. This is another example of an internal source for electric fields in the middle atmosphere (in the stratosphere). These small-scale fields are produced by air turbulence. From D'Angelo et al. [1983].

References

- Barcus, J. R., I. Iversen, and P. Stanuning, Observations of the electric field in the stratosphere over an arctic storm system. *J. Geophys. Res.*, 91, D9, 9881, 1986.
- D'Angelo, N., I. B. Iversen, and M. M. Madsen, Influence of the dawn-dusk potential drop across the polar cap on the high-latitude atmospheric vertical current, *Geophys. Res. Lett.*, 9, 773-776, 1982.
- D'Angelo, N., I. B. Iversen, and M. M. Madsen, Low-frequency ($f \leq 1$ Hz) stratospheric electrical noise measured by balloon-borne sensors, *J. Geophys. Res.*, 88, C9, 5441, 1983.
- Holzworth, R. H., A new source of horizontal electric fields in the midlatitude stratosphere, submitted to *J. Geophys. Res.*, 1989.
- Holzworth, R. H., K. Norville, P. Kintner, and S. Powell, Stratospheric conductivity variations over thunderstorms, *J. Geophys. Res.*, 91, 13,257-13,263, 1986.
- Holzworth, R. H., K. W. Norville, and P. R. Williamson, Solar flare perturbations in stratospheric current systems, *Geophys. Res. Lett.*, 14, 852, 1987.
- Holzworth, R. H., T. Onsager, P. Kintner and S. Powell, Planetary-scale variability of the fair weather vertical electric field, *Phys. Rev. Lett.*, 53, 1398-1401, 1984.
- Iversen, I. B., and M. M. Madsen, Auroral zone electric field measurements with balloons, in *COSPAR: Space Research Volume XVIII*, ed. M. J. Rycroft and A. C. Stickland, Pergamon Press, 1978.
- Madsen, M. M., N. D'Angelo, and I. B. Iversen, Observations of unusual structures of high-latitude stratospheric electric fields, *J. Geophys. Res.*, 88, 3894, 1983.
- Mozar, F. S., W. D. Gonzales, F. Bogott, M. C. Kelley, and S. Schultz, High latitude electric fields and the three-dimensional interaction between the interplanetary and terrestrial magnetic fields, *J. Geophys. Res.*, 79, 56, 1974.
- Volland, H., *Atmospheric Electrodynamics*, Springer, New York, 1984.



6.4 THE USE OF DC-PROBE MEASUREMENTS IN THE MIDDLE ATMOSPHERE PROGRAM

E. V. Thrane

Norwegian Defence Research Establishment
P.O. Box 25, N-2007 Kjeller, Norway

The middle atmosphere is weakly ionized, collision dominated plasma. Rocket-borne dc probes have proven effective in measuring conductivity and electron and ion concentrations in this plasma, and in some cases electron temperatures and ion composition have been observed. During MAP, dc probes have also been used successfully to study turbulence in the middle atmosphere, using the plasma as a passive tracer for the dynamical processes in the nonionized gas. The paper will briefly review basic principles of the dc-probe technique and present examples of results obtained during MAP.

Principles of dc Probes

A "dc" or "electrostatic" probe consists of one or more electrodes inserted as diagnostic tools into the plasma to be studied. An electrode is given a potential (positive or negative) relative to a reference, and the current flowing from the plasma to the electrode is measured.

The terms "dc" or "electrostatic" are used in a broad sense to allow "slow" variations of the potential (on time scales larger than any plasma wave phenomenon)

In most applications in the upper atmosphere the space vehicle itself provides the return electrode in the probe circuitry. The currents must satisfy the following relation:

$$I_e + I_- + I_+ + I_s = 0$$

electrons negative ions positive ions secondary

In order to provide a suitable reference potential the probe/payload area must be $< 10^{-3}$.

Measured Parameters:

Electron density
Ion density
Electron temperature
Conductivity

Types of Probes:

Screened positive ion probes
Nose tip or ogival electron probes
Blunt (patch) probes

The examples are of probes used in MAP.

Experimental characteristics of dc probes

Advantages:

Simple principle and electronic design
Well suited for high resolution *in situ* studies in rocket and balloon payloads

Disadvantages:

Theory complex and difficult to apply
Calibration with other experiments needed to obtain absolute plasma densities
Shock front may influence results
Surface potential difficult to control

Contributions of dc probes to MAP

dc probes have been used extensively to study fine scale structure in the middle atmosphere
From such studies information has been obtained on turbulence and waves that could not easily have been obtained by other means
Combination of such *in situ* studies with ground-based radar and lidar techniques have proved to be a powerful tool in studies of middle atmosphere dynamics as well as the radar reflection mechanisms

Further studies:

Build a data base on middle atmosphere fine scale structure and its variability in time and space
Contribute to the understanding of middle atmosphere waves and turbulence by studying small scales *in situ*
Contribute to the understanding of radar reflection mechanisms in the middle atmosphere
Studies of the microstructure of ion and electron density irregularities in the lower ionosphere

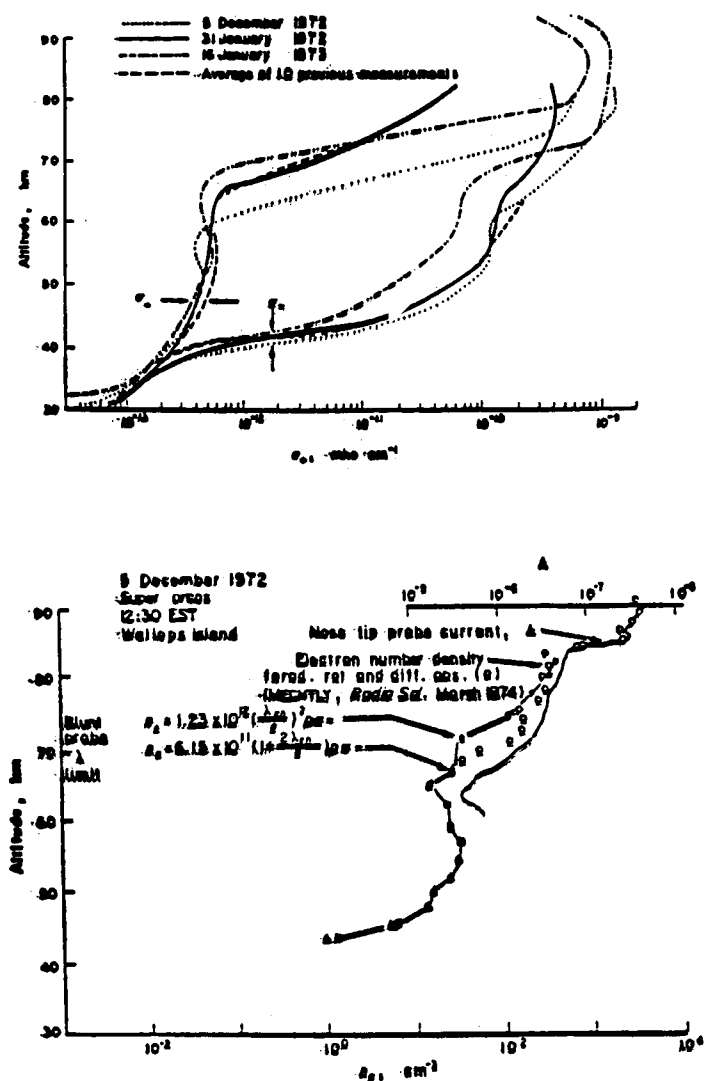


Figure 1. "Classical" use of dc probes. (a) variation of blunt probe conductivity measurements during winter conditions [York et al., 1972], (b) Comparison of height variations of electron density predicted from blunt probe measurements with electron densities from other techniques [York et al., 1982]. The formulae indicated in the figure give the expressions used to derive electron densities from measured conductivities in different height ranges.

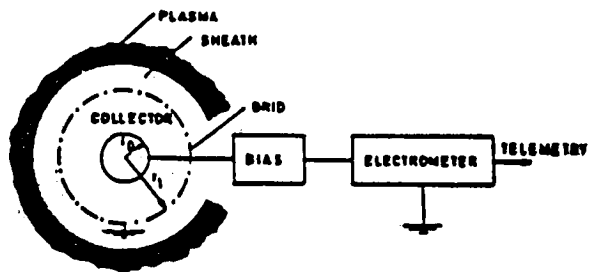


Figure 2. Single grid spherical probe.



Figure 3. Nose tip probe for measuring conductivity during rocket ascent.

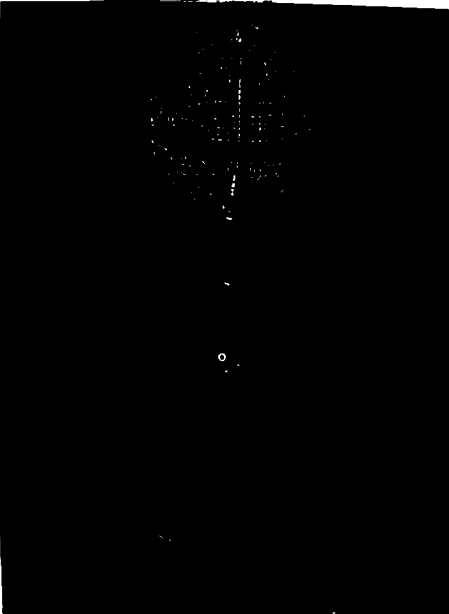
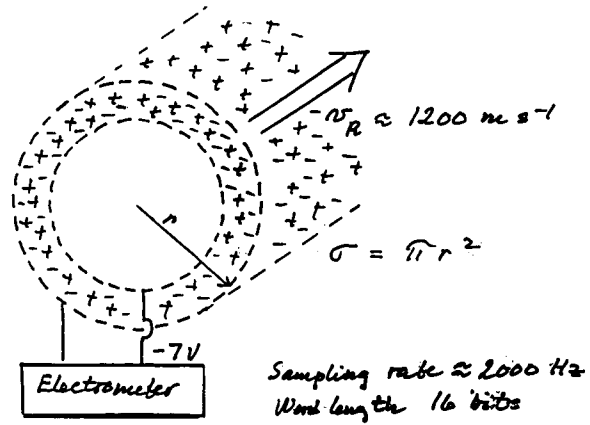


Figure 4. The NDRE positive ion probe flown in MAC/Epsilon.



The current measured by the electrometer will be

$$I = e N_+ \sigma v_R$$

Differentiating (σ and $v_R \approx \text{constant}$) yields the fluctuations:

$$\frac{\Delta N_+}{\langle N_+ \rangle} = \frac{\Delta I}{\langle I \rangle}$$

Using the ions as passive tracers we find

$$\frac{\Delta N_+}{\langle N_+ \rangle} \propto \frac{\Delta n}{\langle n \rangle} \Rightarrow \overline{u^2} \Rightarrow K, \mathcal{E}, \overline{u_i u_j}$$

\uparrow

Measured
scale heights

\uparrow

Energy
equation

\uparrow

Wave
structure

Figure 5. The electrostatic positive ion probe PIP.

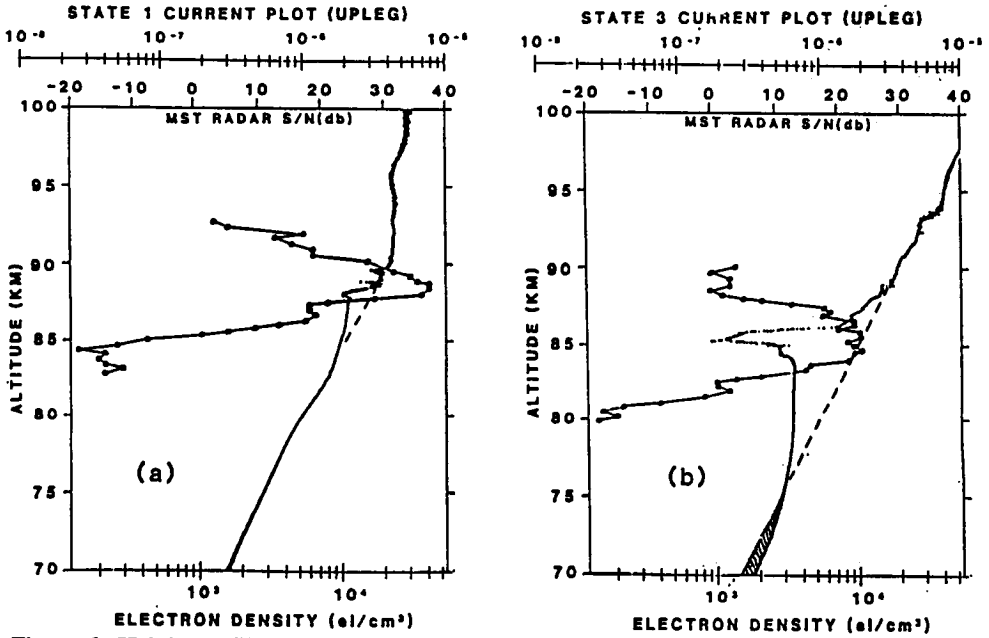


Figure 6. Height profiles of the rocket-borne dc probe results and MST radar echo S/N (solid circles) for the STATE 1 (a) and STATE 3 (b) rocket flights. The dc probe results are given both in probe current (top scale) and tentative electron density values (bottom scale) assuming a constant proportionality between the two. The dashed lines illustrate a more typical D-region profile.

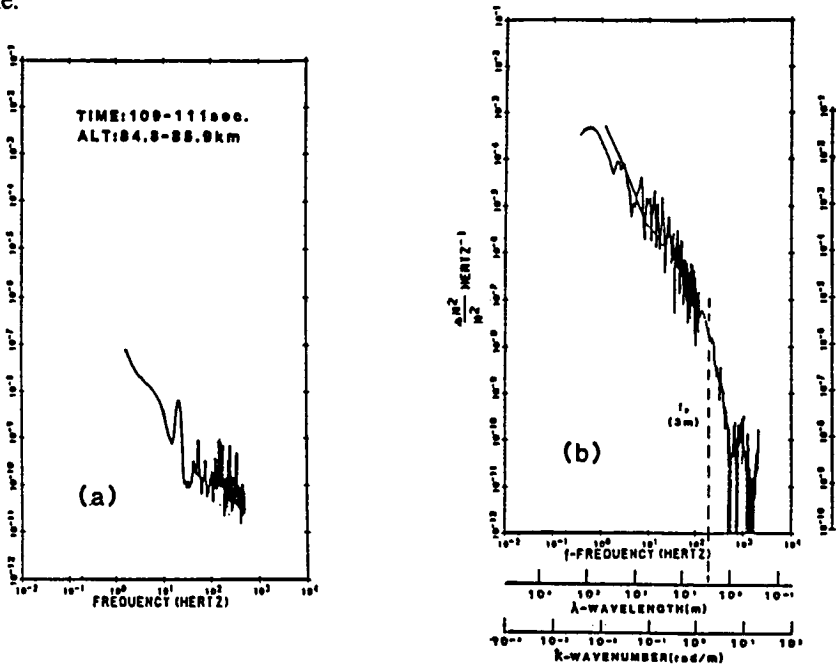


Figure 7. Power spectra of electron density fluctuations from STATE 1 at altitudes where radar echo S/N is the weakest (a - 85 km) and strongest (b - 88 km).

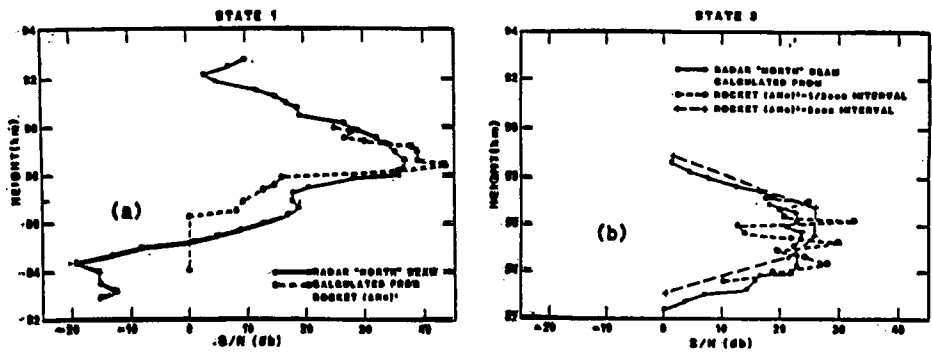


Figure 8. MST radar echo power (S/N measured by the north beam and calculated from the high resolution electron density power fluctuations measured by the rocket probes: STATE 1 results (a) and STATE 3 results (b).

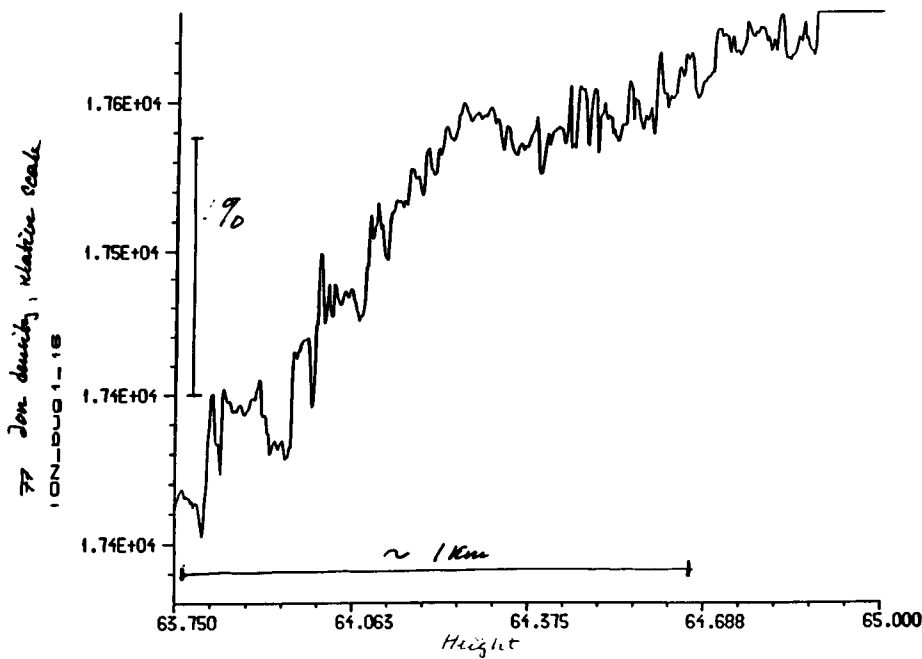


Figure 9. Examples of PIP results from MAC/Epsilon.

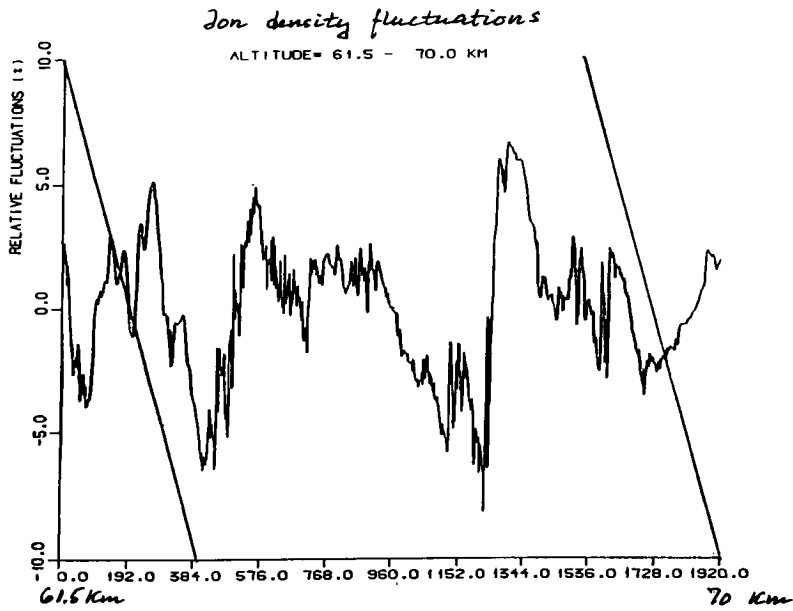


Figure 10. Examples of PIP measurements from MAC/Epsilon.

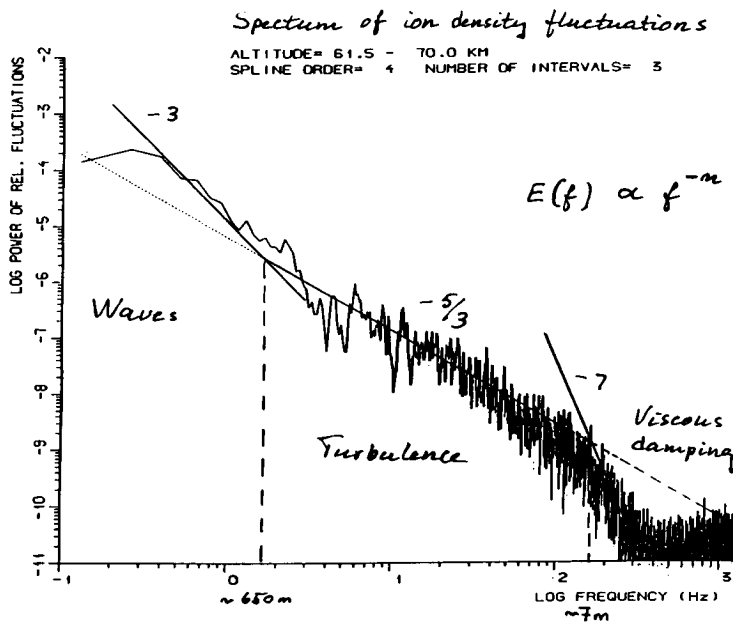


Figure 11. Spectrum from Figure 10.

6.5 RESULTS OF ROCKET MEASUREMENTS OF D-REGION IONIZATION OVER THUMBA IN MAP

D. K. Chakrabarty, G. Beig
Physical Research Laboratory
Navrangpura, Ahmedabad 380 009, India

S. C. Garg, P. Subrahmanyam, K. S. Zalpuri, Y. V. Somayajulu, M. N. M. Rao, C. B. Tandel, and T. R. Murlikrishna

National Physical Laboratory
New Delhi 110012, India

Under MAP, two rockets were launched from Thumba (8.5°N, 76.8°E) around 1030 hrs Lt with identical payloads on 7 and 10 March 1986 for D-region studies. Positive ion densities were measured by spherical probe and Gerdien condenser and electron densities were measured by Langmuir probe and propagation experiments. In both flights a valley in ionization height profile was noticed around 83 km. The density of ionization at this altitude was about $4 \times 10^2 \text{ cm}^{-3}$. A detailed positive ion-chemical scheme was used to reproduce the measured ionization height profiles. The density of NO needed to reproduce the valley in ionization at 83 km came around $5 \times 10^5 \text{ cm}^{-3}$. A photochemical treatment without diffusion process was found inadequate to explain this value of NO. Calculations showed that the value of vertical eddy diffusion needed to reproduce the value of NO was around $10^6 \text{ cm}^2 \text{ s}^{-1}$. Interestingly, the same value of eddy diffusion coefficient was obtained when derived in the manner described by Thrane and his coworkers using only the positive ion current data of spherical probes.

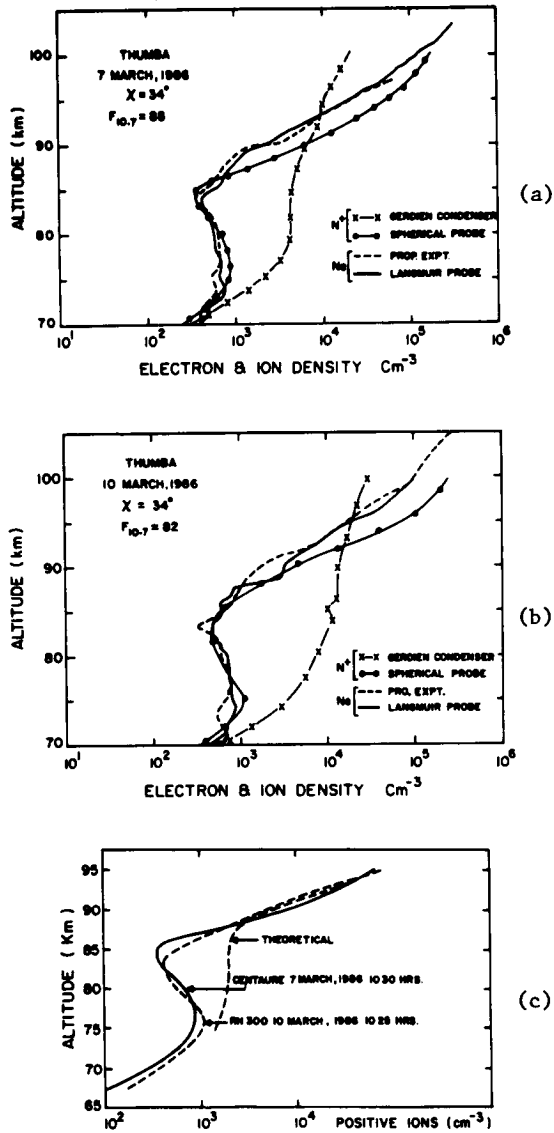


Figure 1. (a) and (b) show the plot of rocket measurements of electron and ion density profiles made at Thumba on 7 and 10 March 1986, respectively. On both days, the rocket carried identical payloads, viz., Langmuir probe, propagation experiment, Gerdien condenser and spherical probe. The Gerdien condenser gives an over estimation of the values of positive ion density below about 90 km and an underestimation above this altitude. Profiles obtained by all other techniques show a ledge preceded by a valley around 83 km. In general, the shapes of electron and ion density profiles on two days are identical but they differ in detail. (c) shows the plot of positive ion density profiles obtained on two days by spherical probe. A day-to-day variability is discernible. The theoretical profile in (c) has been obtained using the measured NO density profile of Torker et al. [1985] at Thumba.

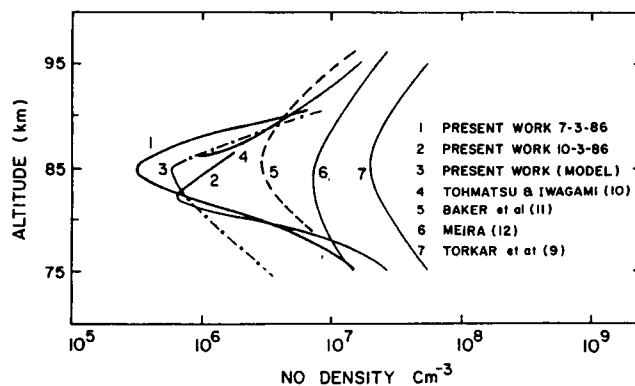


Figure 2. Height distributions of NO density obtained theoretically and experimentally by different workers. Here profile number 1 and number 2 represent the NO density required to reproduce the observed positive ion density profiles of 7 and 10 March 1986. It is to be noted that both the profiles have a valley around 80 - 85 km altitude. Also they differ considerably among themselves and are about an order of magnitude less than that of Baker et al. at this region. Profile number 3 was obtained by an 1D NO program using the eddy diffusion coefficient values derived by the current data of the spherical probe of 7 March 1986 in the manner described by Thrane et al. It is to be noted that we are able to reproduce the NO density above ~ 83 km, but below this altitude the NO values are underestimated.

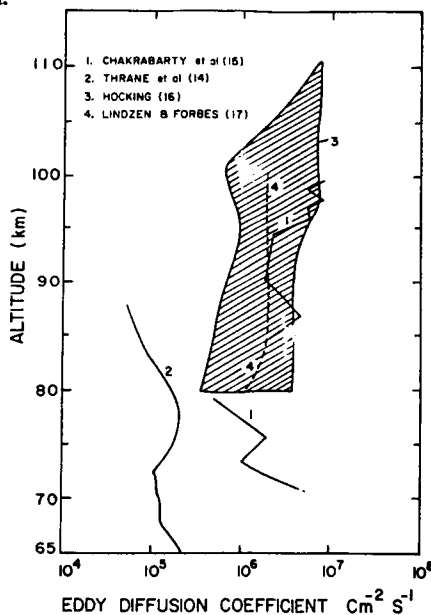


Figure 3. Height distribution of eddy diffusion coefficient given by some authors. Here profile number 1 is derived from the current data of the spherical probe obtained on 7 March 1986 in the manner described by Thrane et al. The profile of the eddy diffusion coefficient has been used in an 1D NO program. The profile of NO thus obtained matches the NO profiles required to reproduce the observed ion density profiles of 7 and 10 March 1986 above ~ 83 km; below this altitude, the NO values are underestimated.

6.6 MODEL REPRESENTATION OF THE AMBIENT ELECTRON DENSITY DISTRIBUTION IN THE MIDDLE ATMOSPHERE

Y. V. Ramanamurty

Radio Science Division, National Physical Laboratory
Dr. K. S. Krishnan Road
New Delhi 110 012, India

While the Langmuir probe controlled by rocket propagation experiments by the University of Illinois at midlatitude revealed the existence of a permanent D-region turning point (DTP), similar measurements over the Thumba equatorial station did not clearly bring out the above daytime feature. Moreover, the calibration constant (ratio of electron density to the current drawn by the Langmuir probe) increased with height (in the 70-100 km region) in the case of the midlatitude observations whereas the recent measurements over Thumba showed a decrease up to about 90 km followed by an increase above 90 km. Secondly, there is the problem of reconciling the station-oriented observations from the COSPAR family with the ground-based radio propagation measurements from the URSI family. Thirdly, new information on Winter in Northern Europe (WINE) and in USSR is available by asking for its incorporation into any global model such as the IRI. This paper presents the results of investigation of the above aspects.

The new analytical description of the electron-density profile in the lower ionosphere envisages the use of the LAY-function which is associated with three nonlinear, geometric parameters. Setting aside the question of a C-layer, three such functions are envisaged; thus, apart from the E-peak data which are used as nodal points, nine geometric parameters are needed to represent the lower ionosphere. Numerical values for noon, night, morning and evening twilight were given by Ramanamurty and Rawer. It is proposed to find the coefficients in a linear combination of the three functions by an optimization procedure inside the IRI program itself.

In order to reach this goal, characteristic features (points or derivatives) of the profile must be known. To that end, we have carefully studied measured profiles from different latitudes. Unfortunately, there are only a few sets of systematic measurements over longer times. These were obtained with different techniques. In the following we consider and compare the (Wallops) series of northern midlatitude profiles published by Mechty et al. [1972] and that of Subbaraya et al. [1983] for a station near the dip equator (Thumba). Both sets were obtained with Langmuir probe measurements, the first one being checked by ground-to rocket propagation experiments.

The crucial problem with Langmuir probes is calibration. While it could be resolved by the Mechty group with point-by-point propagation data, the Subbaraya group had to rely on other evidence. On one occasion (3 March 1973) they flew an in situ resonance probe for comparison. The result is shown in Figure 1a where Mechty's calibration is shown below 95 km. This latter, after some height shift, was matched with the direct calibration (at greater heights) so that the calibration factor increased monotonically with height. In a subsequent publication one of the Indian authors assumed the factor to be constant in the 60 to 100 km height range. Another calibration obtained by comparing with differential wave absorption (1987) led to a height dependence with a clear minimum near 90 km (Figure 1b).

In order to check the quality of the data, the density ratio between high ($F = 135$) and low ($F = 50$) solar activity was plotted as a function of height (Figure 2). It shows rather strange variations. For comparison, the electron production rate taken from theoretical consideration [Deshpande et al.] was dealt with in the same manner and plotted in the same figure. Both curves compare rather poorly. Also, the very small value of the probe curve at 90 km is difficult to understand.

Finally, we show the maximum/minimum density ratio in Figure 3 in more detail. Above 63 km the Wallops data show a ratio greater than one, as expected. The variation with height, when averaged, has a simple shape with a maximum near 80 km. Quite different, the Thumba data show several maxima and minima and ratios less than one between 85 and 95 km.

We conclude that Langmuir probe measurements of electron density in the middle atmosphere should not be accepted unless they are accompanied by simultaneous radio wave propagation experiments.

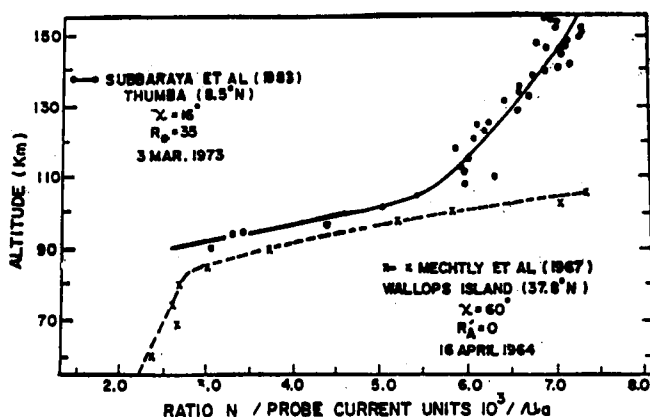


Figure 1. Top curve: in most of the experiments conducted by the Physical Research Laboratory (PRL), Ahmedabad, India, only the Langmuir probe experiment was flown. On 3 March 1973 when the Langmuir probe was calibrated by in situ resonance probe, the variation of the calibration factor, F (the ratio of the electron density, N) measured by resonance probe to the current, I , drawn by the Langmuir probe is shown above. Note that F changes drastically above 90 km. Bottom curve: The height variation of F inferred by Subbaraya et al. [1983] from the results of Mechtly et al. [1967] is shown. The calibration factor F , inferred by Subbaraya et al. [1983] is an ever increasing function of height in the 60 to 100 km region, whereas it is more or less constant below 85 km, according to Mechtly et al. [1967].

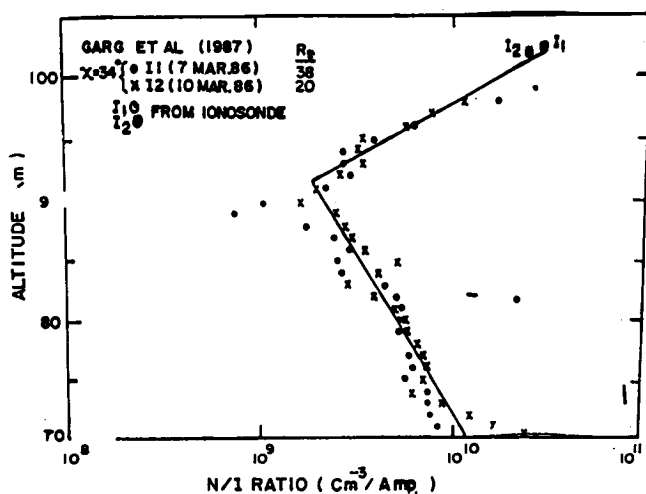


Figure 2. Thumba: N = electron density obtained from absorption experiment flown in rocket. I = current drawn by Langmuir probe flown in the same rocket. Note that N/I decreased up to 90 km by about an order of magnitude.

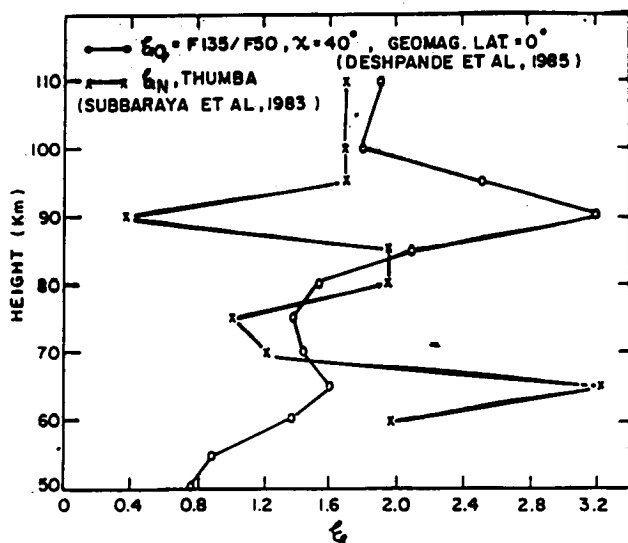


Figure 3.

q = rate of ion production at a particular height

$q_{\max} = q$ at solar maximum

$q_{\min} = q$ at solar minimum

$$\xi_Q = \frac{q_{\max}}{q_{\min}}$$

N = electron density at a particular height

$$\xi_N = \frac{N_{\max}^2}{N_{\min}^2}$$

ξ_Q was based on the work of Deshpande et al. [1985]. ξ_N was derived from the results of Langmuir probe experiments reported by Subbaraya et al. [1983]. ξ_Q and ξ_N are expected to synchronize with each other. Results do not confirm. They are sometimes anticorrelated. Also, ξ_N was less than unity around 90 km (the ledge region) which is not acceptable.

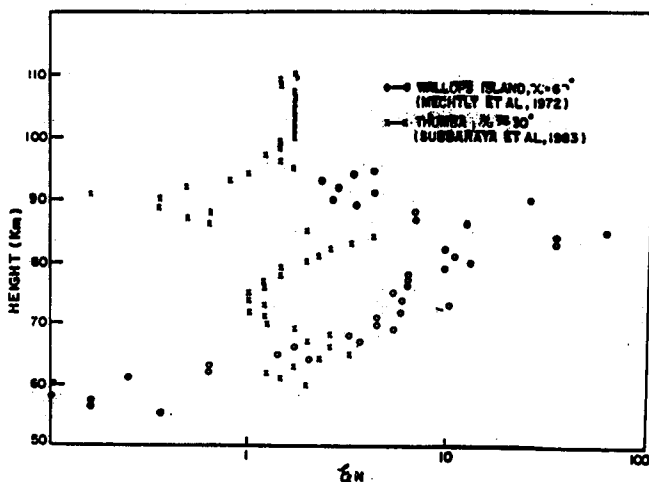


Figure 4. ξ_N for Thumba and Wallops Island are compared. The height variation of ξ_N does not synchronize at Thumba and Wallops Island.

CONCLUSIONS

- The past in situ D-region measurements (especially those involving electron-density measurements by the Langmuir probe technique only) have to be re-evaluated in the light of the discrepancies with the measurements over Wallops Island where in situ calibration of Langmuir probe measurements is done.
- The tentative model representation of the lower ionosphere discussed by Ramanamurty and Rawer [1987] is proposed for the present.
- In future, use of Langmuir probe-cum-propagation experiments is recommended to obtain the necessary data base at different latitudes.

6.7 EFFECT OF VOLCANIC DEBRIS ON STRATOSPHERIC ION CONDUCTIVITY

Y. V. Somayajulu, S. C. Garg, T. John, and K. S. Zalpuri

National Physical Laboratory
Dr. K. S. Krishnan Road
New Delhi 110 012, India

In this paper we report the reduction of stratospheric ion conductivities in the altitude range of 20 - 27 km attributable to the aerosols injected into the stratosphere by the eruption of volcano Nevado Del Ruiz on November 13, 1985. Three balloon experiments were conducted from Hyderabad, India (17.5°N, 78.6°E) carrying a Langmuir probe payload for measuring stratospheric ion conductivities. The first flight took place about 9 months before the volcanic eruption, the second 3 weeks after the eruption and the third about a year later. Lidar observations from Japan, Hawaii, and Europe reported detection of aerosol layers in the 18 - 25 km altitude range attributable to the Nevado Del Ruiz volcanic eruption. A comparison of the conductivity profiles shows that the reduction of ion conductivities is: 57.3% at 20 km and 31% at 25 km. A year after the eruption, conductivities at all heights tended to recover.

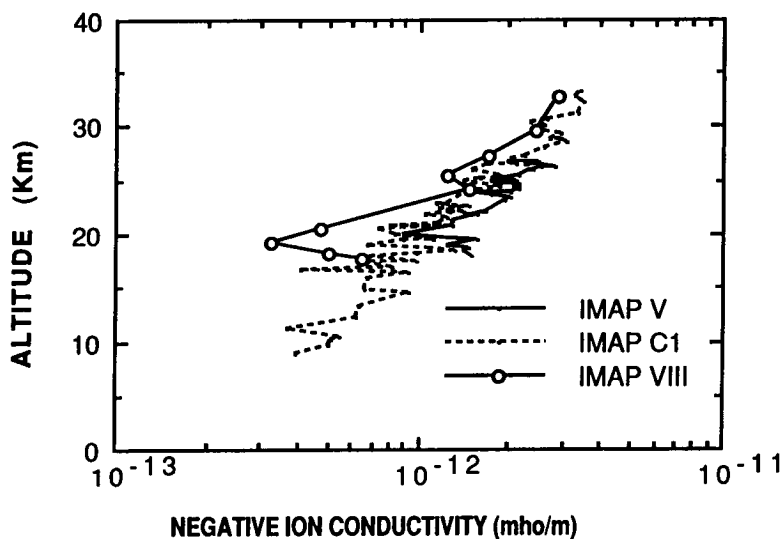


Figure 1. We report the reduction of stratospheric ion conductivities in the altitude range of 20-27 km attributable to the sulfurous material injected into the stratosphere by the eruption of volcano Nevado Del Ruiz on November 13, 1985. Three balloon experiments were conducted from Hyderabad, India (17.5°N, 78.6°E) carrying an electrostatic probe payload for measuring stratospheric ion conductivities. The first flight (IMAP-V) took place about 9 months before the volcanic eruption, the second (IMAP-VIII) about 3 weeks after the eruption and the third (IMAP-C1) about a year later. Lidar observations from Japan, Hawaii, and Europe reported detection of aerosol layers in the 18-25 km altitude range attributable to the Nevado Del Ruiz volcanic eruption. A comparison of the conductivities profiles shows that the reduction of ion conductivities is: 57.3% at 20 km and 31% at 25 km. A year after the eruption, conductivities at all heights tended to recover. Recent ion mass-spectrometer measurements of negative ion composition suggest possible importance of ion nucleation sulphuric acid droplets. It is suggested that the sulfurous material injection from the volcanic eruption of Nevado Del Ruiz can explain the observed stratospheric conductivity reduction.

6.8 RELATIVISTIC MAGNETOSPHERIC ELECTRONS: LOWER IONOSPHERIC CONDUCTIVITY AND LONG-TERM ATMOSPHERIC VARIABILITY

D. N. Baker¹, J. B. Blake², R. Klebesadel³, D. D. Sentman⁴, D. J. Gorney², and P. R. Higbie³

¹NASA, Goddard Space Flight Center, Greenbelt, MD 20771

²Aerospace Corporation, Los Angeles, CA

³Los Alamos National Laboratory, Los Alamos, NM 87545

⁴IGPP, University of California, Los Angeles, CA

Long-term (1979-88) observations of relativistic electrons in the earth's outer magnetosphere show a strong solar cycle dependence with a prominent intensity maximum during the approach to solar minimum (1983-85). This population therefore closely corresponds to the presence of high-speed solar wind streams emanating from solar coronal holes. Using a numerical code, we have calculated the precipitating electron energy deposition in the earth's upper and middle atmosphere. Observed events (typically persisting several days) would have maximum effect in the 40-60 km altitude range with peak energy depositions $> 110 \text{ keV/cm}^3\text{-s}$. We suggest that this electron population could play an important long-term role in modulating lower D-region ionization and middle atmospheric ozone chemistry. We describe methods of observing middle atmospheric and lower ionospheric effects of the electrons including balloon, riometer, and space-based ozone sensor systems. A particularly promising approach may involve the monitoring of global Schumann resonance modes which are sensitive to global changes in the properties of the earth-ionosphere cavity. Present work indicates that Schumann resonance properties are moderately correlated with the flux of precipitating relativistic electrons thus offering the possibility of continuously monitoring this aspect of magnetosphere-atmosphere coupling.

Figure 1. (Following page) Summary of measurements in the 3 - 5 and 5 - 7 MeV energy range for S/C 1979-053 and S/C 1982-019, with data shown as the daily flux averages (electrons/cm²-s-sr-MeV). This highly compressed format shows the long-term behavior of the relativistic electron components from 1980 to 1988. The 5 - 7 MeV channel has been offset downward by one decade in flux for clarity of presentation. No background rate has been subtracted from the counting rates used. Thus, one can observe the smooth, systematic variation of the minimum flux level in each of the energy channels. As discussed previously [Baker et al., *J. Geophys. Res.*, 91, 4265, 1986; Baker et al., *Geophys. Res. Lett.*, 14, 1987] we attribute the minimum count rate in each channel to a galactic cosmic ray component which escapes elimination by the SEE particle analysis system. As shown in our previous analysis, the background variation is plausibly associated with the several hundred MeV/nucleon cosmic ray flux. A variety of analyses and comparisons with other concurrent measurements shows that the large, spiky enhancements above this background level are due almost exclusively to relativistic electron enhancements.

A notable feature of the data is that there were very few significant electron enhancements (i.e., peaks well above background) during 1980. In contrast from late 1981 through early 1986 there were numerous, intense electron spikes. In 1984 and 1985, these increases were particularly intense and frequent -- so much so as to give almost a continuous presence at 6.6 R_E. By late 1986, the relativistic electron flux was waning and individual enhancements were not nearly as large as during 1982-85. A detailed comparison with average solar wind properties shows that relativistic electron enhancements tend to occur only following the passage of solar wind streams $V \geq 600 \text{ km/s}$. thus, the entire run of SEE data is consistent with the earlier findings that very high-energy electrons occur only on the declining edges of high speed solar wind stream structures.

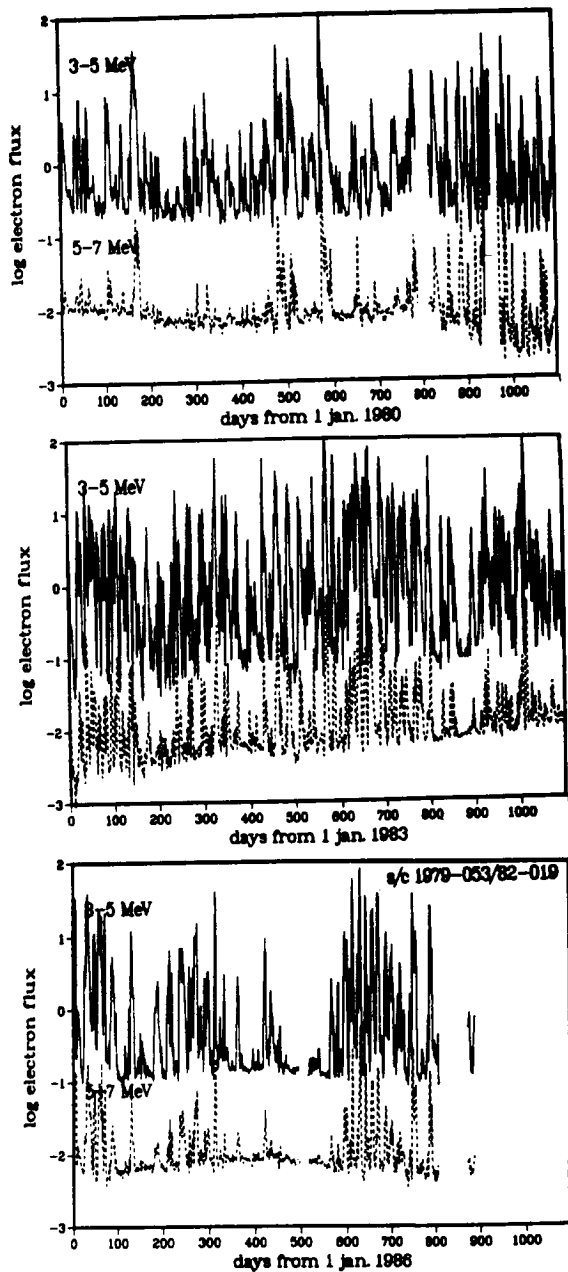


Figure 1.

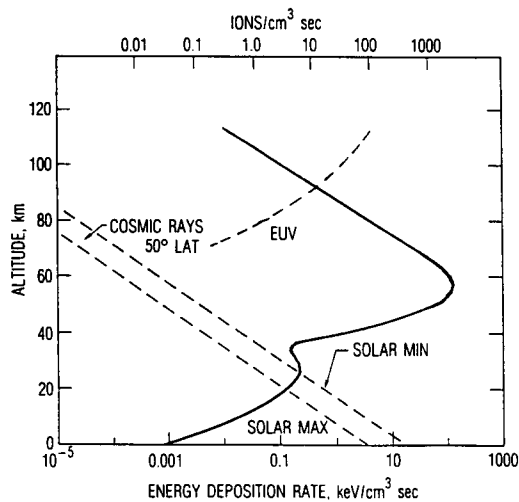


Figure 2. The principal loss mechanism for relativistic electrons in the earth's radiation zone is precipitation into the atmosphere. Normal auroral electron precipitation is confined to a fairly narrow latitudinal band (inv. latitude $\sim 68 - 72^\circ$) i.e., the auroral oval itself. Furthermore, the 20 - 100 keV auroral electrons penetrate only down to ~ 100 km altitude before they are stopped. Unlike these low-energy electrons, multi-MeV electrons are very penetrating. In fact, the ≥ 1 MeV electrons examined here are capable of penetrating down to the lower D region and into the upper stratosphere. The Bremsstrahlung X-rays that such electrons produce when interacting with atmospheric constituents can penetrate even more deeply, and both the primary electrons and the secondary photons can be significant ionization sources.

In order to quantify energy deposition aspects, we have used a numerical transport code to study the interaction of relativistic electrons with earth's atmosphere and ionosphere. The code provides a realistic 1-D representation of vertical atmospheric densities and cross sections. We take as input the measured electron spectrum at $6.6 R_E$ for a particular relativistic electron enhancement, viz., a modest event observed in mid-June 1980. We characterize the high-energy component of this event (≥ 1 MeV) with a spectral from $dJ/dE = 10^3 \exp(-E/587 \text{ keV})$ and use this spectrum in the model atmosphere code. The figure shows the results of this calculation and illustrates energy deposition rate versus altitude. The solid curve shows our estimate of the relativistic electron energy deposition. This calculation shows the very large energy deposition rate in the 40 - 70 km altitude range that occurs during the peak of an electron precipitation event. This deposition is due to the primary electron energy loss. The secondary peaks at ~ 25 km altitude are due to the Bremsstrahlung energy deposition. Even this photon deposition is fairly significant.

For comparison purposes, we have included the energy deposition rates for galactic cosmic rays (both at solar maximum and at solar minimum) at 50° geomagnetic latitude. Near the upper part of the figure we also show the other significant source of ionizing radiation, i.e., the solar extreme ultraviolet (EUV). As can be seen from the figure, at mesospheric and upper stratospheric heights, the relativistic electron energy deposition is dominant during the peak of a multi-MeV precipitation event. Since we are discussing ionizing radiations here, we can use the standard value of 35 eV per ion pair to estimate the ion production rate. We show this scale along the top of the figure. We see that the peak rate is $1000 - 3000 \text{ ions (cm}^3\text{-s)}^{-1}$ at ~ 50 km altitude.

7. WINTER IN NORTHERN EUROPE (WINE)

7.1 THE PROJECT "WINTER IN NORTHERN EUROPE" (MAP/WINE): INTRODUCTION AND OUTLOOK

U. von Zahn

Institute of Physics, University of Bonn
12 Nussallee, 5300 Bonn 1
Federal Republic of Germany

The project "Winter in Northern Europe (WINE)" of the international Middle Atmosphere Program (MAP) comprised a multinational study of the structure, dynamics and composition of the middle atmosphere in winter at high latitudes. Coordinated field measurements were performed during the winter 1983/84 by a large number of ground-based, air-borne, rocket-borne and satellite-borne instruments. Many of the individual experiments were performed in the European sector of the high latitude and polar atmosphere. Studies of the stratosphere, were, in addition, expanded to hemispheric scales by the use of data obtained from remotely sensing satellites. Beyond its direct scientific results, which will be reviewed in the following presentations, MAP/WINE has stimulated quite a number of follow-on experiments and projects which address the aeronomy of the middle atmosphere at high and polar latitudes.

What is special in the winter high latitude middle atmosphere?

1. Strong wave mean flow interactions drive the mesosphere way out of radiative equilibrium. This implies:
 - 1.1 Strong dynamical coupling of the mesosphere to lower atmosphere
 - 1.2 Time scales for transport become smaller than those for many photochemical reactions -- minor constituent distribution depends strongly on horizontal transport (e.g., H_2O ; O ; ...)
2. Neutral and ionized component of the atmosphere affected by geomagnetic and auroral activity (e.g., NO , N_2)
3. Paucity of data

Scientific objectives of the project MAP/WINE

- (a) To study the large scale dynamics of the stratosphere and, in particular, sudden stratospheric warmings (minor and major), their causes, the time evolution of large scale spatial structures and their effects on the mesosphere temperature structure and dynamics.
- (b) To measure the morphology of small scale dynamic features, such as turbulent structures, gravity waves and tides in the winter middle atmosphere, to study the control exerted by gravity waves and tides on the mean flow in the mesosphere and to develop improved parameterizations of the interactions of small scale dynamic processes with mesospheric temperature, structure and mean flow.
- (c) To study the effects of dynamics and temperature structure on the distribution of minor constituents, including ionospheric plasma, in the middle atmosphere.
- (d) To intercompare established and recently developed remote sensing and *in situ* techniques for measuring important mesospheric parameters, such as temperature, wind velocity and direction, turbulence and the water mixing ratio.

Schedule

Intensive field measurements from approximately

December 1, 1983 until February 23, 1984

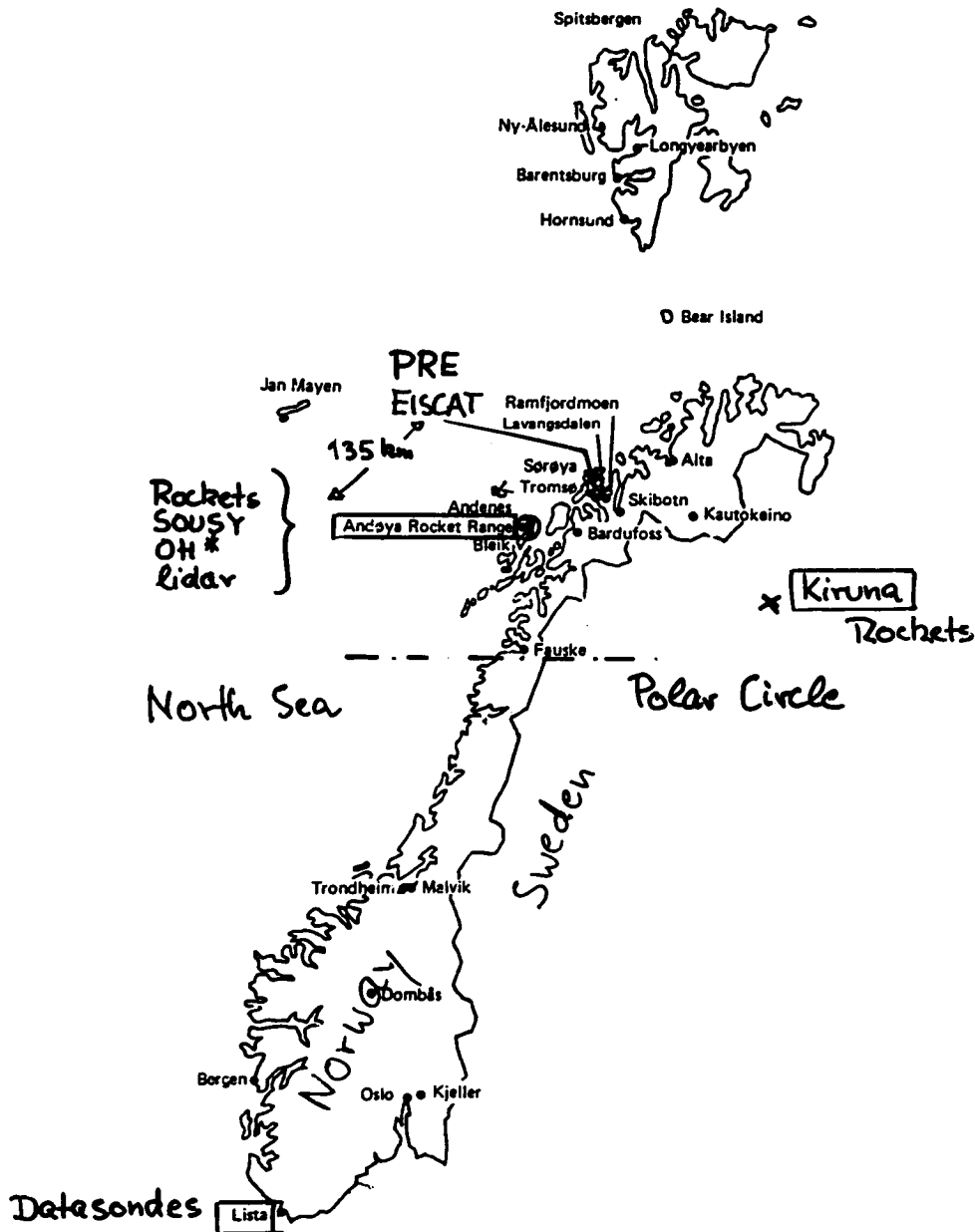
with supporting measurements extending this period on either side by 1 month.

X-X-X-X-X-X-X-X

continuous measurements:	meteor winds, spaced antenna drifts radar, many ground-based techniques
near-continuous measurements:	satellite remote sensing
regularly spaced measurements:	metroket soundings, radiosondes
irregularly spaced measurements:	MST radar, PRE radar, lidar
Scandinavia salvos:	sounding rockets, metrokets, chaff, PRE radar, EISCAT, all other methods as available
USSR salvos:	M-100B rockets with various payloads, ionosondes, PRE radar

Location(s)

- (a) local phenomena studied most intensely in northern Scandinavia, including the sites of
ARR, Kiruna, PRE radar, MST radar, EISCAT, 2 lidar stations,
2 OH*-spectrometers and additional supporting ground-based
observations
- (b) continental scale:
UK, France, Scandinavia, FRG, GDR, Czechoslovakia, USSR
- (c) hemispheric scale:
USA, Canada, northern Europe (plus satellites and metrokets)
("NOAA" + "SME")



Map showing observational sites.

Figure 1. Partial reflection radars (PRE) 2.75 MHz, 109 m; VHF radar (SOUSY), 53.5 MHz, 5.6 m; European Incoherent Scatter Facility (EISCAT) 933 MHz, 0.3 m.

ORIGINAL PAGE
BLACK AND WHITE PHOTOGRAPH



Figure 2. Geographical distribution of the main sites for ground-based observations and rocket launches of the project MAP/WINE.

Salvo Launchings from the Andøya and Kiruna Rocket Ranges

Reg. winter conditions	7. Dec. 1983	(M-T1)	4 metrockets
Special M-T2 salvo	6. Jan. 1984	M-T2,	4 metrockets
Gravity wave salvo	13. Jan. 1984	M-T3,	8 metrockets
↔↔ Metrocket salvo 1 (daylight)	21. Jan. 1984		10 metrockets ↔↔
D-CMET salvo	25. Jan. 1984	M-T4,	3 metrockets
↔↔ Salvo D <i>regular polar vortex</i>	31. Jan. 1984	M-M1, M-T5, M-W1, M-S1.	5 metrockets ↔↔
↔↔ Salvo R 1 <i>peak of minor st. warming</i>	10. Feb. 1984	M-M2, M-T6, M-W2, M-I1.	6 metrockets ↔↔
Salvo R 2	16. Feb. 1984	M-T7,	3 metrockets
Salvo R 3	18. Feb. 1984	M-T8,	7 metrockets
Metrocket salvo 2	19. Feb. 1984		5 metrockets

REVIEWS OF MAP/WINE RESULTS

The Project "Winter in Northern Europe" (MAP/WINE):
Introduction and Outlook.

U. von Zahn (FRG)

Small-Scale Structure and Turbulence Observed in MAP/WINE.
T.A. Blix (Norway)

Middle Atmosphere Thermal Structure during MAP/WINE.
D. Offermann (FRG)

The Soviet Contributions towards MAP/WINE.
Z.T. Rapoport and E.S. Kazimirovsky (USSR)

Mean, Tidal and Fluctuating Winds in the Middle Atmosphere and Lower Thermosphere Observed during MAP/WINE in Northern Scandinavia.

J. Röttger (Sweden)

Large-Scale Dynamics of the Stratosphere and Mesosphere during the MAP/WINE Campaign Winter 1983/84 in Comparison with Other Winters.

K. Petzoldt (FRG)

Middle Atmosphere Minor Species during MAP/WINE.
J.C. Ulwick (USA)

Plasma Phenomena Observed in the MAP/WINE Campaign.
M. Friedrich (Austria)

7.2 SMALL-SCALE STRUCTURE AND TURBULENCE OBSERVED IN MAP/WINE

T. A. Blix

Norwegian Defence Research Establishment
P. O. Box 25
N-2007 Kjeller, Norway

During MAP/WINE small-scale structure and turbulence in the mesosphere and lower thermosphere was studied *in situ* by rocket-borne instruments as well as from the ground by remote sensing techniques. The eight salvoes launched during the campaign resulted in a wealth of information on the dynamical structure of these regions. The paper reviews the experimental results and discusses their interpretation in terms of gravity waves and turbulence. It is shown that eddy diffusion coefficients and turbulent energy dissipation rates may be derived from the *in situ* measurements in a consistent manner. The observations are also shown to be consistent with the hypothesis that turbulence can be created by a process of gravity wave saturation.

DERIVATION OF ϵ AND K

(A) CONSERVATION OF ENERGY (THRANE ET AL, 1985)

(B) STRUCTURE FUNCTION (HOCKING, 1985; TATARSKII, 1961, 1971)

THE STRUCTURE FUNCTION CONSTANT C_E^2 IS GIVEN BY:

$$C_E^2 = a^2 N e^{-1/3} \quad \text{AND} \quad N = K_E \left[\left(\frac{\partial E}{\partial x} \right)^2 + \left(\frac{\partial E}{\partial y} \right)^2 + \left(\frac{\partial E}{\partial z} \right)^2 \right] = K_E \beta M_E^2$$

WHERE:

$$M_E = \frac{\partial E}{\partial z}$$

FROM THE EQUATIONS ABOVE ONE CAN OBTAIN (HOCKING, 1985; BLIX, 1988):

$$\epsilon = \left[a^2 \alpha_1 R_1 \beta \right]^{-3/2} \left[C_E^2 \right]^{3/2} \omega_B^3 M_E^3$$

CRITICAL QUESTIONS:

(1) WHAT IS THE RICHARDSON NUMBER ?

HOCKING (1985): $R_1 = R_1(\text{crit.}) = 0.25$

WEINSTOCK (1978): $R_1 = 0.8$

(2) IS THERE ANY RELATION BETWEEN VARIATIONS IN THE VERTICAL AND HORIZONTAL DIRECTION ?

HOCKING (1985): $\partial E / \partial x = \partial E / \partial y = 0$

BLIX (1988): $\partial E / \partial x = \partial E / \partial y = \partial E / \partial z$

Figure 1. Procedure for deriving turbulence parameters. Good agreement between the two models (A and B) is obtained using $R_1 = 0.8$ instead of 0.25, and $\frac{\partial}{\partial x} = \frac{\partial}{\partial y} = \frac{\partial}{\partial z}$ instead of $\frac{\partial}{\partial x} = \frac{\partial}{\partial y} = 0$.

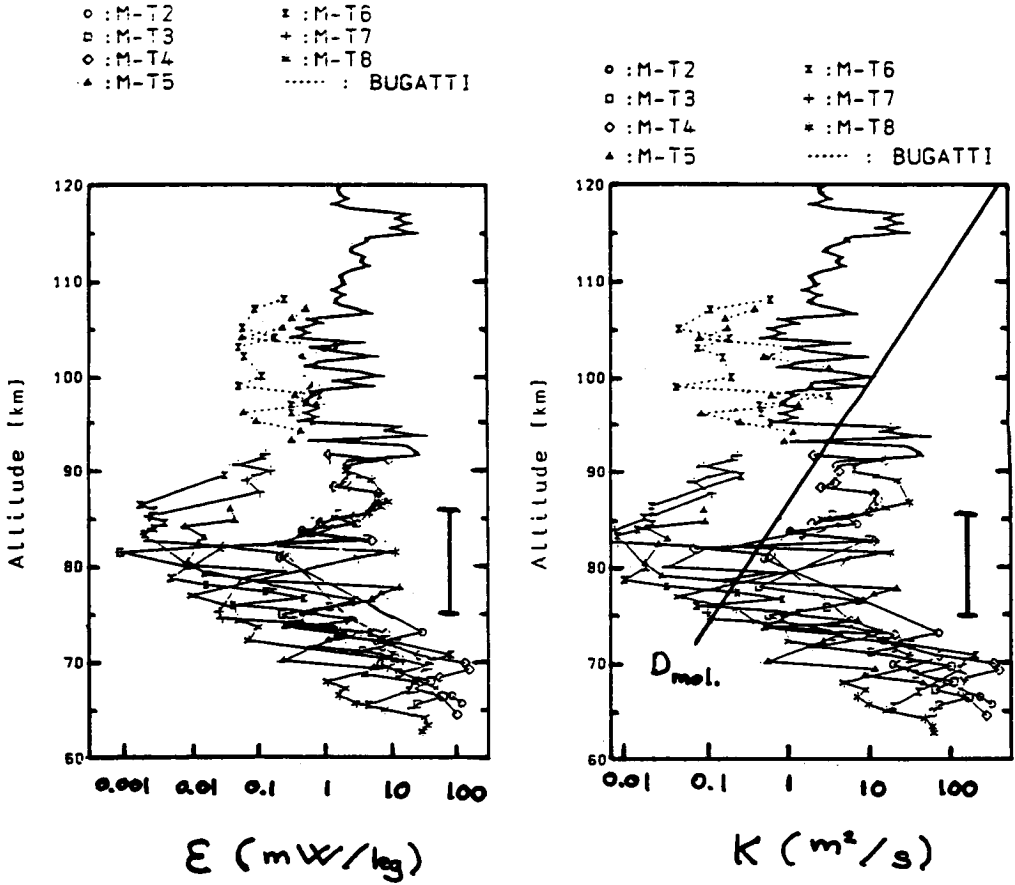


Figure 2. ϵ and K derived from the PIP and BUGATTI flights. Energy dissipation rates ϵ (left panel) and eddy diffusion coefficients K (right panel) derived from the positive ion probe (PIP) and the BUGATTI mass spectrometer flown during MAP/WINE. Note the minimum in turbulence activity at or below the mesopause region (vertical bars in the figure).

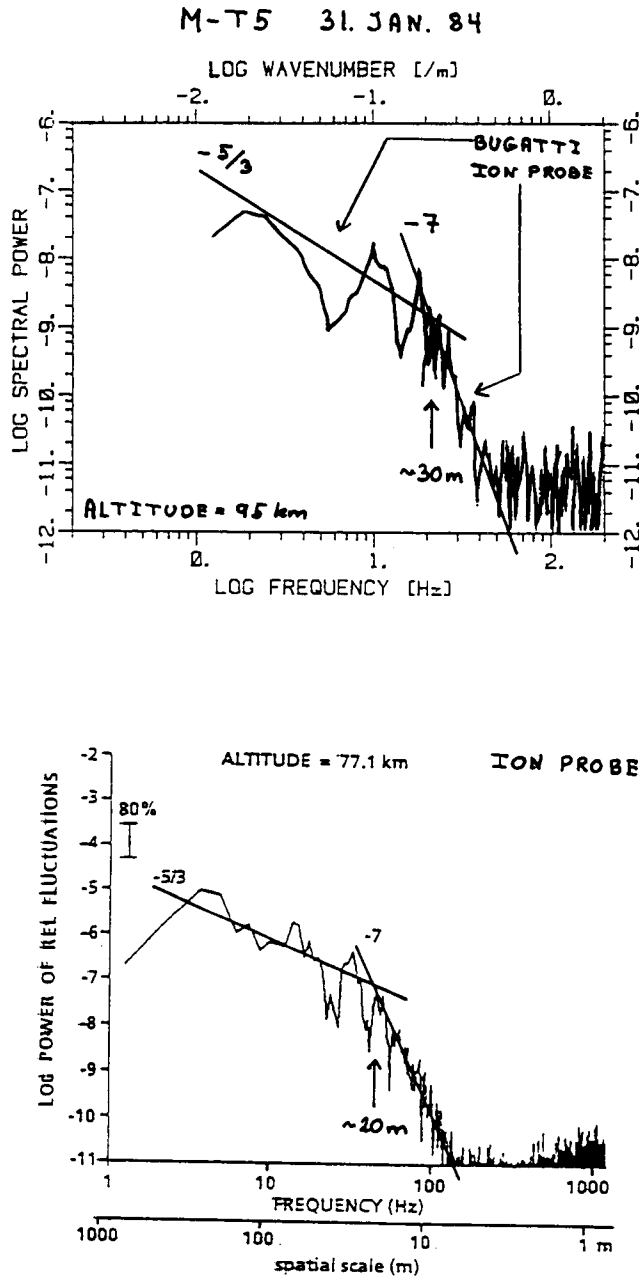
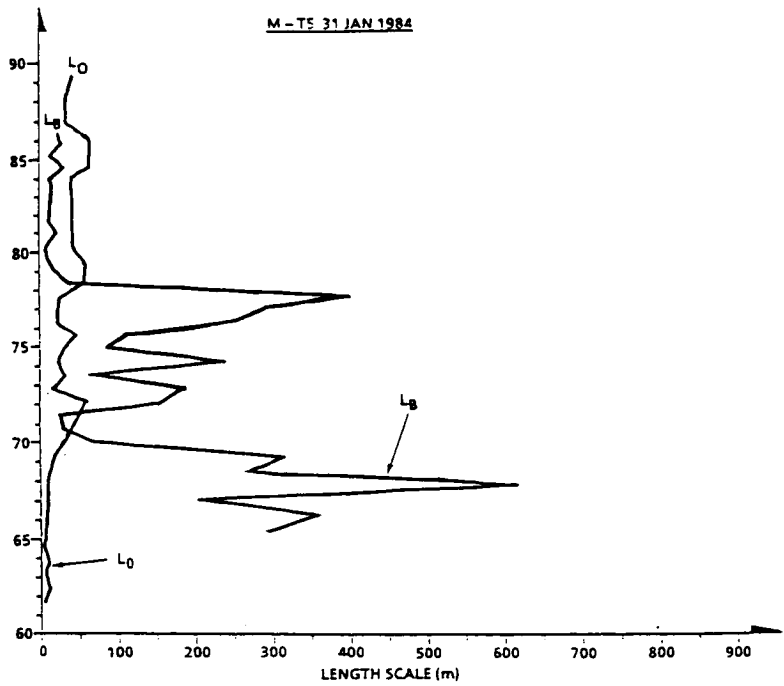


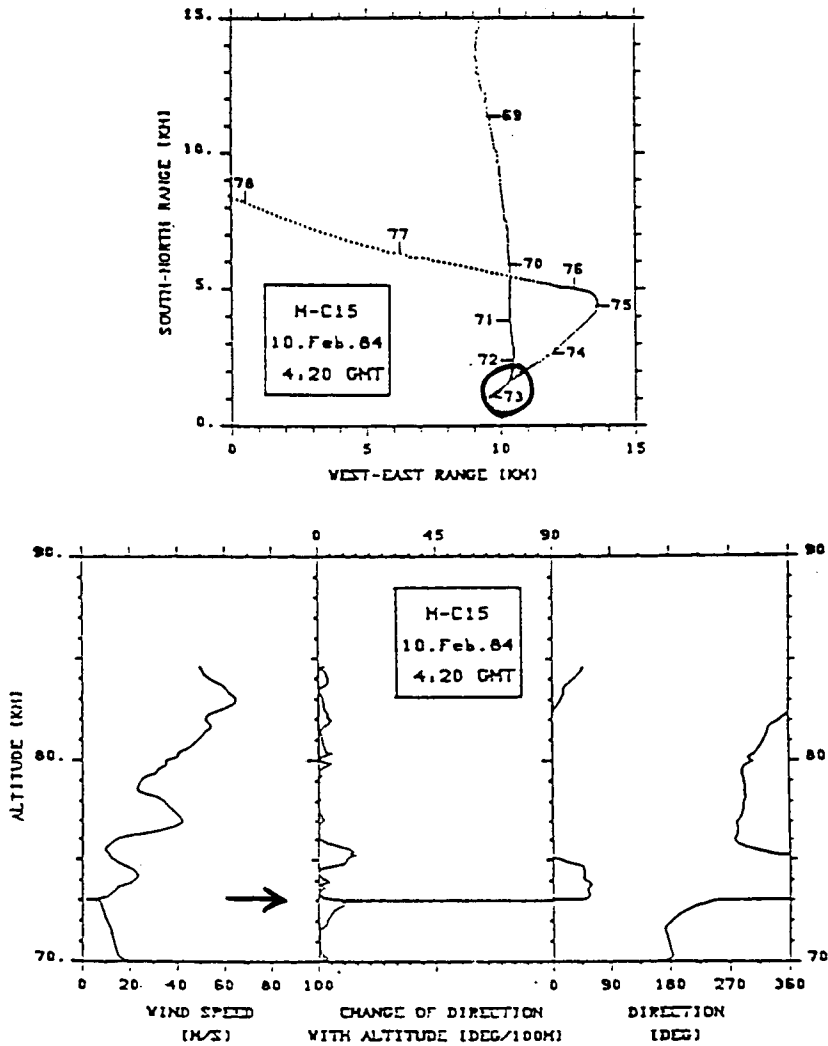
Figure 3. Upper panel: Comparison of spectra at neutral density fluctuations observed with the positive ion probe and the BUGATTI mass spectrometer during flight M-T5 31 Jan 84 at 95 km height. Note break in spectrum from $-5/3$ to -7 at a scale of about 30 m. Lower panel: Spectrum of ion density fluctuations observed with the positive ion probe during flight M-T5 31 Jan 1984 at 77 km height. Note break in spectrum from $-5/3$ to -7 at a scale of about 20 m.

TYPICAL SCALES OF THE OBSERVED TURBULENCE



$$L_B = \left[0.271 M_{\frac{\Delta n}{n}}^2 \right]^{-3/4} \left[C \frac{\Delta n}{n}^2 \right]^{3/4}$$
$$M_{\frac{\Delta n}{n}} = \left[\frac{1}{H_n} - \frac{1}{\gamma H_p} \right]$$

Figure 4. Transition scale L_0 (break in spectral slope from $5/3$ to -7) and buoyancy length scale L_B (derived from the formula shown) versus height from the M-T5 flight 31 Jan 1984.



HIGH LATITUDE (69°N) WINTER

Figure 5. Typical wind corner observed with the foil cloud (chaff) M-C15 on Feb 10 1984. Wind corner at 73 km height is characterized by a minimum in wind speed associated with a sharp change in wind direction with height.

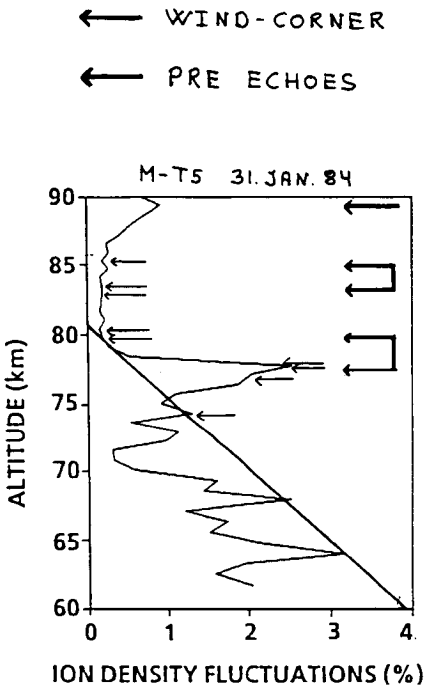


Figure 6. An example showing the correlation between ion density fluctuations (solid curve), wind corners (light arrows) and PRE echoes (heavy arrows). The heavy sloping line is the minimum intensity of ion density fluctuations that can be observed by PRE for normal noise intensity.

	PRE ECHOES	ION DENSITY FLUCTUATIONS	WIND CORNERS
PRE ECHOES	100	78	76
ION DENSITY FLUCTUATIONS	72	100	33
WIND CORNERS	80	30	100

Figure 7. Coincidence rates (in %) between the occurrence rate of PRE echoes, ion density fluctuations and wind corners obtained after a statistical analysis of the salvo launchings during MAP/WINE. One can see that, for example, 80% of the wind corners are associated with PRE echoes, while 33% of the ion density fluctuations are associated with wind corners.

GRAVITY WAVES

- GRAVITY WAVES CREATE CONVECTIVE INSTABILITIES IN PREFERENCE TO DYNAMIC INSTABILITIES FOR HIGH FREQUENCY WAVE MOTIONS
- LINEAR THEORY AND MONOCHROMATIC WAVES
- THE CRITERION FOR CONVECTIVE INSTABILITY IS:

$$\partial T / \partial z + \Gamma < 0 \quad \text{OR} \quad u' > c - U_0$$

WHERE

Γ IS THE ADIABATIC LAPSE RATE

u' IS THE HORIZONTAL PERTURBATION SPEED

c IS THE HORIZONTAL PHASE SPEED OF THE WAVE

U_0 IS THE MEAN WIND

THE INTRINSIC PHASE VELOCITY $c - U_0$ CAN BE FOUND FROM:

$$c - U_0 = (\omega_B / 2\pi) \lambda_z$$

WHERE λ_z IS THE VERTICAL WAVELENGTH

Figure 8. Simple outline of the saturation mechanics for gravity waves.

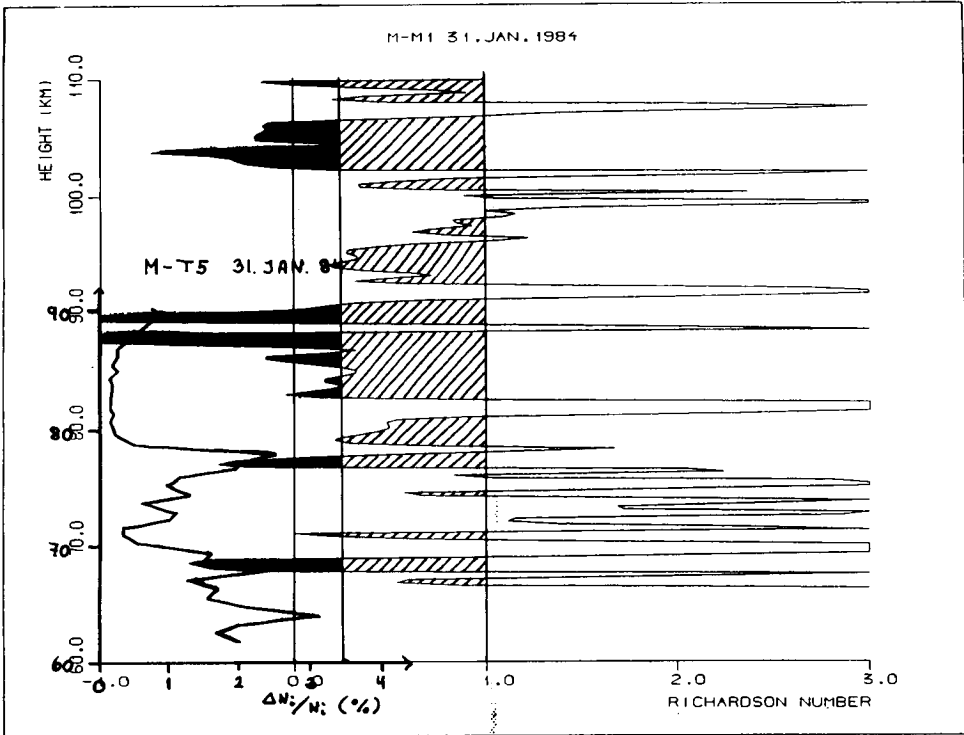


Figure 9. Comparison of Richardson numbers R_i derived from the active falling sphere M-M1 and ion density fluctuations $\Delta N_i/N_i$ (%) derived from the ion probe onboard M-T5 (31 Jan 1984). Good correlation between regions of convective instabilities and significant ion density fluctuations can be seen.

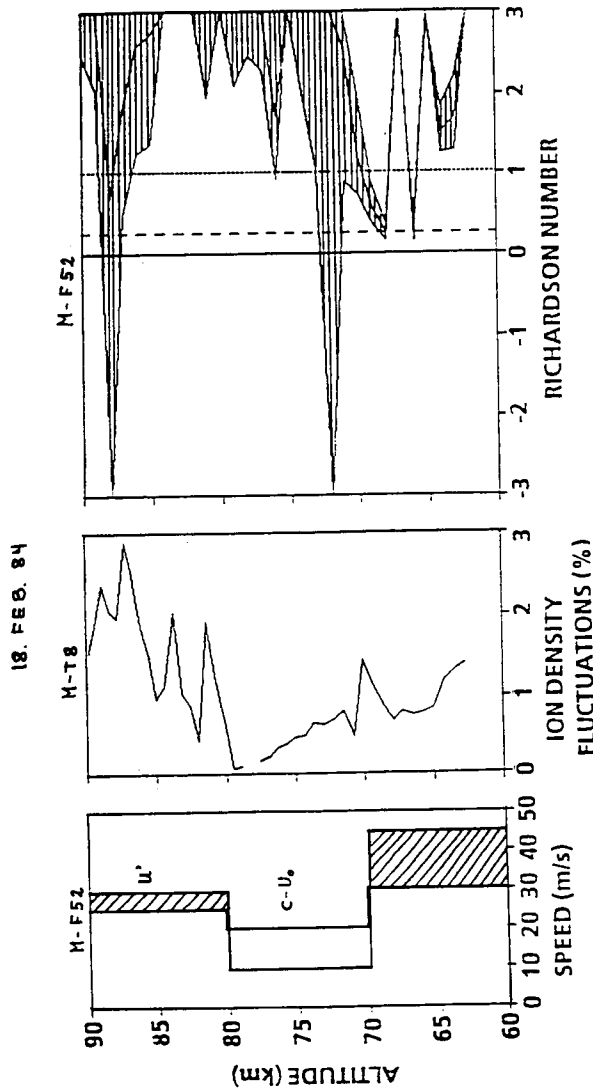


Figure 10. Case study of M-F52 and M-T8 (18 Feb 1984) showing the horizontal perturbation velocity u' the intrinsic phase velocity $c-u$, ion density fluctuations and gradient Richardson number versus height. The hatched areas in the left-hand panel indicate those regions where $u' \geq c-u$. These regions correspond with regions of significant ion density fluctuations.

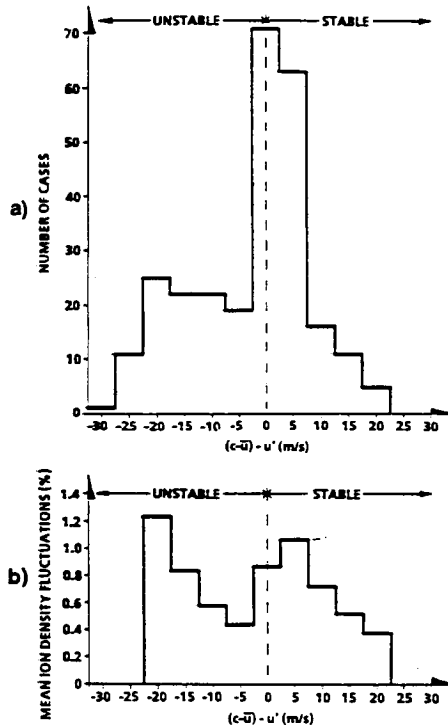


Figure 11. Results of a statistical investigation of the gravity wave saturation criteria ($d = (c - u_0) - u' \approx 0$) and turbulence. (a) Histogram showing number of cases as a function of d in intervals of 5 m/s. (b) Mean intensity of ion density fluctuations as a function of d .

CONCLUSIONS

- Previous disagreement between ϵ and K calculated using two different models have been explained.
- There is a minimum in turbulence at or below the mesopause region.
- There is a close relation between the extent of the intertil subrange, as determined by L_B and l_0 , and the measured turbulence intensities.
- The wind and temperature fields derived from the meteorological rocket measurements have demonstrated that gravity waves are a dominant feature of the mesosphere in winter.
- Turbulent layers are associated with regions of convective and dynamic instabilities.
- The criterion for gravity wave saturation is often fulfilled in the high latitude winter mesosphere.
- There is a positive correspondence between strong turbulence and regions of radar echoes.
- Wind corners are predominantly associated with radar reflections (not with turbulence).

7.3 MIDDLE ATMOSPHERE THERMAL STRUCTURE DURING MAP/WINE

D. Offermann

Physics Department, University of Wuppertal
5600 Wuppertal 1
Federal Republic of Germany

Middle atmosphere temperatures were measured during the MAP/WINE campaign by various ground-based techniques, by rocket instruments, and by satellites. Respective data have been analyzed for atmospheric thermal mean state as well as for long and short period variations. A brief survey of the results is given. Monthly mean temperatures agree well with the new CIRA model. Long period (planetary) waves frequently exhibit peculiar vertical amplitude and phase structures, resembling those of standing waves. Short period oscillations tend to begin breaking well below the stratosphere.

Temperature Measurements during MAP/WINE

<u>Technique</u>	<u>Place/Institution</u>
1. Ground-based	
Lidar	Observatoire de Haute Provence/CNRS
Lidar	Andoya/Bonn University
Near infrared	Andoya/Wuppertal University
OH spectrometers	ESRANGE/Utah State University
OH spectrometers	Lista, Oslo/Wuppertal University; NDRE
OH spectrometer	Zvenigorod/IPA
2. Rockets	
Met. rockets	Heiss Island/CAO
Datasondes	Andoya/Bonn University
Falling spheres (passive)	Andoya/Bonn University; NASA GSFC
Falling spheres (active)	Andoya/AFGL
IR radiometers	Andoya/Wuppertal University
Mass spectrometers	Andoya/Bonn University
IR spectrometer	ESRANGE/Wuppertal University
Datasondes	Lista/NASA GSFC; NDRE
Met. rockets	Volgograd/CAO
3. Satellites	
Stratospheric Sounding Unit	NOAA
SSU	

Figure 1. Techniques used for middle atmosphere temperature measurements during MAP/WINE. For details see the following papers in *J. Atmos. Terr. Phys.*, 49, 1987: v. Zahn, p. 607; Petzold et al., p. 621; Hauchecorne et al., p. 649; Offermann et al., p. 655; v. Zahn, p. 863. Also, Schmidlin, *ESA SP 270 (Sunne)*, 133, 1987; Gerndt, Ph. D., University of Wuppertal, 1986; Brückelmann, Ph.D. University of Wuppertal, 1988; Meyer et al., *ESA SP 229 (Loen)*, 41, 1985; Lübken et al., *ESA SP 229 (Loen)* 259, 1985.

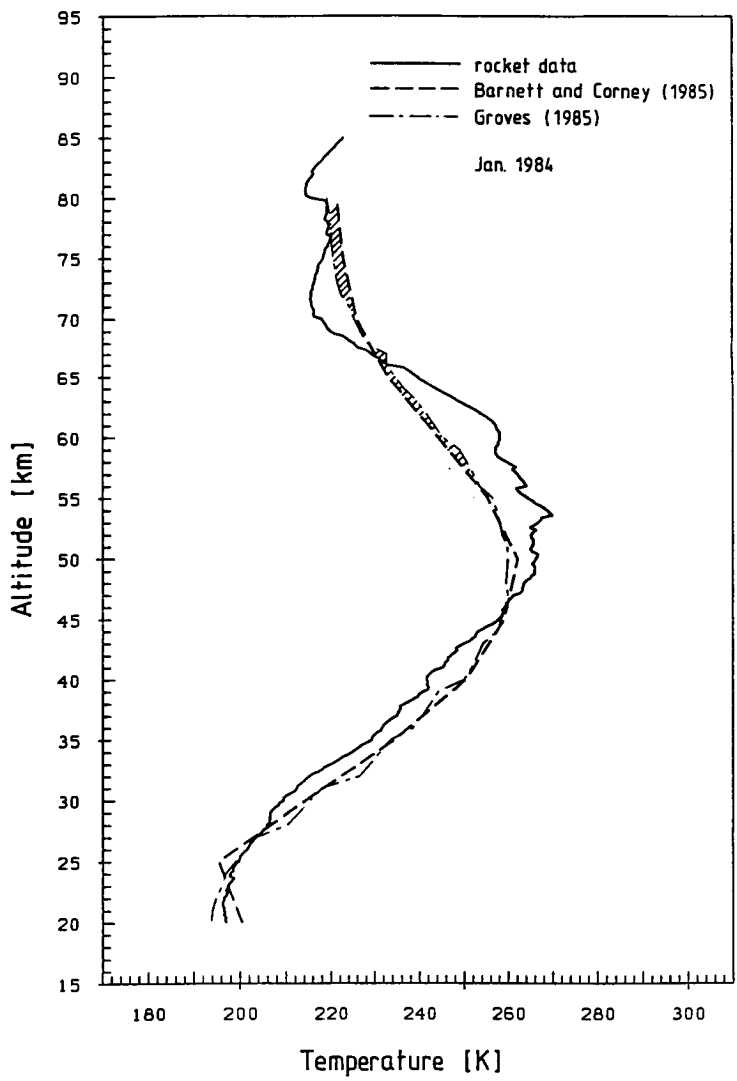


Figure 2. Mean temperature profile calculated from the rocket measurements above Andoya in January 1984. The model profiles of Barnett and Corney (*Handbook for MAP 16*, 47, 1985) and Groves (AFGL-TR-85-0129) are given for comparison. Differences between measured and model profiles in the mesosphere appear to show a precursor structure related to the major stratospheric warming, which occurred by end of February 1984. (For details see Offermann et al., *J. Atmos. Terr. Phys.*, 49, 655, 1987.)

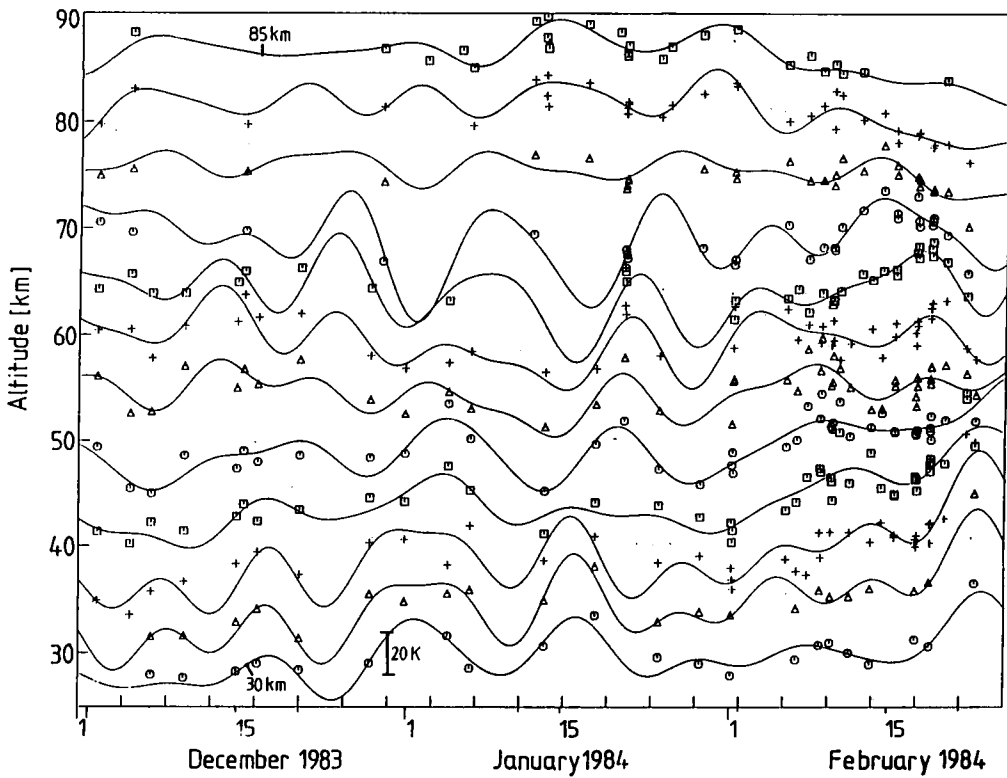


Figure 3. Harmonic least square fit to temperatures measured at given altitudes during the MAP/WINE campaign above Andoya. Analysis is performed at 1 km altitude steps, only part of which is shown here. Five oscillations are superimposed. The periods are 9.6 days, 13.3 days, 17.4 days, 54 days and 144 days. The shorter ones are believed to represent planetary waves (Details of this and the following pictures are given by Offermann et al., *J. Atmos. Terr. Phys.*, 49, 655, 1987.)

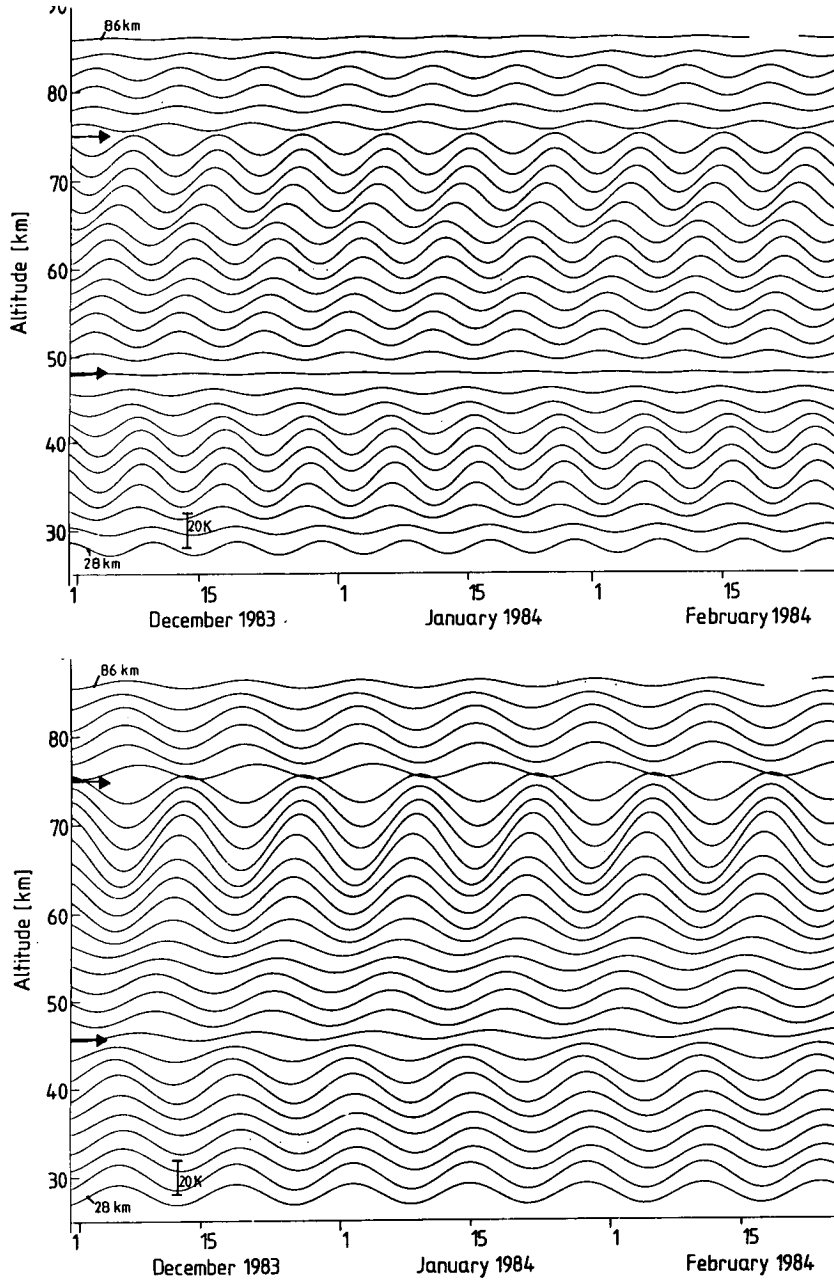


Figure 4. Two components of the harmonic analysis shown in Figure 3 (Andoya): a) period is 9.6 days, b) period is 13.3 days.

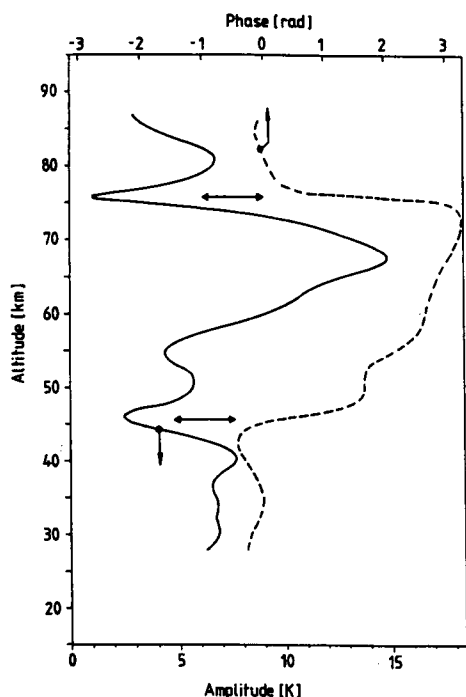


Figure 5. Vertical amplitude and phase structure of the wave with 13.3 days period. Oscillation nodes with amplitude minima and phase jumps (of about 180°) are seen at altitudes of 46 km and 76 km. They are indicative of a standing wave. Similar structures are seen in most of the other oscillations analyzed. They were also found in other winter campaigns in Western Europe.

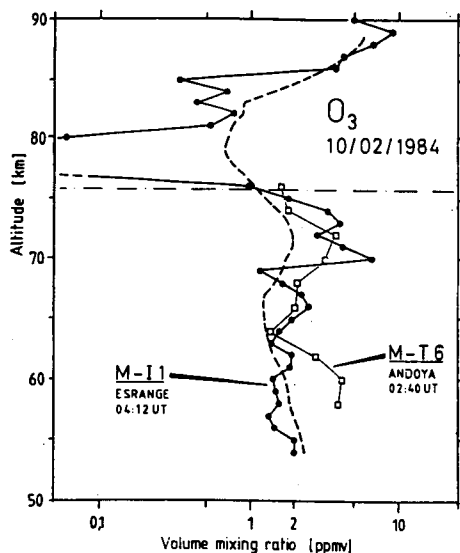


Figure 6. Ozone mixing ratios as measured by infrared rocket experiments (at night). Dashed line is a very approximate mean curve including several other measurements. With respect to this curve, ozone is found to be depleted above 76 km, and enhanced below this level. The level coincides with one of the nodes of the 13.3 d oscillation (Figure 5). Only a small fraction of the ozone deviations can be explained by photochemistry. (For details see Grossmann et al., *J. Atmos. Terr. Phys.*, **49**, 827, 1987.)

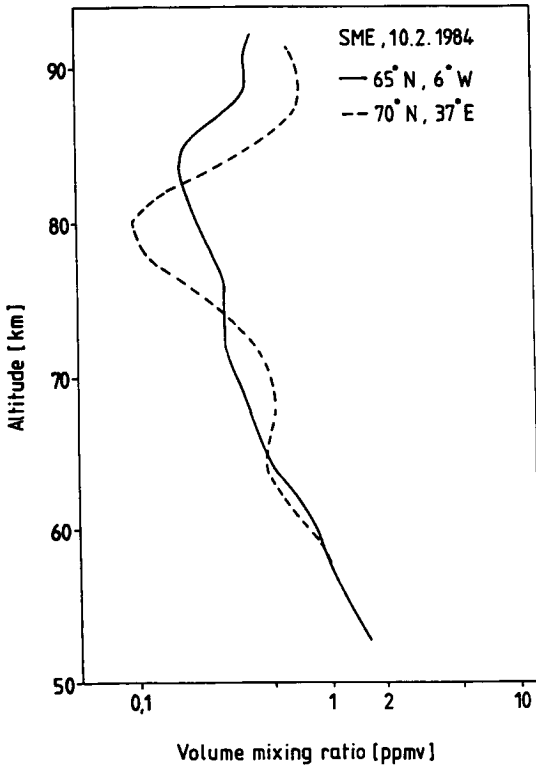


Figure 7. Ozone mixing ratios as measured by the SME satellite at two different longitudes. Measurements are during daytime. Dashed curve is at 378 east and resembles qualitatively the solid curve in Figure 6. Hence the wave structure extended to this longitude at least. The profile at 68 west resembles an undisturbed profile, i.e., a wave with zero phase. If it is assumed that the dashed curve approximately shows the maximum of the wave disturbance, and the solid curve shows zero disturbance, a longitudinal wavelength of 428 results. Hence the disturbance seen is compatible with a planetary wave 2. A similar result was obtained before by Hauchecorne et al. [1987] (see Figure 8).

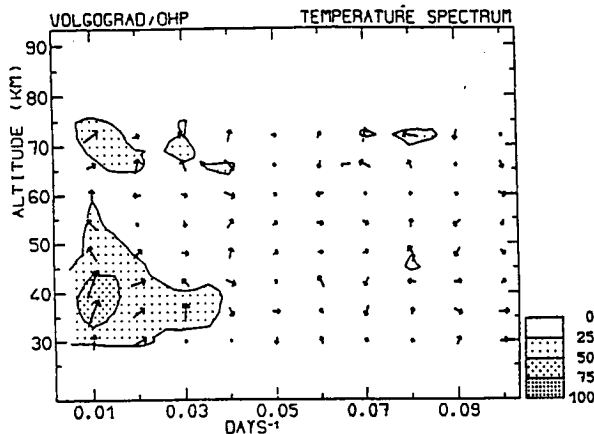


Figure 8. Fourier analysis of temperature measured by lidar and rockets at the Observatoire de Haute Provence (OHP) and at Volgograd, respectively (Hauchecorne et al., *J. Atmos. Terr. Phys.*, 49, 649, 1987). Direction of the arrows gives the phase difference between the two stations. An arrow directed toward right indicates that the maximum occurs sooner at OHP than at Volgograd. The wave at 12.5 days period (45 km, 70 km) shows westward propagation and is interpreted as a planetary wave 2 (second symmetric mode).

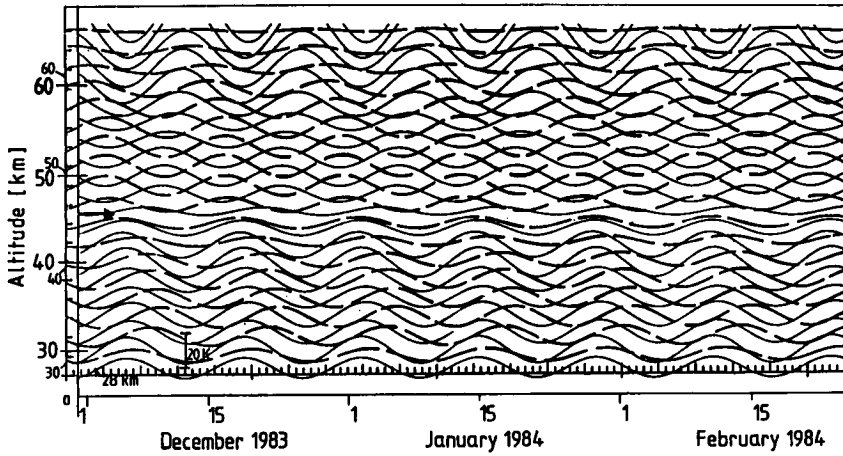


Figure 9. Comparison of an oscillation with 13.3 days period at Andoya (solid lines) and OHP (dashed lines). The lidar data of OHP were analyzed by the same technique as sketched for Andoya above (Figures 3 - 5). An oscillation period of 12.5 days was obtained which is exactly the same as the one of the Fourier analysis of Hauchecorne et al. [1987]. When a period of 13.3 days is prescribed to the OHP data (this picture), an anticorrelation between Andoya and OHP is obtained above the node at 46 km, and a phase shift greater than 90° in most part below it.

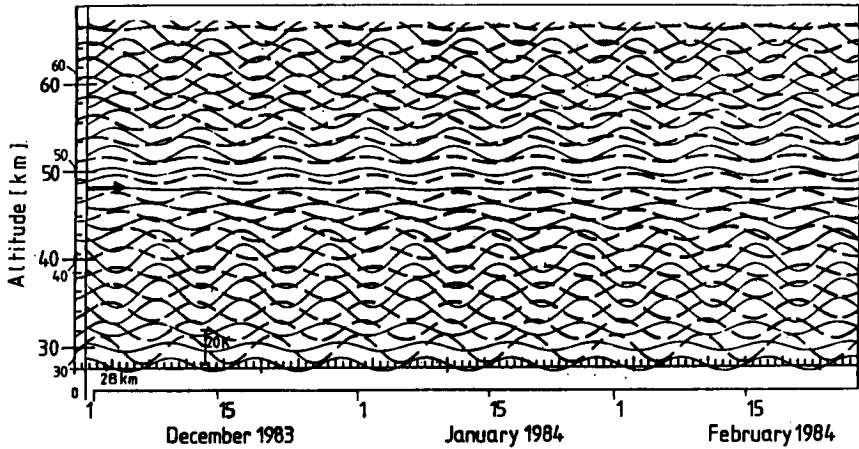


Figure 10. Comparison of an oscillation with 9.6 days period at Andoya (solid lines) and OHP (dashed lines). the 9.6 day value is prescribed to the OHP data. An anticorrelation between the two stations is obtained in most part of the altitude regime, except around the node at 48 km (arrow) and the very lowest altitudes. Please note that a phase reversal occurs at the node (Andoya) similar to and even larger than the one shown in Figure 5 at 46 km.

Wave Summary

Periods observed:	12.5 d - 13.3 d	9.6 d
Vertical structure:		
$\lambda_z/2$:	≈ 30 km	≈ 30 km
Nodes at:	46 km, 76 km	48 km, 76 km
Zonal structure:		
λ_x	180° (wave 2)	?
Meridional structure:		
Nodes at	$50^\circ - 60^\circ$ (?)	$50^\circ - 60^\circ$ (?)

Figure 11. Results obtained from rocket data at Andoya and lidar data at OHP for the two shortest oscillation periods. Meridional structure results are preliminary. Respective analysis is still in progress.

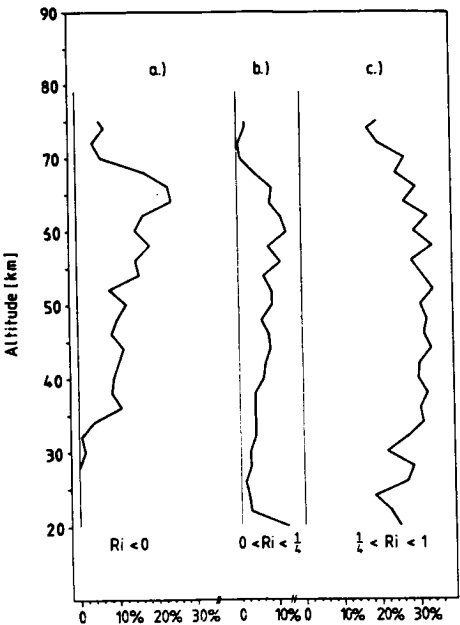


Figure 12. Occurrence frequency of Richardson numbers R_i at Andoya as determined from more than 60 rocket flights during three months. Atmospheric instability sets in as low as 35 km. Above this altitude the atmosphere is unstable ($R_i < 1$) for more than 50% of the time.

7.4 THE SOVIET CONTRIBUTIONS TOWARDS MAP/WINE

Z. Ta. Rapoport

Institute of Terrestrial Magnetism
 Ionosphere and Radio Wave Propagation of the USSR Academy of Sciences
 IZMIRAN, Troitsk, Moscow Region, 142092, USSR

E. S. Kazimirovsky

Siberian Institute of Terrestrial Magnetism, Ionosphere and Radio wave Propagation
 SibIZMIR, Troitsk, USSR

In the winter of 1983/1984, the research institutes of the Soviet Union took an active part in the accomplishment of the project "Winter in Northern Europe" (MAP/WINE) of the Middle Atmosphere Program. Different methods were used to measure temperature, direction and velocity of wind, turbulence, electron concentration in the lower ionosphere, and radio-wave absorption. The study of the stratospheric warmings and the related changes in the mesosphere and lower ionosphere was considered of special importance. The analysis of the obtained data has shown, in particular, that during the stratospheric warmings the western wind in winter time becomes weaker and even reverses. At the same time period the electron concentration and the radio-wave absorption in the lower ionosphere are often reduced. It is also observed that the high absorption zones move from west to east. These results confirm the concept about the role of the cyclonic circumpolar vortex in the transport of the auroral air to temperate latitudes and about the appearance of conditions for the winter anomalous radio-wave absorption.

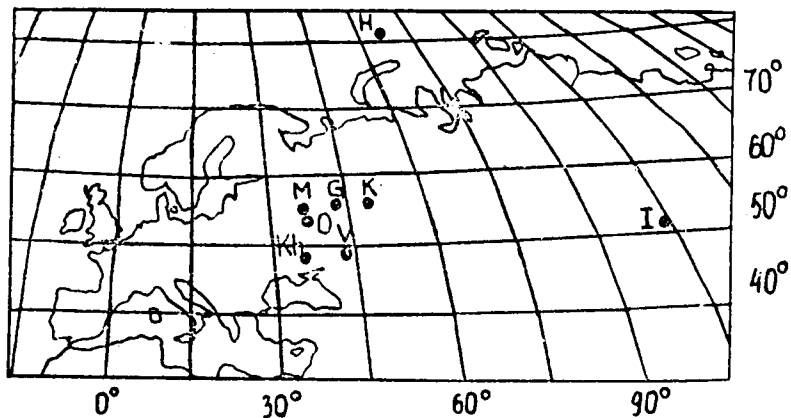


Figure 1. The location of observation sites according to MAP/WINE project. Rocket ranges of Heiss Island and Volgograd are shown, as well as location of Gorky (partial-reflection-method), Obninsk, Krarkov, Kazan and Irkutsk (ionospheric drift measurements by D2 and D1 methods).

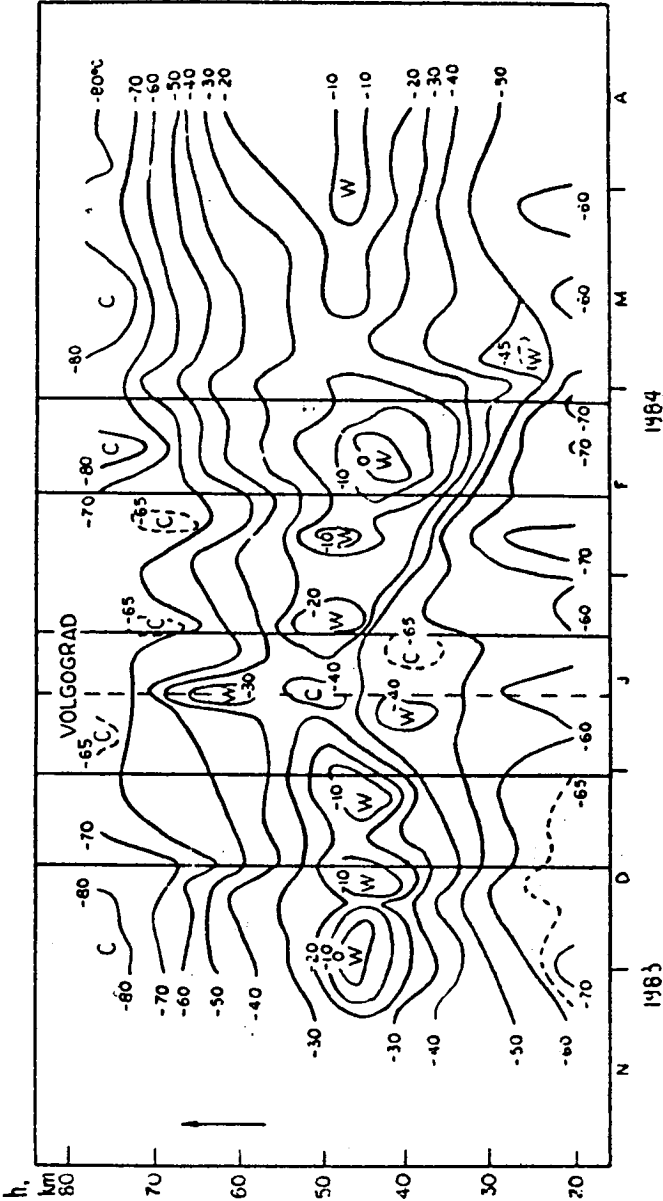


Figure 2. Height-temporal distribution of temperature above Volgograd in winter 1983-1984.

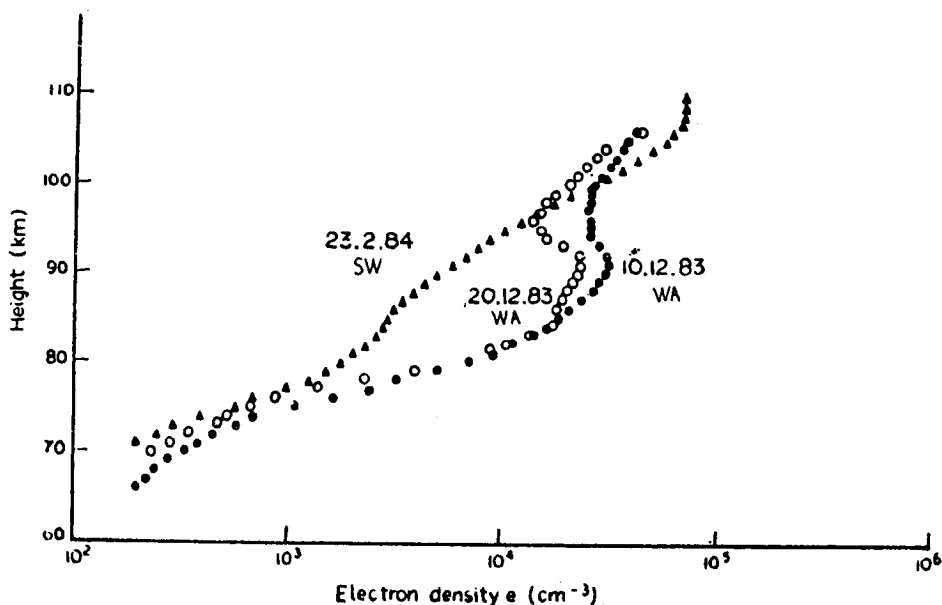


Figure 3. Electron density profiles obtained in Volgograd by the electrostatic probe and by the coherent frequencies technique (above 80 km) at the sun's zenith angle $\chi \approx 78^\circ$ on 10 and 20 December 1983 and 23 February 1984. On 23 February a stratospheric warming and the western wind reverse took place ($L_{2,2} = 33$ dB), on 10 and 20 December the dynamical state was characterized by a stable western wind ($L_{2,2} = 43$ and 50 dB correspondingly).

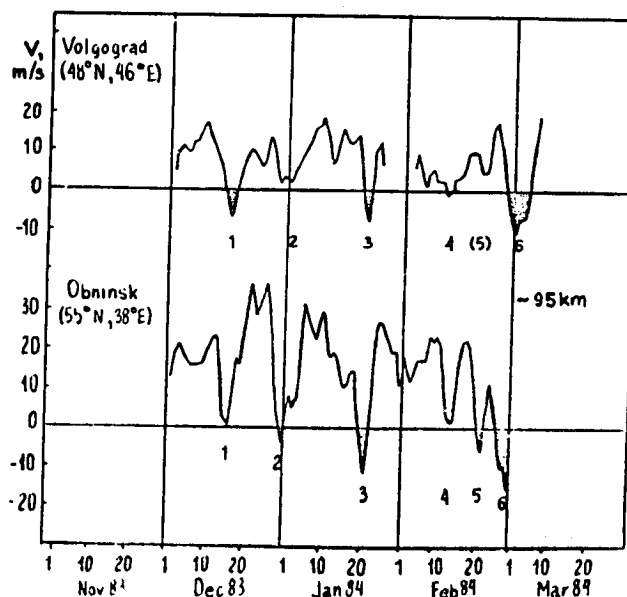


Figure 4. The wind zonal component according to measurements in Volgograd and Obninsk at the height of about 95 km (3 running means 1-2-1 weighting).

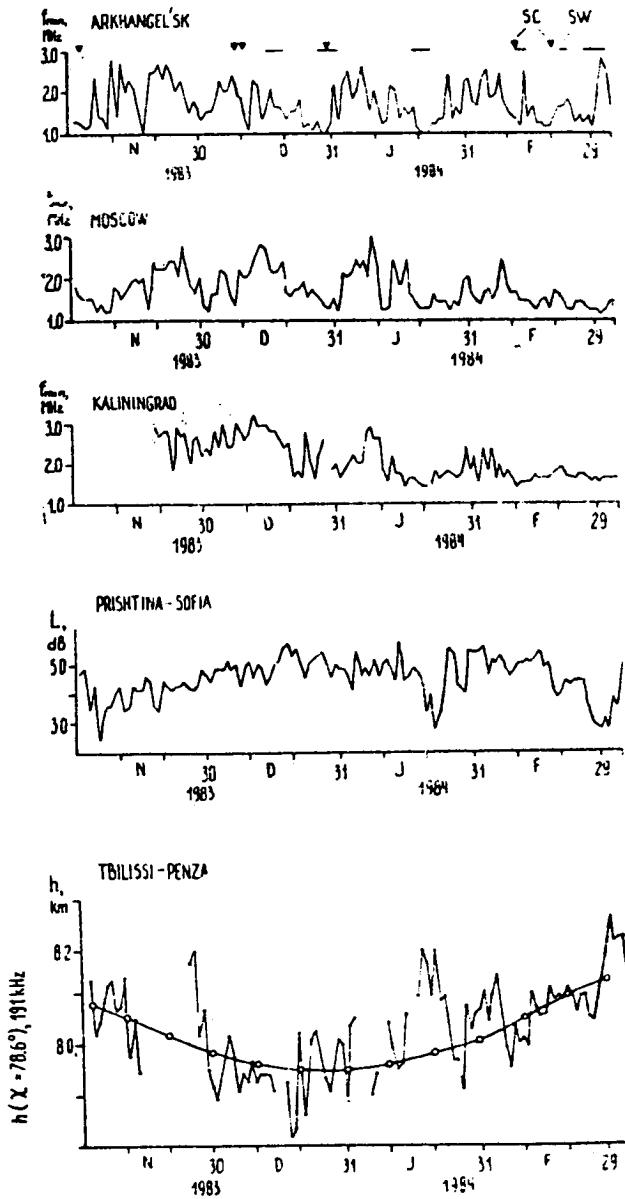


Figure 5. Triangles depict sudden commencements of geomagnetic storms (SC). The horizontal bars point out the periods of stratospheric warmings. Below values of $f_{min} (\cos \chi \approx 0.2)$ (averaged of fore and afternoon values) as indications of absorption for Arkhangelsk, Moscow, and Kaliningrad, the absorption data, obtained at Prishtina-Sofia circuit (A3 method, $f = 1412$ kHz, $d = 170$ km) and the phase height data obtained at Tbilissi-Penza circuit ($f \approx 191$ kHz, $d \approx 1278$ km) are shown.

C-4

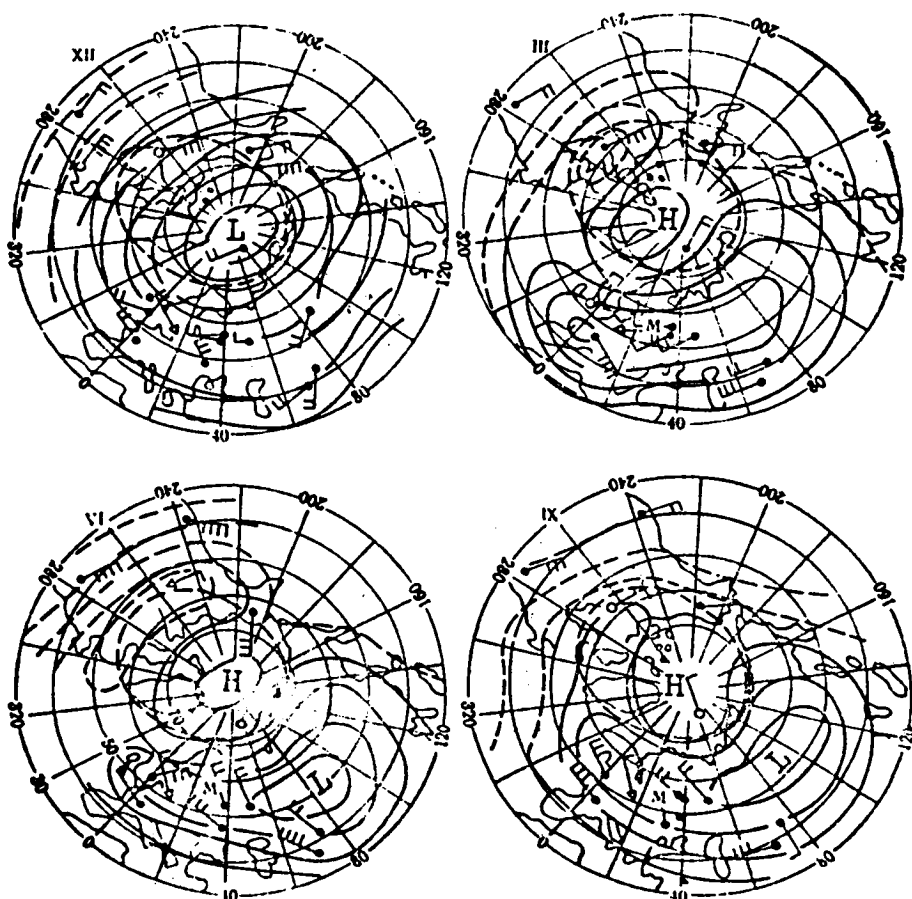


Figure 6. Scheming maps of atmospheric circulation in the Northern Hemisphere obtained by means of different techniques with the involvement of the data of many years for the height of ≈ 95 km for four months (December, March, June, September). An oval at $\Phi_c = 67^\circ$ is depicted on the map showing the location of the auroral zone. Letter M and the point show the location of Moscow, points and flags show the location of observation sites, wind direction and velocity.

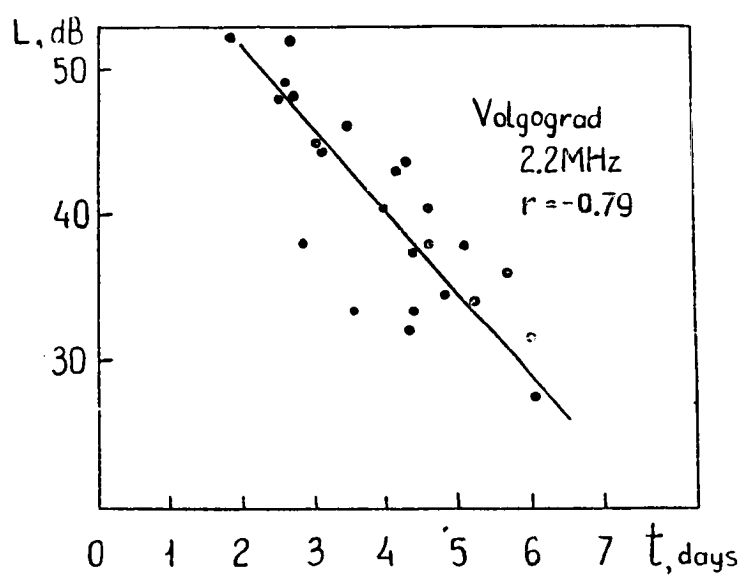


Figure 7. Relationship between absorption L , at 2.2 MHz in Volgograd and the time, t , of the air transport from the auroral zone to the observation site during MAP/WINE campaign. The correlation coefficient between L and t , $r = -0.79$.

7.5 MEAN, TIDAL, AND FLUCTUATING WINDS IN THE MIDDLE ATMOSPHERE AND LOWER THERMOSPHERE OBSERVED DURING MAP/WINE IN NORTHERN SCANDINAVIA

J. Röttger

EISCAT Scientific Association
P. O. Box 812
S-981 28 Kiruna, Sweden

During the MAP/WINE campaign in winter 1983/84 several instrumental techniques, such as meteorological rockets, sounding rockets, MST radar and incoherent scatter radar, were applied to measure wind velocities in the middle atmosphere. Profiles of mean, tidal and fluctuating wind velocities were obtained up to 90 - 100 km altitude. These are compared with profiles from models, measurements at other locations and at other times as well as satellite-derived data. The results are discussed in terms of ageostrophic winds, planetary waves, tidal modes and the possibility of a saturated gravity wave spectrum in the mesosphere.

Observations of mean, tidal and fluctuating winds in the lower thermosphere and middle atmosphere during MAP/WINE

deduced from measurements with

Rockets:
data sondes
chaff clouds
falling spheres

MST Radar

Incoherent Scatter Radar

Publications

- W. Meyer: Untersuchungen groß und kleinskaliger dynamischer Prozesse in der Mesosphäre anhand von Wind- und Dichtemessungen über Nordskandinavien im Rahmen des MAP/WINE Projekts, Bonn University, 1988.
- W. Meyer, C. R. Philbrick, J. Röttger, R. Rüster, H.-U. Widdel, and F. J. Schmidlin, Mean winds in the winter middle atmosphere above northern Scandinavia, *J. Atmos. Terr. Phys.*, 49, 675, 1987.
- J. Röttger, and W. Meyer, Tidal wind observations with incoherent scatter radar and meteorological rockets during MAP/WINE, *J. Atmos. Terr. Phys.*, 49, 689, 1987.
- H. Hass, and W. Meyer, Gravity wave fields above Andöya, *J. Atmos. Terr. Phys.*, 49, 705, 1987.
- H.-U. Widdel, Vertical movements in the middle atmosphere derived from foil cloud experiments, *J. Atmos. Terr. Phys.*, 49, 723, 1987.
- R. Rüster, and J. Klostermeyer, Propagation of turbulence structures detected by VHF radar, *J. Atmos. Terr. Phys.*, 49, 743, 1987.
- E. V. Thrane, T. A. Blix, C. Hall, T. L. Hansen, U. von Zahn, W. Meyer, P. Czechowsky, G. Schmidt, H. -U. Widdel, and A. Neumann, Small scale structure and turbulence in the mesosphere and lower thermosphere at high latitudes in winter, *J. Atmos. Terr. Phys.*, 49, 751, 1987.

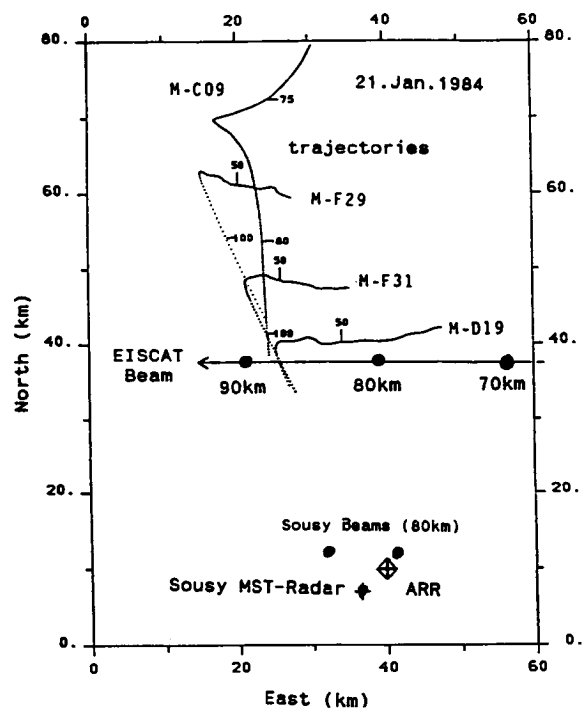


Figure 1. MAP/WINE radar and rocket geometry [after Meyer, 1988].

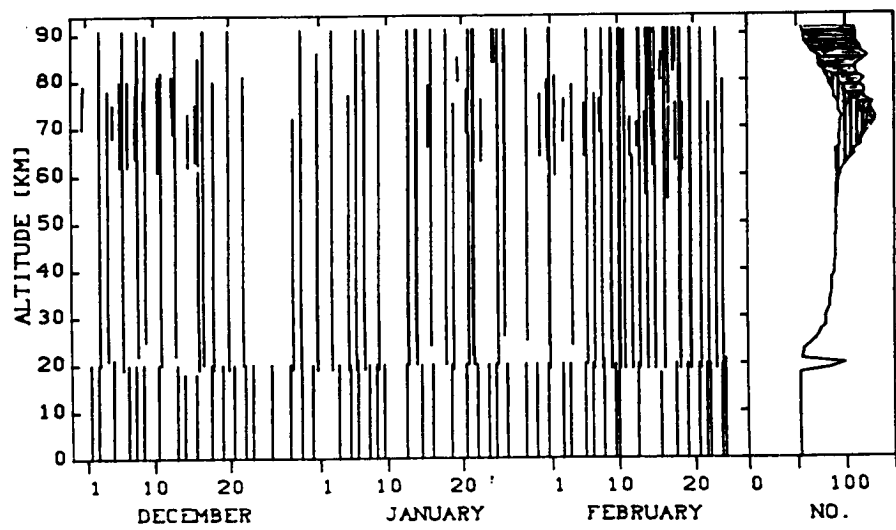


Figure 2. Distribution in time of wind profiles obtained during the period of rocket launched at Andöya (69°N, 16°E). Total number of measurements used for mean wind reduction (right panel): rocket measurements (blank), MST radar (vertically dashed), EISCAT (horizontally dashed). W. Meyer et al.

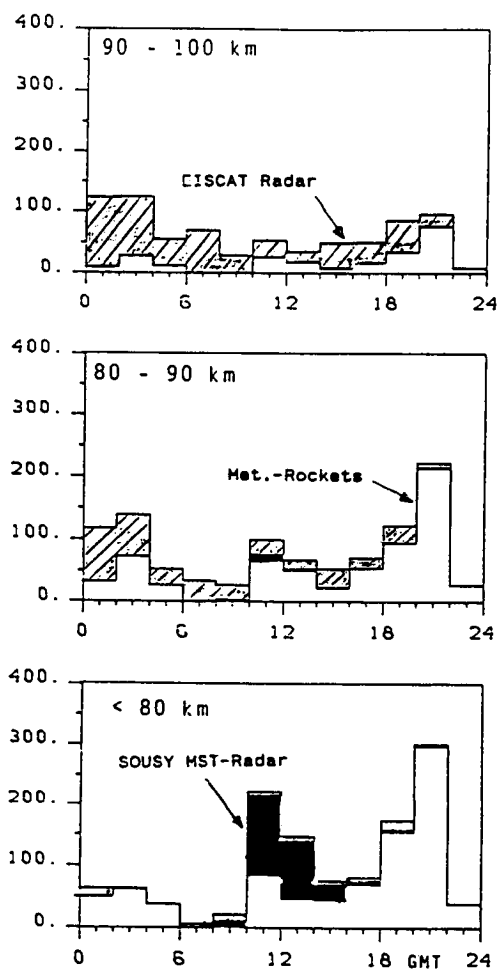


Figure 3. Daily distribution of wind measurements. Meyer [1988].

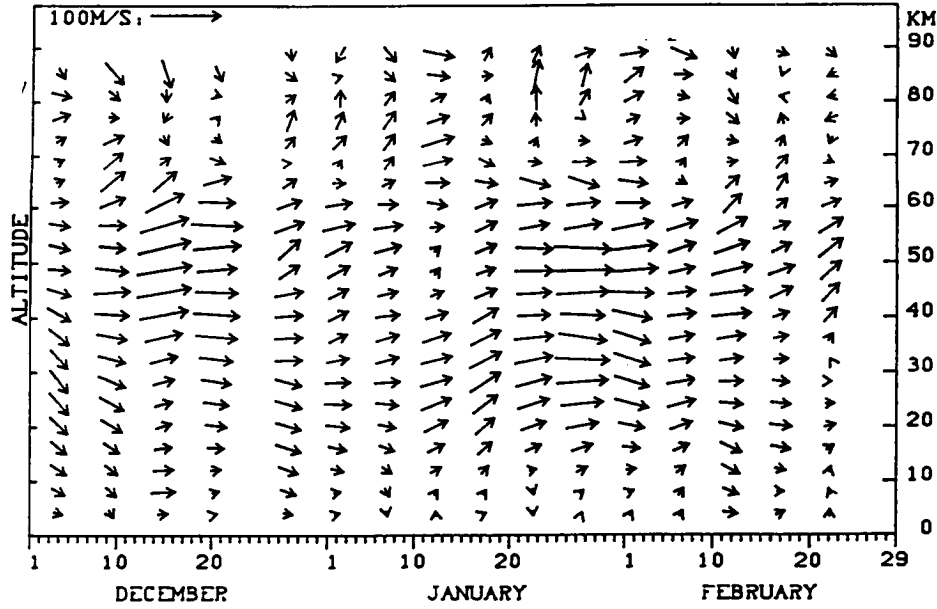
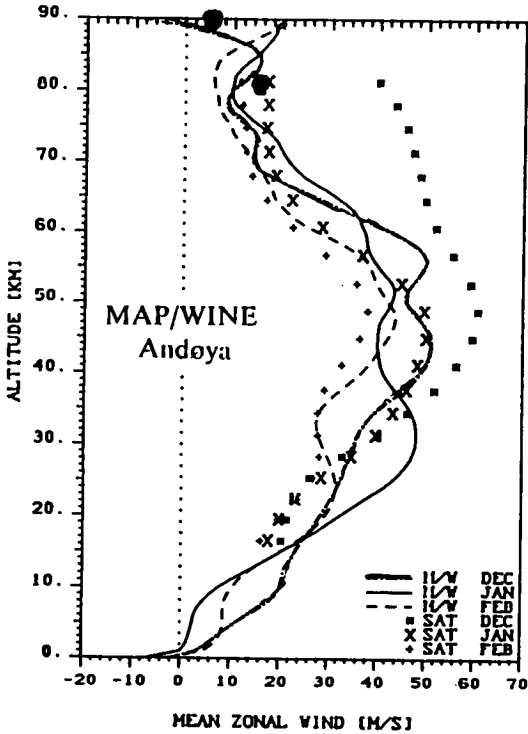


Figure 4. The estimated prevailing wind field above Andöya. Arrows indicate magnitude and direction of the horizontal flow (from the south: upward, from the west: to the right). W. Meyer et al.

W. MEYER *et al.*



D. B. DALSLEY AND A. C. RIDDLE

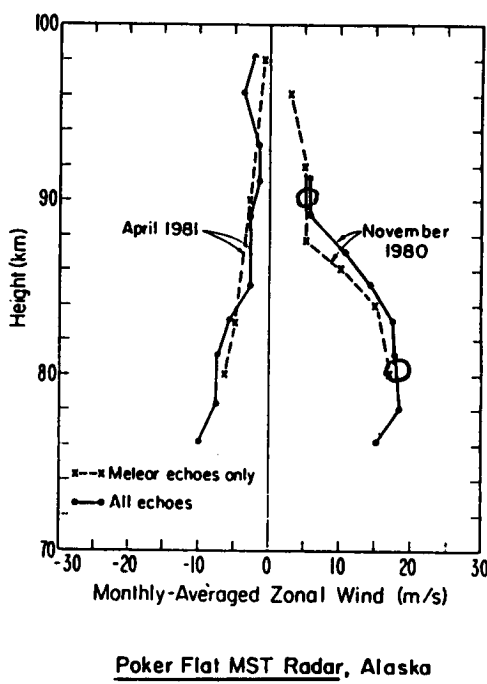


Figure 5. Mean wind profiles during MAP/WINE and at Poker Flat. Meteorological rockets, sounding rockets and radar systems satellite derived winds.

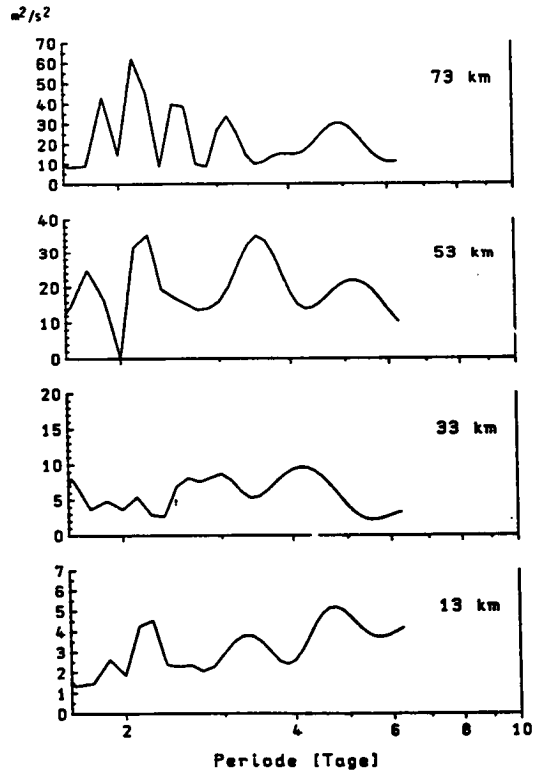


Figure 6. Spectrum of meridional wind component. Meyer [1988].

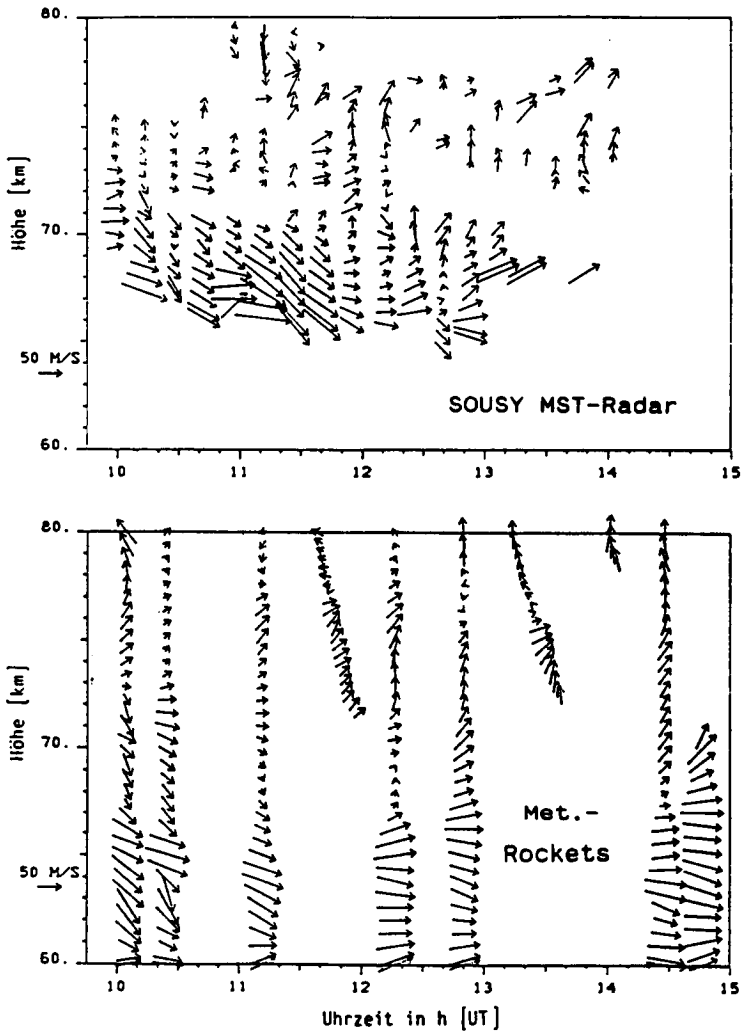


Figure 7. Horizontal wind vectors on 21 January 1984. Horizontale Windvektoren (Südwind: nach oben, Westwind: nach rechts) am 21 Januar gemessen mit dem SOUSY-MST radar (oben) und meteorologischen Raketen (unten). Meyer [1988].

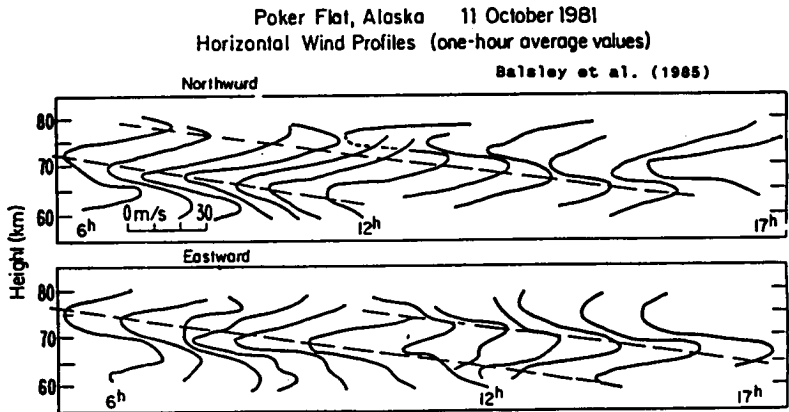
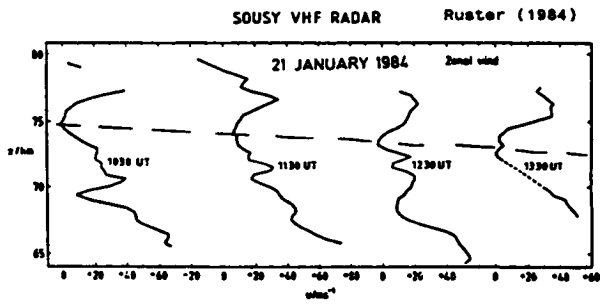
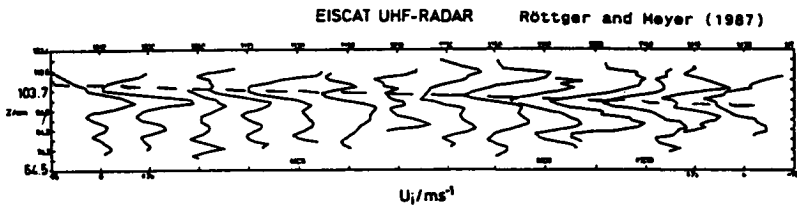


Figure 8. Horizontal wind vectors on 21 January 1984. Meyer [1988].

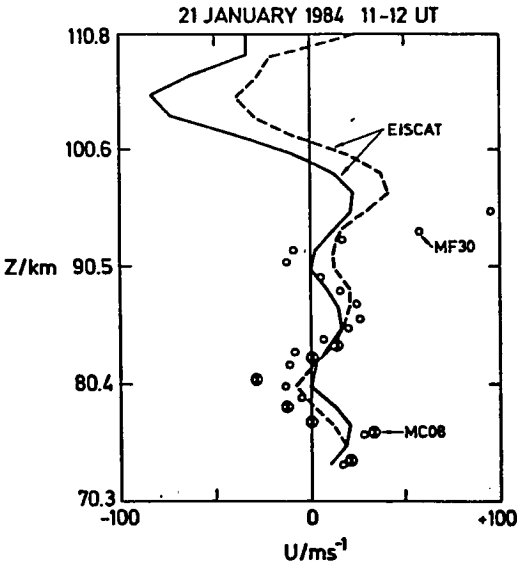


Figure 9. Zonal velocity profiles measured with EISCAT using the matched filter velocity estimates (solid curve 1111 - 1120 UT, dashed curve 1131 - 1140 UT) and falling sphere MF30 (1107 UT) and chaff MC08 (1131 UT) during metrocket salvo 1 on 21 January 1984. Röttger and Meyer [1987].

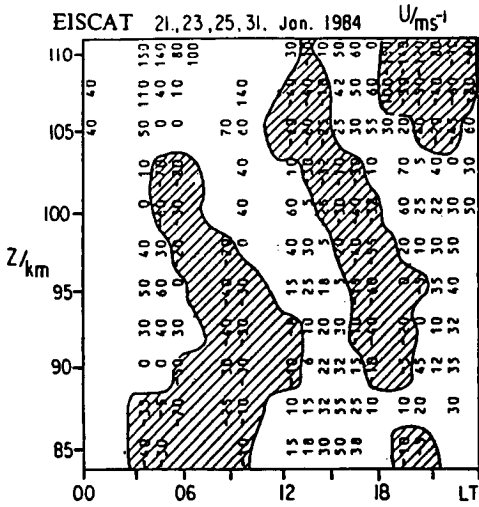


Figure 10. From J. Röttger and W. Meyer.

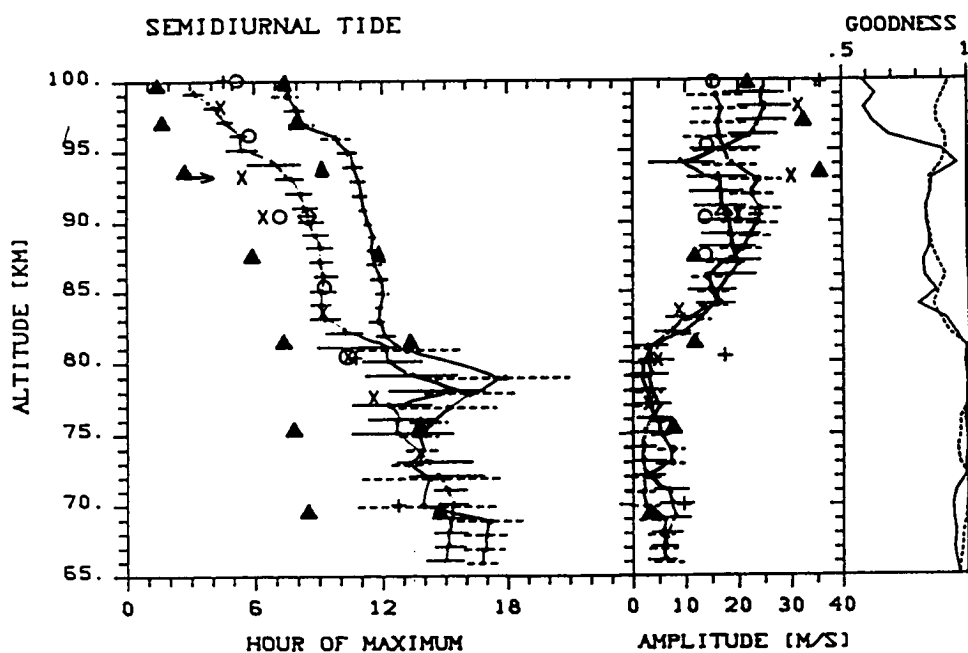


Figure 11. Profiles of amplitude and phase (hour of maximum velocity) of zonal (dashed bars) and meridional (continuous bars) semidiurnal velocity components deduced from all incoherent scatter radar, meteorological rocket and MST radar data. The special characters indicate the maximum of the meridional tidal component (if only zonal components were available, they were shifted by 3 h) obtained from: \blacktriangle Forbes model at 70°N during December solstice [Forbes and Gillette, 1982]; \times winter average of Garchy (48°N) [Fellous et al., 1975]; $+$ average over two winters in Saskatoon [Manson et al., 1983]; \blacklozenge vector average over four winters in Saskatoon [Manson et al., 1983]; \circ 5-day global average deduced from ATMAP high latitude data ($> 43^\circ$) of December 1983 [Forbes, 1985]. J. Röttger and W. Meyer.

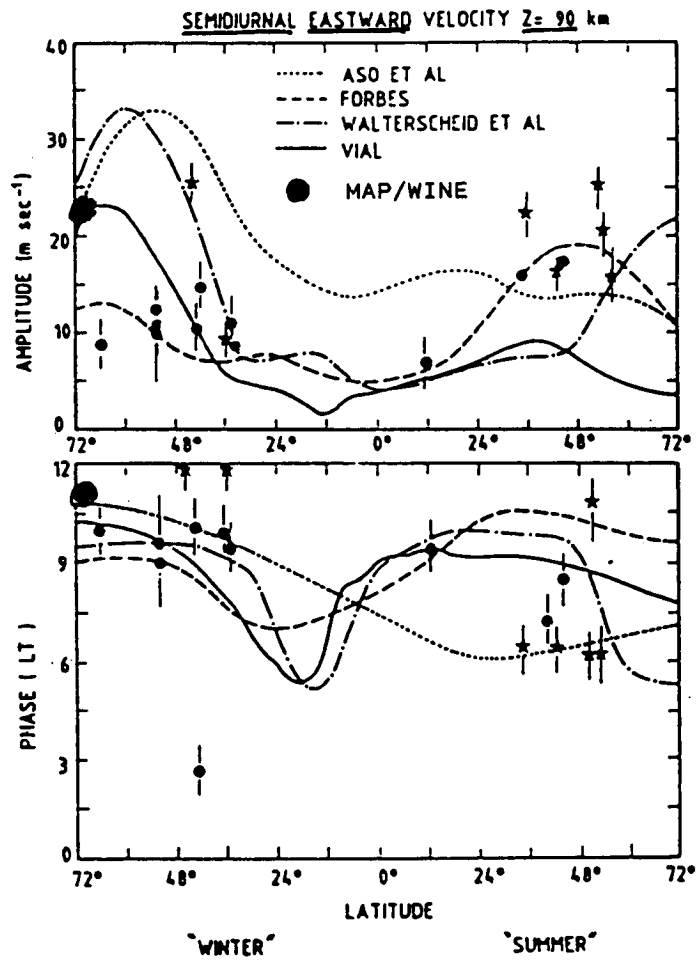


Figure 12. From Forbes [1985].

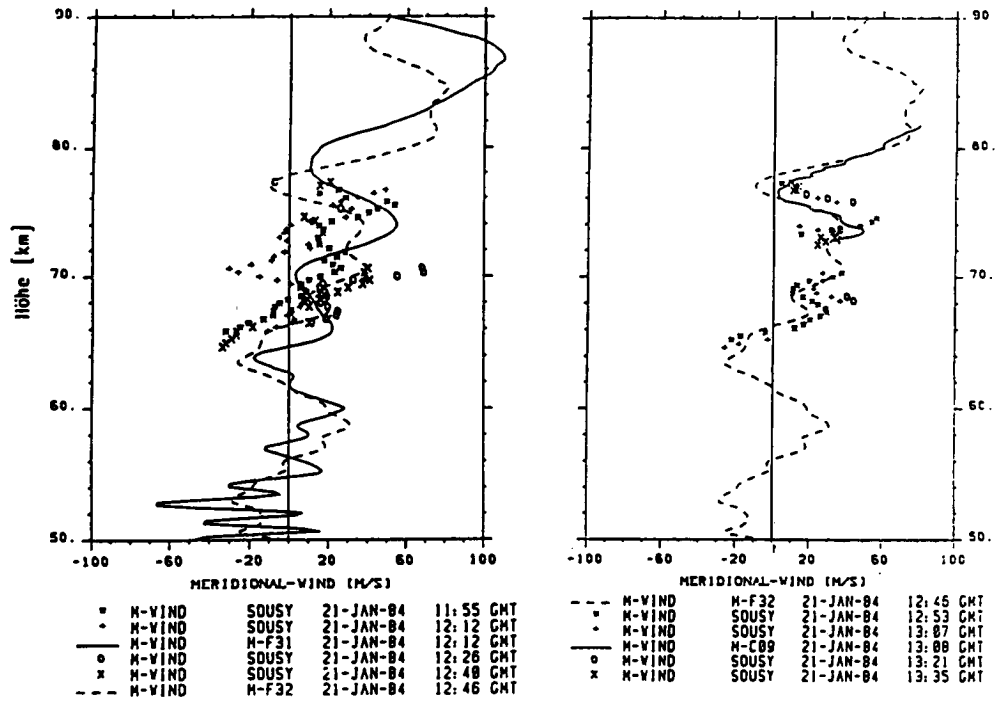


Figure 13. Meridional wind measured with MST radar and rockets. Meyer [1988].

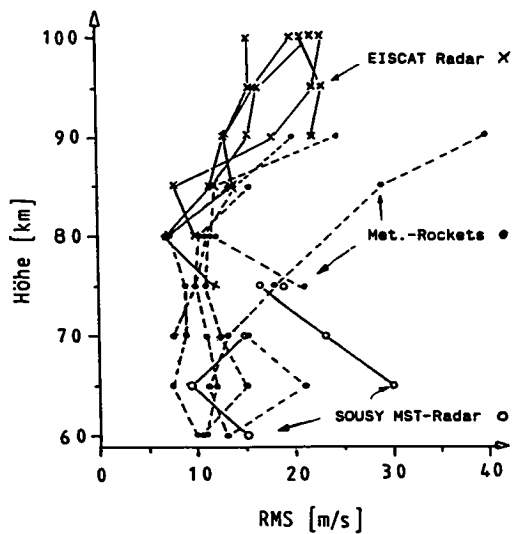


Figure 14. Horizontal wind variations (6 h-rms) Meyer [1988].

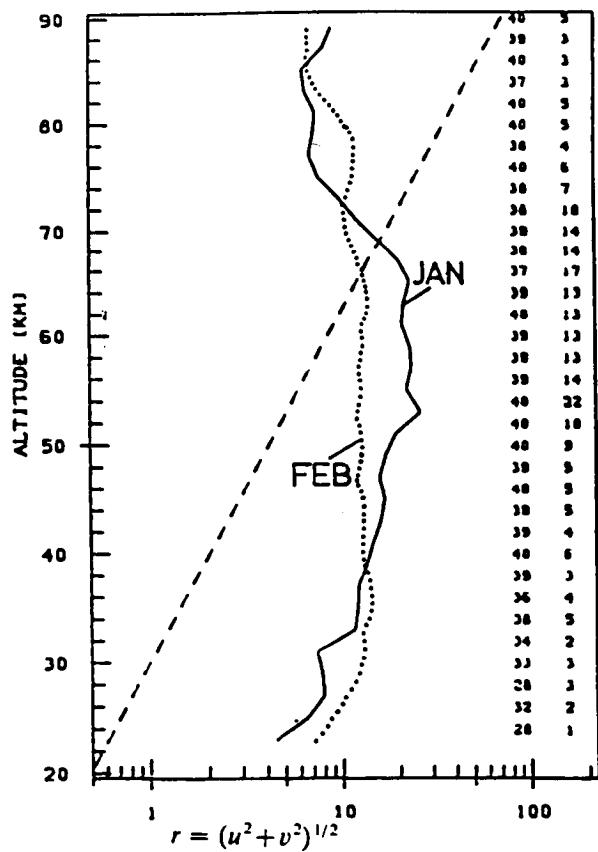
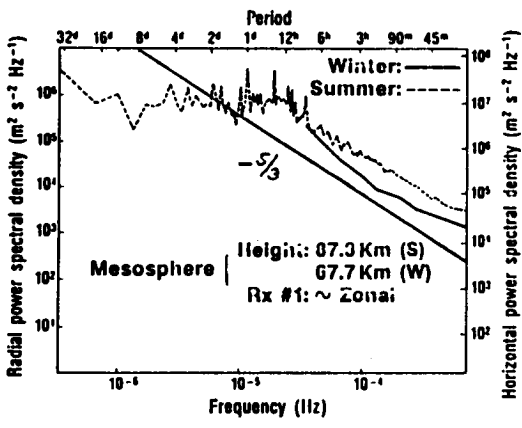


Figure 15. Height profiles of mean horizontal wind fluctuations. H. Hass and W. Meyer.

Poker Flat, Alaska
Horizontal Power Spectral Densities

Balsley and Garello



MOBILE SOUSY RADAR

P. Czechowsky and R. Ruster

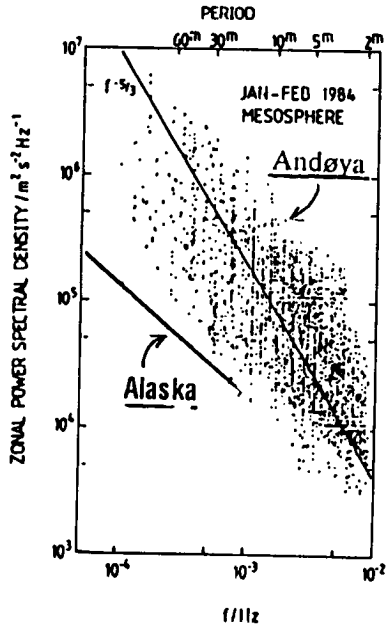


Figure 16.

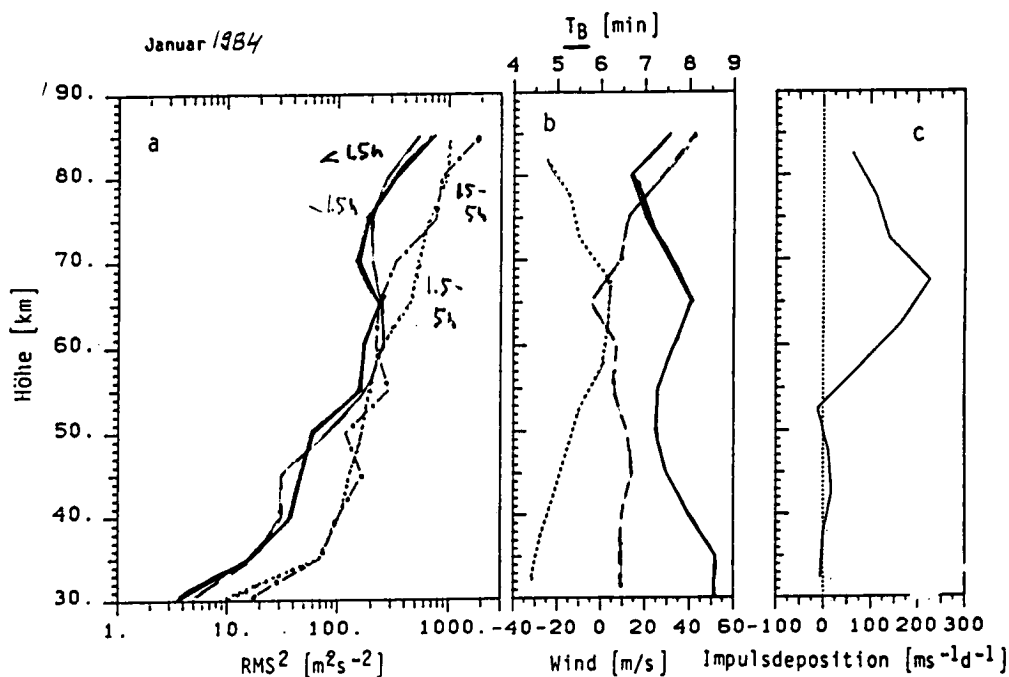


Figure 17. Velocity variability, mean wind and horizontal acceleration. (a) (links): Kurzzeitvariabilität der zonalen (durchgezogen) und meridionalen (strichliert) Windkomponente für Zeitdifferenzen < 1,5 h und 1,5 - 5 h (zonal: strich-punktiert, meridional: punktiert) unter Verwendung von Messungen mit meteorologischen Raketen. (b) (mitte): mittlerer zonaler (durchgezogen) und meridionaler (strichliert) Wind und Brunt-Väisälä-Periode (punktiert). (c) (rechts): Abschätzung der Impulsdeposition aus (a). Meyer [1988].

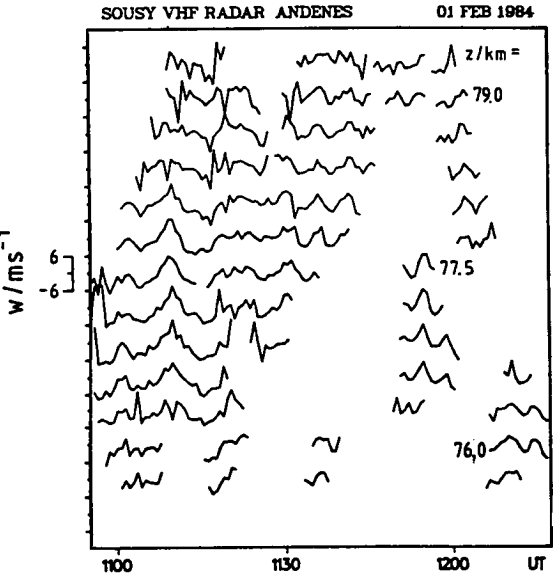


Figure 18. Time variation of vertical velocity w at heights between 76 and 79 km. R. Rüster and J. Klostermeyer.

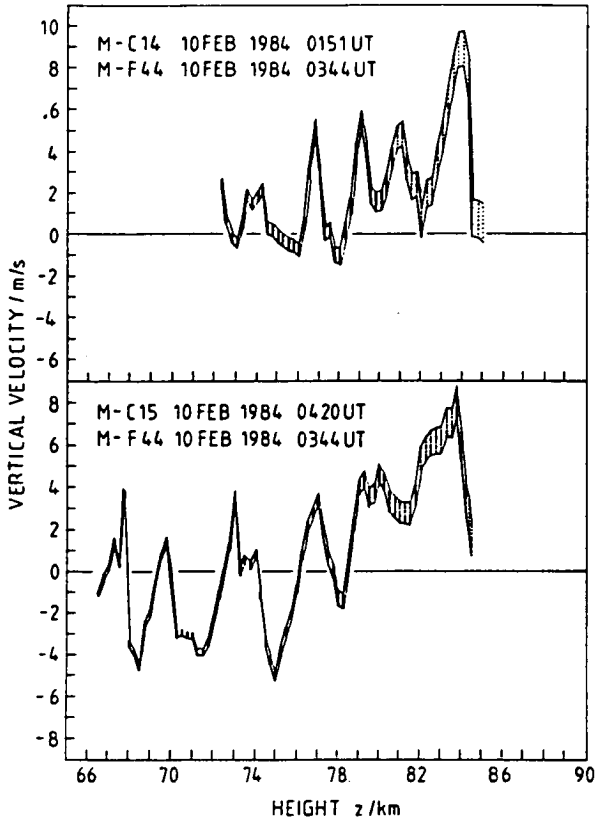
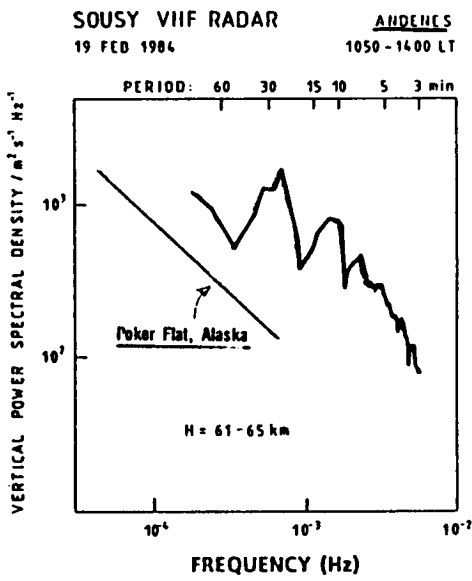
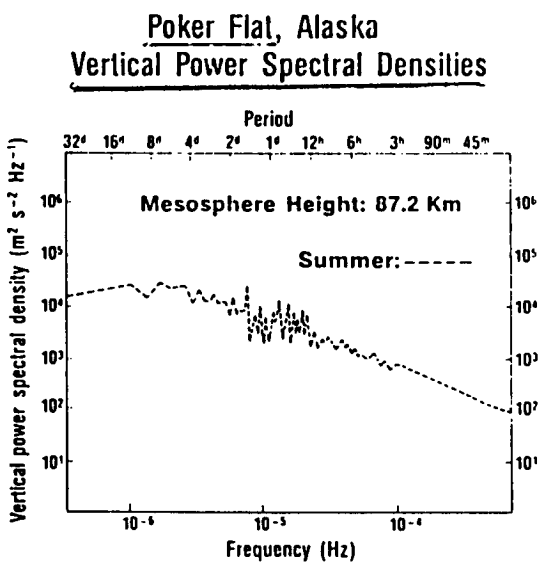


Figure 19. Vertical velocities determined by foil clouds during the fourth salvo (10 February 1984). On both occasions the chaff cloud was intercepted by a wave with upgoing phase which drifted with the wind. H.-U. Widdel.



E. V. THRANE *et al.*



Balsley and Garello

Figure 20.

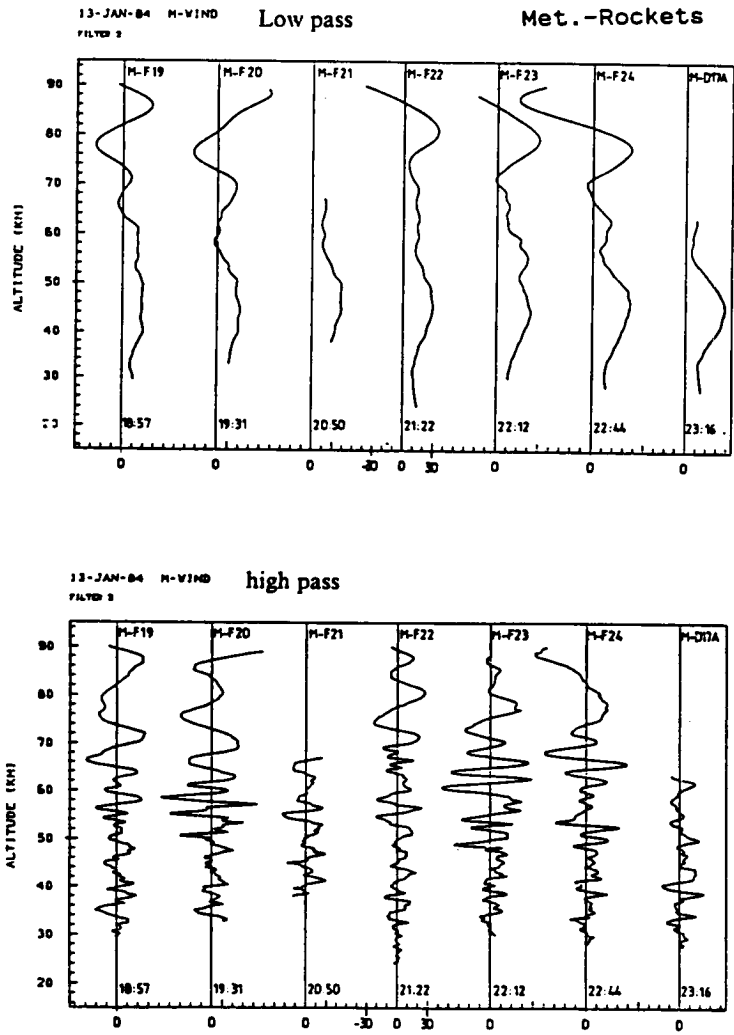


Figure 21. Meridional wind profiles. H. Hass and W. Meyer.

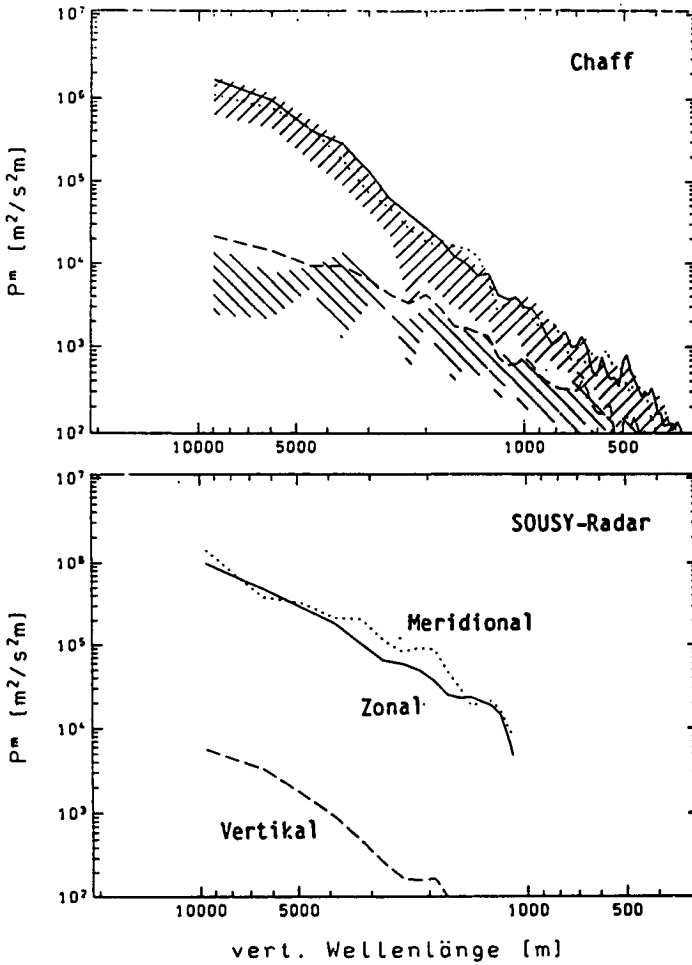


Figure 22. Vertical wave number spectrum. Meyer [1988].

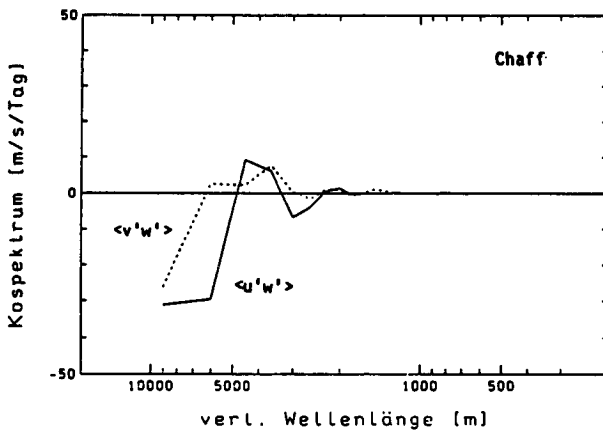


Figure 23. Covariances as function of vertical wave number. Meyer [1988].

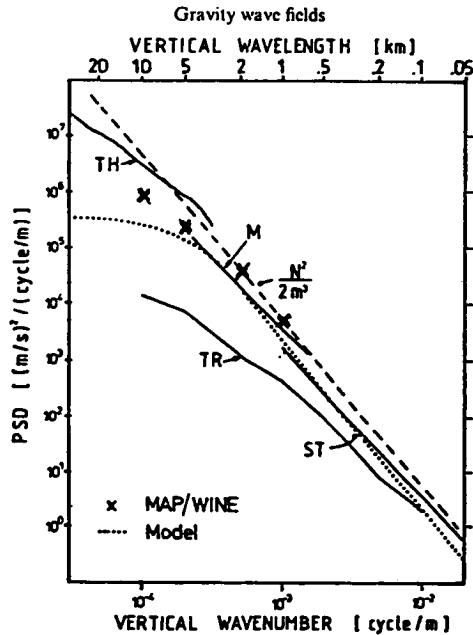


Figure 24. Comparison of observed spectral densities with model spectra [adopted from Smith et al., 1986]. TH = thermospheric spectrum; M = mesospheric spectrum [both Smith et al., 1986]; ST = stratospheric spectrum [Dewan et al., 1984]; TR = tropospheric spectrum [Endlich et al., 1969]; crosses are average of M-F and M-D spectra. Model spectra: dashed line according to equation (i) with $N = 0.02 \text{ rad s}^{-1}$ and dotted line with equation (9) and $m_*^{-1} = 5 \text{ km}$. H. Hass and W. Meyer.

Summary of Middle Atmosphere Dynamics (excl. turbulence) over Northern Scandinavia during Winter 1983/1984 (MAP/WINE)

*Prevailing Winds:

Zonal component is geostrophic, meridional component is ageostrophic in mesosphere.

*Indications of Planetary Waves ($T \sim 2d?$).

*Semidiurnal tide is dominant above mesopause.

*Short-period gravity waves ($T < 6h$) appear to saturate above the lower mesosphere; northern Europe (MAP/WINE) more "active" than Alaska?

*Indication of momentum deposition by short-period gravity waves.

**7.6 LARGE-SCALE DYNAMICS OF THE STRATOSPHERE AND MESOSPHERE
DURING THE MAP/WINE CAMPAIGN WINTER 1983/84
IN COMPARISON WITH OTHER WINTERS**

K. Petzoldt

**Institut für Meteorologie, Freie Universität Berlin
Federal Republic of Germany**

For the MAP/WINE winter temperature and wind measurements of rockets were combined with SSU radiances (Stratospheric Sounder Unit onboard the NOAA satellites) and stratopause heights from the Solar Mesosphere Explorer (SME) to get a retrieved data set including all available information. By means of this data set a hemispheric geopotential height, temperature and geostrophic wind fields eddy transports for wave mean flow interaction and potential vorticity for the interpretation of nonlinear wave breaking could be computed. Wave reflection at critical lines was investigated with respect to stratospheric warmings. The meridional gradient of the potential vorticity and focusing of wave activity is compared with derived data from satellite observations during other winters.

Dynamical Features Shown by the MAP/WINE Data Set Important for Future Studies

- Are the often observed strong minor warmings in the mesosphere the start of sinking motion for photochemically relevant species?
- Is the folded stratopause observed during minor warmings in the stratosphere a mixing layer for potential vorticity and tracers?
- Is the destruction of the mesospheric jet a necessary condition for a major warming in the middle stratosphere, when the downward transported polar minor species will be mixed horizontally into lower latitudes?

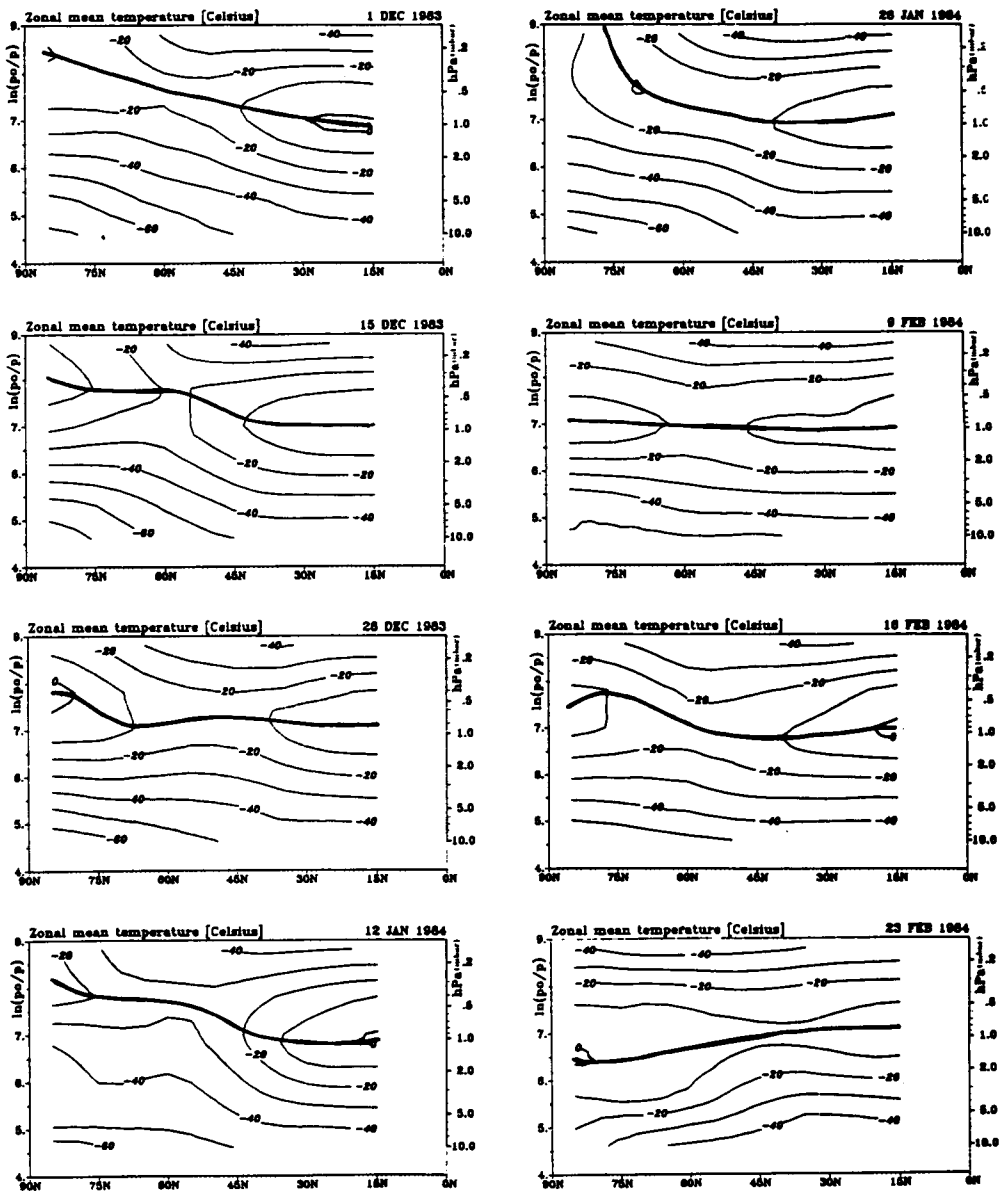


Figure 1.

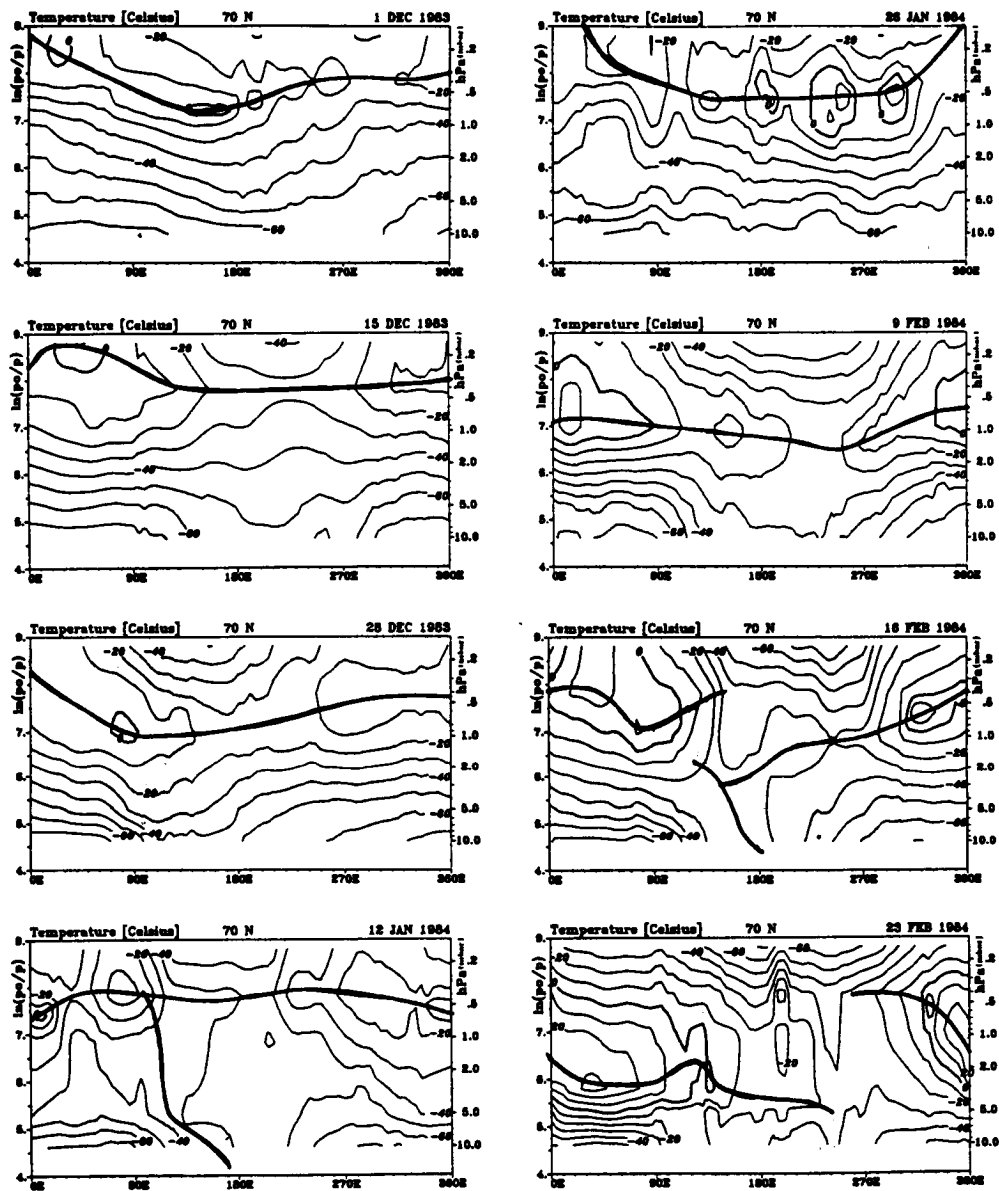


Figure 2.

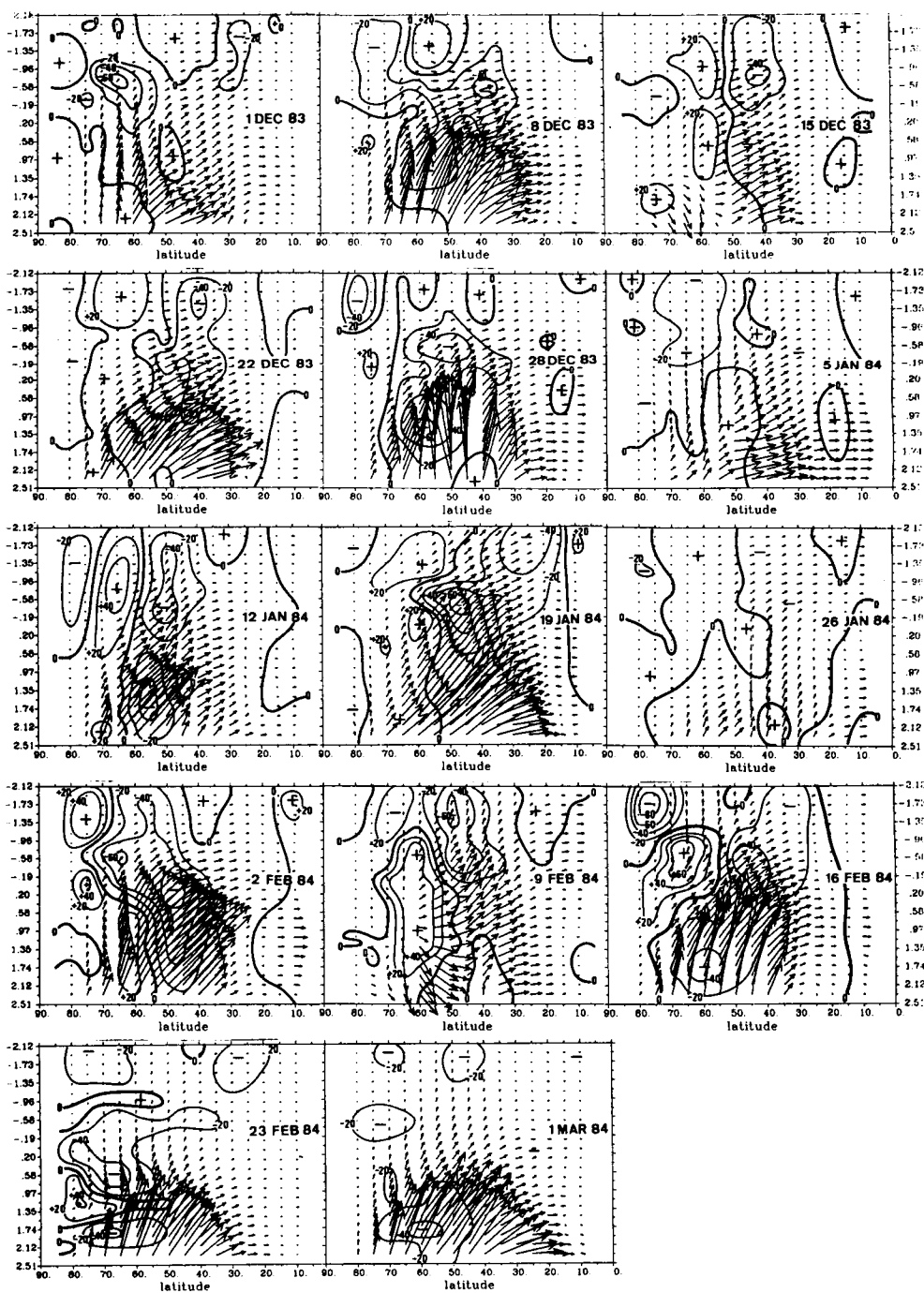


Figure 3. Eliassen-Palm-vector and its divergence ($\text{ms}^{-1}/\text{day}$).

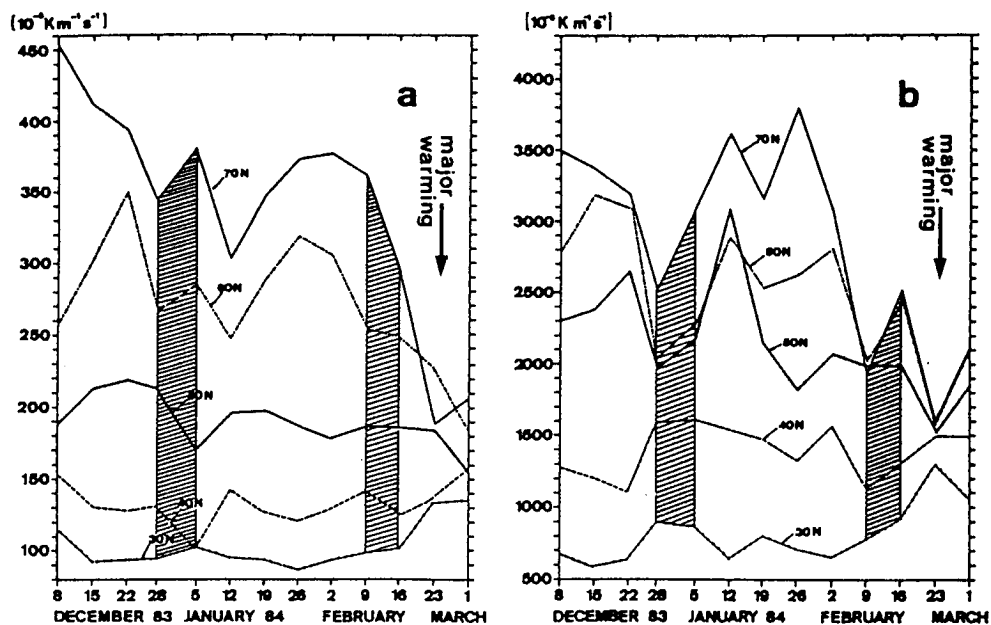


Figure 4. Zonal mean of Ertel's potential vorticity for winter 1983/84 from 30°N to 70°N. (a) at 1200 K isentropic level ~ 39 km. (b) at 220 K isentropic level ~ 54 km (minor warmings are shown as hatched areas).

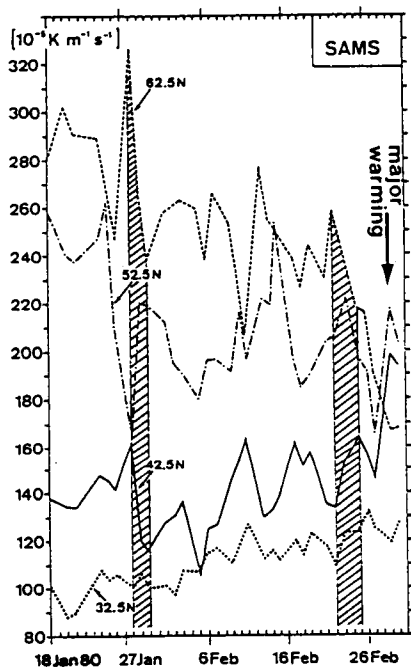


Figure 5. Zonal mean of Ertel's potential vorticity for winter 1979/80 from 32.5°N to 62.5°N at 1200 K isentropic level ~ 39 km (minor warmings are shown as hatched areas).

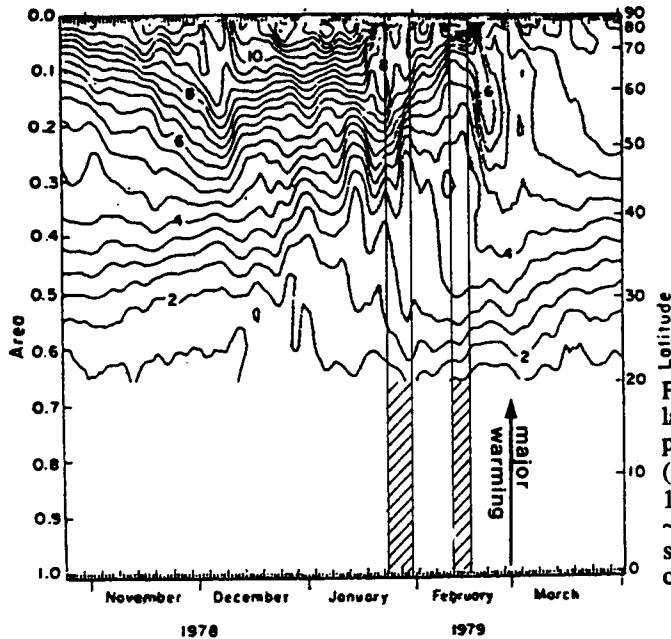


Figure 6. From Butcher et al. [1986] latitude-time sections of zonal mean potential vorticity contours ($gH_0p_0^{-1}10^{-4}K m^{-1}s^{-1}$) for winter 1978/79 at 850 K isentropic level ~ 29 km (minor warmings are shown as hatched areas) by author of this paper.

7.7 PLASMA PHENOMENA OBSERVED IN THE MAP/WINE CAMPAIGN

M. Friedrich

Technical University Graz
Inffeldgasse 12, A-8010 Graz, Austria

The wealth of plasma data gathered in the MAP/WINE campaign allows insight into the generation of electron densities on a large, and the nature of the ions on a small scale. The associated measurements of winds and charged particles help to understand the morphology of the midlatitude ionization which turns out to correlate poorly with geomagnetic activity, but at least slightly with the prevailing winds. A somewhat clearer connection seems to exist between stratospheric warmings and radio wave absorption minima. On the local scale the interpretation of the rocket measurements of positive ions was helped by simultaneous observations of temperatures and atomic oxygen. The relevance of the description "winter anomaly" for high latitude electron density profiles will be examined.

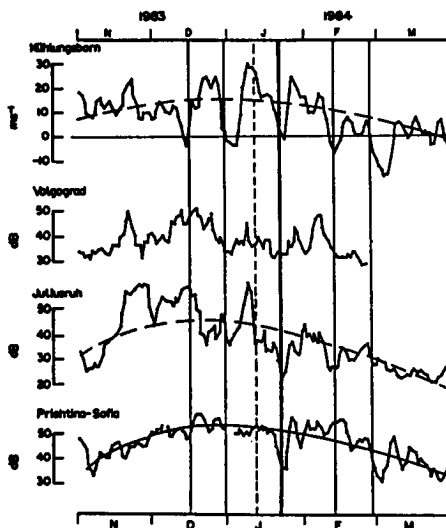


Figure 1. Zonal wind component measured by a meteor radar installation (Kühlungsborn) together with absorption data at three European locations [after Williams et al., *J. Atmos. Terr. Phys.* 49, 777, 1987].

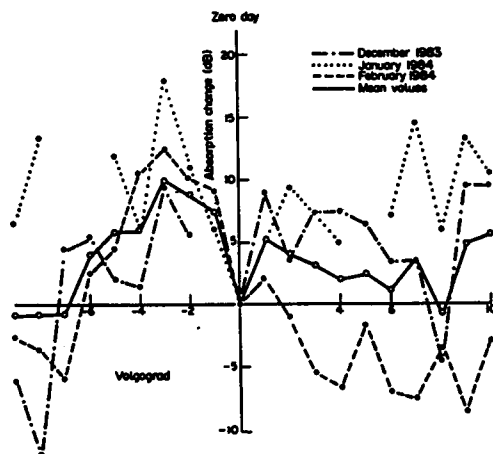


Figure 2. Elapsed time plot of midlatitude absorption(Volgograd) relative to the time of the onset of stratospheric warmings of the MAP/WINE period [after Williams et al., *J. Atmos. Terr. Phys.* 49, 777, 1987].

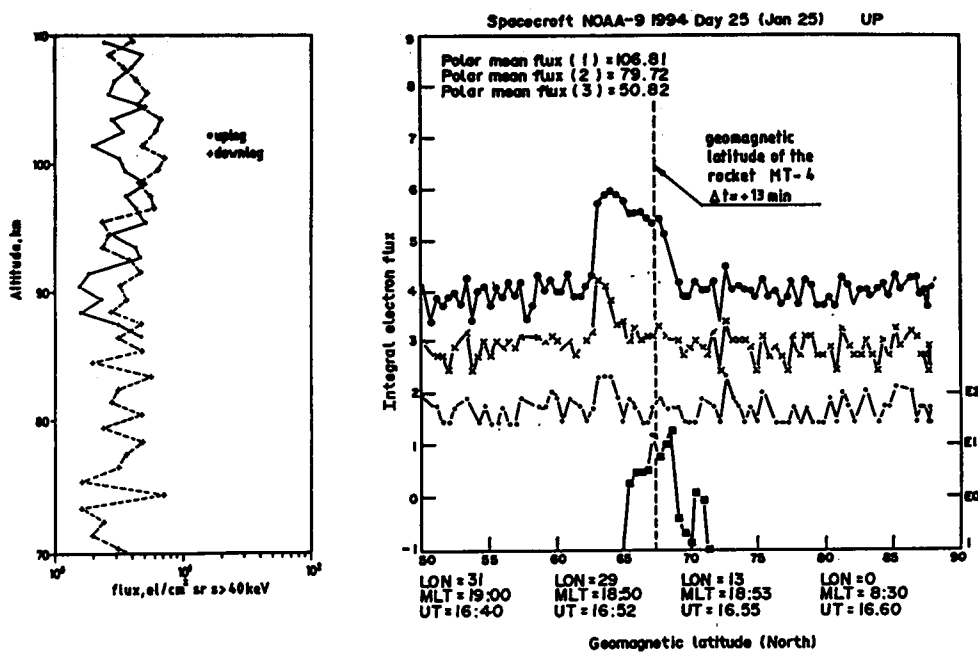


Figure 3. Flux of energetic electrons (> 40 keV) vs. altitude as measured by the rocket-borne Geiger-Müller counters aboard the rocket MT-4 and the corresponding measurements by a TIROS-N satellite. Note that the rocket-borne instrument measured no fluxes exceeding the background, despite the proximity of the satellite's geomagnetic footprint.

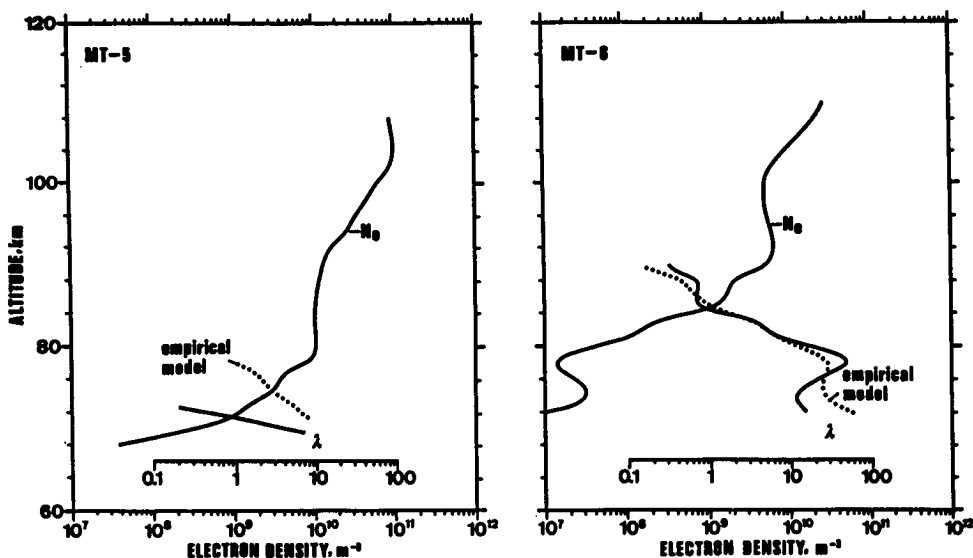


Figure 4. Electron densities and λ (density ratio of negative ions to electrons) for the rocket flights MT-5 and 6.

CONCLUSIONS

A meteorological influence upon the ionosphere has been assumed and is predicted by various models. The observations obtained in the MAP/WINE Campaign have strengthened the following statements:

1. A direct temperature control on radio wave absorption (D-region electron densities) is not evident in the available data, although it can be predicted based on the highly temperature-dependent clustering processes.
2. Daytime absorption tends to decrease after stratospheric warmings which is most probably due to an influence on the chemistry and distribution of minor neutral species (NO, O), rather than a direct temperature influence on the ion chemistry.
3. The only conceivable meteorological influence on the nighttime plasma densities at high latitudes is via the concentration of atomic oxygen, whereas the concentration of NO contributes only marginally to the ion production.
4. To seek a dependence of the electron densities outside the auroral zone on activity inside it was not part of the MAP/WINE Campaign; for completeness it may be added here that such a relation has been found to be, if at all detectable, very poor and only occurring with lags of a few days after the event in the auroral zone [e.g. Torkar et al., *J. Atmos. Terr. Phys.*, 42, 183, 1980].

8. ATMOSPHERIC TIDES MIDDLE ATMOSPHERE PROGRAM (ATMAP)

8.1 THE ATMOSPHERIC TIDES MIDDLE ATMOSPHERE PROGRAM

J. M. Forbes

Department of Electrical, Computer and Systems Engineering
Boston University, Boston, MA 02215

Atmospheric tides, oscillations in meteorological fields occurring at subharmonics of a solar or lunar day, comprise a major component of middle atmosphere global dynamics. The purpose of the 1982-1986 Atmospheric Tides Atmosphere Program (ATMAP) was to foster an interaction between experimentalists, data analysts, and theoreticians and modelers, in order to better understand the physical mechanisms governing tides and their relationships to other scales of motion, and to thereby explain features of observed tidal structures in the mesosphere and lower thermosphere. The ATMAP consisted of seven observational campaigns, five workshops and a climatological study. This paper provides a historical perspective and summary of major results, conclusions, and recommendations for future study which have emerged from the ATMAP.

PURPOSE: Create an interaction among experimentalists, data analysts, theoreticians, and modellers working towards the following goals:

- (1) Delineate the global morphology of middle middle atmosphere tides including temporal and spatial variability on various scales; and
- (2) Elucidate the relationships between tides and other scales of motion (zonal mean circulation, gravity waves, turbulence).

ATMAP PARTICIPANTS

S. Kato (Japan)	S. Avery (USA)
T. Aso	B. Balsley
T. Tsuda	S. Bowhill
S. Miyahara	D. Carter
S. Fukao	R. Clarke
	J. Forbes
G. Elford (Australia)	R. Roper
R. Vincent	R. Walterscheid
G. Fraser (New Zealand)	E. Kazimirovsky (USSR)
	Y. Portnyagin
K. Greisiger (GDR)	J. Rottger (FRG)
R. Schminder	P. Collis
D. Kurschner	R. Ruster
A. Manson (Canada)	P. Czechowsky
C. Meek	
	H. Teitelbaum (France)
C. Reddy (India)	F. Vial
	J. Fellous
G. Cevolani (Italy)	
G. Groves (UK)	

HAMBURG WORKSHOP (1-day)

Global Analyses - Campaigns I, II
 Emphasis on Latitudinal Structures
 Assessment of Numerical Models
 Paucity of Low-Latitude data
 Discussion on Data Analysis Techniques
 Fourier fits, filtering, spectral analysis
 weighting, variable data quality
 Groves technique
 minimum 4-day fit span
 vector average vs. amplitude average

KYOTO WORKSHOP (2-day)

Global Analyses - Campaigns I, II, III, IV
 Emphasis on Vertical Structures
 Typical "High-Latitude" and "Middle-Latitude" Behaviors
 Asymmetries Between Kyoto (35°N) and Adelaide (35°S)
 Paucity of Low-Latitude Data
 Discussion on Tidal 'Variability'
 global (steady-state) vs. local (transient) oscillations
 gravity-wave interactions
 10-day determinations optimum for global consistency
 without removing some real variations of global tides
 Modelling Needs
 hemispheric asymmetries in background winds/temps
 seasonal-latitudinal variations in dissipation
 better seasonal coverage (month-by-month)

PRAGUE WORKSHOP (1/2-day)

June and December Climatologies
 Kyoto/Adelaide Asymmetries with Groves bias removed
 Existence of Interannual Variability Noted
 Discussion on Global Coherence vs. fit span
 Theoretical Relation - $\Phi'/u', v'$
 fit data with orthogonal functions
 formulate l.b.c.'s for thermospheric models
 Guidelines for Construction of Monthly Climatologies

TOULOUSE INTERIM MEETING (1/2-day)

Interim Comparison of Climatologies
 Global Equinox Transition

VANCOUVER WORKSHOP (1/2-day)

Comparative Analyses of Station Climatologies
 Seasonal-Latitudinal Trends in Vertical Structure
 Pre-Helsinki Organization

ATMAP CALENDAR

Campaign I	09 NOV 81 - 03 DEC 81 (Core: 19-22 NOV 81)
Campaign II	02 MAY 82 - 08 MAY 82 (Core: 03-06 MAY 82)
ATMAP Workshop IAMAP, Hamburg, FRG	17 AUG 82
Campaign III	21 NOV 83 - 16 DEC 83 (Core: 06-09 DEC 83)
Campaign IV	15 MAR 84 - 15 APR 84 (Core: 28-31 MAR 84)
Campaign V	01 JUN 84 - 30 JUN 84 (Core 1: 12-15 JUN 84)
Global Thermosphere Mapping Study (GTMS)	(Core 2: 26-28 JUN 84)
Campaign VI	15 SEP 84 - 15 OCT 84
ATMAP Workshop MAP Symposium, Kyoto	05,06 DEC 84
Global Thermosphere Mapping Study (GTMS)	15-17 JAN 85
ATMAP Workshop IAMAP, Prague	14 AUG 85
Interim Meeting COSPAR, Toulouse	6 JUL 86
ATMAP Workshop IAMAP, Vancouver	21 AUG 87
ATMAP Session MAP Symposium COSPAR, Helsinki	22 JUL 88

8.2 ASYMMETRIES IN TIDAL STRUCTURE BETWEEN ADELAIDE AND KYOTO

R. A. Vincent

Physics Department, University of Adelaide
Box 498, Adelaide 5001, Australia

Continuous radar measurements of the wind oscillations caused by the solar diurnal and semidiurnal tides in the 80 - 110 km region of the atmosphere at the geographically conjugate stations of Adelaide (35°S, 138°E) and Kyoto (35°N, 136°E) are compared for the period 1983-1985. At the solstices it is found for both the 24- and 12-hr tides that the NS and EW oscillations tend to be in-phase and out-of-phase, respectively, behavior which indicates strong tidal asymmetries. The asymmetries in the 12-hr tide are consistent with a strong contribution from the (2,3) mode while the asymmetries in the 24-hr tide are ascribed to the effects of mean winds and dissipation acting to distort the (1,1) mode as it propagates up through the middle atmosphere.

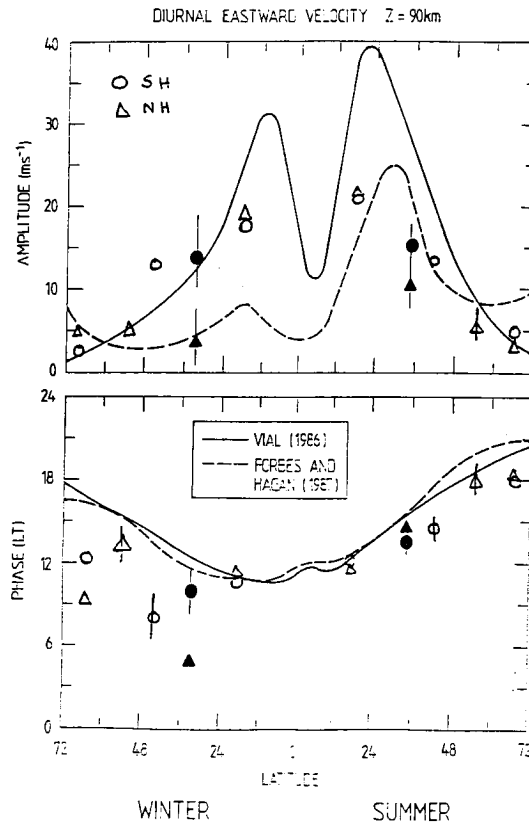


Figure 1. Amplitude and phase of zonal component of diurnal tide at selected stations at solstice compared with recent theory.

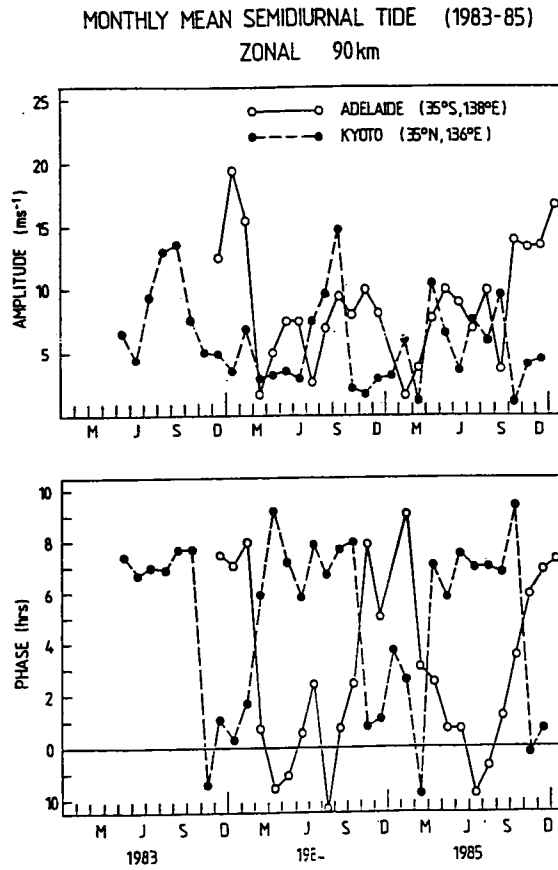


Figure 2. Monthly mean amplitude and phase variations at Adelaide and Kyoto at 90 km.

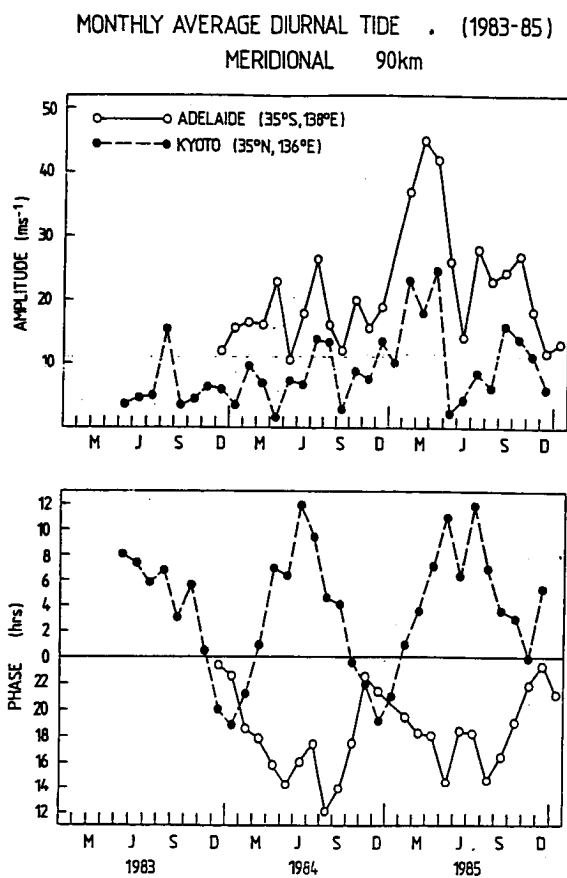


Figure 3. Monthly mean amplitude and phase variations at Adelaide and Kyoto at 90 km.

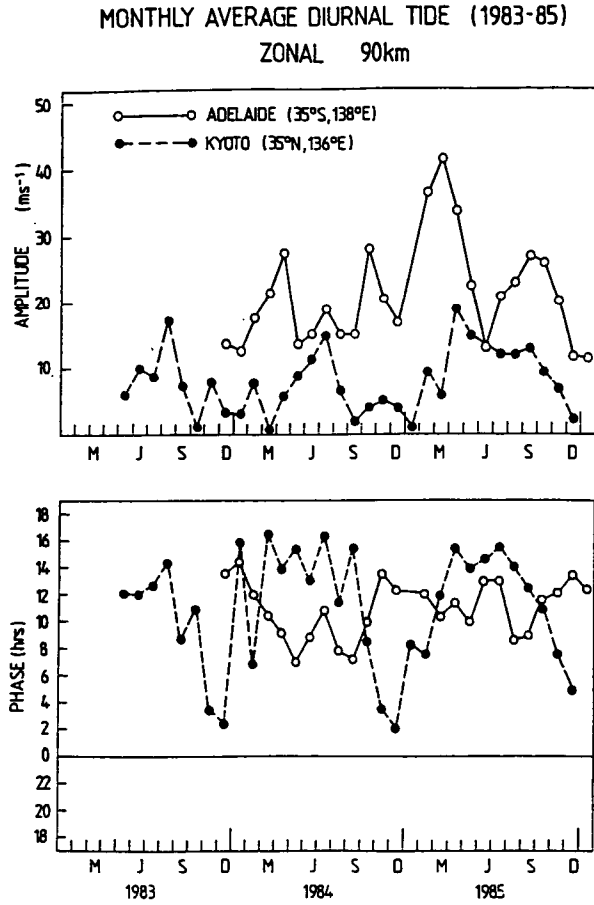


Figure 4. Monthly mean amplitude and phase variations at Adelaide and Kyoto at 90 km.

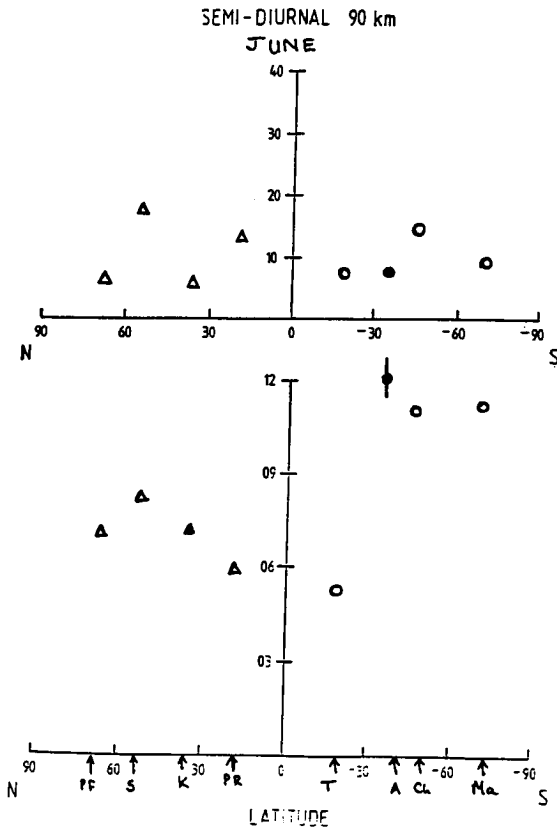


Figure 5. Amplitude and phase of zonal component of semidiurnal tide at selected stations for June solstice.

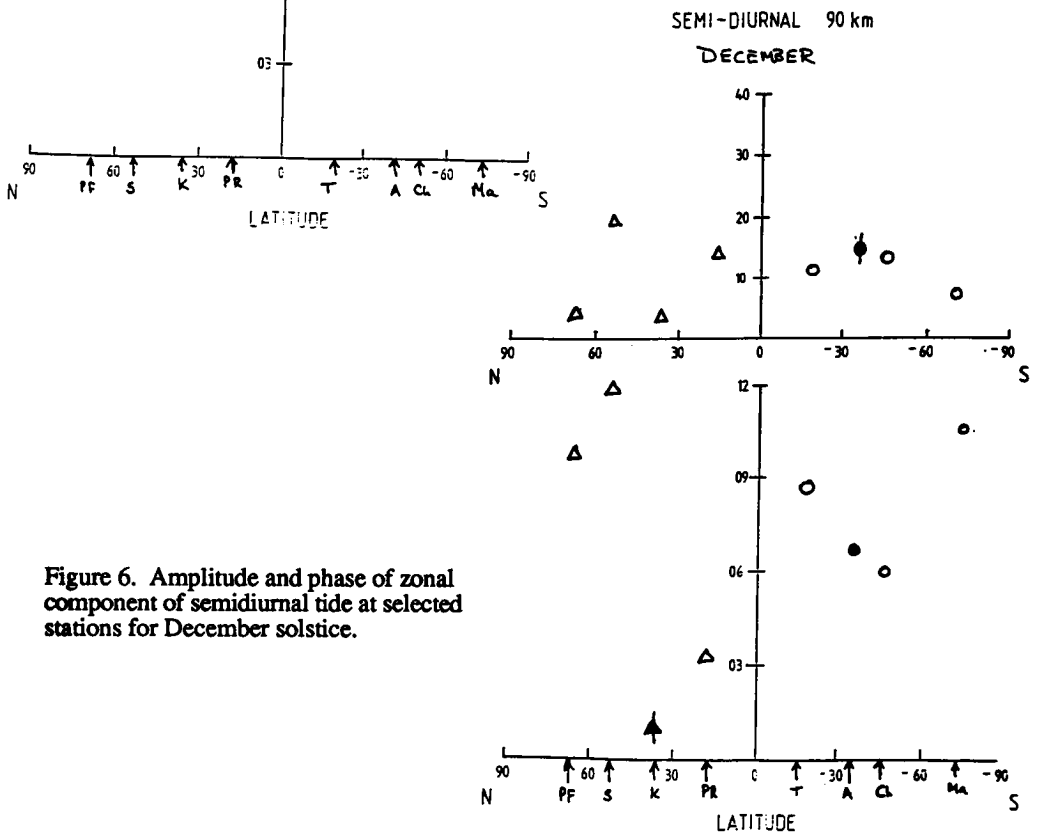


Figure 6. Amplitude and phase of zonal component of semidiurnal tide at selected stations for December solstice.

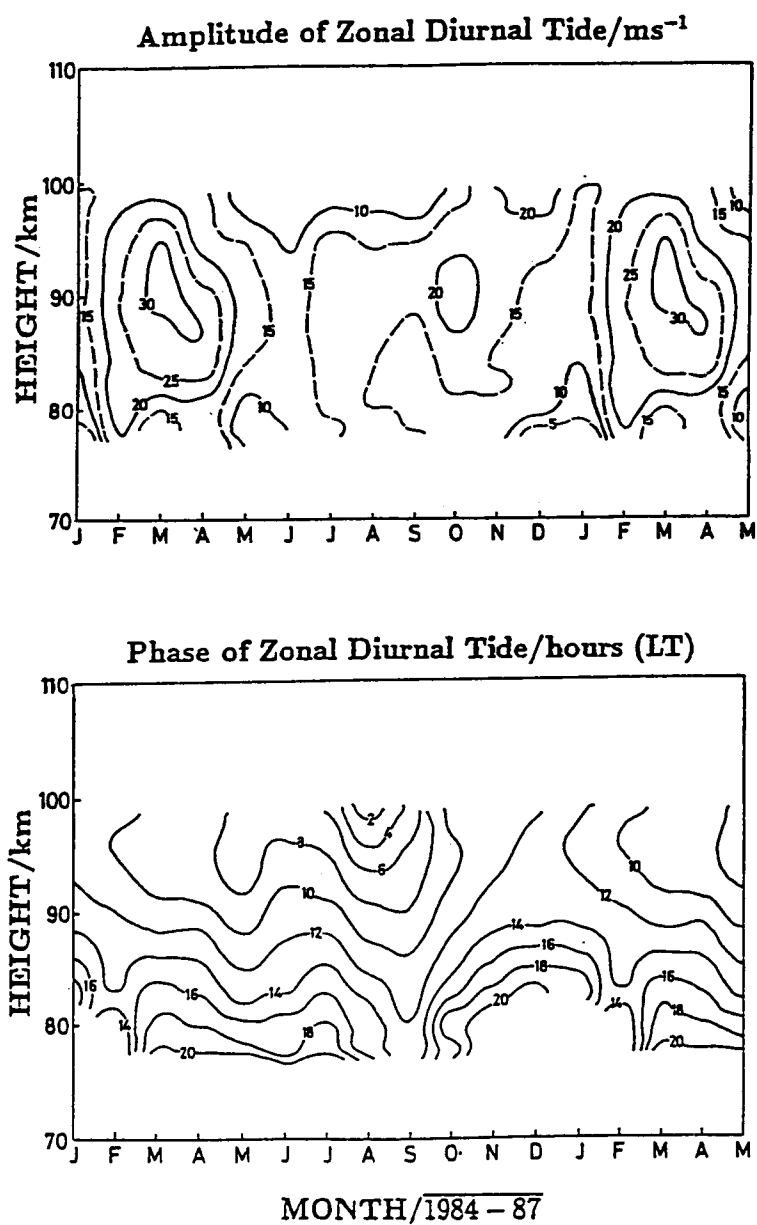


Figure 7. Height-time contour plots of the amplitude and phase of the diurnal tide in the zonal wind component at Adelaide.

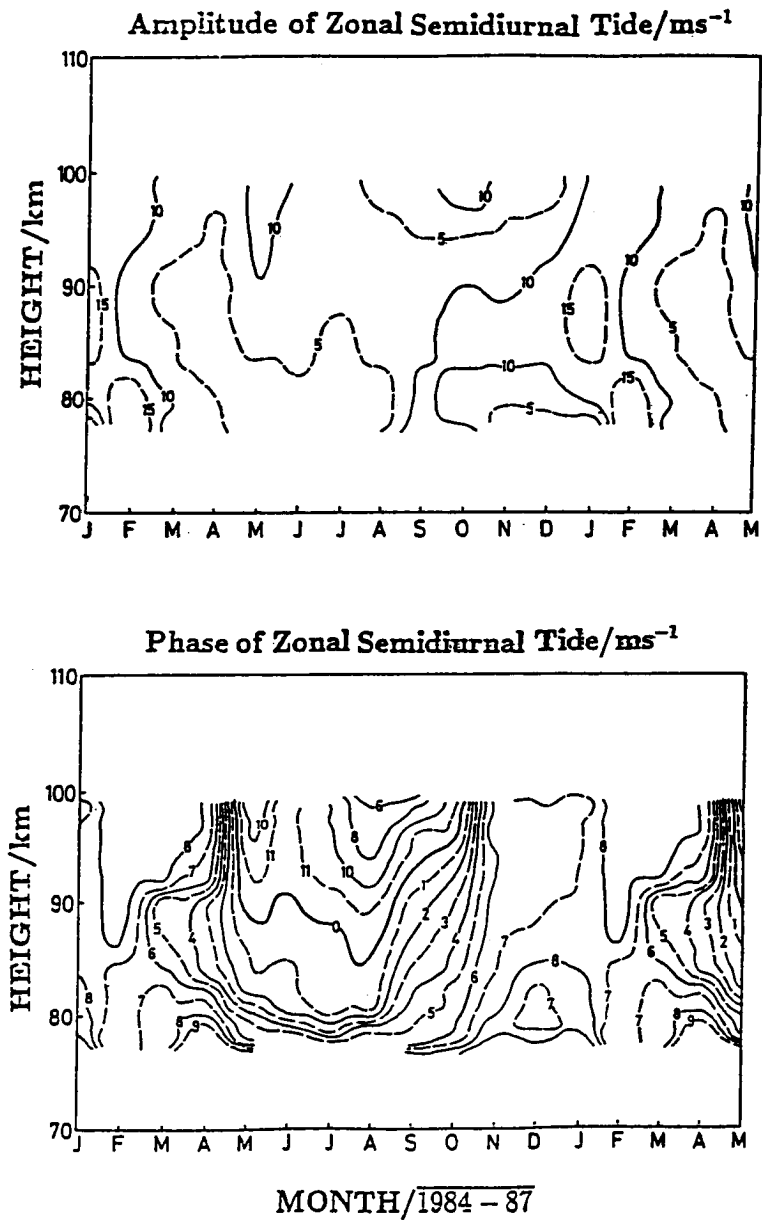


Figure 8. Height-time contour plots of the amplitude and phase of the semidiurnal tide in the zonal wind component at Adelaide.

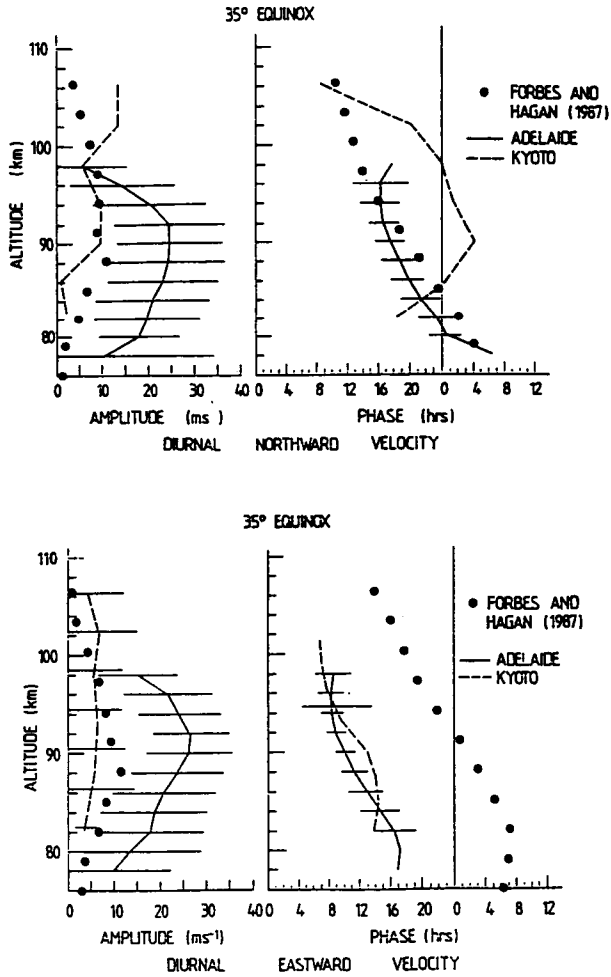


Figure 9. Height profiles of amplitudes and phases.

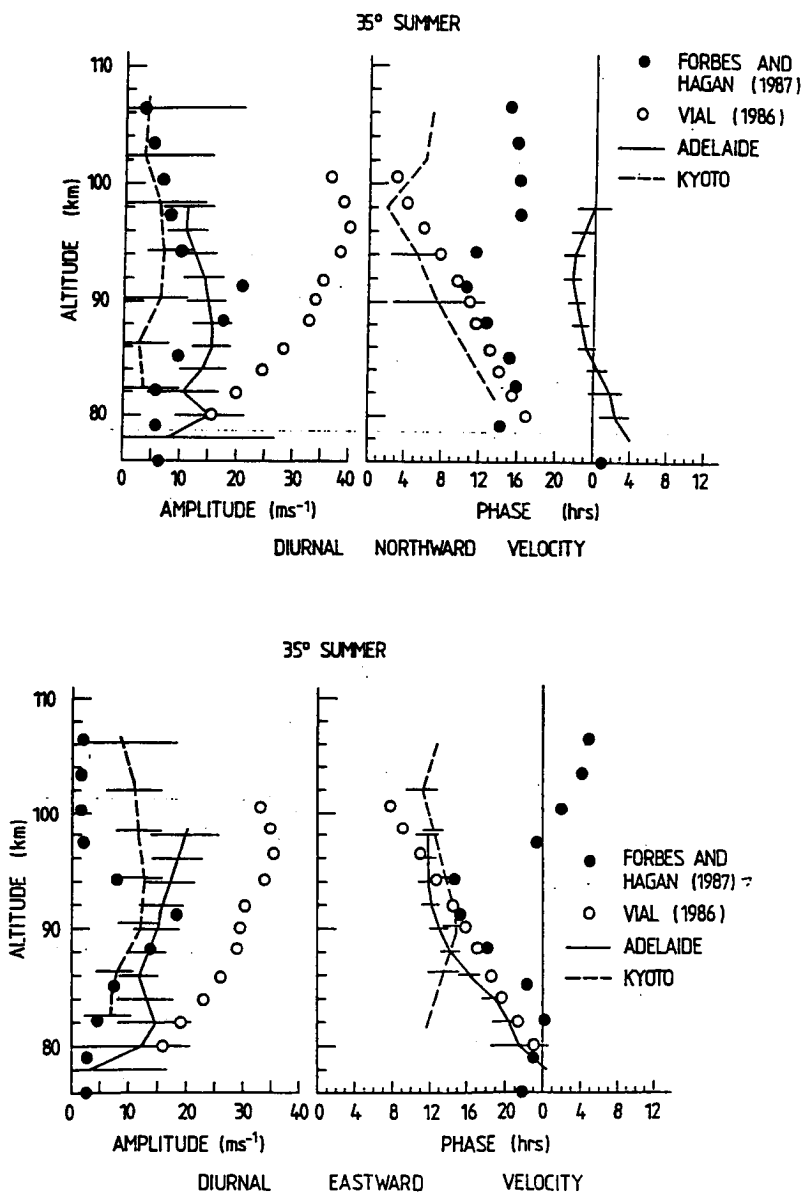


Figure 10. Height profiles of amplitudes and phases

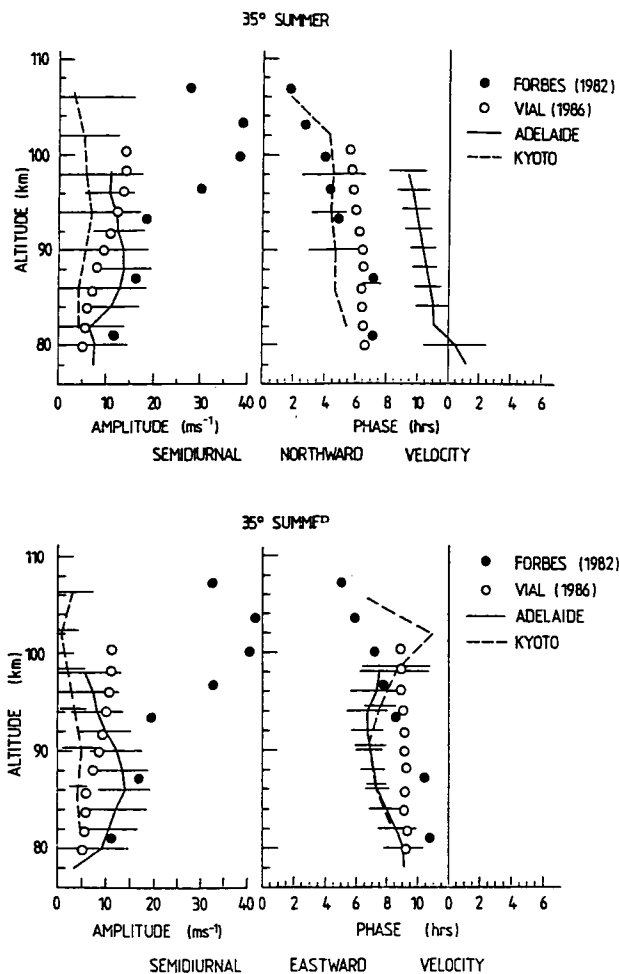


Figure 11. Height profiles of amplitudes and phases.

CONCLUSIONS - DIURNAL TIDE

*Significant phase differences in EW winds

*Amplitudes 2 - 3 times larger at Adelaide
(Lower dissipation in SH?)

*Comparisons with other station pairs gives
reasonable agreement with theory

(Mawson, 68°S, Poker Flat 65°N)
(Christchurch 44°S, Saskatoon, 52°N)
(Adelaide, 35°S, Kyoto, 35°N)
(Townsville, 19°S, Puerto Rico, 18°N)

CONCLUSIONS - SEMIDIURNAL TIDE

*EW components out-of-phase

*NS components in-phase

*Vertical wavelengths -
Long in summer
Short in winter

*Phase vs Latitude plots suggest strong asymmetry

8.3 NONMIGRATING TIDES

S. Kato

Radio Atmospheric Science Center, Kyoto University
Gokanoshō, Uji, Kyoto 611, Japan

Recently we have seen an interesting advancement in the study of nonmigrating tides. There have been two distinct approaches in works on this subject. One is based on mechanistic models as considering nonuniform global distribution of water vapor or heating only on land, solving a set of linear equations. It is found that insolation absorption of the nonuniformly distributed water vapor produces only weak nonmigrating tides in the lower thermosphere; the planetary boundary layer heating on land can explain the enhanced tides on land and those with short vertical wavelengths in the stratosphere. The other approach is novel and uses simulation on the general circulation model (GCM). This realistic model can reproduce tides globally and in many details. The enhancement of two nonmigrating modes as eastward traveling modes with a wave number 3 and westward traveling modes with a wave number 5 is in surprisingly good agreement with observation at sea level, at 700 mb and even at 300 mb.

Table 1. Parameters in various works.

CASE	Heat Source	Model	Resolution etc.
1	Water vapor insolation absorption	EGW dissipation No winds	$s = -2, -1, 0, 1, 2, 3$ for $n = 1$ plus $s = 1$ for $n = 2$ $\Delta z = 0.5 - 1.0 \text{ km}$ $80 < z < 100 \text{ km}$
2,3	GCM(IMR)	GCM(IMR)	$\Delta \theta = 4^\circ$ $\Delta \phi = 5^\circ$ $\Delta z : 12 \text{ levels} \sim 5 \text{ km}$ $P_0 > 1 \text{ mb}$
4	P.B.L.heating	Classical tidal theory only with Newtonian cooling	$ s \leq 20, n \leq 20$ $\Delta z = 40 \text{ m}$ MST region

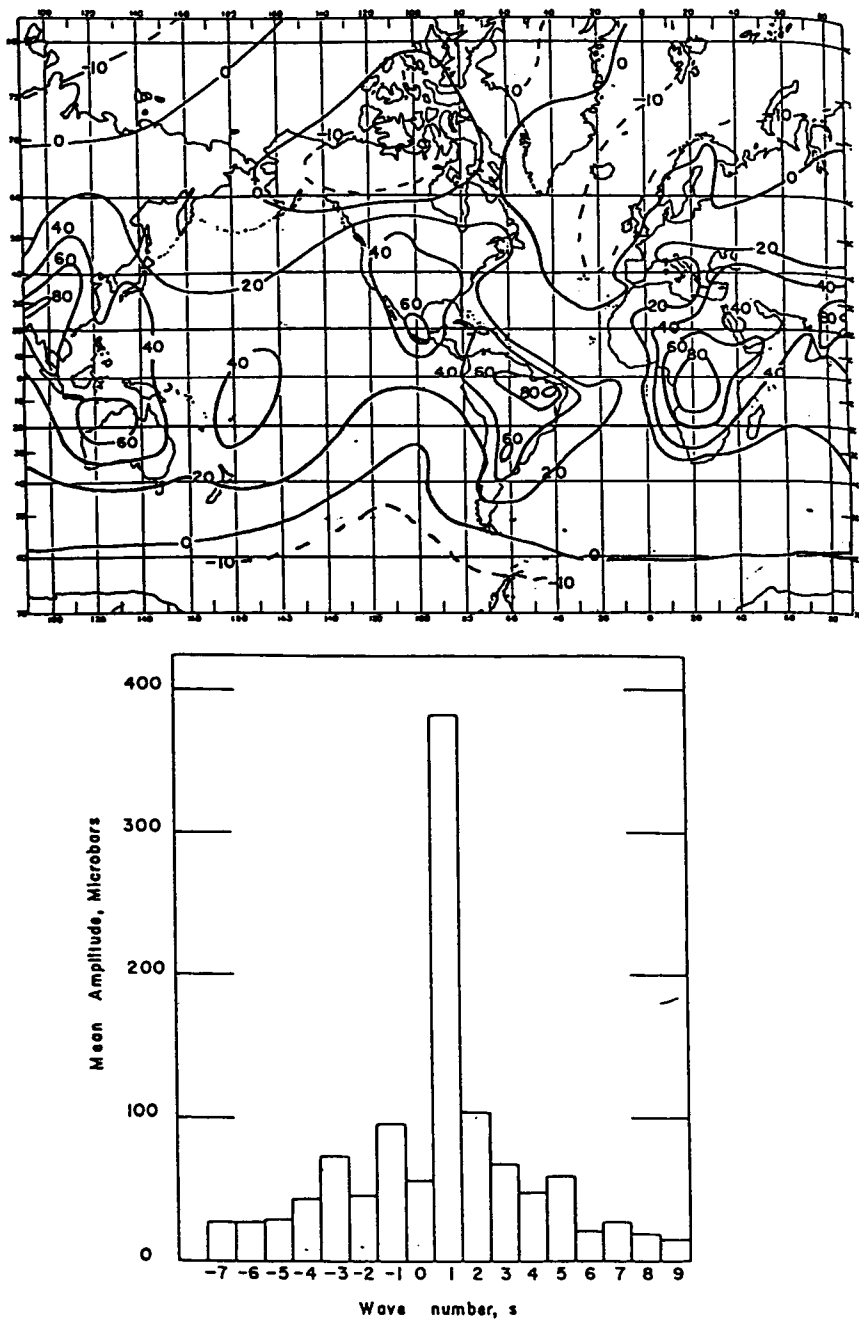


Figure 1. Diurnal tides observed at sea level global distribution (top), wave number spectrum averaged along latitudes (bottom) [Haurwitz, 1965].

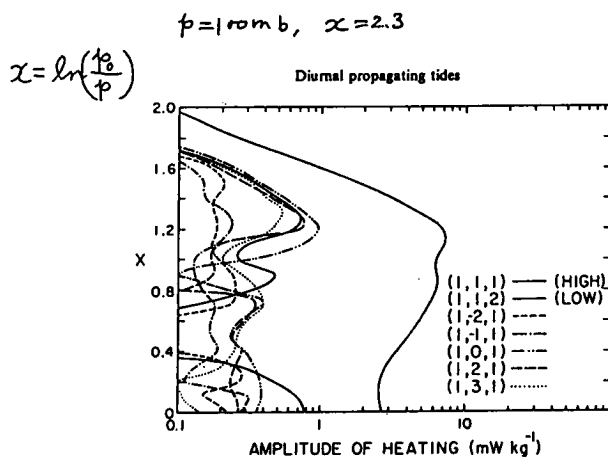


Figure 2. Vertical profiles of diurnal heating in spring equinox for various modes; $x = \ln(P_0/P)$ where P is the atmospheric pressure and P_0 is P at sea level [Forbes and Groves, 1986].

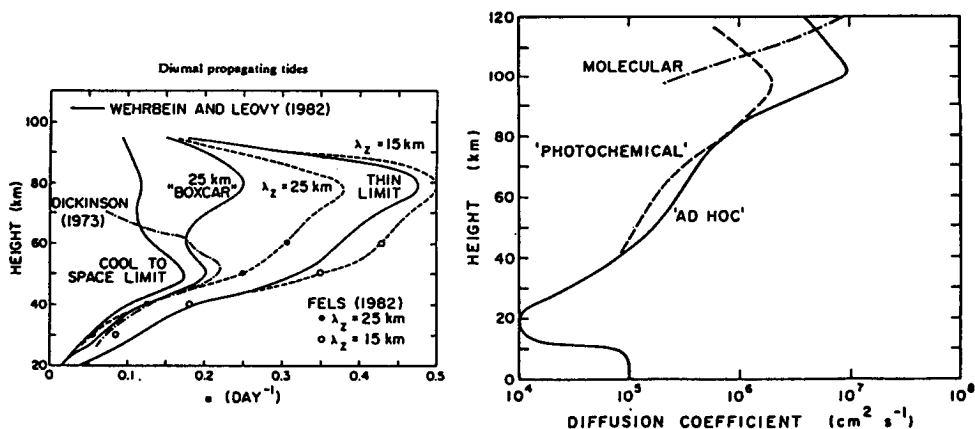


Figure 3. Dissipation rate: Newtonian cooling coefficients. The dashed curves represent profiles used for calculation depending on vertical wavelength λ_z (left), diffusion coefficient (right) [Forbes and Groves, 1986].

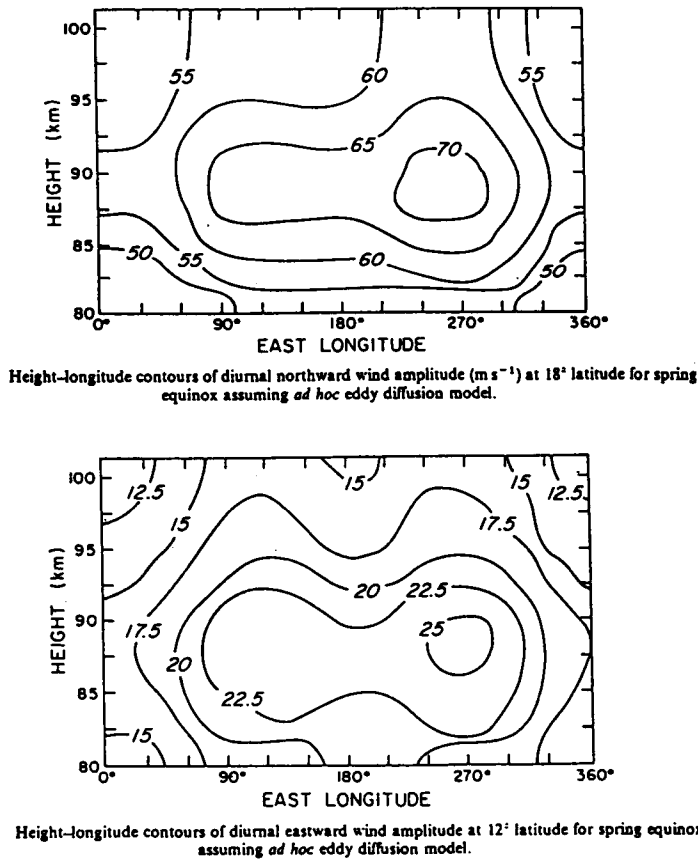


Figure 4. Calculated winds [Forbes and Groves, 1986].

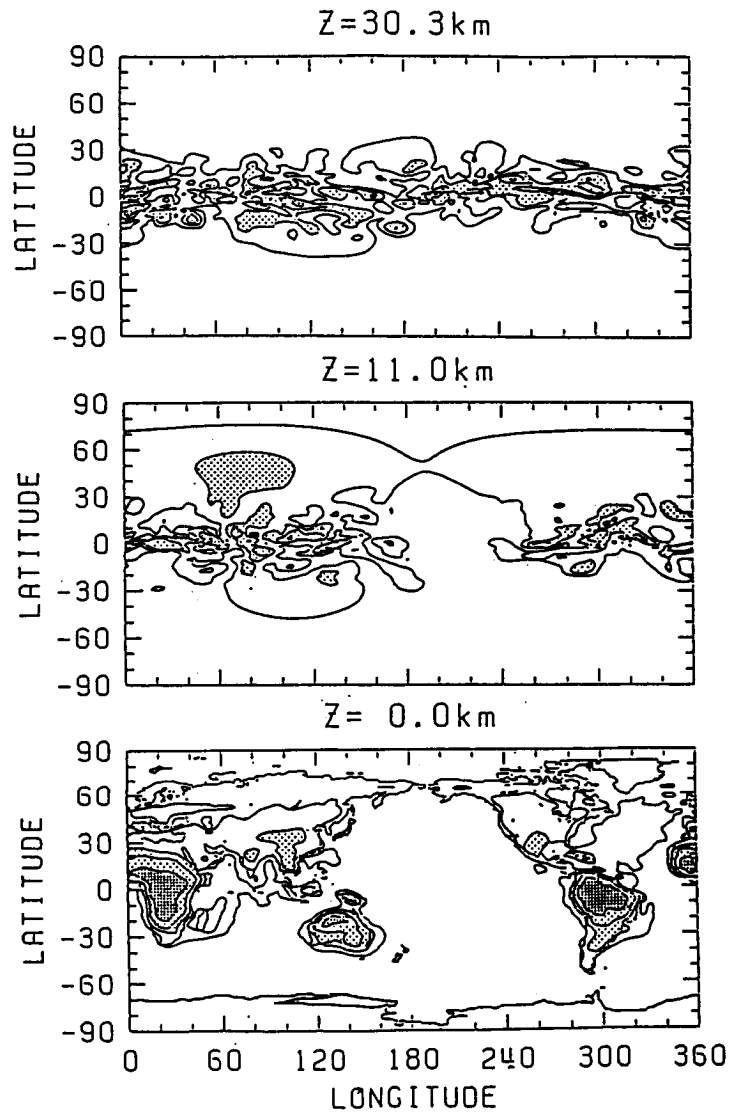


Figure 5. Calculated diurnal pressure tides at equinox [Tsuda and Kato, 1988].

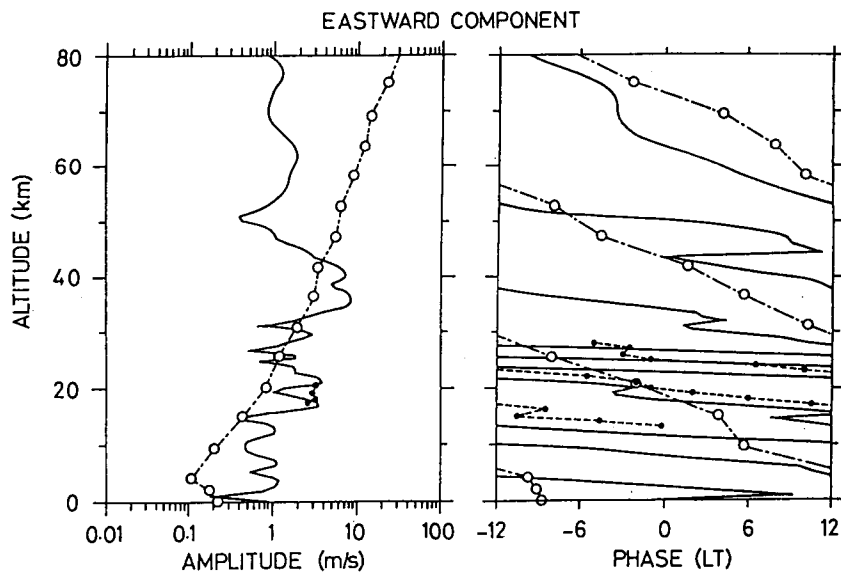


Figure 6. Same as Figure 5 except for vertical profiles of tidal winds.

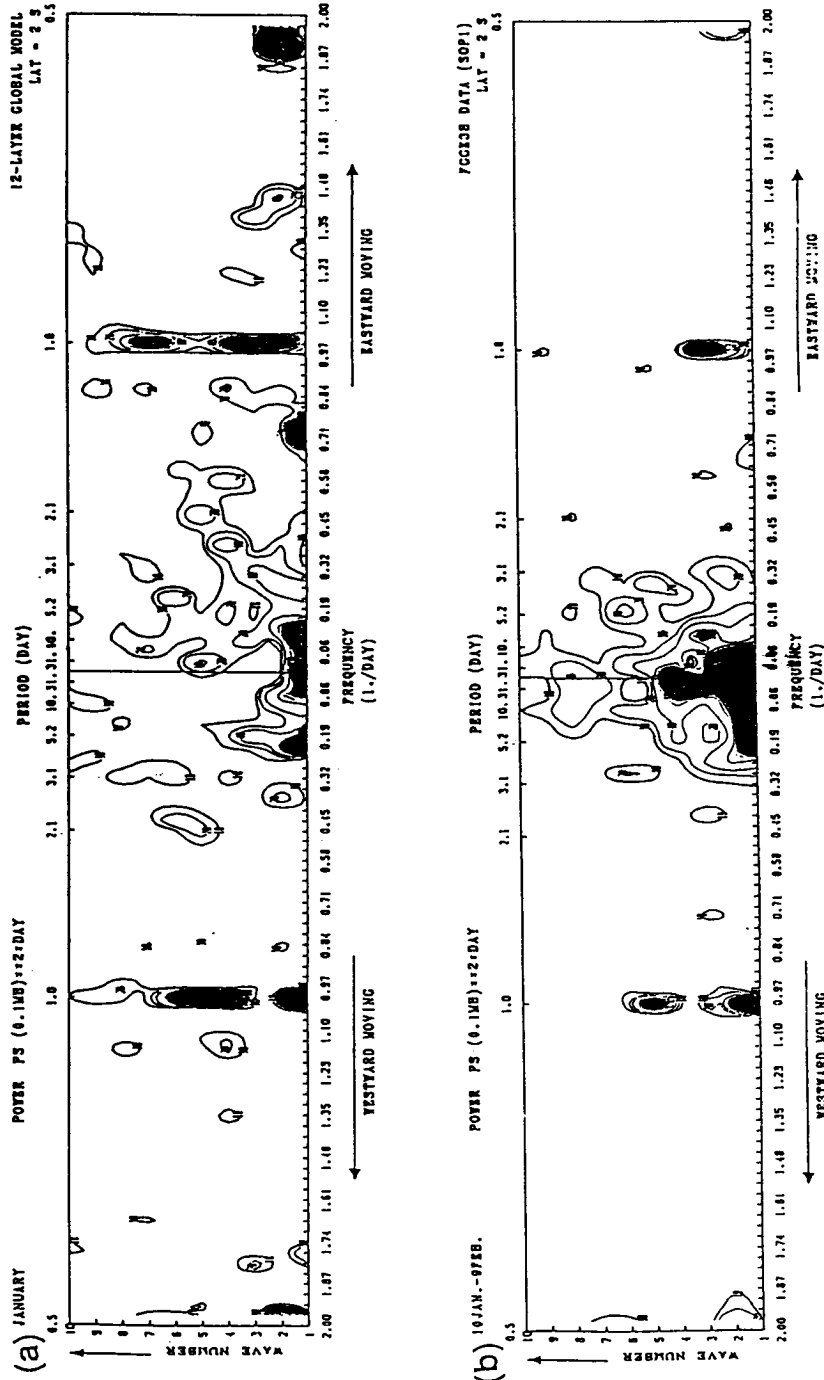


Figure 7. The power spectra of the sea level pressure field in the space-time domain at 2°S from (a) the GCM simulation and (b) FGGE (First GARP Global Experiment) data analysis [Yagai, 1988].

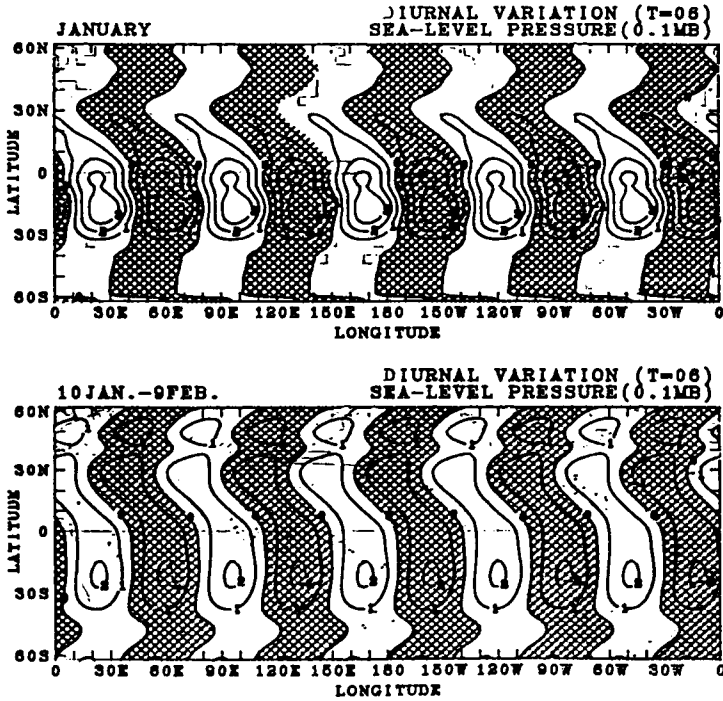


Figure 8. The horizontal map of sea level pressure field of the diurnal mode ($s = 5$) at 0600 GMT from (a) the GCM simulation and (b) FGG data analysis. The contour interval is 0.1 mb, and negative values are shaded.

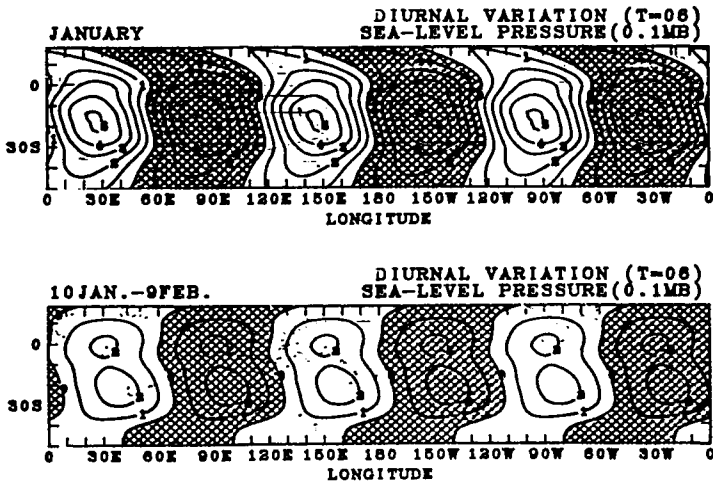


Figure 9. Same as Figure 8 except for $s = -3$.

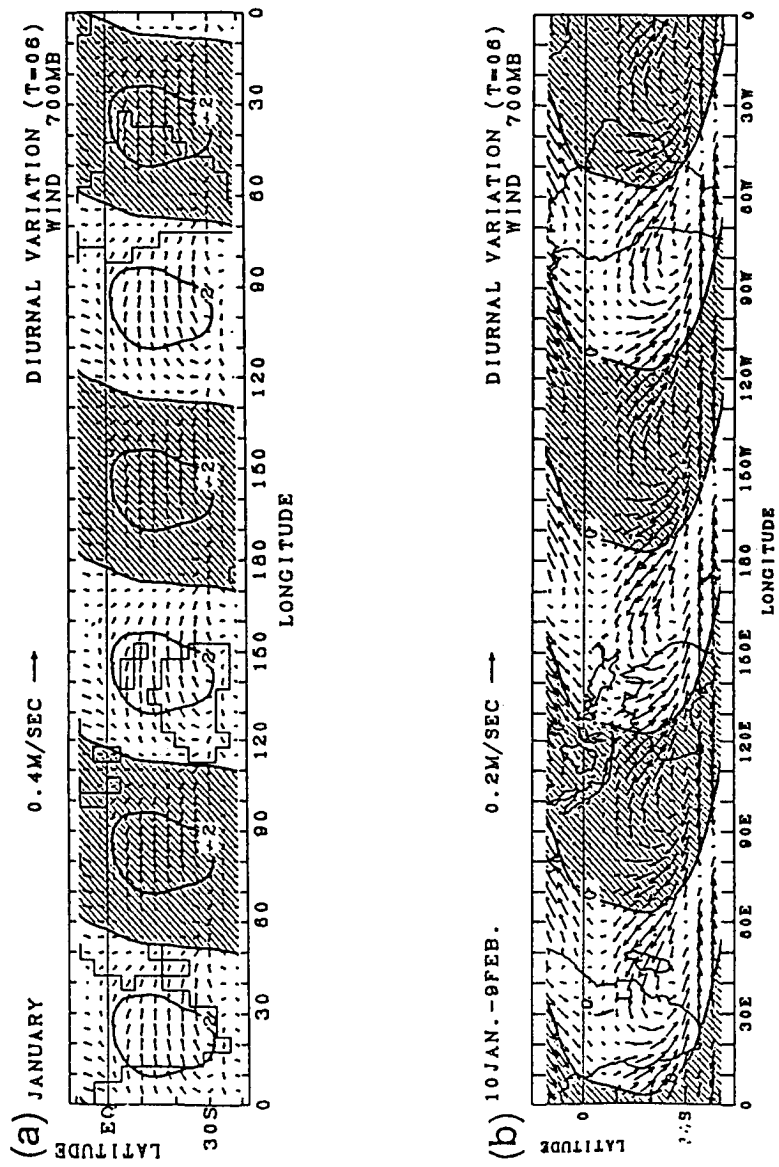


Figure 10. Same as Figure 9 except at 700 mb.

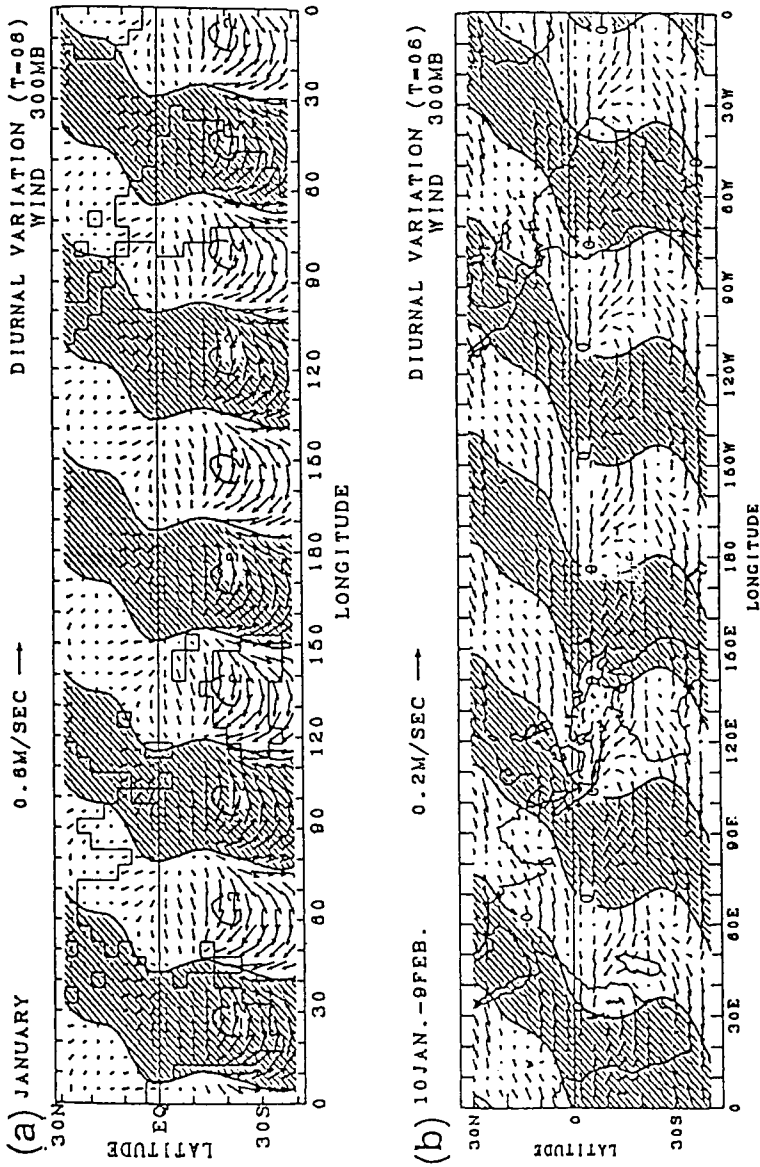


Figure 11. Same as Figure 8 except at 300 mb.

8.4 GLOBAL BEHAVIOR OF THE HEIGHT/SEASONAL STRUCTURE OF TIDES BETWEEN 40° and 60° LATITUDE

A. H. Manson, C. E. Meek

Institute of Space and Atmospheric Studies
University of Saskatchewan, Saskatoon, Sask. S7N 0W0, Canada

H. Teitelbaum

Laboratoire de Meteorologie Dynamique du CNRS
Ecole Polytechnique, 91128 Palaiseau Cedex, France

G. J. Fraser, M. J. Smith

Department of Physics, University of Canterbury
Christchurch 1, New Zealand

R. R. Clark

Electrical and Computer Engineering Department
University of New Hampshire at Kingsbury, Durham, NH 03824

R. Schminder, and D. Kürschner

Karl-Marx Universität, Leipzig, German Democratic Republic

The radars utilized are meteor (2), medium-frequency (2) and the new low-frequency (1) systems: analysis techniques have been exhaustively studied internally and comparatively and are not thought to affect the results. Emphasis is placed upon the new height-time contours of 24-, 12-h tidal amplitudes and phases, which best display height and seasonal structures; where possible high resolution (10 d) is used (Saskatoon), but all stations provide monthly mean resolution. At these latitudes the diurnal tide is generally smaller than the semidiurnal (≤ 10 m/s vs 10 - 30 m/s), and displays more variability. However, there is a tendency for vertical wavelengths and amplitudes to be larger during summer months. On occasions in winter and fall, wavelengths may be less than 50 km. The dominant semidiurnal tide shows significant regular seasonal structure; wavelengths are generally small (~ 50 km) in winter, large in summer (≥ 100 km), and these states are separated by rapid equinoctial transitions. There is some evidence for less regularity toward 40°. Coupling with mean winds is apparent. Data from earlier ATMAP campaigns are mentioned, and reasons for their inadequacies presented.

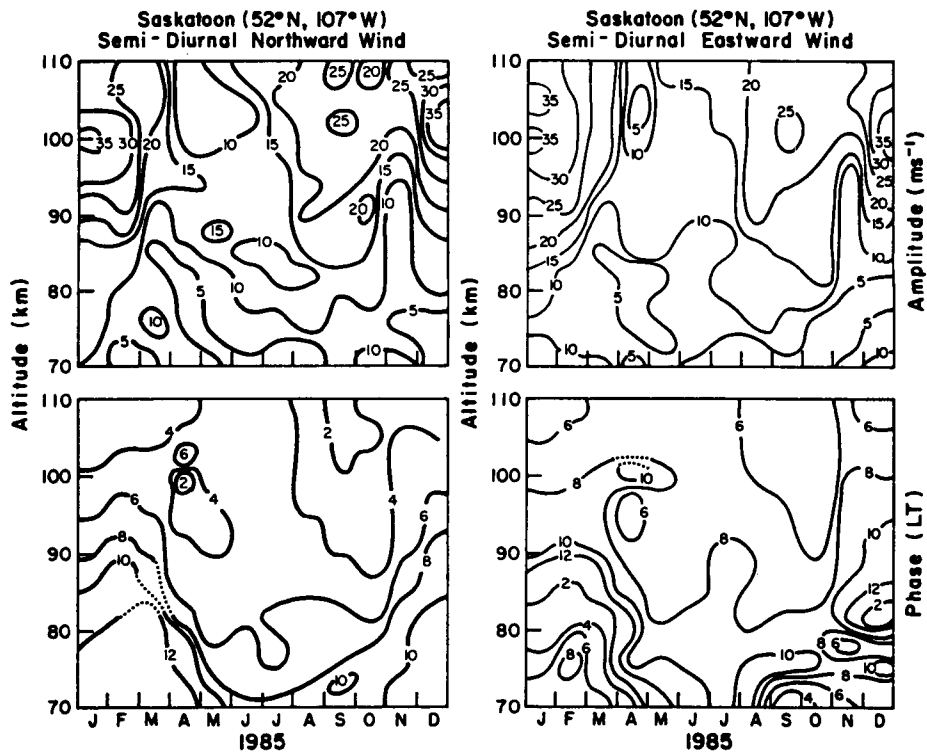


Figure 1. Semidiurnal tidal contours: Saskatoon 1985 (1 month resolution).

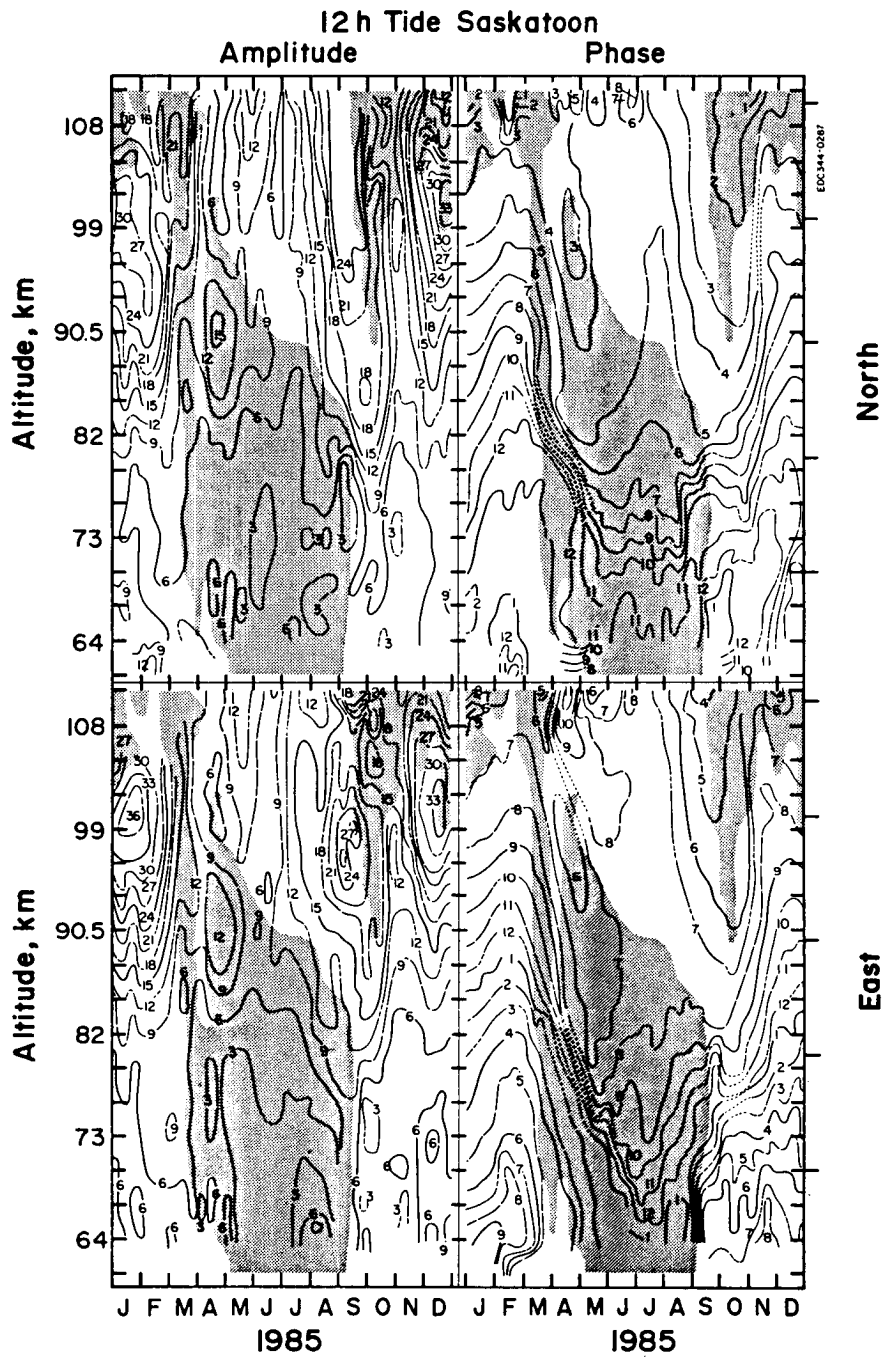


Figure 2. Semidiurnal tidal contours: Saskatoon 1985 (10 d resolution).

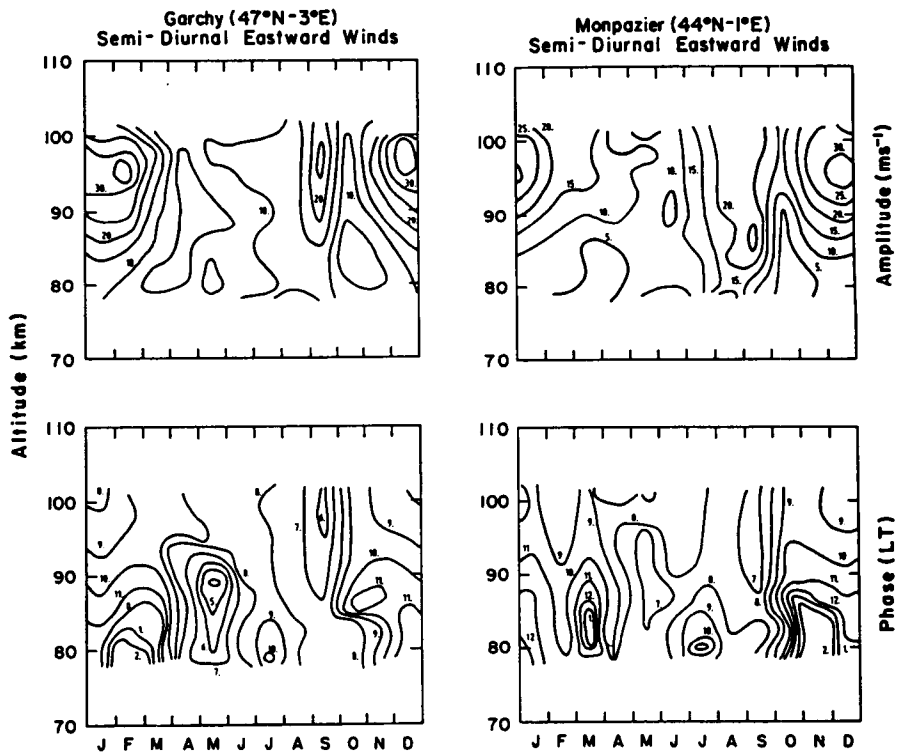


Figure 3. Semidiurnal tidal contours: Garchy 1970-76; Monpazier 1979-80.

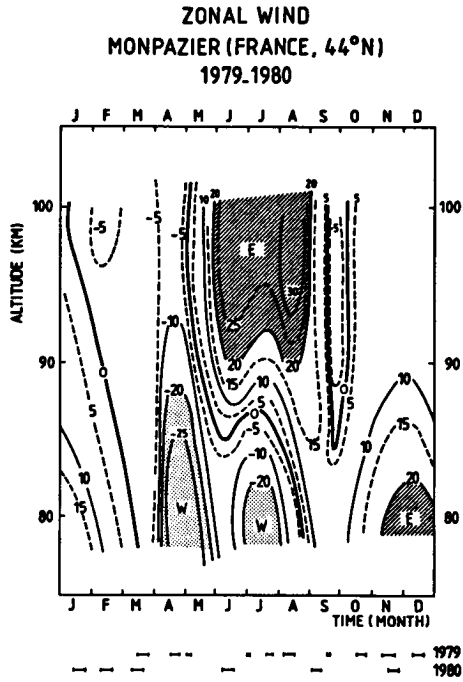
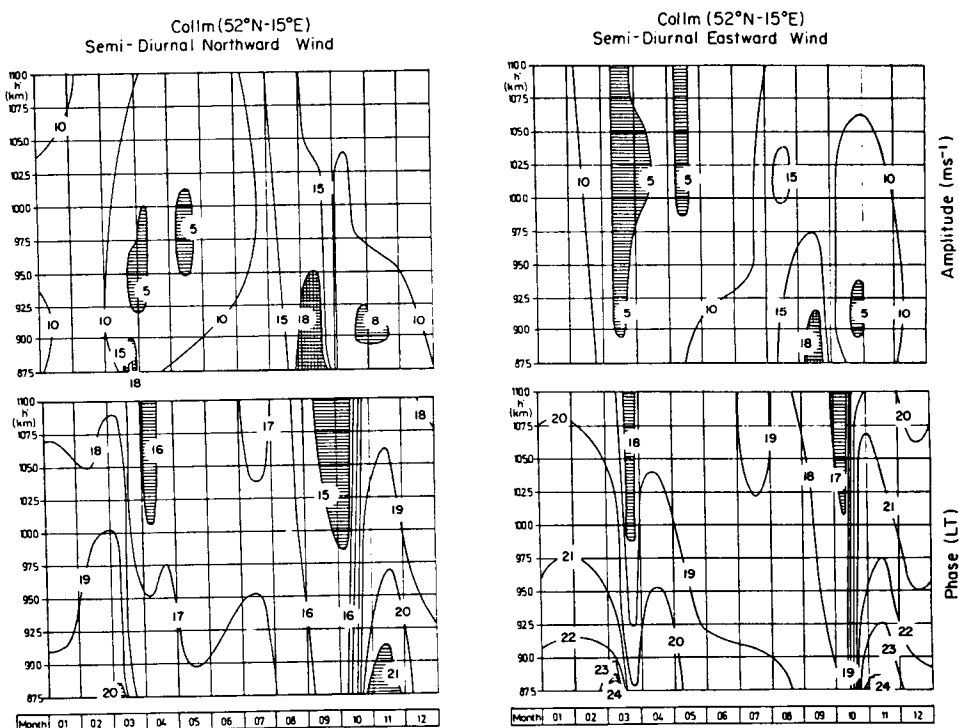


Figure 4. Zonal winds; Garchy and Monpazier.



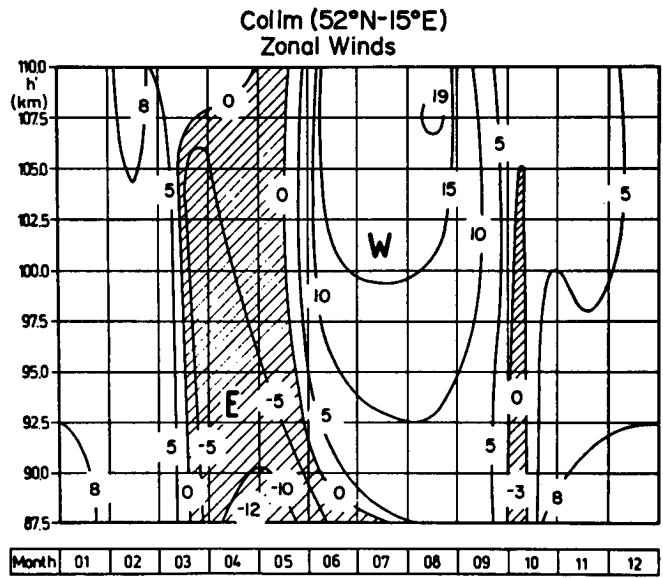


Figure 6. Zonal winds; Collm 1983-86.

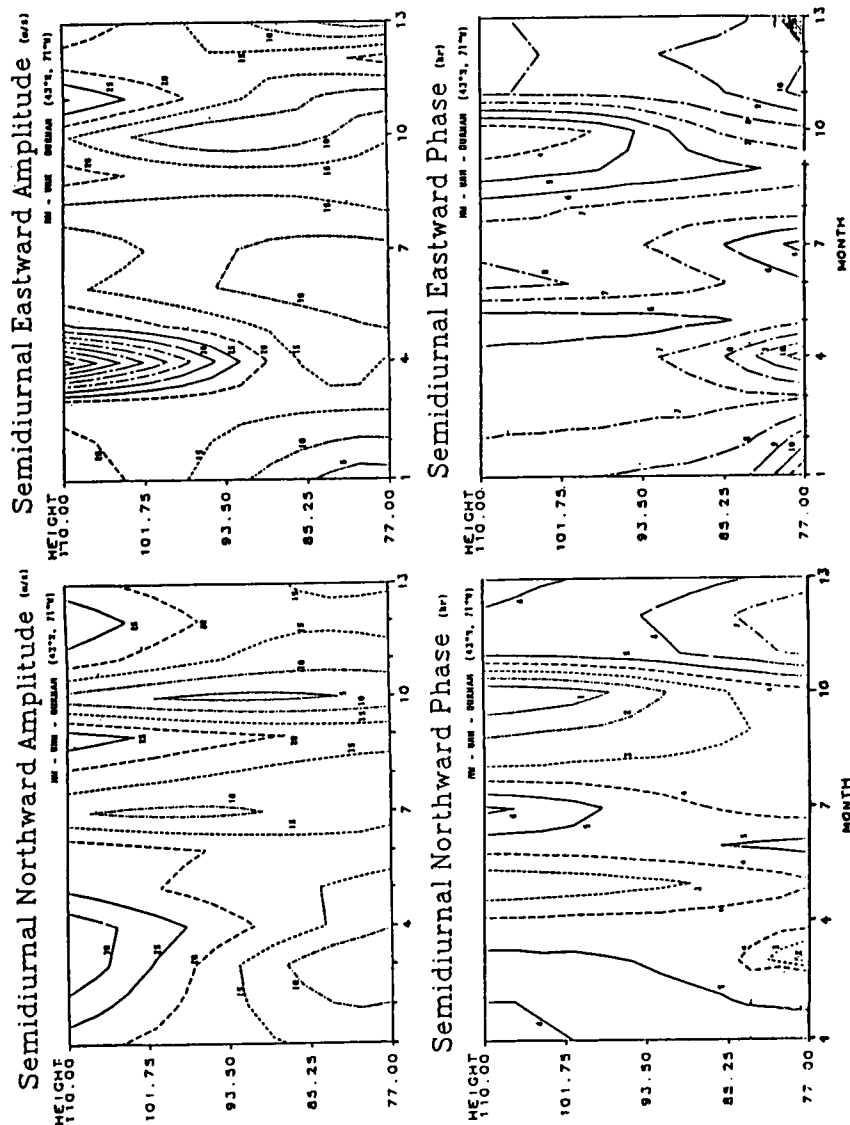


Figure 7. Semidiurnal tidal contours: Durham 1978-84.

ORIGINAL PAGE IS
OF POOR QUALITY

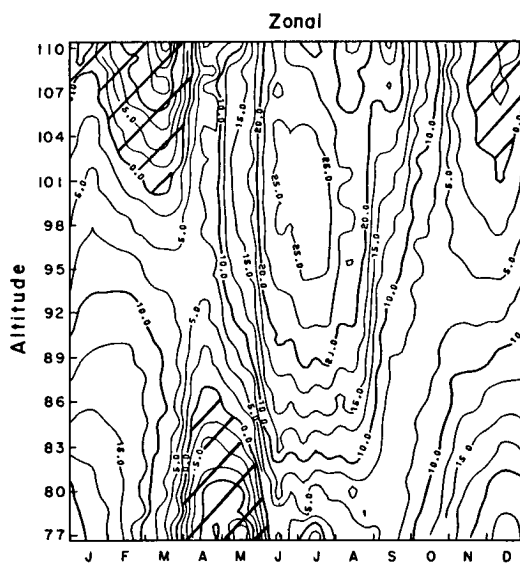
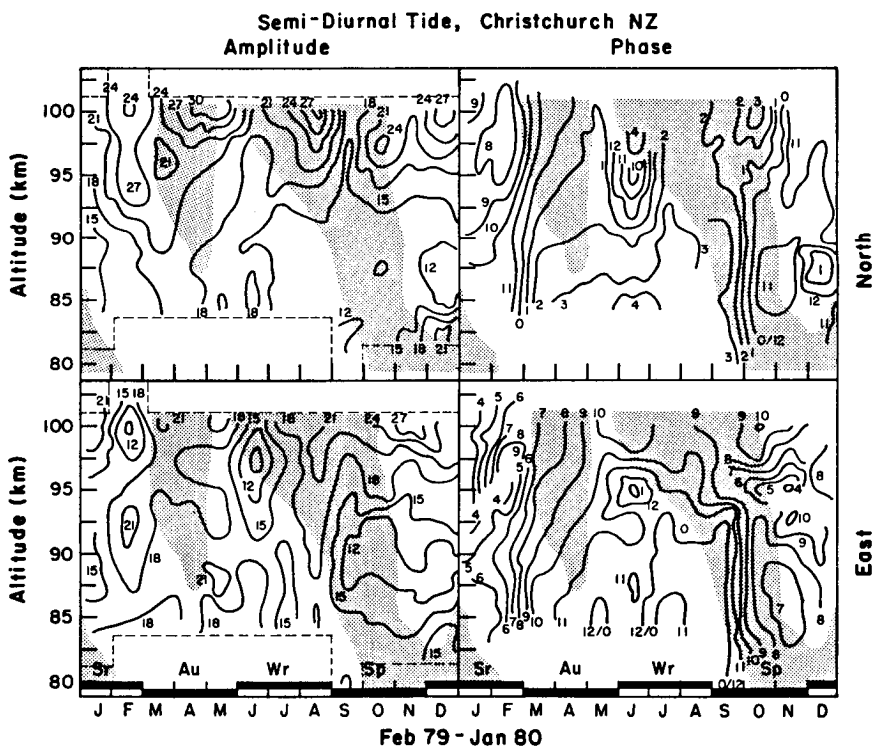


Figure 8. Zonal winds: Durham 1978-84.



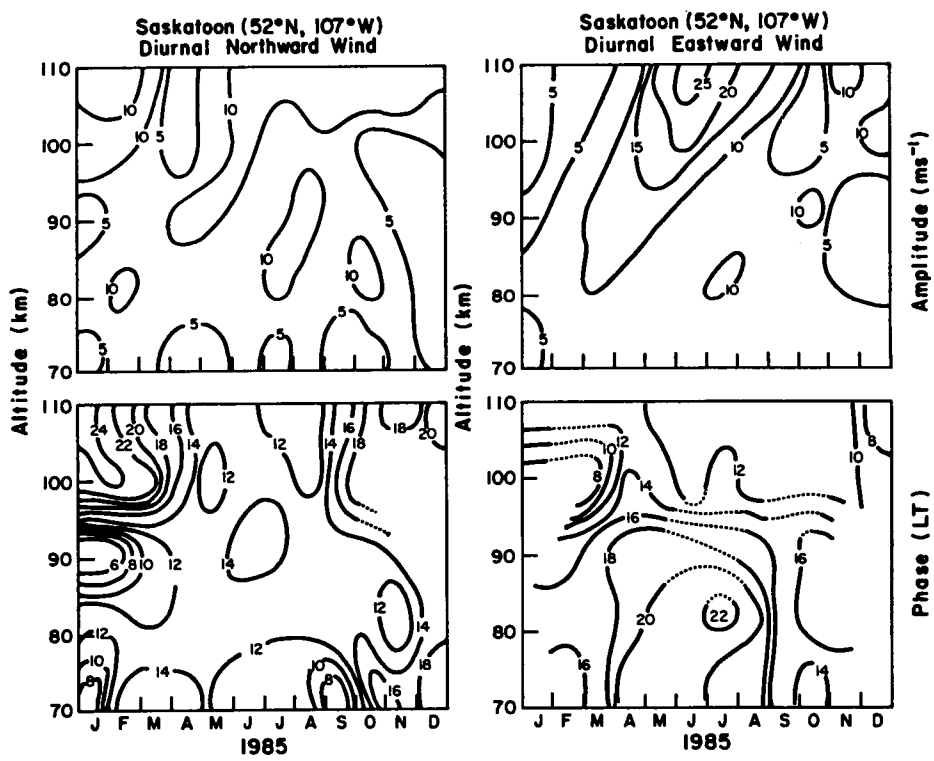


Figure 10. Diurnal tidal contours: Saskatoon 1985 (1 month resolution).

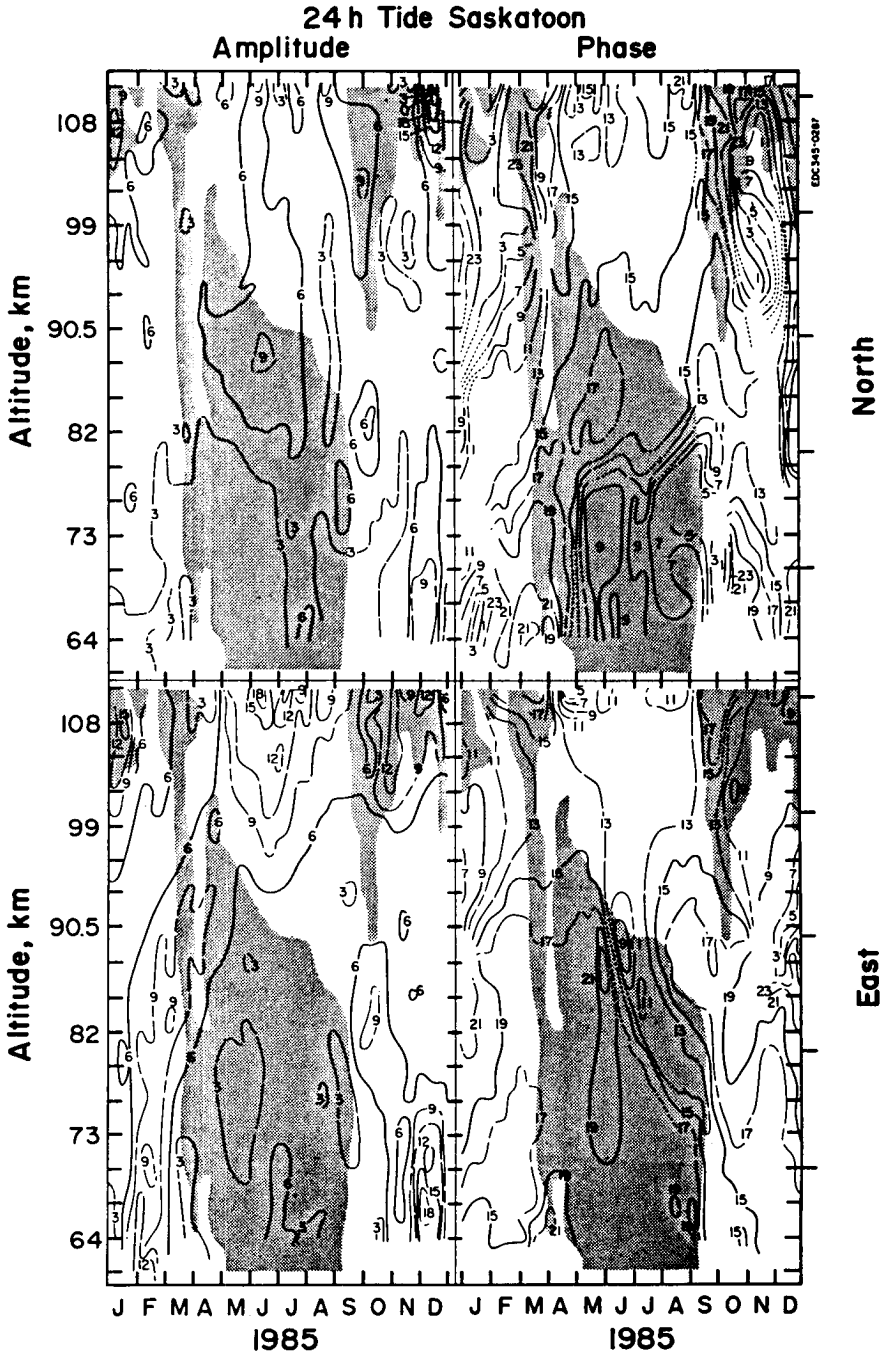


Figure 11. Diurnal tidal contours: Saskatoon 1985 (10 d resolution).

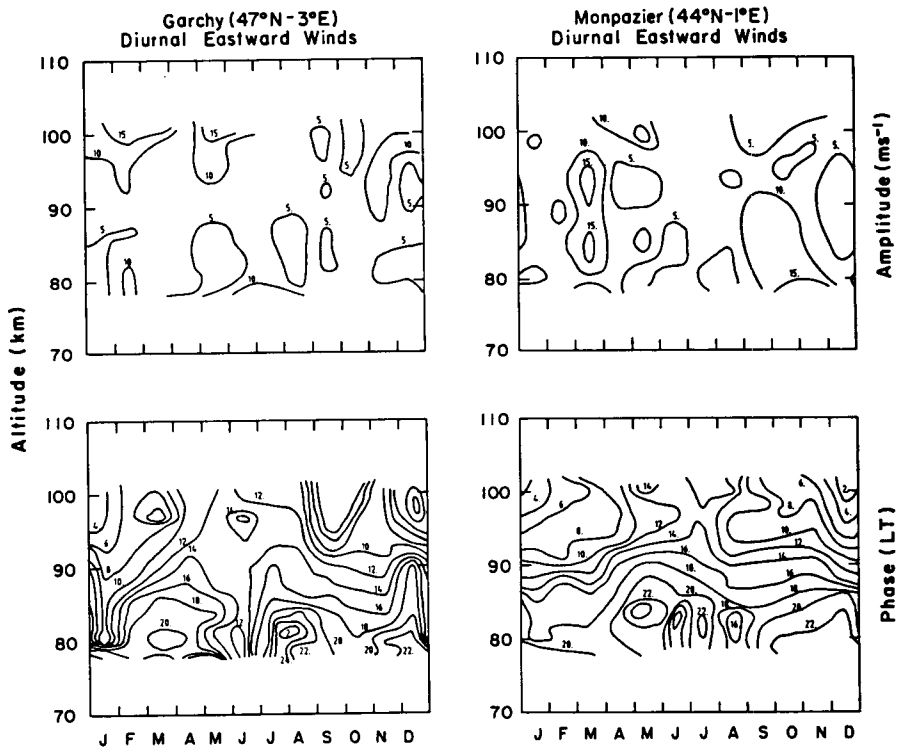


Figure 12. Diurnal tidal contours: Garchy 1970-76; Monpazier 1979-80.

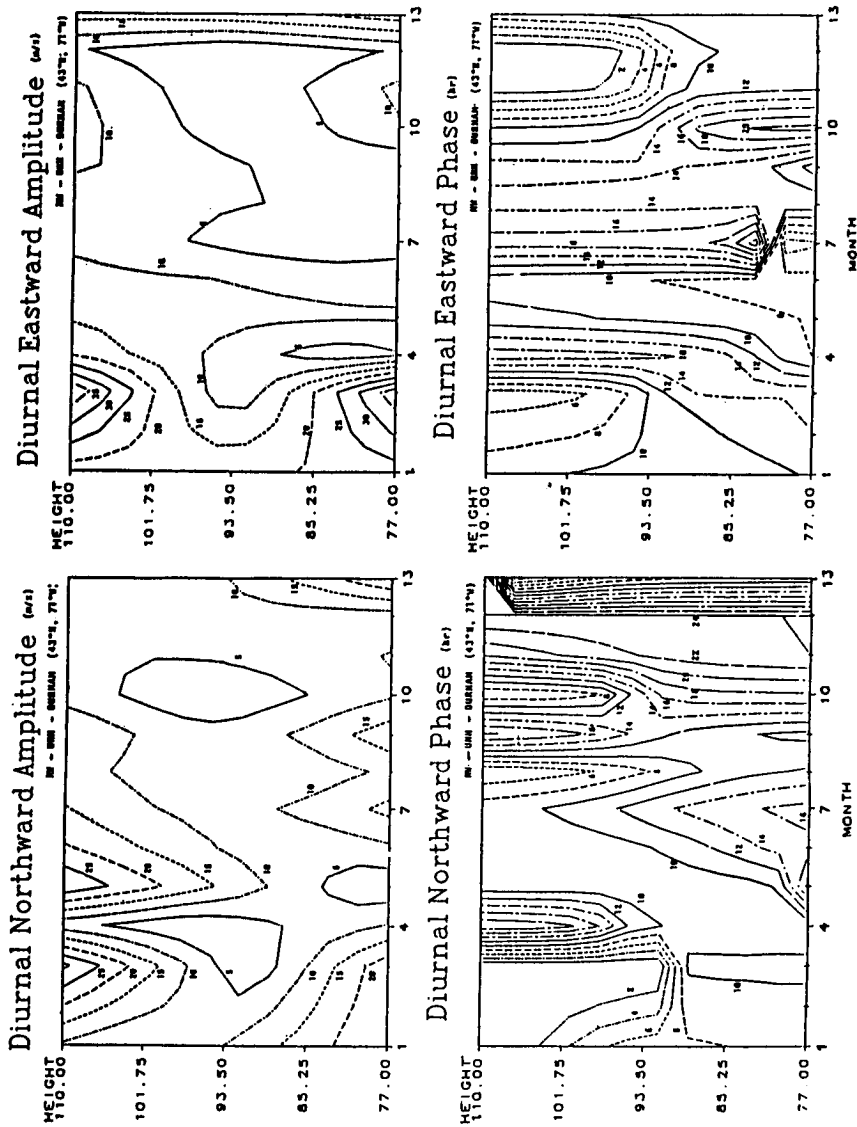


Figure 13. Diurnal tidal contours: Durham 1978-84.

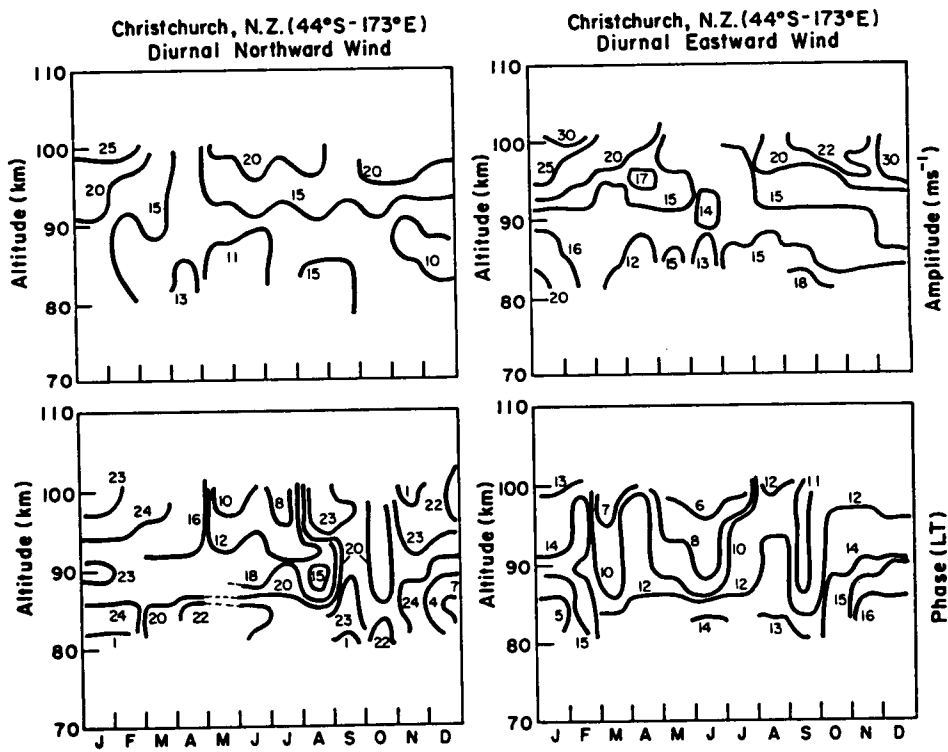


Figure 14. Diurnal tidal contours: Christchurch 1979-80.

8.5 RECENT PROGRESS IN TIDAL MODELING

F. Vial

Laboratoire de Meteorologie Dynamique du CNRS
Ecole Polytechnique, 91128 Palaiseau Cedex, France

J. M. Forbes

College of Engineering, Boston University
110 Cummington Street, Boston, MA 02215

Recent contributions to tidal theory during the last five years are reviewed. Specific areas where recent progress has occurred include: the action of mean wind and dissipation on tides, interactions of other waves with tides, the use of TGCM in tidal studies. Furthermore, attention is put on the nonlinear interaction between semidiurnal and diurnal tides. Finally, more realistic thermal excitation and background wind and temperature models have been developed in the past few years. This has led to new month-to-month numerical simulations of the semidiurnal tide. Some results using these models are presented and compared with ATMAP tidal climatologies.

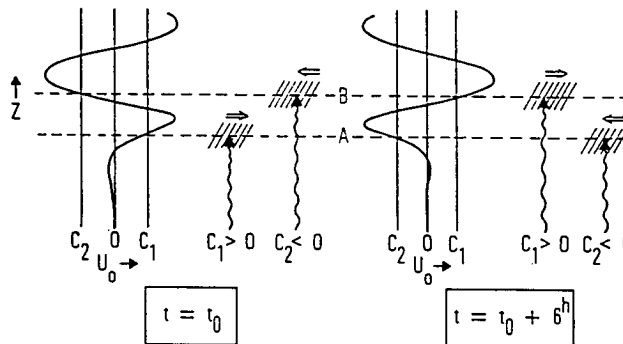


Figure 1. Schematic representation of modulation of wave-mean flow interaction by imposed tidal oscillation. U_0 represents the tidal velocity, c_1 and c_2 the phase velocities of the two waves whose upward propagation is denoted by the wavy lines. The hatched areas indicate regions where the waves are significantly absorbed. The open arrows indicate the sense of the acceleration induced by absorption [Walterscheid, *J. Geophys. Res.*, 86, 9698 1981].

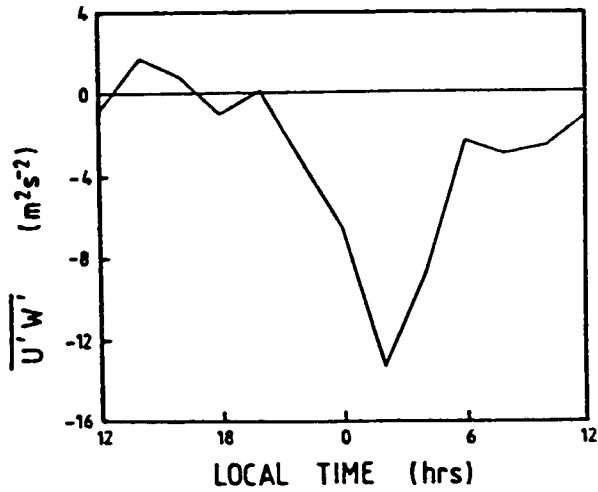


Figure 2. Mean momentum flux as a function of local time as measured with an MF radar at Adelaide (35°) during the 9 - 17 June 1984 period [Fritts and Vincent, *J. Atmos. Sci.*, 44, 605, 1987].

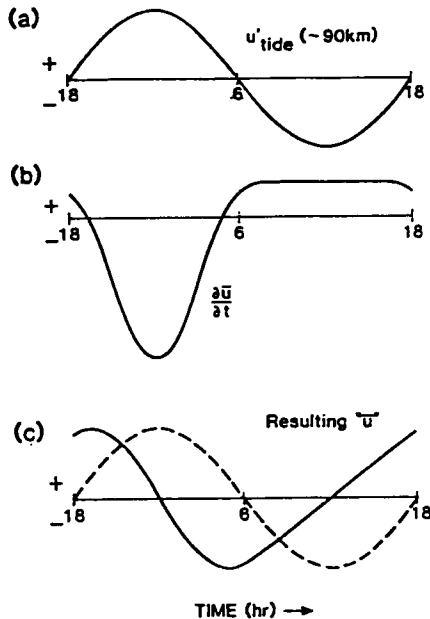


Figure 3. Schematic illustrating the effects of diurnally varying zonal drag on the inferred tidal structure. The results are an altered amplitude and an advanced phase of the apparent tidal motion [Fritts and Vincent, *J. Atmos. Sci.*, 44, 605, 1987].

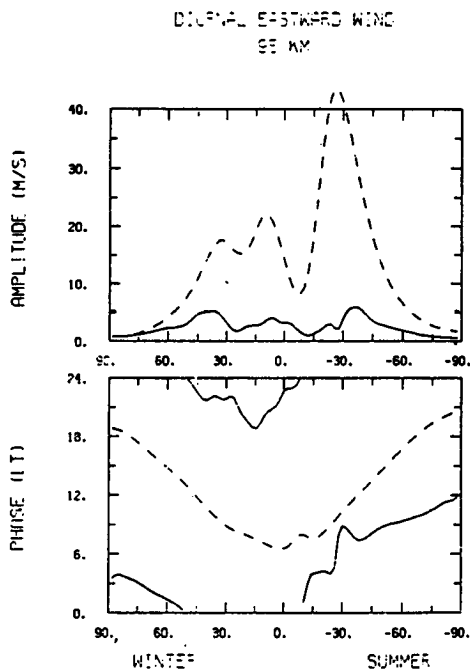


Figure 4. Comparison of the latitudinal structure of amplitude and phase of solar-driven (solid line) and nonlinear (dashed line) diurnal tides at 95 km for solstices conditions [H. Teitelbaum et al., private communication].

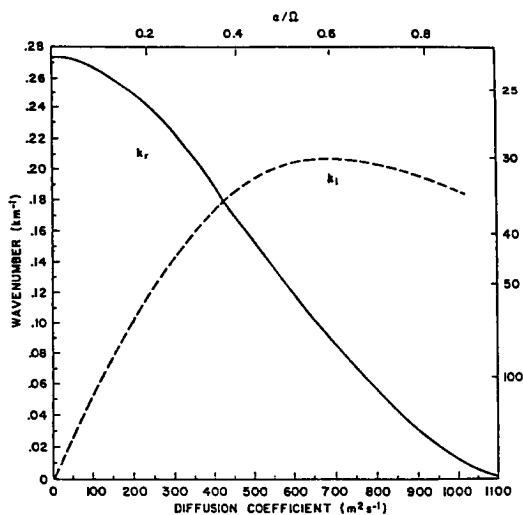


Figure 5. Real and imaginary part of the diurnal tide vertical wave number plotted as a function of eddy diffusion K_{zz} , and equivalently as a function of the Rayleigh friction coefficient α normalized to the earth rotation rate Ω [Forbes and Vincent, Planet. Space Sci., 1988, in press].

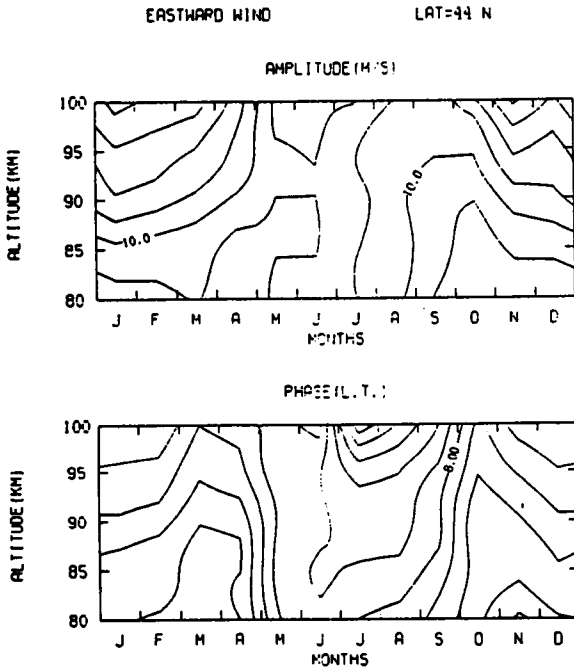


Figure 6. Height vs month contour of amplitude and phase structures at 44° N obtained from monthly simulations of the semidiurnal tide. Contours are plotted with steps of 5 m/s and 1 hour, respectively [Forbes and Vial, 1988, this volume].

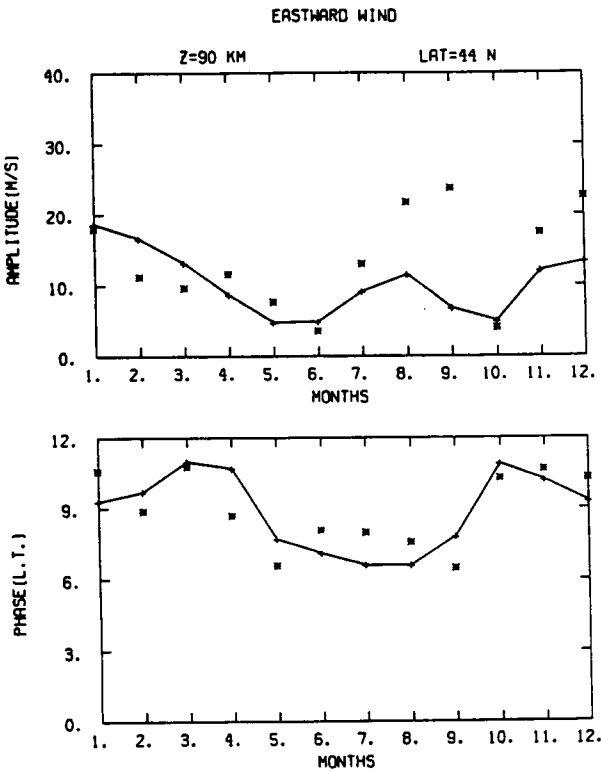


Figure 7. Semidiurnal modeled amplitude and phase at 90 km and 44° N obtained from monthly simulations of the semidiurnal tide. Comparisons are made with monthly tidal climatology data from Monpazier (44°N) [Forbes and Vial, 1988, this volume].

8.6 LONG-TERM VARIATIONS IN MIDLATITUDE SOUTHERN HEMISPHERE MESOSPHERIC WINDS

G. J. Fraser

Physics Department, University of Canterbury
Christchurch 1, New Zealand

This paper presents the monthly mean zonal winds and semidiurnal tides at 80 and 90 km, in January and July, at Christchurch (44°S) for the period 1978-1986. There are significant trends but evidence for solar control of the mean zonal wind and the semidiurnal tide is not conclusive.

OBSERVATIONS

LOCATION: Christchurch 44S 173E

RADAR: Medium frequency partial reflection spaced antenna mode

TIME-SPAN: 1978 - 1986 (no instrumental changes)

MONTHS: January (summer) July (winter)

HEIGHTS: 80 and 90 km
(with supplementary information from other heights)

Note: Summer night-time noise level restricts
summer tidal analysis to above 85 - 87 km

Models for comparison:

THE MEAN ZONAL WIND:

1. Ageostrophic analysis (C.J.Marks,1988) of Barnett and Corney (1985) satellite model
2. Koshelkov (1985) rocket data for 40S and 50S

THE SEMIDIURNAL TIDE:

Forbes and Gillette (1982)

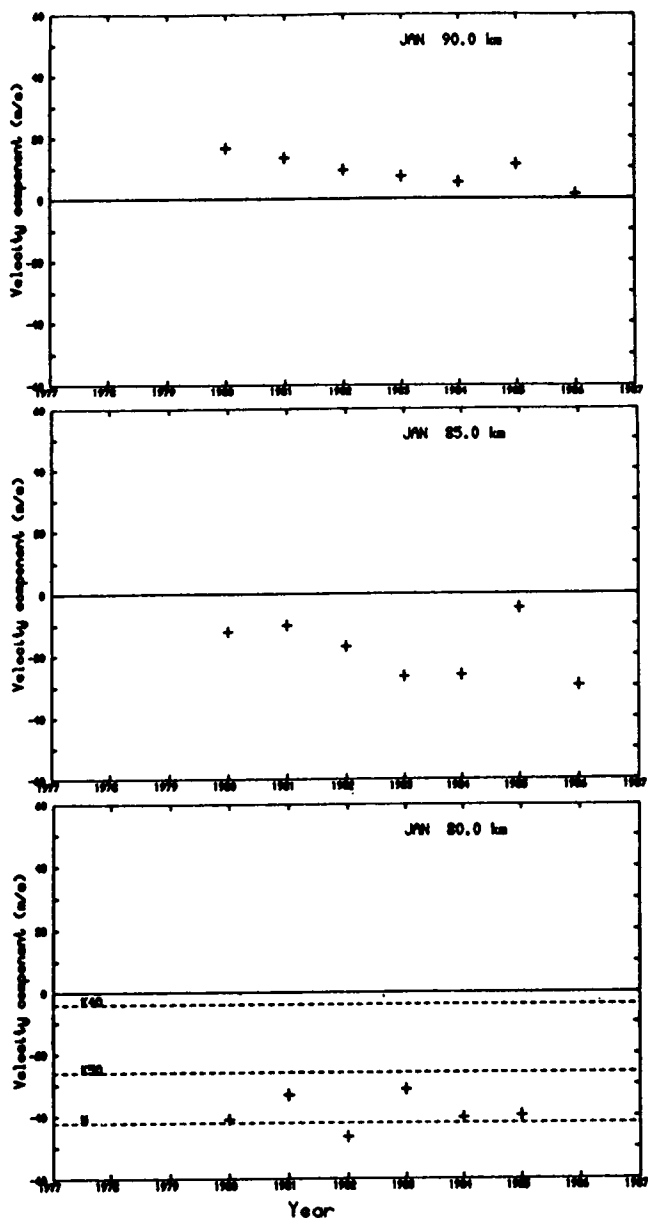


Figure 1. Monthly mean zonal winds in January (summer). At 80 km there is little variation between 1980 and 1986, and agreement with the ageostrophic satellite winds and the 50 S rocket model is good. At 90 km there is a decreasing zonal wind but comparison with 85 km suggests that it may be an increasing easterly trend rather than a decrease in magnitude.

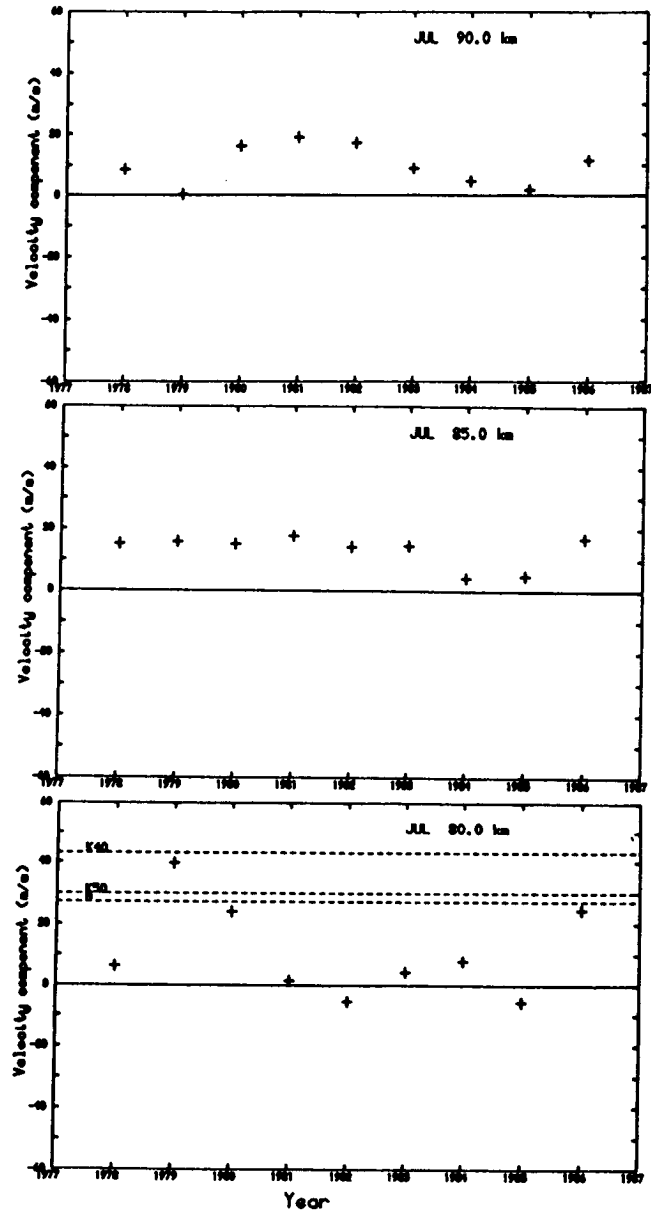


Figure 2. Monthly mean zonal winds for July (winter). At 80 km the winds are variable and agree with the models in only three of the nine years. At 90 km there is a quasi-oscillatory variation with minima in 1979 and 1985. The decreasing trend from 1981 to 1985 resembles that at 90 km in January (Figure 1). At 85 km there is little variation over the nine years apart from the decreases in 1984 and 1985.

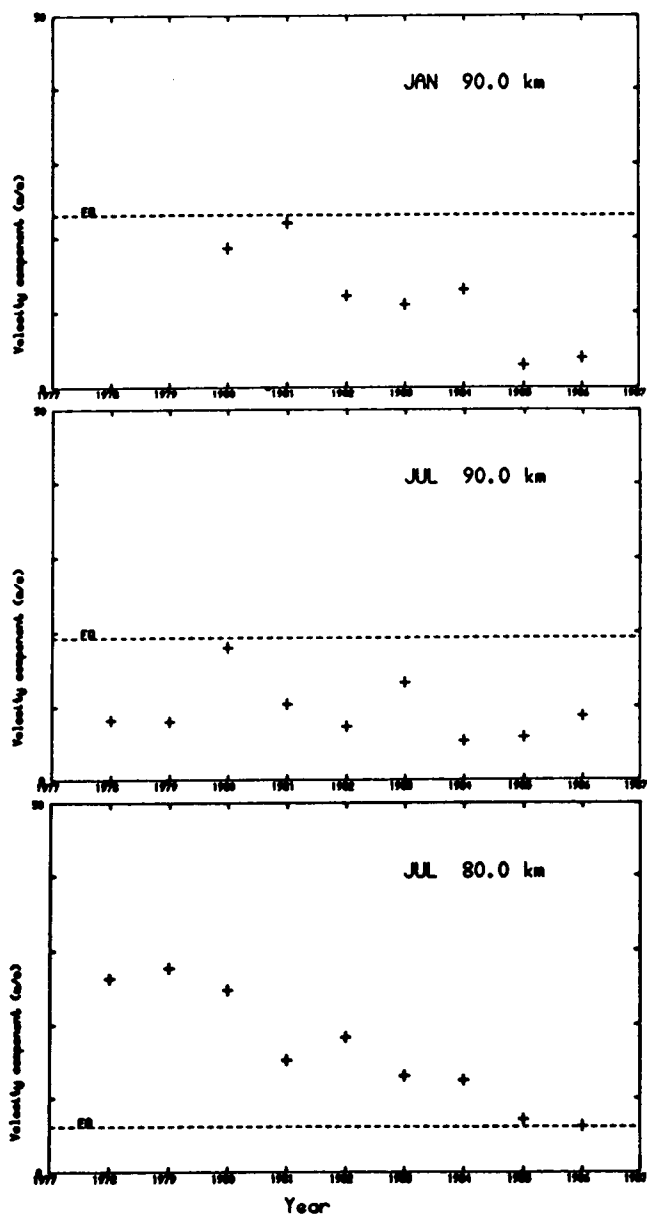


Figure 3. The January semidiurnal tidal amplitude. All three graphs show a general decrease in tidal amplitude over the period studied, to a lesser extent at 90 km in July.

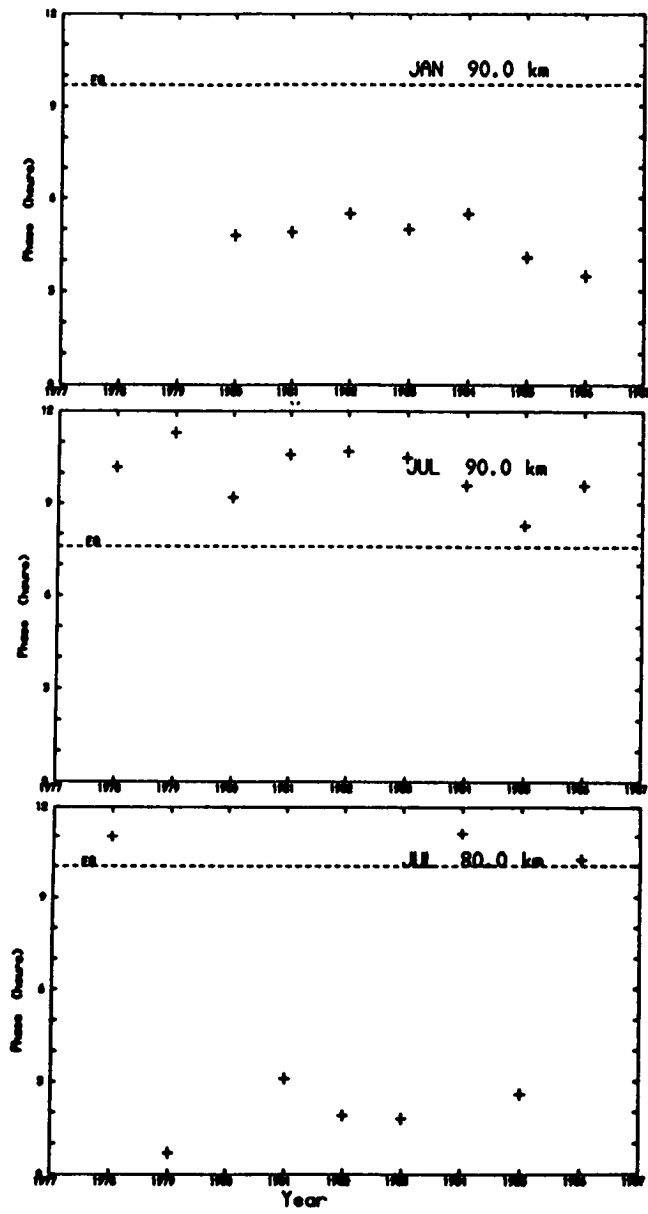
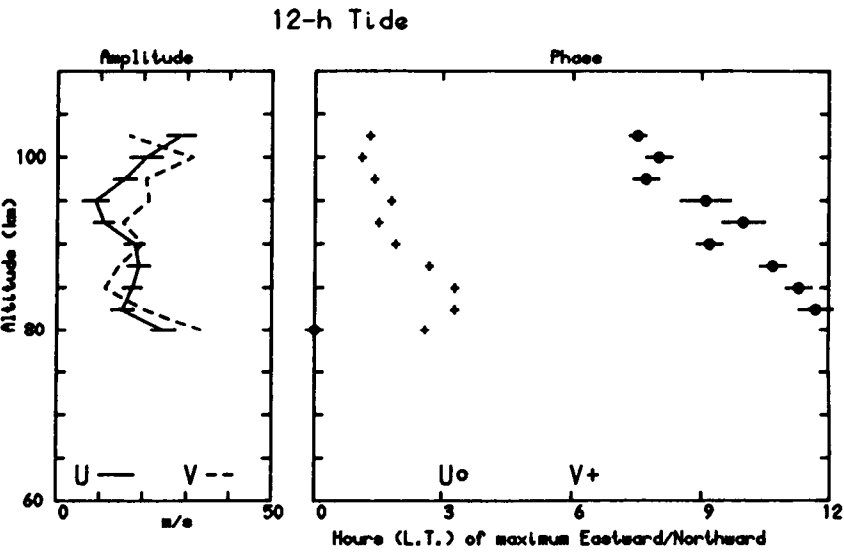


Figure 4. There is no significant trend in tidal phase, in contrast with that observed in the amplitudes (Figure 3).

CHRISTCHURCH 1980 JUL 2 TO 1980 JUL 31



CHRISTCHURCH 1986 JUL 1 TO 1986 JUL 31

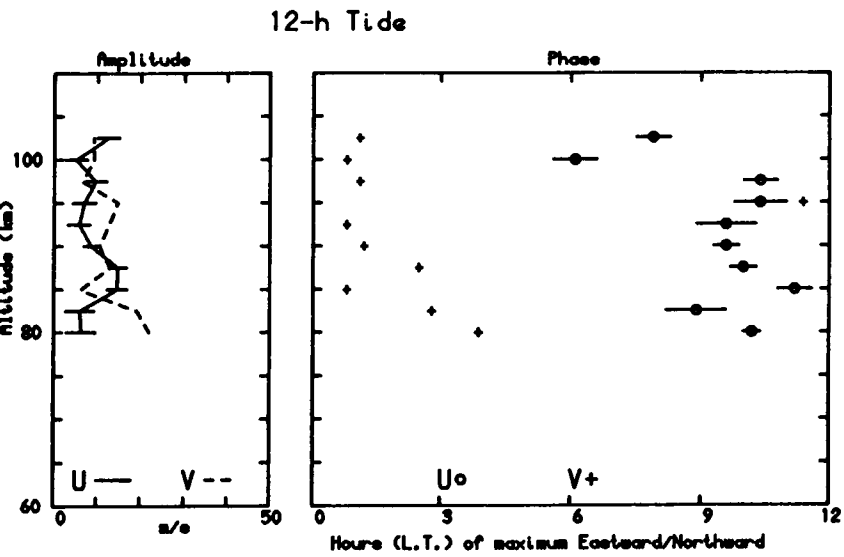


Figure 5. Tidal profiles for July 1980 and 1986. These confirm that the 1986 tides are much weaker than the 1980 tides as shown by the smaller amplitude and fluctuating phase.

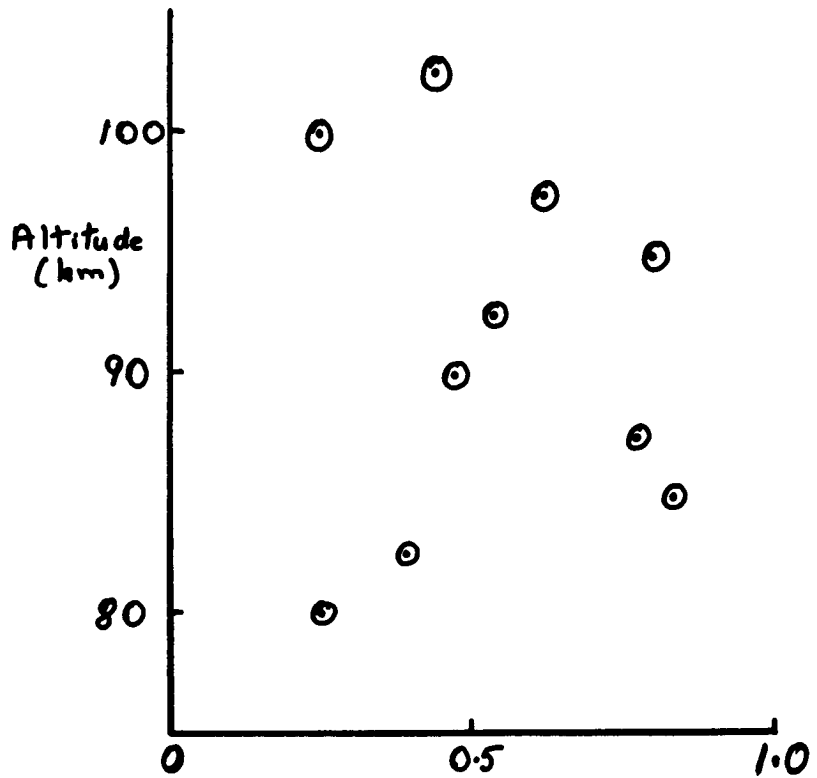
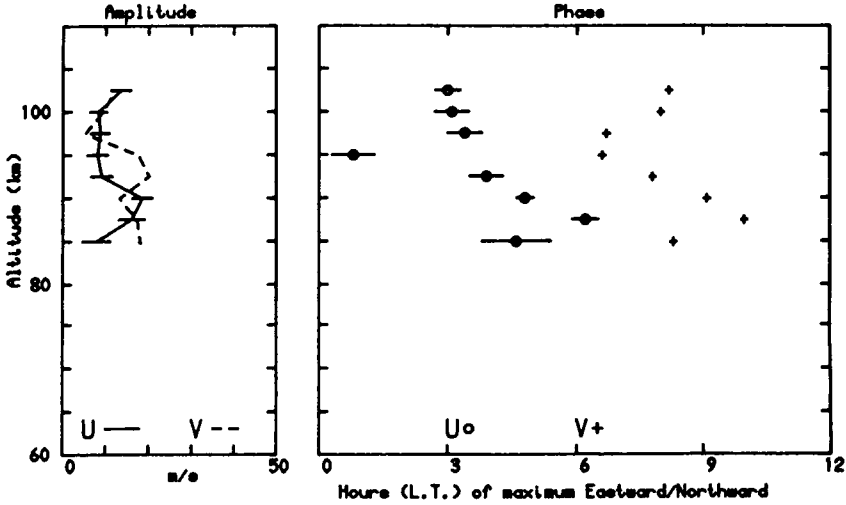


Figure 6. The decrease in amplitude at all heights in July is confirmed by the ratio of 1986 to 1980 amplitudes, taken from the previous diagram. There is some scatter but all the ratios are less than 1.

CHRISTCHURCH 1980 JAN 1 TO 1980 JAN 31

12-h Tide



CHRISTCHURCH 1986 JAN 1 TO 1986 JAN 17

12-h Tide

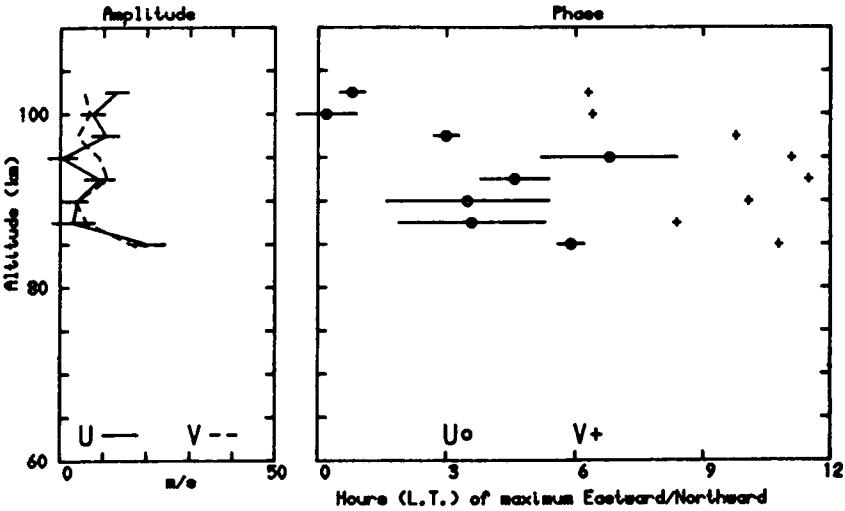


Figure 7. Comparison of the tidal profiles in January is more difficult because the 1986 observations only cover 1 - 17 January and there also are some missing days in that interval. The inadequate nighttime data restricts useful observations to above 85 - 87 km. Within these limitations there is no obvious reduction in tidal amplitude.

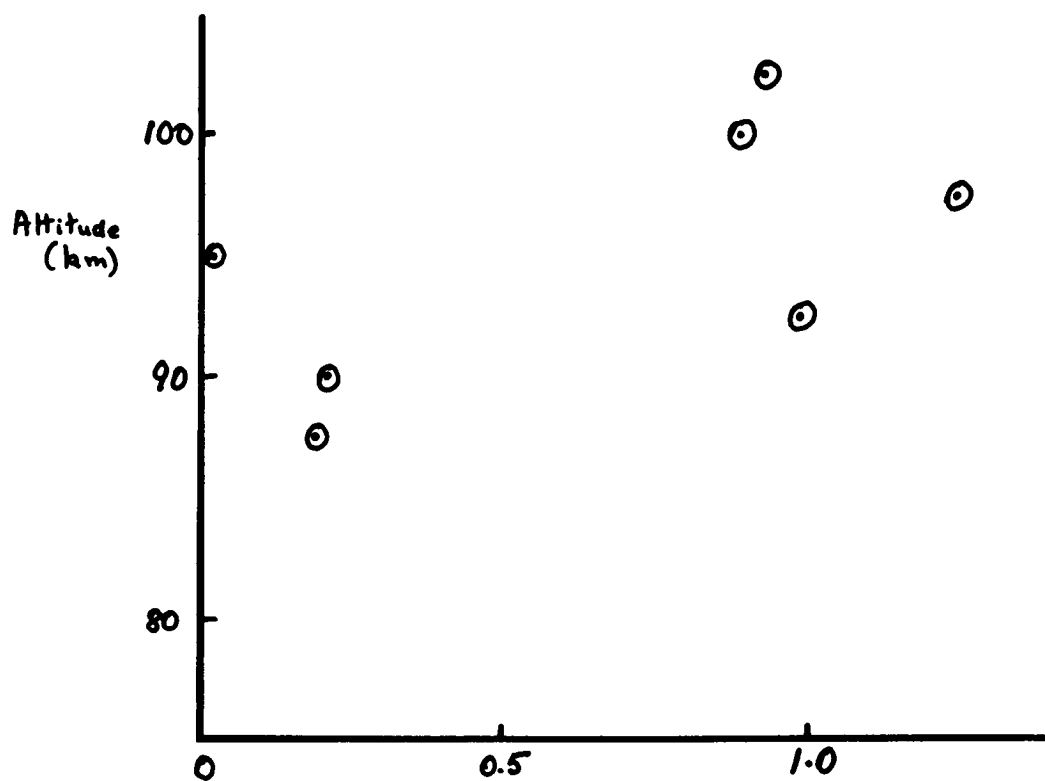


Figure 8. The observational scatter and lack of an obvious trend in January are supported by this plot of the amplitude ratio for 1986 and 1980.

8.7 THE GEOMAGNETIC CONTROL OF THE LOWER THERMOSPHERE WIND SYSTEM OVER EAST SIBERIA

E. S. Kazimirovsky, G. V. Gergasova, E. I. Zhovty, and M. A. Chernigovskaya

SibIZMIR, P. O. Box 4
Irkutsk 33, 664033 USSR

The geomagnetic control of ionospheric D-region dynamics was revealed and confirmed on the basis of radiophysical wind measurements (1978-1983) over East Siberia. The monthly mean parameters of the wind system are different for quiet ($K_p \leq 3$) and disturbed ($K_p > 3$) conditions. There is an increase in stability of the meridional wind with increasing level of geomagnetic activity. The influence of geomagnetic storms on the measured wind is considered on the basis of 31 events. There are effects on the phase of the semidiurnal tidal wind, but variations of amplitude are weak. The effect of the geomagnetic storm depends on the intensity and is more clear-cut for the $A_p > 100$.

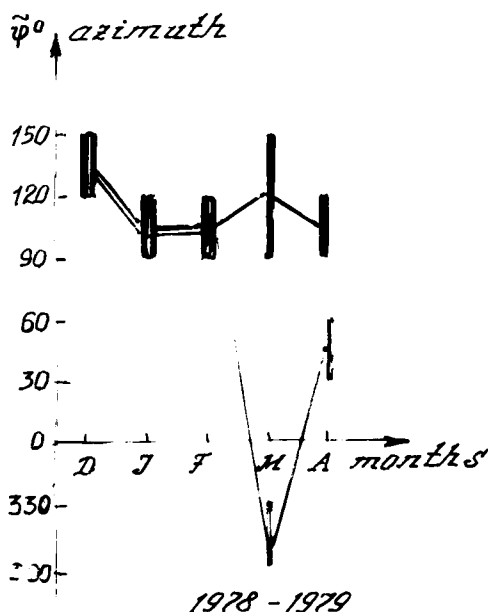


Figure 1. The most probable azimuths of D-region wind over East Siberia for quiet and disturbed conditions.

$$V_k(t) = V_{ak} + \sum_{j=1}^3 V_{jk} \cdot \cos\left[\frac{2\pi j}{12}(t - \tau_{jk})\right] + \delta_k(t), \quad (1)$$

$$k = x, y; \quad j = 1, 2, 3.$$

$$\Delta V_{jk} = |V_{jk}^q - V_{jk}^d|, \quad \Delta \tau_{jk} = |\tau_{jk}^q - \tau_{jk}^d|, \quad (2)$$

$$j = 0, 1, 2, 3; \quad k = x, y.$$

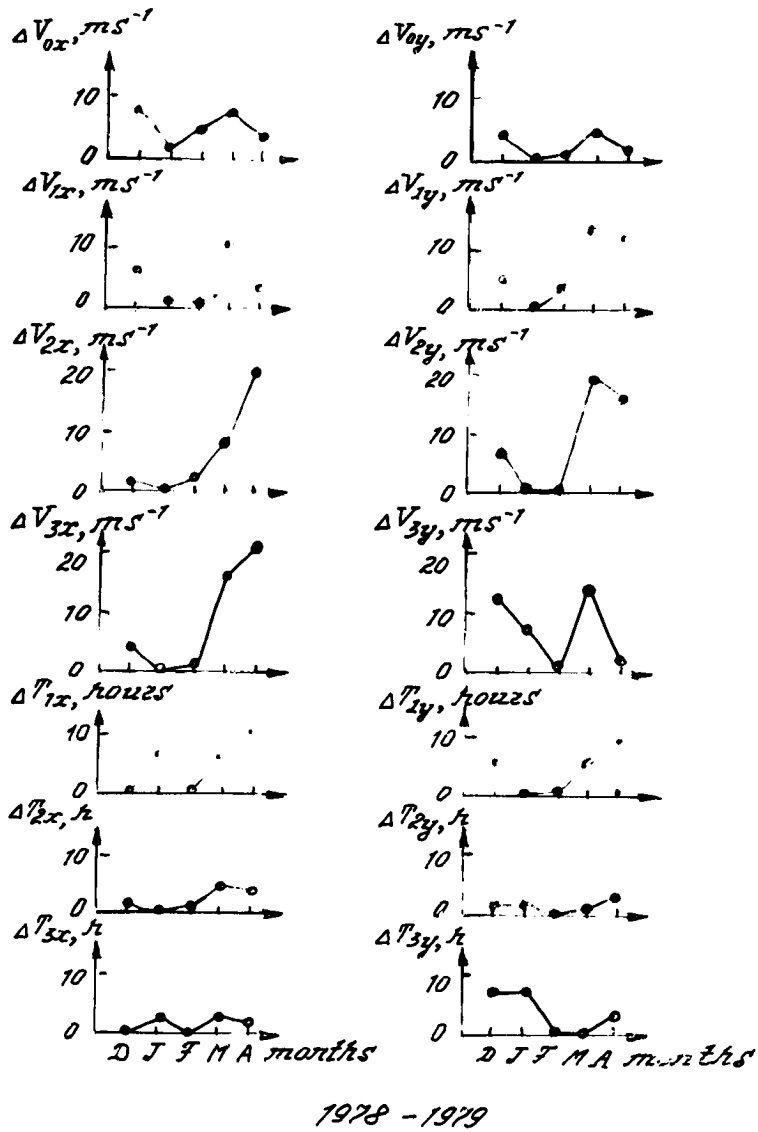


Figure 2. The variations of absolute differences between quiet and disturbed amplitudes and phases (ΔV_{jk} and ΔT_{jk}).

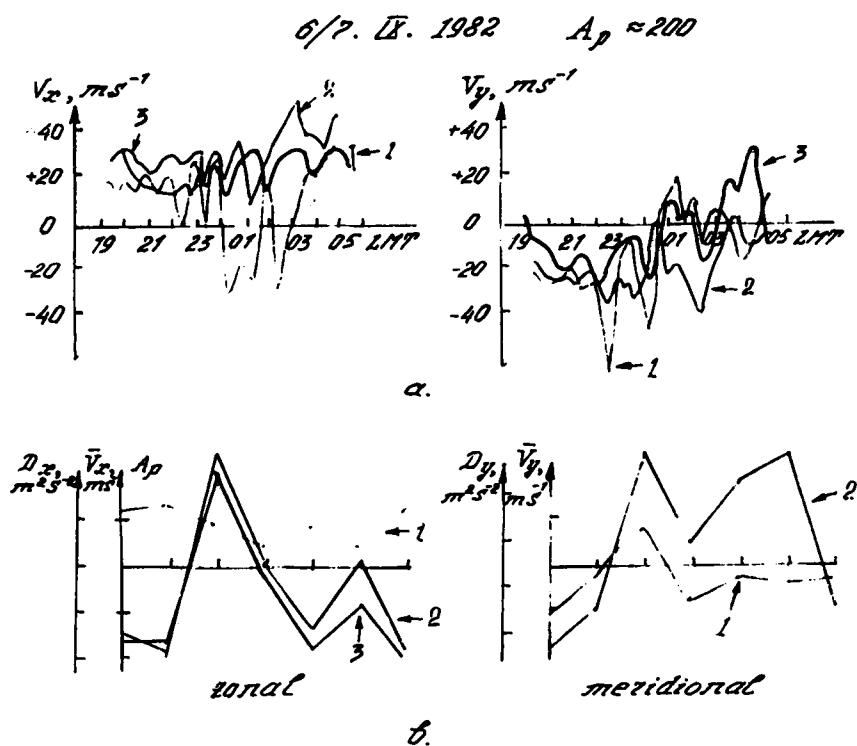


Figure 3. (a) Diurnal variations of prevailing wind (V_x - zonal, V_y - meridional) for the day of magnetic disturbance (curve 1), one day before (curve 2) and one day after (curve 3). (b) The variations of average amplitude (curve 1), dispersion (curve 2) and A_p index (curve 3).

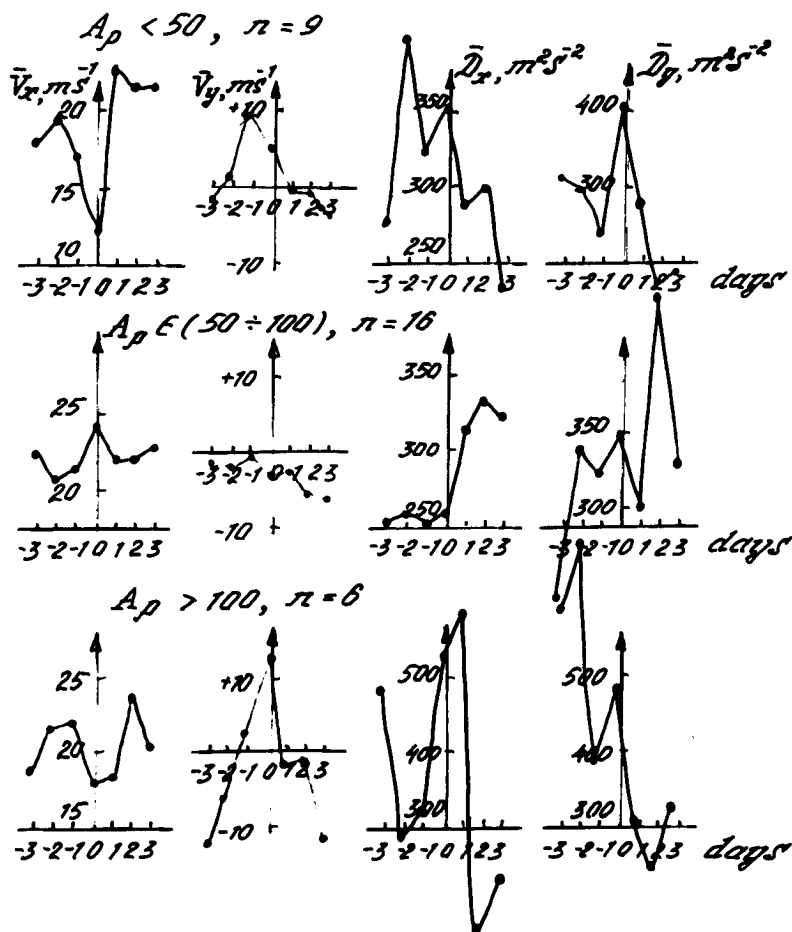


Figure 4. The comparison of geomagnetic storm effects for three levels of geomagnetic activity (V_x - zonal, V_y - meridional, D_x, D_y - dispersions). Superposed epoch method, 0-day with maximal value of A_p .

8.8 MIDLATITUDE SEASONAL BEHAVIOR OF TIDES NEAR THE MESOPAUSE LEVEL

E. S. Kazimirovsky and E. I. Zhovty

SibIZMIR, P. O. Box 4
Irkutsk 33, 664033 USSR

Wind measurements near the mesopause level were provided in Badary (Eastern Siberia, USSR) by the D1 method using a low-frequency (200 kHz) radio transmitter during 1976-1986. The seasonal variations of wind level are analyzed and compared with other midlatitude wind measurements and with some theoretical predictions. It is shown that tidal parameters depend not only on latitude but on the longitude as well. The annual variation of diurnal and semidiurnal tide (zonal and meridional) have maxima in summer and minima in winter. There are significant differences between annual variations of phases for diurnal and semidiurnal tides. These differences are especially distinct for summer and autumn. There is no systematic seasonal variation of the phase of the semidiurnal tide (average value ~ 6 hours).

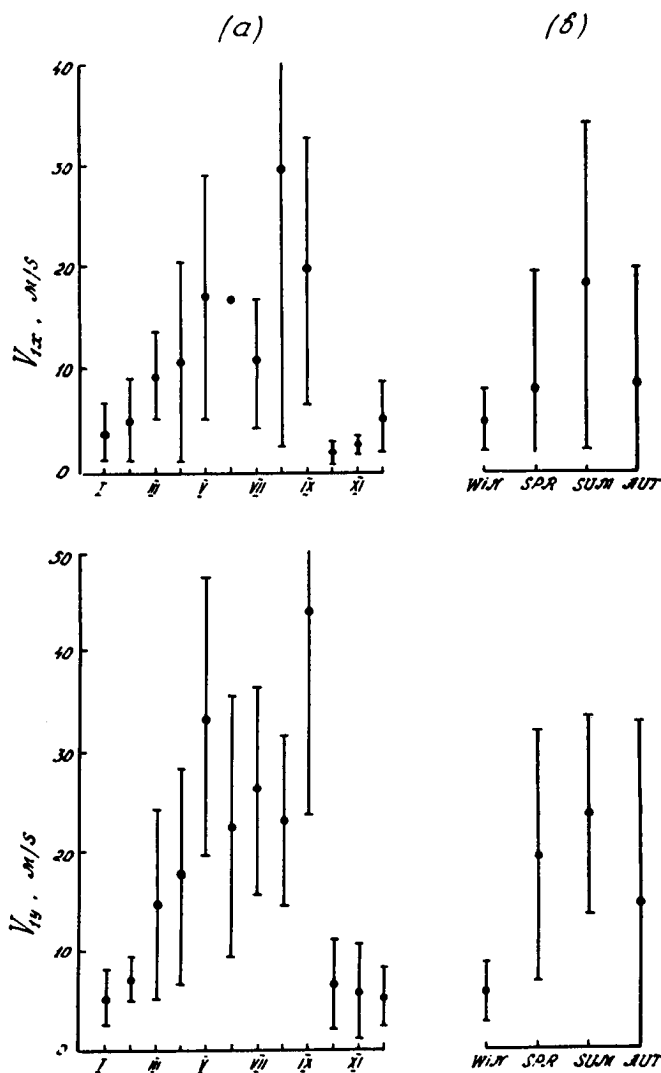


Figure 1. Monthly (a) and seasonally (b) averaged amplitudes for the zonal (V_{ox}) and meridional (V_{oy}) components of diurnal tide.

C-5

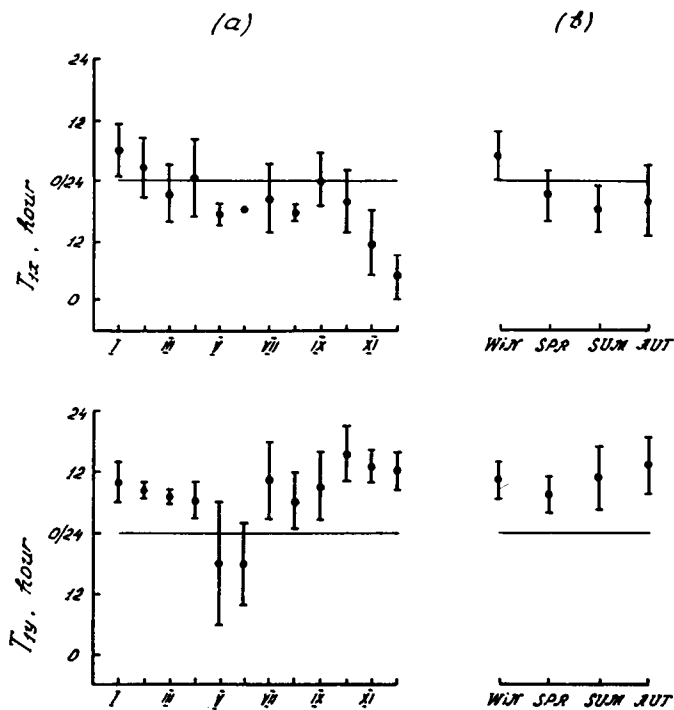


Figure 2. The same as for Figure 1 for the phase of diurnal tide.

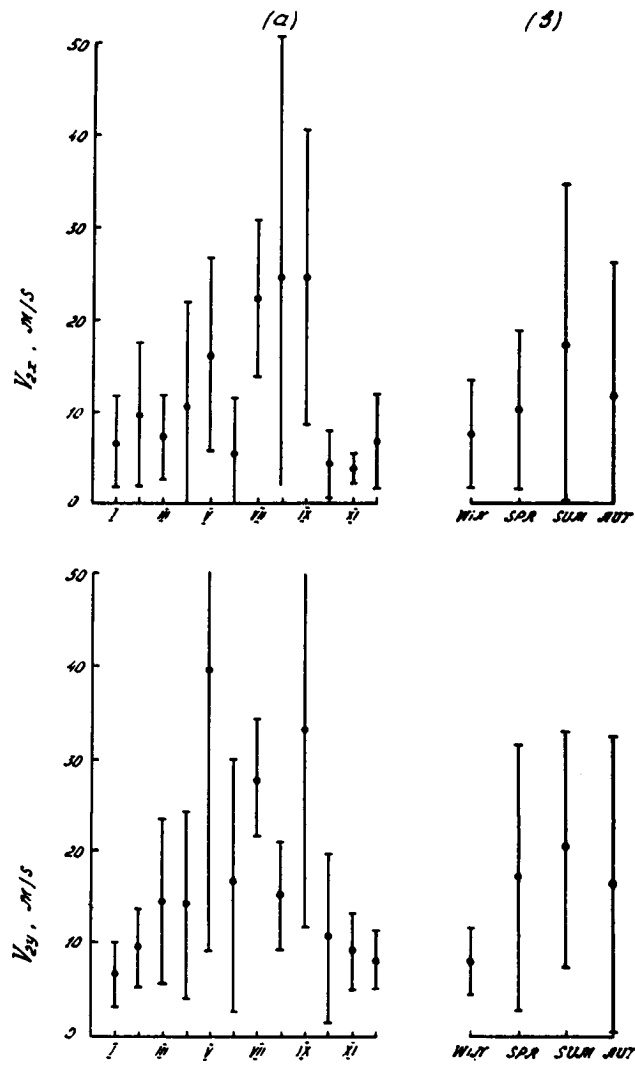


Figure 3. The same as Figure 1 for the amplitude of semidiurnal tide.

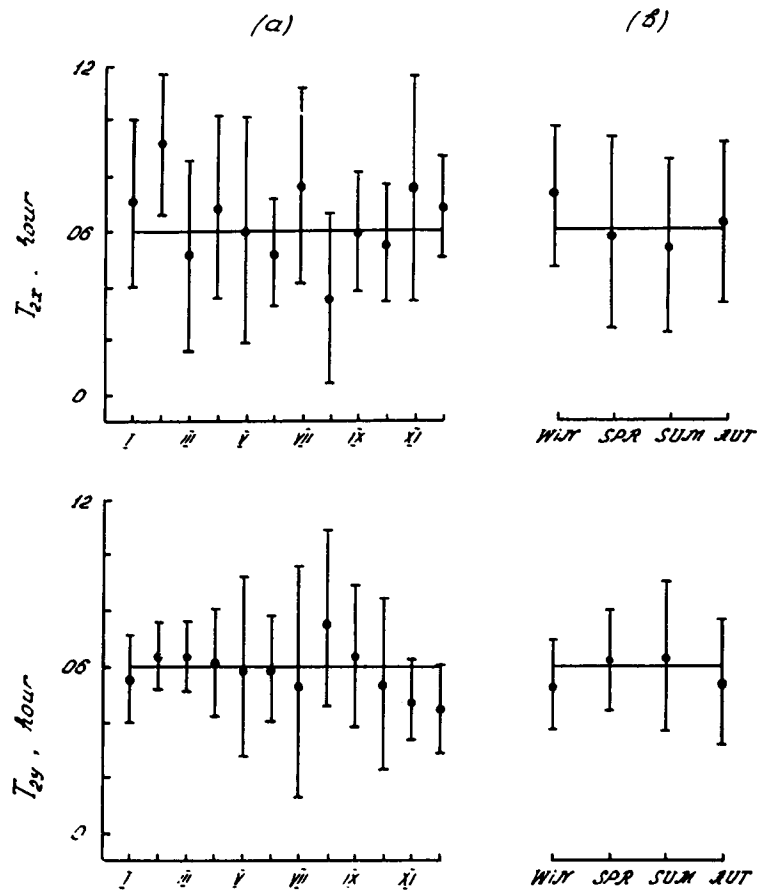


Figure 4. The same as Figure 1 for the phase of semidiurnal tide.

8.9 MEASUREMENTS OF VERTICAL MOTIONS BY THE SASKATOON MF RADAR (1983-85): RELATIONSHIPS WITH HORIZONTAL WINDS AND GRAVITY WAVES

A. H. Manson and C. E. Meek

Institute of Space and Atmospheric Studies, University of Saskatchewan
Saskatoon, Sask., S7N 0W0 Canada

The continuing series of horizontal wind measurements by the spaced-antenna real-time-winds (RTW) method was supplemented by a phase-coherent system for two years. Vertical motions are inferred from the complex autocorrelation functions, and an RTW system provides 5 min samples from 60 - 110 km. Comparisons with full interferometric 3-D velocity measurements confirm the validity of this approach. Following comparisons and corrections with the horizontal winds, mean summer and winter (24-h) days of vertical motions are shown. Tidal fluctuations are evident (≤ 1 m/s). In summer the motions are downward, consistent with data from Poker Flat, and the suggestion of Coy et al. [1986] that these represent Eulerian motions. The expected upward Lagrangian motion then results from adding up upward Stokes' drift. The winter motions are more complex, and are discussed in the context of gravity wave fluxes and possible meridional cells. The divergence of the vertical flux of zonal momentum is also calculated and found to be similar to the coriolis torque due to the meridional winds.

Coy, L., D. C. Fritts, and J. Weinstock, *J. Atmos. Sci.*, 43, 2636, 1986.

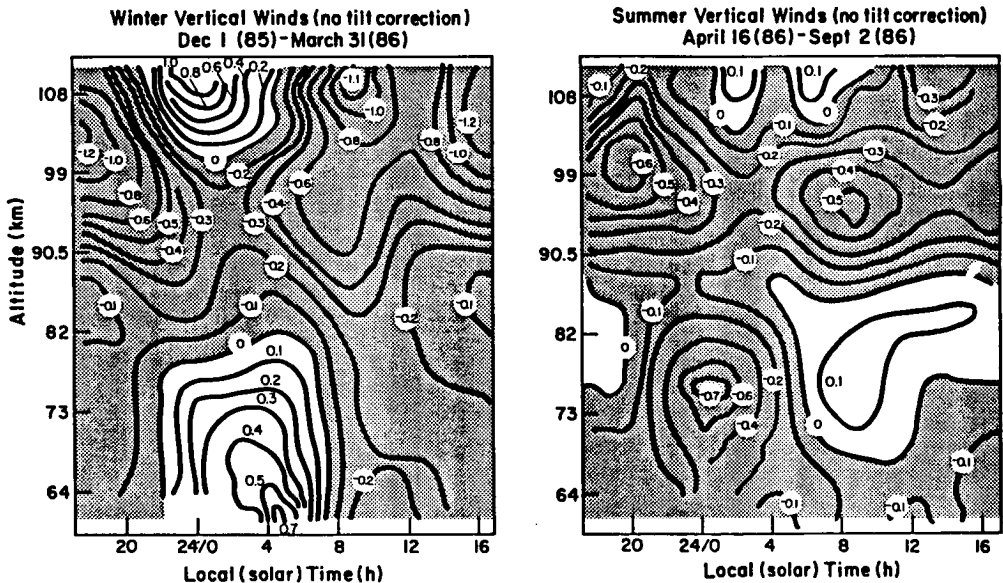


Figure 1. Mean vertical winds: above 99 km, data apply to a 5-km layer near 105 km.

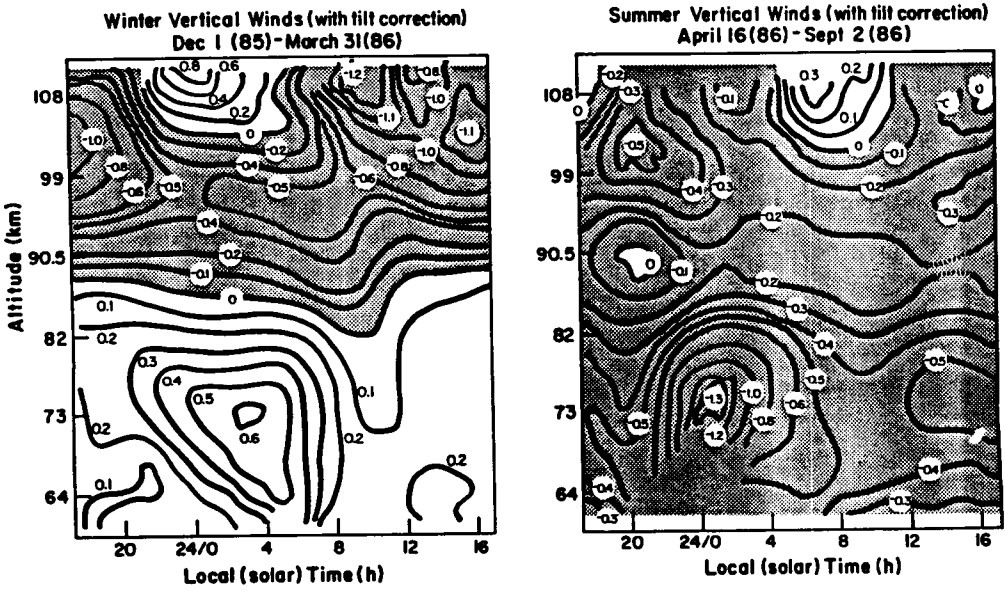


Figure 2. Mean vertical winds: tilt correction applied.

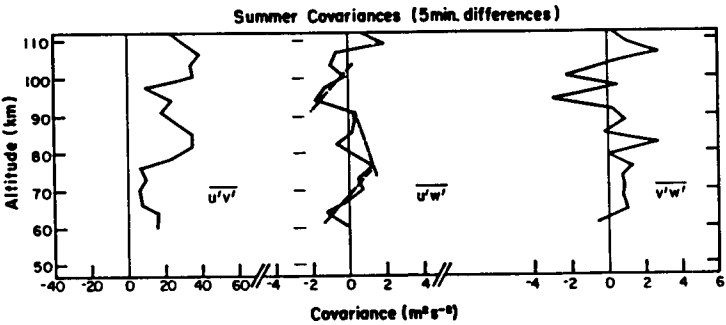


Figure 3. Covariances of wind perturbations ($10 < \tau < 100$ min).

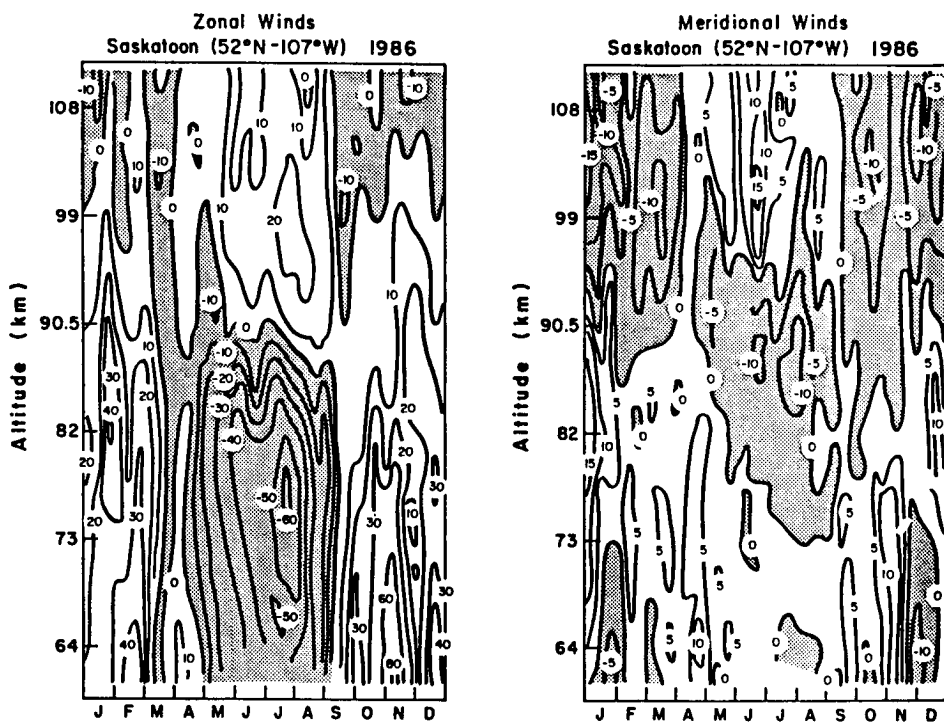


Figure 4. Mean circulation (as for Figure 1).

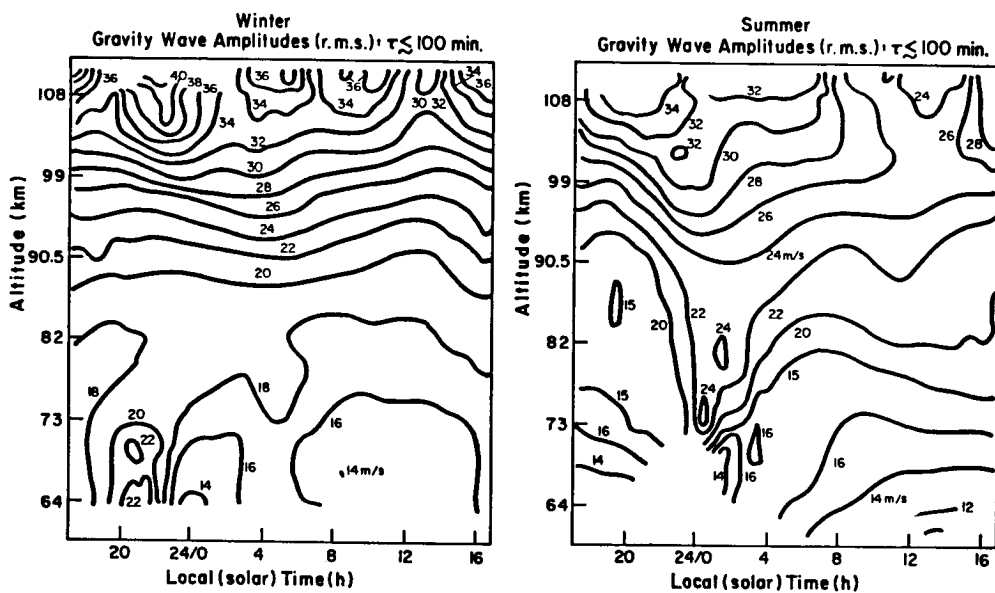


Figure 5. Gravity wave amplitudes 1985/6 (as for Figure 1).

8.10 NONLINEAR INTERACTION BETWEEN THE DIURNAL AND SEMIDIURNAL TIDES: TERDIURNAL AND DIURNAL SECONDARY WAVES

H. Teitelbaum and F. Vial

Laboratoire de Meteorologie Dynamique du CNRS
Ecole Polytechnique, 91128 Palaiseau Cedex, France

A. H. Manson

Institute of Space and Atmospheric Studies
University of Saskatchewan, Saskatoon, Saskatchewan, Canada S7N 0W0

R. Giraldez

Laboratorio Ionosferico de la Armada de la Republica Argentina
SENID and CONICET, Av. del Libertador 327, 1839 Vicente Lopez
Province Buenos Aires, Republica Argentina

M. Masseboeuf

CNET, CNRS, CRPE
4 Avenue de Neptune
94107 Saint-Maur des Fosses, France

Many years of measurements obtained using French meteor radars at Garchy (latitude 47°N) and Montpazier (latitude 44°N) are used to show the existence of an 8-hour oscillation. Some examples of the structure of this wave are displayed and compared with measurements performed at Saskatoon (latitude 52°N) and Budrio (latitude 45°N). This wave can be interpreted as the solar-driven terdiurnal tide, or as the result of the nonlinear interaction between the diurnal and semidiurnal tides. Both hypotheses are tested with numerical models. Incidentally, the possible existence of a 24-hour wave resulting from this interaction is also studied.

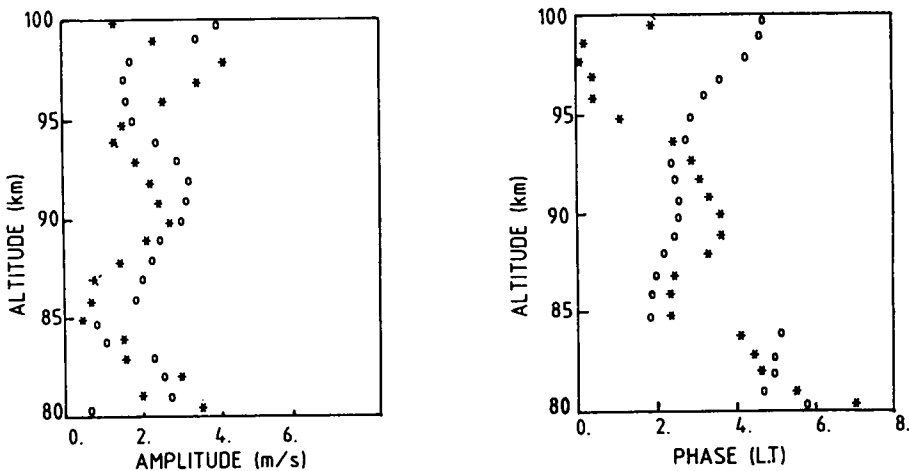


Figure 1. Amplitude and phase of terdiurnal tide (eastward wind), deduced from two simultaneous campaigns carried out at Garchy (47°N) and Montpazier (44°N) during the 8-20 July 1976 period.
o - Garchy, * - Montpazier.

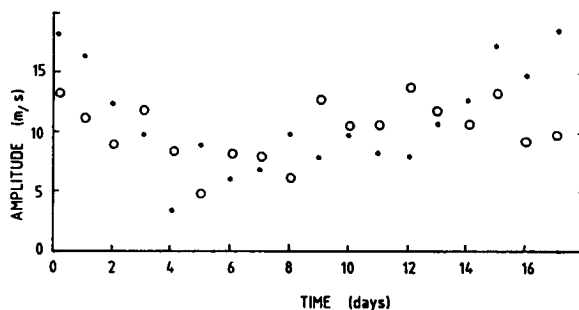


Figure 2. Short-time variation of the diurnal and terdiurnal tides for a single campaign. Garchy, 6 to 28 January 1976 period. Mean <90 - 95 km> eastward wind • - diurnal tide, o - terdiurnal tide.

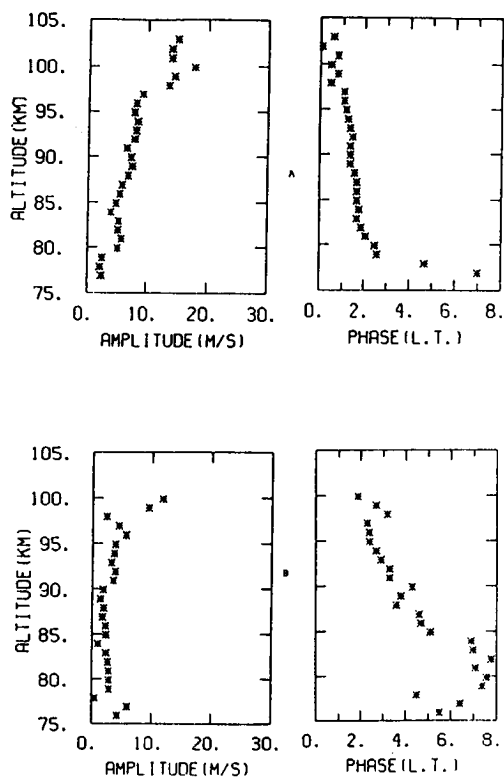


Figure 3. Terdiurnal monthly mean climatology for typical winter (a) and summer (b) months. Eastward wind at Garchy (47°N).

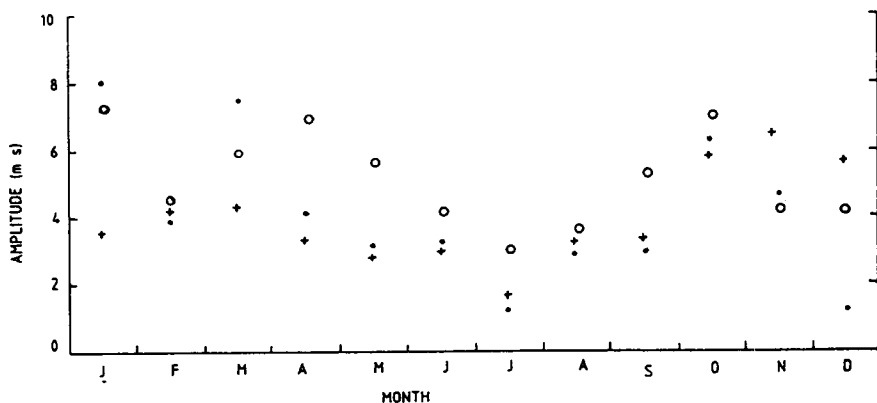


Figure 4a. Terdiurnal monthly mean climatology for all the months of the year and 94 km altitude: amplitude of the eastward wind at three different latitudes. • - Garchy (47°N), + - Montpazier (44°N), o - Saskatoon (52°N).

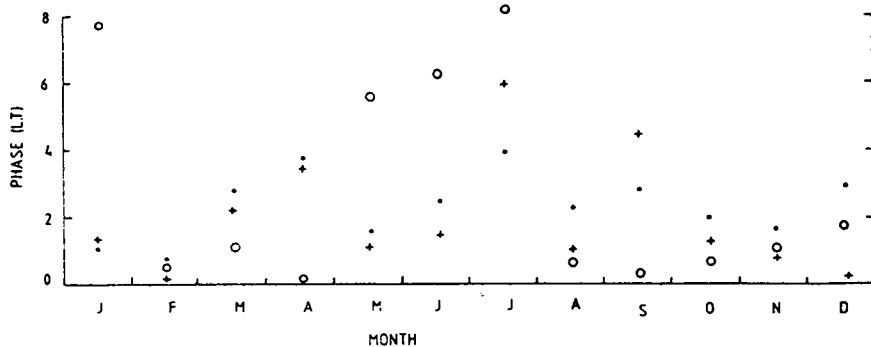


Figure 4b. The same as Figure 4a but for the phase. • - Garchy (47°N), + - Montpazier (44°N), o - Saskatoon (52°N).

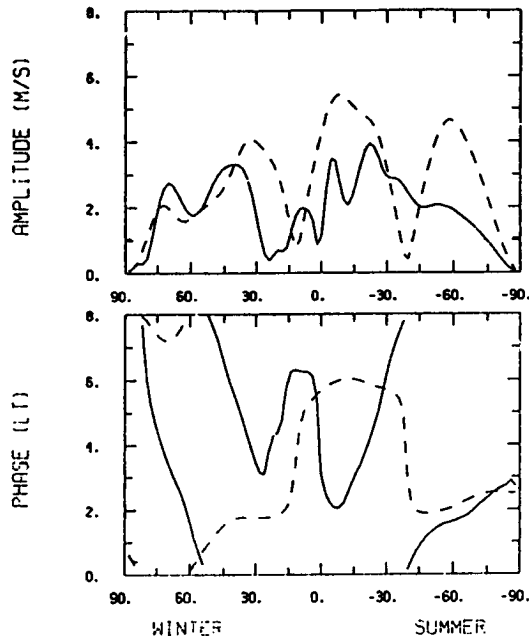


Figure 5. Latitudinal variation of the terdiurnal tide (eastward wind), for solstice conditions at 95 km altitude. The theoretical solar-driven and nonlinear waves are shown. The nonlinear wave is a secondary wave generated by the nonlinear interaction of the diurnal and semidiurnal tides. - - - solar-driven wave, — - nonlinear wave.

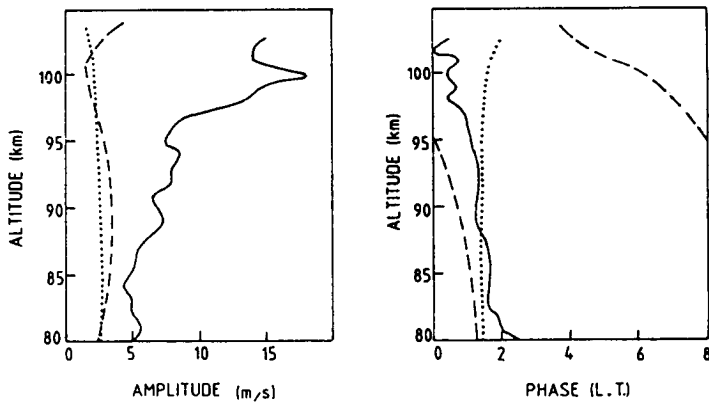


Figure 6. Eastward wind profile corresponding to the terdiurnal tide at 47° latitude in winter. Comparison of the data with the calculated solar-driven wave and with the superposition of the solar-driven and the nonlinear waves. — - data, . . . - solar-driven, - - - solar-driven plus nonlinear.

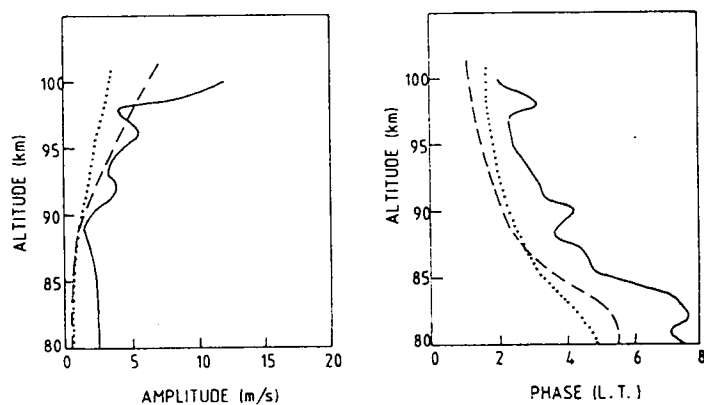


Figure 7. The same as in Figure 6 but in summer.

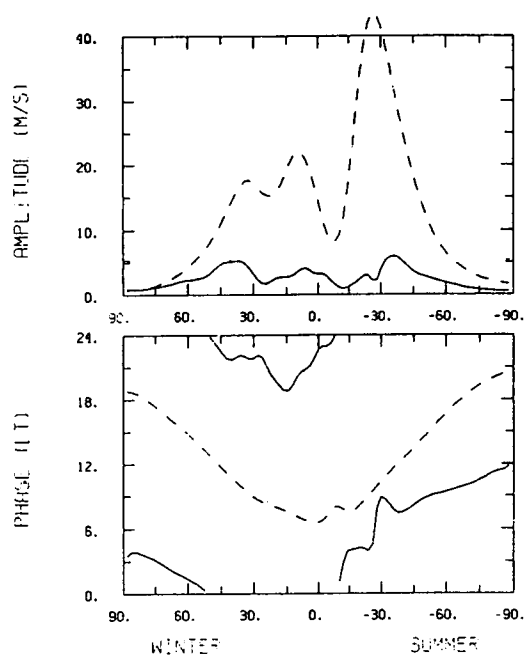


Figure 8. Latitudinal variation of the amplitude and phase of the diurnal nonlinear secondary wave for solstice conditions at 95 km altitude. The solar-driven diurnal tide is also shown. — - nonlinear secondary diurnal tide, --- - solar-driven diurnal tide.

9. MIDDLE ATMOSPHERE COOPERATION/ SUMMER IN NORTHERN EUROPE (MAC/SINE) AND MAC/EPSILON

9.1 THE MAC/SINE AND MAC/EPSILON CAMPAIGNS

E. V. Thrane

Norwegian Defence Research Establishment
P. O. Box 25, N-2007 Kjeller, Norway

Two major international campaigns dedicated to the study of middle atmosphere dynamics in high latitudes were successfully completed in 1987. MAC/SINE (Middle Atmosphere Cooperation/Summer in Northern Europe) was carried out during the period 7 June - 19 July, whereas MAC/Epsilon took place in the period 12 October - 15 November. In both campaigns a large number of ground-based and rocket techniques were used in a concerted effort to map the dynamical structure of the middle atmosphere over Northern Europe. Although the analysis of the observations has only just started, it is clear that a large and unique data set has been obtained, which we believe will provide new insight into the dynamical processes in this interesting region of the atmosphere. The paper will present a brief overview of the campaigns, their scientific aims, organization and structure.

Organization of MAC/SINE and MAC/Epsilon

Operation Center: Andoya Rocket Range

Project Scientist: Prof. E. V. Thrane

Deputy Project Scientist: Prof. U. von Zahn

Technical Coordinator: Mr. A. Gundersen

Logistics, Technical Management: Deutsche Forschungs- und Versuchsanstalt für Luft- und Raumfahrt eV., Koeln, Mr. O. Röhrig
Deutsche Forschungs- und Versuchsanstalt für Luft- und Raumfahrt E.V, Wessling, Mr. K. Zdarsky
NASA/GSFC Wallops Flight Facility, Mrs. D. L. Frostrom
Norwegian Space Center, Oslo, Mr. A. Gundersen

Sponsoring Organizations: Bundesministerium für Forschung und Technologie, Bonn
Deutsche Forschungsgemeinschaft, Bonn
National Aeronautics and Space Administration, Washington, DC
Norwegian Space Centre, Oslo
National Agencies in the Participating Countries

Measurements of Dynamical Processes

In order to map the dynamical processes in the middle atmosphere we must be able to measure:

Wind speed, density, temperature and pressure as well as small fluctuations of these parameters.

The problem:

To find experimental methods that work where the density is $1/1000\ 000$ of the air density at ground level. For studies of turbulence the accuracy must be better than 0.1%.

A solution:

Measurements of easily detectable trace constituents, such as positive ions.

Scientific goals:

To study dynamical processes, winds, waves and turbulence in the high latitude middle atmosphere.

To study the interaction between ionospheric/auroral phenomena and the nonionized upper atmosphere.

To study the effects of the ionosphere/middle atmosphere on radio wave propagation in high latitudes.

Experimental tools:

Rockets, SINE:

- 27 Falling spheres (Andoya)
- 28 Chaff (Andoya)
- 4 NASA instrumented rockets (Andoya)
- 12 USSR instrumented rockets (Heiss Island)
- 7 USSR instrumented rockets (Volgograd)
- 4 USSR instrumented rockets (Prof Zubov)

Rockets, Epsilon:

- 5 European instrumented rockets (built in Norway)
- 8 NASA instrumented rockets
- 12 Falling spheres (Andoya)
- 9 chaff (Andoya)
- 18 USSR instrumented rockets (Heiss Island)
- 17 USSR instrumented rockets (Volgograd)

Rocket launches from Andoya Rocket Range during MAC/SINE

Regular met.rocket firings Mondays, Wednesdays and Fridays at 1100 h UT
In addition, several salvos were launched to study specific phenomena:

- | | |
|-------------------------------|--------------|
| Chaff Salvo 1: | 24 June 1987 |
| Chaff Salvo 2: | 26 June 1987 |
| Chaff Salvo 3: | 1 July 1987 |
| Turbulence/Gravity Wave Salvo | 14 July 1987 |
| EISCAT Salvo | 15 July 1987 |
| Sodium/Chaff Salvo | 15 July 1987 |

GROUND-BASED EXPERIMENTS IN MAC/EPSILON

REV. 9 June 87

EXPERIMENT	OBSERVED PARAMETERS	LOCATION	REAL TIME	OPERATION
<u>PARTIAL REFLECTION</u>	e ⁻ DENSITY TURBULENCE	RAMFJORDMOEN	N Y	CD
<u>PRE DRIFT</u>	WINDS	RAMFJORDMOEN	Y	C
<u>PARTIAL REFLECTION</u>	TURBULENCE	VOLGOGRAD	N	C
<u>SOUSY VHF RADAR</u>	TURBULENCE WINDS	BLEIK	Y N	CD
<u>EISCAT</u>	e ⁻ DENSITY, A WINDS	RAMFJORDMOEN	N Y	B
<u>MS-RADAR</u>	WINDS	SASKATOON	N	C
<u>GLOBMET</u>	WINDS	USSR (7x1)	N	C
<u>METEOR RADAR</u>	WINDS	VOLGOGRAD	N	C
<u>HF-CIRCUIT</u>	PROPAGATION CONDITIONS	ANDENES-ALTA	N	C
<u>IONOSONDES</u>	IONOSPHERIC CONDITIONS	ANDENES, RAMFJORDMOEN	Y	A
<u>A1-ABSORPTION</u>	ABS. 2.2 MHz	VOLGOGRAD	N	C
<u>RIOMETERS</u>	ABSORPTION	ANDENES, FINLAND (9x), KIRUNA (KGI), RAMFJORDMOEN	Y	C
<u>MAGNETOMETERS</u>	GEOMAGNETIC CONDITIONS	ANDENES, FINLAND (Nx), KIRUNA (KGI), RAMFJORDMOEN	Y	C
<u>UB LIDAR</u>	TEMPERATURE NA-DENSITY, DENSITY	ANDENES	N Y	CS
<u>UI LIDAR</u>	NA-DENSITY, WINDS	LONGYEARBYEN	N	CS
<u>CNRS LIDARS</u>	DENSITY, TEMPERATURE	SKIBOTN, ON SHIP	N	CS

A EVERY 20 MINUTES
 B SOME(10?) NIGHTS 15-21 UT
 C CONTINUOUS
 CD CONTINUOUS DURING COUNTDOWNS
 CS CONTINUOUS WHEN CLEAR SKY

GROUND-BASED EXPERIMENTS IN MAC/EPSILON (CONT'D)
REV. 29 MAY 87

EXPERIMENT	OBSERVED PARAMETERS	LOCATION	REAL TIME	OPERATION
IR MERIDIAN SCANNER	?	ANDENES	N?	CS
IR INTERFEROMETER (LOWE)	AURORAL, AIRGL. EMISS., TEMPERATURE?	SKIBOTN?	N?	CS
IR INTERFEROMETERS (WARE)	AURORAL, AIRGL. EMISS., TEMPERATURE?	KIRUNA (KGI)	N?	CS
SPECTROMETERS (WITT)	AURORAL, AIRGL. EMISS.	ANDENES, KIRUNA (KGI)	Y	CS
PHOTOMETER (PETERSON)	AURORAL, AIRGL. EMISS.	SKIBOTN?	Y	CS
PHOTOMETERS (WITT)	AURORAL, AIRGL. EMISS.	ANDENES	Y	CS
PHOTOMETER (ARR)	AURORAL, AIRGL. EMISS.	ANDENES	Y	CS
IMAGERS (2 PETERSON)	AURORAL, AIRGLOW STRUCTURE	SKIBOTN?	Y?	CS
IMAGER (TAYLOR)	AURORAL, AIRGLOW STRUCTURE	SODANKYLÄ	Y?	CS
ALL-SKY CAMERA	AURORAL STRUCTURE	ANDENES	N	CD
ALL-SKY CAMERA (PETERSON)	AURORAL STRUCTURE	KIRUNA (KGI)	N?	CS
VIDEO CAMERA (PETERSON)	AURORAL, AIRGL. STRUCTURE?	SKIBOTN?	Y?	CS
FABRY-PEROT ETALONS (3 + 1 OH + 1 TRIPLE)	WINDS	KILPISJÄRVI, KIRUNA (KGI), SVALBARD	N	CS
STEREO OH TV (TAYLOR)	WAVES	IVALO- SODANKYLÄ	Y	CS
ALL-SKY IMAGING (REES)	OH- VARIABILITY	KIRUNA (KGI)	N?	CS

CD CONTINUOUS DURING COUNTDOWNS
CS CONTINUOUS WHEN CLEAR SKY

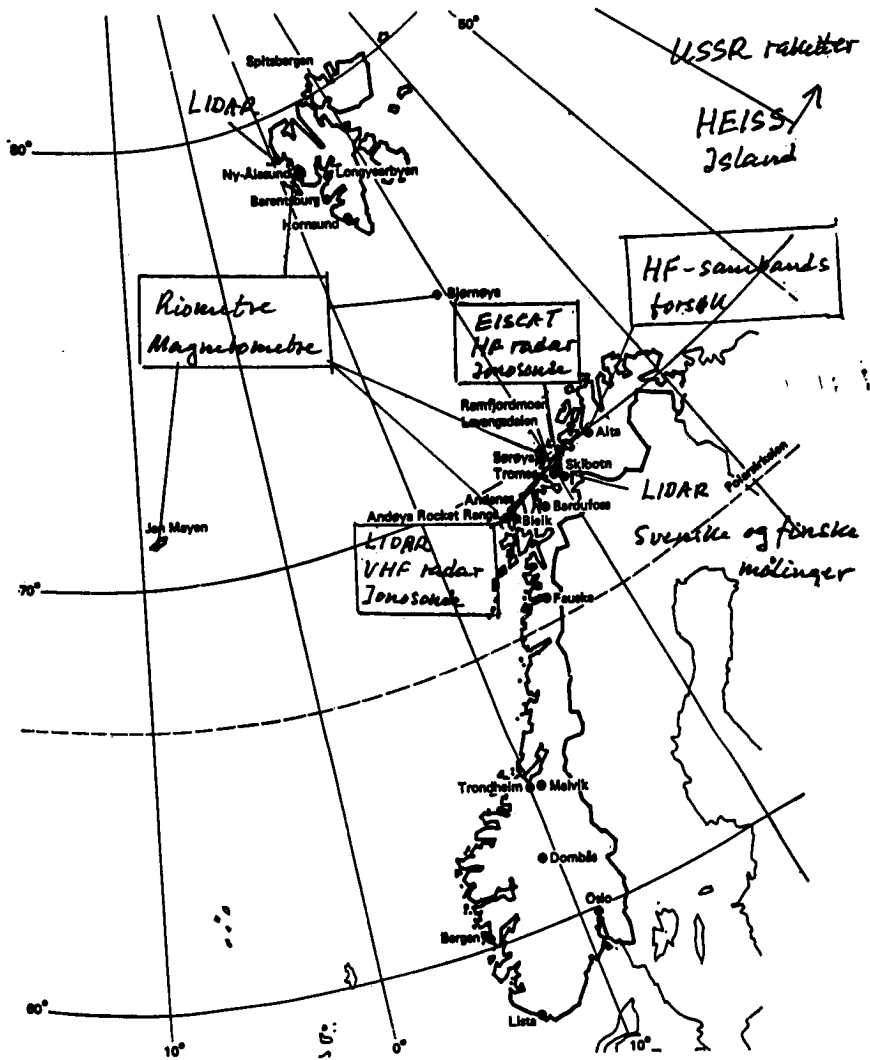


Figure 1. More than 50 ground-based instruments.

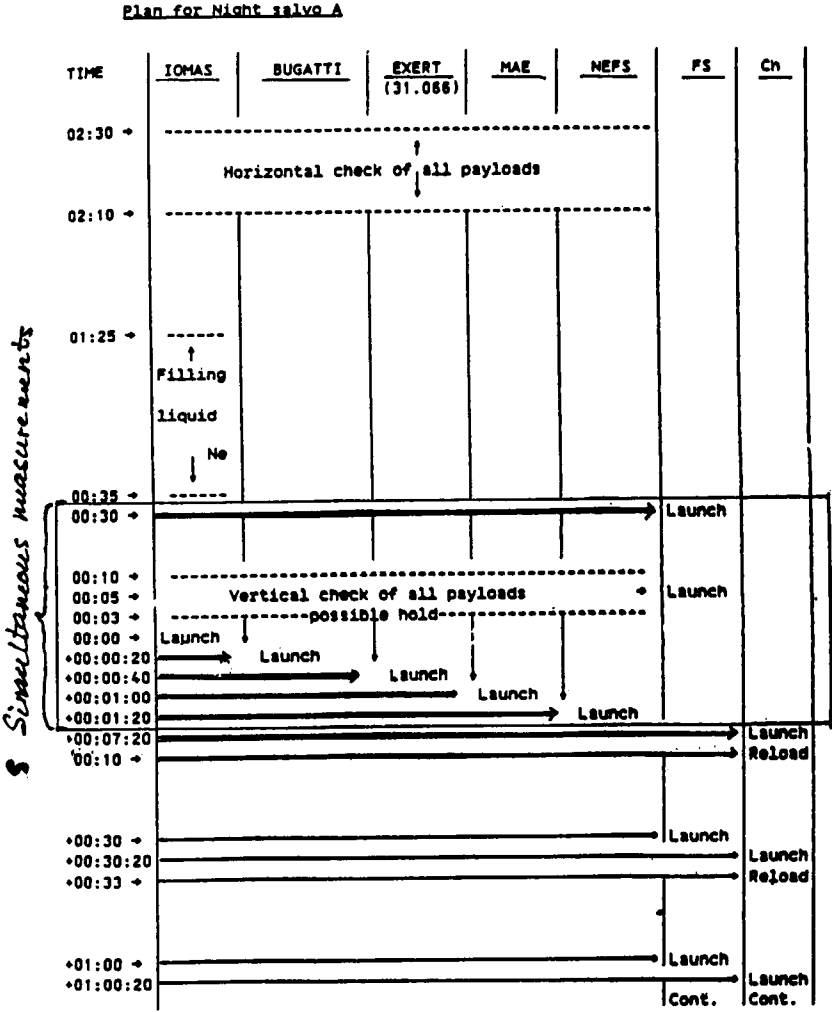


Figure 2. Simultaneous measurements made with 24 rocket experiments.

OVERVIEW OF THE MAC/EPSILON CAMPAIGN

Four salvos were launched during the campaign:

Day Salvo: 15 October

Launch criteria: Presence of turbulence (PRE, SOUSY)
 Presence of gravity waves (PRE, EISCAT, LIDAR)
 Riometer absorption between 0.2 and 2 dB
 Clear sky sufficient for LIDAR results

All launch criteria fulfilled

Night Salvo A: 21 October

Launch criteria: Presence of turbulence (PRE, SOUSY)
 Presence of gravity waves (PRE, EISCAT, LIDAR)
 Riometer absorption between 0.2 and 2 dB
 Clear sky sufficient for LIDAR results

All launch criteria fulfilled

Night Salvo A1: 28 October

Launch criteria: Presence of turbulence (PRE, SOUSY)
 Presence of gravity waves (PRE, EISCAT, LIDAR)
 Riometer absorption between 0.2 and 2 dB
 Presence of pulsating aurora
 Clear sky sufficient for LIDAR results

All launch criteria fulfilled

Night Salvo B: 12 November

Modified launch criteria: Presence of turbulence (PRE, SOUSY)
 Presence of gravity waves (PRE, EISCAT, LIDAR)
 Riometer absorption between 0.2 and 2 d

Modified launch criteria fulfilled.

HOW DID IT GO?

The data analysis is progressing well!

MAC/SINE

Very interesting observations were made by rockets and ground-based instruments. Summer conditions in high latitudes were mapped in greater detail than previously. Of particular importance are layers observed near the mesopause.

47 out of 55 met rockets from Andoya worked, success rate 87%

All instrumented rockets from Andoya worked, success rate 100%

The ground-based instruments performed well.

MAC/Epsilon

Four salvos were launched from Andoya. The launch criteria were fulfilled for three of these. The last salvo was launched under modified conditions. A very good series of measurements of turbulence was obtained.

18.5 out of 21 met rockets from Andoya worked, success rate 88%

Out of 55 rocket instruments launched from Andoya 51 worked, success rate 93%

Most ground-based instruments gave good results.

9.2 DYNAMICS OF THE UPPER MIDDLE ATMOSPHERE (80 - 110 KM) AT TROMSÖ, JUNE - DECEMBER 1987, USING THE TROMSÖ/SASKATOON M.F. RADAR

A. H. Manson and C. E. Meek

Institute of Space and Atmospheric Studies
University of Saskatchewan, Sask., S7N 0W0, Canada

A real-time-winds (RTW) system from Saskatoon operated with the Tromsö M.F. (partial reflection) radar on a continuous basis, June - December 1987. Profiles with 3 km resolution were obtained every 5 minutes -- weak ionization, and few geomagnetic disturbances limited the observations normally to 80 - 110 km. However, daily mean winds, tidal characteristics (24-, 12-h) such as amplitudes, phases and wavelengths, and gravity wave characteristics (intensities, mean directions) are available throughout this interval, which includes MAC-SINE and Epsilon. This is particularly valuable in defining the background state for some experiments, e.g., rockets, and for comparison with related parameters from the lidar and other radars (EISCAT, SOUSY-VHF). Comparisons with dynamical parameters from Saskatoon (52°N) are made: the zonal circulation was weaker at Tromsö, tidal amplitudes smaller, and summer 12-h tidal wavelengths shorter (~ 80 km vs ~ 100 km). The fall transition for this tide occurred in September, earlier than observed elsewhere. Initial comparisons with other experimental systems are also made.

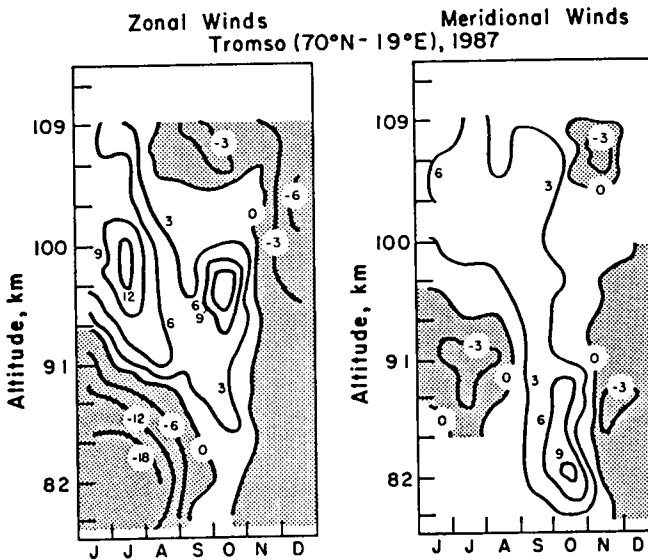


Figure 1. Mean winds: above 100 km values refer to a ~5 km layer near 100 km.

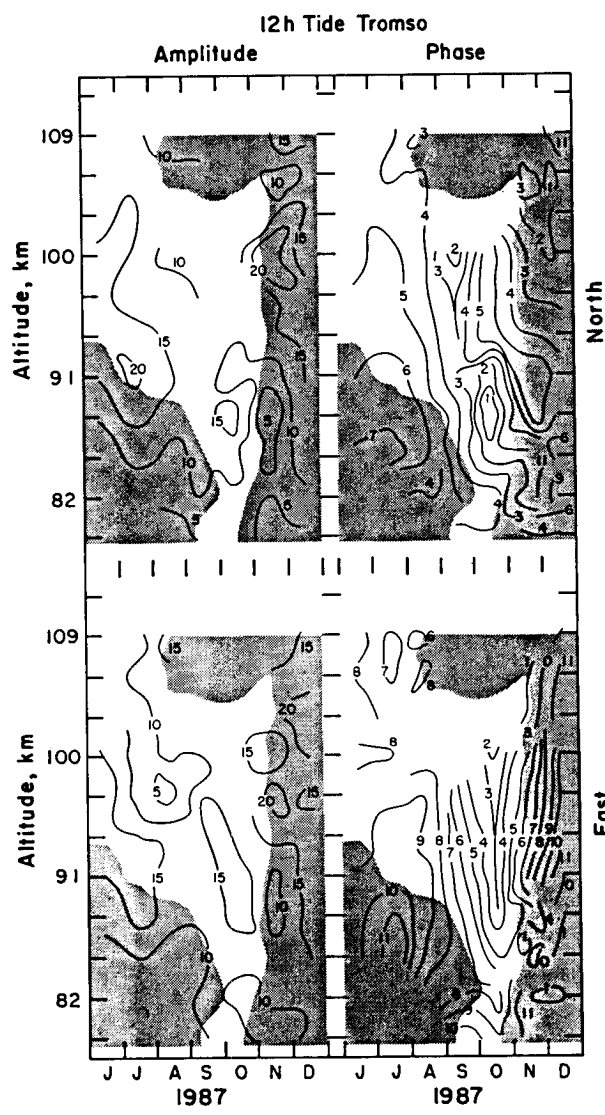


Figure 2. Semidiurnal tides.

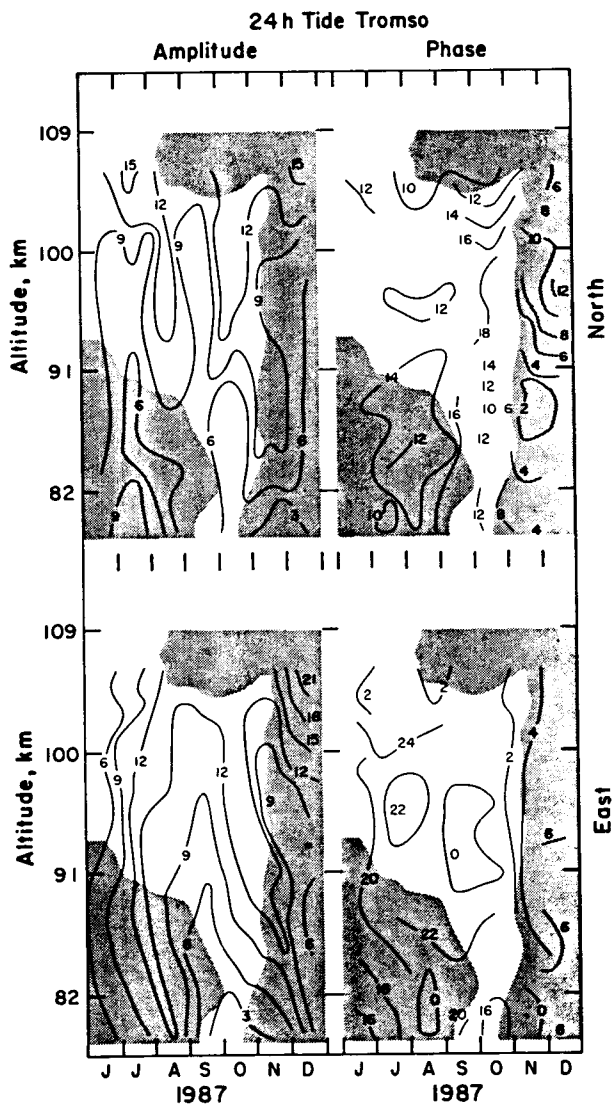


Figure 3. Diurnal tides.

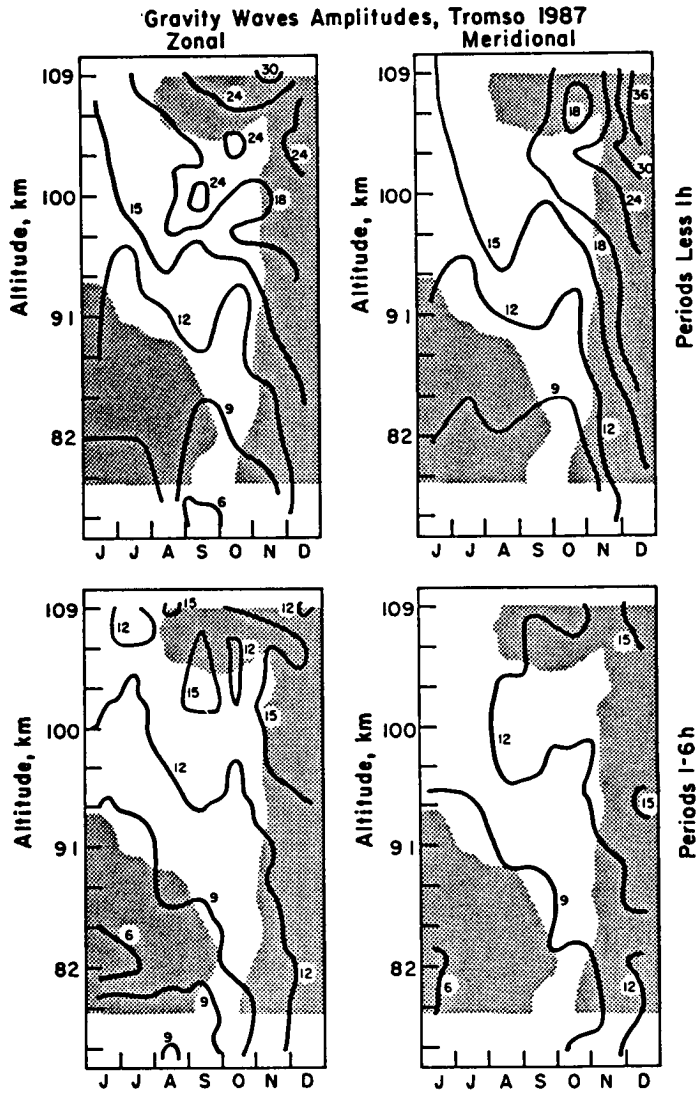


Figure 4. Gravity wave amplitudes.

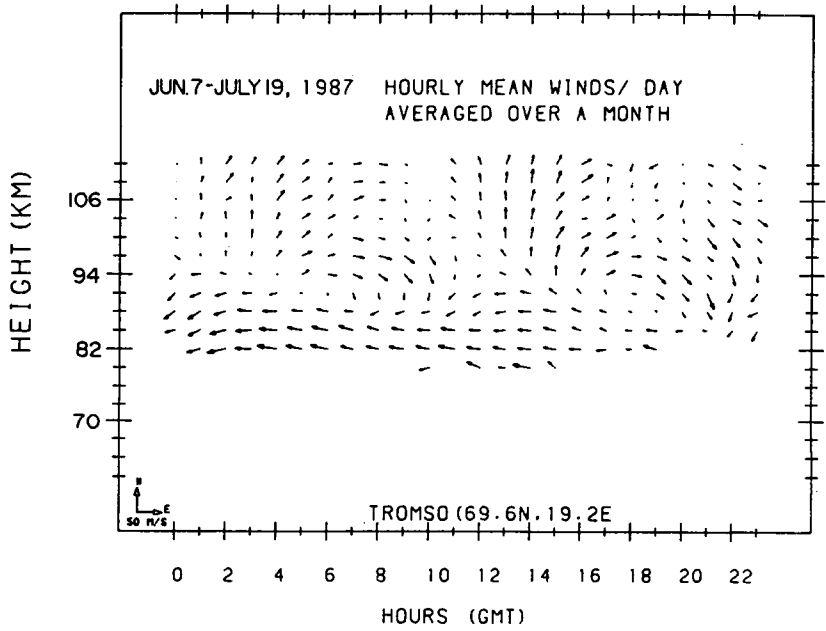


Figure 5. Mean day for SINE.

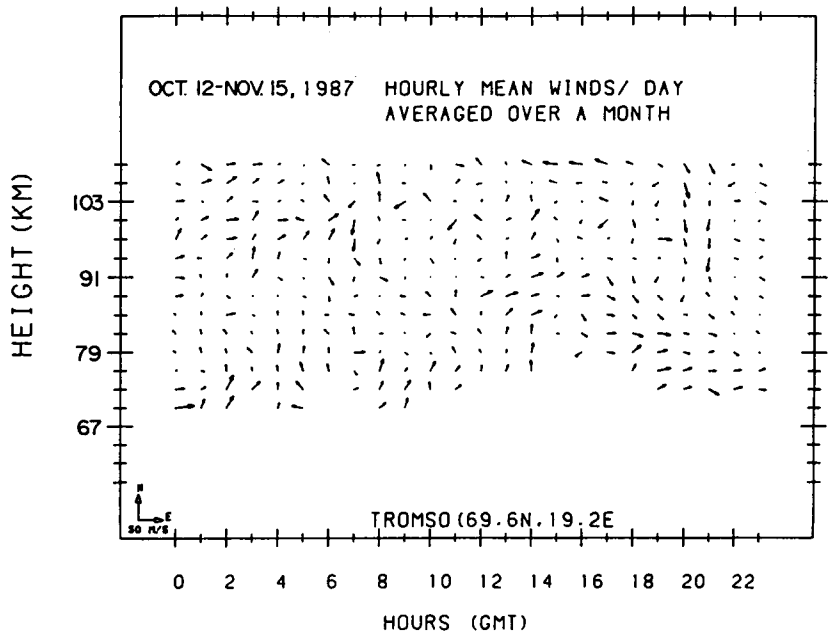


Figure 6. Mean day for Epsilon.

9.3 VHF RADAR MEASUREMENTS IN THE SUMMER POLAR MESOSPHERE

R. Rüster, I. M. Reid, P. Czechowsky, and G. Schmidt

Max-Planck-Institut für Aeronomie, Postfach 20
D-3411 Katlenburg-Lindau, FRG

Measurements in the mesosphere over Andoya/Norway (69°N, 16°E) have been carried out using the mobile SOUSY-VHF radar with an extended beam configuration during the MAC/SINE campaign in summer 1987. First results of a 48-h and a 3-h observational period for heights between about 83 and 91 km are presented. Zonal mean winds are characterized by a strong westward flow of up to 50 ms^{-1} , whereas the equatorward directed meridional component is weaker. The dominating semidiurnal tide has amplitudes up to 30 ms^{-1} and a vertical wavelength of about 55 km. The diurnal tide is less pronounced. The total upward flux of horizontal momentum takes values of $-2 \text{ m}^2\text{s}^{-2}$ near 84 km and increases with increasing height, reaching a maximum value of $22 \text{ m}^2\text{s}^{-2}$ for both the zonal and meridional components. However, measurements of the horizontal isotropy of the wave field suggest significant anisotropy. The major contribution to the momentum flux is from the 10 min - 1 h period range below about 87 km, and from the 1 - 6 h period range above this height.

Figure 1 shows a characteristic height-time plot of the echo power received in the vertically point beam for 24 h. VHF-radar echoes from the summer polar mesosphere are typically observed in the height range from about 83 to 92 km. A more detailed discussion of the layered structure, the aspect sensitivity and other characteristic features is the subject of the subsequent paper by Czechowsky et al.

The average height profile of the observed wind components is presented in Figure 2. The solid and dashed curves refer to the zonal and meridional components, respectively. As expected, the zonal wind field in summer is characterized by a strong westward flow up to altitudes of about 92 km. Above that height the results indicate a change of westward to eastward flow. The meridional wind pattern reveals a summer equatorward motion. The vertical component is on average about 10 cm/s and it shows a clear directional change from downward to upward around 87 km. According to Coy et al. [1988] this time average velocity (Eulerian average) may not be directly related to the averaged parcel motion (Lagrangian average) due to the Stokes drift resulting from upward propagating waves.

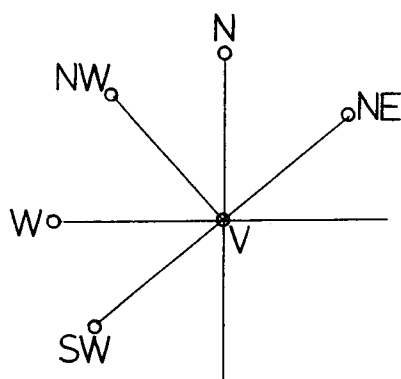
The main propagating tidal wave at high latitudes in summer is the semidiurnal tide. Figure 3 presents the height profiles of the amplitude A and local time of maximum T_{max} for both the zonal and meridional components. At all heights the amplitude of the zonal component exceeds that of the meridional one. Both amplitudes vary between about 15 and 30 ms^{-1} . The apparent vertical wavelength resulting from the very stable phase variation with height is estimated to be about 55 km.

Figure 4 (a) shows the total upward flux of momentum for the 10 min to 48 h period range (solid line) and for the 12 - 48 h period range (dashed line). Note that the contributions of the 12 and 24 h tides have been removed. The 12 - 48 h contribution is relatively small at heights below 87 km, and insignificant above this height. The total upward flux of horizontal momentum takes values of $-2 \text{ m}^2\text{s}^{-2}$ near 84 km, and increases with increasing height, reaching a maximum value of $22 \text{ m}^2\text{s}^{-2}$ for both the zonal and meridional components. However, measurements of the horizontal isotropy of the wave field suggest significant anisotropy. This is shown in Figure 4(b). In the 12 - 48 h period range, the zonal component is dominant, while in the 10 min - 48 h range the height variation is somewhat more complicated. The w^2 -data (Figures 4c, 5c) consistently show a strong decrease in magnitude with decreasing frequency, i.e., the Doppler shift of the measured frequencies is likely to be negligible.

The contributions to both the flux and anisotropy from motions in the 10 min - 12 h period range are presented in Figure 5(a),(b). (a) shows that the major contribution to the momentum flux is from the 10 min - 1 h period range below about 87 km, and from the 1 - 6 h period range above this height. It is also evident that each of the three period ranges tends to increase with height, reaching maximum values near 89 - 90 km. The anisotropy (Figure 5(b)) for the 6 - 12 h period range indicates dominance of the meridional component above 87 km, with little consistent variation below this height. This is possibly consistent with removal of a portion of the zonal component through filtering. In the 1 - 6 h period range the anisotropy varies with height and is somewhat suggestive of a wave motion of about 2 km vertical wavelength. The 10 min - 1 h period range also shows a wave-like variation.

The upward flux of horizontal momentum for a 3-h period showing some of the strongest echoes observed during the whole campaign is presented in Figure 6 for periods between 120 and 160 min, between 10 and 53 min, and between 53 and 160 min. The mean number of 5 min data points for the NE and SW beam is given in parenthesis for each height. The maximum number possible is 30. In the 10 - 160 min interval, values range from 15 to 66 m^2s^{-2} . The largest values occur above the peak in the vertical power profile, and the most abrupt increase is noted in the first range above the 3 dB point of the vertical power profile (shaded area). Below 86 km the major contribution to the total flux comes from the 53 - 160 min interval. Above 86 km, motions in the 53 - 160 min and 10 - 53 min period ranges contribute approximately equally. The anisotropy of the horizontal wind fields is shown in Figure 6b. For the 10 - 160 min and 10 - 53 min period ranges, the largest variations are noted just above the peak vertical power, while in the 53 - 160 min period range, the maximum anisotropy occurs near the peak. The zonal component dominates the 10 - 160 min period range, with the major contribution coming from those motions in the 10 - 53 min period range. These would appear to be the first unbiased mesospheric measurements of the anisotropy term made with Doppler radar [After Reid, et al., *Geophys. Res. Lett.*, in press].

Table 1. Beam configuration used in the measurements; the Reynolds stress tensor; the terms that have been obtained directly from the variances of the radial velocities.



$$\begin{pmatrix} \overline{u'^2} & \overline{u'v'} & \overline{u'w'} \\ \overline{v'w'} & \overline{v'^2} & \overline{v'w'} \\ \overline{w'u'} & \overline{w'v'} & \overline{w'^2} \end{pmatrix}$$

$$\overline{u'w'} + \overline{v'w'} = (\overline{V_{NE}'^2} - \overline{V_{SW}'^2}) / \sqrt{2} \sin 2\theta_{E_1}$$

$$\overline{v'^2} - \overline{u'^2} = (\overline{V_N'^2} - \overline{V_W'^2}) / \sin^2 \theta_{E_2} - 2 (\overline{u'w'} + \overline{v'w'}) \cot \theta_{E_2}$$

Table 2. Summary of the observational results.

SOUSY VHF Radar23 – 25 June 198716 June 1987Andenes/Norway(83 – 91 km)

Mean Winds	: $\bar{u} \approx -50 \rightarrow -10 \text{ ms}^{-1}$; $\bar{v} \approx -10 \rightarrow -30 \text{ ms}^{-1}$
Tide (12 h)	: $A \approx 20 \rightarrow 30 \text{ ms}^{-1}$; $\lambda_z \approx 55 \text{ km}$
Tide (24 h)	: $A \approx 10 \text{ ms}^{-1}$; $(\lambda_z = 10 \text{ km?})$
$(\overline{u'w'} + \overline{v'w'})_{total}$: $-2 \rightarrow 20 \text{ m}^2 \text{ s}^{-2}$ (for 48 h)	; $20 \rightarrow 60 \text{ m}^2 \text{ s}^{-2}$ (for 3 h)

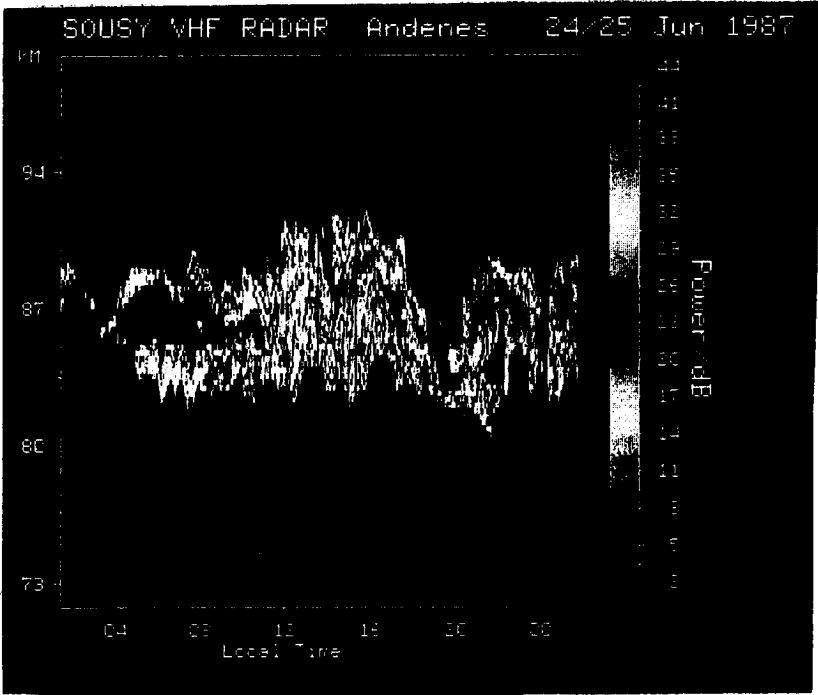


Figure 1.

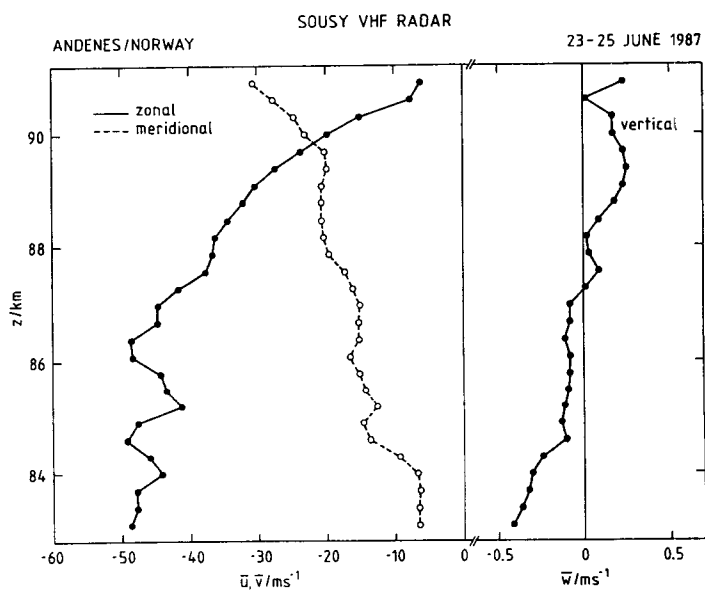


Figure 2.

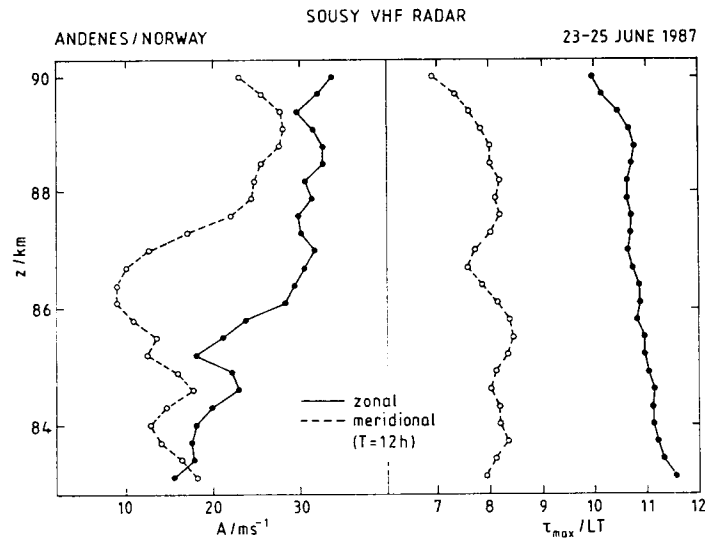


Figure 3.

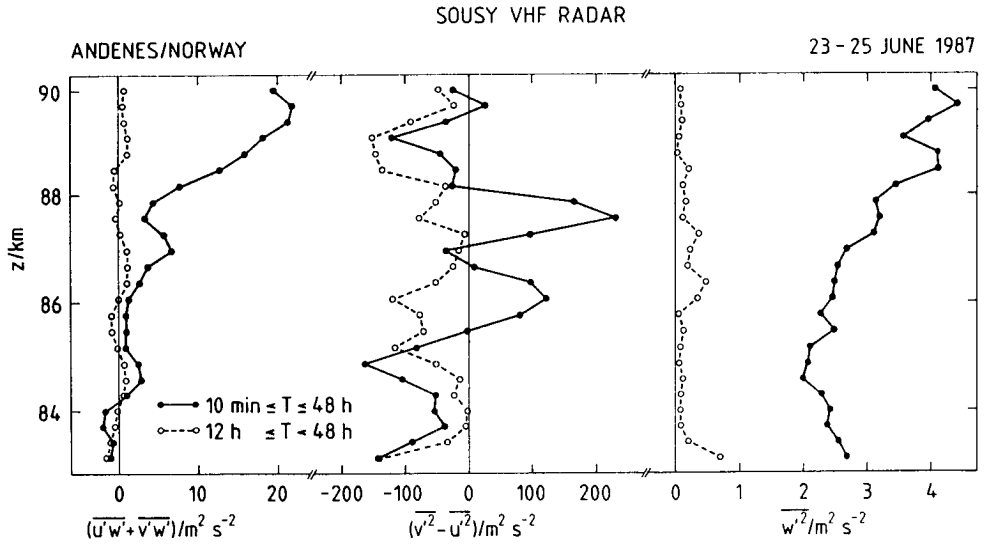


Figure 4.

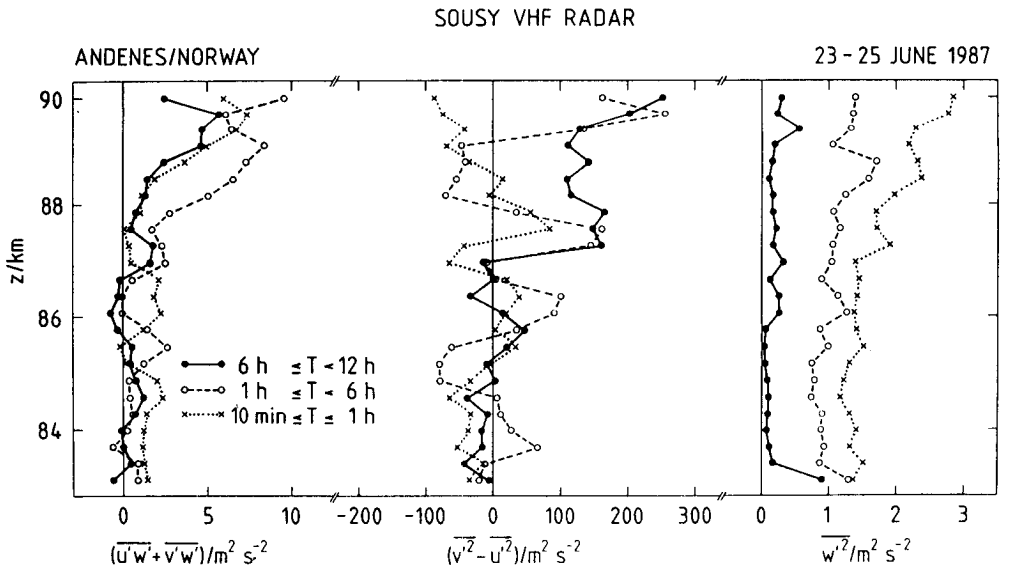


Figure 5.

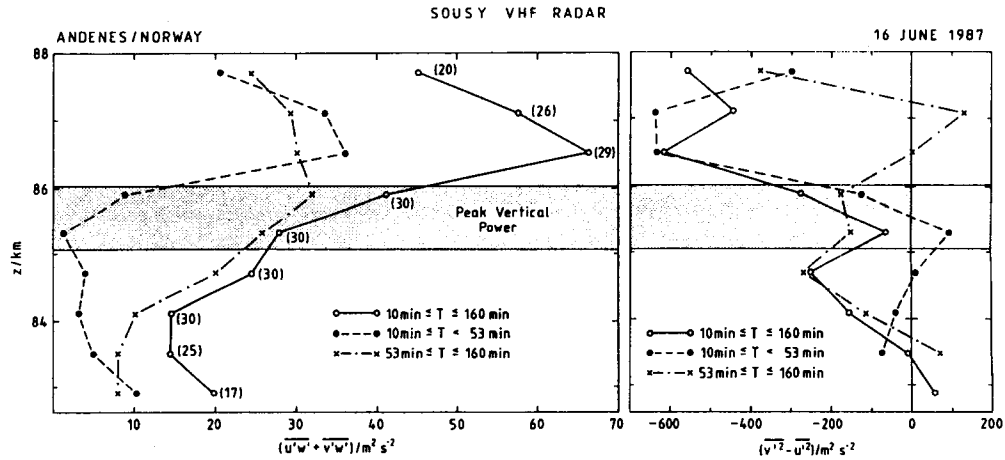


Figure 6.

9.4 VHF RADAR MEASUREMENTS OVER ANDOYA (NORTHERN NORWAY)

P. Czechowsky, I. M. Reid, R. Rüster, and G. Schmidt

Max-Planck-Institut für Aeronomie
Postfach 20, 3411 Katlenburg-Lindau, FRG

The Mobile SOUSY Radar has been operated during the MAP/WINE, the MAC/SINE, and MAC/Epsilon campaigns at Andoya in Northern Norway. This paper presents a comparison between summer and winter results, in particular the generation and development of the scattering regions, the different power spectral densities and the aspect sensitivities which were derived from six different beam directions.

In summer 1983 the Mobile SOUSY VHF Radar was installed in Andenes on the island of Andoya in Northern Norway, with the aim of investigating backscattering structures and dynamics in the polar middle atmosphere. The object of this paper is to compare and summarize summer and winter results obtained during several campaigns within the last five years.

Typical summer echoes occur only during the three months from June to August. They are characterized by persistent, intense layers, centered around an altitude of 86 km, with echo powers of up to 60 dB above noise.

During the fall, winter and spring periods, echoes are observed predominantly at daytime within the height range from about 50 to 85 km. They often take the form of street-like structures separated by about 3 to 4 km. We have selected for this presentation some representative examples from the different campaigns.

Table 1. Summary of Echo Region Characteristics over Andoya.

Characteristics	Winter	Summer
Height interval of of echo occurrence	50 - 85 km	75 - 95 km
Typical signal to noise ratio	3 - 25 dB	30 - 60 dB
Height of echo power maximum	variable between 50 and 85 km	86 km on average
Echo occurrence	at daytime in connection with radio wave absorption	continuous during day and night, 15% diurnal variation
aspect sensitivity	intermittent; high at the top and bottom of the layers	continuous and high throughout the whole layer
dominating periods	gravity wave periods	tidal (12 h dominates) and long period gravity wave periods
spectral width	relatively constant in height	minimum near maximum power

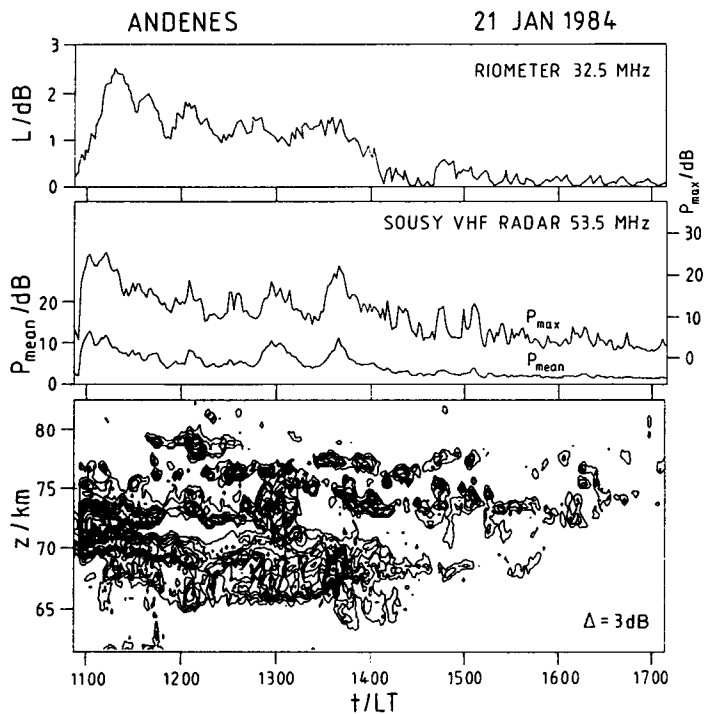


Figure 1. Absorption (L) as measured on 21 January 1984 with a 32.5 MHz riometer located at Andenes near the SOUSY radar facility (top), maximum echo power (P_{max}) and mean echo power (P_{mean}) measured in the 65 to 80 km height region as a function of time (center), and a contour plot of the echo power as a function of height and time (bottom).

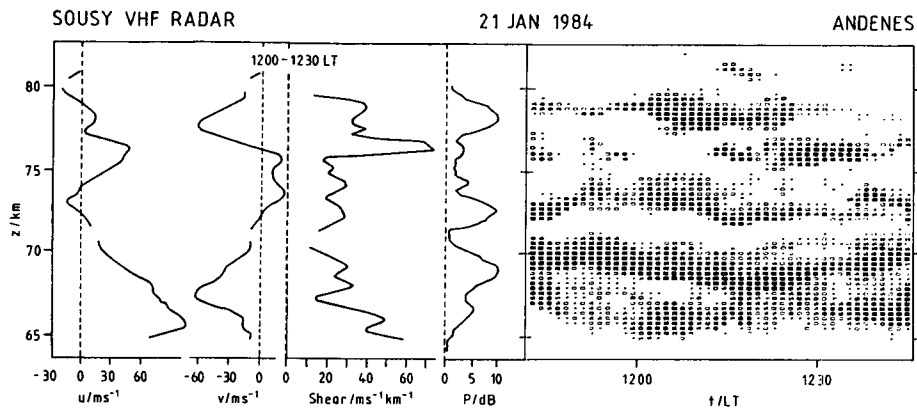


Figure 2. Height profiles of the mean zonal (u) and meridional (v) wind velocities for 1200 - 1230 LT on 21 January 1984 (left), and the corresponding mean echo intensity (P), and mean shear (center). A section of the bottom panel of Figure 1 is shown as a height time intensity plot (right).

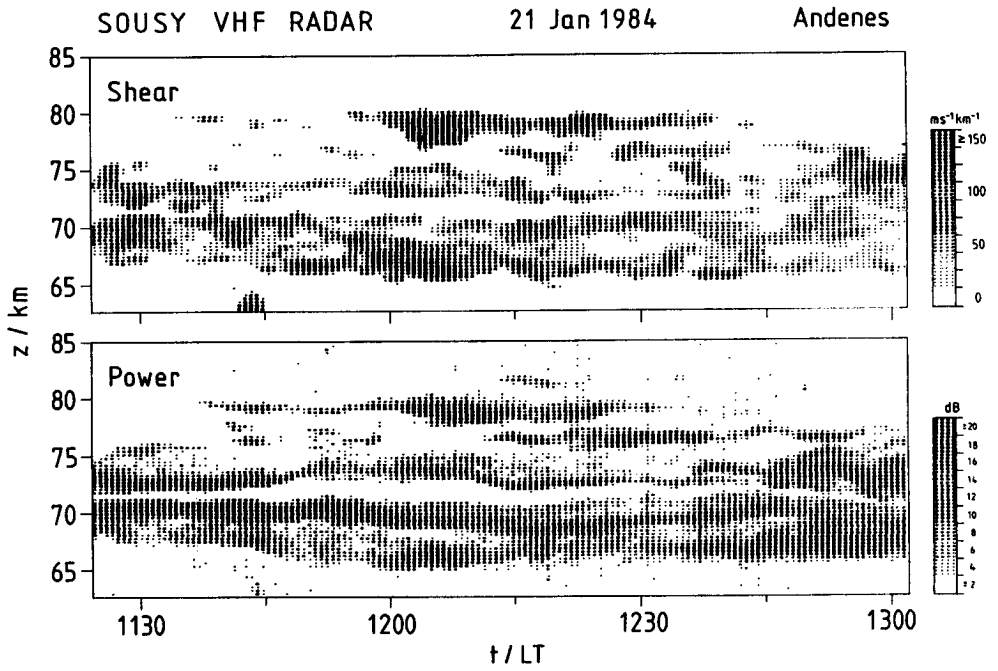


Figure 3. Height-time intensity plots of shear (top) and echo power (bottom) for 1118 - 1305 LT on 21 January 1984.

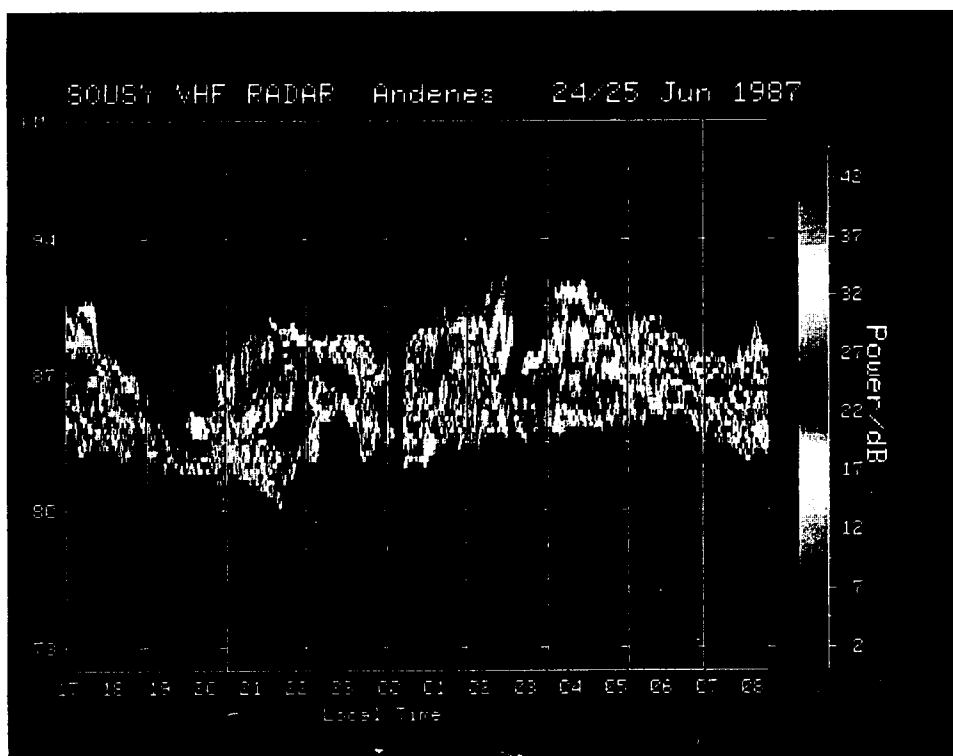


Figure 4. Height-time plot of the variation of the echo power for a period of about 15 h which is typical for the MAC/SINE campaign 1987. The characteristic double peak structures with vertical separations of around 5 to 10 km are often observed to move downwards with apparent velocities between 0.1 and 2.5 m/s and tend to oscillate in height with a period of about 12 h.

ORIGINAL PAGE
BLACK AND WHITE PHOTOGRAPH

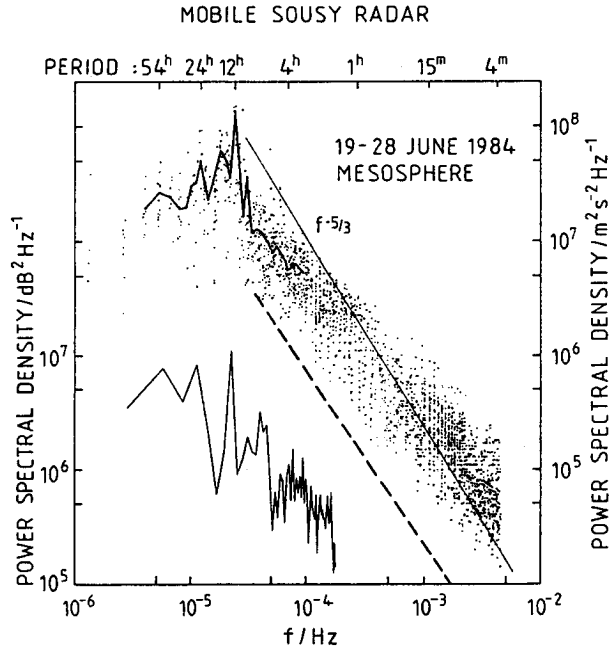


Figure 5. Power spectral density of zonal velocity for the entire summer campaign 1984 (scale on left). The lower curve shows the power spectral density of echo power (scale right). Spectral peaks are evident in both curves at 54, 24, 12, and 8 h. The straight line represents summer results from Poker Flat for a height of 87.3 km [Balsley and Garello, 1985].

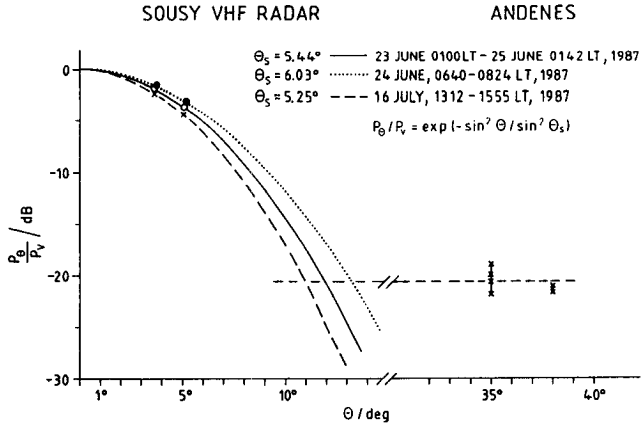


Figure 6. Backscattered power relative to that received in the vertical beam (crosses, dots and circles) plotted as a function of zenith angle, for three different periods. The powers measured at $\theta = 35^\circ$ and $\theta = 38^\circ$ (crosses) are observed in the two grating lobes of the antenna. The fall-off in power up to $\theta = 15^\circ$ represents the equation:

$$P_\theta / P_{\text{vert}} = \exp(-\sin^2 \theta / \sin^2 \theta_s)$$

$\theta_s = \text{half width of the backscatter angular polar diagram.}$

9.5 EISCAT OBSERVATIONS DURING MAC/SINE AND MAC/EPSILON

J. Röttger

EISCAT Scientific Association
Box 705, S981 27 Kiruna, SwedenU.-P. Hoppe
Norwegian defence Research Establishment
P. O. Box 25, N-2007 Kjeller, Norway

C. Hall

The Auroral Observatory
N-9001 Tromsø, Norway

The EISCAT incoherent scatter radar facility in Tromsø, Norway was operated during the MAC/SINE campaign for 78 hours in the period 10 June - 17 July 1987, and during the MAC/Epsilon campaign for 90 hours in the period 15 October - 5 November 1987. The VHF (224 MHz) radar operations during MAC/SINE yielded most interesting observations of strong coherent echoes from the mesopause region. We will present characteristic data of these polar mesospheric summer echoes. The UHF (933 MHz) radar operations during MAC/Epsilon were done with 18° off zenith beam and allow us to deduce meridional and horizontal wind components as well as radial velocity spectra in addition to the usual electron density profiles in the D and lower E regions. Some results from the VHF and UHF radars indicating the presence of gravity waves will be examined.

Table 1. EISCAT Observations During MAC/SINE

Campaign duration:	7 June - 19 July 1987
EISCAT operation:	10 June - 17 July 1987
Total observation time:	78 hrs on 16 days, mostly 9 - 13 UT
Location:	69.6°N, 19.2°E
Transmitted frequency:	224 MHz
Peak transmitter power:	2 MW
Duty cycle:	8%
Beam position	vertical
Height range	74 - 113 km
Height resolution:	105 km
Scattering volume:	~ 1 km ³
Time resolution:	10 s

Results:

- Very strong backscatter from 85 ± 4 km, nearly continuous
- Theory of radio scattering in the lower ionosphere must be modified
- High resolution observation of vertical motions:
 $\Delta w < 1$ cm/s; $\Delta t = 10$ s; $\Delta z = 1.05$ km

Table 2. EISCAT Observations During MAC/Epsilon

Campaign duration:	12 October - 15 November 1987
EISCAT operation	15 October - 5 November 1987
Total observation time:	90 hr on 15 days
Location:	69.6°N, 19.2°E
Transmitted frequency:	933 MHz
Beam position:	18° zenith angle, alternately 180° and 270° azimuth
Cycle time:	20 minutes
Height range:	75 - 106 km
Height resolution:	1 km
Scattering volume:	~ 1 km ³
Time resolution:	5 minutes

Results:

- Raw electron density as a function of time and height
- Zonal and meridional winds as a function of time and height

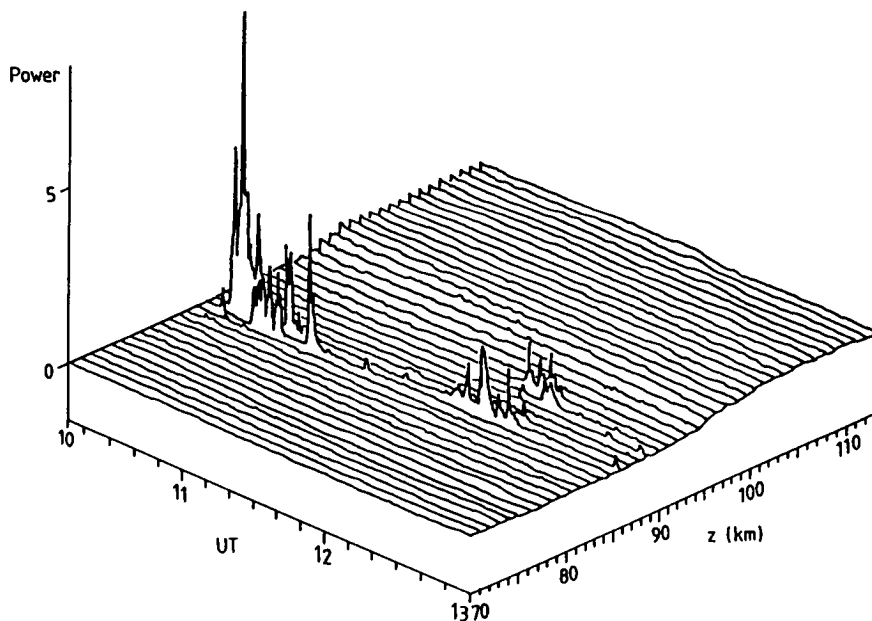


Figure 1. The backscattered power profile as a function of height and time on 10 June 1987. The height resolution is 1.05 km, the time resolution is 10 s. The power scale is arbitrary, but linear.

Log average power 224 MHz
70°N ; June-July 1987
43 hrs averaged ; 10-14 LT

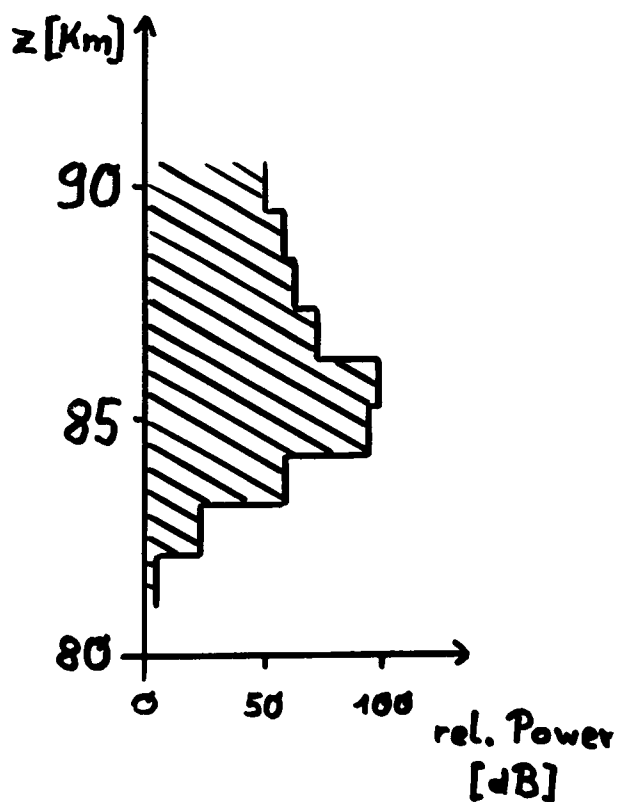


Figure 2. Log averaged power.

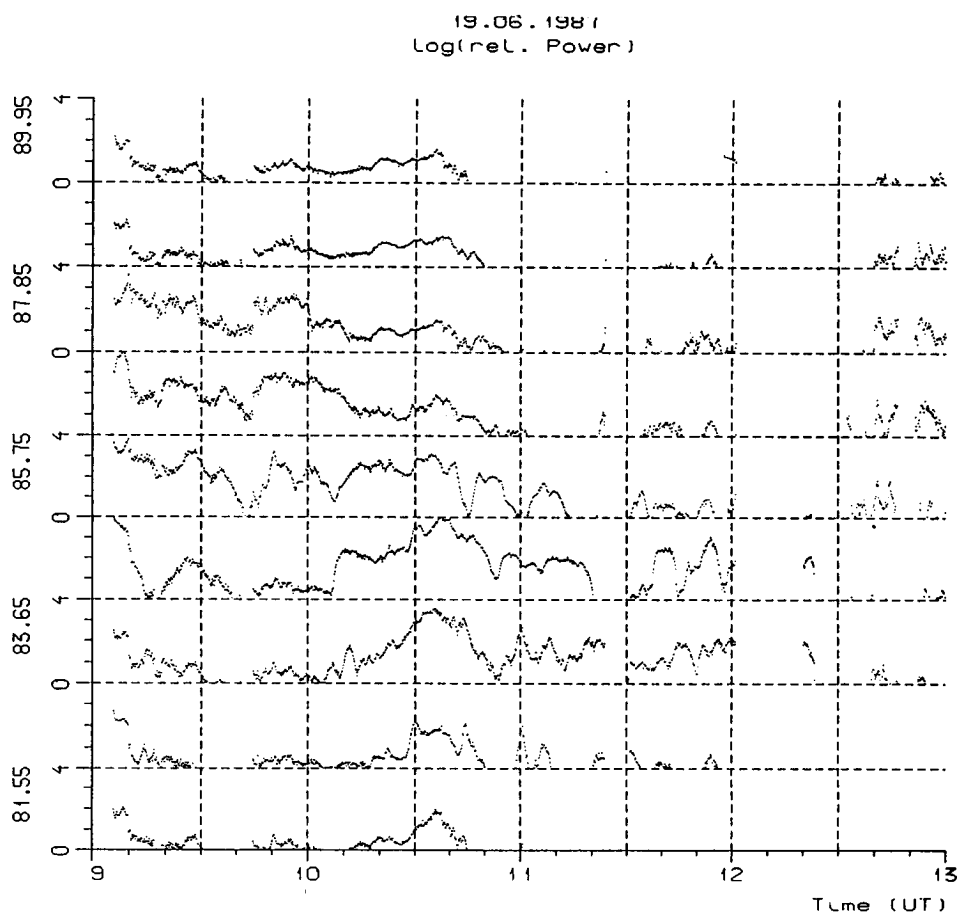


Figure 3. Log (rel. power) at nine heights.

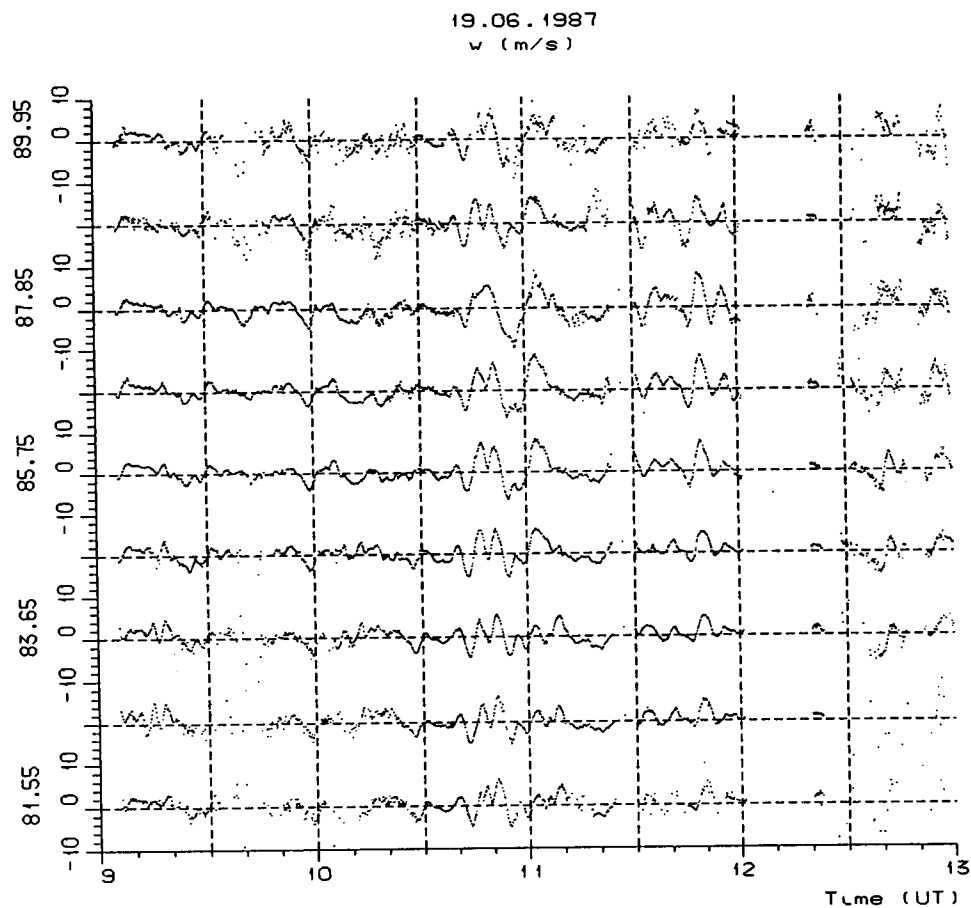


Figure 4. Vertical velocities at nine heights.

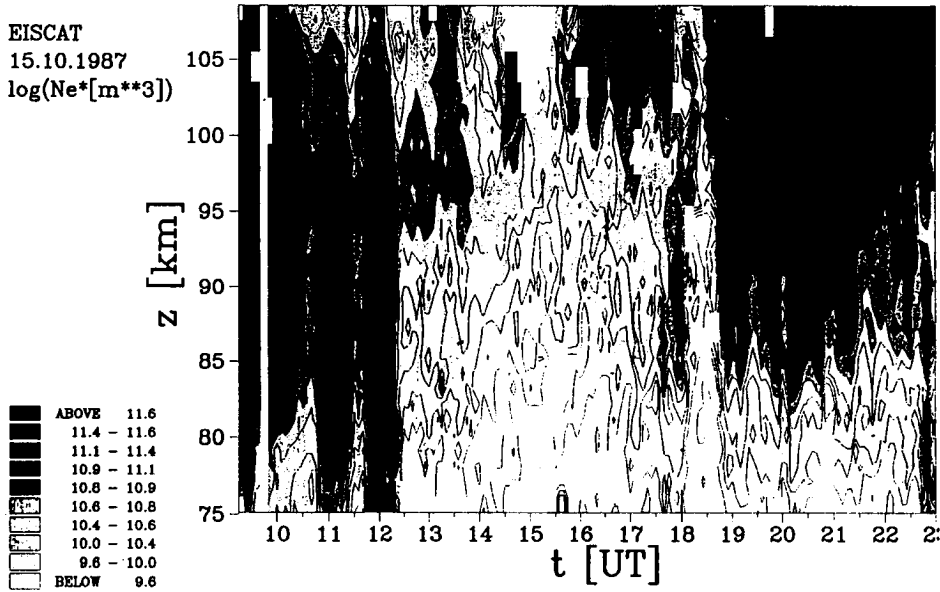


Figure 5. Raw electron density.

ORIGINAL FILE
BLACK AND WHITE PHOTOGRAPH

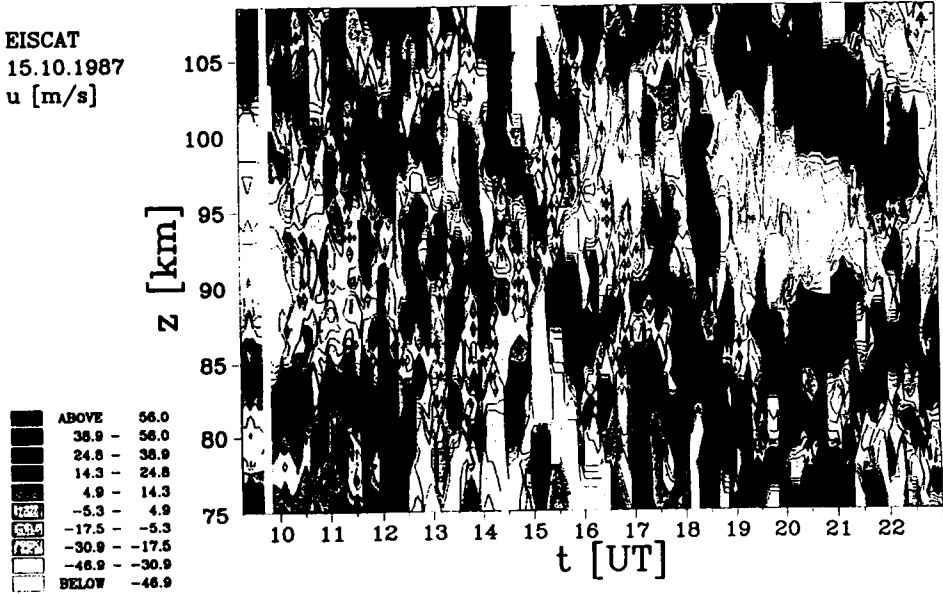


Figure 6. Zonal velocity.

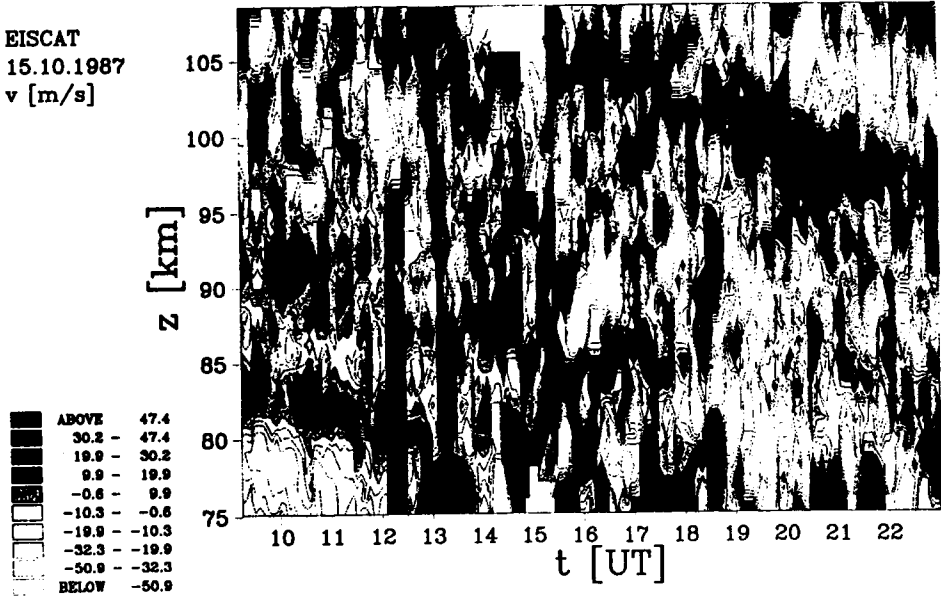


Figure 7. Meridional velocity.

9.6 A COMPARISON OF RESULTS OBTAINED FROM FOIL CHAFF CLOUDS AT 69° NORTHERN LATITUDE DURING WINTER, SUMMER AND AUTUMN

H. U. Widdel

Max-Planck-Institut für Aeronomie
Postfach 20, 3411 Katlenburg-Lindau, FRG

U. von Zahn

Physikalisches Institut der Universität Bonn
Nussallee 12, D-5300 Bonn 1, FRG

Results from high-resolution foil chaff experiments flown during the campaigns MAP/WINE (December 83 - February 84), MAC/SINE (June/July 87) and Epsilon (October/November 87) at Andenes (Northern Norway) are compared to each other and the differences in wind direction and wave activity during the different seasons are worked out.

Table 1. Types of Chaff.

Maximum height (km)	Thickness (μm)	width: (mm)	length (mm)	Mass-over area ratio (g/m^2)	Designation:
≤ 85	10	8,5	24	13,6	heavy(H)
≤ 93	2,5	9	24	3,4	light(L)
≤ 96	1,5	8	24	2,37	super hight(SL)
≤ 102	1	8	24	1,7	extra light(EL)

The foil chaff method is best suited for the investigation of fine structures of atmospheric motions in the middle atmosphere. The type of chaff to be used for such purposes should be selected and matched to the height at which such investigations are to be performed. The 1 micrometer thick material is a new development rather difficult to handle and gets very close to the physical limit of height up to which the chaff method can sensibly be used at all (108 km depends upon latitude and season).

Table 2. Summary of Data Available for Analysis.

Season	Campaign	Period	Number of flight per kind of chaff	
WINTER:	MAP/WINE	Dec. 83-Feb. 84	H:2 L:14(16)	SL:- EL:-
SUMMER:	MAC/SINE	Jun. 87-July 87	H:5 L:17	SL:- EL:-
SUMMER:	MAC/Sodium	Jun. 88-July 88	H:- L:-	SL:3 EL:7
AUTUMN:	MAC/EPSILON	Oct. 87	H: L:3(+1)	SL:4 EL:-

Height coverage:

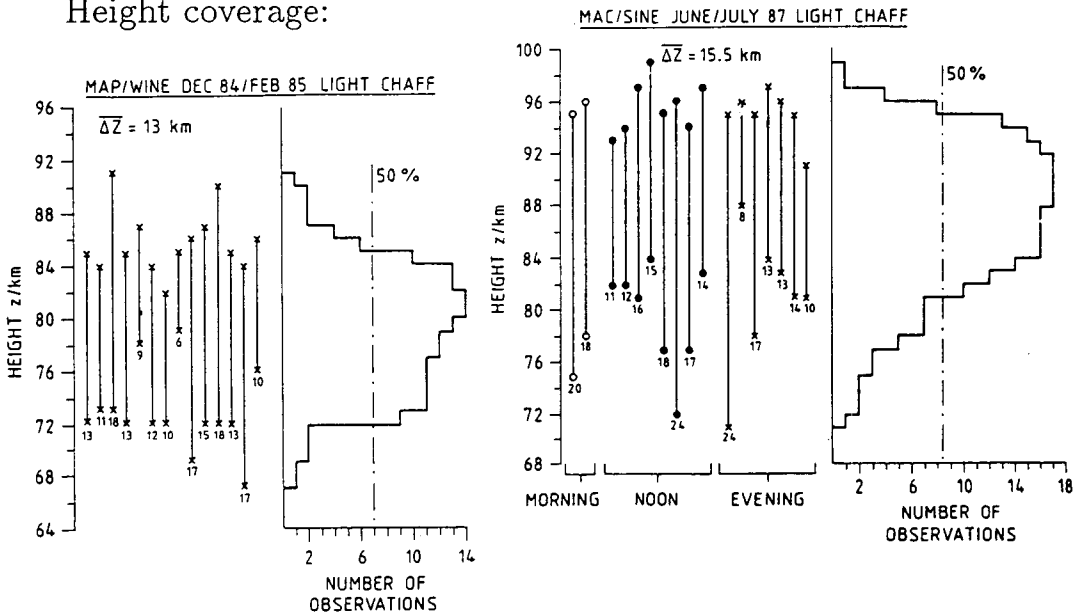
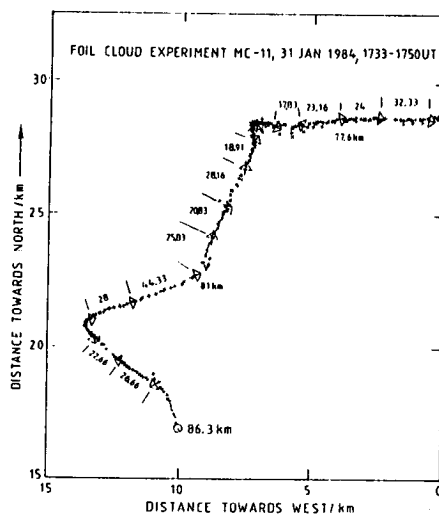
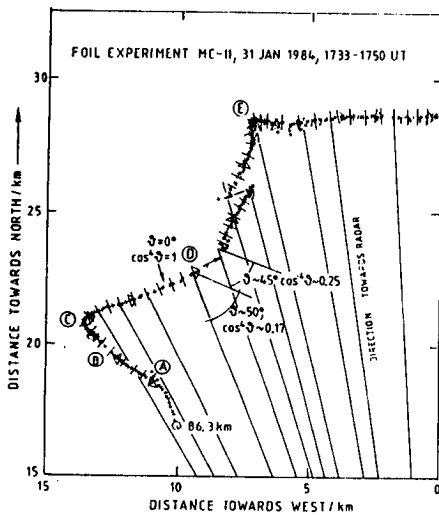
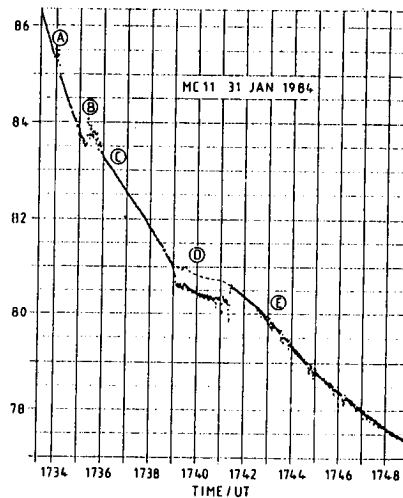
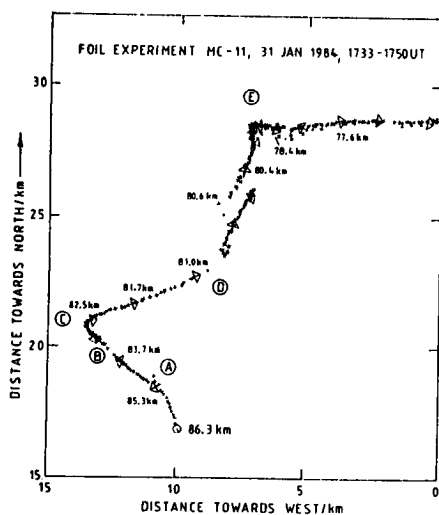


Figure 1. The histograms show that the height coverage of measurements was different in winter and summer. This was caused by different performance of the rockets. The average height coverage of 15 km during summer agrees quite well with predictions obtained from a theoretical description of the flight behavior of foil chaff.

Figure 2. (Following page) Example for a winter measurement. All data raw, uncorrected radar tracking data. (a) Projection of the trajectory onto the earth's surface (to be read like a map, north at top). Note offset at "D" marks at 1 minute interval. (b) Height versus time plot which shows some irregularities (marked A to E). These irregularities (height jumps of order 500 m) occur when the direction changes (see Figure at left). (c) Explanation of the jump seen at point "D" and an example how to correct it. The foils fly with their longitudinal axis perpendicular to the direction of fall and to the direction of drift in the wind. The return power received by the radar varies with the fourth power of the angle between the radar wave polarization plane and the dipole's longitudinal axis. The could had a certain vertical extent (~500 m) and was oriented "oblique" in space as the result of several shears it passed. At "D" the orientation of the foils change and the radar moves to the bottom end of the cloud. (d) "Repaired" trajectory. Note that the drift velocity is "modulated" (~5 m/s). (e) Vertical velocities of air derived from the chaff data using independent temperature and density data (falling sphere flown close in time to launch of chaff). Note that disturbances A to D are seen at or close to the crest of an upgoing wave motion. They were never seen at maximum downward motion. Dotted lines take into account roll-in of the chaff results suggest that it did not occur (inner curve).



M-C 11 31 JAN 84 1731UT LAUNCH TIME
M-F 39 31 JAN 84 1823UT LAUNCH TIME

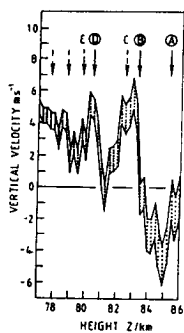


Figure 2.

Figure 3. (Following page) Winter data: second example suggesting quasi-acoustic disturbances connected with breaking of waves. Upper right: height vs time plot (A) with echo record (B,C) and variation of radar cross section (D). One notes that the plot becomes transiently noisy at fairly regular intervals ($\sim 4 - 5$ min) and that the cloud is eventually destroyed by a violent event at 72 km. Before that, quasi-regular oscillations are seen and the echo record tells that these were motions in the cloud which did not change its size. The trajectory map was broken for reasons of clearer visibility of details. Middle left: the trajectory is shown from $z = 81.5$ km to $z = 75.2$ km. The disturbances No. 3 and 4 are hidden in the loop and manifest themselves as "curl-ups", No. 5 as some data scatter after having passed the loop, but No. 6 (and 7) are clearly seen as scatter across the trajectory (left, top). An enlargement (bottom, left) plotted at a higher data rate (1 per second) shows that No. 6 comprised in fact two consecutive events separated by only a short time (arrow). Explanation is that the foils behave like Rayleigh disks and were turned out of orientation by an acoustic wave and the scatter represents the true extension of the foil cloud as is supported by the echo records. Entering the heights in which the noise was observed into the plot of vertical motions one notes that they are located about symmetrically to the crests of upgoing motions. Assuming acoustic disturbances caused by the breaking of waves, this can be understood: in contrast to ocean waves, there is no significant change in acoustic impedance between medium and wave and the noise is seen on both sides of the wave.

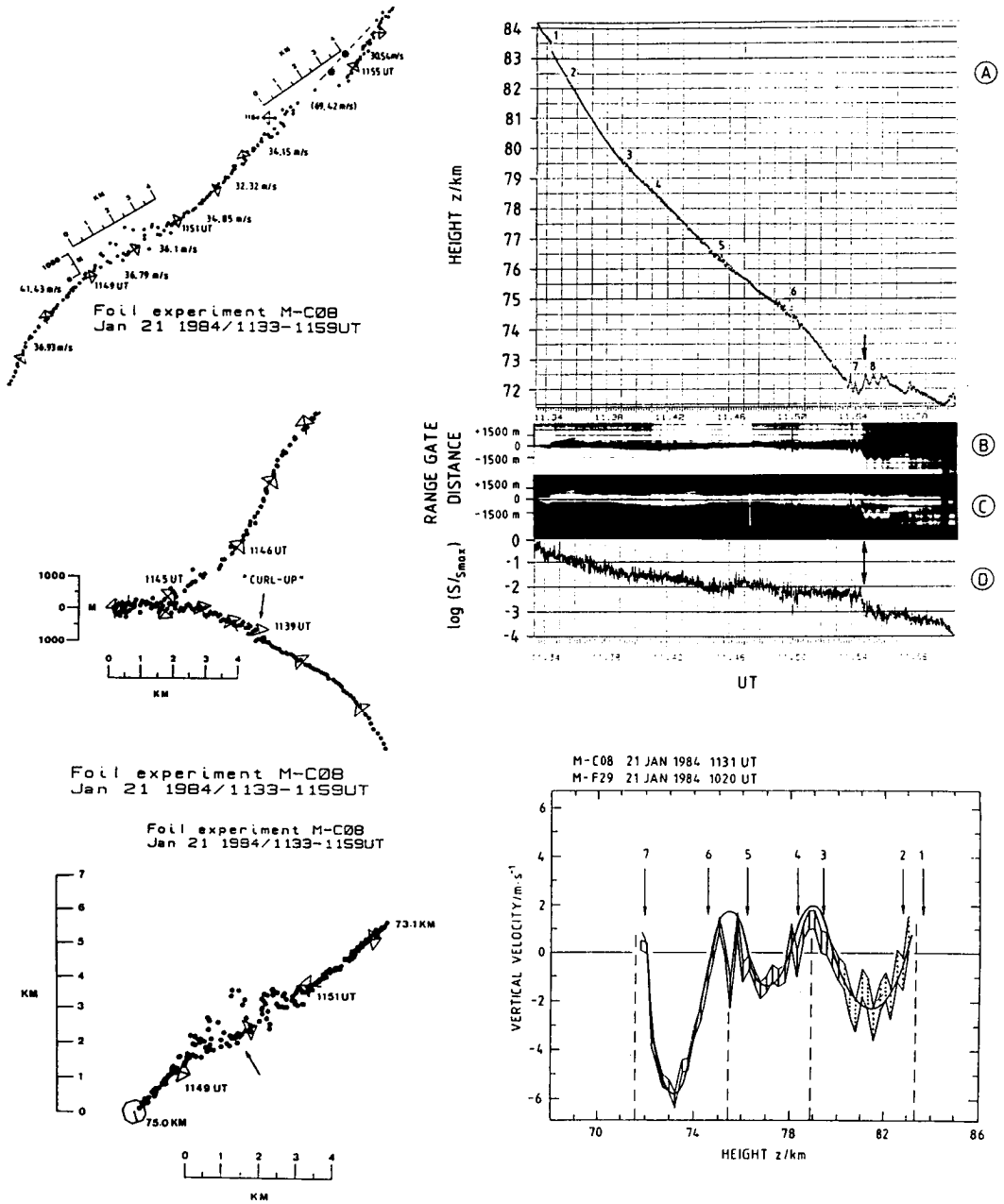


Figure 3.

ORIGINAL PAGE IS
OF POOR QUALITY

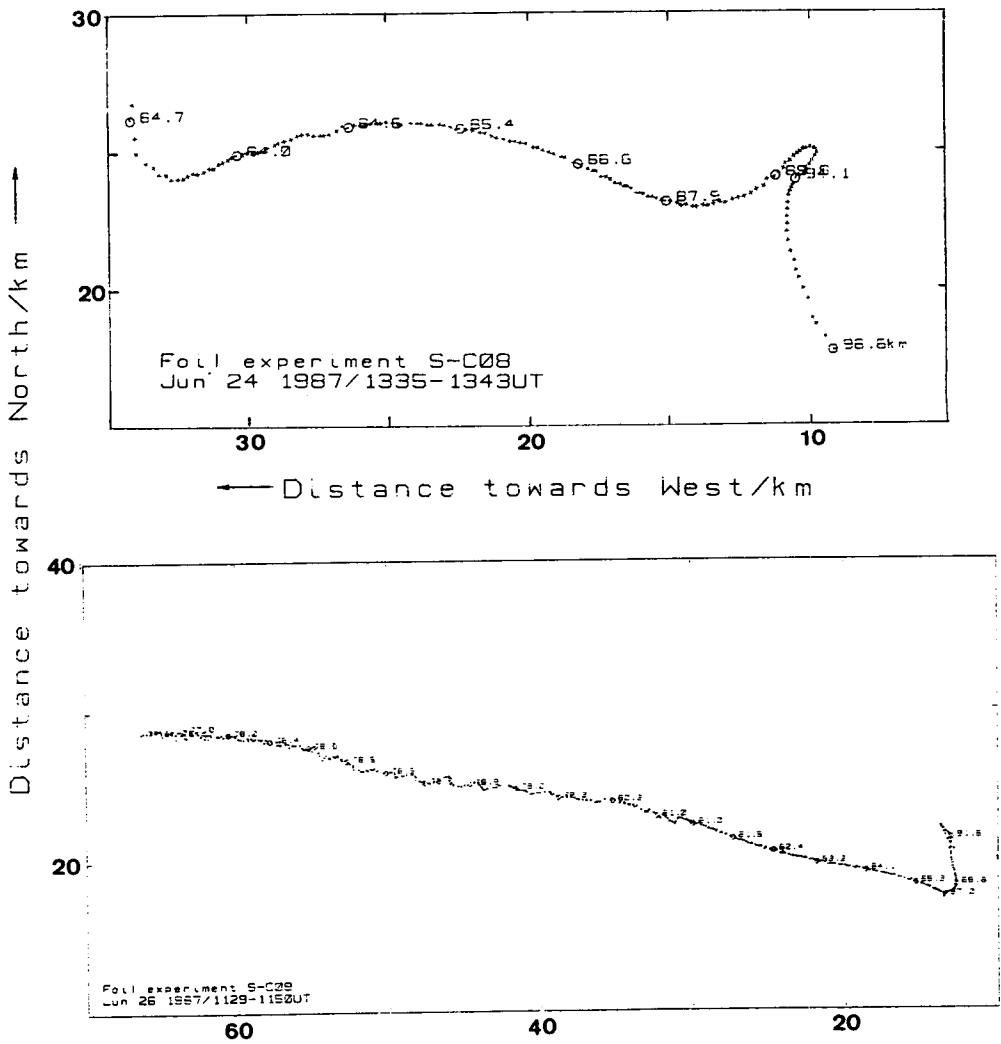


Figure 4. Summer measurement. No wind corners were observed below 88 km but rather uneventful drifts towards west (or south) in which strong turbulence and/or "billows" (vortices) were imbedded. Upper figure: very rapid destruction of cloud below 84 km. Lower figure: "Billows show up below 81 km. Rapid destruction (disappearance of the radar echo within a few seconds) was a salient feature of the summer measurements.

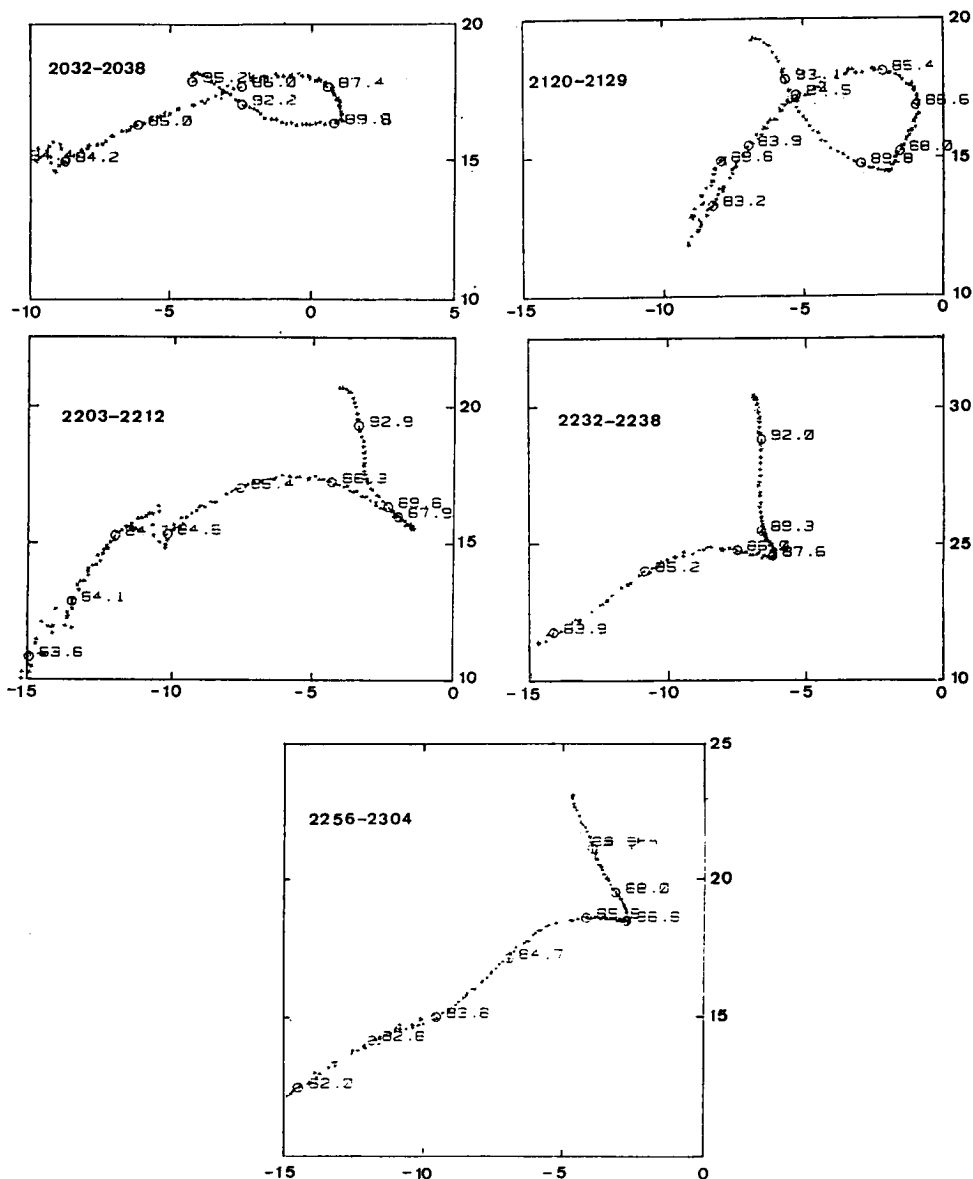


Figure 5. "Wind corners" were not seen during summer below 88 km, but above. Development of a "wind corner" shortly before local midnight between 88 and 89 km and its decay (15 July 1988). Note degradation of tracking data (resp. destruction of cloud flight 2120 UT) at the 83 - 84 km level caused by turbulence.

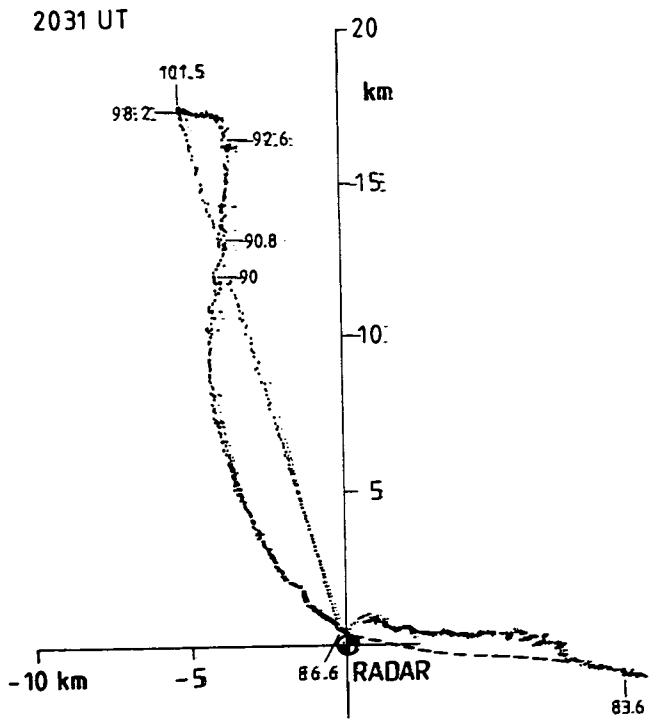


Figure 6. Second example for a development of a wind corner (24 June 1988) observations made with 1.5 μm and 1 μm chaff. 2031: No wind corner (note difference to 5!).

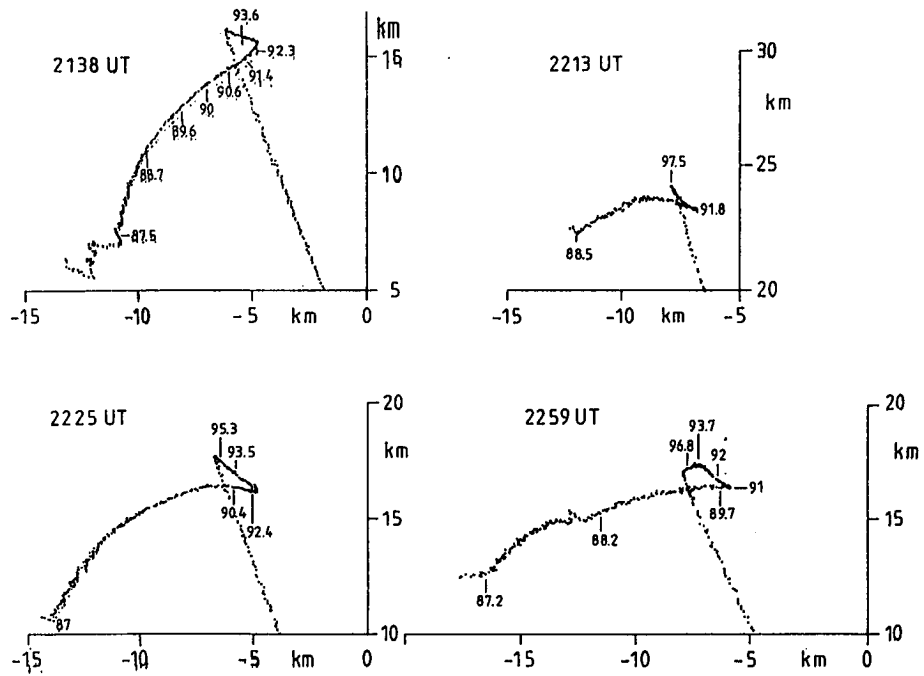


Figure 7. Development of wind corner which subsides. Note destruction of cloud at the 87-88 km level. Comparing 5 to 7 it looks as if the formation of wind corners is associated with a region of strong turbulence 4 - 6 km lower in height.

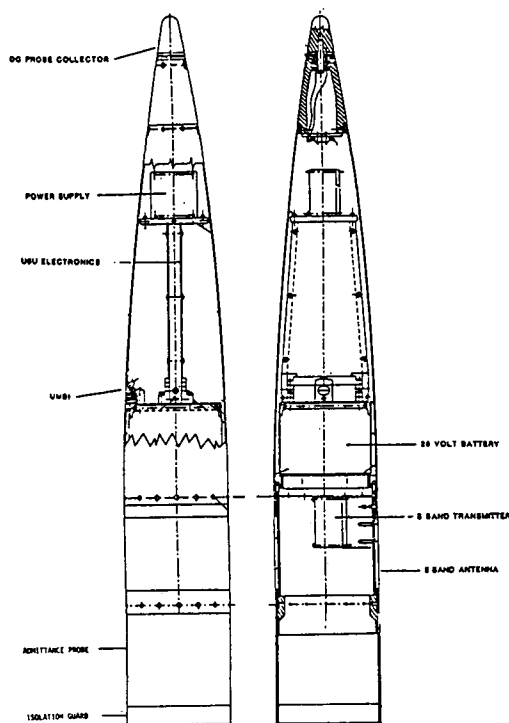
9.7 ROCKET MEASUREMENTS OF ELECTRON DENSITY IRREGULARITIES DURING MAC/SINE

J. C. Ulwick¹

Stewart Radiance Laboratory, Utah State University
Logan, UT 84321

Four Super Arcas rockets were launched at the Andoya Rocket Range, Norway, as part of the MAC/SINE campaign to measure electron density irregularities with high spatial resolution in the cold summer polar mesosphere. They were launched as part of two salvos: the turbulent/gravity wave salvo (3 rockets) and the EISCAT/SOUSY radar salvo (one rocket). In both salvos meteorological rockets, measuring temperature and winds, were also launched and the SOUSY radar, located near the launch site, measured mesospheric turbulence. Electron density irregularities and strong gradients were measured by the rocket probes in the region of most intense backscatter observed by the radar. The electron density profiles (8 - 4 on ascent and 4 on descent) show very different characteristics in the peak scattering region and show marked spatial and temporal variability. These data are intercompared and discussed.

¹Permanent address: 139 Great Road, Bedford, MA 01730



MAC/SINE SUPER ARCAS

Figure 1.

INSTRUMENTATION

DC PROBE: ON ALL FOUR SUPER ARCAS ROCKETS

TECHNIQUE - COLLECTION OF DC ELECTRON CURRENT OF ISOLATED TIP HELD AT FIXED +3-VOLT BIAS POTENTIAL WITH RESPECT TO ROCKET SKIN.

MEASUREMENT - HIGH RESOLUTION (SPATIAL TO ABOUT 10 CM) OF ELECTRON CURRENTS PRESUMED APPROXIMATELY PROPORTIONAL TO ELECTRON DENSITY.

RF PROBE: ON TWO OF FOUR SUPER ARCAS ROCKETS

TECHNIQUE - THE ROCKET BODY IS SPLIT (ISOLATED) AND FED AS A DIPOLE ANTENNA WHOSE RF ADMITTANCE AT 3 MHz IS TELEMETERED TO THE GROUND.

MEASUREMENT - LOW RESOLUTION ELECTRON DENSITY PROFILES.

MAC SINE SUPER ARCAS ROCKETS SUMMARY

<u>ROCKET NO.</u>	<u>SALVOE</u>	<u>LAUNCH DATE/TIME</u>	<u>APOGEE</u>	<u>REMARKS</u>
NASA 15.244 S-SA 1/L	TURBULENT GRAVITY WAVES	DAY 195 14 JULY 87 1000 L.T. (0800 UT)	95.4 KM	GOOD DC PROBE ASCENT & DESCENT
NASA 15.245 S-SA 2/H	TURBULENT GRAVITY WAVES	DAY 195 14 JULY 87 1129 L.T.	96.1 KM	GOOD DC PROBE ASCENT & DESCENT GOOD RF PROBE ASCENT & DESCENT
NASA 15.247 S-SA 3/H	TURBULENT GRAVITY WAVES	DAY 195 14 JULY 87 1455 L.T.	92.5 KM	GOOD DC PROBE ASCENT & DESCENT GOOD RF PROBE ASCENT & DESCENT
NASA 15.246 S-SA 4/L	EISCAT/SOUSY	DAY 196 15 JULY 87 1432 L.T.	97.7 KM	GOOD DC PROBE ASCENT & DESCENT

MS'T radar

$$\sigma = \frac{2\pi c k_B (T_s + \alpha T_c)}{P_T A_e \alpha^2 F_i} \left(\frac{r}{\Delta r} \right)^2 \frac{S}{N} \quad \text{Balsley and Gage [1980]}$$

$$\sigma = 1.15 \times 10^{-17} S/N \text{ m}^{-1}. \quad \text{Poker HST}$$

$$\sigma = C S/N \text{ m}^{-1}. \quad \text{Soucy}$$

Rocket

$$\sigma(k) = -n \left(\frac{\pi}{8} \right) k^2 \frac{f_p^4}{4f^4} \left(\frac{S_n(k)}{N_e^2} \right) \quad \text{Royruik and Smith [1984]}$$

$$\text{Poker } S/N = \frac{3.91 \times 10^{-11} (-n) N_e^2 V_R}{2\pi} \left(\frac{\Delta N_e}{N_e} \right)^2 \quad \text{where:}$$

n = Slope PSD
 N_e = Elec. Density
 V_R = Rocket Velocity

$$\text{Soucy } S/N = C (-n) N_e^2 V_R \left(\frac{\Delta N_e}{N_e} \right)^2 \quad \left(\frac{\Delta N_e}{N_e} \right)^2 = \text{Power at } f_o$$

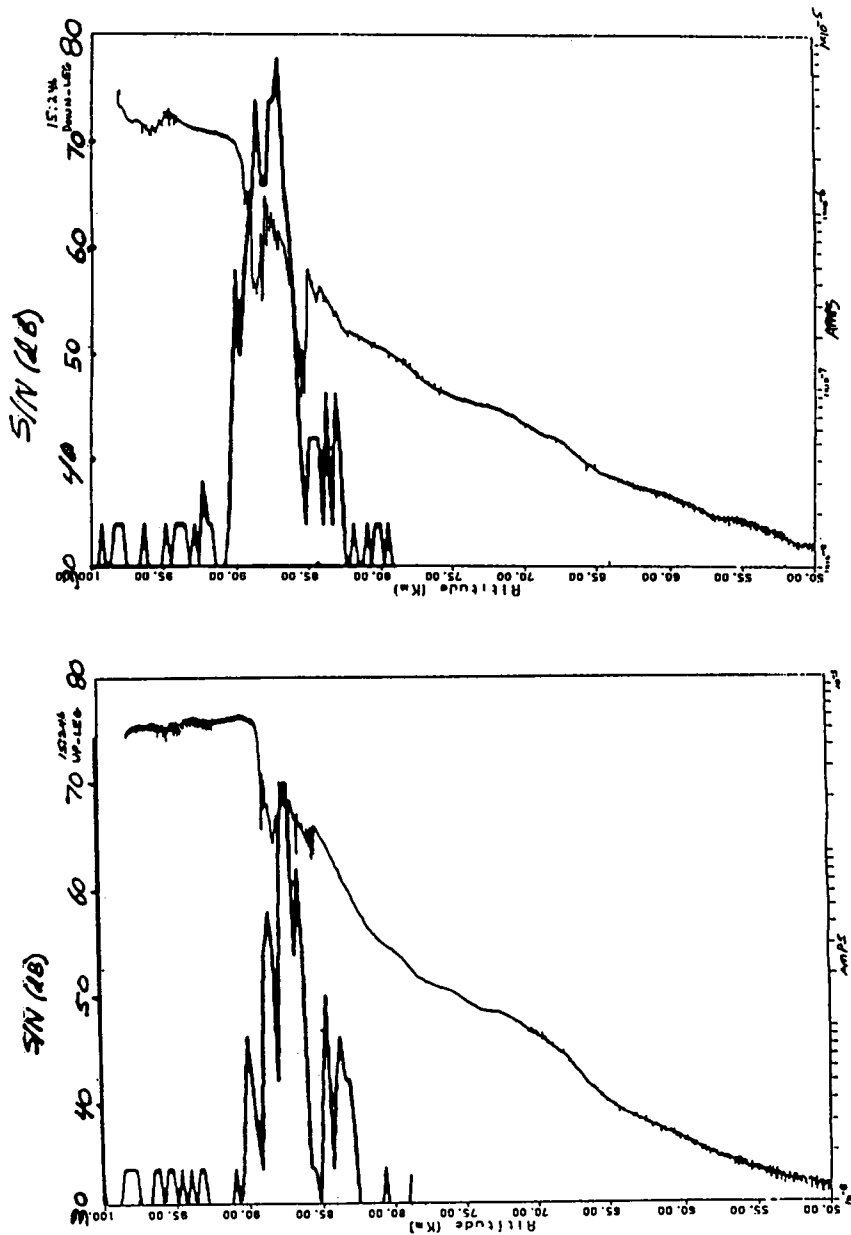


Figure 2.

ORIGINAL PAGE IS
OF POOR QUALITY

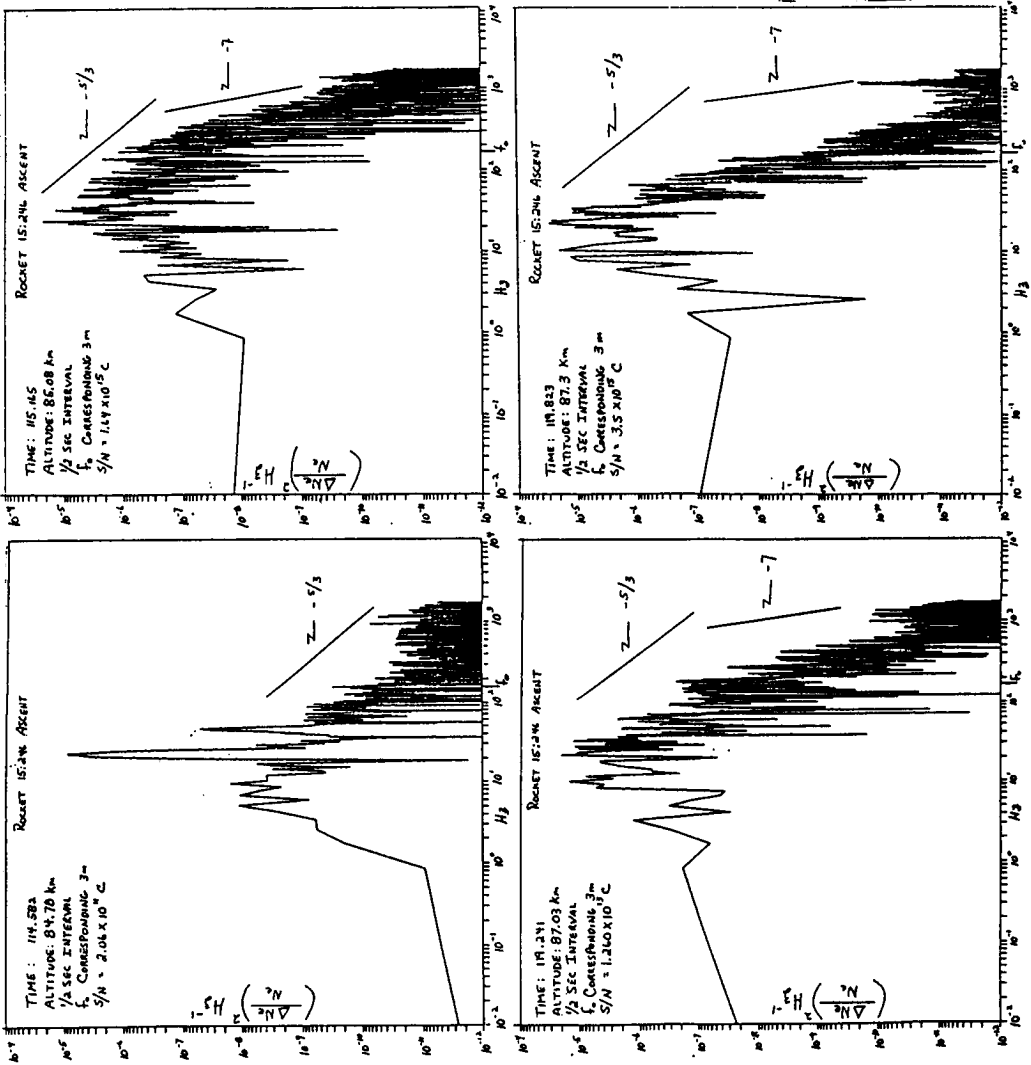


Figure 3.

9.8 TURBULENT SMALL-SCALE NEUTRAL AND ION DENSITY FLUCTUATIONS AS MEASURED DURING MAC/EPSILON

F.-J. Lübken, W. Hillert, U. von Zahn

Physics Institute, University of Bonn
Nussallee 12, D-5300 Bonn 1, FRG

T. Blix, and E. Thrane

Norwegian Defence and Research Establishment
N-2007 Kjeller, Norway

During the MAC/Epsilon campaign (Fall 1987, from Andoya, Northern Norway, 69°N, 16°E) a total of four altitude profiles of neutral gas number densities and six profiles of ion number densities were measured with high spatial resolution in the height range from 60 to 120 km. First results of these rocket-borne experiments will be presented with emphasis on small-scale turbulent density variations and related turbulent parameter as structure function constants and energy dissipation rates.

Raw-Data: $n(z)$; $n_{N_2}(z)$; $I(z)$

Relative Fluctuations: (data-fit)/fit

Spectral Analysis:

1. Power spectral density (PSD)
2. Spectral index ξ : $PSD \sim K_z^\xi$
3. Structure function constant C_n^2 :
 $PSD(k_z) = 0.125 * C_n^2 * k_z^{-5/3}$

Turbulent vertical velocity:

$$w^2 = 1.1 * \{g/4M\}^{3/2} * \{C_n^2\}^{3/2} / \omega_B$$

with

$$M = (1/n) * (dn_{\text{pot}}/dz) = 1/H_n - 1/\gamma H_p$$

Energy dissipation rate: $\epsilon = 0.4 w^2 \omega_B$

Eddy diffusion coefficient: $k = 0.8 \epsilon / \omega_B^2$

3 Instruments:

*Mass-spectrometer ("BUGATTI") n_{N_2} , (n_{Ar} , n_{He} , n_{Kr})

*Ionization-gauge ("TOTAL") n_{tot} ; Δn

*Positive ion probe ("PIP") I_i

Background temperature and -density from:

*BUGATTI and TOTAL: $90 \leq z \leq 125$ km

*Passive falling sphere: $45 \leq z \leq 90$ km

*LIDAR (MAC-E-T3 only): $82 \leq z \leq 97$ km

Small Scale Turbulence Measurements with BUGATTI PIP and TOTAL durch MAC/EPILON

MAC-E-T	Salvo	Launch	Apogee	BUGATTI	PIP	TOTAL
1	Day	Oct. 15, 1987 10:52:00 UT	127.0 km	Apogee - 94.0	63.4-120.0 km	117.-66,9 km
2	Night A	Oct. 21, 1987 21:33:00 UT	126.0 km	/	64.3-120.0 km	/
3	"	" + 20 sec	125.6 km	/	61.9-120.0 km	117.-64,2 km
4	Night B	Nov. 21, 1987 00:21:00 UT	126.0 km	/	64,9-120.0 km	/
5	"	" + 20 sec	124.2 km	/	67,0-120.0 km	117.-60,9 km

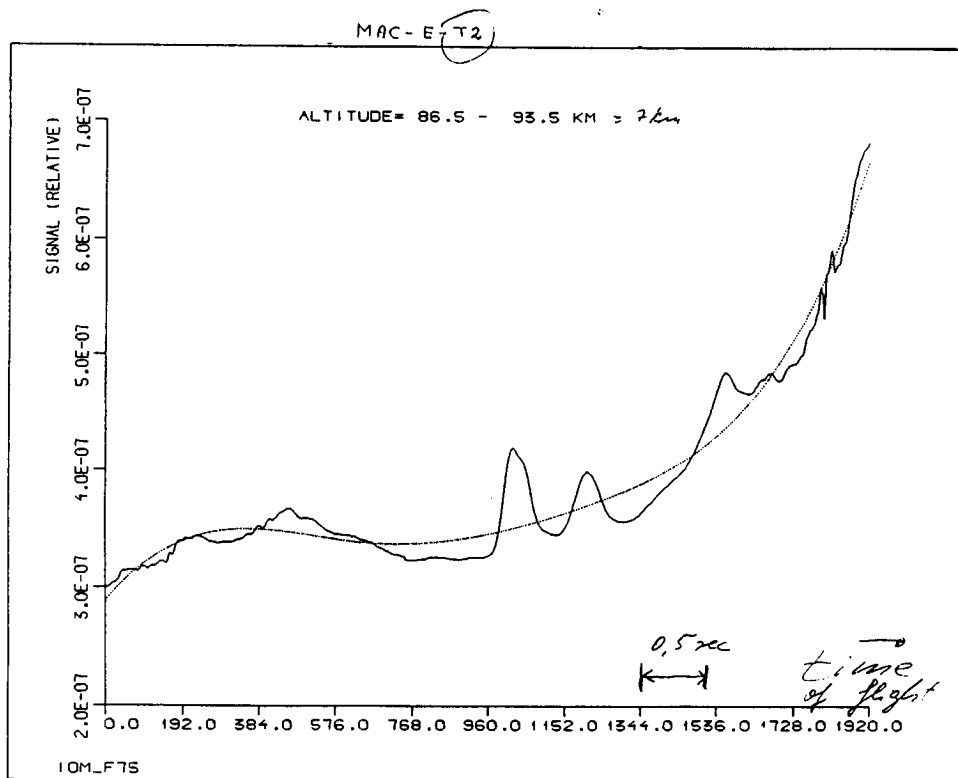


Figure 1.

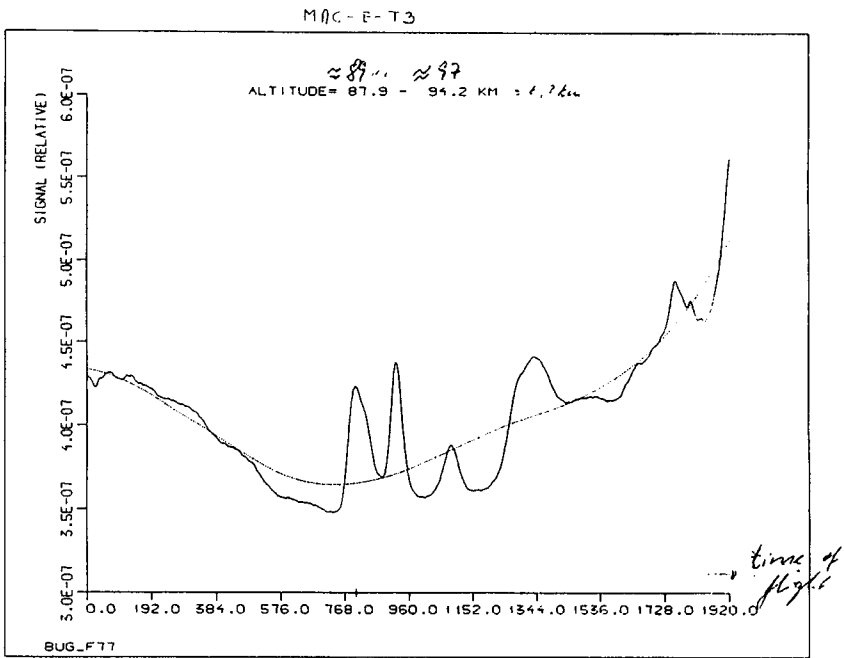


Figure 2.

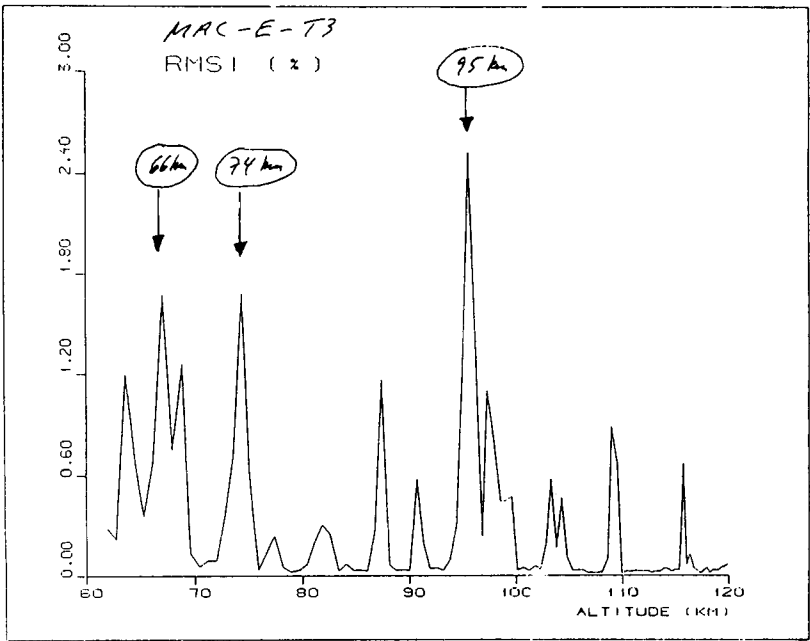


Figure 3.

MAC-E-T3

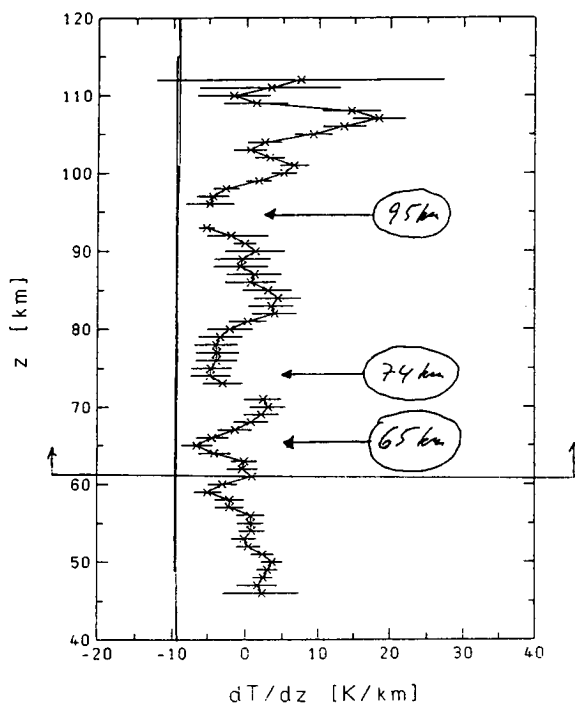


Figure 4.

MAC-E-T3: 64. km

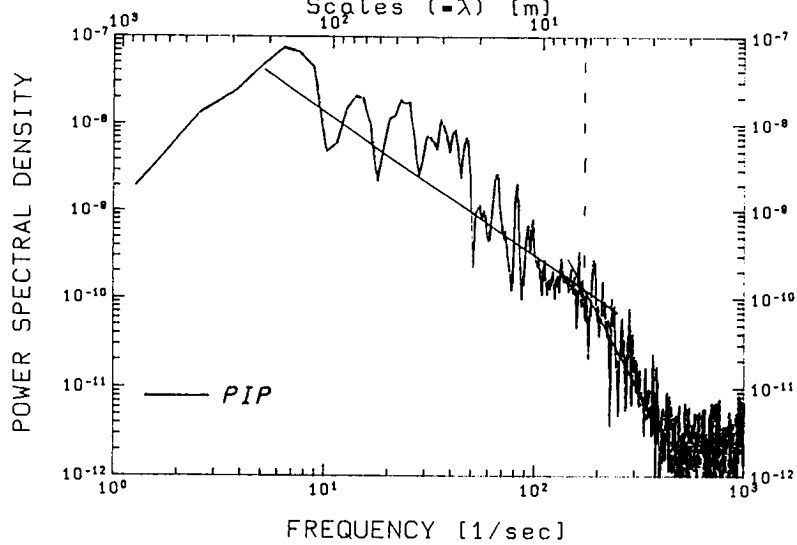
Scales ($=\lambda$) [m]

Figure 5.

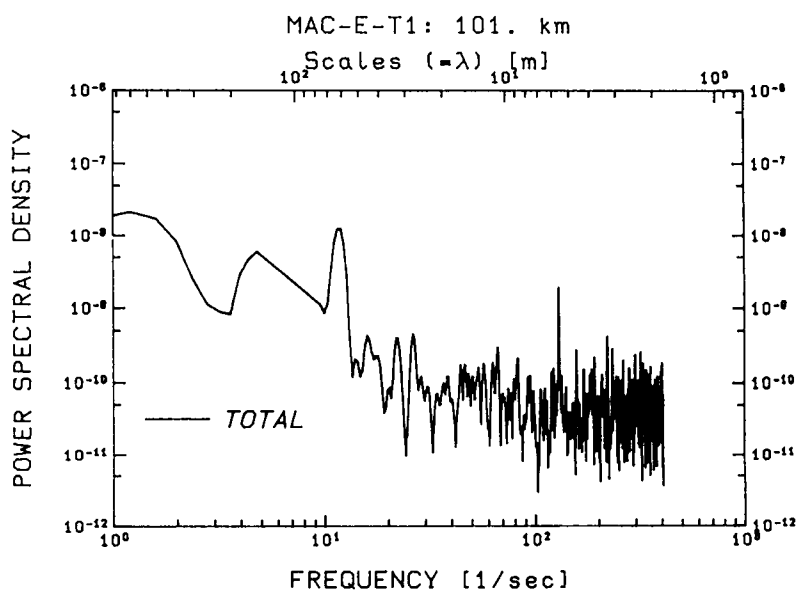


Figure 6.

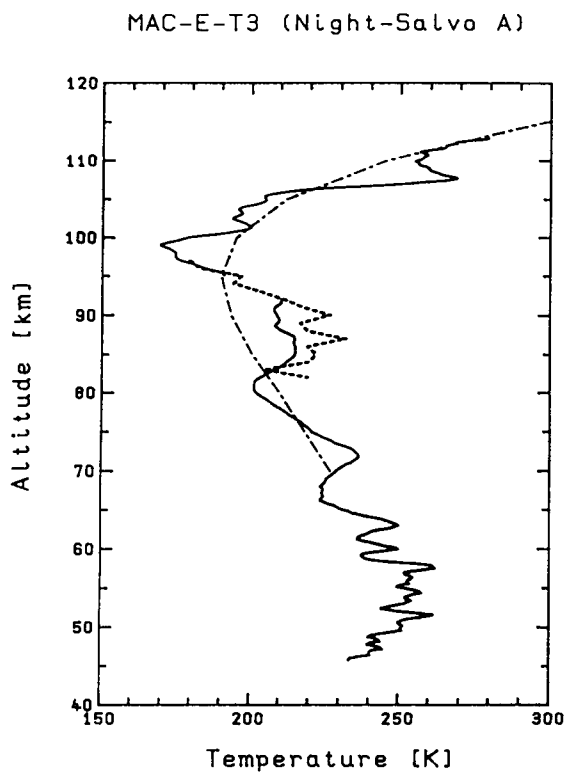


Figure 7.

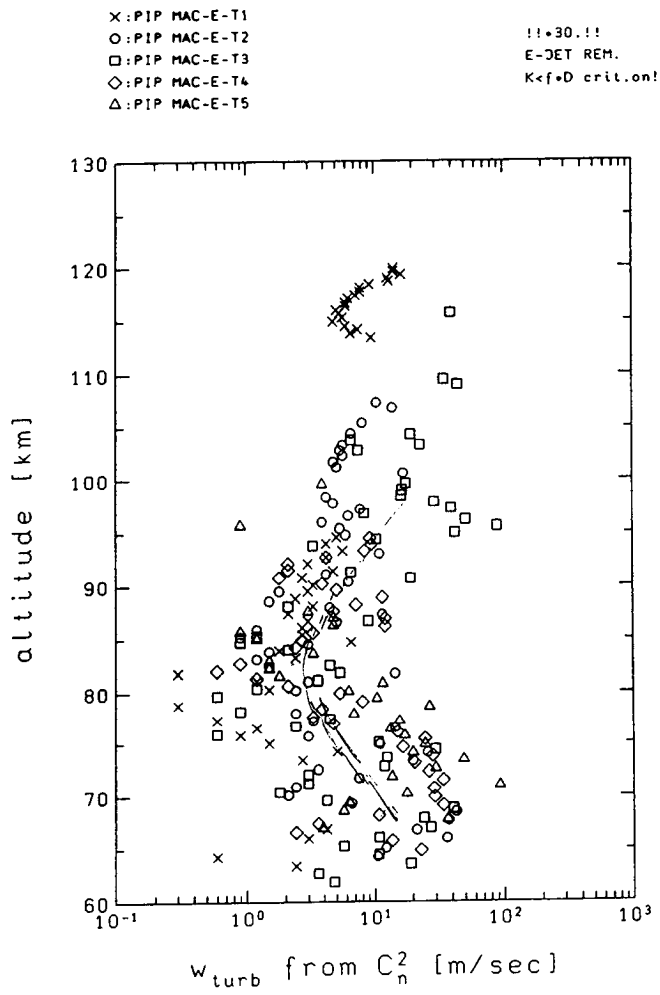


Figure 8.

9.9 MIDDLE ATMOSPHERE MEASUREMENTS OF SMALL-SCALE ELECTRON DENSITY IRREGULARITIES AND ION PROPERTIES DURING THE MAC/EPSILON CAMPAIGN

S. P. Blood, J. D. Mitchell, and C. L. Croskey

Communications and Space Sciences Laboratory
Department of Electrical Engineering, The Pennsylvania State University
University Park, PA 16802

Rocket payloads designed to measure small-scale electron density irregularities and ion properties in the middle atmosphere were flown with each of the three main salvos of the MAC/Epsilon campaign conducted at the Andoya Rocket Range, Norway, during October to November 1987. Fixed-bias, hemispheric nose tip probes measured small-scale electron density irregularities, indicative of neutral air turbulence, during the rocket's ascent; and subsequently, parachute-borne Gerdien condensers measured the region's polar electrical conductivity, ion mobility and density. One rocket was launched during daylight (October 15, 1052:20 UT), and the other two launches occurred at night (October 21, 2134 UT; November 12, 0021:40 UT) under moderately disturbed conditions which enhanced the detection and measurement of turbulence structures. A preliminary analysis of the real-time data displays indicates the presence of small-scale electron density irregularities in the altitude range of 60 to 90 km. Ongoing data reduction will determine turbulence parameters and also the region's electrical properties below 90 km.

TABLE 1 MAC/Epsilon Campaign--Penn State Experiments

Launch Date--Time (Flight No.)	Probe	Measurements	Launch Conditions
15 Oct. 1987--1052:20 UT (30.038)	Nose Tip	$I_e, \Delta N_e/N_e$	Daytime
	Gerdien Condenser	$\sigma_{\pm}, k_{\pm}, N_{\pm}$	Disturbed
	Booms	E field	
	Rigid Electrode	I_{Max}	
21 Oct. 1987--2133:40 UT (31.066)	Nose Tip	$I_{+}, \Delta N_{+}/N_{+}$	Nighttime
	Booms	E Field	Disturbed
21 Oct. 1987--2134:00 UT (30.036)	Nose Tip	$I_e, \Delta N_e/N_e$	Nighttime
	Gerdien Condenser	$\sigma_{\pm}, k_{\pm}, N_{\pm}$	Disturbed
	Booms	E field	
	Rigid Electrode	I_{Max}	
28 Oct. 1987--0021:00 UT (31.067)	Nose Tip	$I_e, \Delta N_e/N_e$	Nighttime
	Booms	E field	Disturbed
	Blunt	σ_{\pm}	
12 Nov. 1987--0021:40 UT (30.037)	Nose Tip	$I_e, \Delta N_e/N_e$	Nighttime
	Gerdien Condenser	$\sigma_{\pm}, k_{\pm}, N_{\pm}$	Disturbed
	Booms	E field	
	Rigid Electrode	I_{Max}	

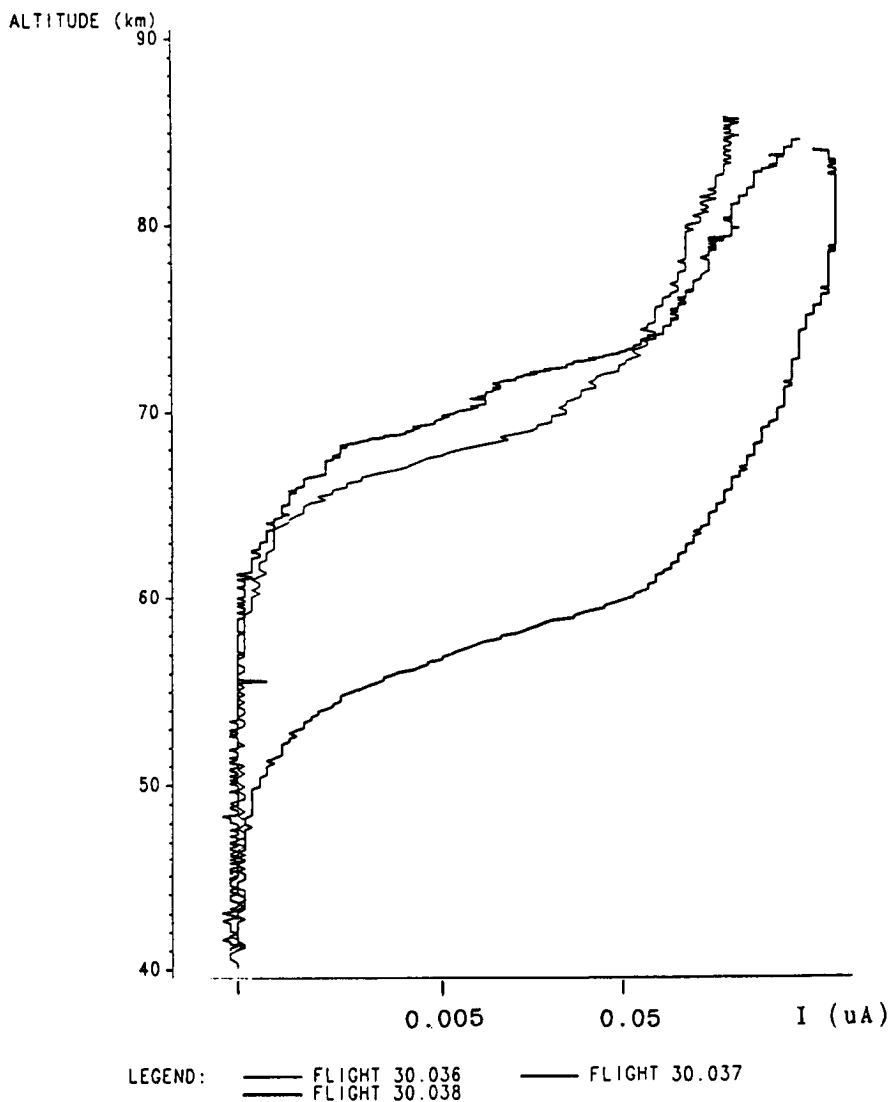


Figure 1. Nose tip probe electron current measurements for flights 30.036, 30.037 and 30.038. The different currents, for the same altitude, are indicative of relative electron concentrations. The electron number densities are the largest for the daytime flight 30.038 (salvo 1). In comparing the two nighttime current profiles, the electron concentration for salvo 2 (flight 30.036) was larger below 73 km and smaller above that altitude. Large scale (≥ 1 km) wave-like structures are noticeable in the electron current measurements, particularly at altitudes above 70 km.

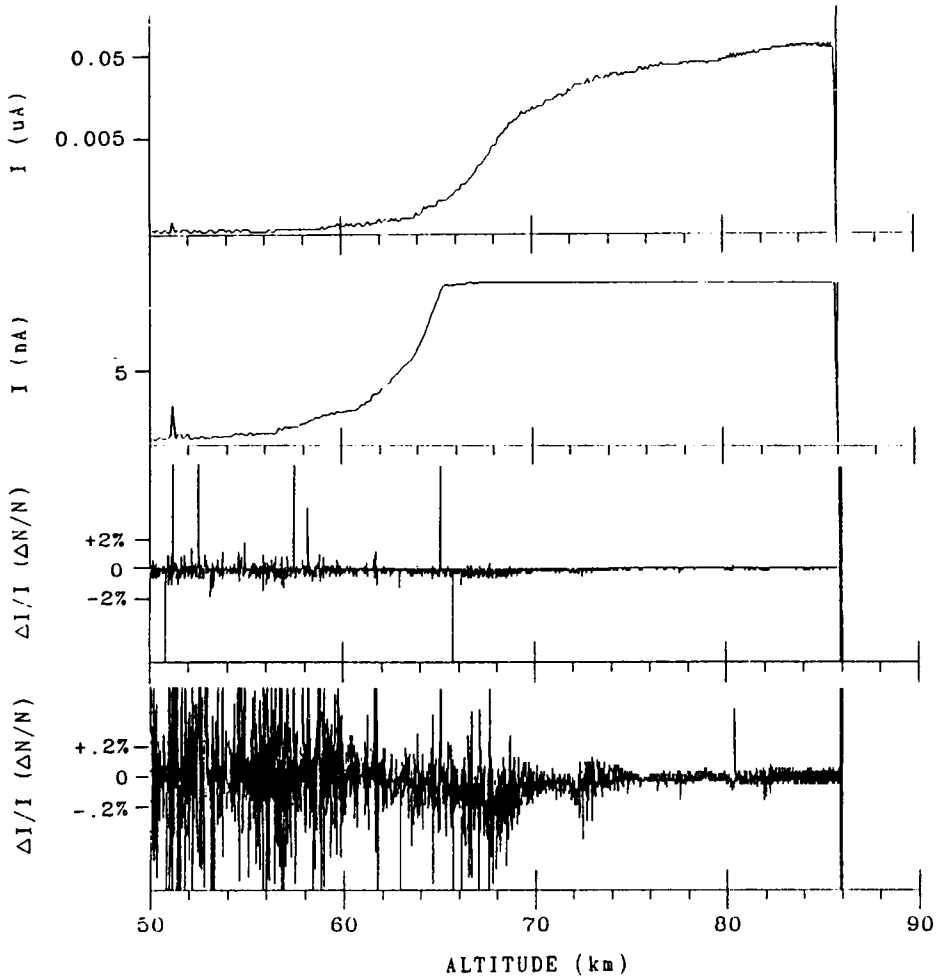


Figure 2. Nose tip probe dc and ac (amplified) electron current measurements for flight 30.036 (salvo 2). The dc electron current measurements (upper two panels) indicate the presence of free electrons at altitudes above approximately 64 km. Noticeable ac current variations (electron density fluctuations) at 68 km and 72-74 km indicate possible regions of small-scale turbulence. A power density spectrum for the small-scale electron density irregularities at 74 km showed a slope of $-5/3$ for frequencies of 10 - 200 Hz, indicating turbulence in the inertial subrange. A spectral index of -7 at higher frequencies, indicative of the viscous range, also was determined.

2134 UT - 21 OCTOBER 1987 (30.036)

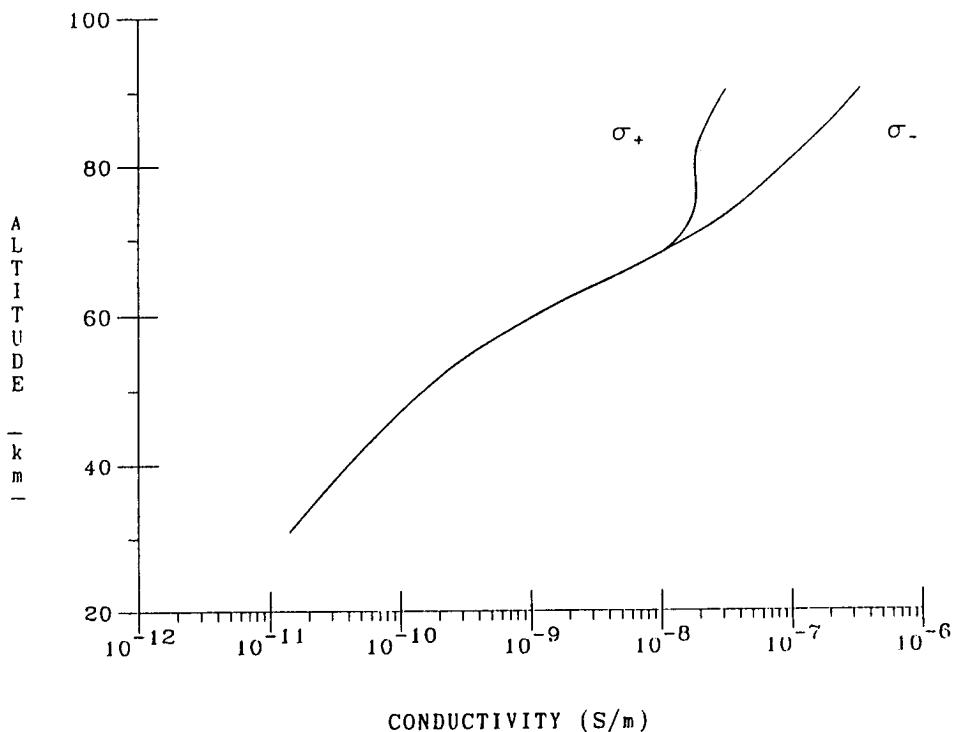


Figure 3. Profiles of positive and negative electrical conductivity obtained for flight 30.036 (salvo 2) by a parachute-borne Gerdien condenser. The altitude dependence for conductivity indicates the presence of auroral ionization sources above approximately 50 km (supported by the energy deposition measurements of Goldberg et al.) The relatively larger negative conductivity values above 65 - 70 km signifies the region where free electrons are present, which is consistent with the nose tip probe data of Figures 1 and 2.

9.10 PRELIMINARY MEASUREMENTS OF AURORAL ENERGY DEPOSITION AND MIDDLE ATMOSPHERE ELECTRODYNAMIC RESPONSE DURING MAC/EPSILON

R. A. Goldberg

NASA/Goddard Space Flight Center
Code 696, Greenbelt, MD 20771

On the nights of October 21 and 28, 1987 (UT), two Nike Orion payloads (NASA 31.066 AND 31.067) were launched from Andoya, Norway, as part of the MAC/Epsilon campaign, to study auroral energetics and their effect on the middle atmosphere. Each payload carried instrumentation to measure relativistic electrons from 0.1 to 1.0 MeV in 12 differential channels, and Bremsstrahlung X-rays from > 5 to > 80 keV in 5 integral channels. In addition, instrumentation to measure ion densities and electric fields were also included on these and, in the case of 31.066, on other near simultaneous payloads. The first flight, 31.066, was launched under pre-magnetic midnight conditions during relatively stable auroral conditions. Flight 31.067 was launched during post-breakup conditions, at which time pulsations of approximately 100 seconds duration were evident. The measured radiations including their spectral characteristics are compared for these two events, to appraise their effect on the electrodynamic properties of the middle atmosphere as determined by other rocket-borne measurements.

31.066/31.067 MAC/EPSILON

Scientific Team

<u>Instrument</u>	<u>Investigators/affiliation</u>
Solid state detector	R. A. Goldberg, NASA/GSFC
X-Ray detector	J. R. Barcus, Univ. Denver
Geiger tube	R. A. Goldberg, J. R. Barcus
Nosetip probe	J. D. Mitchell, S. Blood, Penn. State Univ.
Conductivity probe	L. C. Hale, C. L. Croskey, Penn. State Univ.
Positive ion probe	E. Thrane, T. Blix, NDRE
3D-Electric field	L. C. Hale, C. L. Croskey
Wind Spectrometer	F. A. Herrero, NASA/GSFC

Figure 1. During MAC/Epsilon two Nike Orion rockets were launched from Andoya, Norway, to study auroral energetic radiation and middle atmosphere response in both a neutral and electrodynamic sense. Each payload carried the listed instrument complement. The figure also lists the scientific team. Upon reaching about 90 km, each payload was despun and pointed along the earth's magnetic field, thereby permitting radiation measurements in a controlled pitch angle environment.

ORIGINAL PAGE IS
OF POOR QUALITY

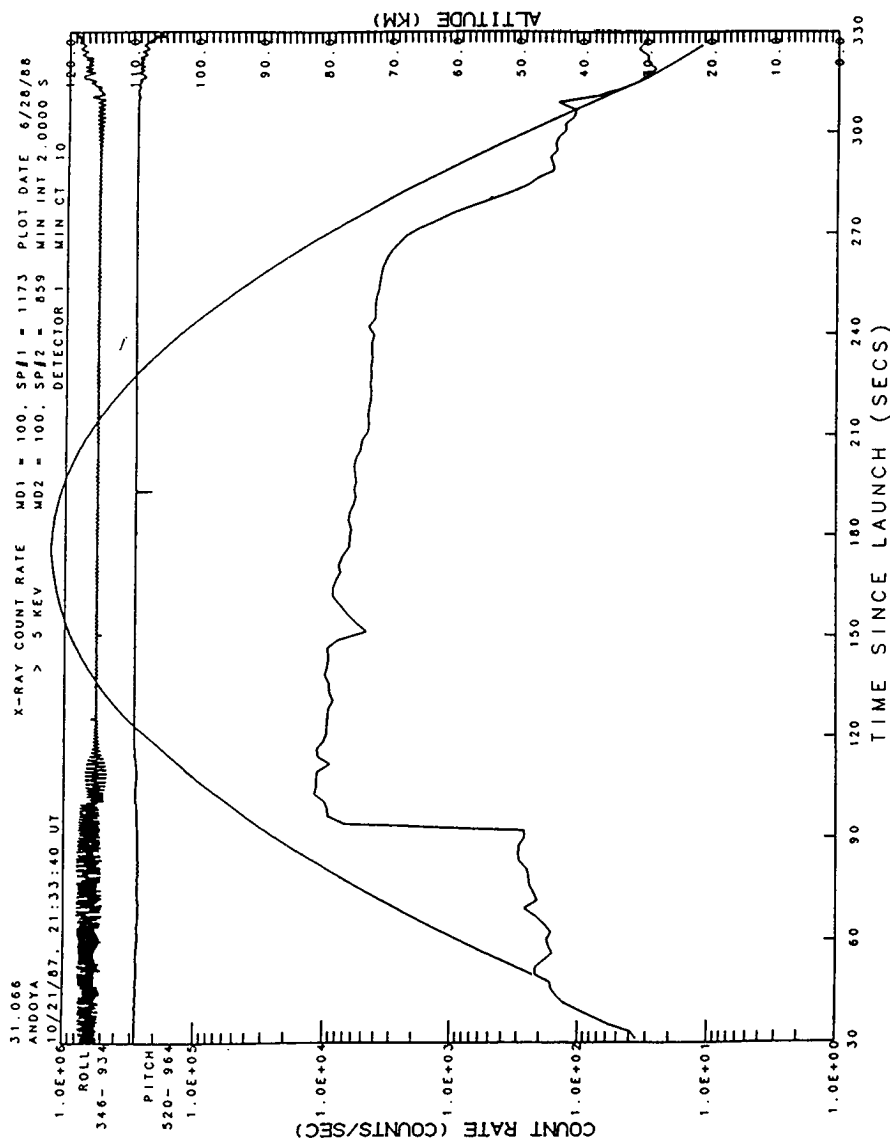


Figure 2. The first payload, 31.066, was launched on the night of October 21, 1987, as part of a near simultaneous 5 rocket series. Launch occurred during the recovery phase of a magnetic substorm with the local sidereal time a little less than 1 dB absorption. The figure displays count rates measured by the forward-looking X-ray scintillator detector in the 75 keV channel along with the trajectory as a function of time. Also shown are the magnetic pitch and roll exhibiting the despin and magnetic field alignment. From detector exposure at nose cone deployment near 90 km, X-ray detector count rates show a linear decline with time. Comparison with the solid-state detector data (12 differential channels above 90 keV) shows similar characteristics, implying that the X-ray detector is primarily responsive to relativistic electrons above 90 km.

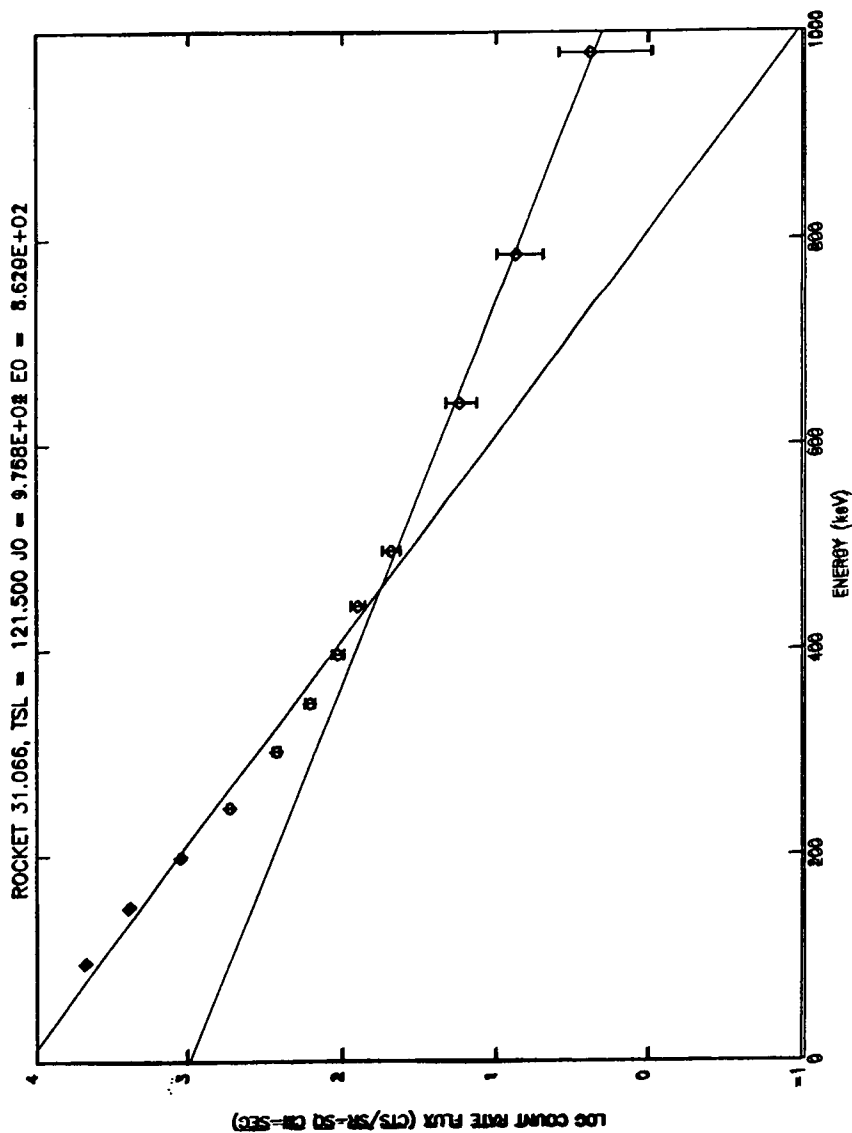


Figure 3. The integral spectrum shown here was obtained from the solid-state detector during the 1 second period about 121.5 s into the flight. It shows a two-component spectrum with a break point near 450 keV, having E_0 folding energies of about 86 and 162 keV below and above 450 keV, respectively. These values for $1 E_0$ were maintained throughout the flight.

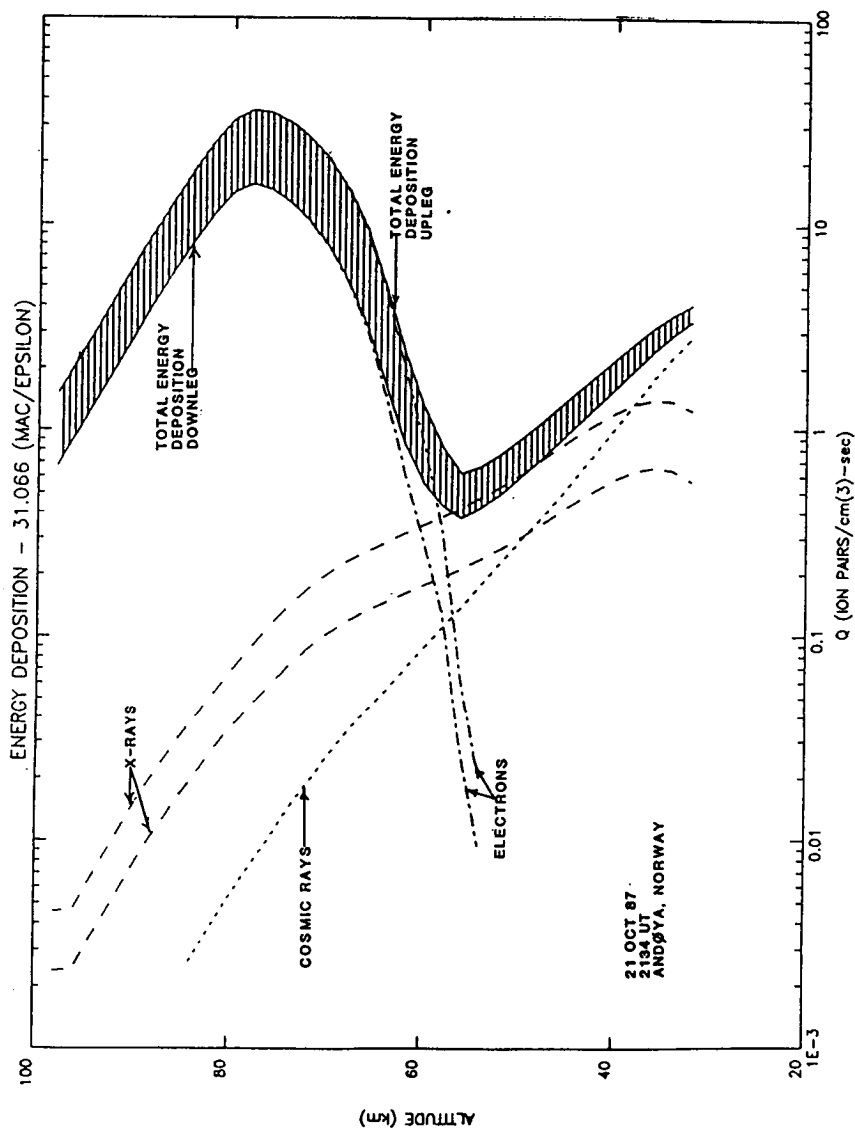


Figure 4. The X-ray and relativistic electron measurements have been used to calculate an energy deposition profile within the atmosphere, given as an ion-pair production rate. The upper and lower bounds of the decaying flux are given by the upper and lower boundaries of the shaded curve. Individual contributions from X-rays, electrons, and cosmic rays (modeled) are provided. The figure shows a peak in energy deposition near 85 km (for electrons > 90 keV), which remains well above the cosmic ray background to altitudes below 60 km. The dominant flux is controlled by electrons throughout this entire height range.

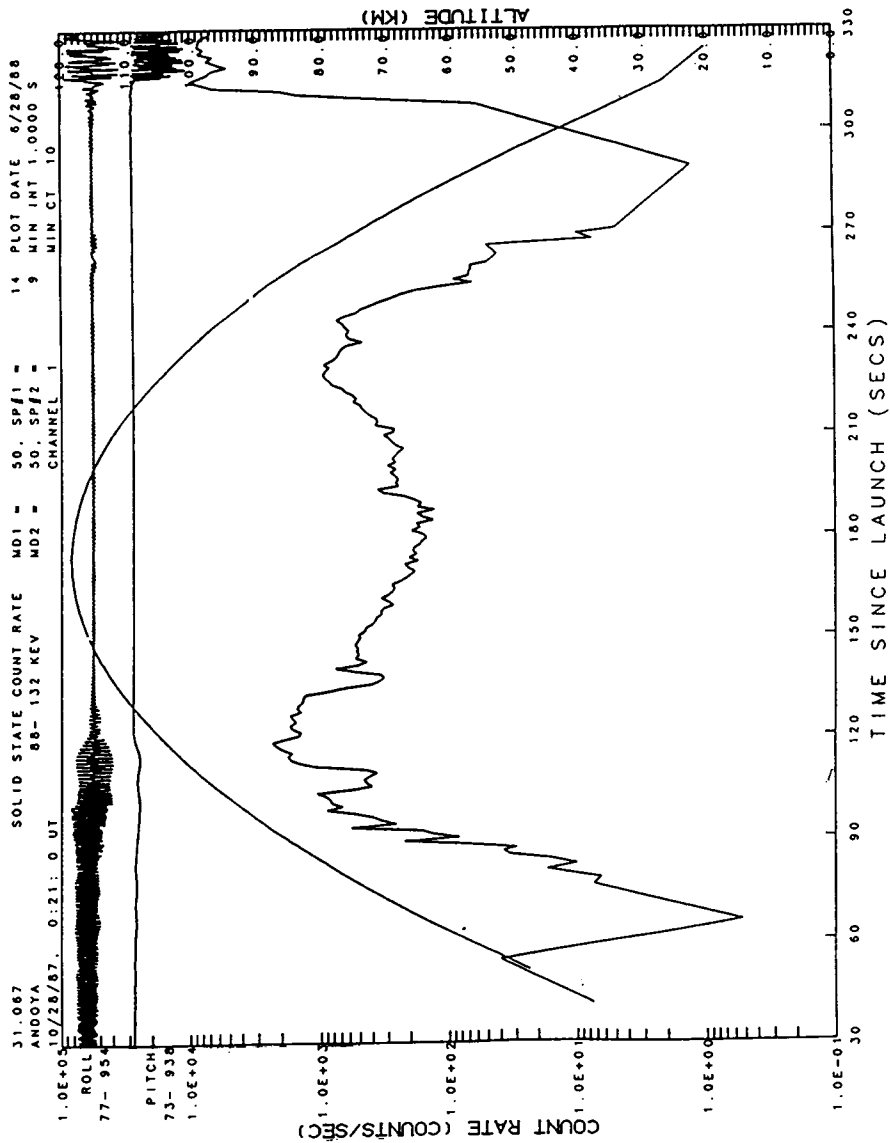


Figure 5. On October 28, 1987, the second Nike Orion (31.067) was launched as a solo rocket during a brief recovery phase of a large magnetic storm (geomagnetic absorption ~ 2 dB). The figure shows count rates from the first channel (88 - 132 keV) of the solid-state detector, which exhibits large pulsations during the early and late portions of the flight.

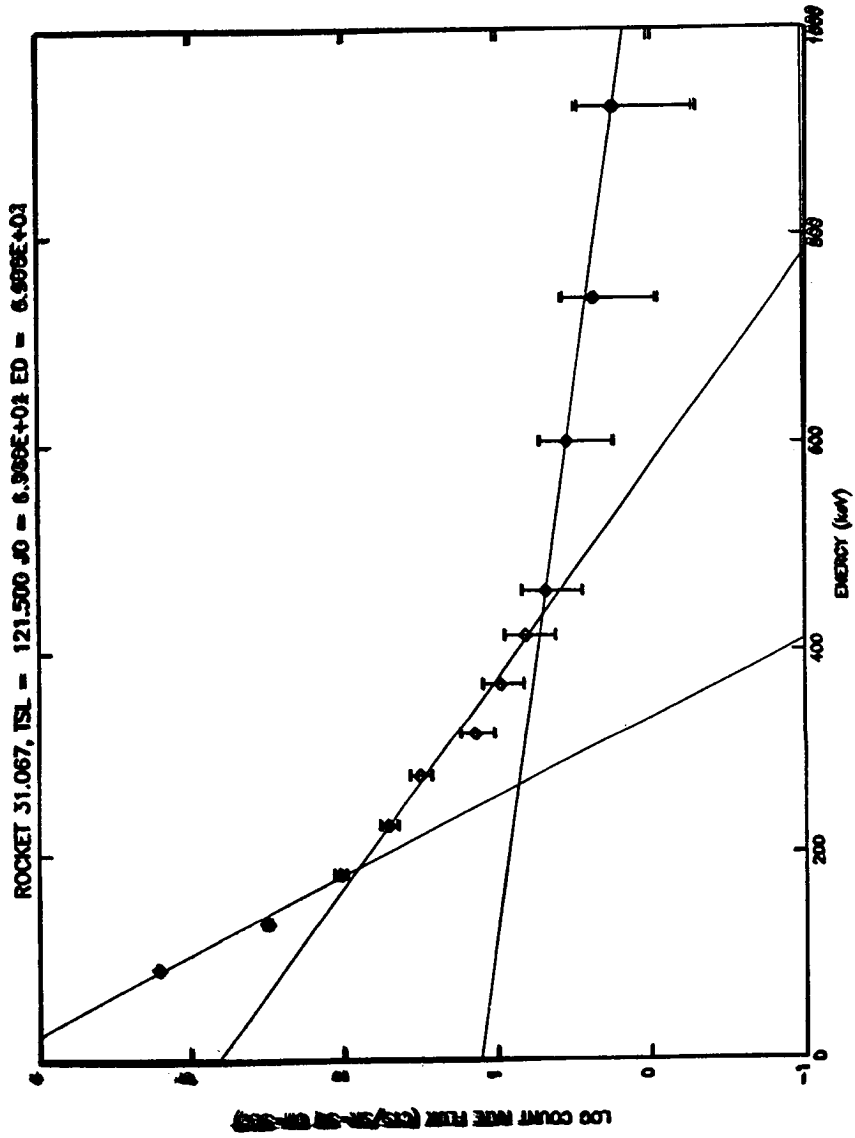


Figure 6. The solid-state detector in this case showed a 3-component spectrum, with the addition of a steep low-energy component. This low energy component (< 100 keV) should have produced large quantities of Bremsstrahlung X-rays, which were seen by the X-ray detectors aboard this payload.

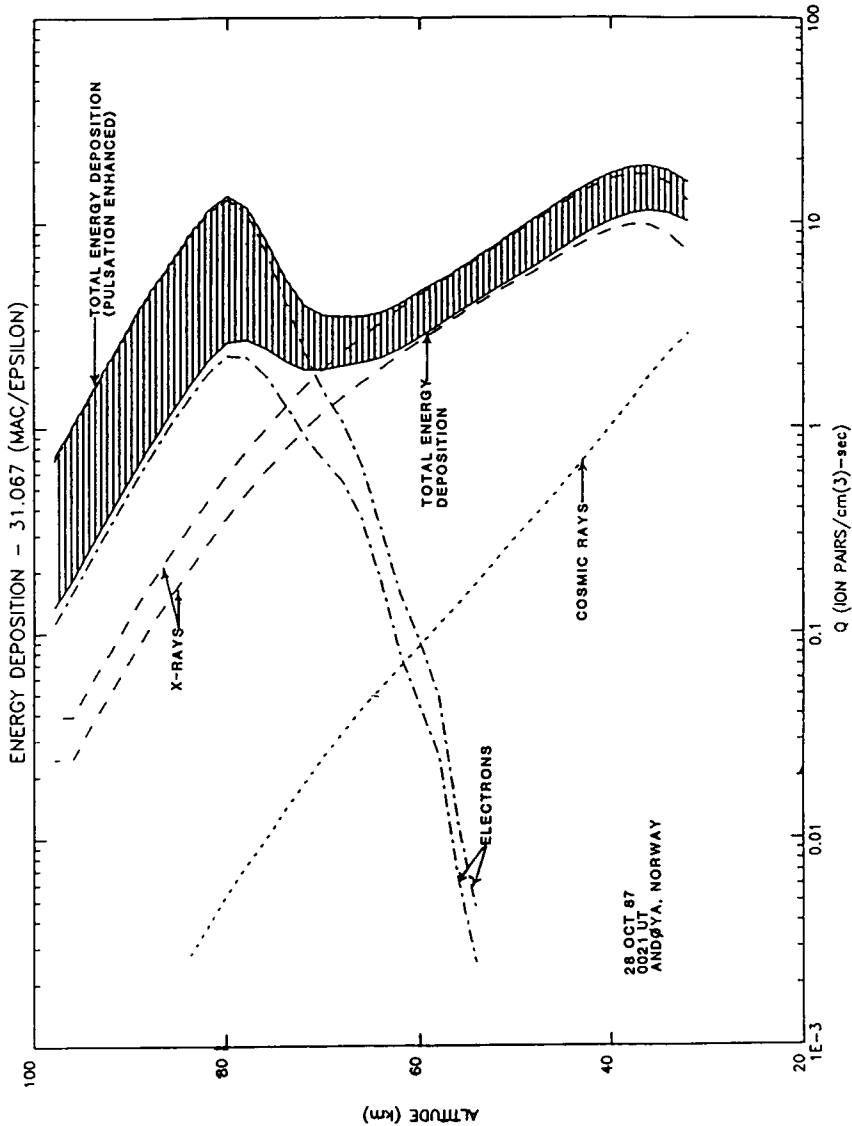


Figure 7. The data obtained from X-ray and particle data on 31.067 were used to determine the energy deposition profiles shown here. The lower and upper bounds on the curves are our current best estimate of the stable and pulsation enhanced contributions. Although the electrons produce an enhancement in the energy deposition peak near 80 km, the dominant source of radiation on this flight was from Bremsstrahlung X-rays, which penetrated significantly below 40 km. These were probably produced by the huge flux of lower energy electrons, not present on the night of the 31.066 flight.

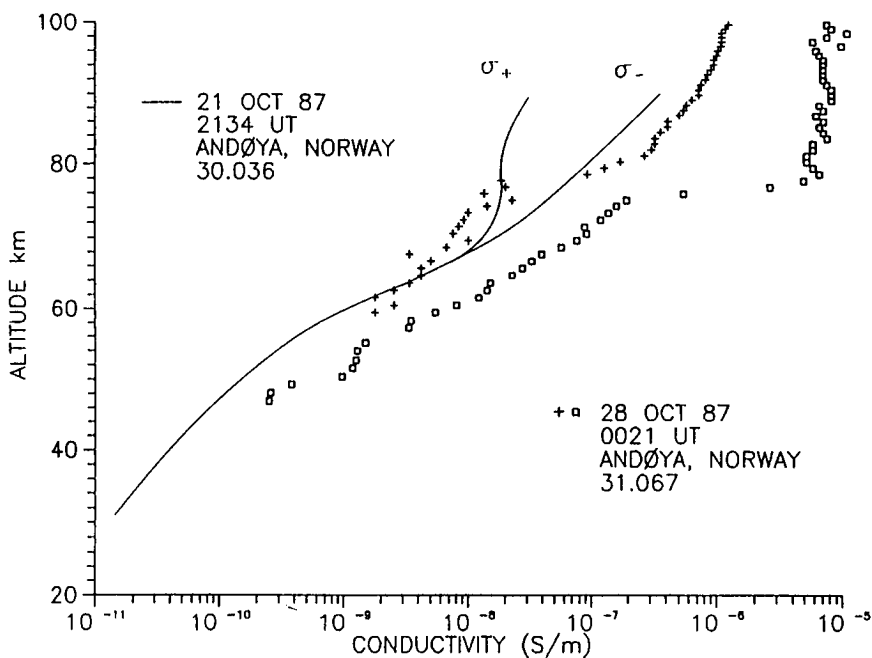


Figure 8. This figure shows conductivity profiles obtained during each rocket flight. On October 21, 1987 (31.066), there is a change in slope near 60 km, reflecting an enhancement in the conductivity profile which demonstrates a departure from cosmic rays as the primary ionizing source. Above 65 km, the positive and negative conductivity curves separate, indicating the presence of free electrons. For the night of October 28, 1987 (31.067), the huge source of Bremsstrahlung X-rays maintains free electrons down to approximately 50 - 55 km, with an enhanced conductivity above the expected cosmic ray level to much lower altitudes. The conductivity profiles obtained on both nights are thereby consistent with the measured energy deposition profiles. The enhanced conductivities above 80 km for October 28 are attributed to the lower energy electrons (< 90 keV) which were not directly measured in spectral form on either flight and thereby not reflected in the energy deposition curves at this time.

9.11 POSITIVE ION COMPOSITION IN THE POLAR D AND E REGIONS MEASURED DURING MODERATE IONOSPHERIC ABSORPTION

P. Lämmerzahl and D. Krankowsky

Max-Planck-Institut für Kernphysik
Postfach 103980, D-6900 Heidelberg, FRG

During the MAC/Epsilon campaign a mass spectrometer probe was flown on a rocket launched from Andoya (Norway) on 12 November 1987 at 0021 UT providing partial ion density profiles in the altitude range between < 50 km and 125 km. Due to the short sampling period of 0.17 seconds structural features could be observed at ~ 150 m height resolution in the regimes where metal ions occur and where cluster ions are dominant. The observations were made during stable ionospheric absorption of 1 - 1.5 dB. Preliminary results are presented and discussed.

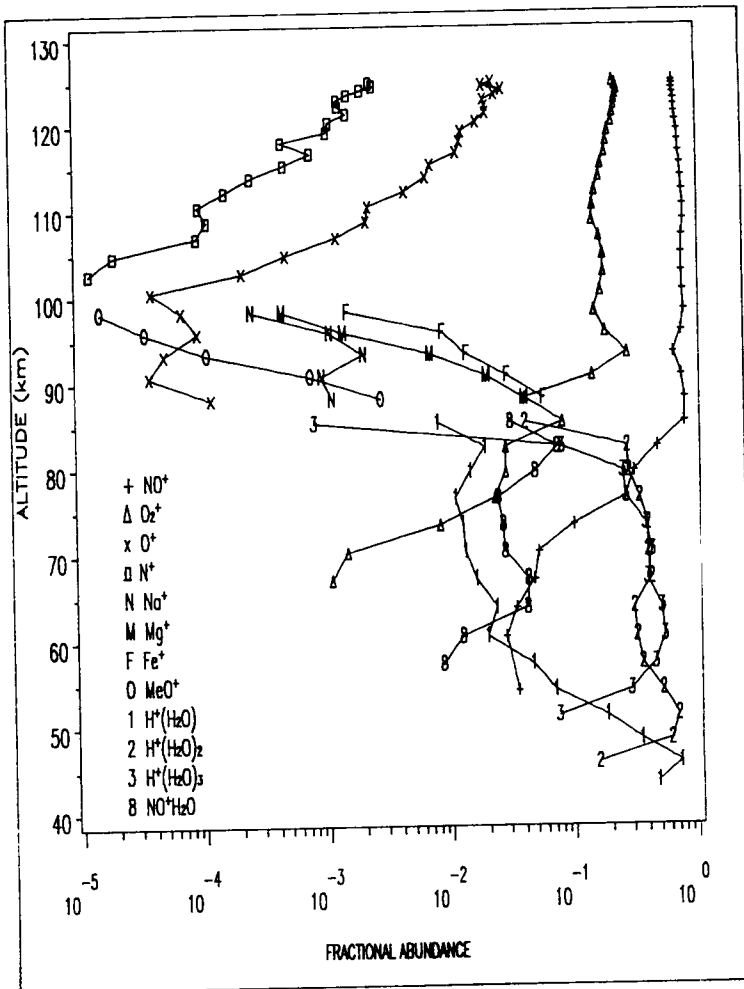


Figure 1.

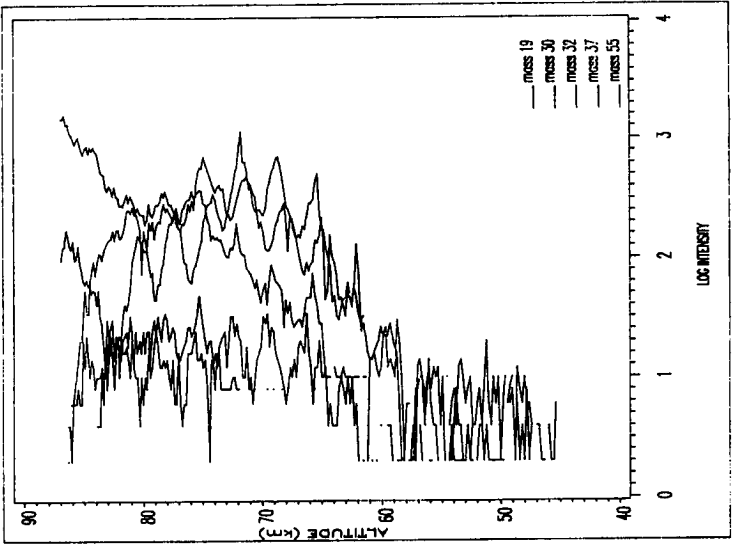


Figure 2.

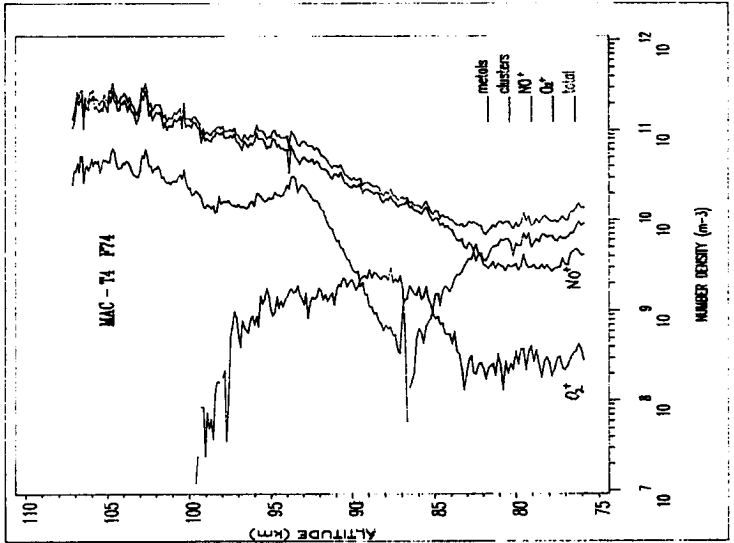


Figure 3.

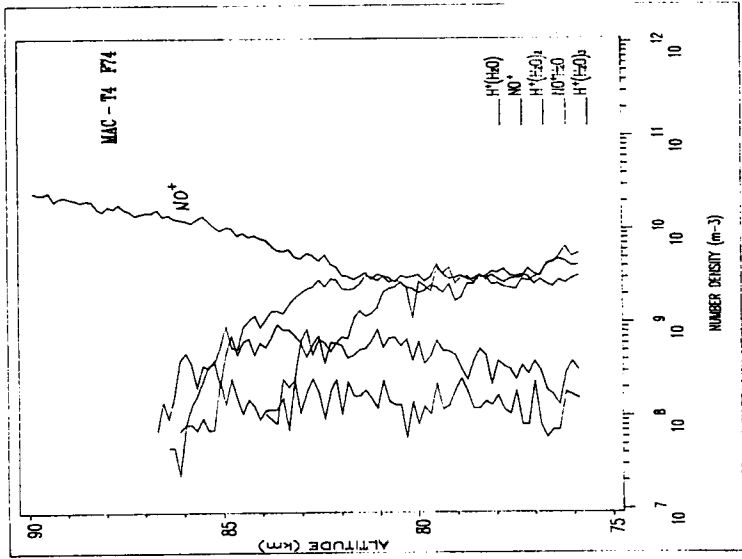


Figure 4.

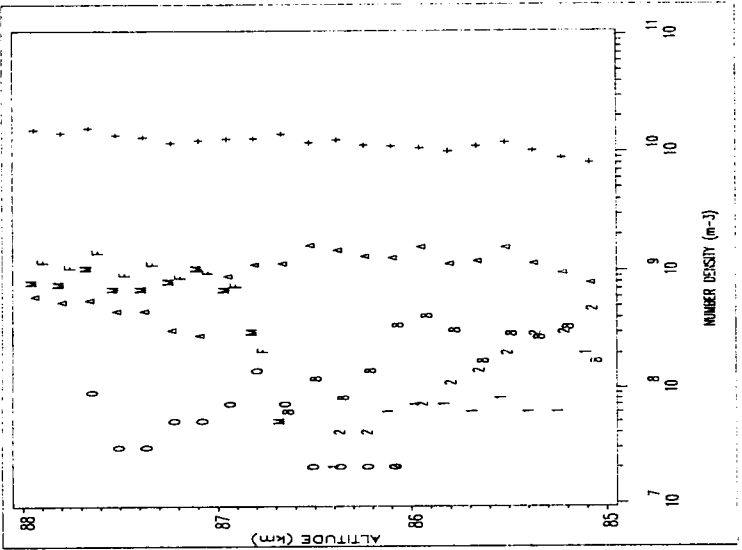


Figure 5.

9.12 CASE STUDY OF MODELED AND MEASURED D-REGION PLASMA DENSITIES

M. Friedrich

Department of Communications and Wave Propagation
 Technical University Graz
 Inffeldgasse 12, A-8010 Graz, Austria

Two of the many sounding rockets launched as part of the MAC/Epsilon campaign are particularly suited to test the validity or quality of D-region models. The measurements covered atomic oxygen, neutral temperatures and fluxes of charged particles. With these parameters as inputs, one is thus in the position to assess their relevance for the measured parameters, i.e., ion composition, transition heights of clusters and negative ions and total plasma density. The two IOMAS payloads are believed to be the only night flights with associated measurements of atomic oxygen extending below the ledge at about 80 km.

Table 1. List of Rocket Salvos During the Campaign MAC/Epsilon.

date y,m,d	time UTC	zenith angle deg	payload codes	available data
1987-10-15	10:52	78°	T1	q,N ⁺
1987-10-21	21:33	120°	T2, T3	q,N ⁺ ,N _e ,O
1987-11-12	00:21	127°	T4, T5	q,N ⁺ ,N _e ,O,NO

N⁺ density of positive ions, N_e electron density, q ion pair production rate by energetic electrons (> 40 keV), O atomic oxygen density, NO nitric oxide density.

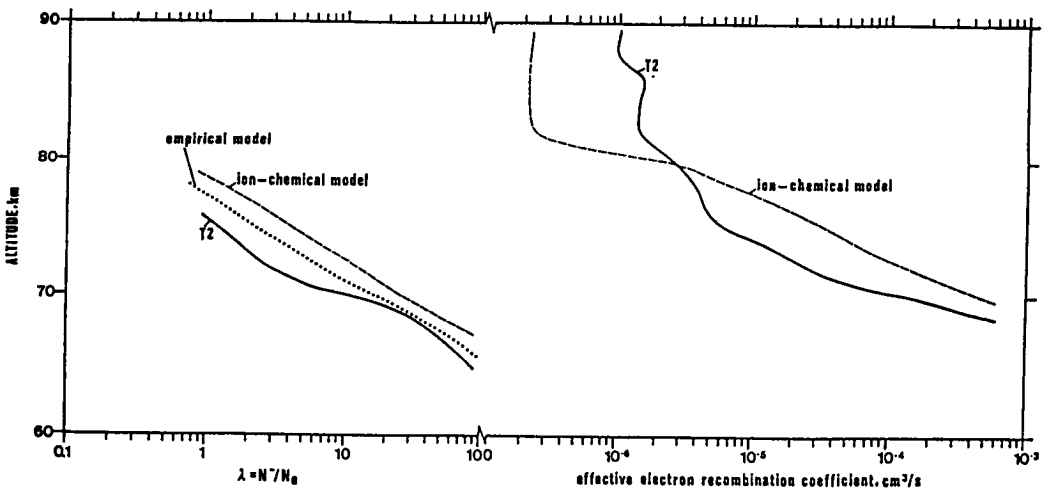


Figure 1. Ratio $\lambda = N^+/N_e$ derived from the rocket flight T2 and the corresponding results from a statistical analysis [Torkar and Friedrich, *J. Atmos. Terr. Phys.*, in press] and an ion-chemical model [Torkar and Friedrich, *J. Atmos. Terr. Phys.*, 45, 369, 1983] (left panel). Right panel: effective electron recombination coefficient derived from payload T2 together with the result of the theoretical model [Torkar and Friedrich, *J. Atmos. Terr. Phys.*, 45, 369, 1983].

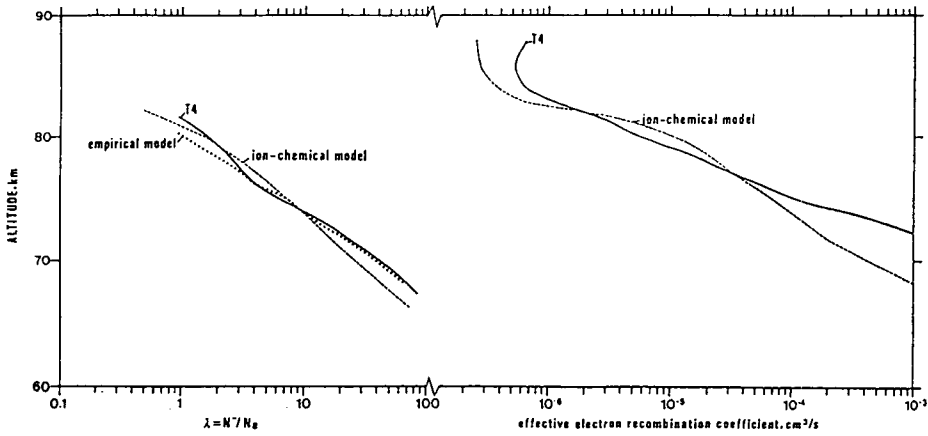


Figure 2. Same as for Figure 1 but for rocket flight T4.

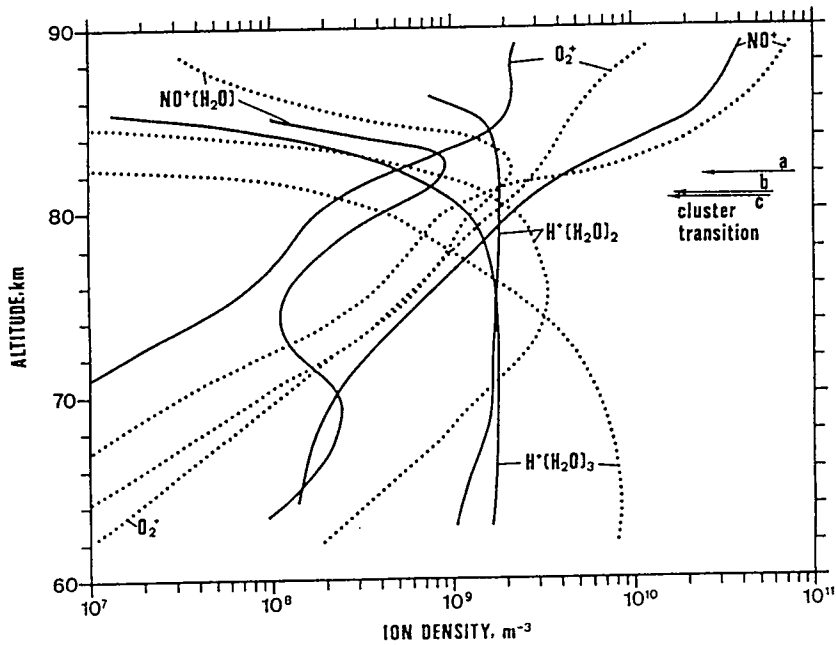


Figure 3. Measured and modeled partial densities of the five most abundant positive ions of the rocket flight T4. Full lines = measurement, dotted lines = ion-chemical modeling. Transition height from cluster to molecular ions: a = statistical model, b = measured, c = ion chemical model.

**10. OBSERVATIONS OF, AND SOURCES OF THE SPATIAL AND
TEMPORAL VARIABILITY OF OZONE IN THE MIDDLE ATMOSPHERE
ON CLIMATOLOGICAL TIME SCALES (OZMAP)
AND EQUATORIAL DYNAMICS**

10.1 SEASONAL VARIATIONS OF OZONE TRENDS

G. Entzian

Academy of Sciences of the GDR
Institute for Atmospheric Research and Geomagnetism
Berlin 1199, GDR

K. H. Grasnick

Meteorological Service of the GDR
Meteorological Main Observatory
Potsdam 1500, GDR

J. Taubenheim

Academy of Sciences of the GDR
Institute for Atmospheric Research and Geomagnetism
Berlin 1199, GDR

The long-term trends (least-square linear regression with time) of ozone content at seven European, seven North American, three Japanese and two tropical stations during 21 years (1964-1984) are analyzed. In all regions negative trends are observed during the 1970s, but are partly compensated by limited periods of positive trends during the late 1960s and late 1970s. Solely the North American ozone data show negative trends in all 10-year periods. When the long-term ozone trends are evaluated for each month of the year separately, a seasonal variation is revealed, which in Europe and North America has largest negative trends in late winter and spring. While in Europe the negative trends in winter/spring are partly compensated by positive trends in summer, in North America the summer values reach only zero, retaining the significant negative trend in annual mean values. In contrast to the antarctic ozone hole, the spring reduction of ozone in Europe and in North America is associated with stratospheric temperatures increasing in the analyzed period and therefore is consistent with the major natural ozone production and loss processes.

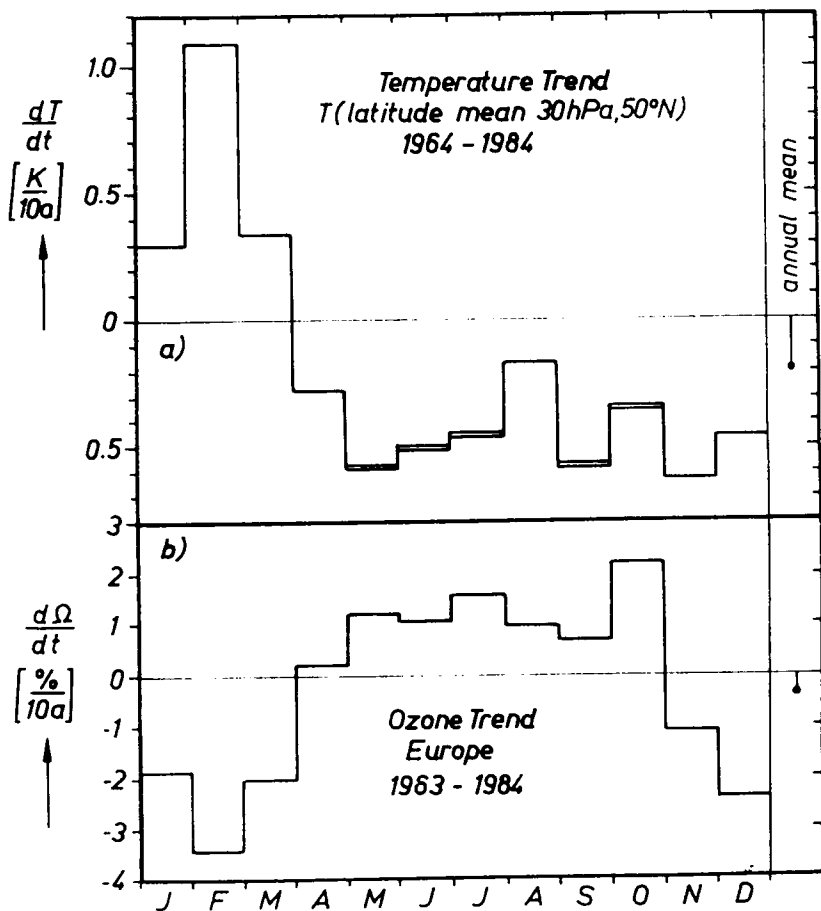


Figure 1. Seasonal trend variation: (a) Temperature trend; latitude mean 50°N, 30 hPa 1964-1984; (double lines indicate statistically significant (>95% values)). (b) Trend of total ozone: mean of seven European stations 1963-1964; at right margin: trend of annual mean values over the total available time (all values in percent per 10 years). Antiphase of temperature and ozone trend (Jan - Oct) suggests the effect of normal production and loss processes, while in-phase variations (Nov - Dec) require additional processes like transport. Reactions with anthropogenic substances should be carefully considered taking into account that their interactions with dynamical processes on the Northern Hemisphere will be different from those on the Southern Hemisphere.

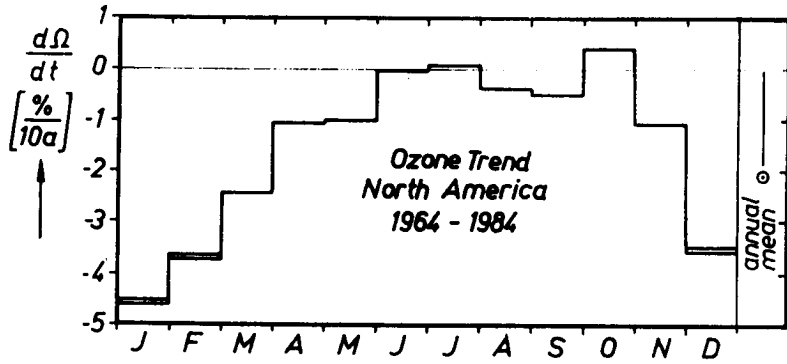


Figure 2. As Figure 1(b), but for the mean of seven North American stations. The negative trend during almost all months can possibly be explained by compensation of stratospheric ozone decrease by tropospheric ozone increase being less in North American than in Europe.

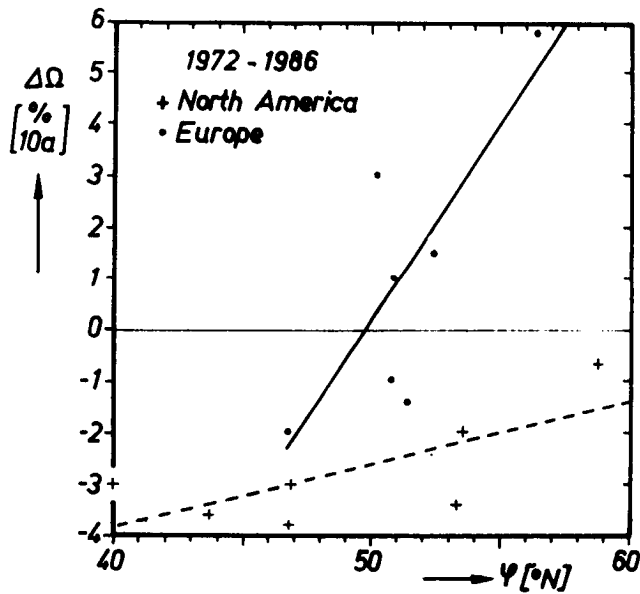


Figure 3. Latitude dependence of total ozone trend of annual mean values (1972-1986) of seven European and seven North American stations.

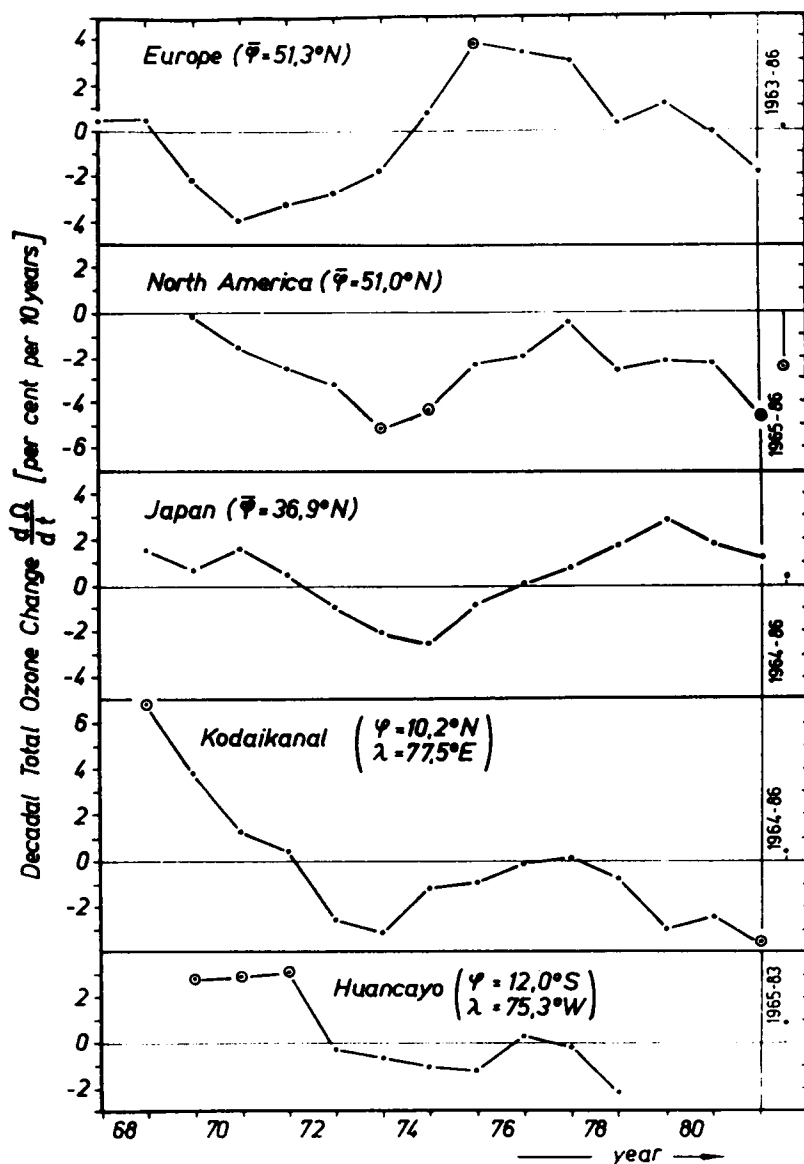


Figure 4. Time variability of trends in total ozone, from linear slopes calculated for sliding 10-year intervals in different regions. At right margin: trend over the total available period. Positive and negative trends partly compensate each other in almost all analyzed regions except North America. See Figure 2 for possible explanation. The general ozone decrease since the end of the 1970s is connected with natural processes like El Chichon eruption, El Nino / Southern Oscillation and the phase of the QBO during 1982/83.

10.2 STRATOSPHERIC TEMPERATURE - OZONE RELATIONSHIPS 1978 - 1986

M. E. Gelman, R. M. Nagatani, A. J. Miller, and K. W. Johnson

Climate Analysis Center, W/NMC53 World Weather Building
5200 Auth Road, Washington, DC 20233

Global stratospheric temperature and geopotential height at eight pressure levels (70, 50, 30, 10, 5, 2, 1, and 0.4 hPa) have been derived at NMC daily since October 1978. These fields are based on NOAA operational satellite sounder information. Comparable daily global fields of stratospheric ozone (30 to 0.4 hPa and total ozone) have been derived from the SBUV instrument on Nimbus 7 and are now derived from the operational NOAA SBUV/2 instrument. The ozone and meteorological fields are verified against ground-based measurements (Umkehr, balloon, rocket, lidar) to determine fields of temperature and ozone has been assembled. We will discuss some of the interesting features of correlation between the synoptic patterns of the two data sets as well as their change with time. Seasonal as well as interannual variations in the patterns of correlation will be compared in the Northern and Southern Hemisphere polar regions. Other outstanding features in both the temperature and ozone fields will be highlighted.

* C - 6

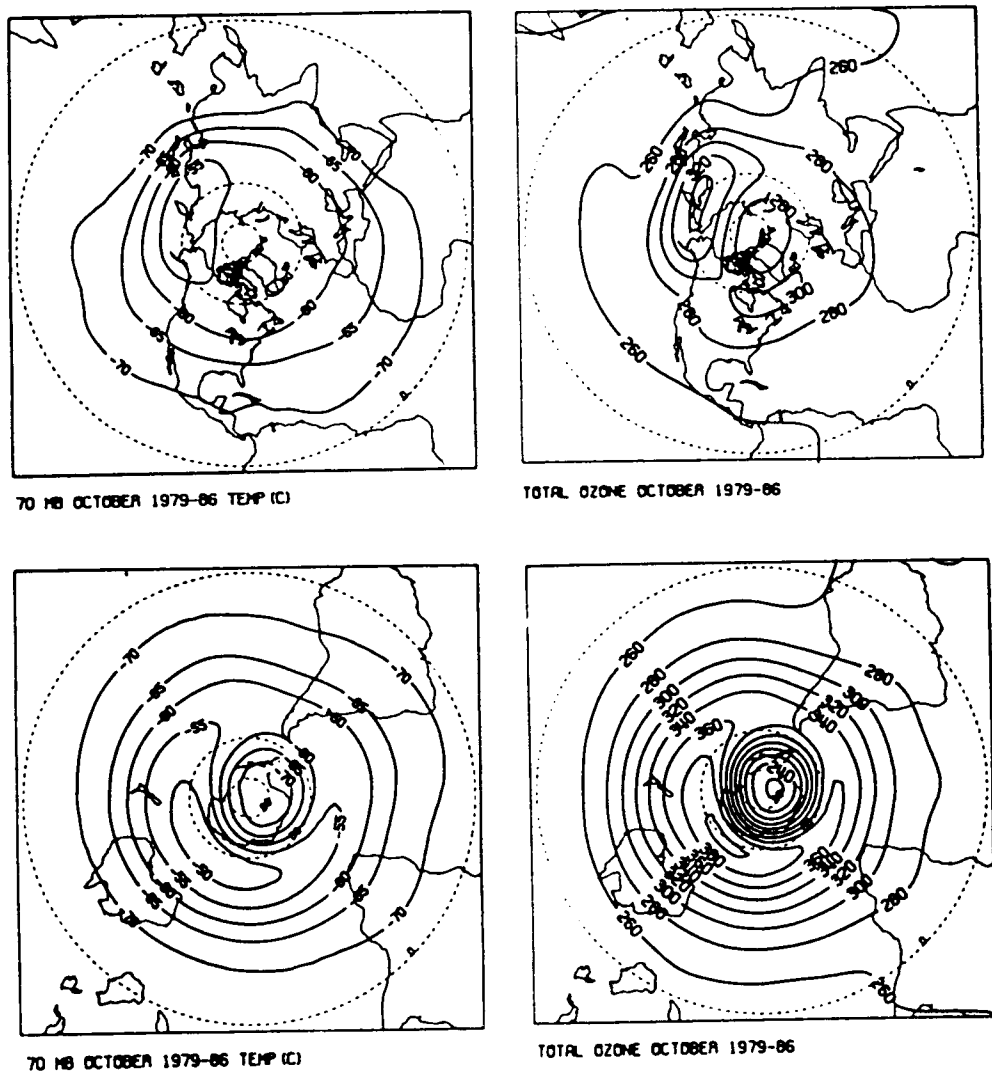
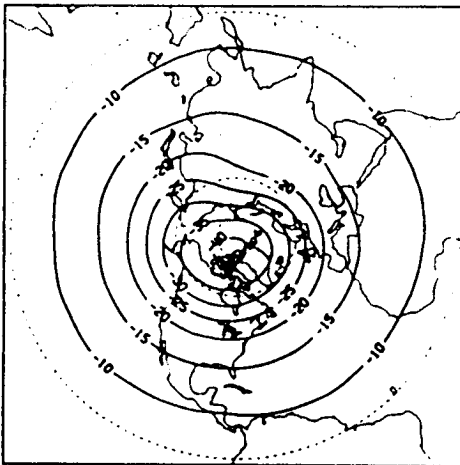
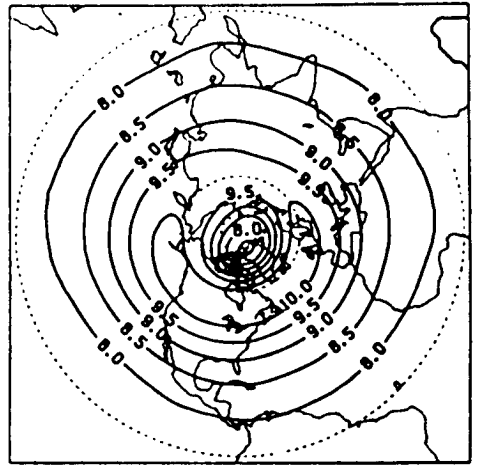


Figure 1(a).

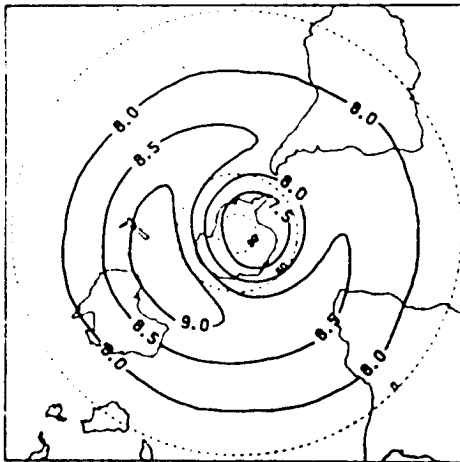
Figure 1. (a) and (b) show the 1978-86 mean October 70 hPa and 2 hPa temperature and ozone maps for the Northern and Southern Hemispheres [Nagatani et al., NOAA Tech. Rep. NWS 40, 1988]. At 70 hPa, the warmest air over each polar region is shown in the area of highest ozone, and the lowest temperatures are seen over the longitudinal region with lowest ozone. However, at 2 hPa the reverse is seen in both polar regions, with low temperatures generally associated with high polar ozone, and high temperatures in the area of lowest ozone. These features are well known and are generally explained as showing that the distribution of ozone in the lower stratosphere is dynamically driven, whereas in the upper stratosphere photochemical processes dominate.



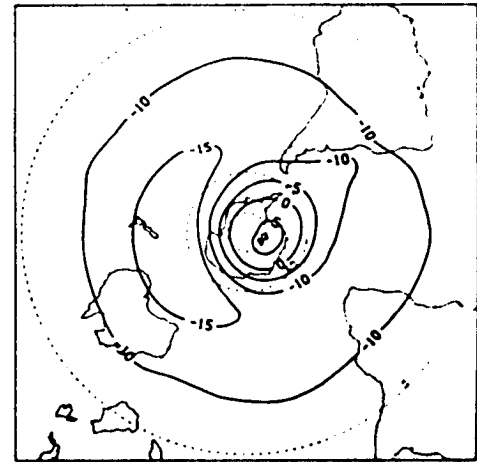
2 MB OCTOBER 1979-86 TEMP (C)



2 MB OCTOBER 1979-86



2 MB OCTOBER 1979-86



2 MB OCTOBER 1979-86 TEMP (C)

Figure 1(b).

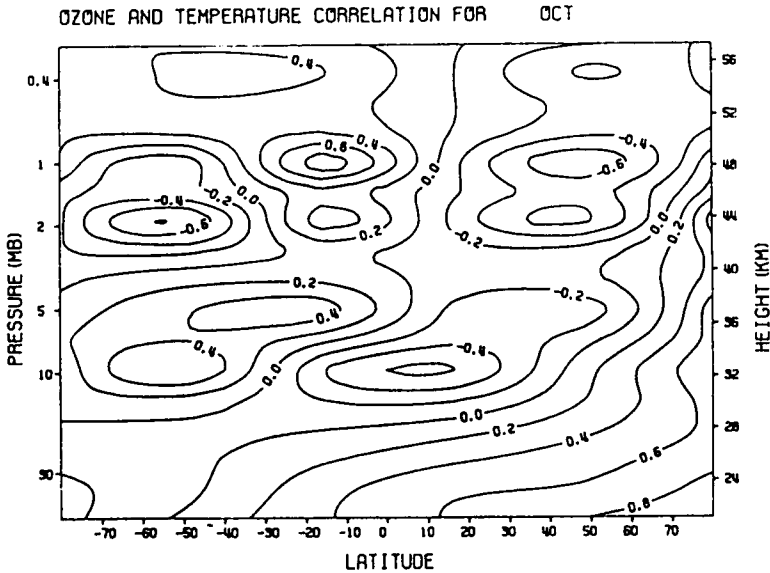


Figure 2. Shown are the correlations of ozone and temperature for October, January, and July for 30 to 0.4 hPa for all latitudes. The patterns of correlation for the north and south polar regions in October are similar because this is a winter month in each hemisphere for the stratosphere. There is positive correlations at lower levels and strong negative correlations at upper levels. For January and July, each winter hemisphere polar region again shows a similar correlation pattern to that of October. However, the polar latitudes in the July summer Northern Hemisphere show negative correlations at lower levels and positive correlations at upper levels. This is different from the January summer Southern Hemisphere which shows positive correlations at lower levels and negative correlations at higher stratospheric levels, similar to the pattern in the winter hemisphere. The summertime circulation is dominated by zonal flow, so that correlations may represent only small eccentricity from this pattern.

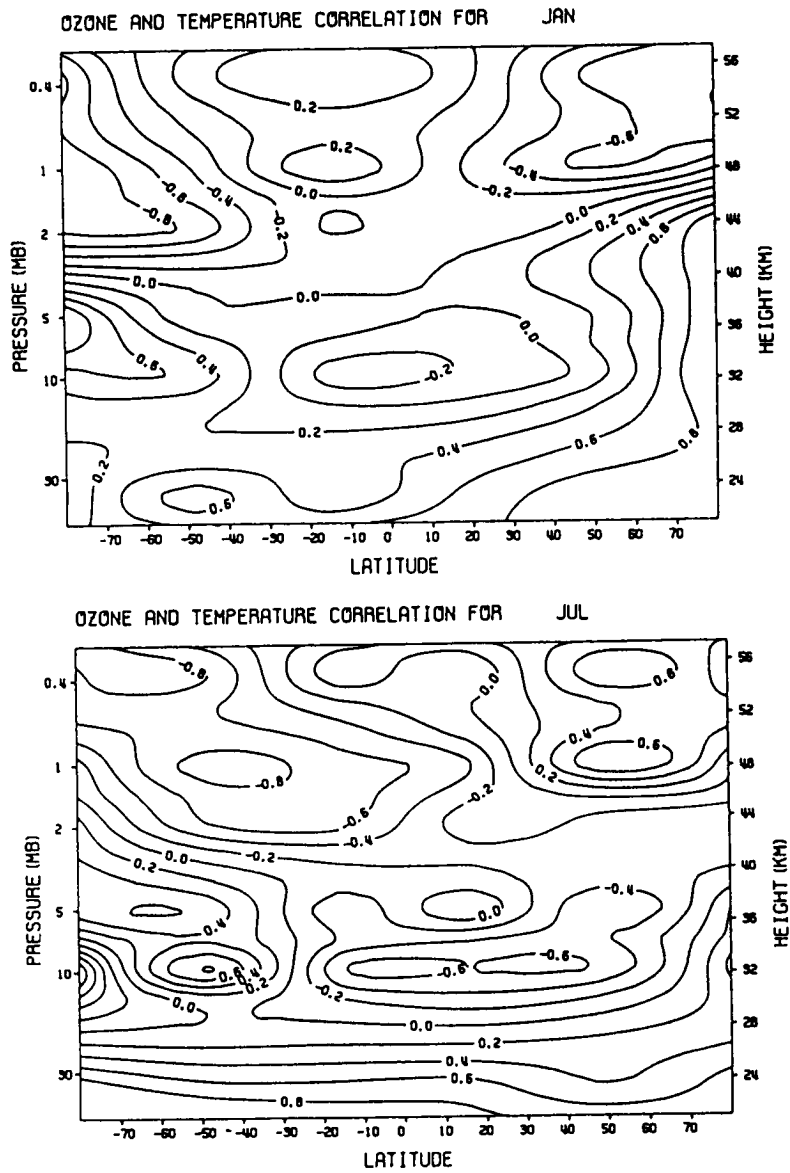


Figure 2 Continued.

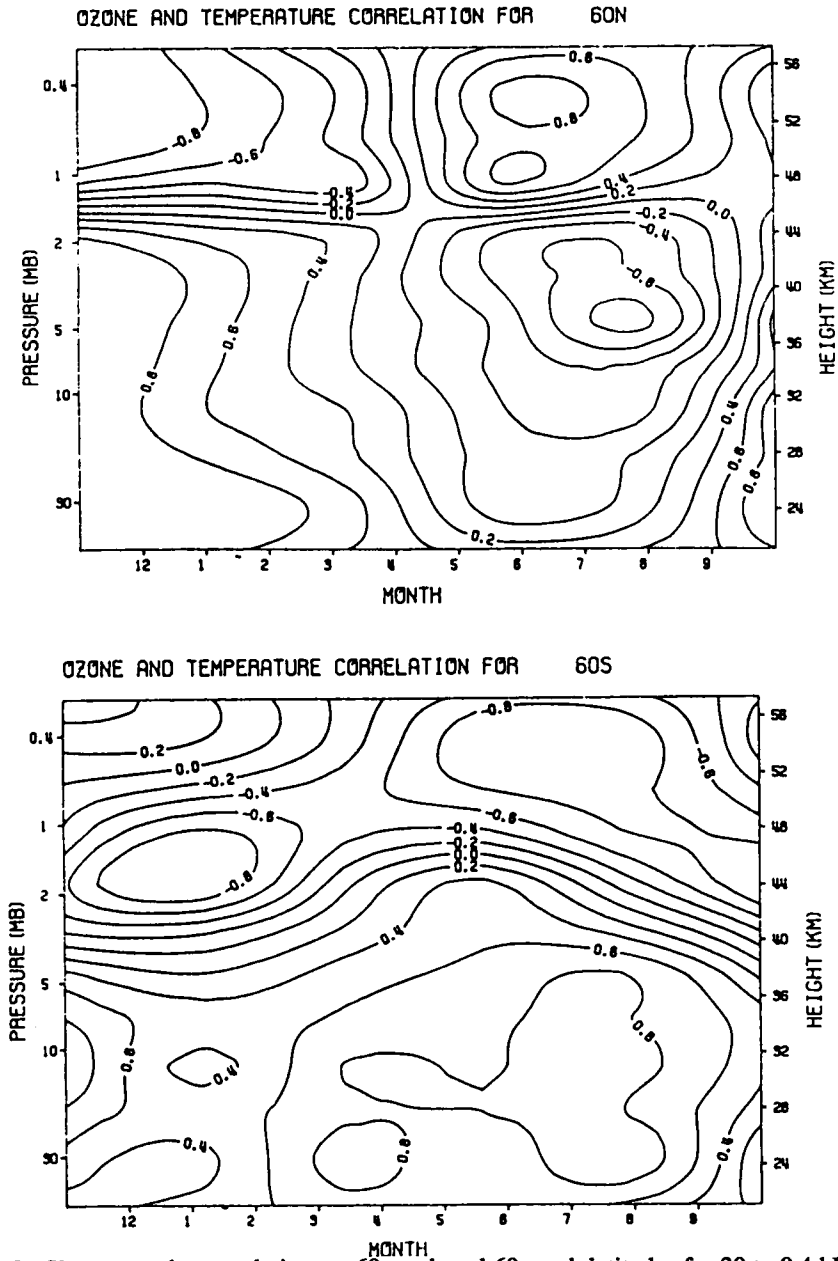


Figure 3. Shown are the correlations at 60 north and 60 south latitudes for 30 to 0.4 hPa and for each of the 12 months. Again, the patterns of correlation shown are similar for the north and south polar regions for the respective winter months, with strong positive correlations of greater than 0.8 at lower levels and strong negative correlations at upper levels. This sense of correlations agrees with the synoptic picture shown in Figures 1 and 2 and with our discussion of those figures.

10.3 SUBTROPICAL MIDDLE ATMOSPHERE DYNAMICS OBSERVED BY THE CHUNG LI RADAR

I. J. Fu,* C. H. Liu,**, J. Röttger,*** and J. K. Chao*

*National Central University, Chung Li, Taiwan, **University of Illinois, Urbana, IL 61801,
***Eiscat Scientific Association, Kiruna, Sweden

ABSTRACT

The Chung Li radar (24.91°N; 121.24°E) has been operating since 1986. A five-beam observational configuration has been used on a regular basis to study the various dynamics processes in the atmosphere-lower stratosphere height region. Due to its geographical location, the annual Typhoon and Mei-Yu seasons provide good opportunities to study the various interesting dynamic processes such as instabilities, generation of gravity waves, wave-mean field interaction, etc. Three-dimensional air motions due to these fronts will be presented. Special cases of gravity wave generation, propagation and their effects on the turbulent layers will be discussed.

INTRODUCTION

The Chung Li VHF radar is located in the northern part of Taiwan. Since late 1986, it has been in full operation. The radar is situated approximately 50 km southwest of Taipei. The geographical position of the radar is 24.91°N; 121.24°E. It is in the subtropical region. There are several interesting annual meteorological phenomena that are special in this area. There is the Mei-Yu season that usually occurs during the months of May and early June. The Typhoon season starts about July and lasts until approximately the end of September. The Chung Li radar is in the position to observe some of the dynamical behavior of the upper troposphere and lower stratosphere in this interesting region. In this paper, some of the results based on the data base for the past year or so will be presented.

Table 1 summarizes the parameters for the Chung Li radar.

TABLE 1. Chung Li Radar.

Frequency	52 MHz
Average Power	4 kW
Duty Cycle	2%
Minimum Pulse	1 μs
Antenna	3 phased arrays, 64 Yagi each
Beam Positions	Vertical and 4 oblique at 17°

POSITION OF TROPOPAUSE IN THE SUBTROPICAL REGION

With the radar beam pointed upward, the position of the tropopause can be determined using the procedure developed by Gage and Green [1979]. Figure 1 shows the long-term behavior of the tropopause heights at Chung Li.

HUMIDITY CONTRIBUTIONS TO ECHO POWER -- EFFECTS OF TYPHOON

Because the Chung Li radar is on a subtropical island, it is expected that humidity in the troposphere will play a very important role in providing echo returns of the radar signals. Indeed, from the very beginning of Chung Li operation, it has been noticed that echo power decreases sharply above 7 or 8 km. Since radiosonde data are available at Chung Li either on site or at a distance approximately 30 km away, it is possible to model the "dry" term and "wet" term contributions to the echo power [Gage and Balsley, 1980; Röttger, 1984]. Figure 2 shows such a

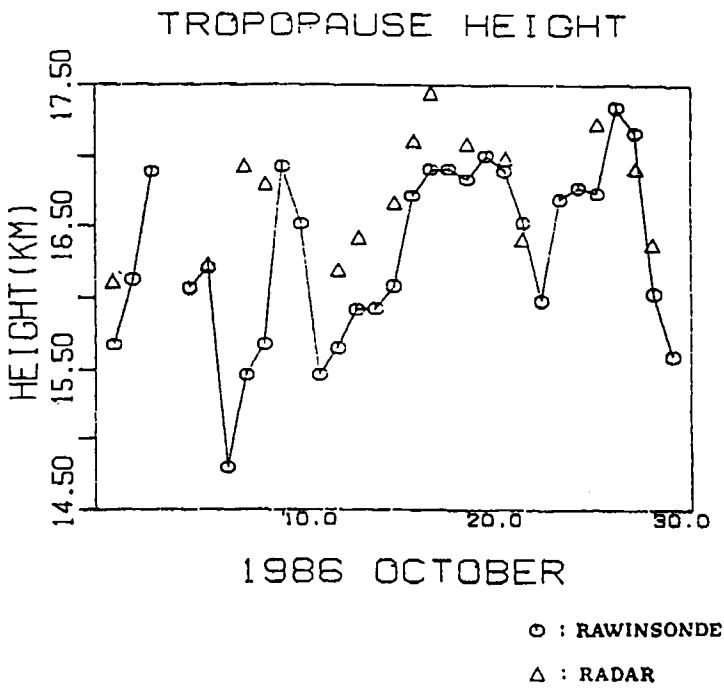


Figure 1.

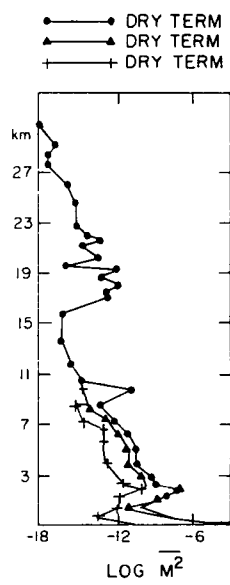


Figure 2.

model. It is apparent that the contribution from humidity dominates in the height region from 2 to 8 km. This is quite different from the usual reflectivity profile where temperature fluctuations dominate above 4 ~ 5 km [Gage and Balsley, 1980; Röttger, 1984].

Another interesting phenomenon observed at Chung Li is that whenever there is a Typhoon passing through, or near the Island, the VHF radar gets echoes from higher range gates, sometimes up to 4 range gates at 300 m height resolution. Figure 3 shows such an example. This perhaps is due to the fact that the Typhoon has caused the uplift of the humid air from the lower height which in turn contributes to the enhanced echo power.

SPECTRA OF VELOCITY FLUCTUATIONS

The Chung Li radar can be used for 5-beam observations of the atmospheric dynamics. The experimental setup will be for beam 1 to be upward, beams 2 and 4 oblique at 17° east and west, respective, beams 3 and 5 oblique at 17° north and south, respectively. Spectra of velocity fluctuations at each beam are computed. Figure 4 shows the results of such an experiment. The spectra from the four oblique beams are quite similar and are shown as averaged spectra. Using the procedure developed by Scheffler and Liu [1985], a model gravity wave spectrum can be found that fits the observed oblique spectra quite well. Using these parameters it is possible to predict the vertical spectrum if the observed velocity fluctuations are entirely due to gravity waves. This predicted spectrum can then be compared with the observed spectrum. Figure 4b shows such a comparison. There is reasonable agreement between the two spectra, especially the level and the shape. The weather conditions for this data set are in general quiet. Similar observations were carried out during a more active situation. This was during the period of the passage of the Mei-Yu front. Figure 4c shows the averaged spectra for the oblique beams. When a gravity wave model was used to transfer the oblique spectra to vertical spectra and compared with observed spectra, much greater discrepancies were found. Figure 4d shows the comparison. The predicated spectra are about an order of magnitude higher than the observed ones, indicating that on these oblique beams there probably are contributions to the velocity fluctuations other than gravity waves.

CONCLUSION

In this paper, results from the Chung Li radar are presented giving examples on the special features in this subtropical upper atmosphere observed by the radar. More statistical analysis on the data accumulated are being carried out and will be communicated in the near future.

ACKNOWLEDGMENT

The work described in this paper was supported in part by the National Science Foundation under grant ATM 87 11938.

REFERENCES

- K. S. Gage and J. L. Green, Tropopause detection by partial specular reflection with VHF radar, *Science*, 203, 1238-1240, 1979.
- K. S. Gage and B. B. Balsley, On the scattering and reflection mechanisms contributing to clear air radar echoes from the troposphere, stratosphere and mesosphere, *Radio Sci.*, 15, 243-257, 1980.
- J. Röttger, The MST radar technique, *Handbook for MAP*, 13, 187-232, 1984.
- A. O. Scheffler and C. H. Liu, On observations of gravity wave spectra in the atmosphere by using MST radar *Radio Sci.*, 20, 1309-1322, 1985.

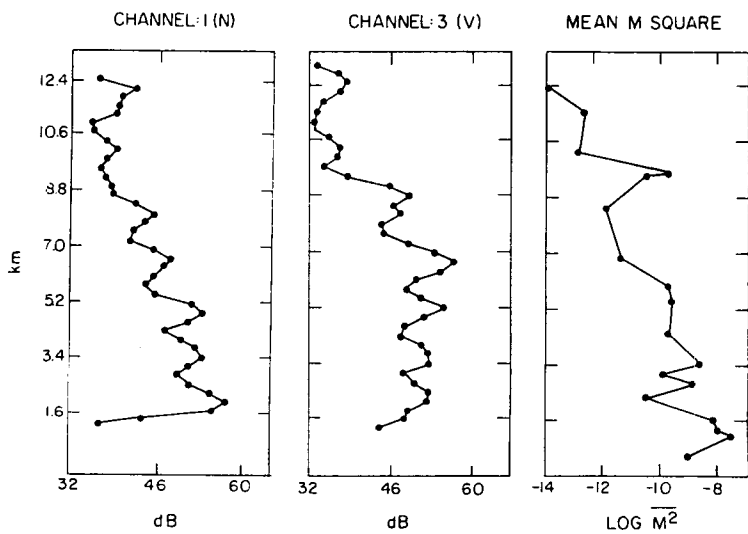


Figure 3.

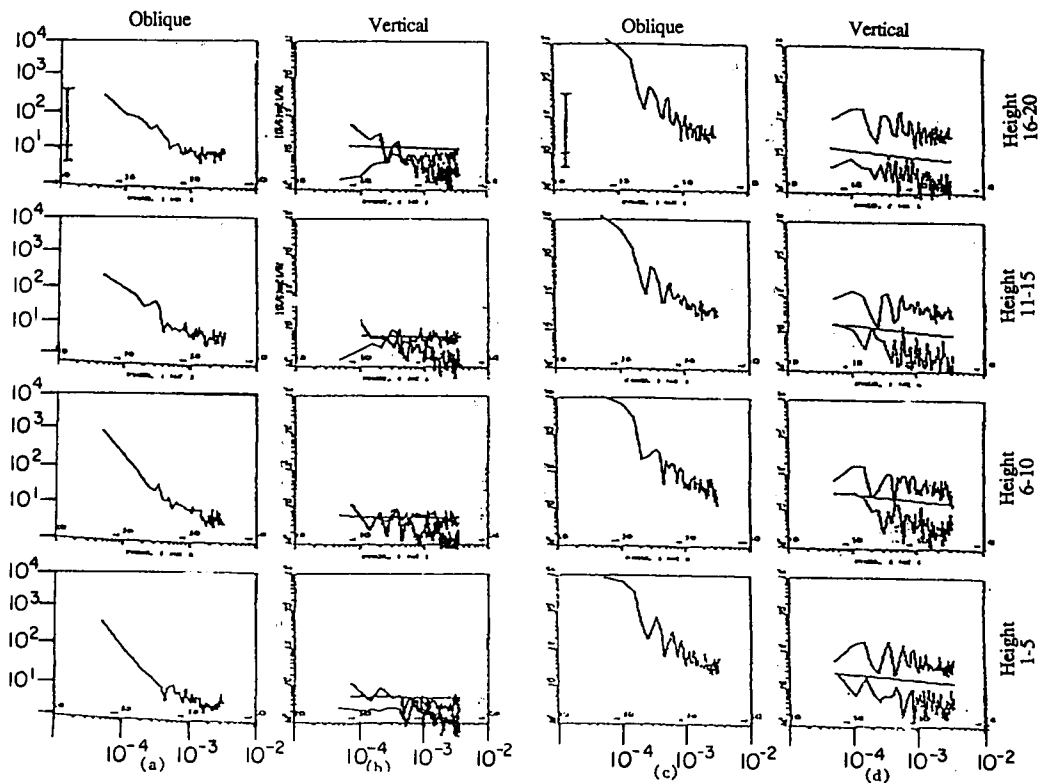


Figure 4.

POSTER SESSION**P.1 WIND AND WAVES IN THE MIDDLE ATMOSPHERE
OBSERVED WITH THE MU RADAR**

S. Fukao, T. Tsuda, T. Sato, M. Yamamoto, and S. Kato

**Radio Atmospheric Science Center
Kyoto University, Uji Kyoto 611 Japan**

The VHF-band MU radar at Shigaraki, Japan, has been in full operation successfully since April 1985. This paper will focus on dynamical features found primarily in the data obtained by the radar during a one-year period from December 1985 to November 1986. These include: basic wind observations, quasi-monochromatic gravity waves generated by the jet stream or through a geostrophic adjustment process, seasonal variation of the mesoscale wind variability, the momentum flux due to gravity wave motions, and saturated gravity wave spectrum. A short discussion will be added to the relationship between turbulent layers and ambient wind field in the mesosphere.

ZONAL WIND FOUR CONTINUOUS DAY AVERAGE

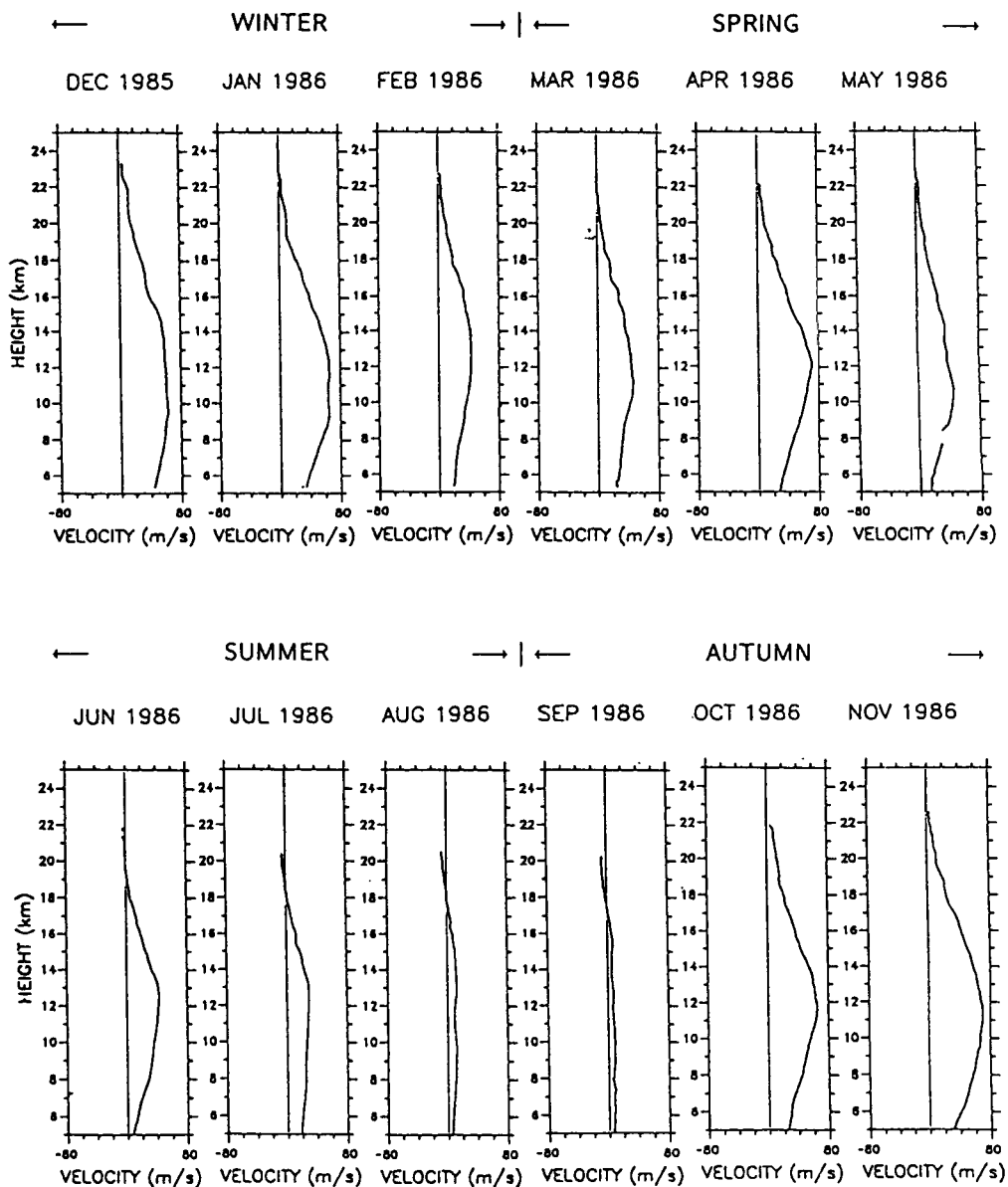


Figure 1. Zonal wind averaged over four continuous days each month. A typical seasonal wind change in Japan is observed with the subtropical jet predominating in winter and weak in summer.

ZONAL & VERTICAL VARIANCE DEC 1985 - NOV 1986

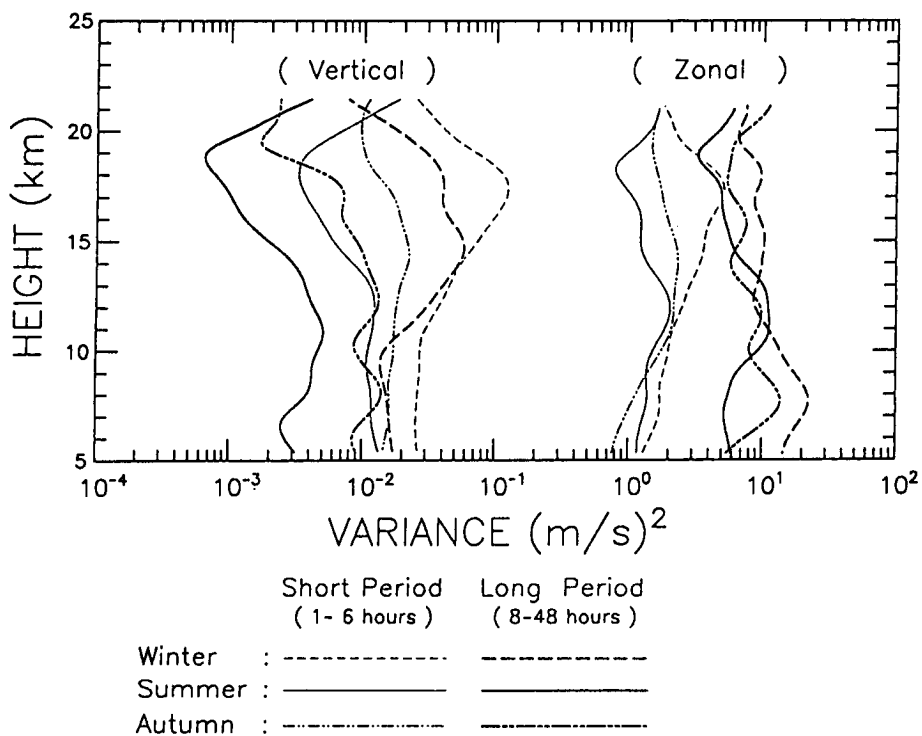


Figure 2. Horizontal and vertical velocity variance for two period ranges during summer, autumn and winter. The gravity wave characteristics are reflected here with wave front being more vertical with increasing periods.

MEAN PSD OF HOURLY MEAN FLUCTUATIONS DEC 1985 – NOV 1986 STRATOSPHERE

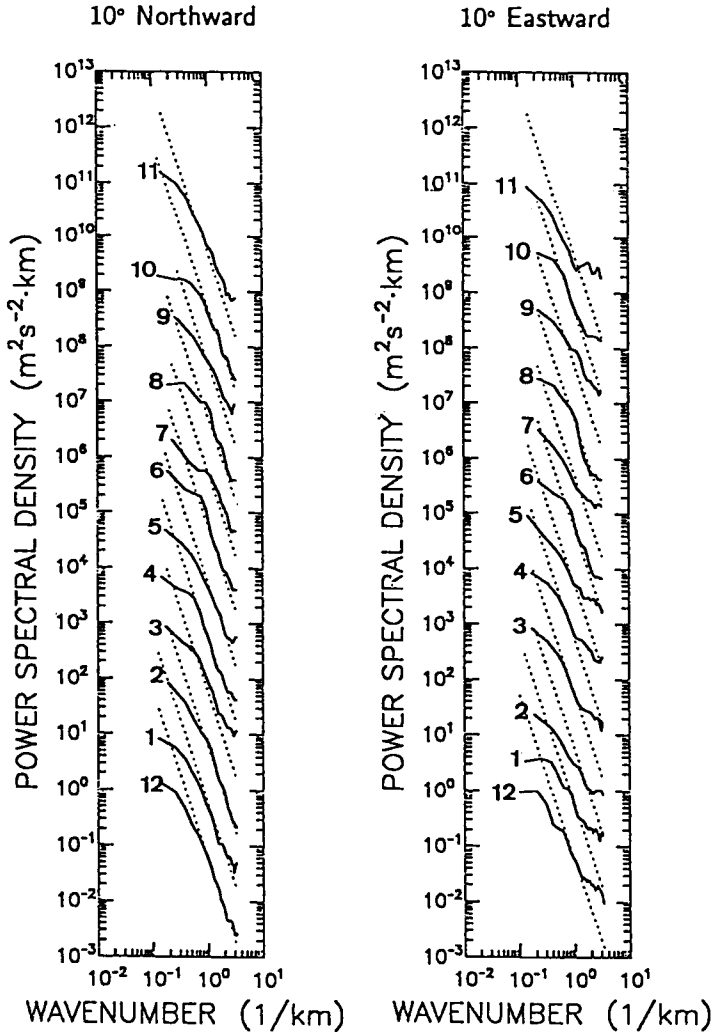


Figure 3. Monthly change of power spectral densities (PSD) of northward and eastward radial velocity in the stratosphere (left) and troposphere (right) compared to a theoretical saturated spectrum. PSD changes little despite the conspicuous seasonal change of the mean wind, suggesting that nonorographic sources are important for middle atmospheric gravity waves.

MEAN PSD OF HOURLY MEAN FLUCTUATIONS
DEC 1985 – NOV 1986
TROPOSPHERE

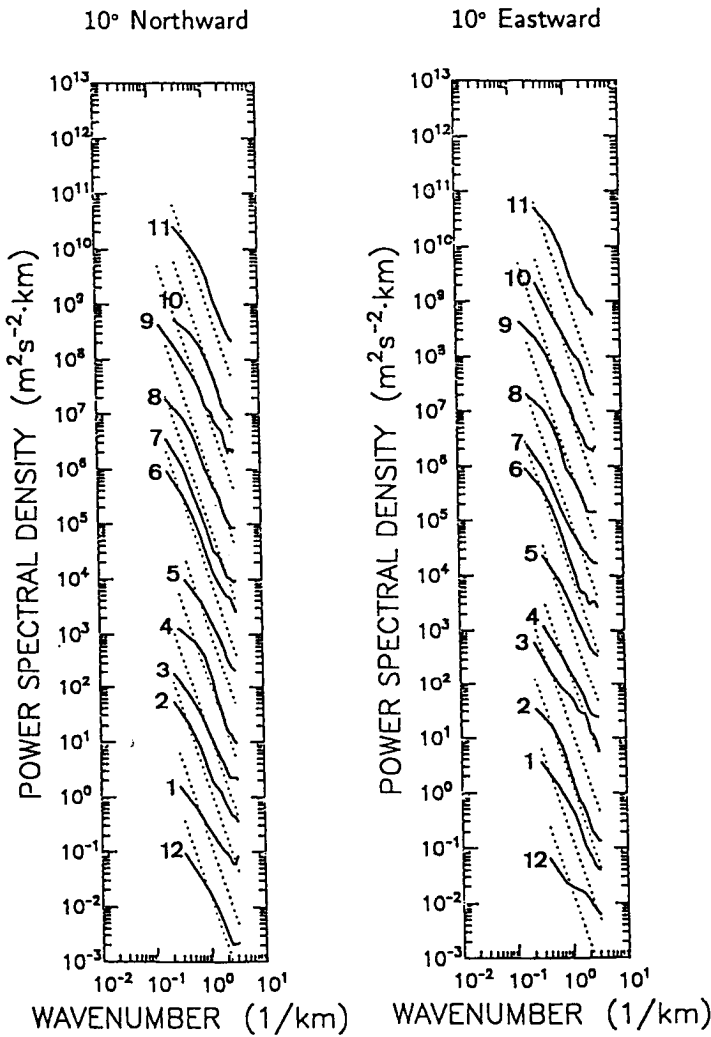


Figure 3. Continued.

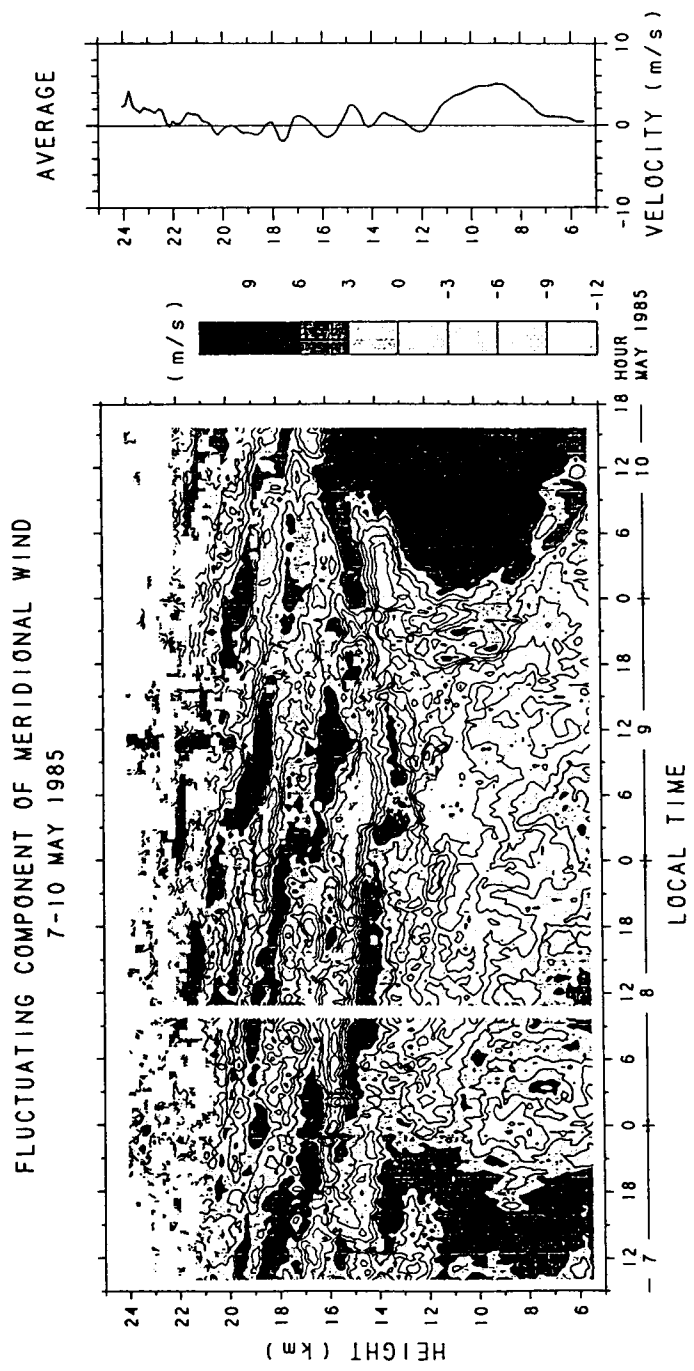


Figure 4. Cross section of meridional wind perturbation relative to the mean wind averaged over the whole observational period.

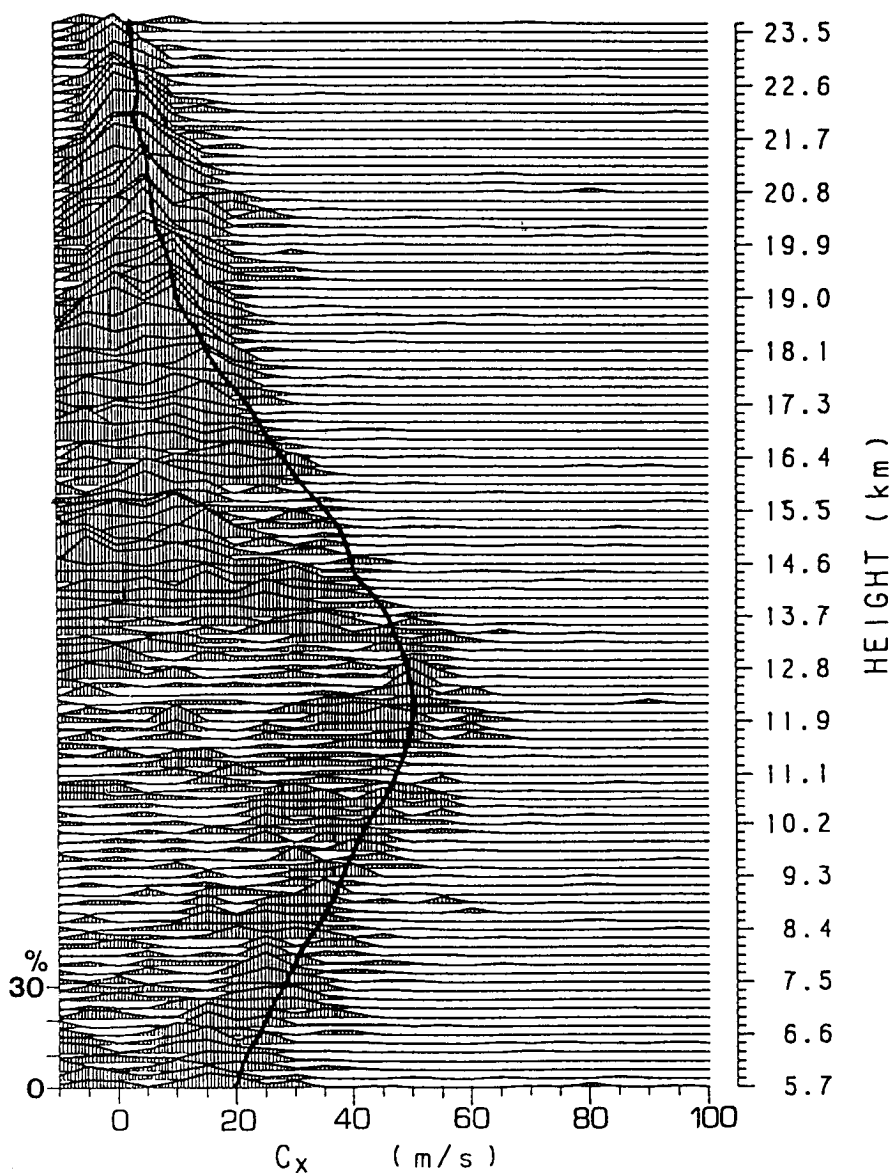


Figure 5. Histogram of the zonal phase velocity analyzed from 30 min average hodographs compared to the mean zonal wind (thick curve). The scale is correct for the lowest spectral curve.

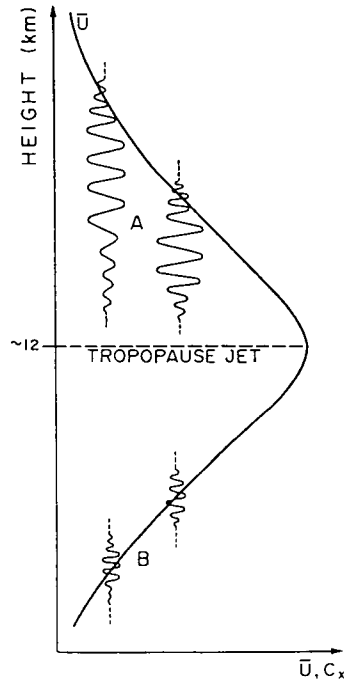


Figure 6. A wave selection model.

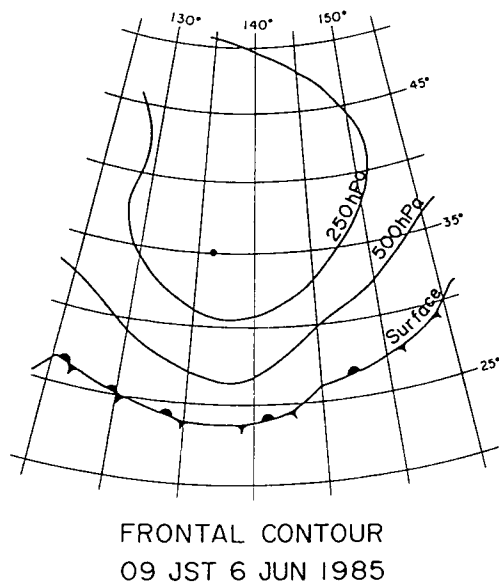


Figure 7. Frontal contours at 09 LST June 1985.

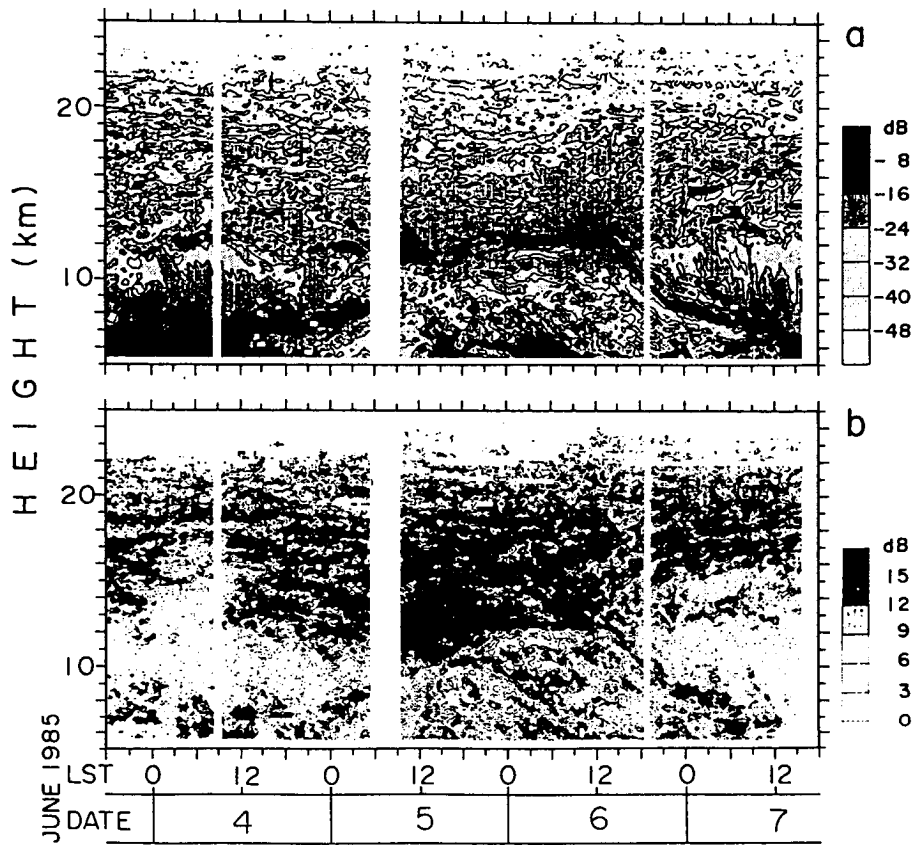


Figure 8. (a) Vertical echo power (in an arbitrary unit) and (b) echo power ratio of the zenith to the 10° oblique direction, showing a structure of the cold air dome.

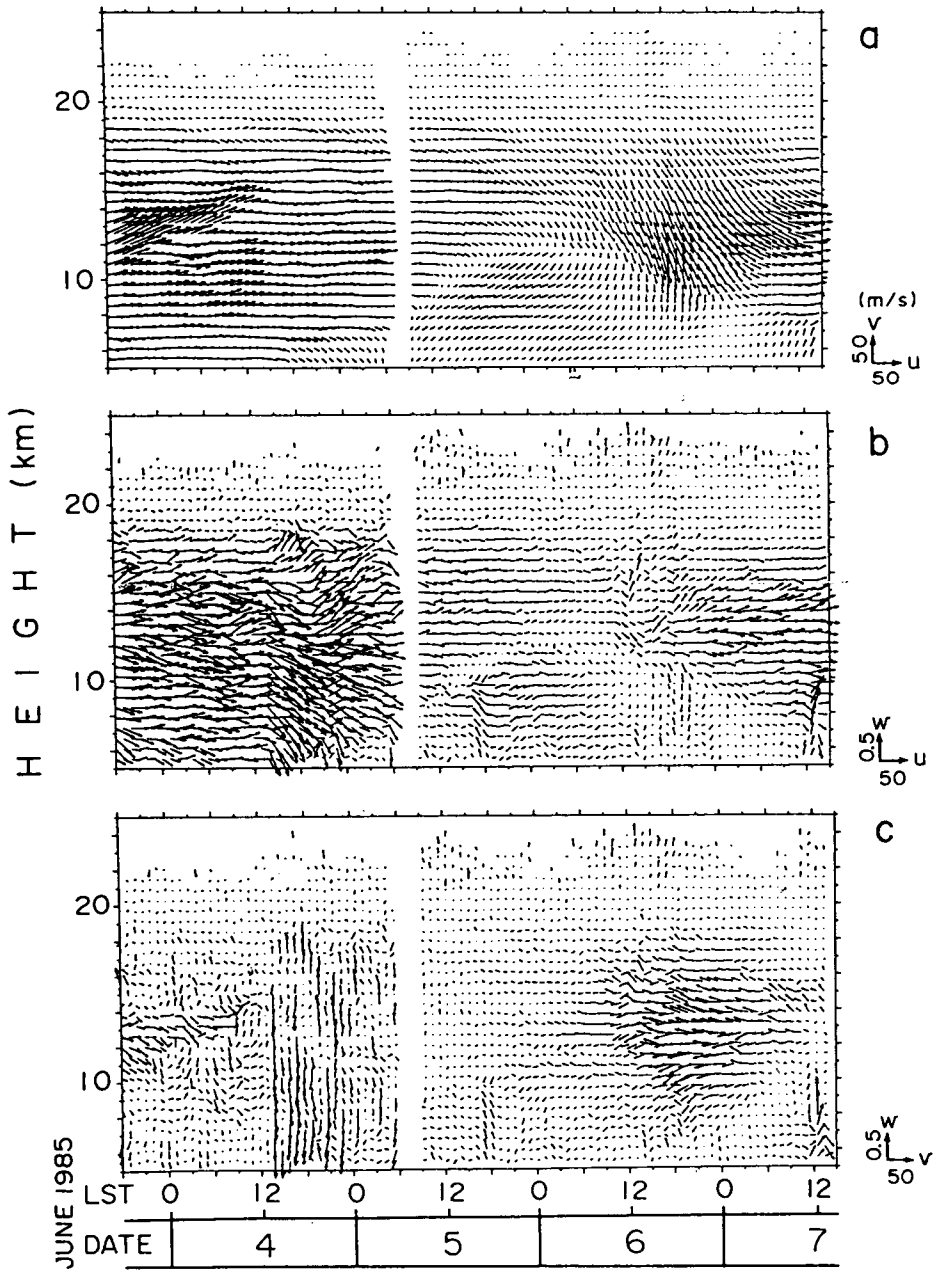


Figure 9. (a) Zonal-meridional, (b) zonal-vertical, and (c) meridional-vertical winds. u , v and w denote eastward, northward, and upward winds, respectively.

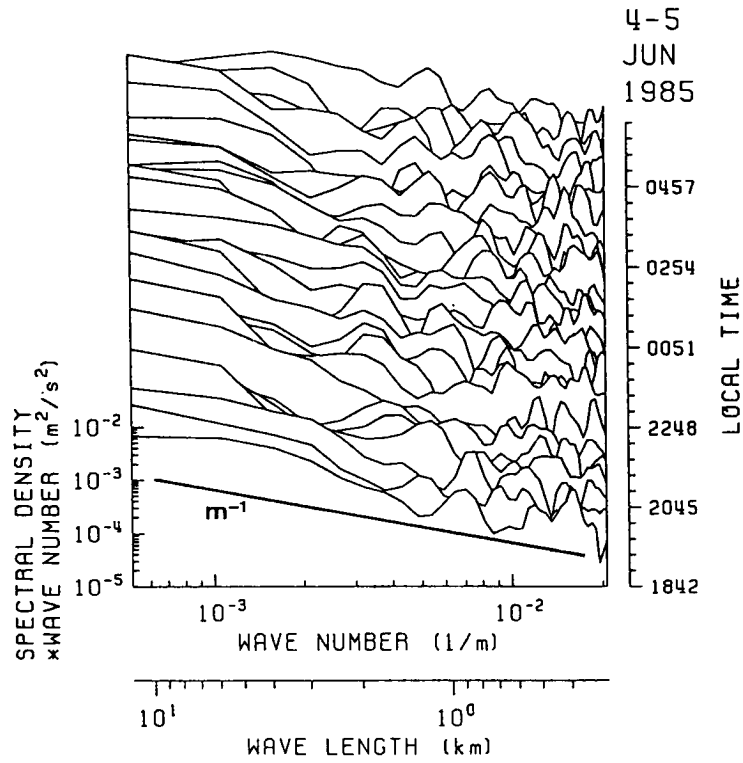


Figure 10. Area-preserving vertical wave number spectra of w .

P.2 SEASONAL VARIATION OF TURBULENCE INTENSITIES IN THE UPPER MESOSPHERE AND LOWER THERMOSPHERE MEASURED BY RADAR TECHNIQUES

W. K. Hocking

Department of Physics and Mathematical Physics
University of Adelaide, GPO Box 498, Adelaide, SA 5001

Since February 1985, the 2-MHz narrow beam radar operated by the University of Adelaide in Australia has been used to measure the short-term root-mean-square fluctuating velocities of radio wave scatterers in the upper middle atmosphere (80 - 100 km). These measured fluctuations are caused by a mixture of turbulence and gravity waves, and under certain reasonable assumptions the turbulent contribution can be extracted. The results of these measurements were discussed in detail by Hocking [1988]. This paper summarizes these results and extends the data set to include 1987.

Hocking, W. K., *J. Geophys. Res.*, 93, 2475, 1988.

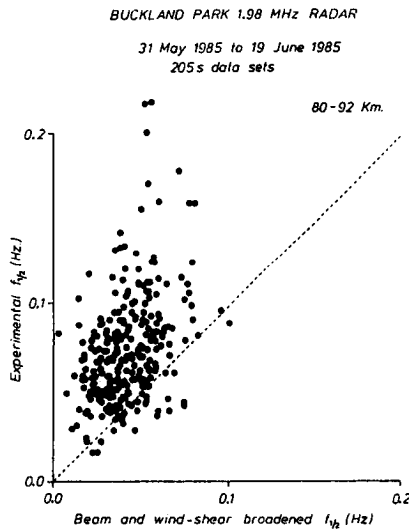


Figure 1. Scatter plot of experimental spectral half-power half width, compared to the half-power half width expected for isotropic scatterers in the absence of any fluctuating motions of the scatterers.

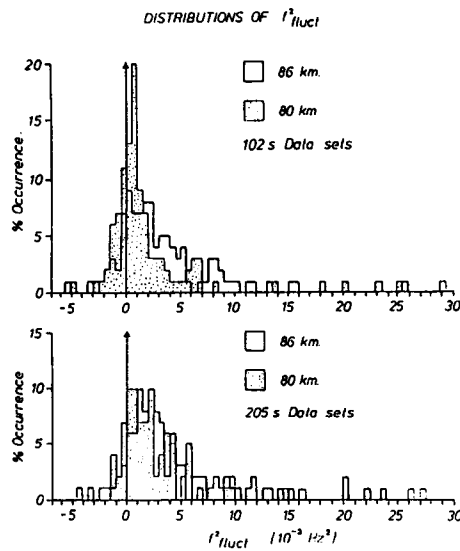


Figure 2. Histograms of frequency of occurrence of various classes of spectral width, $f_{(fluct)}$ being the spectral width measured after the removal of beam and wind-shear broadening. Values for $f_{(fluct)}$ greater than about 0.010 - 0.015 clearly lie in the "tail" of the distribution, and may arise due to effects unrelated to turbulence. For statistical reasons, some values were negative, but by far the majority were positive (generally > 85%) indicating real contributions due to turbulence and wave effects.

CONTRIBUTION OF TURBULENCE TO MEAN
SQUARE SPECTRAL WIDTHS.

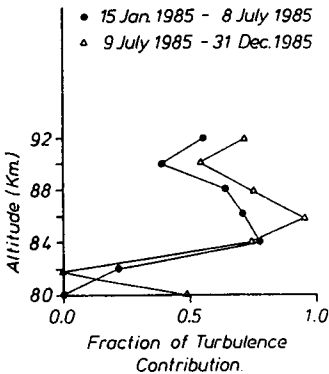


Figure 3. Fraction of experimentally observed spectral widths due to the turbulence for spectral widths deduced from 102 s data set. The remaining contribution was due to gravity waves of short period.

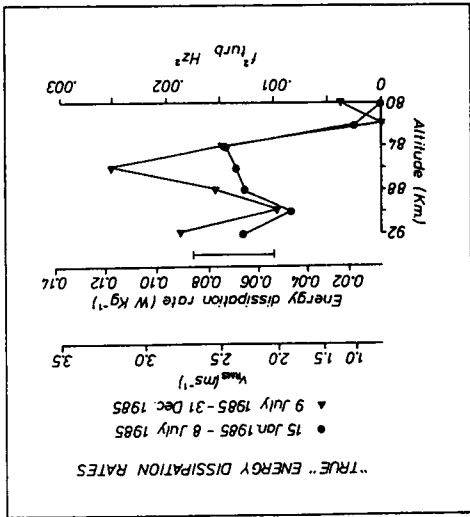


Figure 4. Height profiles of energy dissipation rates deduced for the periods January to June 1985, and July to December 1985, after removal of contamination due to gravity waves. The typical "standard error" is also given, although again it must be noted that a large part of this is due to natural fluctuation.

ENERGY DISSIPATION RATE TIME SERIES
ADELAIDE AUSTRALIA 1985/1986

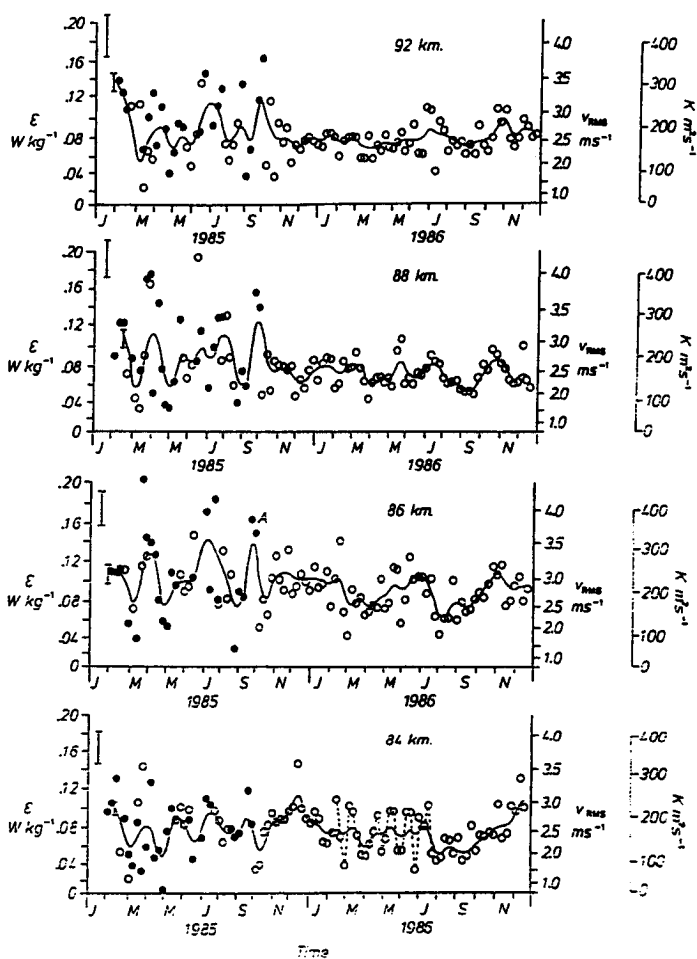


Figure 5. One-week averages of turbulent energy dissipation rates as a function of time for altitudes of 84, 86, 88 and 92 km. The 90-km plot is fairly similar to 92 km. Solid dots represent data collected using 102 s data lengths, and the open circles represent data collected using 205 s data lengths. The solid lines represent five point running means of the weekly averages. Error bars for individual means are shown (top left) and error bars for the running mean are also given. Note that the vertical spacing of the axis is not uniform, because $f^2_{\text{(fluct)}}$ was actually plotted, and then the axis rescaled. RMS fluctuating velocities are also shown to the right. The energy dissipation rates have also been plotted as "eddy diffusion coefficients", K , where $K = c\varepsilon/N^2$, N being the Brunt-Väisälä frequency and c being taken as 1.0.

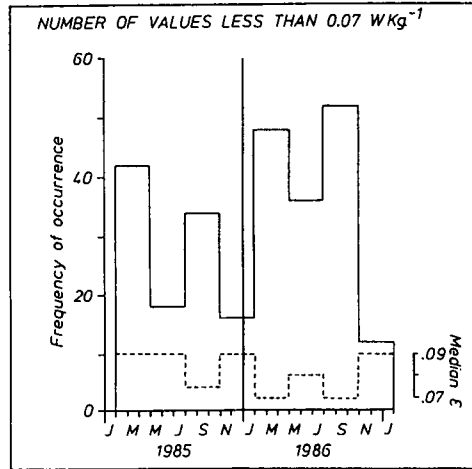


Figure 6. Histograms of the frequency of occurrence of values of less than 0.07 W kg^{-1} , in 3-month intervals (solid line). The dashed line shows the medians of the 1985 and 1986 data in the same 3-month groups for all data at the heights 84, 86, and 88 km.

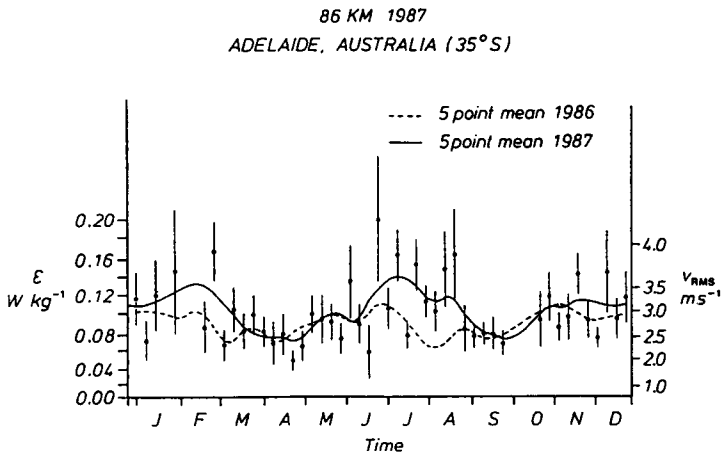


Figure 7. One week averages of ϵ , and a five-point running mean for 1987. The 1986 five-point running mean is also superimposed. These data show the clearest evidence of any of the three years 1985=1987 for a semiannual oscillation. (In 1987, all data were recorded using 102 s data blocks.)

P.3 A COMPARISON OF RADAR MEASUREMENTS OF ATMOSPHERIC TURBULENCE INTENSITIES BY BOTH C_n^2 AND SPECTRAL WIDTH METHODS

W. K. Hocking, K. Lawry, and D. Neudegg

Department of Physics and Mathematical Physics
University of Adelaide, Box 498, Adelaide SA 5001, Australia

There are two main techniques by which turbulence intensities in the atmosphere can be measured by radars. One is to utilize the absolute backscattered power received by the radar, and use this to deduce C_n^2 . With appropriate assumptions, this parameter can then be converted to an energy dissipation rate. The second method utilizes the width of the spectrum of the signal received by the radar. Neither of these techniques have been used a great deal, and they have never been properly compared. Thus it has not been possible to determine the validity of the assumptions made in applying each technique, nor has it been possible to determine the limitations of each method. This paper presents the first comparisons of the two techniques. Measurements were made with the Adelaide VHF ST radar, and the results of the comparisons will be discussed.

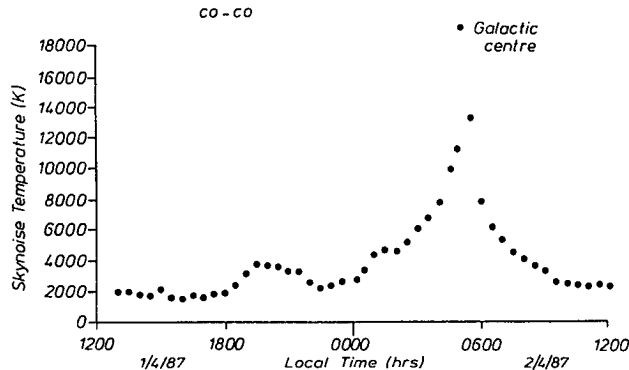


Figure 1. Sky noise temperature as a function of time of day.

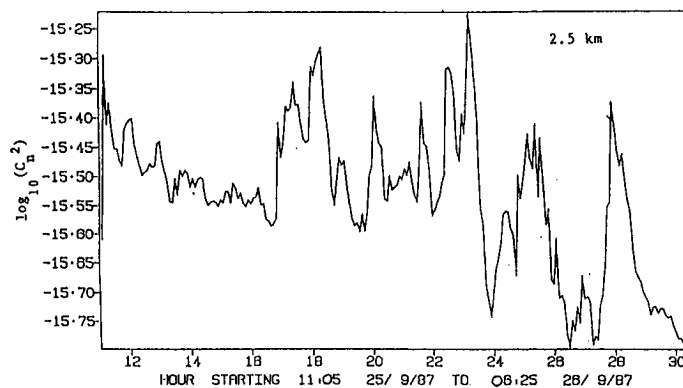


Figure 2. Typical C_n^2 values plotted over a 20-hour period in 1987.

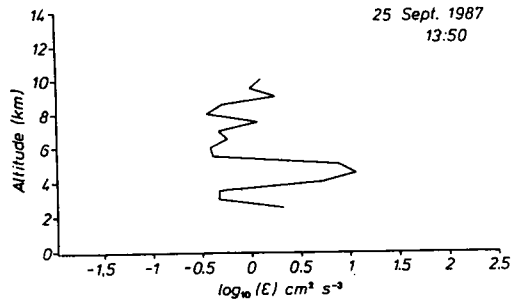


Figure 3. Typical height profile of energy dissipation rates determined by the C_n^2 method.

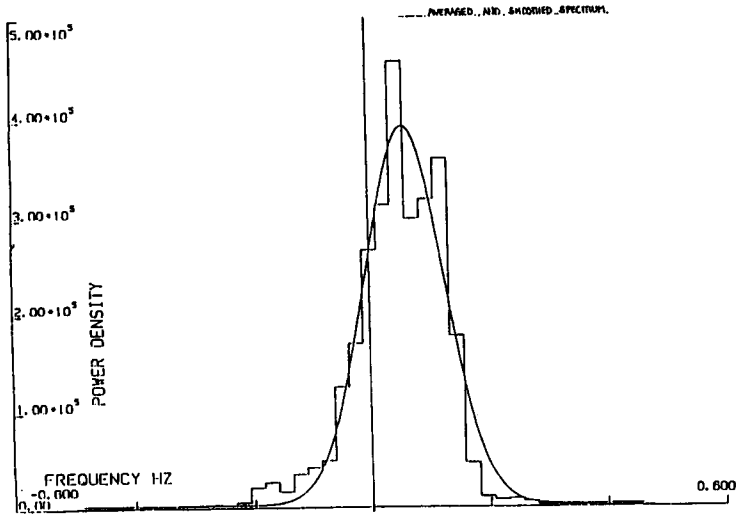


Figure 4. Typical spectrum recorded with the Adelaide VHF radar. The spectral points have been averaged into frequency bins and then a Gaussian function (plus constant offset) fitted to the spectrum.

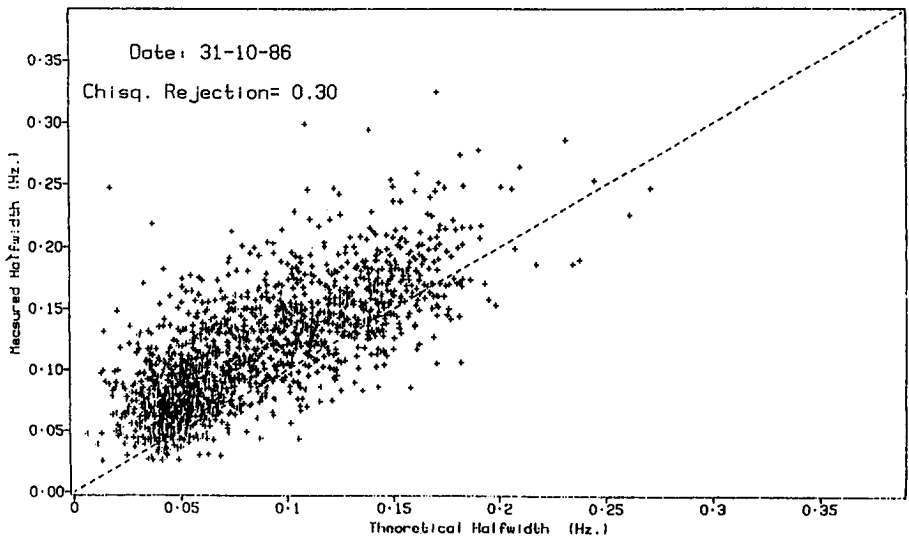


Figure 5. Scatter plot of experimental spectral half-power-half-widths versus the half width expected due to beam and wind-shear broadening ("instrumental"). If the only causes of the spectral widths were instrumental, the points should be scattered symmetrically about the broken line. Instead, they are predominantly above this line, indicating an extra contribution due to turbulence. There are points below the line, which arise due to statistical effects and also possibly due to the effects of specular reflectors, although attempts have been made to remove the latter contribution. By using sufficient averaging, these statistical fluctuations are reduced.

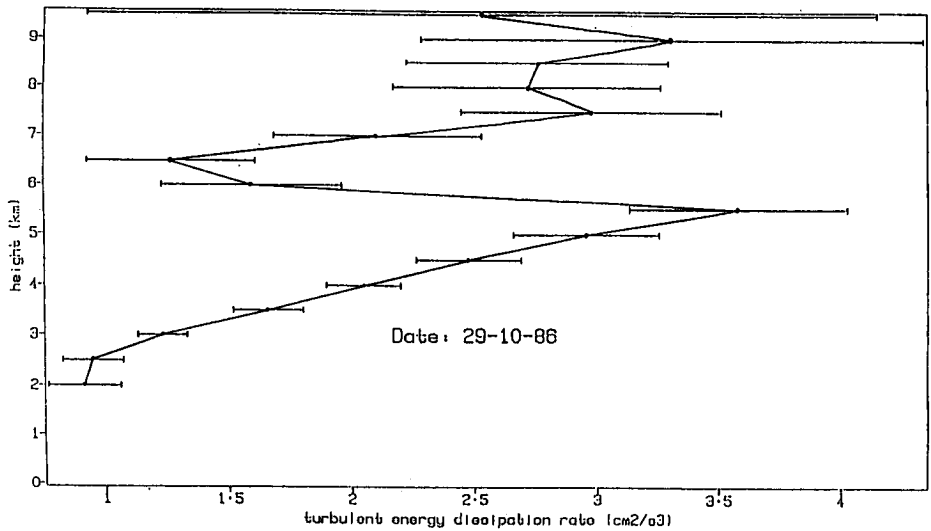


Figure 6. Typical height profile of mean energy dissipation rates, averaged over a 24-hour period.

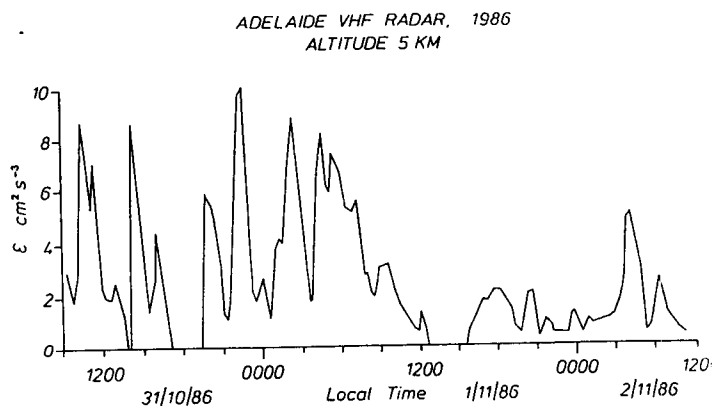


Figure 7. Time sequence of hourly mean turbulent energy dissipation rates for an altitude of 5 km in October and November 1986.

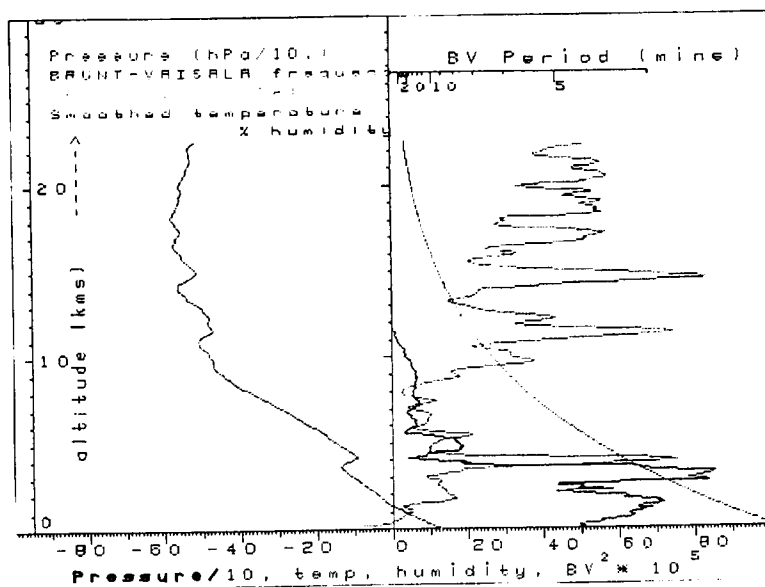


Figure 8. Height profiles of temperature, humidity and Brunt-Väisälä frequency for October 31, 1986 at 0730 local time (30 October 1986 at 2200 GMT). This radiosonde release was made just prior to the data runs shown in Figure 7.

P.4 MU RADAR OBSERVATION OF A MESOSPHERIC GRAVITY WAVE BREAKING CAUSED BY CONVECTIVE INSTABILITY

Y. Muraoka¹, T. Sugiyama², K. Kawahira³, T. Sato⁴, T. Tsuda⁴, S. Fukao⁴, and S. Sato⁴

¹Department of Physics, Hyogo College of Medicine
Nishinomiya, Hyogo 663, Japan

²Department of Physics, Kyoto University
Kyoto 606, Japan

³Toyama National College of Technology, Toyama
Toyama 939, Japan

⁴Radio Atmospheric Science Center, Kyoto University
Uji, Kyoto 611, Japan

In our recent measurements of mesospheric winds with the MU radar at Shigaraki (34.9°N, 136.1°E), Japan, we obtained a couple of wind velocity data showing that a monochromatic inertia-gravity wave was propagating vertically in the mesosphere. The data show that the velocity amplitude of the wave did not increase exponentially above a height and further show that the wave form had broken down at a level. Evaluating the changes of the atmospheric stability in the wave field from the measured wind data and from the estimated wave parameters, we were able to show that the breakdown of the wave had been connected with the occurrence of convective instability in the wave field.

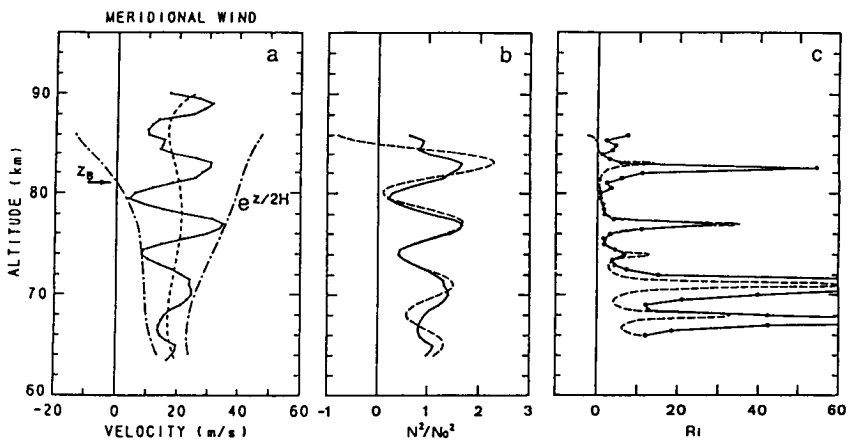


Figure 1. A comparison between height profiles of (a) meridional wind velocity, (b) normalized total static stability (N^2/N_0^2) and (c) Richardson number (Ri). In the panel (a), the full line represents the wind velocity obtained from the measurement during the period of 1430 - 1635 LT on 20 September 1985. The dashed and dot-dashed lines indicate the background mean flow and an exponential growth of the velocity perturbation, respectively. In the panels (b) and (c), the full and dashed lines represent the values evaluated from the measured wind velocity and from the estimated wave parameters, respectively.

Table 1. Characteristics of the Gravity Wave Motion Observed in the Mesosphere on 20 September 1985 and the Related Mean Atmospheric Parameters.

Quantities	Notations	Values
Wave Field		
Vertical wavelength	$\lambda_z=2\pi/ m $	6 km
Horizontal wavelength	$\lambda_x=2\pi/k$	400 km
Period	$2\omega/\pi$	5.6 h
Vertical phase velocity	ω/m	30 cms ⁻¹ downward
Horizontal phase velocity	ω/k	20 ms ⁻¹ southward
Ratio of the intrinsic to inertial frequency	f/ω	0.3
Doppler-shifted horizontal phase velocity	$c=\omega/k+\bar{u}$	0 ms ⁻¹
Mean Field*		
Meridional wind velocity	\bar{u}	20 ms ⁻¹ northward
Vertical wind velocity	\bar{w}	20 cms ⁻¹ downward
Brunt-Väisälä frequency	N_0	0.021 s ⁻¹
Scale height	H	6.2 km
Temperature	T	210 K

*Evaluated around 75 km altitude.

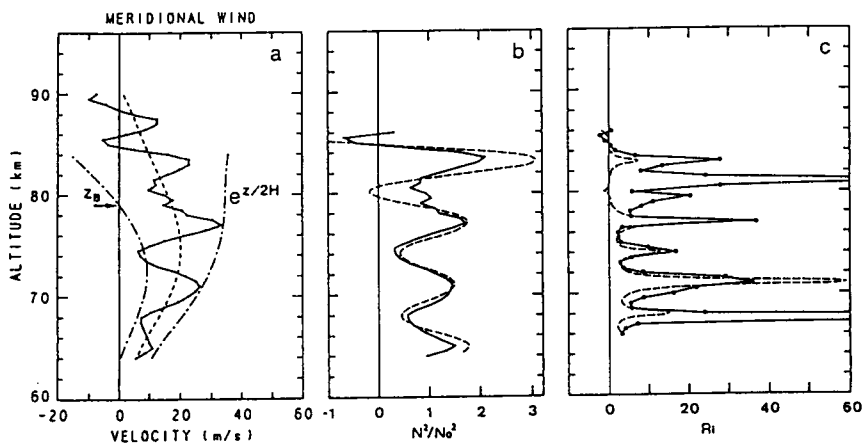


Figure 2. Same as Figure 1 except for the observation during the period of 1202 - 1406 LT on 20 September 1985.

P.5 A NUMERICAL STUDY OF SCALAR GRADIENTS IN KELVIN-HELMHOLTZ BILLOWS

J. W. Parker

Department of Electrical and Computer Engineering
University of Illinois, 1406 W. Green, Urbana, IL 61801

S. A. Bowhill

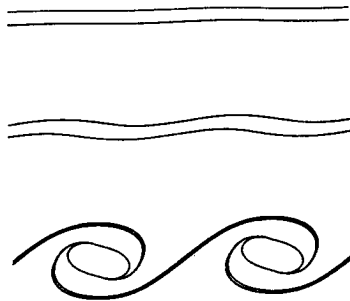
Department of Electrical Engineering
University of Lowell, 1 University Avenue, Lowell, MA 01854

A high-resolution numerical technique is used to model the development of a periodically perturbed shear layer imbedded in an initially vertical gradient of a passive scalar. The technique follows the development of the vorticity through an initial linear growth stage and well into the nonlinear development of Kelvin-Helmholtz billows, in the zero-viscosity, zero-diffusion limit. The resulting scalar distribution rapidly develops regions of extremely sharp scalar gradients, which wind around the periodically spaced vortical low-gradient cores. Vertical cross sections through different parts of the billow structure are presented and compared with rocket measurements of electron density fine structure in the mesosphere. Gradient limits imposed by finite diffusion are calculated, and implications for atmospheric radar observations are discussed.

What is the Kelvin-Helmholtz Instability ?

A region of fluid shear is unstable.

Disturbances grow, billows form.



Rockets, radar observe advected scalar quantities (temperature, ionization).

What happens to scalar distribution?

What features should show up in rocket, radar data?

Linear perturbation of vortex layer:


$$y = \frac{1}{2}h + \varepsilon e^{\sigma + i(\alpha x - \frac{\phi}{2})}$$
$$y = -\frac{1}{2}h + \varepsilon e^{\sigma + i(\alpha x + \frac{\phi}{2})}$$

implies

$$\sigma = \pm \frac{\Omega}{2} \sqrt{e^{-2kh} - (kh - 1)^2}$$
$$\phi : e^{i\phi} = e^{kh} [1 - kh \pm i \sqrt{e^{-2kh} - (kh - 1)^2}]$$

Thus, for this choice of phase angle, amplitude grows as

$$e^{\sigma}$$

We may measure this amplitude as the vertical extent of the vorticity boundaries, less h.

A semilog plot of amplitude vs. time should show unit slope in this linear growth phase of development.

Linear perturbation of vortex layer:

$$y = \frac{1}{2}h + \varepsilon e^{\sigma + i(\alpha x - \frac{\phi}{2})}$$
$$y = -\frac{1}{2}h + \varepsilon e^{\sigma + i(\alpha x + \frac{\phi}{2})}$$

implies

$$\sigma = \pm \frac{\Omega}{2} \sqrt{e^{-2kh} - (kh - 1)^2}$$
$$\phi : e^{i\phi} = e^{kh} [1 - kh \pm i \sqrt{e^{-2kh} - (kh - 1)^2}]$$

Thus, for this choice of phase angle, amplitude grows as

$$e^{\sigma}$$

We may measure this amplitude as the vertical extent of the vorticity boundaries, less h.

A semilog plot of amplitude vs. time should show unit slope in this linear growth phase of development.

Equations:

For 2-d incompressible, unbounded fluid, velocity may be found from the vorticity distribution:

$$du(x,y) = \frac{-\omega}{2\pi} (y-y') dA$$

$$dv(x,y) = \frac{\omega}{2\pi} (x-x') dA$$

With zero viscosity, a 2-d barotropic fluid is governed by

$$\frac{d\omega}{dt} + \mathbf{u} \cdot \nabla \omega = 0$$

A moving fluid element cannot change its vorticity.

We will begin with a bounded region of constant vorticity. Boundary determines flow.

We apply Green's theorem to obtain

$$u = -\omega \int_C \psi_0(x-x', y-y') dx'$$

$$v = -\omega \int_C \psi_0(x-x', y-y') dy'$$

$$\psi_0 = \frac{1}{2\pi} \ln \sqrt{(x-x')^2 + (y-y')^2}$$

is stream function for point vortex. We use periodic form.

In zero diffusion limit, may also use

$$\frac{dN}{dt} + \mathbf{u} \cdot \nabla N = 0$$

Numerical procedure:

1. Define contours by markers, interpolating function
2. Compute marker velocities based on vorticity boundaries.
3. Move markers one time step with integration technique.
4. Insert markers as needed to faithfully represent curves .

Limitations:

1. 2-d: no way to represent 3rd dimension instabilities, vortex stretching of fully developed turbulence.
2. No way to incorporate buoyancy, viscosity, or diffusion.
3. Complexity increases with time: n squared.

Advantages:

1. High resolution, only limited by accumulated error.
2. Sharp gradients may be represented faithfully
3. Higher order 2-d instabilities not artificially suppressed.
4. Vortex behavior of flow easily visualized.
5. Faster than other methods for simple boundaries.

Results:

1. Linear growth from small disturbance (method check).
2. Maximum instability billow in initial vertical scalar gradient.
3. Cuts across scalar map compared to rocket data.

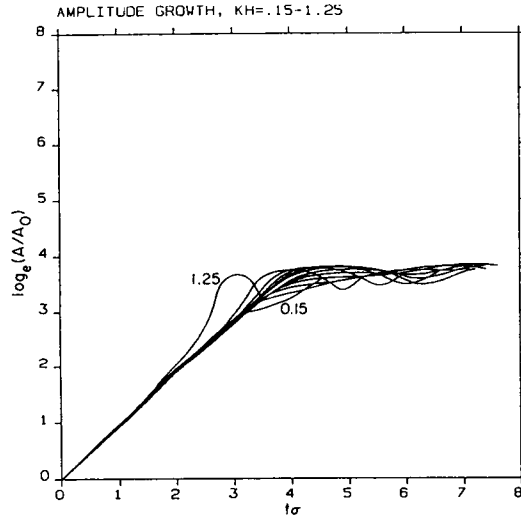


Figure 1. Billow amplitudes vs. time scaled by growth factor for $kh = 0.15, 0.25, 0.35, 0.45, 0.55, 0.65, 0.75, 0.85, 0.95, 1.05, 1.15, \text{ and } 1.25$.

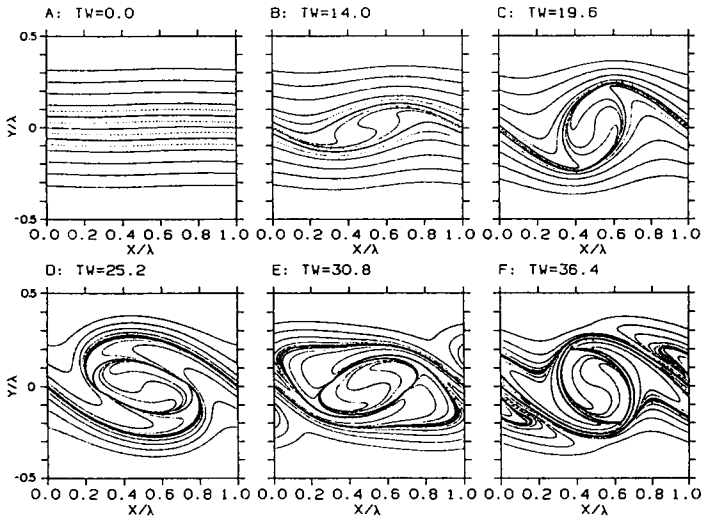


Figure 2. Scalar development in billow with time. (a) initial condition, with constant scalar vertical gradient. contours at $y/\lambda = \pm 0.06$ are also boundaries of vorticity region. (b) $t\omega = 14.0$. (c) $t\omega = 19.6$. (d) $t\omega = 25.2$. (e) $t\omega = 30.8$. (f) $t\omega = 36.4$.

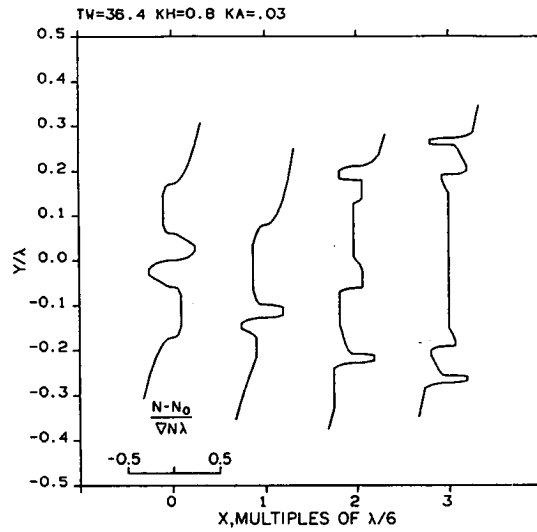


Figure 3. Vertical cross sections of scalar for pattern of Figure 2(f), through stagnation point, two intermediate locations between stagnation point and core, and core center.

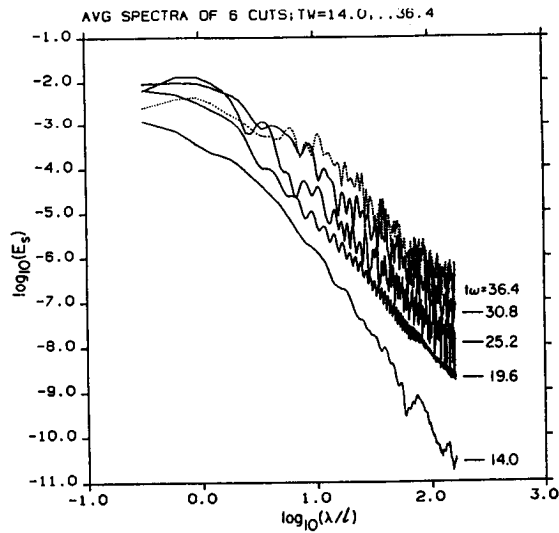


Figure 4. Log average of six energy spectral densities from cuts through scalar irregularities in simulated billows.

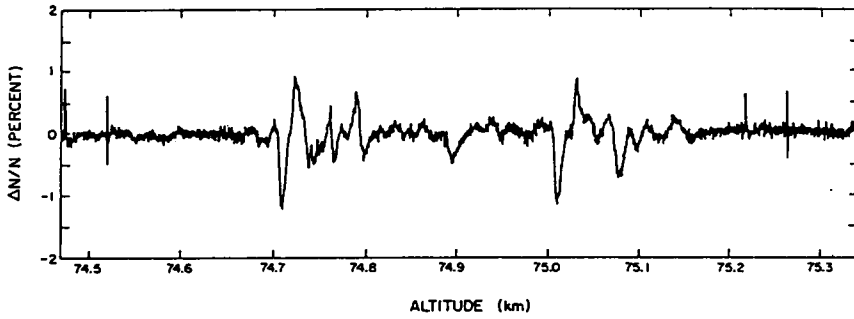


Figure 5. Reconstruction of digital electron density data for a portion of 28 May 1975 Peru rocket shot [Stoltzfus et al., *Adv. Space Res.*, 4(6), 143, 1984].

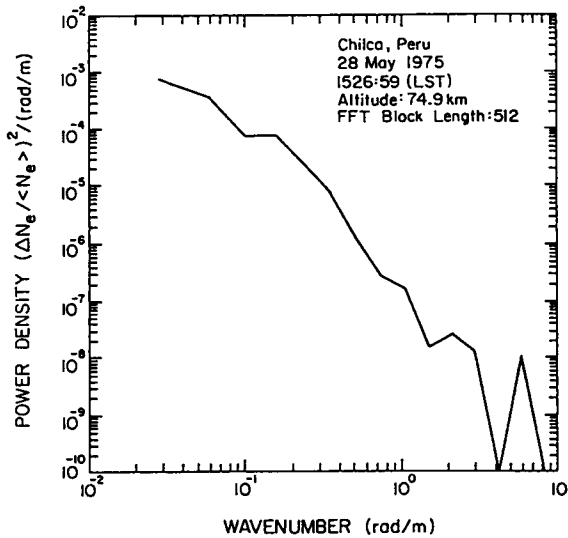


Figure 6. Power spectrum from 28 May 1975 Peru rocket shot. Spectrum is average of spectra from two parts of data of Figure 4, with noise estimate subtracted, and smoothing in wave number domain.

P.6 ESTIMATIONS OF MODEL PARAMETERS FOR GRAVITY WAVE SPECTRA OBSERVED BY MST RADAR

A. O. Scheffler, C. H. Liu, and S. J. Franke

Department of Electrical and Computer Engineering
University of Illinois, Urbana, IL 61801

ABSTRACT

The general theory of MST radar observations of gravity wave spectra is developed in this paper. This effort extends the previous results to include anisotropy and Doppler effects for the spectra, as well as the consequences for the multibeam configuration. The relationships between the observed one- or two-dimensional spectra for the line-of-sight velocity in the gravity wave spectra are derived. Expressions for cross spectra, as well as covariances between velocities observed on different beams, are computed. Using these results, studies are carried out to show how model parameters for gravity wave spectra can be estimated from the observed quantities. Model parameters include the variance, power-law indices, anisotropy parameters, Doppler parameters, mean scale sizes, etc. Cases with different numbers of beams will be investigated.

INTRODUCTION

Recently, MST radars have been used by many investigators to study the spectra of velocity fluctuations in the middle atmosphere [Balsley and Carter, 1982; Meek et al., 1985; Scheffler and Liu, 1985; Scheffler and Liu, 1986; Smith et al., 1985; Franke et al., 1988, VanZandt, 1985]. Attempts have been made by these authors to interpret the observed spectra in terms of internal gravity waves. Based on the Garrett-Munk model spectrum for ocean waves, VanZandt [1985] proposed a similar model spectrum for atmospheric waves. Features of the model spectrum have been compared to observed spectra [Smith et al., 1985; Franke et al., 1988].

In this paper, we generalize the model spectrum for the atmosphere to include different types of asymmetry in the model. We then derive relations between radar observed quantities and the model parameters. Based on these relations, we propose several observational configurations and data processing schemes in order to determine, experimentally, some of the parameters in the model spectrum.

MODEL GRAVITY WAVE SPECTRUM

For a general GM type spectrum for gravity waves the following form is assumed:

$$E(\phi, k_z, \omega) = E_0 A_z(k_z, \omega) B(\omega) F(\phi, \omega) \quad (1)$$

E_0 is the energy density constant; k_z^* is the vertical wave number bandwidth; p and t are the frequency and wave number power law indices, respectively. The corresponding three algebraic model functions are defined as

$$A_z(k_z, \omega) = \left(1 + \frac{\omega}{|\omega|} \frac{k_z}{|k_z|} S_v \right) \frac{(t-1)k_z^{*t-1}}{(k_z^* + |k_z|)^t} \quad (2a)$$

$$B(\omega) = \frac{p-1}{\omega_1^{1-p} - \omega_b^{1-p}} |\omega|^{-p} \text{ for } \omega_1 \leq |\omega| \leq \omega_b, \text{ and } B(\omega) = 0 \text{ elsewhere} \quad (2b)$$

$$F(\phi, \omega) = \frac{1+S_h}{2} \frac{a}{1 - \frac{\omega}{|\omega|}(1-a^2)^{1/2} \cos(\phi-\phi_a)} + \frac{1-S_h}{2} \frac{a}{1 - \frac{\omega}{|\omega|}(1-a^2)^{1/2} \cos(\phi-\phi_a)} \quad (2c)$$

where $a = (1-e^2)^{1/2}$.

The A_z function is based upon the familiar GM 75 vertical wave number function introduced in the symmetric model with bandwidth k_z^* . However, the vertical symmetry fraction S_v , has been added to model the upward/downward propagation asymmetry of gravity waves for two different cases. The spectral shape is the same for the $\pm k_z$ (upward/downward) branches, but the levels of these two branches are altered so that they are proportional to $1 \pm S_v$. A physically realistic spectrum requires that $|S_v| \leq 1$. The extreme example of $S_v = \pm 1$ therefore corresponds to solely upward/downward propagation. Any case of $S_v \neq 0$ adds one degree of freedom to the model to represent vertical asymmetry.

The B function retains the same symmetric power law form as previously assumed. In comparison to Garrett and Munk, however, a double-sided form is emphasized throughout this paper to be consistent with even symmetry of the four-dimensional wave energy spectrum necessary to represent a real velocity field in the space-time domain. This physical requirement is also the reason for introducing the sign of ω dependence to the A and F functions in order to model the vertical and azimuthal asymmetries. Complete separability is therefore not possible in the asymmetric spectrum, but $\phi - k_z$ separation is still assumed. If so desired, however, the model presented here is simple enough to be represented as the sum of four completely separable products when the \pm branches of ϕ , k_z , and ω are treated individually.

The F function has been introduced to model the azimuthal dependence of the gravity wave spectrum. This function is essentially the sum of two ellipses in the azimuthal plane whose pairs of foci lie on opposite sides of the origin but along the same axis inclined by the angle ϕ_a from the x-axis. The eccentricity of both ellipses is e , which is determined by the azimuthal shape factor a . The azimuthal symmetry factor S_h controls the relative sizes of the two ellipses in varying degrees, from waves propagating with bilateral symmetry, $S_h = 0$, to those propagating only toward one axial direction, $S_h = 1$. The minimum value for the shape fraction is $a = 0$, which represents propagation only in the vertical plane inclined by ϕ_a from the x-axis. Nonzero shape factors lead to general three-dimensional spectra. The case for a maximum value of $a = 1$ corresponds to azimuthal isotropy for which $F(\phi, \omega) = 1$.

The following normalizations apply to the general model for the functions A, B, and F:

$$\frac{1}{2} \int_{-\infty}^{\infty} A_z(k_z, \omega) dk_z = \frac{1}{2} \int_{-\infty}^{\infty} B(\omega) d\omega = \int_{\omega_i}^{\omega_b} B(\omega) d\omega = \frac{1}{2\pi} \int_{2\pi}^0 F(\phi, \omega) d\phi = 1 \quad (3)$$

Finally, the spectrum becomes the symmetric Boussinesq model spectrum for the special case of $S_v = 0$ and $a = 1$.

GRAVITY WAVE SPECTRA AND VARIANCES OBSERVED BY RADAR

We shall proceed to derive the relation which involve the observed frequency spectrum and velocity variance from a given radar beam and the wave spectrum $E(\vec{k}, \omega)$. For a positioned radar beam, $\vec{r} = r \hat{B}$, with range r and beam direction

$$\hat{B}(\theta_B, \phi_B) = \cos \phi_B \sin \theta_B \hat{x} + \sin \phi_B \sin \theta_B \hat{y} + \cos \theta_B \hat{z} \quad (4)$$

By closely following the procedure in Scheffler and Liu [1985], the observed velocity fluctuation along the beam direction is found to be

$$\vec{V}_{ob}(r,t) = \vec{V}(rB,t) \cdot \hat{B} \quad (5)$$

where \vec{V} is the velocity fluctuation associated with the waves, including the three components U, V and W.

From (4) and (5), we can derive the frequency spectrum for the observed velocity fluctuation:

$$\begin{aligned} E_{ob}(\omega) = & E_V(\omega) \cos^2\phi_B \sin^2\theta_B + E_V(\omega) \sin^2\phi_B \sin^2\theta_B + E_W(\omega) \cos^2\theta_B \\ & + \text{Re}E_{UV}(\omega) \sin 2\phi_B \sin^2\theta_B + \text{Re}E_{UW}(\omega) \cos\phi_B \sin 2\theta_B \\ & + \text{Re}E_{VW}(\omega) \sin\phi_B \sin 2\theta_B \end{aligned} \quad (6)$$

where the rectilinear spectral components $E_U(\omega)$, $E_V(\omega)$, $E_W(\omega)$, $E_{UV}(\omega)$, and $E_{VW}(\omega)$ are the autospectra and cross spectra of the velocity components, respectively. They can be related to the general model spectrum for the wave, eq (1), through manipulations following the procedure outlined in Scheffler and Liu /3/. The effects of Doppler shift due to background wind can also be included [Scheffler and Liu, 1986].

The general expression for the velocity covariance $\overline{V_{ob}^2}$ at a given radar beam can be obtained by integration of the frequency autospectrum

$$\langle V_{ob}^2 \rangle = \int_0^\infty E_{ob}(\omega) d\omega \quad (7)$$

which yields

$$\begin{aligned} \langle V_{ob}^2 \rangle = & \langle U^2 \rangle \cos^2\phi_B \sin^2\theta_B + \langle V^2 \rangle \sin^2\phi_B \sin^2\theta_B + \langle W^2 \rangle \cos^2\theta_B \\ & + \langle UV \rangle \sin 2\phi_B \sin^2\theta_B + \langle UW \rangle \cos\phi_B \sin 2\theta_B + \langle VW \rangle \sin\phi_B \sin 2\theta_B \end{aligned} \quad (8)$$

where the rectilinear variance components are

$$\begin{aligned} \langle U^2 \rangle = & E_o \left[1 - \frac{2}{p+1} \frac{a+(1-a)\sin^2\phi_a}{1+a} \right] \\ \langle V^2 \rangle = & E_o \left[1 - \frac{2}{p+1} \frac{a+(1-a)\cos^2\phi_a}{1+a} \right] \\ \langle W^2 \rangle = & E_o \frac{p-1}{3-p} \left(\frac{\omega_i}{\omega_b} \right)^{p-1} \\ \langle UV \rangle = & E_o \frac{1}{p+1} \frac{1-a}{1+a} \sin 2\phi_a \\ \langle UW \rangle = & -E_o S_V' S_h' \left(\frac{1-a}{1+a} \right)^{1/2} \frac{\bar{\omega}}{\omega_b} \cos\phi_a \\ \langle VW \rangle = & E_o S_V' S_h' \left(\frac{1-a}{1+a} \right)^{1/2} \frac{\bar{\omega}}{\omega_b} \sin\phi_a \end{aligned} \quad (9)$$

where

$$\bar{\omega} = \frac{\omega_b}{\int_{\omega_i} \omega B(\omega) d\omega} \quad (10)$$

PARAMETER ESTIMATION FOR GENERAL MODEL GRAVITY WAVE SPECTRUM

We will now make use of the variance formulae obtained in the preceding section to outline a parameter estimation procedure for the general model spectrum. Let us assume that we have simultaneous and continuous Doppler radar velocity time series at the same altitude for at least three beams pointing in nonparallel directions. Then the frequency spectra and cross spectra can be computed from these beams. Analysis of the spectral slopes can determine the frequency power index, p . The Brunt Vaisala frequency, ω_b , might also be estimated from these spectra or by other means such as from background wind and temperature profiles. The inertial frequency can be computed from the earth's rotational period and latitude of the radar site.

Using a 5-beam configuration where beam 1 points upward in the vertical direction, beams 2 and 4 obliquely to the east and west at an angle θ_B , respectively, and beams 3 and 5 obliquely to the north and south at an angle θ_B , respectively. If we denote the velocity covariances measured by the i th beam as $\langle V_i^2 \rangle$, then the covariances for the wave associated velocity components can be computed from the $\langle V_i^2 \rangle$:

$$\begin{aligned} \langle W^2 \rangle &= \langle V_1^2 \rangle \\ \langle U^2 \rangle &= (\langle V_2^2 \rangle + \langle V_4^2 \rangle - 2\langle W^2 \rangle \cos^2 \theta_B) / (2\sin^2 \theta_B) \\ \langle V^2 \rangle &= (\langle V_3^2 \rangle + \langle V_5^2 \rangle - 2\langle W^2 \rangle \cos^2 \theta_B) / (2\sin^2 \theta_B) \\ \langle UW \rangle &= (\langle V_2^2 \rangle - \langle V_4^2 \rangle) / (2\sin^2 \theta_B) \\ \langle VW \rangle &= (\langle V_3^2 \rangle - \langle V_5^2 \rangle) / (2\sin^2 \theta_B) \end{aligned} \quad (11)$$

If a sixth beam is added, say at $\phi_6 = 45^\circ$, then it is possible to obtain

$$\langle UV \rangle = \frac{\langle V_6^2 \rangle - (\sqrt{2}+1)(\langle V_2^2 \rangle + \langle V_3^2 \rangle)/4 + \frac{\sqrt{2}-2}{c}(\langle V_4^2 \rangle + \langle V_5^2 \rangle)/4}{\sin^2 \theta_B}$$

With these six measured variances in eq. (11), the solution of eq. (9) allows for the quantitative estimation of four parameters for the model spectrum: E_0 , a , $\tan 2\phi_a$, and $|S_{vh}| = |S_v|$. Under the set of assumptions made here, this leaves two degrees of freedom since there are six velocity variances in all. Due to this redundancy, it is possible to check the consistence of the wave spectrum hypothesis by computing some of the parameters in more than one way.

Let us first examine the case of E_0 . Inspection of (9) shows that it is determined by $\langle W^2 \rangle$, or $\langle U^2 \rangle$, and $\langle V^2 \rangle$,

$$E_0 = \frac{3-p}{p-1} \left(\frac{\omega_b}{\omega_i} \right)^{p-1} \langle W^2 \rangle, \text{ or } E_0 = \frac{p+1}{2p} (\langle U^2 \rangle + \langle V^2 \rangle) \quad (12)$$

The second way to obtain E_0 from velocity variances is from the horizontal components. If $\langle W^2 \rangle$ is obtained directly from a vertical radar measurement it may be contaminated with a horizontal velocity component depending on the possible sloped layer and the precise nature of the

scattering mechanism. On the other hand, the value of E_0 obtained by decomposition of oblique velocity variance measurements can be compared to the one found by $\langle W^2 \rangle$ to check the effect of the contamination. Greater consistency could be achieved for the parameter estimation scheme applied here if $\langle W^2 \rangle$ were also determined by decomposition from an oblique beam configuration. The scattering mechanisms for multiple beams at a fixed oblique zenith angle are much likelier to be caused by the same process than the vertical beam. This is especially the case of θ_B greater than about 2.5° where turbulent scatter dominates. A way to obtain $\langle W^2 \rangle$ from oblique measurements is to add the 7th beam at a different beam angle θ_B' with ϕ_B , say, at 135° . Then

$$\langle W^2 \rangle = \frac{A \sin^2 \theta_B' - B \sin^2 \theta_B}{\sin(\theta_B' - \theta_B) \sin(\theta_B' + \theta_B)} \quad (13)$$

where

$$A = \frac{1}{4} [\langle V_2^2 \rangle + \langle V_3^2 \rangle + \langle V_4^2 \rangle + \langle V_5^2 \rangle]$$

$$B = \frac{1}{2} [\langle V_6^2 \rangle + \langle V_7^2 \rangle] - \frac{\sqrt{2}}{4} [\langle V_3^2 \rangle - \langle V_5^2 \rangle] \left(\frac{\sin 2\theta_B'}{\sin 2\theta_B} \right)$$

Even if the observed velocity variances are obtained under identical scattering mechanisms, a discrepancy between E_0 computed from (12) could still arise if the mesoscale atmospheric energy spectrum $E(k, \omega)$ is not entirely due to waves. The presence of two-dimensional atmospheric turbulence could contribute to a significant increase in the horizontal variance components without having an effect on the vertical variance which would still be due mainly to wave fluctuations. This provides a way to examine the contribution of 2-D turbulence to the overall observed velocity fluctuations.

The azimuth width factor, a , can be solved from (9). The most straightforward solution is:

$$\frac{1-a}{1+a} = \frac{[(\langle U \rangle - \langle V^2 \rangle)^2 + (\langle UV \rangle)^2]^{1/2}}{\langle U^2 \rangle \langle V^2 \rangle} \quad (14)$$

Note that for the case of an azimuthally isotropic spectrum, such that $a = 1$ and so $\langle U^2 \rangle - \langle V^2 \rangle = \langle UV \rangle = \langle UW \rangle = \langle VW \rangle = 0$. Then the remaining parameters, ϕ_a and S_{vh} cannot be determined by velocity variances alone. However, if $0 \leq a \leq 1$, then we can continue this approach to solve these two parameters also.

The solution to ϕ_a is quite straightforward.

$$\tan 1\phi_a = \frac{2\langle UV \rangle}{\langle U^2 \rangle - \langle V^2 \rangle} \quad \text{or} \quad \tan \phi_a = \frac{\langle VW \rangle}{\langle UW \rangle} \quad (15)$$

The two possible solutions to ϕ_a cannot be distinguished by variances alone without other knowledge or an assumption about the sign of S_v . A spectrum which consists of mainly downward phase propagation will, for example, have a negative S_v , and then (9) can be used to determine the quadrant of ϕ_a . The magnitude of the vertical-horizontal propagation factor S_{vh} can be found for $a \neq 1$ through the vertical fluxes of the zonal and meridional momenta.

$$|S_{vh}| = |S_v| S_h \left(\frac{1+a}{1-a} \right)^{1/2} \left(\frac{\omega_h}{\bar{\omega}} \right) [\langle UW^2 \rangle + \langle V^2 \rangle]^{1/2} / E_0 \quad (16)$$

This completes all the possible ways to estimate the parameters of the general model spectrum by using the nine variance components. Although these variances do include the momentum fluxes, they do not determine all the parameters in our model. Spatial information must also be available in order to determine k_z^* and S_v (or S_h). A vertical or nearly vertical observed wave number spectrum can be directly applied to estimate k_z^* such as was done by Scheffler and Liu [1985]. However, a two-dimensional data set is required to completely determine the propagation factors S_v or S_h . The energy density content of each of the two branches of an observed $k_z - \omega$ velocity spectrum could, for instance, be used to estimate S_v . This parameter could also be determined from the same data set, but in the time domain by using the phase propagation correlation technique.

CONCLUSIONS

In this paper we derived the general expressions for various autospectra and cross spectra, as well as different types of variances for velocity fluctuations observed by multibeam MST radars. Assuming that these fluctuations are due to the presence of gravity waves, the radar-observed quantities are related to parameters of the general model gravity wave spectrum. These relations are used to design observational configurations such that the model parameters can be determined from the observed data.

The procedure can be summarized as follows. With one beam, pointing vertically, one can determine the spectral indices p and t ; also E_0 , and possibly S_v by 2-D spectral analysis. With five beams, one vertical, two symmetrically off vertical in the E-W directions, and two N-S directions, one can then determine the azimuthal asymmetry parameters, a , and the principal direction of the propagation ellipse, ϕ_a . With two additional beams, one with the same beam zenith angle but with different azimuth angle, one with different zenith angle, sufficient redundancy can be provided for checking the consistency of the assumption that the observed velocity fluctuations are due to gravity waves.

Finally, it should be mentioned that the major effort in this procedure is based on the variances of the observed quantities. This in many ways is more suitable for the purpose in determining model parameters than procedures that use spectral information alone.

ACKNOWLEDGMENT

The work described in this paper was supported by the National Science Foundation under grant ATM 87 04947.

REFERENCES

- B. B. Balsley, and D. A. Carter, The spectrum of atmospheric velocity fluctuations at 8 km and 86 km, *Geophys. Res. Lett.*, **9**, 465-468, 1982.
- C. E. Meek, I. M. Reid, and A. H. Manson, Observations of mesospheric wind velocities. II. Cross sections of power spectral density for 48-8 h, 8-1 h, 1 h - 10 min over 60-110 km for 1981, *Radio sci.*, **20**, 1383-1402, 1985.
- A. O. Scheffler, and C. H. Liu, On observation of gravity wave spectra in the atmosphere by using MST radar, *Radio Sci.*, **20**, 1309-1322, 1985.
- A. O. Scheffler, and C. H. Liu, The effects of Doppler shift on gravity wave spectra observed by MST radar, *J. Atmos. Terr. Phys.*, **48**, 1225-1231, 1986.
- S. A. Smith, D. C. Fritts, and T. E. VanZandt, Comparison of mesospheric wind spectra with a gravity wave model, *Radio Sci.*, **20**, 1331-1338, 1985.
- S. J. Franke, C. H. Liu, I. J. Fu, R. Ruster, P. Czechowsky, and G. Schmidt, Multi-beam radar observations of winds in the mesosphere, submitted to *Geophys. Res.*, 1988.
- T. E. VanZandt, A model for gravity wave spectra observed by Doppler sounding systems, *Radio Sci.*, **20**, 1323-1330, 1985.

P.7 SPECTRAL ANALYSIS OF TEMPERATURE AND BRUNT-VÄISÄLÄ FREQUENCY FLUCTUATIONS OBSERVED BY RADIOSONDES

T. Tsuda, T. E. VanZandt

NOAA Aeronomy Laboratory, R/E/AL3
325 Broadway, Boulder, CO 80303

S. Kato, S. Fukao, and T. Sato

Radio Atmospheric Science Center
Kyoto University, Uji, Kyoto 611 Japan

Recent studies have revealed that vertical wave number spectra of wind velocity and temperature fluctuations in the troposphere and the lower stratosphere are fairly well explained by a saturated gravity wave spectrum. But N^2 (N: Brunt-Väisälä (BV) frequency) spectra seem to be better for testing the scaling of the vertical wave number spectra in layers with different stratifications, because its energy density is proportional only to the background value of N^2 , while that for temperature depends on both the BV frequency and the potential temperature. From temperature profiles observed in June-August 1987 over the MU Observatory, Japan, by using a radiosonde with 30 m height resolution, N^2 spectra are determined in the 2 - 8.5 km (troposphere) and 18.5 - 25 km (lower stratosphere) ranges. Although individual spectra show fairly large day-by-day variability, the slope of the median of 34 spectra agrees reasonably with the theoretical value of -1 in the wave number range of $6 \times 10^{-4} \sim 3 \times 10^{-3}$ (c/m). The ratio of the spectral energy between these two height regions is about equal to the ratio of N^2 , consistent with the prediction of saturated gravity wave theory.

RADIOSONDE LAUNCHED AT MU OBSERVATORY

6 30 8: 8 -	7 3 8: 7
7 6 14:23 -	7 11 20:22
7 29 20:21 -	7 31 21:15
8 20 14:45 -	8 20 14:45
8 29 5:26 -	9 4 0: 7

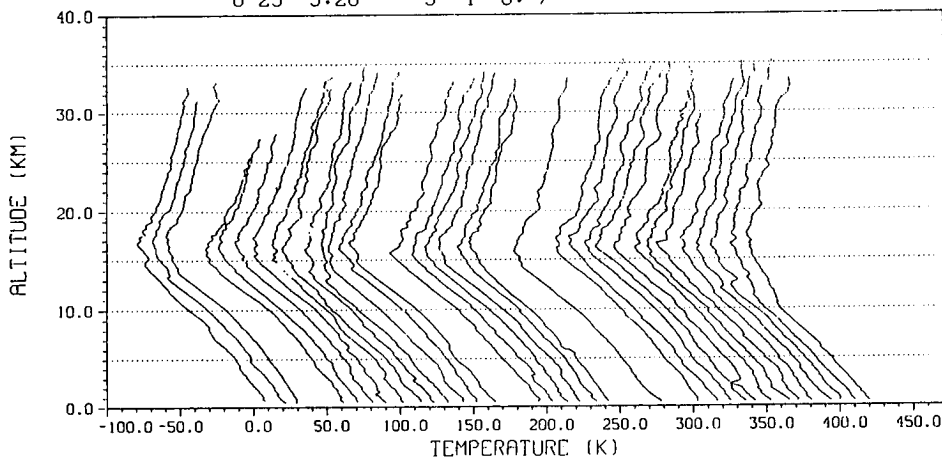


Figure 1. Temperature profiles observed by radiosondes launched from the MU radar site from 30 June to 4 September 1987. The campaign periods are listed above. Successive profiles are displaced by 10 K, and the beginning of each campaign is displaced by 20 K.

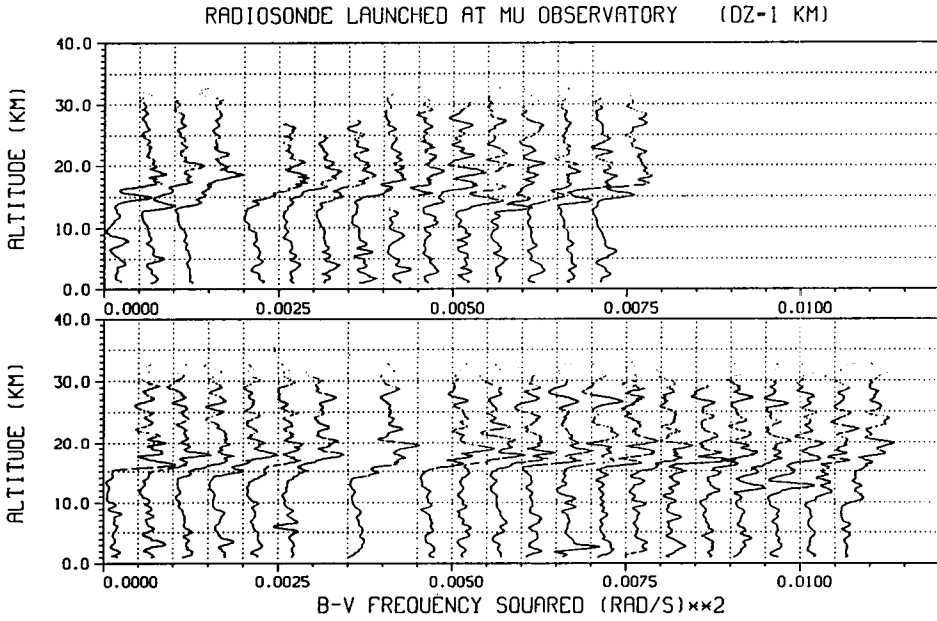


Figure 2. N^2 profiles determined from the temperature profiles plotted in Figure 1. The spacing for a calculation of the vertical derivative is 990 m. Successive profiles are displaced by $5 \times 10^{-4} \text{ (rad/s)}^2$.

RADIOSONDE LAUNCHED AT MU OBSERVATORY

12 22 14:28 - 12 26 4:56
 2 17 8:43 - 2 18 20:25
 2 23 15: 1 - 2 25 19:55

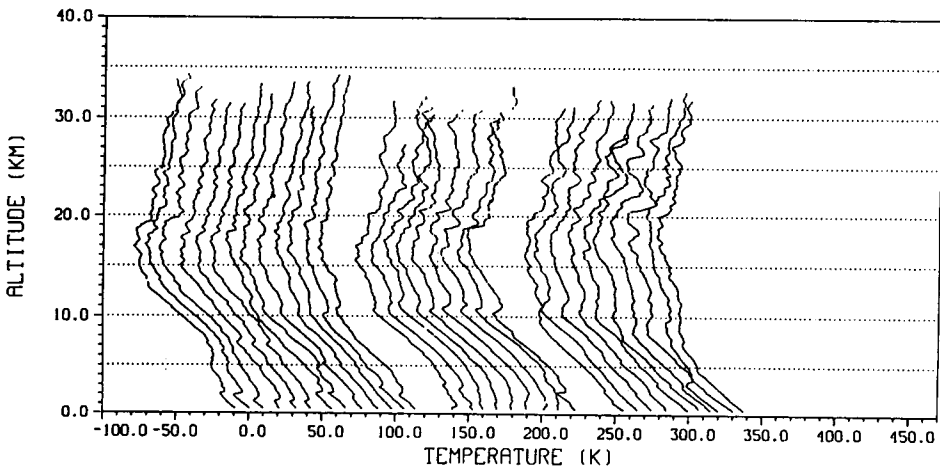


Figure 3. The same as Figure 1 except for the winter campaigns from 22 December 1986 to 25 February 1987.

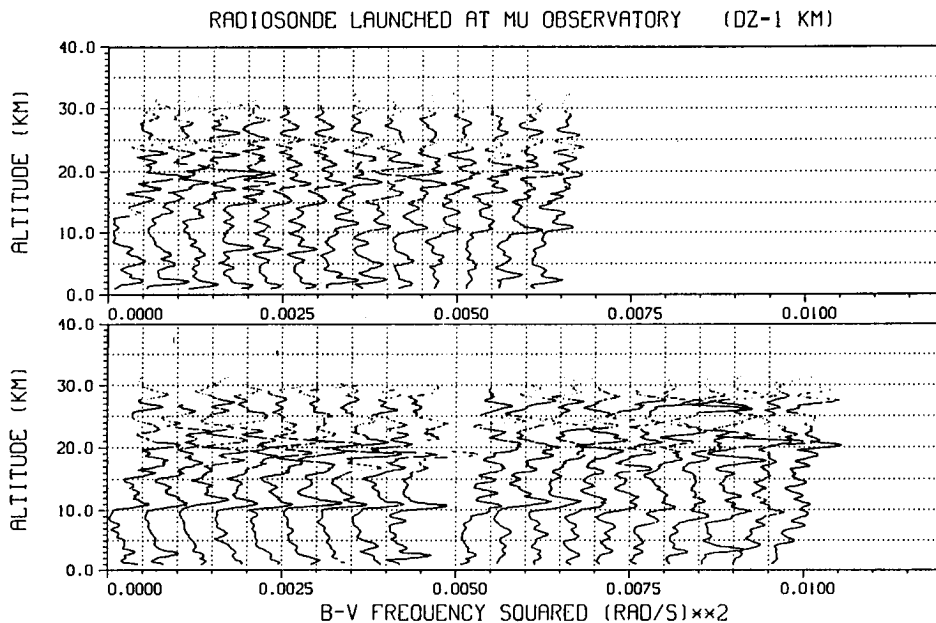


Figure 4. The same as Figure 2 except for the winter campaigns.

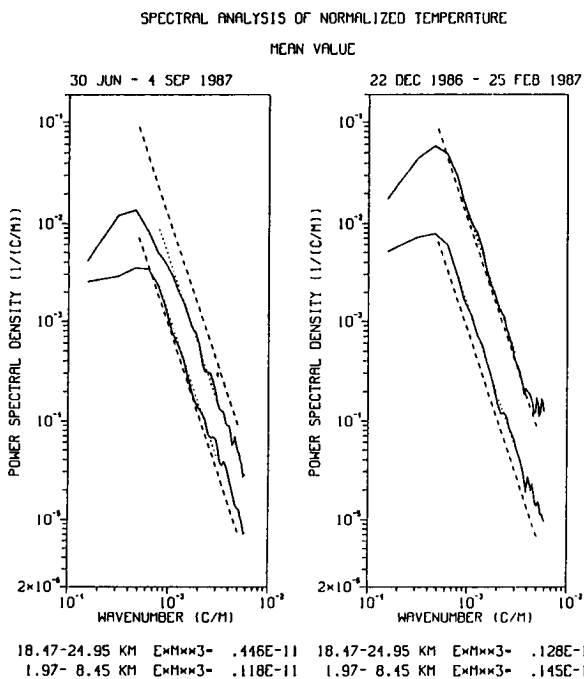


Figure 5. Mean vertical wave number spectra of normalized temperature perturbations in summer (left panel) and winter (right panel). The spectra with larger amplitudes are from 18.5 - 24.5 km altitude, while the others are from 2.0 - 8.5 km. The dashed curves correspond to a saturated gravity wave spectrum [Smith et al., 1987]. The dotted lines are the best-fits determined from the mean value of $F(m)m^3$ averaged for $m = 8 \times 10^4$ to 3×10^3 , where $F(m)$ and m are power spectral density and wave number, respectively.

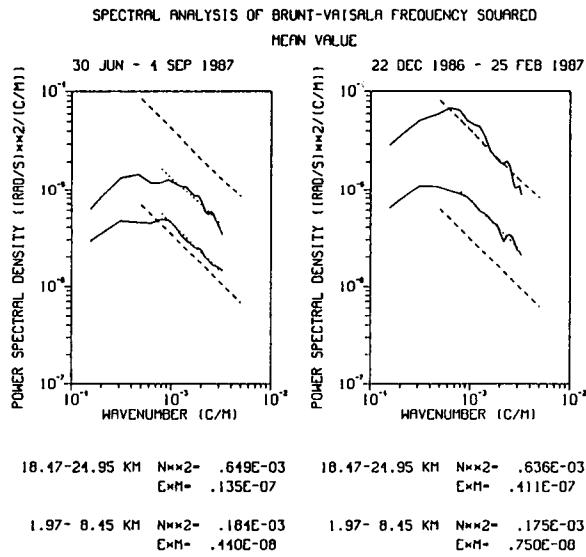


Figure 6. Same as Figure 5 except for N^2 spectra. The vertical spacing to calculate N^2 is 150 m. The median value of background N^2 in each height range is shown at the bottom of the pane, which is used to calculate the theoretical predictions plotted in Figures 5 and 6.

RADIOSONDE LAUNCHED FROM MU OBSERVATORY AT 20:21 ON 7/29 1988

BAND-PASS-FILTER CUTOFF= 900.0 .0 (M)
 HT RANGE FOR VARIANCE= 900.0 (M)
 HT DIFF FOR B.V. FREQ=1230.0 (M)

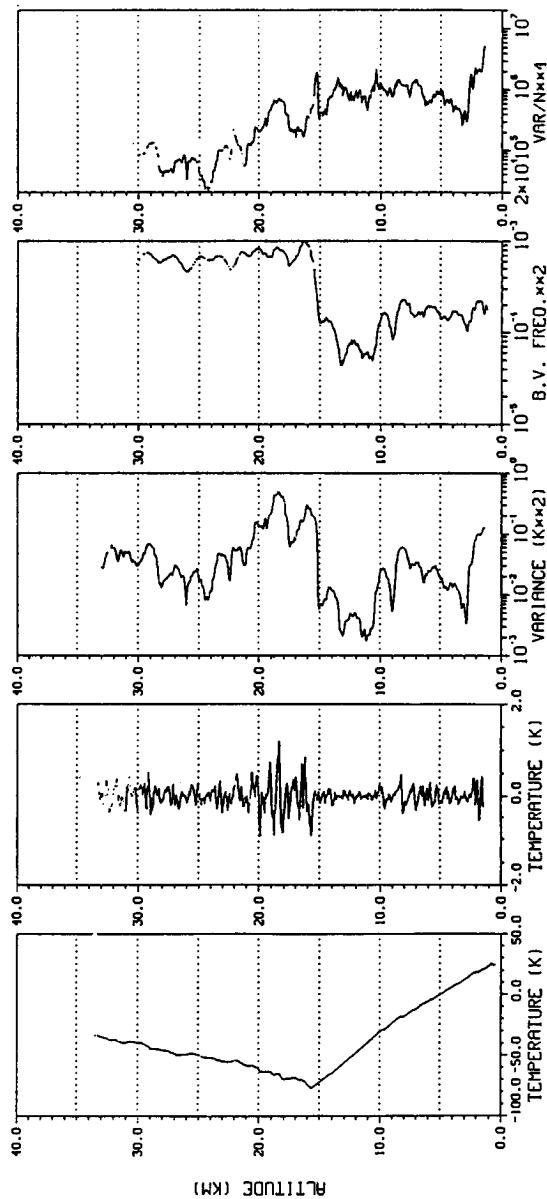


Figure 7. Vertical profiles of temperature, perturbed temperature T' , variance of temperature, N^2 and $\langle T'^2 \rangle / N^4$ (from left to right panels) measured on 29 July 1987. T is extracted by using a high-pass filter with a cutoff at 900 m. The vertical spacings for the calculations of $\langle T'^2 \rangle$ and N^2 are 900 and 1230 m, respectively. Note that $\langle T'^2 \rangle$ becomes very small just below the tropopause and then becomes large just above the tropopause, while the corresponding variation in $\langle T'^2 \rangle / N^4$ near the tropopause is relatively small.

RADIOSONDE LAUNCHED FROM MU OBSERVATORY AT 19:55 ON 2/25 1988

BAND-PASS-FILTER CUTOFF= 900.0 .0 (M)
HT RANGE FOR VARIANCE= 900.0 (M)
HT DIFF FOR B.V. FREQ=1230.0 (M)

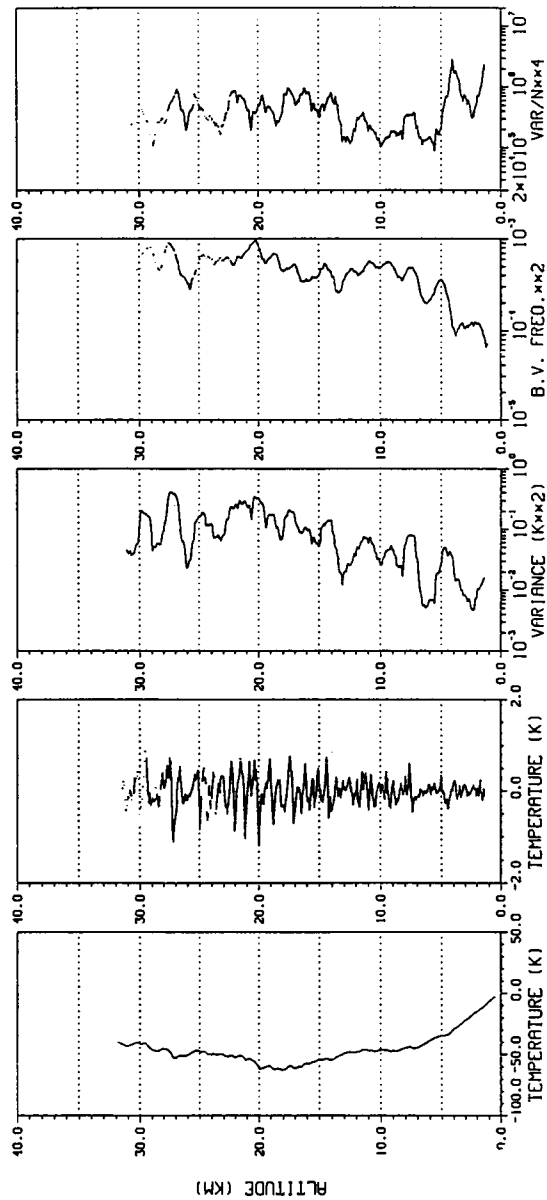


Figure 8. The same as Figure 7 except for the observation on 25 February 1987.

RADIOSONDE LAUNCHED AT MU OBSERVATORY

BAND-PASS-FILTER CUTOFF= 900.0 .0 (M)

HT RANGE FOR VARIANCE= 900.0 (M)

HT DIFF FOR B.V. FREQ=1230.0 (M)

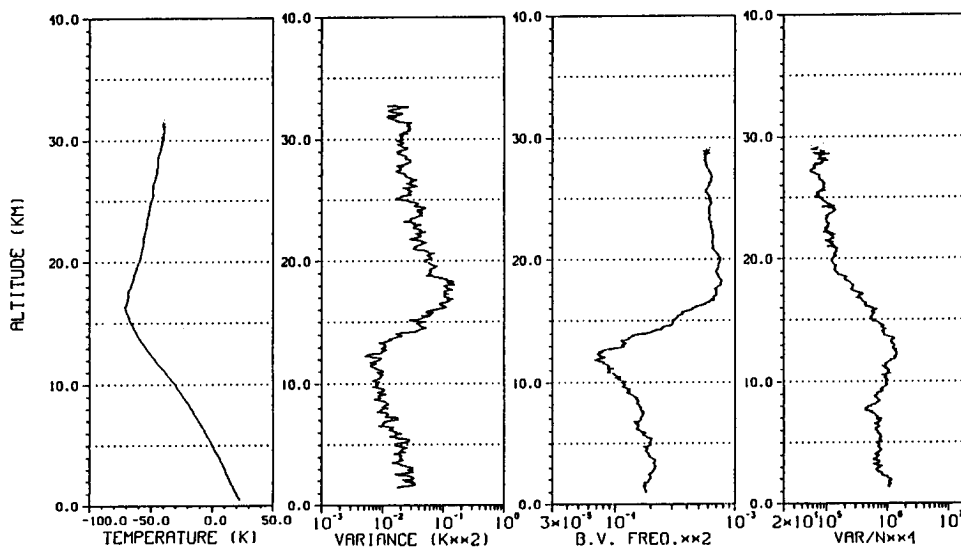


Figure 9. Profiles of temperature $\langle T^2 \rangle$, N^2 , and $\langle T^2 \rangle / N^4$ determined as the median of 34 observations in summer months. Note that $\langle T^2 \rangle / N^4$ is fairly constant in the troposphere and stratosphere, although their amplitudes differ by a factor of about 8.

RADIOSONDE LAUNCHED AT MU OBSERVATORY

BAND-PASS-FILTER CUTOFF= 900.0 .0 (M)
HT RANGE FOR VARIANCE= 900.0 (M)
HT DIFF FOR B.V. FREQ=1230.0 (M)

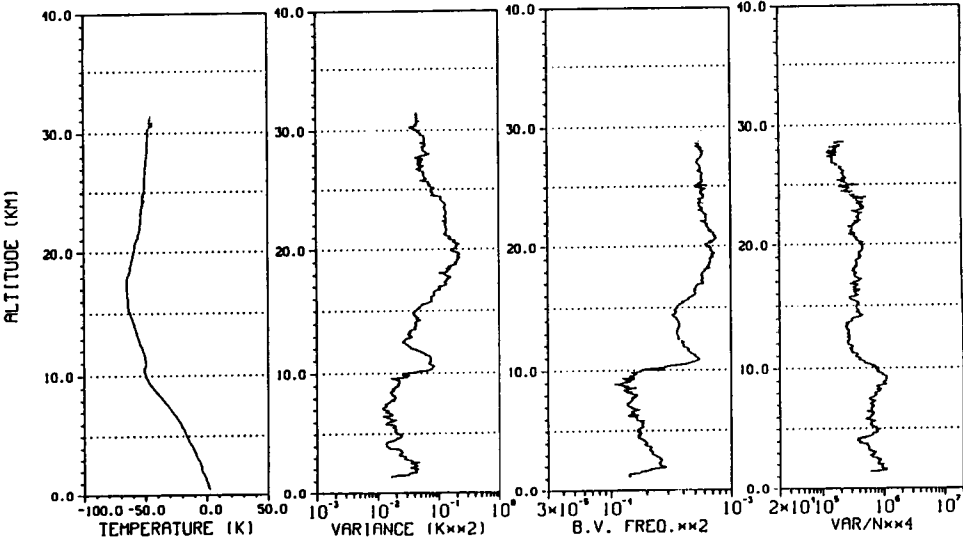


Figure 10. The same as Figure 9 except for 32 winter observations. The difference in $\langle T^2 \rangle / N^4$ between the troposphere and stratosphere is smaller than in the summer case.

P.8 OBSERVATIONS OF GRAVITY WAVES IN THE MESOSPHERE
WITH THE MU RADAR

T. Tsuda, S. Kato, T. Inoue, T. Yokoi, M. Yamamoto, S. Fukao, and T. Sato

Radio Atmospheric Science Center,
Kyoto University, Uji, Kyoto 611, Japan

We have observed wind motions at 60 - 90 km altitudes with the MU radar during daylight hours (0800 - 1600 LT) from 13 to 31 October 1986. Quasi-monochromatic gravity waves were evident on 16 of the 19 days of observations. They were characterized by typical vertical wavelength of 5 to 15 km and intrinsic periods centered at about 9 hours. The propagation direction of the gravity waves, determined by the gravity wave dispersion relation, was mostly equatorward.

The vertical wave number spectra of the horizontal components of the mesoscale wind fluctuations are explained well by saturated gravity wave theory. the frequency spectrum of vertical wind component has a slope of $+1/3$, while the oblique spectra have a slope of $-5/3$ up to 4×10^{-3} (c/s); these agree fairly well with model gravity wave spectra. Doppler shift effects on the frequency spectra are recognized at higher frequencies.

We also determined upward flux of horizontal momentum flux induced by waves with periods from 10 min to 8 hours, and we estimated westward and northward body forces of 5.1 and 4.0 m/s/day, respectively.

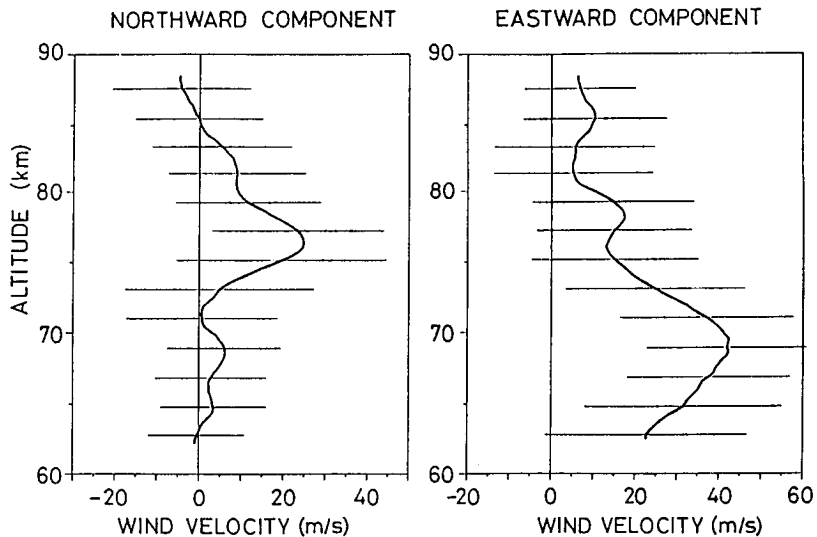


Figure 1. Mean northward (left) and eastward (right) horizontal wind velocity profiles determined from MU radar observations 13 - 31 October 1986. A running average for 2 km altitude is applied. The error bars indicate standard deviations of fluctuating wind components.

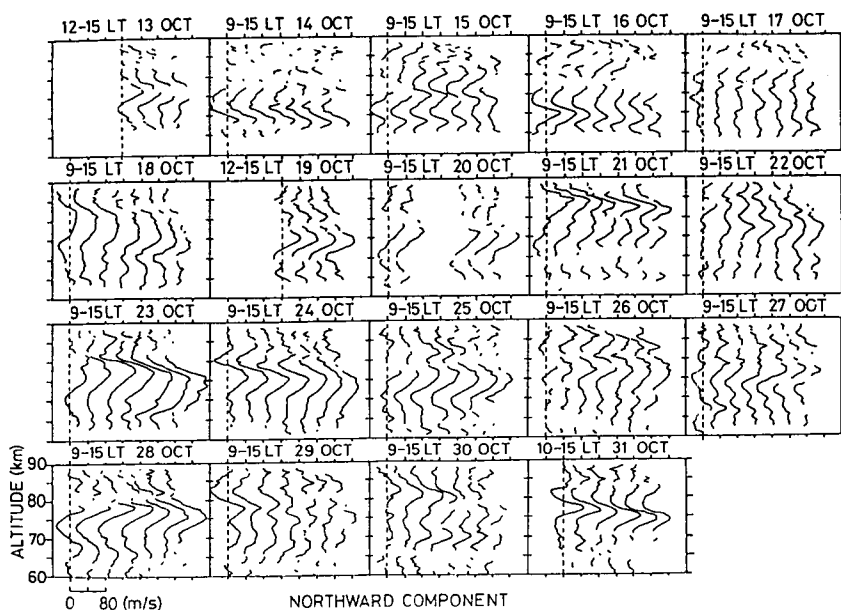


Figure 2. The northward component of wind velocity profiles. Data are averaged for 2 hours by shifting the averaging period by one hour. The dashed line indicates 0 m/s for the first profile, and other profiles are successively shifted by 40 m/s.

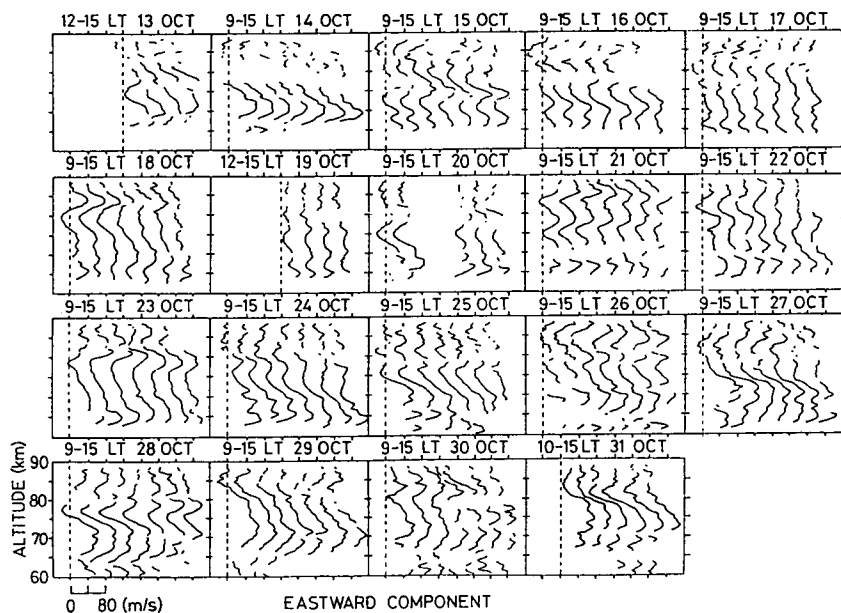


Figure 3. The same as Figure 2 except for the eastward component.

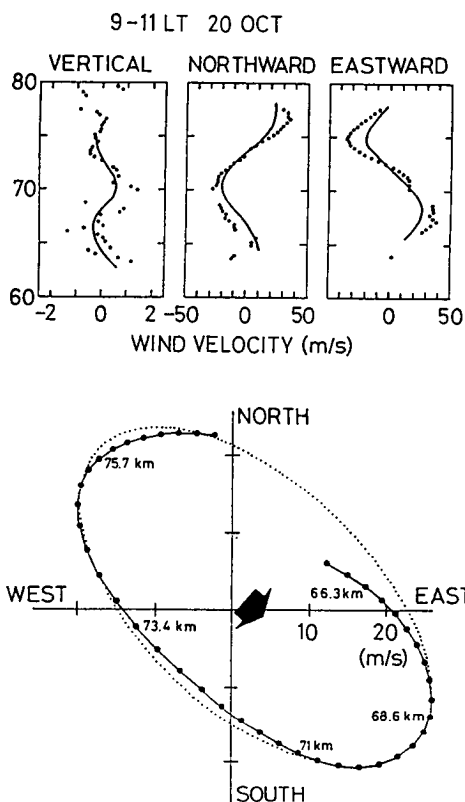


Figure 4. Vertical profiles of the three wind components observed at 9 - 11 LT on 20 October 1986 (top) and the corresponding hodograph (bottom). Dots in the top panels show original data, while the solid curves correspond to the profiles after band-pass filtering with cutoffs at 6 and 24 km. The solid curve in the bottom panel is the hodograph of the filtered wind velocities, and the dotted curve is a least-squares fit of an ellipse to the hodograph, from which the intrinsic wave period was estimated to be 10.9 hours. The thick arrow indicates the propagation direction of this wave.

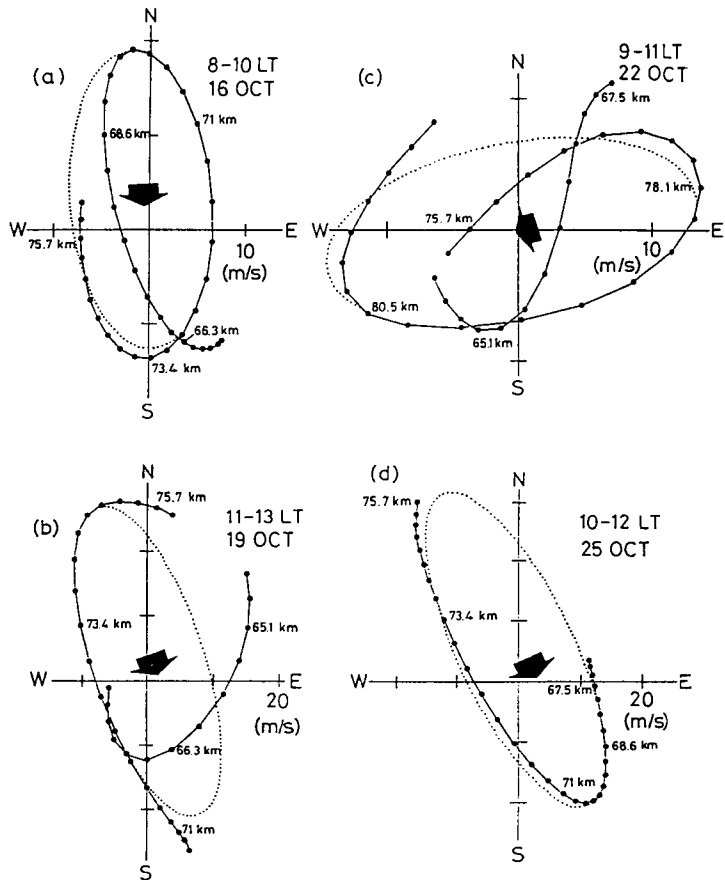


Figure 5. Four examples of the hodographs and the propagation direction.

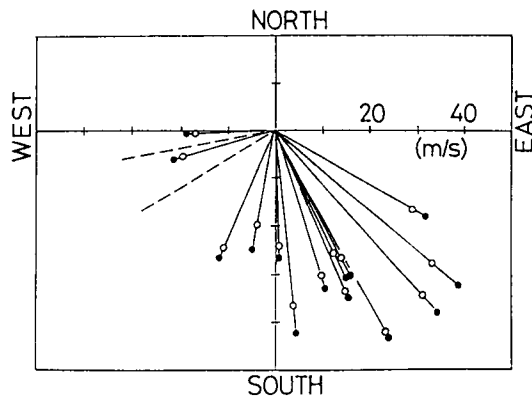


Figure 6. Distribution of horizontal phase (full circle) and group (open circle) velocities. Only the propagation direction was determined for two cases indicated by a dashed line. The mean amplitudes of the horizontal phase and group velocities were 35.3 and 31.6 m/s, respectively.

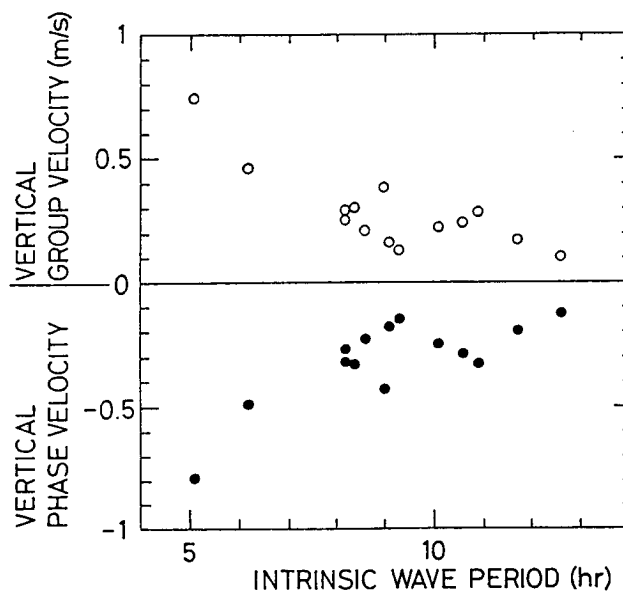


Figure 7. Distribution of the intrinsic period and vertical group (open circle) and phase (full circle) velocities. The mean intrinsic period was 8.6 hours, and the mean vertical group and phase velocities were 0.31 and -0.28 m/s, respectively.

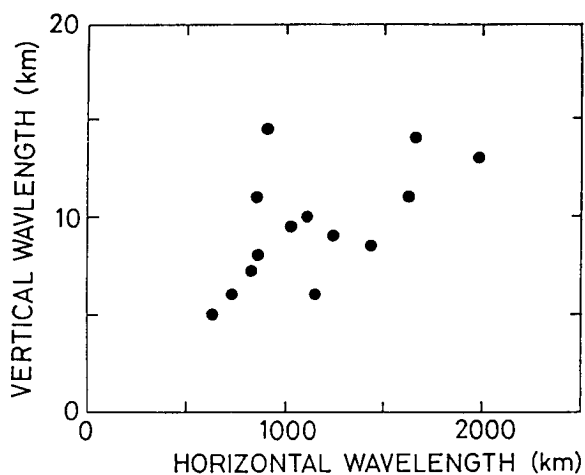


Figure 8. Distribution of the horizontal and vertical wavelength. The mean values were 1100 and 9.5 km.

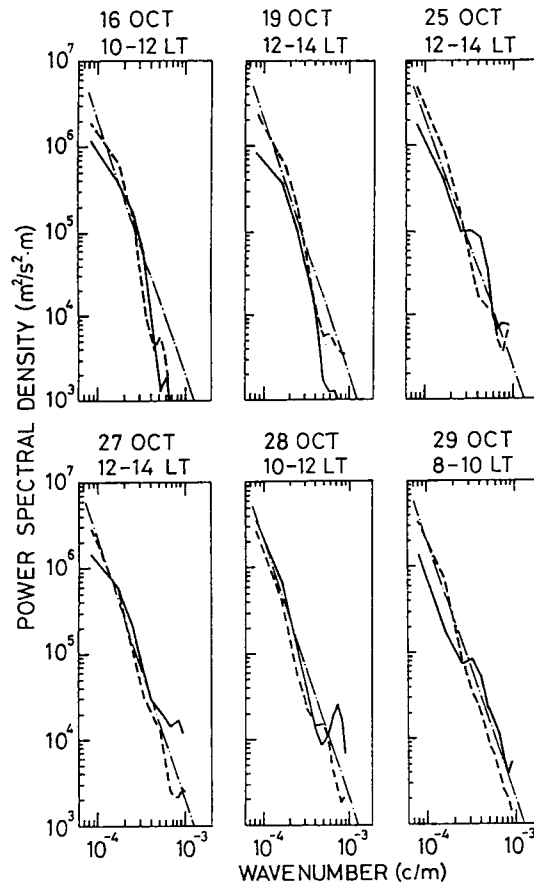


Figure 9. Vertical wave number spectra. The solid and dashed lines show the zonal and meridional components, respectively. The chained line corresponds to the model spectrum predicted by saturated gravity wave theory [Smith et al., 1987].

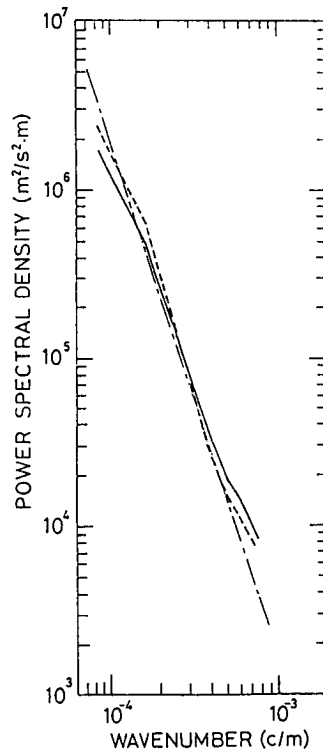


Figure 10. The same as Figure 9 except for a mean spectrum averaged for 13 - 31 October 1986.

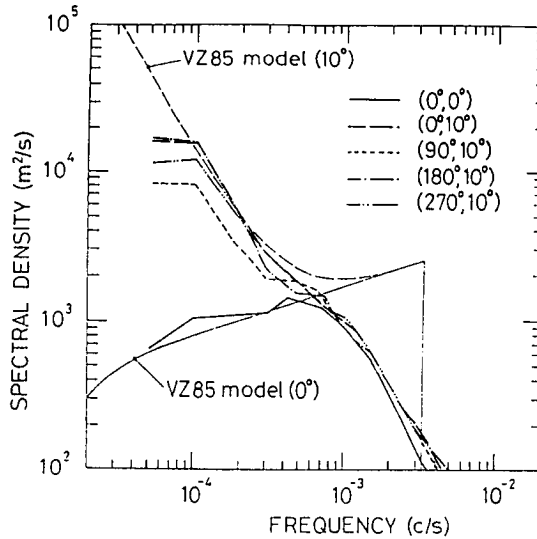


Figure 11. Frequency spectra of vertical and radial (10°) wind velocities observed on 18 - 31 October 1986 compared with a model spectrum proposed by VanZandt [1985] (indicated as VZ85).

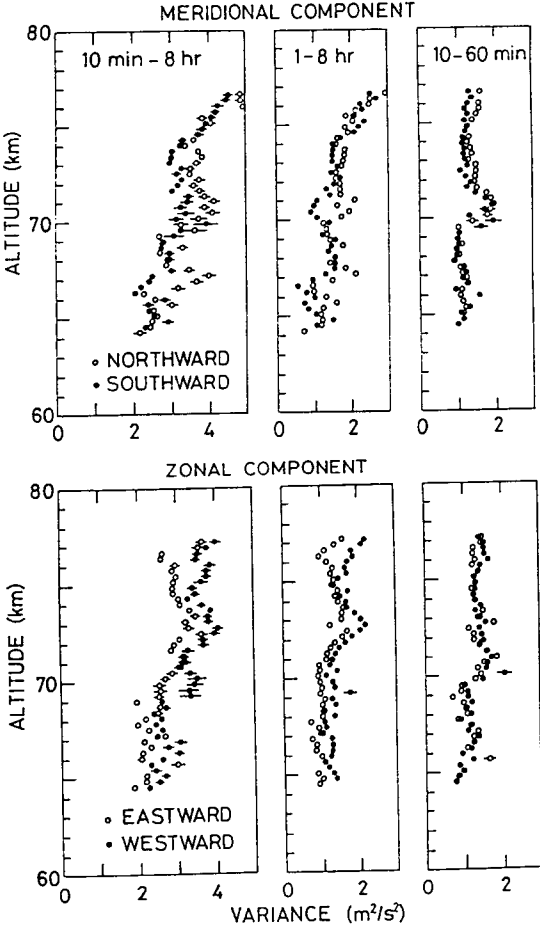


Figure 12. Variance of radial wind velocities for meridional (top) and zonal (bottom) components determined independently at each height. Left, center and right panels correspond to the variance contributed from wave components with periods from 10 min to 8 hours, 1 to 8 hours, and 10 to 60 min, respectively.

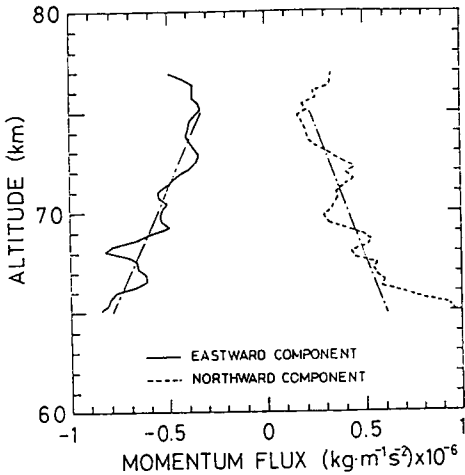


Figure 13. Vertical profiles of the eastward and northward components of momentum flux for wave periods ranging from 10 min to 8 hours. The mean accelerations at 60 - 75 km is 5.1 and 4.0 m/s/day for eastward and northward components, respectively.

P.9 MEASUREMENT OF VERTICAL VELOCITY USING CLEAR-AIR DOPPLER RADARS

T. E. VanZandt, J. L. Green

NOAA/Aeronomy Laboratory, R/E/AL3
325 Broadway, Boulder, CO 80303

G. D. Nastrom

Meteorology Research, Control Data Corporation
Minneapolis, MN 55440

K. S. Gage, W. L. Clark, and J. M. Warnock

NOAA/Aeronomy Laboratory, R/E/AL3
325 Broadway, Boulder, CO 80303

We have constructed a new clear-air Doppler radar, called the Flatland radar, in very flat terrain near Champaign-Urbana, Illinois. The radar wavelength is 6.02 m. The radar has been measuring vertical velocity every 153 s with a range resolution of 750 m almost continuously since March 2, 1987. We find that the variance of vertical velocity at Flatland is usually quite small, comparable to the variance at radars located near rough terrain during periods of small background wind. The absence of orographic effects over very flat terrain suggests that clear-air Doppler radars can be used to study vertical velocities due to other processes, including synoptic scale motions and propagating gravity waves. For example, near rough terrain the shape of frequency spectra changes drastically as the background wind increases. But at Flatland the shape at periods shorter than a few hours changes only slowly, consistent with the changes predicted by Doppler shifting of gravity wave spectra. Thus it appears that the short-period fluctuations of vertical velocity at Flatland are almost entirely due to the propagating gravity waves.

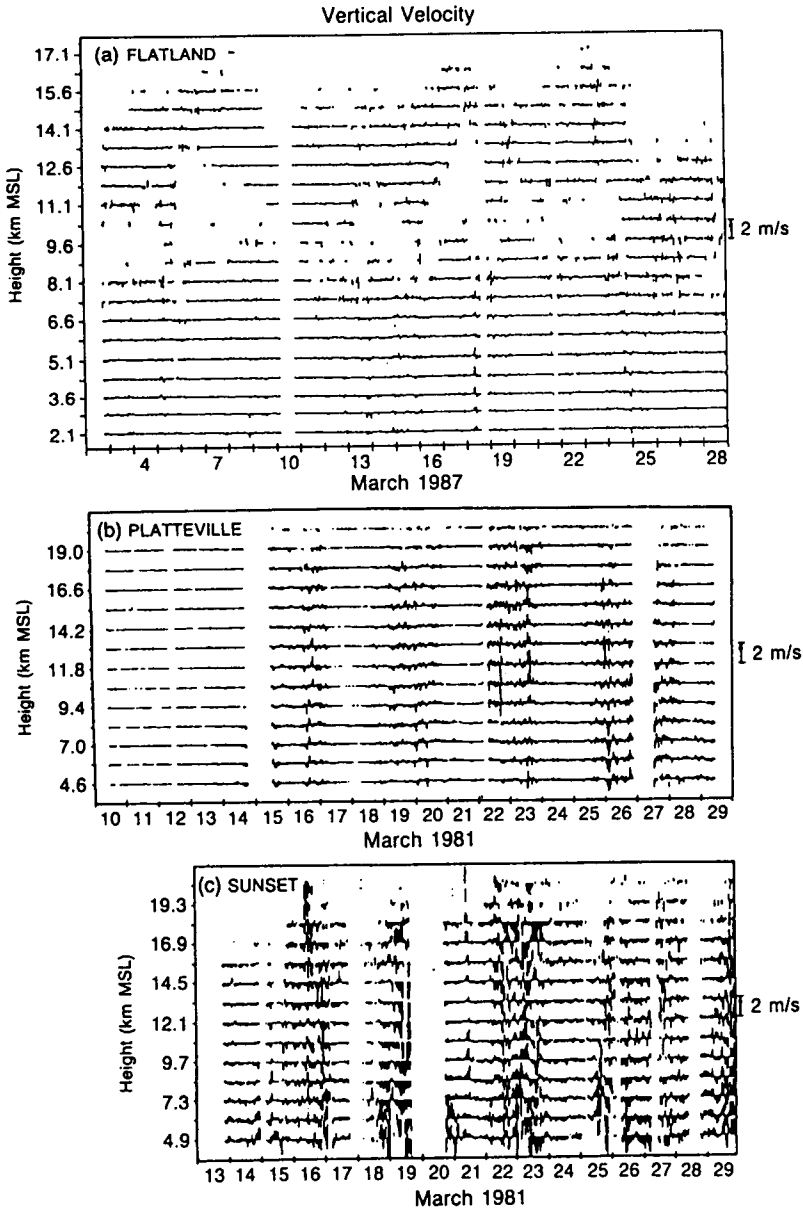


Figure 1. Time series of 15-minute averages of w . Panel (a) is from the Flatland radar, in very flat terrain, panel (b) is from the Platteville radar, in moderately flat terrain but 80 km east of the 4000 m crest of the Front Range of the Rocky Mountains, and panel (c) is from the sunset radar, in rough terrain 16 km east of the crest. It can be seen that the variance of w increases with increasing roughness of the terrain.

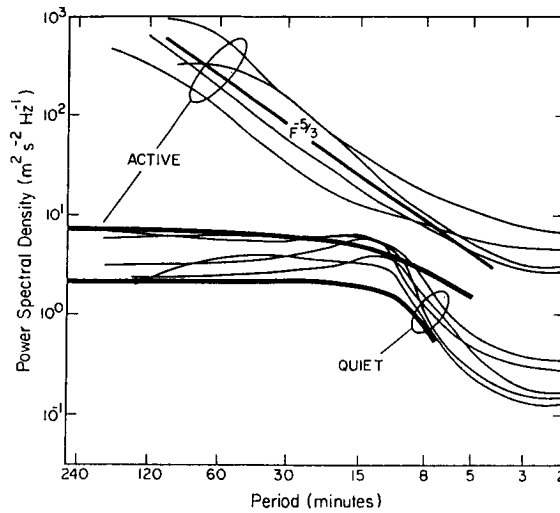


Figure 2. Frequency spectra of w in the troposphere. The lower two thick curves are from the Flatland radar at 5.3 km and the thin curves are from southern France [Ecklund et al., 1985] between 3.85 and 6.10 km. The thick reference line labeled $F^{-5/3}$ has a spectral slope of $5/3$. The spectra labeled QUIET were obtained when the wind was ≤ 5 m/s and those labeled ACTIVE, when the wind was ≥ 20 m/s. At Flatland the ACTIVE spectrum is similar to the QUIET spectrum, but with a slightly flatter shape and greater amplitude. In southern France, the ACTIVE spectra are much steeper than the QUIET spectra with much larger spectral amplitudes. The difference between Flatland and southern France is presumably due to the absence of mountains near Flatland.

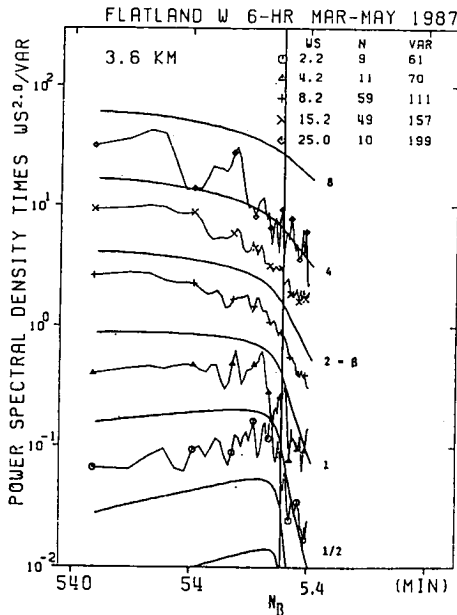


Figure 3. Comparison between observed spectra stratified by wind speed and Doppler-shifted model spectra. The mean Flatland spectra at 3.6 km are stratified into bins according to the mean wind speed WS at the middle of the 6-hour time series. WS, the number of spectra N entering the mean, and the variance VAR for each bin are given in the upper right-hand corner.

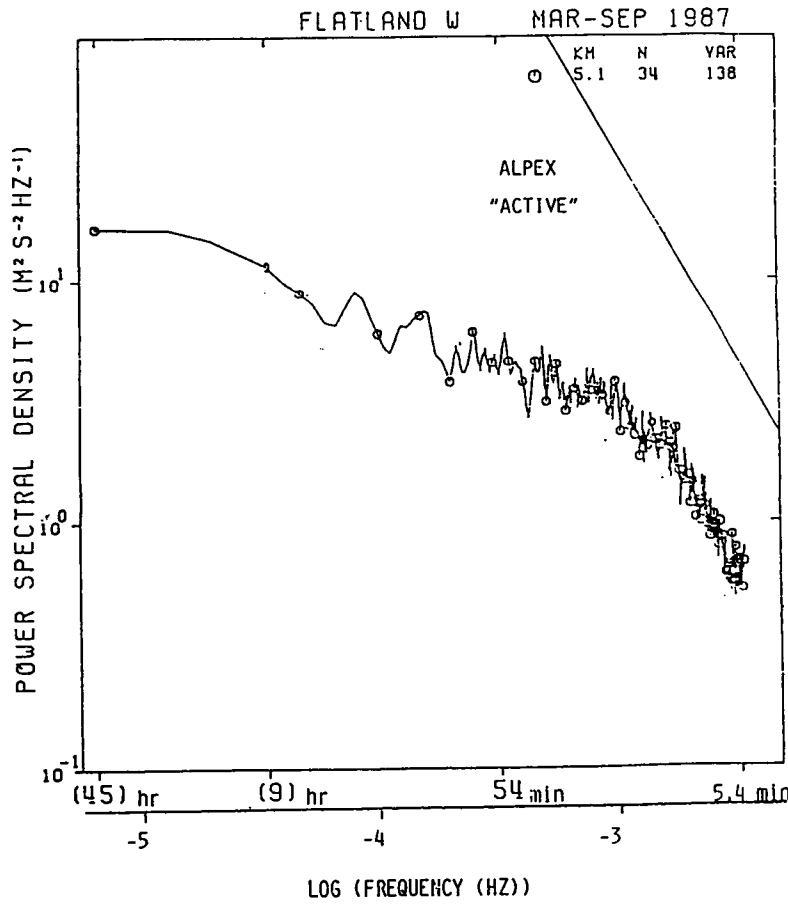


Figure 4. Mean frequency spectrum of w from 45 h time series.

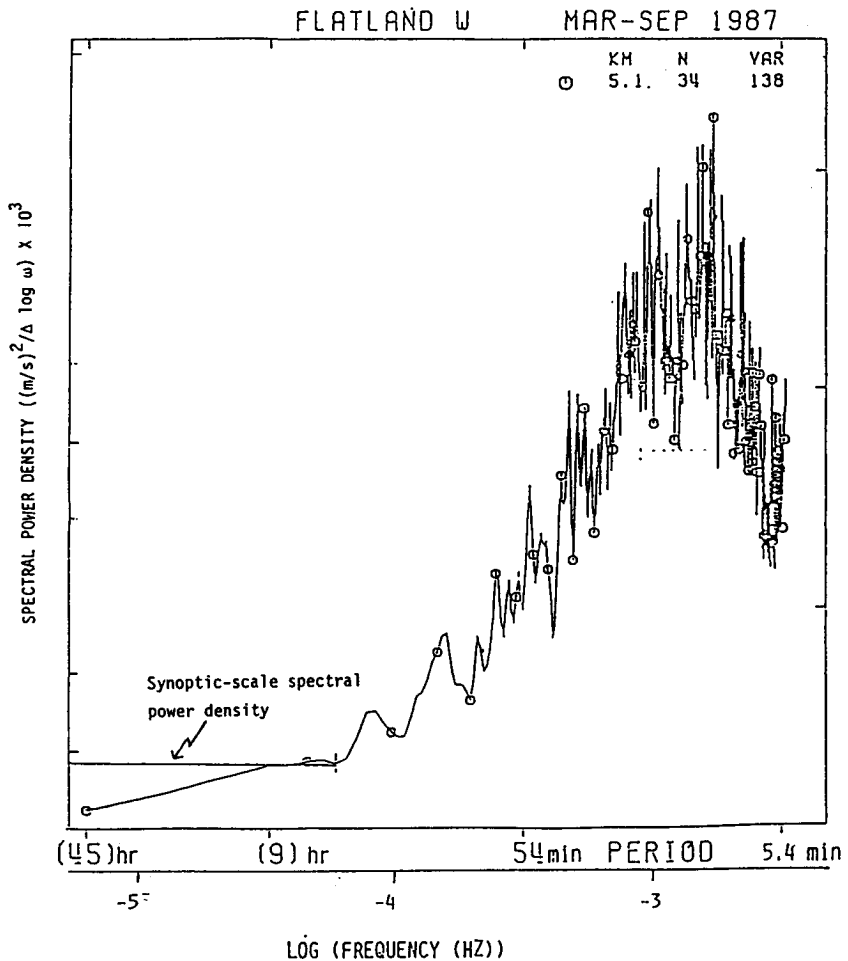


Figure 5. The same spectrum in area-preserving form, so that the contribution to the variance is proportional to the area under the spectrum. The horizontal line in the lower left-hand corner is the estimated spectral density due to synoptic-scale vertical motions, with a variance equal to 12.5 (cm/s)^2 , distributed uniformly from 7 days to 5 hours. The fact that the observed spectral density is \approx this level suggests that synoptic-scale vertical velocities can be measured by clear-air Doppler radars located in very flat terrain.

CONCLUSIONS

The conclusions of this study are:

1. The fluctuations of vertical velocity with periods $\leq 6 \text{ h}$ are dominated by gravity waves.
2. The observed variance with periods $\geq 6 \text{ h}$ is comparable with the estimated variance of vertical velocity due to synoptic-scale motions.
3. These results suggest that clear-air Doppler radars located in very flat terrain can be used to study vertical velocity due to gravity waves and synoptic-scale motions.

P.10 PICTURE OF THE GLOBAL FIELD OF "QUASI-MONOCHROMATIC" GRAVITY WAVES OBSERVED BY STRATOSPHERIC BALLOONS AND MST RADARS

M. D. Yamanaka

Institute of Earth Science, Yamaguchi University
1677-1 Yoshida, Yamaguchi-shi, Yamaguchi 753, Japan

In MAP observations we have found that (i) gravity waves in selected or filtered portions of data are fit for monochromatic structures, whereas (ii) those in fully continuous and resolved observations take "universal" continuous spectra. It is possible to explain (ii) by dispersion of "quasi-monochromatic" (or slowly varying) wave packets observed locally as (i), since the medium atmosphere is unsteady and nonuniform. Complete verification of the wave-mean flow interactions by tracking individual wave packets seems hopeless, because we cannot distinguish the wave-induced flow from the basic flow independent of the waves. Instead, we go back to the primitive picture before MAP, that is, the atmosphere is just like an entertainment stage illuminated by cocktail lights of quasi-monochromatic gravity waves. The wave parameters are regarded as functions of time and spatial coordinates. The observational evidences (i) and (ii) suggest that the wave parameter field is rather homogeneous, which can be explained by interference of quasi-monochromatic wave packets.

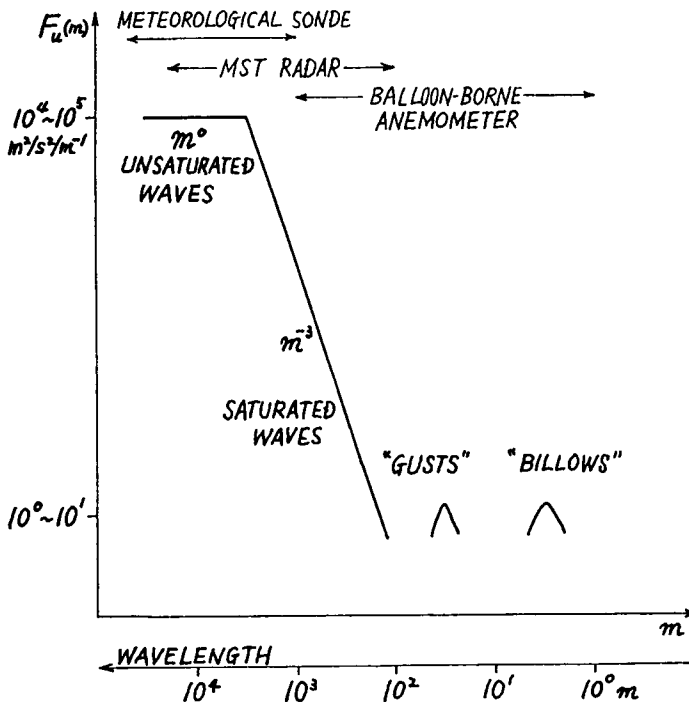


Figure 1. A model of vertical wave number (m) spectrum for stratospheric internal gravity waves and turbulence observed mainly during MAP.

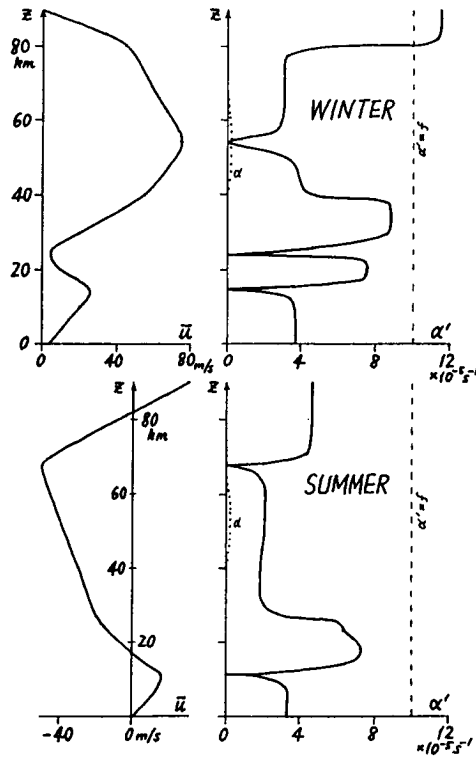


Figure 2. Rayleigh-type damping coefficient α' calculated for typical values of parameters in the midlatitude stratosphere ($f = 10^{-4} \text{ s}^{-1}$, $N = 2 \times 10^{-2} \text{ s}^{-1}$; $|\partial \bar{u} / \partial z|$ is obtained from a model profile shown in the left-hand side). Dashed line shows $\alpha' = f$. Dotted curve shows the Newtonian cooling coefficient.

P.11 HIGHER ORDER DISPERSION IN THE PROPAGATION OF A GRAVITY WAVE PACKET

K. C. Yeh and B. Dong

Department of Electrical and Computer Engineering
University of Illinois, 1046 W. Green, Urbana, IL 61801

To the first order of approximation, the complex amplitude of a wave packet in an anisotropic and dispersive medium is convected with the group of velocity. However, a gravity wave is a vector wave. Its wave packet must be formed by superposition of various wave numbers with corresponding frequencies, as is the case for scalar waves, and additionally by superposing many eigenmodes which also depend on the wave number. To represent the vector wave packet self-consistently, it is found that a gradient term must be included in the expansion. For a Gaussian wave packet, this gradient term is shown to have important implications on the velocity vector as represented by its hodograph. Numerical results show that the hodograph is influenced by the location of the relative position of interest from the center of a Gaussian pulse. Higher order expansion shows that an initial Gaussian wave packet will retain its Gaussian shape as it propagates, but the pulse will spread in all directions with its major axis undergoing a rotation. Numerical results indicate that these higher order dispersive effects may be marginally observable in the atmosphere.

1. Introduction

Of all experiments on atmospheric gravity waves, the wave trains are observed to be, sometimes, quasi-sinusoidal but always to have finite extent in time and in space. To predict the outcome of such waves in the atmosphere requires the study of propagation of a wave packet. By nature, the propagation of such atmospheric waves is both dispersive and anisotropic. Even though the dispersive effects have been studied for some time for both one-dimensional and higher dimensional waves, the additional anisotropic effects do not seem to have received much attention. In this paper both dispersion and anisotropy will be taken into account. It will be shown that when the Earth's rotation is considered, the otherwise closed hodograph may become open for a wave packet. Due to the action of a Coriolis force, a monochromatic wave is accompanied by a hodograph rotating in the clockwise sense in the Northern Hemisphere and counter-clockwise in the Southern Hemisphere. However, the polychromatic nature of a wave packet may change both the ellipse ratio and the sense of rotation. The combined dispersive and anisotropic effects on the propagation of a Gaussian wave packet is investigated in this paper.

2. Mathematical Formulation

For simplicity the atmosphere will be assumed to be inviscid and isothermal. Let the first order perturbations in the atmosphere associated with the propagation of gravity waves be described by a five-dimensional vector \mathbf{F} where the first component is proportional to the entropy perturbation per unit mass, the second component is proportional to the pressure perturbation and the third through fifth components are proportional to the perturbed velocity. The last three components of \mathbf{F} thus determine the nature of a hodograph.

The linearized hydrodynamic equations can be cast into an equation with a dyadic operator operating on \mathbf{F} . By a judicious choice of \mathbf{F} , this operator consists of both time and spatial differentiation but is of constant coefficients. Thus Fourier transform in time and space is permitted and the analysis of the resulting equations produces eigenmodes, $\tilde{\mathbf{u}}(\mathbf{k})$. For a wave packet, the eigenmodes are assumed to have a narrow spectrum. By expanding to the second order, the state vector \mathbf{F} can be related to the eigenmodes $\tilde{\mathbf{u}}(\mathbf{k}_0)$ at the carrier wave number \mathbf{k}_0 through the following equation

$$F(\vec{r}, t) = [A(\vec{r}, t) \tilde{u}(\vec{k}_0) + j \nabla A \cdot \nabla_{\vec{k}_0} \tilde{u}] \exp j[\omega(\vec{k}_0)t - \vec{k}_0 \cdot \vec{r}] \quad (1)$$

where A is the complex envelope function. Readers interested in the detailed proof should consult Dong and Yeh [1989].

To the first order, the complex envelope function is found to have the form

$$A(\vec{r}, t) = A(\vec{R}) \quad (2)$$

where $\vec{R} = \vec{r} - \vec{\nabla}_g t$. In this case, the envelope is thus convected with a group velocity $\vec{\nabla}_g$ undistorted. Even in this order, the state vector F given by (1) in general may have a non-negligible gradient term. When this happens, F is not a simple convection alone; it undergoes a time-dependent change while being convected. This is most easily demonstrated from numerical calculations of a Gaussian pulse. The results are shown in Figure 1 where the hodograph at three fixed positions are plotted as a function of time starting at its peak. In order to illustrate the three-dimensional nature of the velocity orbits, four different projections have been used. They show that even at a point where the Gaussian peak would pass through (i.e., at the origin in Figure 1), the hodograph is still clockwise but open. For a point away from the Gaussian peak, the ellipse ratio or the sense of rotation or both may change as demonstrated by plots of Figure 1 at plus or minus five wavelengths away from the Gaussian peak.

When expanding to the second order, the complex envelope function A itself is found to distort with time as it propagates with the group velocity, since now, instead of (2) it becomes

$$A(\vec{r}, t) = A(\vec{R}, t) \quad (3)$$

One way to describe the variation of A as it propagates is to define a surface S on which the magnitude is $\exp(-1/2)$ of its value at the Gaussian peak, i.e.,

$$|A(\vec{R}, t)| = |A(\vec{0}, t)| \exp(-1/2) \quad (4)$$

It has been found that the surface S is a surface of spheroid, the three axes of which L_1 , L_2 and L_3 , will change with time. The peak of the Gaussian wave packet $|A(\vec{0}, t)|$ normalized by its initial value $A(\vec{0}, 0) = A_0$ as given by the ratio A/A_0 in Figure 2 decreases with time. This is caused entirely by dispersion. Furthermore, this ellipsoid undergoes a rotation as indicated by the angle α . Both the pulse dispersion and the rotation of the ellipsoid are clearly depicted in Figure 3 which plots the projection of the S surface on the xz -plane at successive instants. Successively, the initially sharply peaked Gaussian pulse becomes reduced at its peak value, coupled simultaneously with a more dispersed pulse in the spatial domain and a rotation of its major axis.

3. Conclusion

A theory describing the propagation of a wave packet in a dispersive and anisotropic medium has been developed. This theory is applied to gravity waves. It is found that important new features are manifested. The calculations that have been carried out assume a Gaussian pulse with half-width equal to five wavelengths. As many observations, even in the best of times, only show a few oscillations, there is need to extend the study to narrower Gaussian pulses for which the dispersive effects are expected to be even more important. In preparation for such investigations, the theory must be extended to a higher order than that given by (1), which is now in progress.

Acknowledgment: This research was supported by the National Science Foundation under grant ATM 87-04947.

Reference

Dong, B., and K. C. Yeh, Polarization and dispersion of a Gaussian gravity-wave packet, *Ann. Geophysicae*, to appear in January 1989 issue.

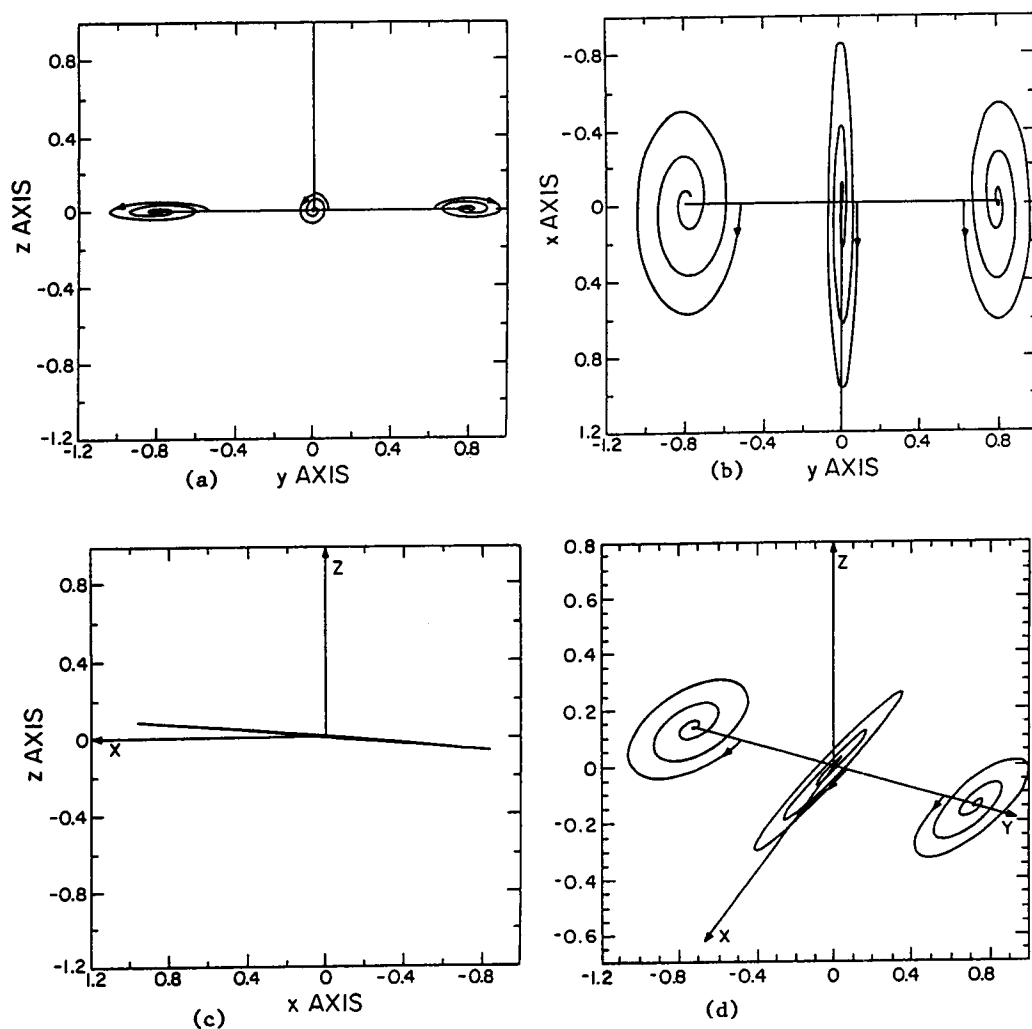


Figure 1. Projection of 3-D hodographs of the velocities of a Gaussian gravity wave packet having a period 55.6 min and a propagation vector 5° away from downward direction. (a) front view (from x-axis), (b) top view (from z-axis), (c) side view (from y-axis), and (d) view from a point at $\theta = 25^\circ$ and $\phi = 65^\circ$.

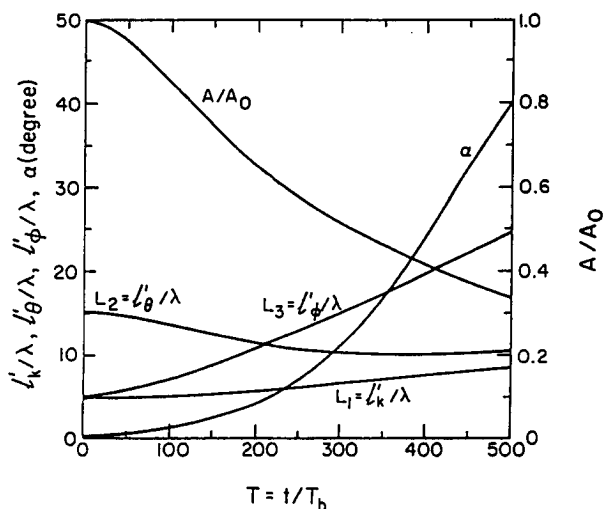


Figure 2. The propagation of a Gaussian packet can be described by the motion of a spheroid. The three axes of the ellipsoid L_1, L_2, L_3 normalized by the wavelength λ vary with time as shown. The temporal variation of the magnitude at the center of the Gaussian packet normalized by its initial value at $t = 0$ is shown as the curve A/A_0 using the right scale. The rotating angle α uses the left scale. The initial parameters of the wave packet are: $l_k = 5\lambda$, $l_\theta = 15\lambda$, $l_\phi = 5\lambda$, $\theta_0 = 175^\circ$, $\phi_0 = 0^\circ$.

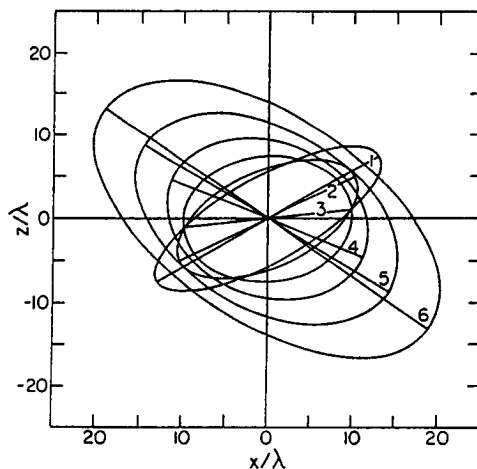


Figure 3. The projection of the ellipsoidal surface S at successive times on the plane xoz . The time increment used is $200 T_b$. As time increases, the spreading and rotation of the Gaussian packet can be visualized. The angle α determines the orientation of the major axis of the ellipse and is measured from the axis at $t = 0$ marked by 1. The initial parameters of the wave packet are identical to those used in Figure 3.

P.12 GRAVITY WAVE CLIMATOLOGY AT MIDLATITUDE FROM RAYLEIGH LIDAR DATA

R. Wilson, M. L. Chanin, and A. Hauchecorne

Service d'Aeronomie du CNRS
BP 3, 91371 Verrieres-le-Buisson Cedex, France

Atmospheric sounding of the middle atmosphere by Rayleigh scattering has been performed in France for several years, from two stations with different orographic situations: one in the Alps, the Observatoire de Haute Provence (44°N, 6°E), one on the Atlantic coast at Biscarosse (44°N, 1°W). The vertical profiles of density and temperature are obtained with a temporal and spatial resolution of, respectively, 15 mn and 300 m between 30 and 80 km. A statistical study of the atmospheric fluctuations due to gravity waves has been performed and the main results of this study will be presented: climatology of the gravity wave activity, distribution of energy versus vertical wave number and altitude, comparison of the observations at the two sites. Conclusions will be presented on the saturation of the wave field, the filtering by the mean wind, the transfer of energy and momentum into the atmosphere.

Climatology

Data base

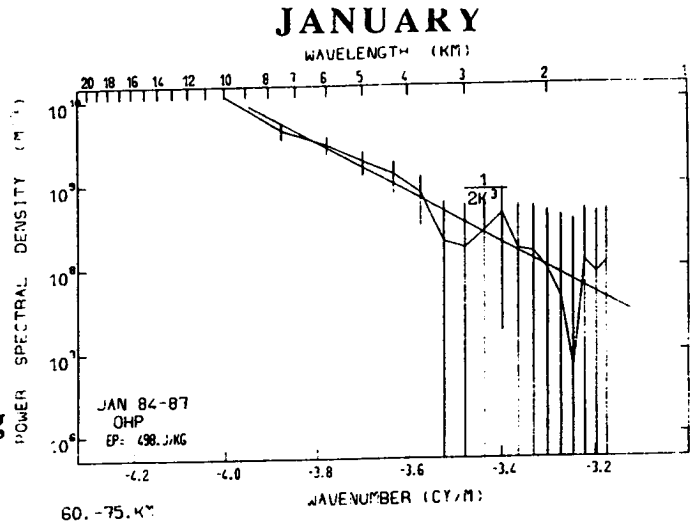
This study is based upon the monthly means of either the power spectral density (Figures 1, 2, 3) and of the variance obtained by demodulation (Figures 4, 5). The data based extended over 4 years at O.H.P. and 2 years at Biscarosse. The fluctuations of temperature are associated with vertical displacement of air, then are related to the potential energy of the wave field which is used here to define the "activity".

Main results

- The amplitude of the temperature fluctuations are far from the (convective) saturation value in the stratosphere, in all seasons and for wavelength greater than 1 km. In the lower mesosphere (45-60 km), the saturation value is reached for waves smaller than 2-3 km wavelength. In the upper mesosphere (60-75 km) the wave field is completely saturated in a statistical sense for wavelengths up to 8 km, especially in winter.
- The climatology exhibits essentially the same features at the two stations (Figures 4,5). Nevertheless the activity is weaker at Biscarosse in winter, and identical during summer and equinoxes after the reversal of the zonal wind (Figures 6,7).
- In the stratosphere the activity presents a clear annual variation with a maximum in winter, a minimum in summer, with a seasonal ratio of 3.
- In the mesosphere an annual variability is also observed but less pronounced. The seasonal ratio is 1.5. A weak semiannual component is also present with a minimum of activity during the equinoxes.

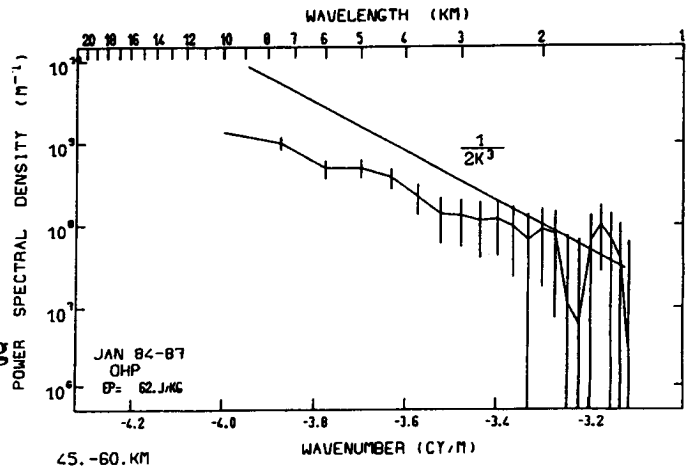
60-75 Km

$E_p = 498 \text{ J/Kg}$



45-60 Km

$E_p = 62 \text{ J/Kg}$



30-45 Km

$E_p = 27 \text{ J/Kg}$

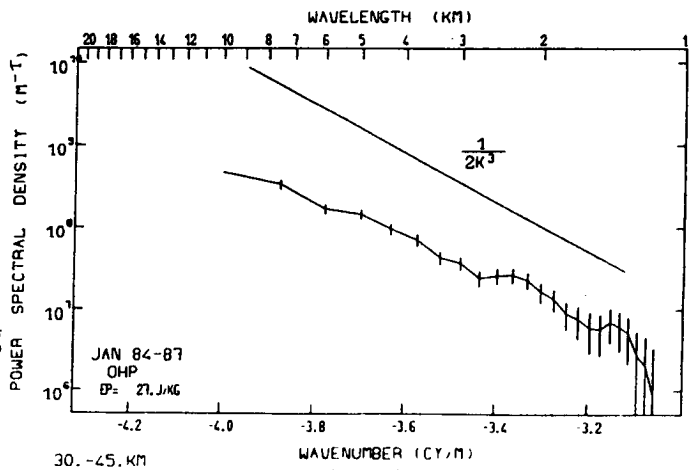
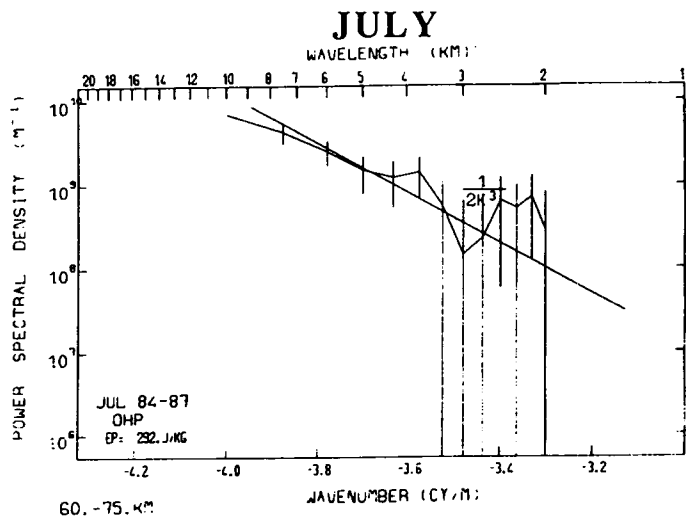
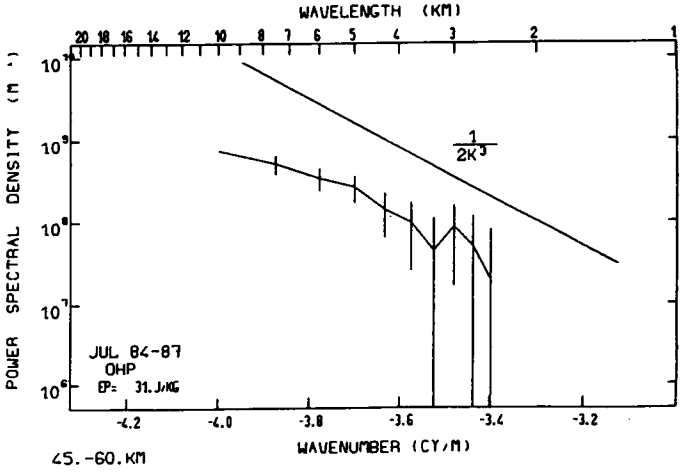


Figure 1.

60-75 Km
Ep=292J/Kg



45-60 Km
Ep=31 J/Kg



30-45 Km
Ep= 8 J/Kg

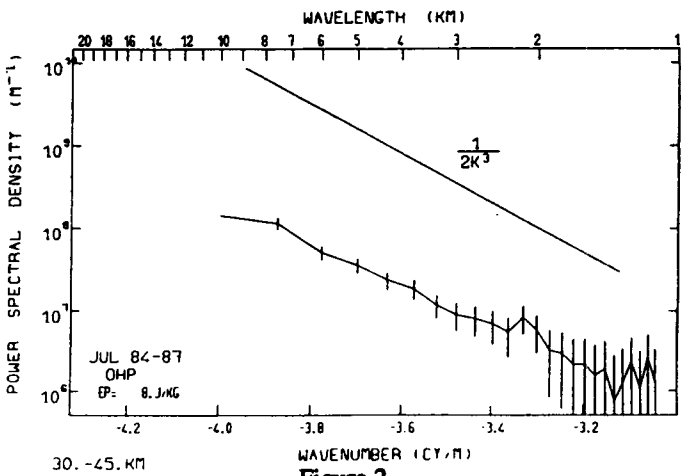
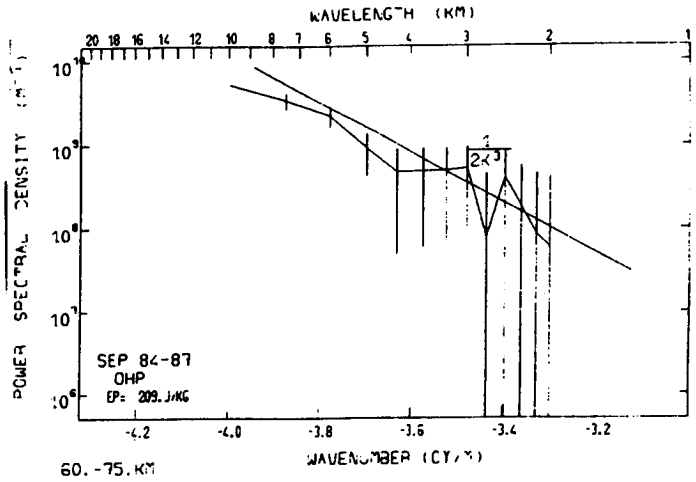


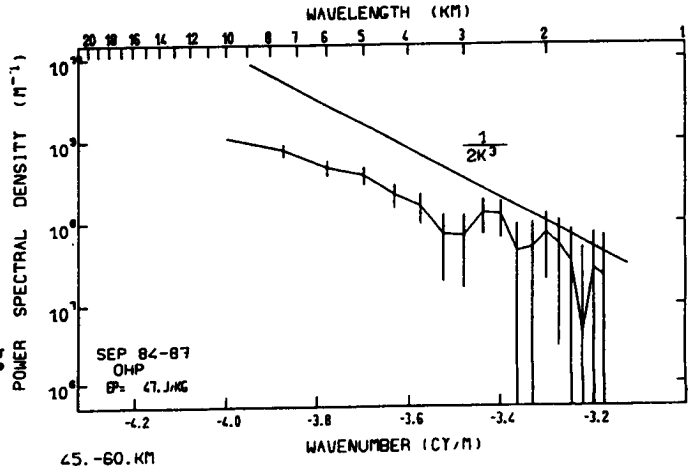
Figure 2.

SEPTEMBER

60-75 Km
 $E_p=209 \text{ J/Kg}$



45-60 Km
 $E_p=47 \text{ J/Kg}$



30-45 Km
 $E_p=8 \text{ J/Kg}$

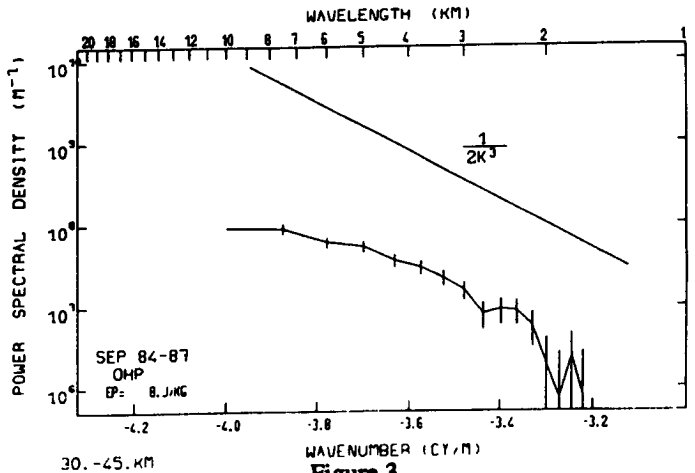


Figure 3.

Seasonal variation of the variance at O.H.P. for $\lambda = 8$ km

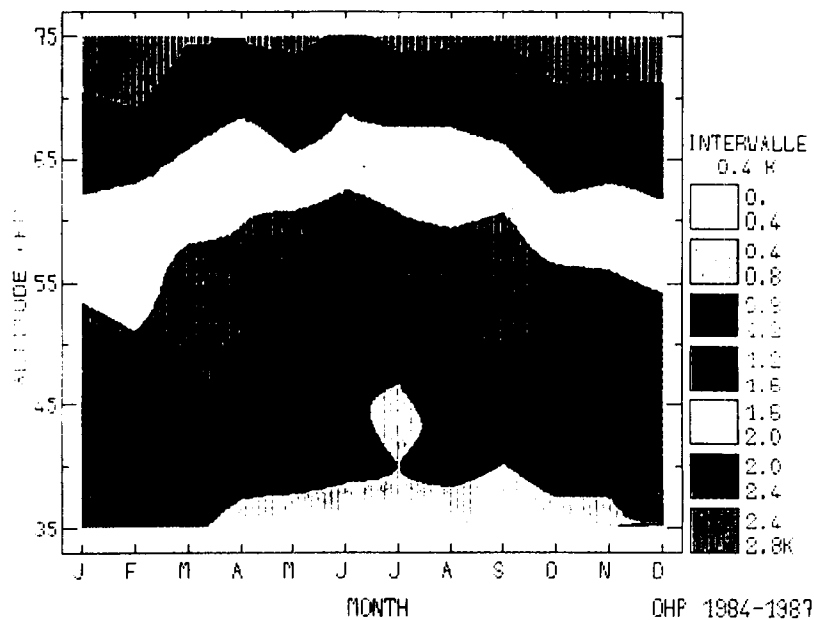


Figure 4.

Seasonal variation of the variance at Biscarosse for $\lambda = 8$ km

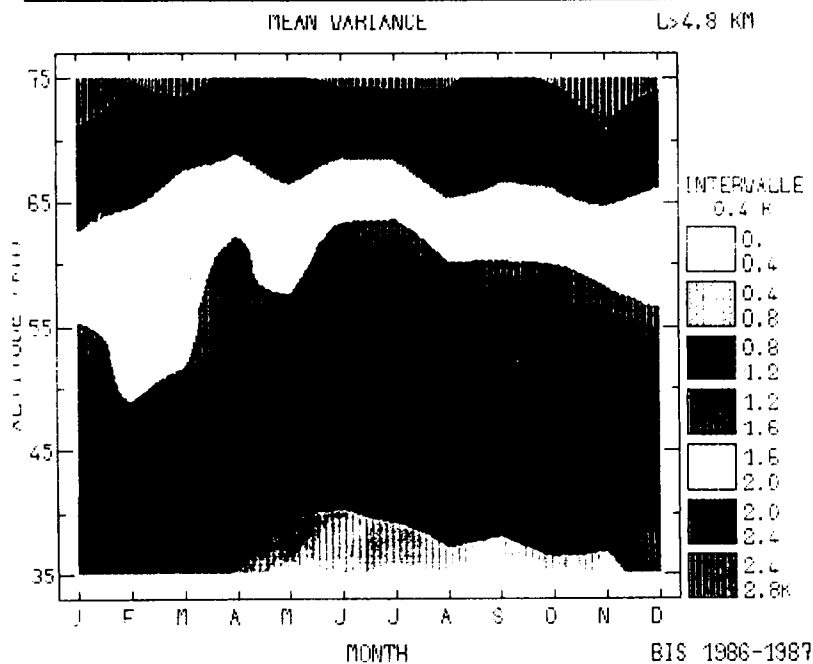


Figure 5.

Comparison of power spectral density for July at the two stations.

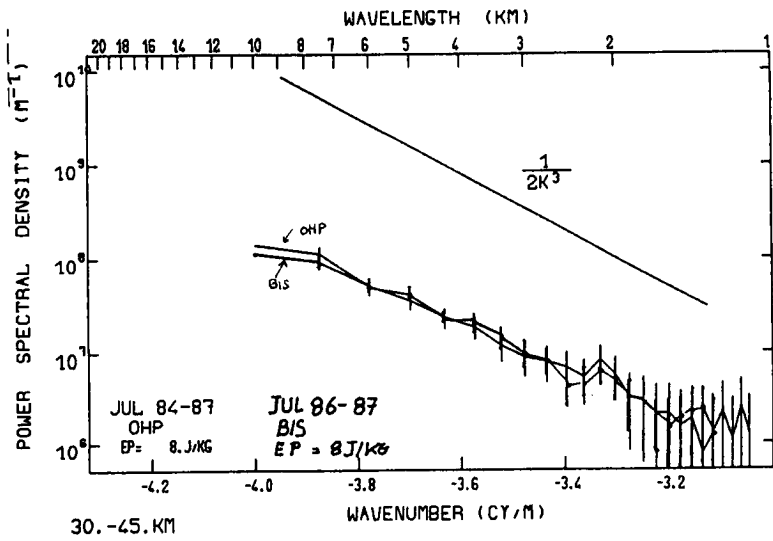


Figure 6.

Comparison of power spectral density for January at the two stations.

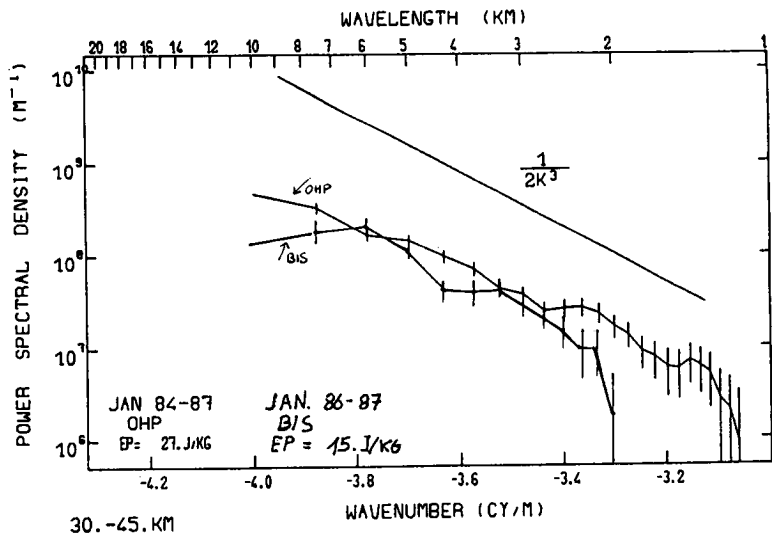
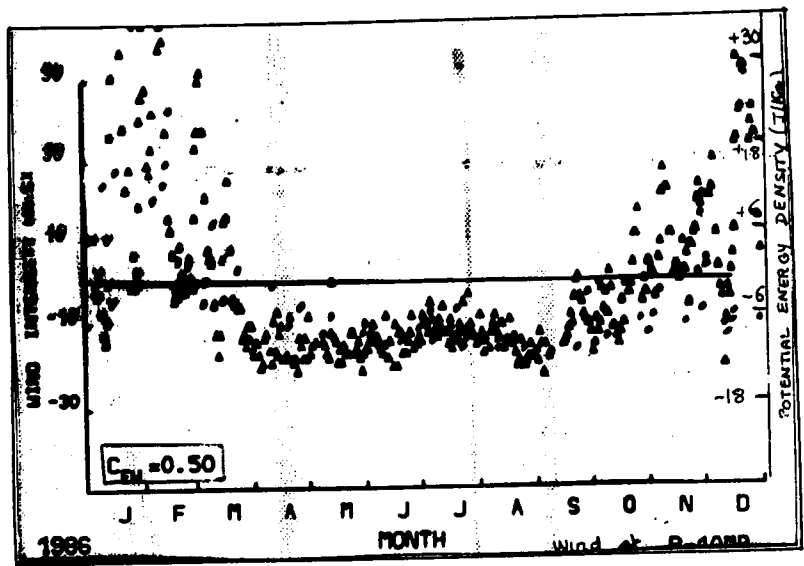


Figure 7.

Seasonal variation of potential energy density and zonal mean wind at 10 mb (from N.M.C.)



The correlation coefficient is 0.5

Figure 8.

ranges compared with a spectral model

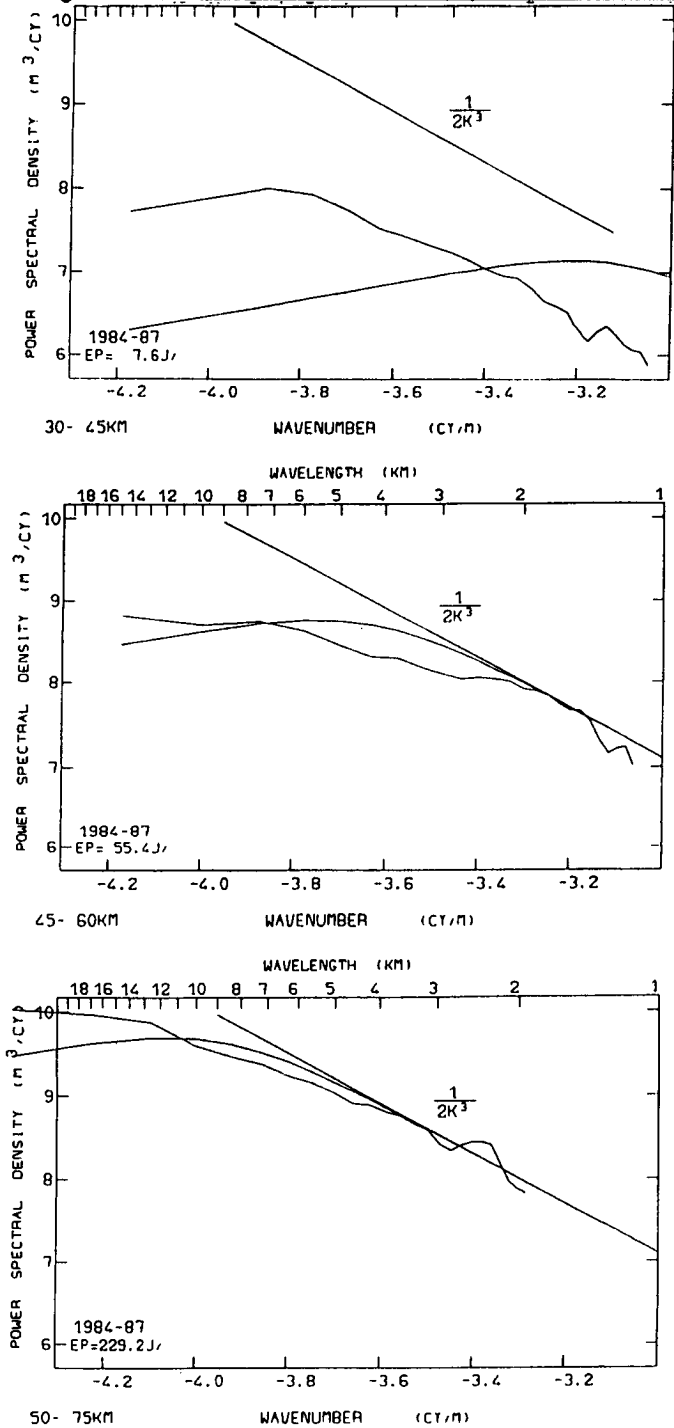


Figure 9.

Variance of temperature fluctuations as a function of altitude
($\lambda = 8 \text{ km}$)

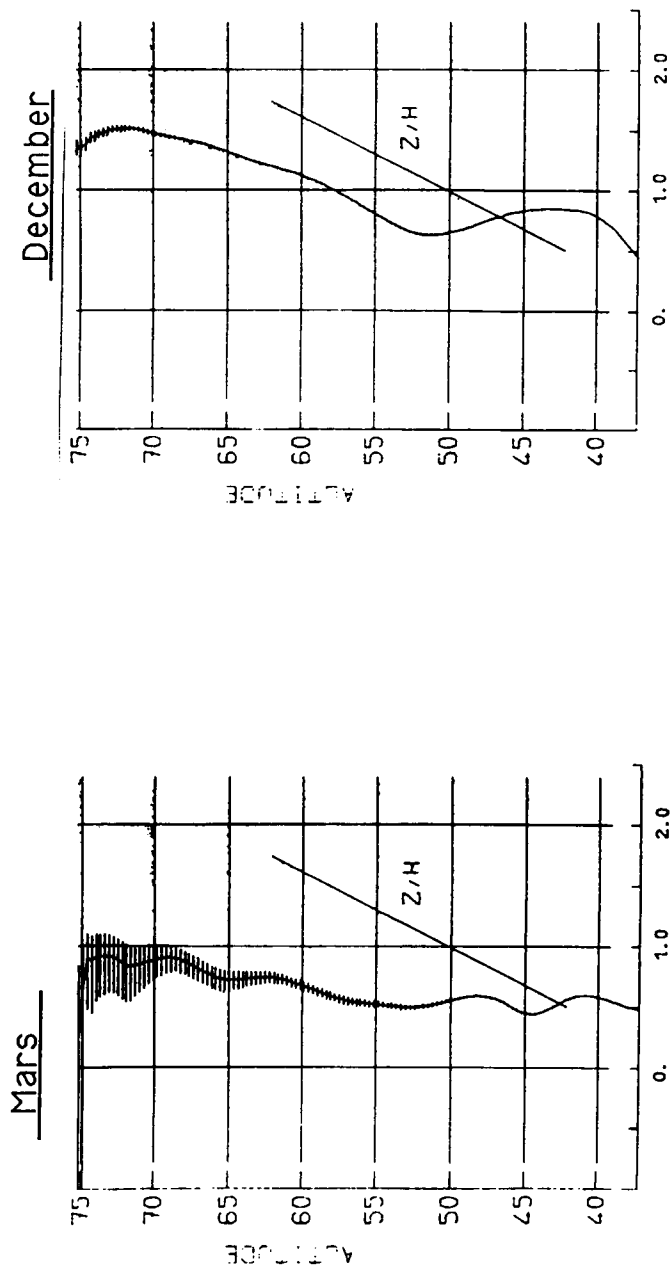


Figure 10.

Interpretation

The variability of the gravity wave activity is induced first by the sources, second by the transmission of the wave field through the atmosphere.

- Due to the different locations of the two stations, the orographic source should be more important at OHP. The activity is observed to be higher in winter. However it is not the case during weak wind conditions, or wind reversal periods, when stationary waves (orographics) cannot propagate (because they reach critical levels).

- The growth of the variance of temperature fluctuations for wavelength of 8 and 5 km (which are generally associated with low frequency modes) is much weaker in March than in September, especially in the mesosphere. This indicates that the wave energy propagation is much easier in strong wind conditions. This is confirmed by the observed minimum of activity in the mesosphere during equinoxes. It should be noticed that for all seasons the growth of amplitude is very weak in the upper stratosphere, even if the waves are not convectively saturated.

- The positive correlation between mean wind intensity above the OHP (from N.M.C. data) and wave activity (daily mean of the potential energy) emphasizes again the importance of wind conditions on wave activity. Even at the lower level a strong gravity wave activity is associated with strong wind intensity.

- The wave field is far from saturation in the stratosphere and lower mesosphere for wavelengths greater than 2-3 km. The power spectral indices is close to minus 2. In the mesosphere the waves are saturated (in winter) and the spectral index is minus 3.

DRAFT MINUTES
MAP STEERING COMMITTEE MEETING
July 18, 1988, Espoo, Finland

1. Welcome and Introductory Remarks

The Chairman welcomed everyone. He mentioned that MAC is winding down and that this may be the next to last Steering Committee Meeting.

2. Approval of Agenda

With one addition to "Other Business", the Symposium in Czechoslovakia, the Agenda was approved.

3. Minutes of 1987 Meeting, Vancouver

The minutes of the Vancouver Meeting were approved.

4. Committee Reports

Data Management - I. Hirota gave the report and urged adherents to cooperate in supplying information for the MAP Data Catalogue (Appendix 1).

Publications - B. Edwards reported (Appendix 2). In addition to the future volumes listed in the report, other volumes may include the GLOBMET meeting in USSR; Middle Atmosphere Reference Models of Minor Species for COSPAR International Reference Atmosphere, the MAC-Epsilon/MAC-SINE Workshop in October 1988, papers from the International School on Atmospheric Radar, and papers from the IAGA Symposium "Solar Activity Forcing of the Middle Atmosphere".

R. A. Vincent discussed the current status of the MAP Summary Document. There was one additional contributor, Dr. Brasseur, on Neutral Atmospheric Chemistry. S. A. Bowhill suggested that when the Document is ready, it should be sent to the Steering Committee members for a fast review before final publication.

5. MSG Reports

There were no Study Group Reports.

6. Project Reports

AMA: M. Yamamoto reported that most of the observations have been completed. Only the polar circumvent balloon test flight experiment was not completed due to sensor failure, but will continue during the STEP period, with approximately 100 kg payload.

ATMAP - A. H. Manson reported.

DYNAMICS - Labitzke reported (Appendix 3).

GLOBMET - Vincent mentioned a resolution from the Second GLOBMET Symposium and Roper provided the report (Appendix 4)

GRATMAP - D. C. Fritts reported.

MAC-Epsilon - MAC/SINE - E. Thrane reported (Appendix 5).

MAE - R. A. Goldberg reported (Appendix 6).

MASH - A. O'Neill reported (Appendix 7).

NIEO - S. Kato reported (Appendix 8).

SSIM - P. C. Simon reported.

SUPERCAMP - E. Kopp reported (Appendix 9).

GLOBUS NO_x - J. P. Pommereau provided the report (Appendix 10).

WINE - U. von Zahn reported (Appendix 11).

Bowhill proposed MAC/REP (Relativistic Electron Precipitation) as a MAC project, subject to international participation.

PRECEDING PAGE BLANK NOT FILMED

7. Workshops/Symposia

Add to the list: MASH Workshop in April 1989

MAC-Epsilon- MAC-SINE Workshop April 1989

IAGA Symposium on "Solar Activity Forcing of the Middle Atmosphere", April 1989, Czechoslovakia

IAMAP-IAGA MAP Symposium 21-28 July; 2 - 7 August IAMAP

IGBP Symposium 29-30 July

8. Coordination with STEP

Bowhill reported the discussions during the STEP Steering Committee meeting and the preliminary plan of STEP is to set up Working Groups. He noted that MAP activities will have a home in STEP. A. D. Danilov expressed concern that in many countries MAP has been established successfully as a major atmospheric research field. When STEP begins in 1990, the national MAP organization would be replaced by STEP organizations and funding situations for MAP activities might suffer. Bowhill mentioned that he understood the problem. However, each country has its own organizational procedures, the Steering Committee would not be able to influence them.

The Steering Committee endorsed the preliminary plans for the STEP organization.

9. Regional Consultative Group Report

None

10. Reports from Representatives of the Countries

Kato mentioned the International School on Atmospheric Radar (ISAR) to be held November 24-28, 1988, in Kyoto, just prior to the MST Radar Workshop.

E. S. Kazimirovsky reported for USSR (Appendix 12).

G. Witt reported for Sweden.

S.-Y. Su reported for Taiwan.

von Zahn reported for FRG (Appendix 13).

B. R. Clemesha furnished the report for Brazil (Appendix 14).

J. Lastovicka furnished the report for Czechoslovakia (Appendix 15).

L. Thomas furnished the report for the UK (Appendix 16).

P. Bencze furnished the report for Hungary (Appendix 17).

11. Other Business

A letter from Dr. Lastovicka concerning sponsorship of the IAGA Symposium "Solar Activity Forcing of the Middle Atmosphere" was discussed. It was decided that MAC would be a co-sponsor of the Symposium.

The list of attendees is given in Appendix 18 and the Agenda for the meeting in Appendix 19.

12. Next Meeting

The next meeting of the Bureau will be during the IAGA meeting at Exeter, UK, July 1989.

Appendix 1

MAP DATA MANAGEMENT REPORT: STATUS OF MAP DATA CATALOGUE

I. Hirota and G. Hartmann
(Co-chairmen of MAP-DM)

During the MAPSC meeting in Vancouver in August 1987, we decided to compile a MAP Data Catalogue, as a volume of MAP Handbook, following the format of the Japanese MAP Data Catalogue published in January 1987. In October 1987, Prof. Liu, Secretary of SCOSTEP, sent a letter to the national MAP representatives to ask to collect a one-page data catalogue for each type of experiment conducted in each country during the period of MAP/MAC. The deadline for submission to the MAP-DM chairman (I. Hirota) was 1 June 1988. However, only a small number of countries have sent their catalogues by the deadline, in response to our request. They are:

Czechoslovakia (1), Finland (2), France (4), Japan (34) and USSR (23).

(): number of subjects

We will send a letter again to the national MAP representatives who have not made the report yet, to urge them to collect the data catalogue of their countries, by setting the deadline for submission as 1 December 1988.

We should like to emphasize the importance of the exchange of information in the MAP/MAC community and the need for international cooperation.

Appendix 2

PUBLICATIONS REPORT

B. Edwards

Volume 26 of the HANDBOOK FOR MAP consists of the Minutes and attachments of the MAPSC Vancouver Meeting plus a writeup and short abstracts of the papers presented at the Noctiluent Cloud Workshop in Boulder earlier this year. The manuscript is prepared and will be shipped to NASA for printing and distribution shortly.

Possible future volumes include:

MAP Data Catalog
MAP Summary Document
Extended abstracts from the MAP Symposium
Extended abstracts from the MST Workshop to be held in Kyoto
Minutes and related material generated at this meeting

C-7

Appendix 3

THE STRATOSPHERIC WINTER 1987/88: An Unusually Early Major Midwinter Warming

B. Naujokat, K. Labitzke, R. Lenschow, K. Petzoldt and R. -C. Wohlfart

Abstract

The main features of the stratospheric-mesospheric circulation during the winter of 1987/88 are described. The winter had three distinct periods: a very early major warming in December which started at the end of November, a very cold midwinter with a stable vortex in January and February and a major final warming in March which started at the end of February and led to an early transition to the summer circulation around mid-April. The ECMWF-prognoses for the 30-hPa heights are compared with the Berlin analyses. Finally, it is briefly referred to the connection of total ozone amount with low-stratospheric temperatures over northern Europe during the last three winters.

1. Introduction

As in the years before, the main features of the stratospheric circulation during the winter are described. We have combined data from various sources in order to give as complete an overview of the middle atmosphere as possible. Mandated by WMO, during the winter the STRATALERT BERLIN message is prepared daily and is transmitted through the Global Telecommunication System to the Meteorological Centres. We are responsible also for the GEOALERT/STRATWARM messages, which have to be issued when the magnitude of the warming reaches hemispheric extent.

For the preparation of these messages during the last winter, the Meteorological Office, Bracknell, U. K., transmitted daily maps of radiances of the SSU (Stratospheric Sounding Unit, on board the NOAA satellites) and derived 10- and 1-hPa charts. Some of these data were used in Figures 1, 13, and 14.

The European Centre for Medium Range Weather Forecasts (ECMWF), Reading, U. K., transmitted daily 3- and 5-day prognoses for the 30-hPa level. Figure 18 is based on these prognoses.

The University of Saskatchewan, Saskatoon, Canada, the Geophysical Observatory Collm, GDR, and the University of Sheffield, U. K. transmitted information on the prevailing winds in the upper mesosphere, part of which is shown in Figure 14. A detailed contribution from the measurements at Collm has been submitted to us and is shown in Figure 15.

The Service d'Aeronomie du CNRS, Verrières le Buisson, France, transmitted temperature profiles of the middle atmosphere as measured by lidar over Haute Provence and Biscarosse, France. They contributed to this publication with Figure 16.

From the Geophysical Institute of the Czechoslovak Academy of Sciences, Praha, CSSR, we received a contribution on the ionospheric radio wave absorption over Central Europe, which is shown in Figure 17.

The Physical Institute of the University Oslo, Norway sent to us daily values of total ozone from Dobson measurements at Oslo, Tromsø, and Longyearbyen together with satellite measurements from the TIROS 10 infrared spectrometer. The Dobson measurements at Oslo are used in Figure 19.

The 500-hPa data of Figure 7 are derived from gridpoints which are transmitted daily by the Deutscher Wetterdienst, Offenbach.

The Stratospheric Research Group, F. U. Berlin, analyzed daily maps for the 50-, 30- and 10-hPa levels, using radiosonde and rocketsonde data as well as thickness values derived from satellite soundings (SATEM). From these analyses characteristic quantities were derived which are used in all Figures displaying data of the 50-, 30- and 10-hPa levels.

2. Description of the Main Circulation Features of the Winter of 1987/88

It should be stated that this winter was exceptional in nearly every way. It belonged to the "westerly category" as defined by Labitzke [1982], i.e. the Quasi-Biennial Oscillation

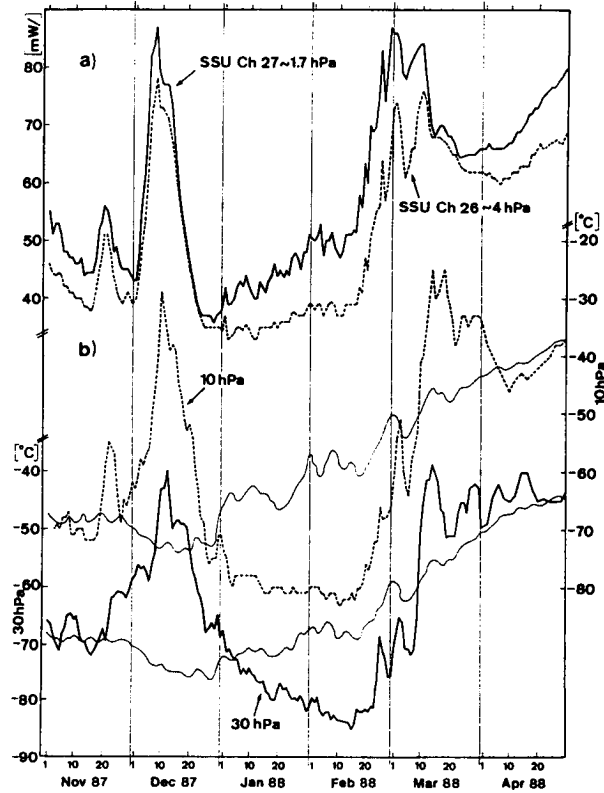


Figure 1. March of radiances and temperatures over the North Pole: a) Radiances [$\text{mW/m}^2 \text{sr cm}^{-1}$] of channel 27 and 26 of the SSU, maximum weight around 1.7 and 4 hPa (courtesy Meteorological Office, Bracknell, U. K.) b) Temperatures [$^{\circ}\text{C}$] at 10 and 30 hPa (thin lines are daily 20-year means)

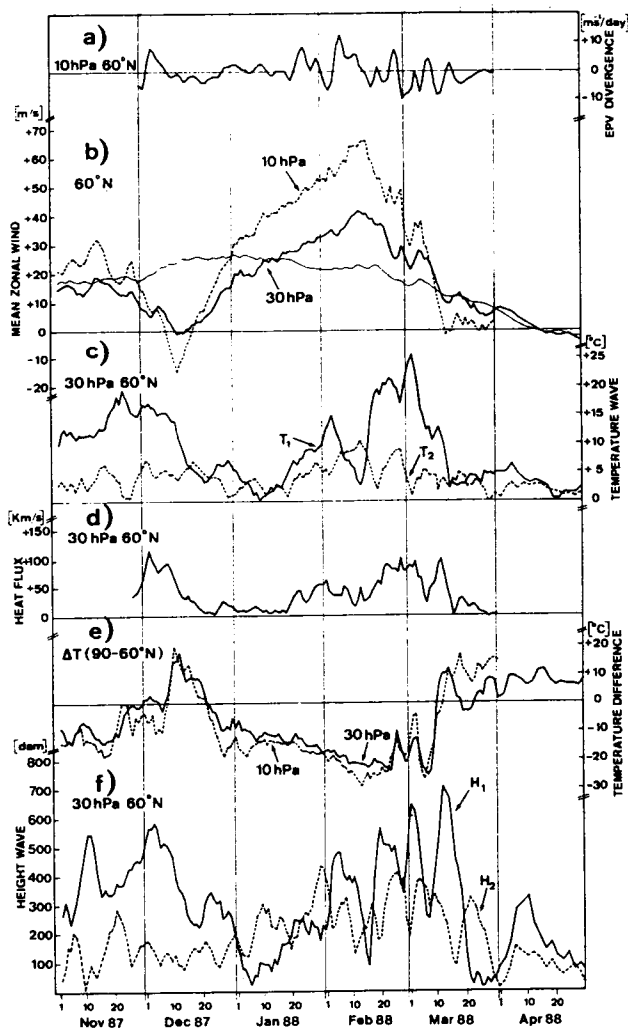


Figure 2. Derived quantities (daily values) describing the winter 1987/88: a) Divergence of the Eliassen-Palm-Vector [$\text{m s}^{-1}/\text{day}$] at 60°N , 10 hPa (3-day running means with 1-2-1 weighting) b) Mean zonal wind [m/s] at 60°N , 10 and 30 hPa c) Amplitudes of temperature waves 1 and 2 [$^\circ\text{C}$] at 60°N , 30 hPa d) Heat flux [K m/s] at 30 hPa through 60°N e) Temperature differences [$^\circ\text{C}$] between 60°N and the Pole, 10 and 30 hPa f) Amplitudes of height waves 1 and 2 [geopot. m] at 60°N , 30 hPa (thin lines in b) and e) are daily 20-year means)

1987/88

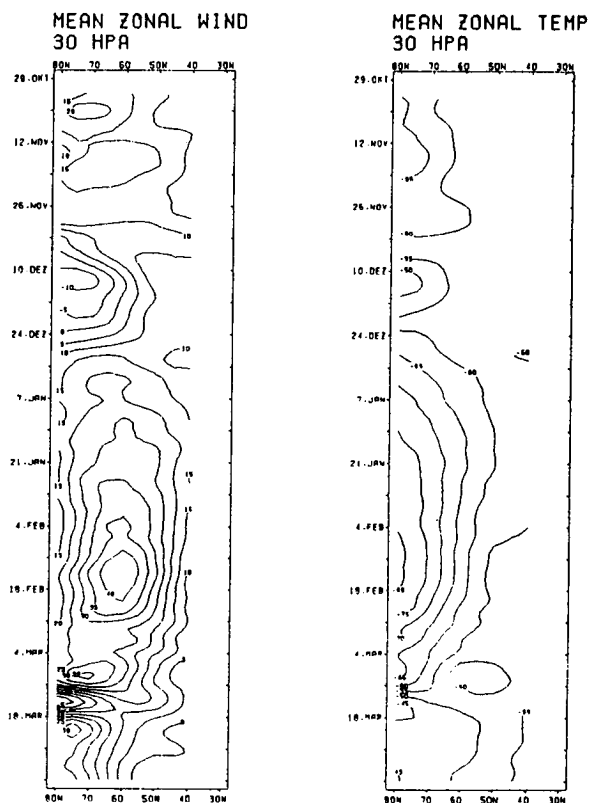


Figure 3. Meridional time sections from November 1987 to March 1988 of mean zonal wind [m/s] and mean zonal temperature [°C] at 30 hPa.

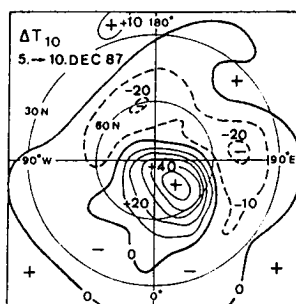


Figure 4. 10-hPa temperature changes [K] over the Northern Hemisphere from 5 to 10 December 1987.

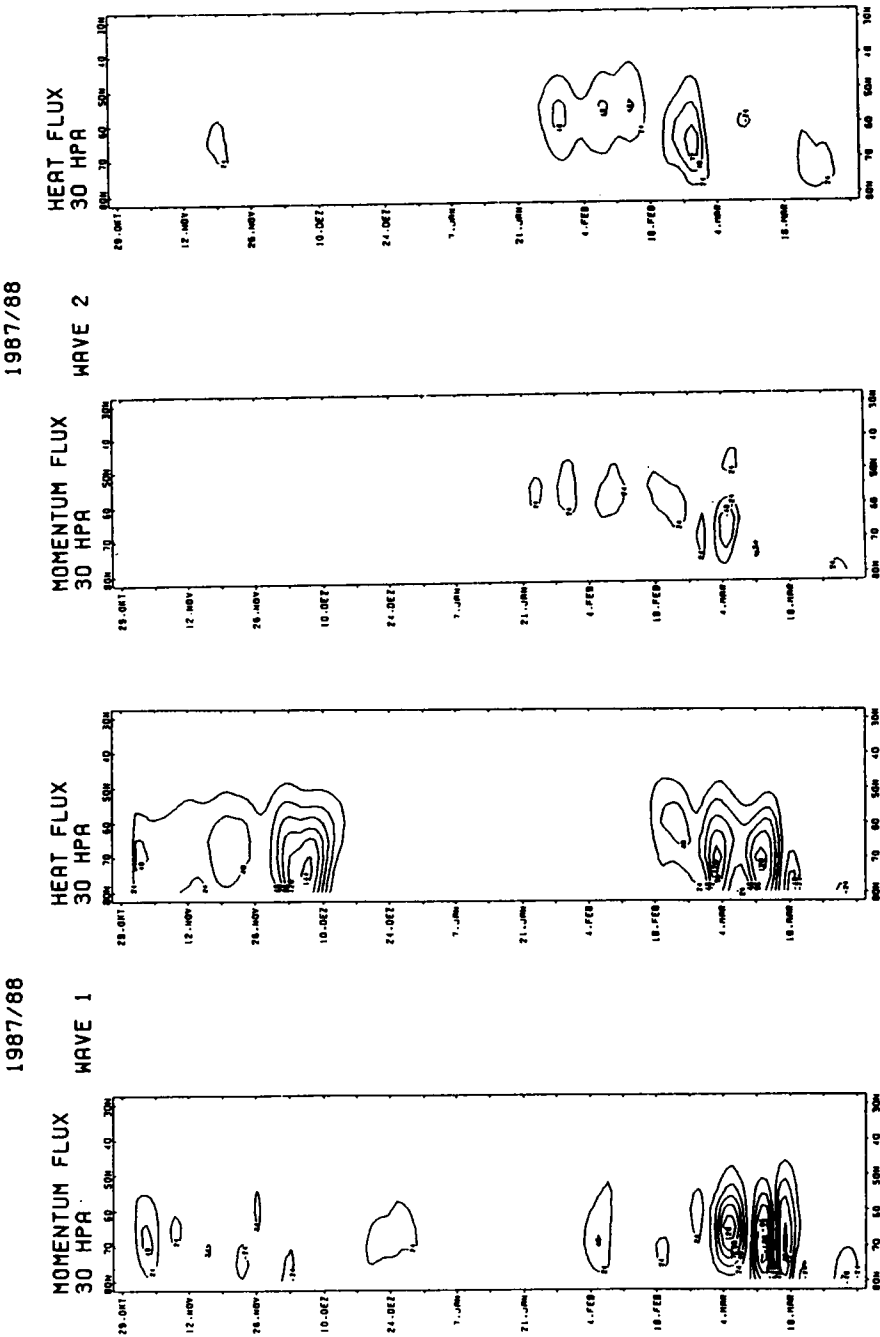


Figure 5. Meridional time sections from November 1987 to March 1988 of zonally averaged eddy momentum transport [m^2/s^2] and eddy heat transport [K m/s] by the planetary waves 1 and 2 at 30 hPa.

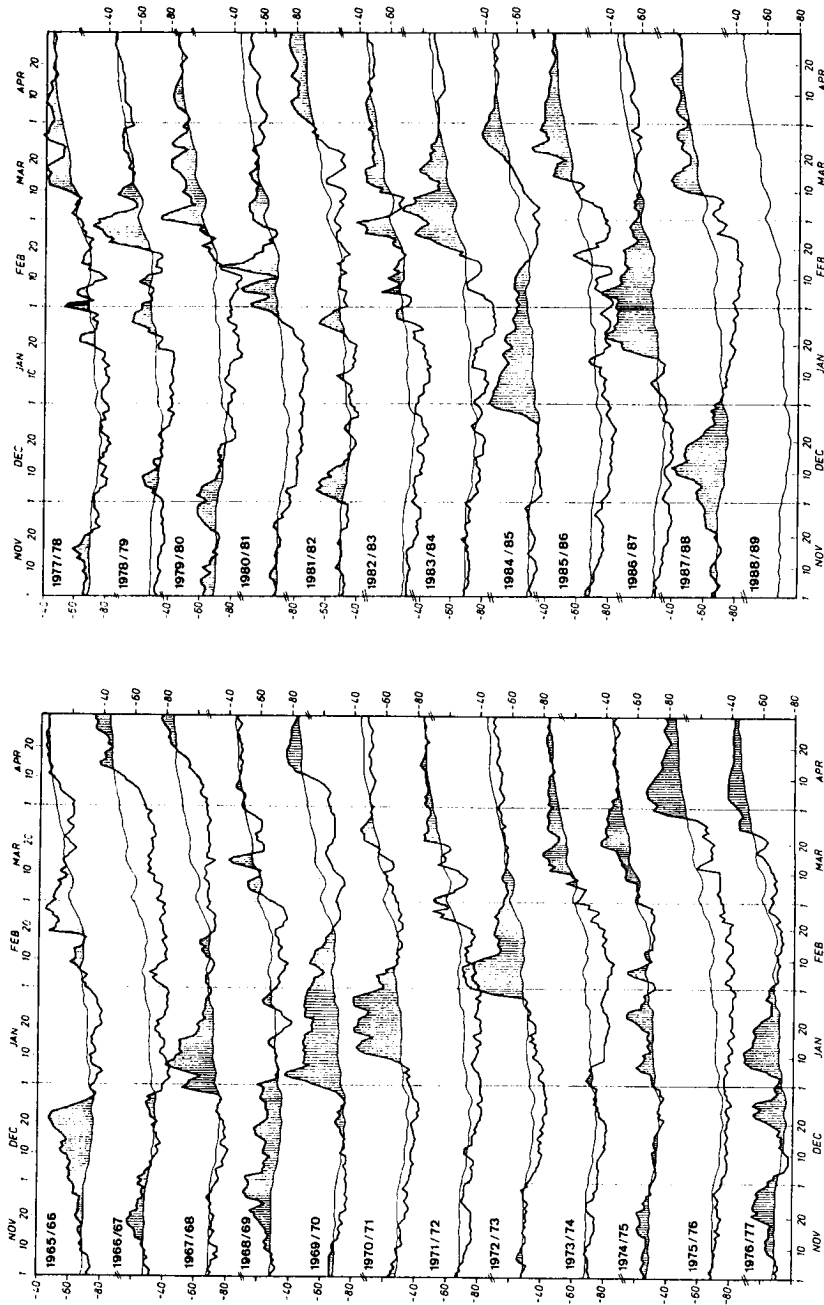


Figure 6. March of 30-hPa temperatures [$^{\circ}\text{C}$] over the North Pole during all winters since 1965/66 and deviations from the daily 20-year means 1965/66 - 1984/85 (thin lines).

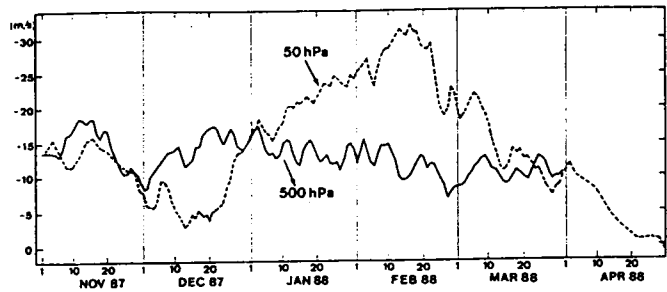


Figure 7. Mean zonal wind [m/s] at 60°N in 50 hPa and at 50°N in 500 hPa.

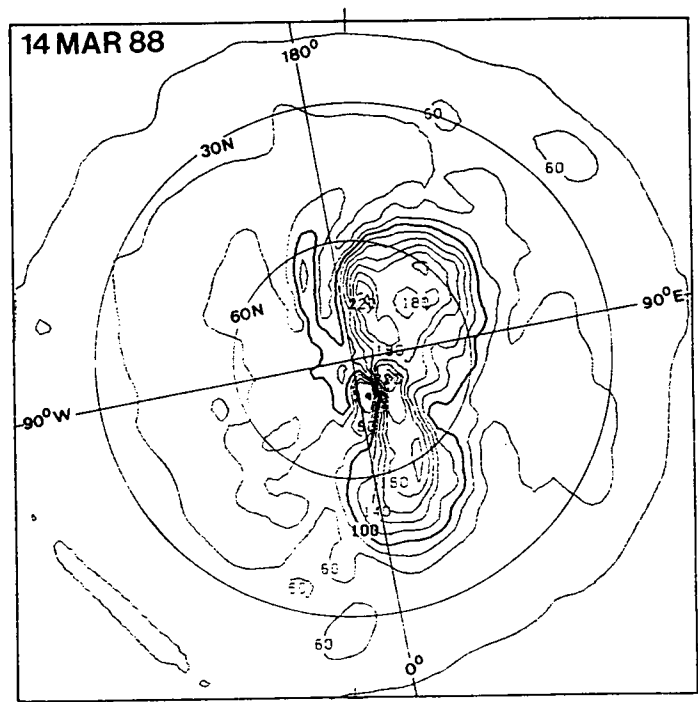
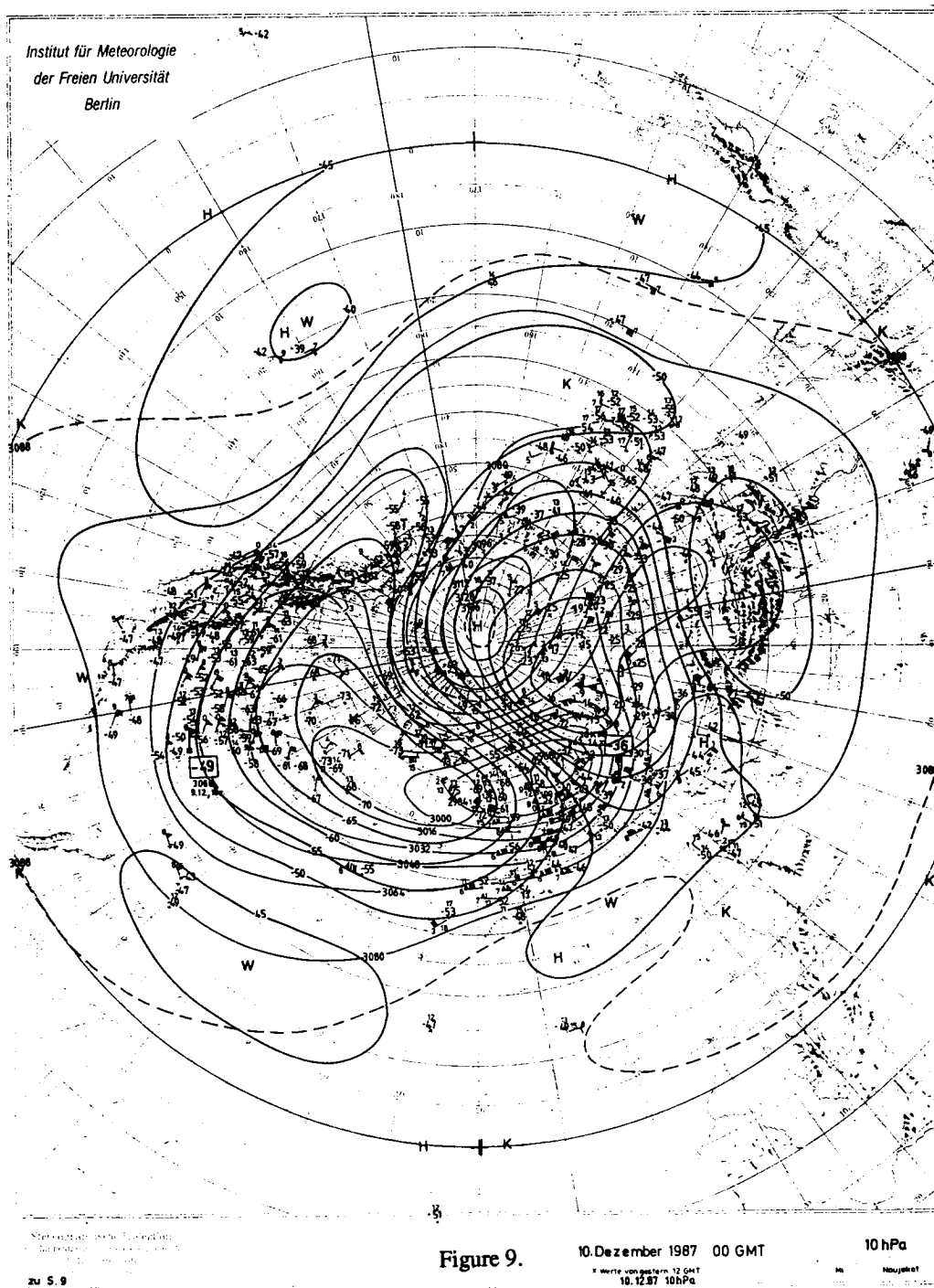
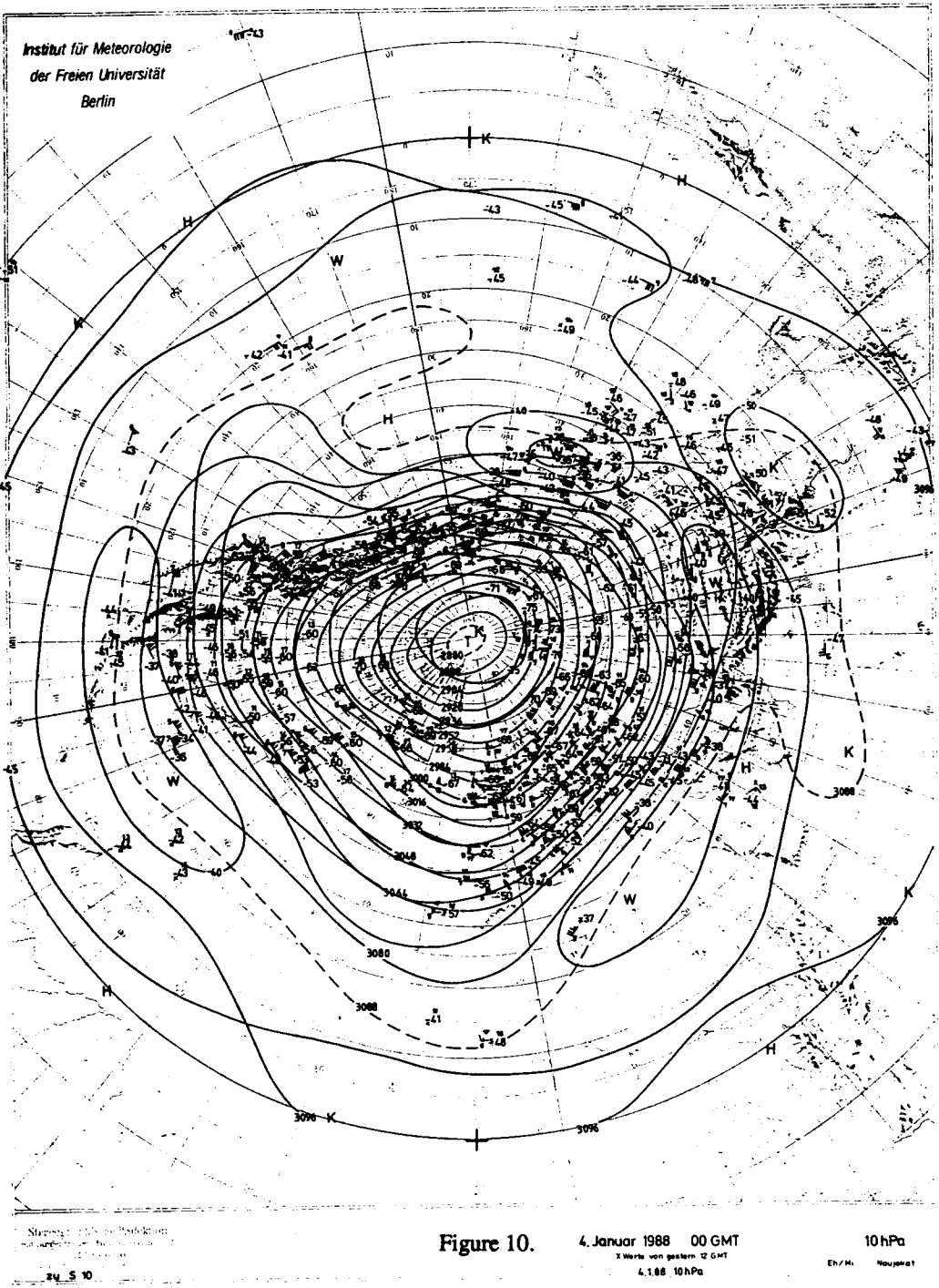


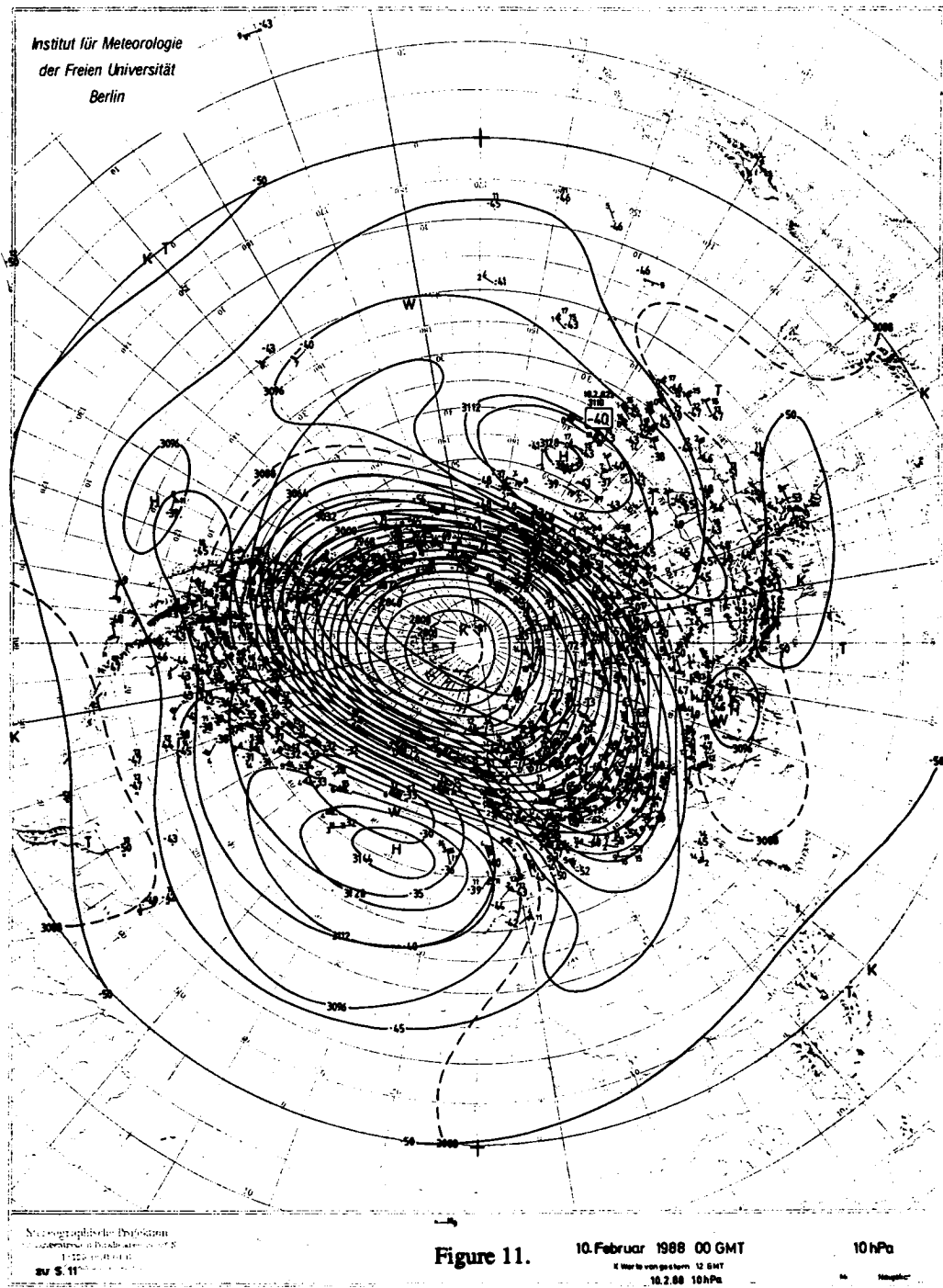
Figure 8. Potential vorticity [$\text{K hPa}^{-1}\text{s}^{-1}\times 10^5$] at the 30-hPa level.



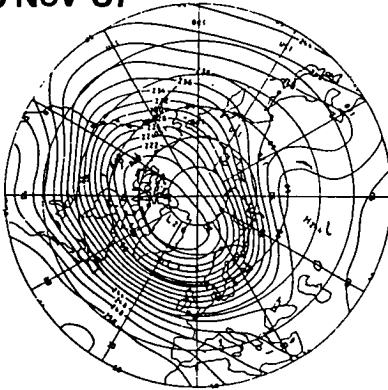
ORIGINAL PAGE IS
OF POOR QUALITY



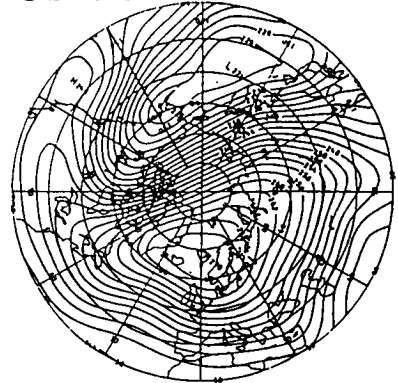
ORIGINAL PAGE IS
OF POOR QUALITY



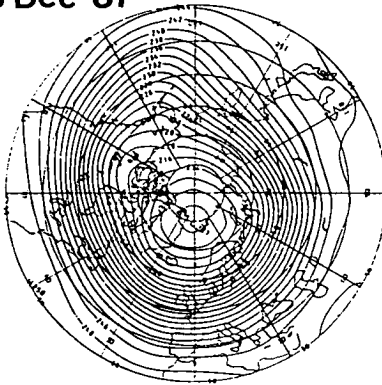
15 Nov 87



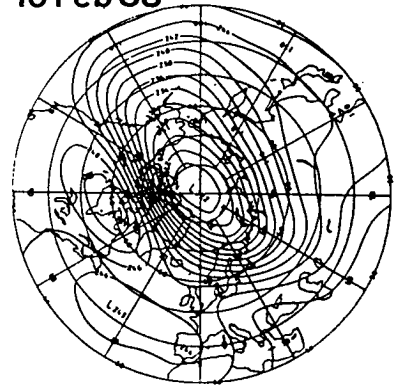
8 Dec 87



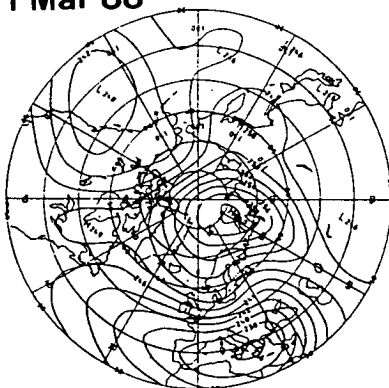
28 Dec 87



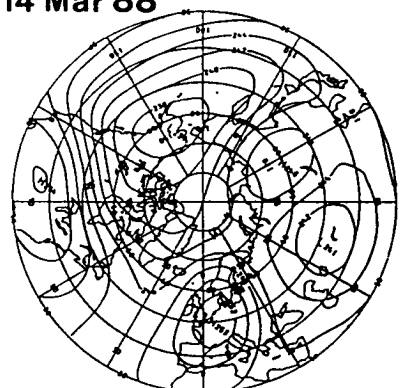
10 Feb 88



1 Mar 88



14 Mar 88



SSU Channel 27 Radiance [K]

Figure 13. Charts of radiances [K] at channel 27 of the SSU, maximum weight around 1.7 hPa (courtesy Meteorological Office, Bracknell, U.K.)

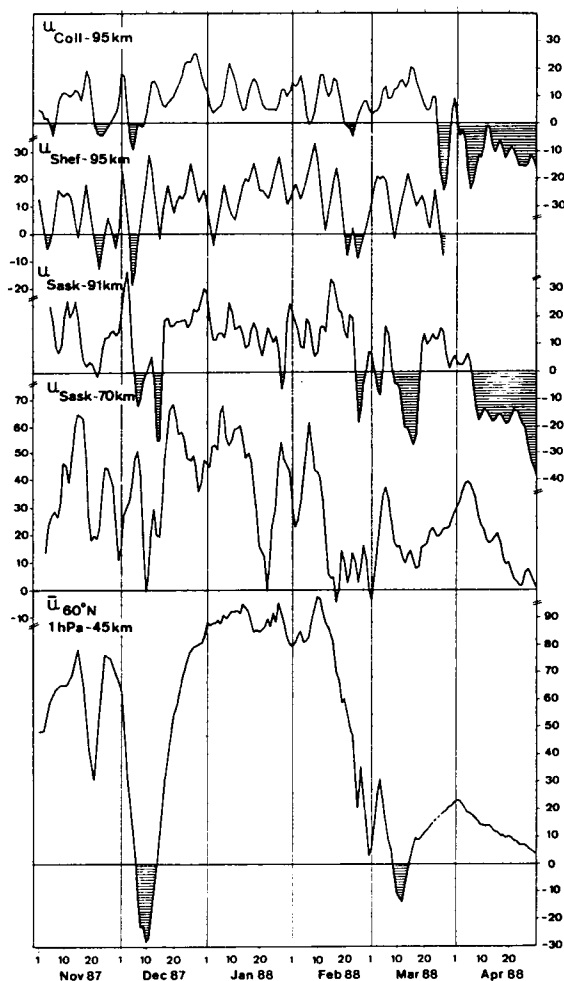


Figure 14. Upper stratospheric and mesospheric winds [m/s]:

u_{COLL} : Prevailing zonal winds over Central Europe (51N,13E) around 95 km from low frequency drift measurements; 3-day running means with 1-2-1 weighting (courtesy Geophys. Obs. Collm, GDR)

u_{SHEF} : Zonal winds over Great Britain (around 55N,02W) around 95 km measured by meteor wind radar; periods of less than 4 days removed (courtesy University of Sheffield, U.K.)

u_{SASK} : Zonal winds over Canada (52N, 107W) around 91 km (tidally corrected) and around 70 km (with tidal contamination) measured by partial reflection radar; 3-day running means with 1-2-1 weighting (courtesy University Saskatchewan, Canada)

$u_{60^{\circ}\text{N}}$: Mean zonal wind at 60°N, 1 hPa (around 45 km) derived from SSU satellite data (courtesy Meteorological Office, Bracknell, U. K.)

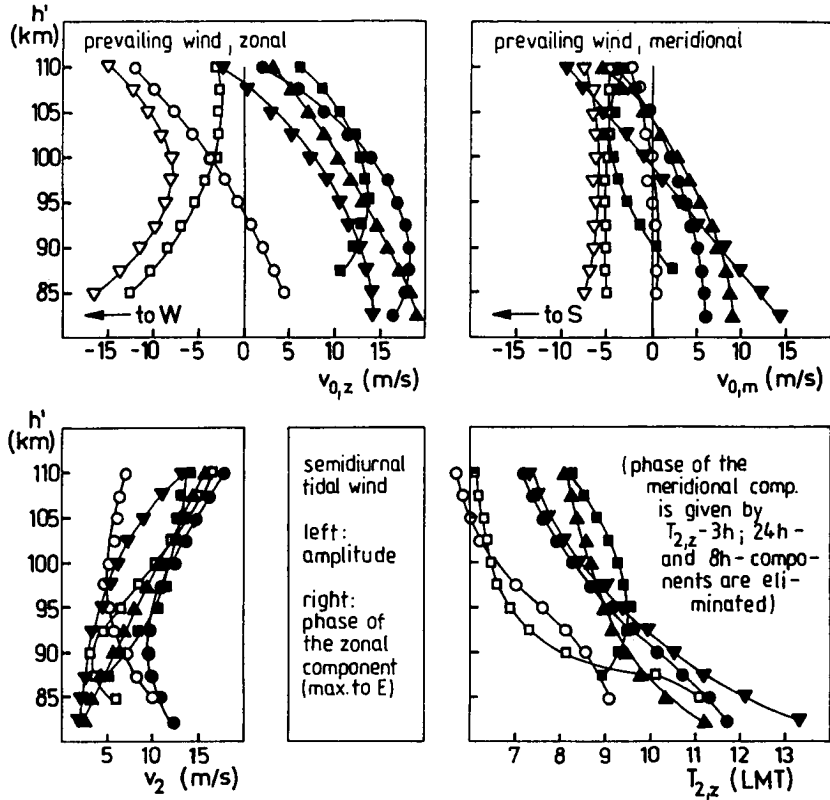


Figure 15. Wind profiles obtained from D1 measurements on 3 measuring paths (177, 225, and 272 kHz) over Central Europe (52N, 15E) between 80 and 110 km altitude in winter 1987/88 and spring 1988:

- December 1987 (without stratwarm-influenced days)
- December 1987 (stratwarm-influenced days, 03-08)
- ▲ January 1988
- ▼ February 1988
- March 1988 (01-13)
- March 1988 (23-31)
- ▽ April 1988

(courtesy Geophysical Observatory Collm, GDR)

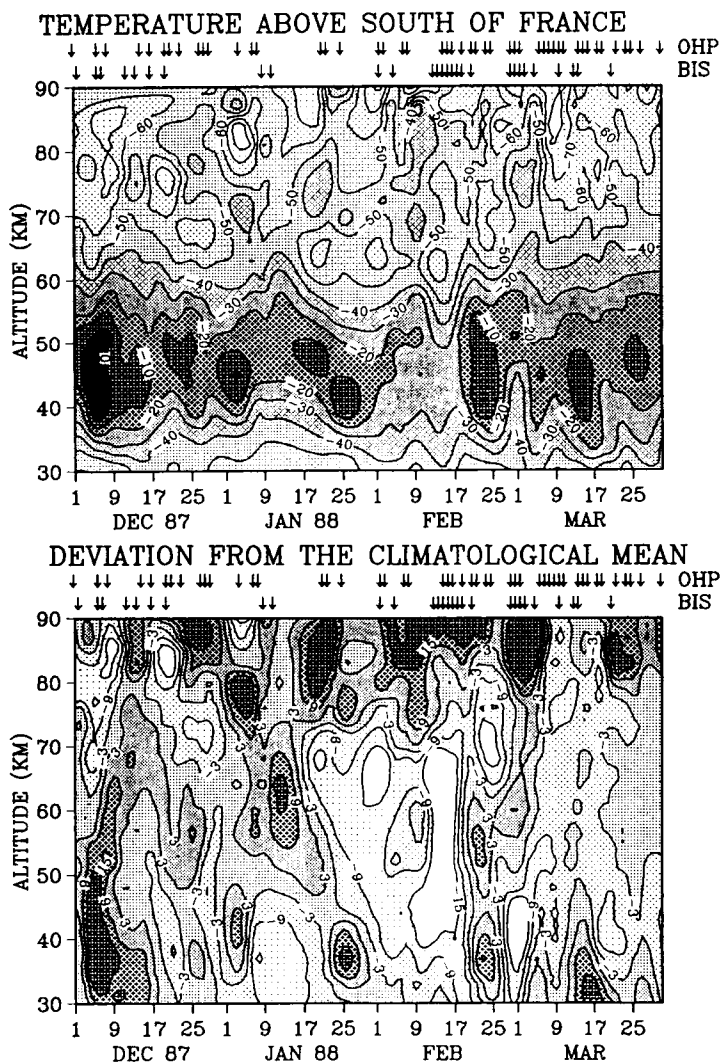


Figure 16. Time-height section of temperature [$^{\circ}\text{C}$] and temperature deviation [K] from the 1981-1987 climatological mean above the south of France, observed by Rayleigh lidar. The arrows indicate the nights of measurements at the Observatory of Haute-Provence (OHP,44N,06E) and of Biscarrosse (BIS,44N,01W) (courtesy Service d'Aeronomie du CNRS, Verrieres-le-Buisson, France).

ORIGINAL PAGE IS
OF POOR QUALITY

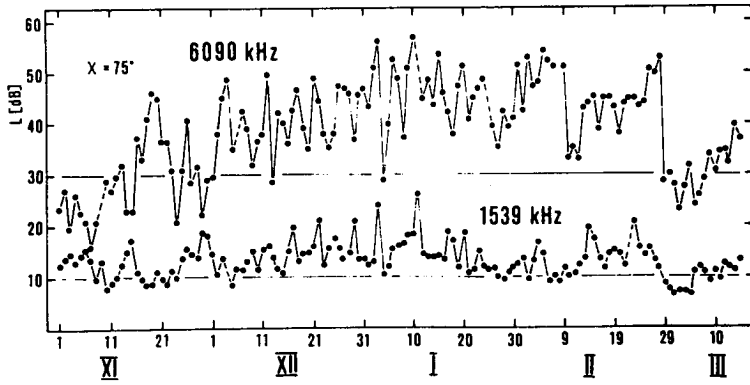


Figure 17. Radio wave absorption [dB] over Central Europe (courtesy Geophysical Institute Prague, CSSR).

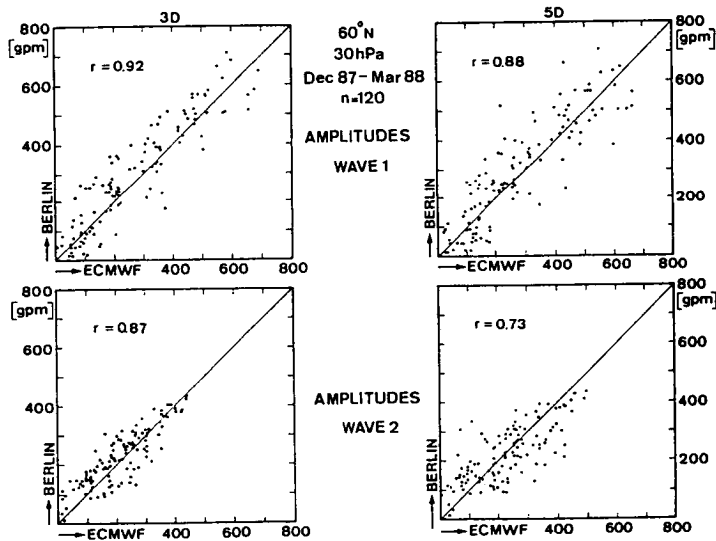


Figure 18. Comparison of amplitudes [m] of 30 hPa height waves 1 and 2 between the Berlin analyses and the ECMWF 3 and 5 day prognoses, respectively.

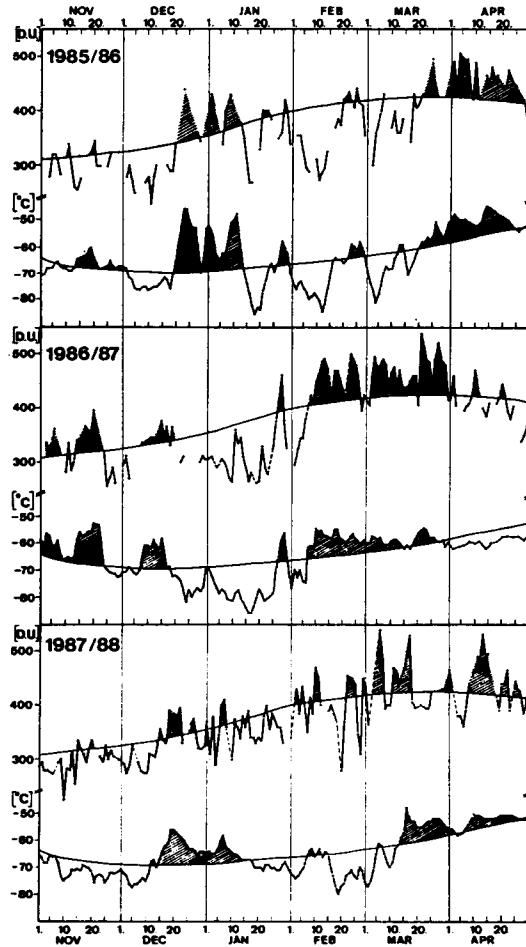


Figure 19. Daily values of total amount of ozone [D.U.] from Dobson measurements at Oslo (courtesy Physical Institute, University of Oslo, Norway) and of 30-hPa temperatures [°C] at 60N,10E during the last three winters; thin lines are the zonal mean at 60N and the monthly mean at 60N,10E, respectively.

(QBO) was in the westerly phase, so a relatively undisturbed winter could be expected with an enhanced tendency for the development of a cold wave two pattern. Labitzke and Van Loon [1988] have shown that the polar stratospheric temperatures in midwinter are significantly positively correlated with the solar cycle when the equatorial winds in the lower stratosphere are westerly. The only major midwinter warmings within the westerly category have occurred during the sunspot maxima of the last three solar cycles. All that was true of January and February; an extremely cold polar region was observed, fully in accordance with the statistics of Labitzke and Van Loon.

However, a major warming took place in December; it was the earliest observed since they were detected in 1952. The marches of 30-hPa temperatures at the North Pole for the last 23 winters (Figure 6) show that considerable positive deviations from the daily 20-year means have occurred in former years too. These have been Canadian warmings, which are typically connected with an intensified Aleutian anticyclone moving into Canada and displacing the polar vortex towards Siberia. The most intense Canadian warming, of December 1965, has been described in detail by Labitzke [1977]. Previously, a major warming never started before mid-December and a break-down of the stratospheric wintertime circulation was never observed before the beginning of January.

Usually, late and not very pronounced final warmings happened after major midwinter warmings. This year an intense final warming was observed with features similar to a major warming, leading to an early reversal from the winter to the summer circulation.

2.1 The Unusually Early Major Warming in December

The first warming pulse, preceded by a first peak in the amplitude of height wave one (Figure 2f), had already occurred in November, clearly discernible in the march of temperatures and radiances over the North Pole (Figure 1) at all stratospheric levels. The radiance chart of channel 27 with the maximum weight around 1.7 hPa (Figure 13) shows the first indication of the developing warm area over western Siberia on 15 November. The normal seasonal increase of the westerly winds at the mid-latitudinal belt, shown by the zonal mean at 60N (Figure 2b), was interrupted. The decrease was strongest in the upper stratosphere but was also detected in the mesosphere over Europe and Canada (Figure 14). While in the upper stratosphere the temperatures then decreased for a short time and the zonal winds from the west temporarily strengthened again, the rise of temperatures and the decrease of the westerlies continued in the lower stratosphere. Figure 7 shows that the mean zonal flow at middle latitudes also weakened in the troposphere from the middle of November.

During the last days of November the planetary wave one intensified again (Figure 2f), transporting a considerable amount of heat, the maximum of the winter, northwards through 60N at the 30-hPa level (Figures 2d and 5). The temperatures and radiances over the North Pole (Figure 1) rose again. This development was very similar to the previous year when an intense minor warming occurred in the upper stratosphere at the beginning of December [Naujokat et al., 1987] but did not penetrate to the lower levels. In the latter year there was already a diminished zonal flow and a warm polar region in the lower stratosphere when the additional warming pulse occurred.

In our first note on this unusual event [Naujokat et al., 1987] we have shown how impressively the whole of the stratosphere warmed, accompanied by the typical cooling of the mesosphere, by means of two rocket observations over Heiss Island (81N, 58E) from 24 November and 8 December. The same is visible in the lidar data over southern France (Figure 16). The hemispheric extent can be seen from the temperature changes at the 10-hPa level from 5 to 10 December (Figure 4) which exceeded +55 degrees over the Barents Sea. The radiance chart of 8 December (Figure 13) and the 10-hPa chart of 10 December (Figure 9) show the large warm area over high latitudes and the cold air displaced far to the south. An anticyclone had nearly reached the North Pole.

On 9 December the criteria for a major warming were fulfilled: the temperature gradient between 60N and the Pole was reversed (Figure 2e) and polewards of 60N an eastward flow governed the stratosphere and mesosphere up to the mesopause region (Figures 2b, 3, and 14). The mesospheric wind profiles over Central Europe (Figure 15) for the stratwarm-influenced days of December show the reversal of the prevailing wind direction and the spring-

like phase position of the semidiurnal tidal wind. In contrast to the major warming of January 1987 the response of the lower ionosphere to these processes was not very pronounced, as indicated by the behavior of the radio-wave absorption over Central Europe (Figure 17).

2.2 The Extremely Cold Midwinter in January and February

The re-establishment of the wintertime circulation rapidly progressed during the second half of December. The mesospheric wind profiles over Central Europe (Figure 15) show the development of a very strong winter circulation with a northward directed meridional wind component up to at least 100 km and small values for the vertical wavelength of the semidiurnal tidal wind. In the upper stratosphere the lowest temperatures of the winter were reached at the end of December (Figures 1a and 13) and at the beginning of January the zonal mean wind at 60N reached speeds of around 90 m/s at the 1-hPa level (Figure 14). At the same time, a well developed vortex was found again over the Pole in the lower stratosphere (Figure 10) and the zonal flow exhibited only small zonal asymmetries. This is also expressed by the very small amplitudes of both planetary height waves (Figures 2c and 2f). In the following weeks a cold wave two pattern developed in the lower and middle stratosphere. There was nearly no eddy heat transport in January (Figures 2d and 5) and the polar region steadily cooled; extremely low temperatures were reached around the middle of February (Figures 1b, 3, and 11) accompanied by very high wind speeds at middle latitudes (Figures 2b and 3). The charts of the radiances from channel 27 with maximum weight around 1.7 hPa (Figure 13) and of the 10-hPa level (Figure 11) from 10 February demonstrate the cold polar region. At the 30-hPa level the mean monthly temperature deviations from the 20-year average were almost as strongly negative in February as they were positive in December [Geb and Naujokat, 1988].

2.3 The Major Final Warming in March

At the end of January/beginning of February some minor warmings developed in the strong jet surrounding the elongated polar vortex but it was not before 20 February that there was a significant northward eddy heat transport at the 30-hPa level, mainly by an amplifying planetary wave one (Figures 2c, 2d, 2f, and 5). The radiances and temperatures over the North Pole started to rise once more (Figure 1) and in the upper stratosphere the peak of the warming was reached on 1 March, as shown by the radiance chart of this day (Figure 13). This upper stratospheric warming is also clearly visible in the lidar data over southern France (Figure 16). In the middle and lower stratosphere an additional warming pulse was necessary (Figures 2d and 5) to complete the reversal of the temperature gradient over high latitudes around the middle of March. The mean zonal wind at 60N, which had been weakening since the middle of February throughout the stratosphere and mesosphere (Figures 2b, 7, and 14), was temporarily from the east at the upper levels down to the 10-hPa level. The 10-hPa chart of 14 March (Figure 12) shows the warm air covering the hemisphere north of 50N and a well developed anticyclone over Greenland. The two centres of the split vortex were displaced towards Siberia and Europe; values of low potential vorticity were found in high latitudes at the 30-hPa level (Figure 8).

At the same time, a weaker than normal late winter cooling began in the upper stratosphere with decreasing temperatures and increasing winds (Figures 1a, 13, and 14), which was also discernible in the upper mesosphere (Figures 14 and 16). At the end of March, however, the spring reversal was accomplished at those high levels (Figures 14 and 15) and the lower ionosphere responded with a broad minimum of radio-wave absorption (Figure 17).

In the stratosphere the circulation reversal was completed around the middle of April (Fig. 2b), i.e. an early transition to the summer conditions took place.

3. Comparison between ECMWF-Prognoses and Berlin Analyses

The daily transmitted 3- and 5-day forecasts of the 30-hPa heights were again of great help for the preparation of the STRATALERT messages. During the major warming in December the amplification of height wave one and the non-development of height wave two (compare Figure 2f) was as well predicted as the short reversal of the mean zonal wind at 60°N

(see Figure 2b). The development of a cold wave two pattern in January with the peak at the end of the month was correctly predicted and the four amplitude peaks of wave one in February and March were also in good agreement, although there were some differences in magnitude. Also well predicted was the rapid decrease of the planetary wave activity at the end of March in connection with the final warming. Comparing the amplitudes at 60°N as analyzed in Berlin and as forecast by the ECMWF (Figure 18), the agreement is not as good as in the year before, as can be seen from the correlation coefficients. The reason might be that the planetary wave activity was not very pronounced during this winter: wave two was weak most of the time and wave one also hardly reached 700 decameters. In general, there seems to be a tendency in the forecasts to overestimate the amplitude changes, i. e. strong waves have often been predicted too strong and weak waves too weak.

4. Total Ozone and 30-hPa Temperatures at Norway

In Figure 19 the daily values of total ozone at Oslo are shown together with the 30-hPa temperatures at the nearest gridpoint from the Berlin Analyses for the last three winters. They all behaved in a difference manner. In 1985/86 and 1986/87 the ozone strongly corresponded to the temperatures, and the positive deviations were related either to a wave two pattern of the circulation or to a major warming event like the major final warming in March 1986 and the major midwinter warming in February 1987. In the winter 1987/88 the agreement is not as good as in the years before. After the early major warming in December the ozone distribution seems to remain disturbed during the following months and even the final warming is not so clearly related as in 1986.

Acknowledgements

For watching the middle atmosphere wintertime circulation, preparing the daily STRATALERT and the GEOALERT messages, and providing material for this report we should like to thank the groups mentioned in the Introduction. Special thanks go to A. O'Neill, Bracknell, E. Klinker, Reading, A. H. Manson, Saskatoon, R. Schminder and D. Kürschner, Collm, H. G. Mueller, Sheffield, A. Hauchecorne, Verrières leBuisson, J. Lastovicka, Praha, and S. H. H. Larsen, Oslo. Further, we should like to thank the members of the Stratospheric Research Group, F. U. Berlin for their untiring effort and assistance and the Deutscher Wetterdienst for arranging the direct transfer of the ECMWF prognoses.

References

- Geb, M. and B. Naujokat, 1987/88: Nordhemisphärischer Klimabericht zum November 1987, Dezember 1987, Januar 1988, Februar 1988, März 1988. Beilagen zur Berliner Wetterkarte, KNH XI/87, KNH XII/87, KNH I/88, KNH II/88, KNH III/88.
- Labitzke, K., 1977: Interannual variability of the winter stratosphere in the northern hemisphere. *Mon. Wea. Rev.*, **105**, 762-770.
- Labitzke, K., 1982: On the interannual variability of the middle stratosphere during the northern winters. *J. Meteor. Soc. Japan*, **60**, 124-139.
- Labitzke, K., and H. van Loon, 1988: Associations between the 11-year solar cycle, the QBO, and the atmosphere. Part I: The troposphere and stratosphere on the northern hemisphere in winter. *J. Atmos. Terr. Phys.*, **50**, 197-206.
- Naujokat, B., K. Labitzke, R. Lenschow, K. Petzoldt, and R. -C. Wohlfart, 1987: The stratospheric winter 1986/87: A major midwinter warming 35 years after they were first detected. Beilage zur Berliner Wetterkarte, SO 9/87.
- Naujokat, B., R. Lenschow, K. Labitzke, K. Petzoldt, and R. -C. Wohlfart, 1987: First note on the unusually early major stratospheric warming in December 1987. Beilage zur Berliner Wetterkarte, SO 16/87.

Appendix 4

GLOBMET

R. G. Roper

The GLOBAL METeor Observations System has continued to function as a combined atmospheric dynamics, meteor/atmosphere interaction and meteor astronomy program under MAC, with, of course, the atmospheric dynamics portion of the program being of primary interest to MAC.

The most direct input of wind data has been to ATMAP (the Atmospheric Tides in the Middle Atmosphere Project) and to the global modeling of the mean atmospheric circulation at meteor heights, with the Soviet Union taking a major role in the latter.

Most recently, the Second GLOBMET Symposium (held in Kazan, USSR, July 11-16, 1988) provided a forum for almost 100 scientists from the worldwide meteor community to present the results of their research. This community has, since the First GLOBMET Symposium (in Dushanbe, USSR, August 1985 -- proceedings published as MAP Handbook No. 25) established ties which led to a much more informal atmosphere, with a greater number of papers presenting the results of joint efforts, and significantly more personal interaction, resulting in detailed discussions, several leading to proposals of mutual cooperation in the future. The proceedings of GLOBMET II will be published as a MAP Handbook

At GLOBMET II, the problem of starting (continuing) a working body for future coordination of meteor research after MAC was discussed in depth; IAGA, IAMAP, IAU, and URSI, or at least the appropriate divisions, commissions or working groups in each, are to be contacted soliciting their reactions as to how best to perpetuate what, to date, has been a very fruitful alliance under MAP/MAC.

RESOLUTION

Second GLOBMET Symposium:

noting the remarkable progress in the study of meteor phenomena under the GLOBMET Project especially; in the provision of complex observations for Meteor Geophysics and Meteor Astronomy, in the development of up-to-date multi-purpose observing systems for measuring geophysical and astronomical parameters of meteors and in the measurement of the middle atmosphere at different heights,

bearing in mind the necessity of combining these methods with other techniques which study the middle and upper atmosphere, as well as the necessity of close cooperation among research groups which use meteor radars, MST and ST radars, partial reflection radars, lidars and other techniques,

recommends that a working body should be established to coordinate these activities in the form of an interunion commission on atmospheric radars which will include representatives from [IAGA, IAMAP, URSI, IAU, SCOSTEP, IUPAP]

requests that these international organizations support this proposal, and

recommends, as a first step to develop cooperation, that a working group on atmospheric radars be formed.

Appendix 5

THE MAC/SINE AND MAC/EPSILON CAMPAIGNS

A report to the MAP Steering Committee
and campaign participants

Eivind V. Thrane
Project Scientist

1. Introduction

Two major international campaigns dedicated to the study of middle atmosphere dynamics in high latitudes were successfully completed in 1987. MAC/SINE (Middle Atmosphere Cooperation/Summer In Northern Europe) was carried out during the period 7 June - 19 July, whereas MAC/EPSILON took place in the period 12 October - 15 November. In both campaigns a large number of ground-based and rocket techniques were used in a concerted effort to map the dynamical structure of the middle atmosphere over Northern Europe. Although the analysis of the observations has only just started, it is clear that a large and unique data set has been obtained, which we believe will provide new insight into the dynamical processes in this interesting region of the atmosphere. In the following a preliminary report on the campaigns will be given. The report will serve two purposes: a) to inform the MAP Steering Committee about the projects and b) to give campaign participants and other interested parties an overview of the information available to date on the rocket launches and observational schedules for the ground-based experiments.

2. MAC/SINE

The MAC/SINE campaign was carried out during the period 7 through 19 July 1987. The primary purpose of the project was to study dynamical processes, winds, waves, and turbulence in the high latitude summer middle atmosphere. Measurements were carried out using a combination of instrumented sounding rockets, meteorological rockets, and ground-based radar and lidar techniques. The ground-based techniques provided extensive series of synoptic measurements, whereas the rocket program comprised regular launches of metrockets as well as launches of 6 "salvos" constructed to study specific phenomena.

The observational program was very successful, and a preliminary review of the data shows that the summer, high latitude mesosphere is a complex and variable medium. It is hoped that the results will throw new light on a number of interesting specific phenomena as well as increase our understanding of the general summer circulation.

The ground-based measurements were, as far as possible, made continuously throughout the whole campaign period. The mode of operation is indicated in Table 1. More detailed information on some of the most important instruments is given below.

The SOUSY radar provided a very extensive set of measurements of winds, waves and turbulence, mainly between 80 and 90 km where persistent echoes were normally observed from early morning to the afternoon hours.

The PRE radar observed drifts in the D region throughout the campaign, and detailed measurements of ordinary and extraordinary echo amplitudes were made during all rocket launches. In striking contrast to winter measurements very few echoes were observed below 80 km.

The EISCAT VHF radar was operated successfully for nearly 60 hours as part of the campaign. The normal operation times were from 09-13 UT on Mondays, Wednesdays and Fridays. The measurements will provide information on vertical winds, electron density and possibly ion composition. Of particular interest was the observation of very intense echoes from a very thin layer near the mesopause.

Table 1. GROUND-BASED EXPERIMENTS IN MAC/SINE Rev. 17 Sept 87

EXPERIMENT	OBSERVED PARAMETERS	LOCATION	REAL TIME	OPERATION
PARTIAL REFLECTION	e ⁻ DENSITY TURBULENCE	RAMFJORDMOEN	N Y	CD
PRE (MF) RADAR	WINDS	RAMFJORDMOEN	Y	C
PARTIAL REFLECTION	TURBULENCE	VOLGOGRAD	N	C
SOUSY VHF RADAR	TURBULENCE WINDS	BLEIK	Y N	CD, AFTER 15 JUNE
EISCAT	e ⁻ DENSITY, λ WINDS	RAMFJORDMOEN	N Y	B
MS-RADAR	WINDS	SASKATOON	N	C
GLOBMET	WINDS	USSR (7x)	N	C
METEOR RADAR	WINDS	VOLGOGRAD	N	C
HF-CIRCUIT	PROPAGATION CONDITIONS	ANDENES-ALTA	N	C
IONOSONDES	IONOSPHERIC CONDITIONS	ANDENES, RAMFJORDMOEN	Y	A
A1-ABSORPTION	ABS. 2.2 MHZ	VOLGOGRAD	N	C
RIOMETERS	ABSORPTION	ANDENES, FINLAND (9x), KIRUNA (KGI), RAMFJORDMOEN	Y	C
MAGNETOMETERS	GEOMAGNETIC CONDITIONS	ANDENES, FINLAND (Nx), KIRUNA (KGI), RAMFJORDMOEN	Y	C
UB LIDAR	NA-DENSITY, DENSITY	ANDENES	Y	CS, AFTER 28 JUNE
UI LIDAR	NA-DENSITY, WINDS	LONGYEARBYEN	N	CS
CNRS LIDARS	DENSITY, TEMPERATURE	SKIBOTN, ON SHIP	N	CS
FABRY-PEROT TRIPLE ETALON	WINDS	KIRUNA (KGI)	N	? CS ?

A EVERY 20 MINUTES

B ON REGULAR LAUNCH DAYS FROM 9-13 UT; 9-19 UT POSSIBLE FROM 29 JUNE

C CONTINUOUS

CD CONTINUOUS DURING COUNTDOWNS

CS CONTINUOUS WHEN CLEAR SKY

The Bonn University LIDAR. Successful observations of the mesospheric sodium layer were made during the last part of the campaign and these were extended for several weeks beyond the end of SINE. Very interesting results were obtained on the fine structure of the sodium layer, its total density and diurnal variation.

The sequence of rocket launches for Andøya Rocket Range is given in Table 2. Note that the rockets in the six salvos are grouped together.

As the Table shows, the regular met-rocket (Viper 3A Falling Sphere) launches were carried out on Mondays, Wednesdays and Fridays at or near 11:00 UT.

Three Chaff salvos were launched to study detailed wind and wave structure in the mesosphere. These typically contained 4 chaff rockets and 2 falling spheres.

The Turbulence/Gravity Wave salvo was launched on 14 July during conditions with very strong and variable echoes observed with the 50 MHz SOUSY and the 2.75 MHz PRE radars. The radars indicated strong winds and turbulence above 80 km, and the electron probe on the first and second Super-Arcas payloads showed interesting detailed structures in the mesopause region. The third Super-Arcas was launched as a reference during conditions with no significant radar echoes.

The EISCAT salvo was launched on 15 July, using the EISCAT VHF radar and the SOUSY as primary diagnostic tools. During the salvo strong echoes were observed from layers near the mesopause on both radars, and exceptionally strong structures were observed at this level by the Super-Arcas electron probe. Sodium lidar observations were also made during this salvo.

The Sodium/Chaff salvo was launched before midnight on 15 July during a period with magnetic activity and particle precipitation. The main diagnostic tool was the Bonn University sodium lidar, but SOUSY, PRE and the ionosondes were also in operation. Development of sudden Sodium layers were observed during this salvo. The chaff rockets launched into these layers should yield in situ information on the dynamical structure of the mesopause region during such conditions.

2.1 Rocket Launches in the USSR

HEISS ISLAND	VOLGOGRAD
10 June	10 June
13 June	
17 June	17 June
20 June	
24 June	
	25 June
27 June	
01 July	01 July
04 July	
08 July	08 July
11 July	
15 July	15 July
18 July	
	22 July

Parameters measured: Profiles of temperature, wind, electron concentration all to 80-85 km. At Volgograd also turbulent energy dissipation rate at 75-80 km.

2.2 Reports on Ground-Based Measurements

Table 2. Rocket Launches during MAC/SINE

<u>Launch time (UT):</u>		<u>Remarks</u>
S-F1	10/6	13:40 116-20 km (collapse: 30 km); noisy AGC above 70 km.
S-F2	12/6	11:00 115-22 km (collapse: 28 km); noisy AGC above 77 km.
S-F3	15/6	11:24 109-28 km (collapse: 29 km); noisy AGC above 77 km; spikes in AGC below.
S-C1/H	15/6	11:57 Booster failure; missing ejection charge.
S-F4	17/6	11:03 115-27 km (collapse: 29 km); noisy AGC above 75 km.
S-F5	19/6	11:05 113-26 km (collapse: 28 km); noisy AGC above 80 km.
S-F6	22/6	11:29 114-27 km (collapse: 29 km); noisy AGC above 70 km; spikes in AGC below.
S-C2/H	22/6	12:30 83-71 km; O.K.
S-C3/H	22/6	13:11 Dart Failure; no ejection of foils.
<u>Chaff salvo No. 1:</u>		
S-F7	24/6	11:00 105-27 km (collapse: 28 km); noisy AGC above 70 km; spikes in AGC below.
S-C4/L	24/6	11:20 93-82 km; O. K.
S-C5/L	24/6	11:53 94-82 km; O. K.
S-C6/L	24/6	12:25 Dart failure; no ejection of foils.
S-C7/L	24/6	12:40 97-81 km; O. K.
S-C8/L	24/6	13:33 99-84 km; O. K.
S-F8	24/6	13:58 112-26 km (collapse: 28 km); noisy AGC above 75 km; spikes in AGC below.
<u>Chaff salvo No. 2:</u>		
S-F9	26/6	11:00 115-26 km (collapse: 28 km); some spikes in AGC down to collapse altitude.
S-C9/L	26/6	11:27 95-77 km; O. K.
S-C10/H	26/6	12:01 Dart failure; no ejection of foils.
S-C11/L	26/6	12:44 96-72 km; O. K.
S-C12/H	26/6	13:36 86-71 km; O. K.
S-F10	26/6	14:12 114-26 km (collapse: 28 km); noisy AGC above 70 km; spikes in AGC below.
S-F11	29/6	11:06 112-26 km (collapse: 28 km); noisy AGC above 75 km; spikes in AGC below.
<u>Chaff salvo No. 3:</u>		
S-F12	1/7	21:08 112-30 km (collapse: n.a.).
S-C13/L	1/7	21:28 95-71 km; O. K.
S-C14/H	1/7	22:15 82-62 km; O. K.
S-F13	1/7	23:05 113-28 km (collapse: 29 km);
S-C15/L	1/7	23:34 96-88 km; O. K.
S-C16/H	1/7	23:49 83-67 km; O. K.

S-F14	3/7	11:00 112-26 km (collapse: 28 km).
S-F15	6/7	12:40 105-26 km (collapse: 29 km).
S-F16	8/7	13:00 107-26 km (collapse: 29 km).
S-F17	10/7	12:12 107-26 km (collapse: 28 km).
S-F18	13/7	19:55 106-27 km (collapse: 51 km).
<u>Turbulence/gravity wave salvo:</u>		
S-SA1/L	14/7	08:00 95-0 km; Success.
S-F19	14/7	08:11 108-37 km (collapse: 40 km).

S-F20	14/7	08:32	115-30 km (collapse: n.a.).
S-C17/L	14/7	08:52	95-75 km; O. K.
S-SA2/H	14/7	09:29	96-0 km; Success.
S-C18/L	14/7	09:43	96-78 km; lost track at T + 11 min, reacquired separated cloud at T + 16 min; O. K.
S-C19/H	14/7	10:19	80-63 km; O. K.
S-F21	14/7	11:02	116-28 km (collapse: 34 km).
S-C20/L	14/7	11:30	Dart failure; no ejection of foils.
S-C21/L	14/7	12:03	94-77 km; O. K.
S-SA3/H	14/7	12:55	93-0 km; Success.
S-C22/L	14/7	13:07	Dart failure; no ejection of foils.

EISCAT salvo:

S-SA4/L	15/7	12:32	98-0 km; Success.
S-F22	15/7	12:46	107-30 km (collapse: n.a.).
S-C23/L	15/7	13:06	97-83 km; O. K.

Sodium/chaff salvo:

S-C24/L	15/7	20:30	95-78 km; O. K.
S-F23	15/7	21:01	117-45 km (collapse: n.a.).
S-C25/L	15/7	21:17	97-84 km; O. K.
S-F24	15/7	21:43	112-38 km (collapse: n.a.)
S-C26/L	15/7	22:01	96-83 km; O. K.
S-C27/L	15/7	22:30	95-81 km; O. K.
S-C28/L	15/7	22:54	91-81 km; O. K.

S-F25	17/7	11:00	111-27 km (collapse: 29 km).
S-F26	19/7	11:07	115-85 km; Failure.
S-F27	19/7	11:21	111-25 km (collapse: 28 km).

(Additional information that is not in the Campaign Supplement Handbook of September 1987)

Experiment: PRE(MF) radar (Ramfjordmoen): Success: Yes

Periods of Successful Operation: June 7-19, 21-24, 26-27, 29-30, July 1-15, 17, 27 - Oct

Approximate Date When First Results are Available: Today

In What Form: Magnetic tapes with 5 min profiles, or 1-h profiles, or tidal characteristics (1D and 4D fits). All with 3 km resolution, tabulations or time series plots, or vector plots available for any intervals upon request.

Experiment: MF-Radar (Saskatoon): Success: Yes

Periods of Successful Operation: 1 June - 1 December

Approximate Date When First Results are Available: Today

In What Form: Magnetic tapes with 5 min profiles, or 1-h profiles, or tidal characteristics (1D and 4D fits). All with 3 km resolution, tabulations or time series plots, or vector plots available for any intervals upon request.

Experiment: 2.2 MHz Partial Reflection (Volgograd): Success: Yes

Periods of Successful Operation:

Approximate Date When First Results are Available:

In What Form:

Experiment: <u>Riometers</u> at	- Hornsund	77° 00'N	15° 36'E
	- Kevo	69 45	27 01
	- Kilpisjärvi	69 03	20 47
	- Ivalo	68 36	27 25
	- Sodankylä	67 25	26 24
	- Apukka	66 34	26 01
	- Oulu	65 06	25 59
	- Höytiä	62 24	25 22
	- Nurmijärvi	60 31	24 39

Success: Yes

Periods of Successful Operation: Campaign period (continuous)

Approximate Date When First Results are Available: Today

In What Form: Listings of absorption at the first minute of each hour and of maximum absorption during each hour. Paper recordings at 60 mm/h from Kilpisjärvi and Sodankylä also digital recordings with 1 s resolution.

Experiment: Riometer (Kiruna): Success: Yes

Periods of Successful Operation: Campaign period without 2/3 July

Approximate Date When First Results are Available: Today

In What Form: Paper recordings, tape.

Experiment: Magnetometer (Kiruna): Success: Yes

Periods of Successful Operation: Campaign period without 10-13 July

Approximate Date When First Results are Available: Today

In What Form: Paper recordings, tape.

Experiment: Radio Wave Absorption (Volgograd): Success: Yes

Periods of Successful Operation:

Approximate Date When First Results are Available:

In What Form:

Experiment: Wind in Meteor Zone (Volgograd): Success: Yes

Periods of Successful Operation:

Approximate Date When First Results are Available:

In What Form:

Experiment: Wind in Meteor Zone (Kharkov): Success: Yes
 Periods of Successful Operation: 11 June - 19 July
 Approximate Date When First Results are Available:
 In What Form: Meteor radar phasemeter.

Experiment: Wind in Meteor Zone (Obninsk): Success: Yes
 Periods of Successful Operation: 12 June - 19 July
 Approximate Date When First Results are Available:
 In What Form: Meteor radar phasemeter without coordinates

Experiment: Wind in Meteor Zone (Dushanbe): Success: Yes
 Periods of Successful Operation: Wednesdays from 10 June - 15 July
 Approximate Date When First Results are Available:
 In What Form: Meteor radar phasemeter without coordinates

Experiment: A3-Absorption at 6090 and 1539 kHz (CSSR): Success: Yes
 Periods of Successful Operation: 1 June - 31 August (6090 kHz not on 14 June)
 Approximate Date When First Results are Available: Today
 In What Form: Tables of half-hour averages and absorption at $\chi = 75$.

Experiment: A3-Absorption at 272 kHz (CSSR): Success: Yes
 Periods of Successful Operation: 1 June - 31 August (not on a few days in July)
 Approximate Date When First Results are Available: Today
 In What Form: Tables for several const. zenith angles for June (evaluation slowly progresses).

Experiment: SID-Monitoring (CSSR): Success: Yes
 Periods of Successful Operation: Campaign period
 Approximate Date When First Results are Available:
 In What Form:

Experiment: LF Phase Reflection Heights at 162 kHz (CSSR): Success: Yes
 Periods of Successful Operation:
 Approximate Date When First Results are Available: Today
 In What Form: Tables for $\cos \chi = 0.2$

Experiment: OH*-Temperatures (Wuppertal): Success: Yes
 Periods of Successful Operation: Reasonable quality: 9-19 May, 24 May- 7 June, 29 June -
 23 July: Good quality: 26 July - 8 Aug, 13-22 Aug (with gaps)
 Approximate Date When First Results are Available: Today
 In What Form: Lists of preliminary nightly mean temperatures.

Experiment: OH*-Temperatures at 41.8°N, 42.8°E: Success: Yes
 Periods of Successful Operation: June 21-29, 29-30, July 1-2, 5, 17, 18-19, 20-21, 27
 Approximate Date When First Results are Available: Today
 In What Form: Hard copies.

Experiment: Fmin at Moscow, Kalinigrad, Rostov-on-Don, Arkhangelsk: Success: Yes
 Periods of Successful Operation: During campaign period
 Approximate Date When First Results are Available: Today
 In What Form: Hard copies.

Experiment: Sodium Lidar (University of Bonn): Success: Yes
 Periods of Successful Operation: 08 Jul 2210-0002 UT 06 Aug 1900-2248
 14 Jul 0741-2315 07 Aug 1959-2400
 15 Jul 1840-2204 08 Aug 0002-0102

24 Jul 2010-0001	08 Aug 1249-1405
25 Jul 0013-0158	08 Aug 1829-2400
25 Jul 1330-0001	09 Aug 0002-0111
26 Jul 0002-1341	09 Aug 1113-1340
29 Jul 1507-1729	09 Aug 1829-2400
30 Jul 1526-1617	10 Aug 0003-0149
31 Jul 1206-1258	12 Aug 2250-2400
01 Aug 0941-1232	13 Aug 2036-2124
05 Aug 1241-2400	14 Aug 2040-2400
06 Aug 0005-1248	15 Aug 0002-0031

Temperature measurements from 5 August

Approximate Date When First Results are Available: 15 Jan 1988: List of sudden sodium layers
 15 Feb 1988: Plots of initial NA-density profiles
 15 Mar 1988: Plots of initial temperature profiles

In What Form: See above.

3. MAC/EPSILON

This campaign was planned as a case study of middle atmosphere turbulence by means of instrumented sounding rockets, meteorological rockets and ground-based observations. The campaign comprised four salvos in which all rocket and ground-based techniques were concentrated in time and space to make detailed measurements during events with strongly developed turbulence. During the campaign period the ground-based techniques were exploited to map the general behavior of the middle atmosphere during autumn/early winter conditions. The campaign took place in the period 12 October - 15 November 1987.

3.1 Overview of the MAC/Epsilon Campaign

Four salvos were launched during the campaign:

Day Salvo: 15 October

- Launch criteria:
- Presence of turbulence (PRE, SOUSY)
 - Presence of gravity waves (PRE, EISCAT, LIDAR)
 - Riometer absorption between 0.2 and 2 dB
 - Clear sky sufficient for LIDAR results

All launch criteria fulfilled.

Night Salvo A: 21 October

- Launch criteria:
- Presence of turbulence (PRE, SOUSY)
 - Presence of gravity waves (PRE, EISCAT, LIDAR)
 - Riometer absorption between 0.2 and 2 dB
 - Clear sky sufficient for LIDAR results

All launch criteria fulfilled.

Night Salvo A1: 28 October

- Launch criteria:
- Presence of turbulence (PRE, SOUSY)
 - Presence of gravity waves (PRE, EISCAT, LIDAR)
 - Riometer absorption between 0.2 and 2 dB
 - Presence of pulsating aurora
 - Clear sky sufficient for LIDAR results

All launch criteria fulfilled.

Night Salvo B: 12 November

- Modified launch criteria:
- Presence of turbulence (PRE, SOUSY)
 - Presence of gravity waves (PRE)
 - Riometer absorption between 0.2 and 2 dB

Modified launch criteria fulfilled.

Success rates of rockets:

Falling spheres:	11 successful out of 12	Success rate: 92%
Chaff:	7.5 successful out of 9	Success rate: 83%
Instrumented rockets:	52 successful instruments out of 55	Success rate: 95%

3.2 Rocket Launches:

Day Salvo:

<u>Rocket Designation:</u>	<u>Launch Time:</u> UT	<u>Height:</u> km	<u>Comments:</u>
MAC-E-F1 (Viper 3a)	87.10.15 10:47:00	113.5	Success
MAC-E-T1 (Bugatti)	87.10.15 10:52:00	127.0	Success
TY1-1690 30.038 UE(XRG)	87.10.15 10:52:20	81	Success
TY2-1691 31.063 UE(NEFS)	87.10.15 10:52:40	181	Success
MAC-E-C1/L (Str.Super/Loki)	87.10.15 10:57:00	86.7-75.5	Success
TY1-1696(FS Str.Super/Loki)	87.10.15 11:32:00	93.4	Success
MAC-E-C2/H(Str.Super/Loki)	87.10.15 11:33:00	96.3	Failure: No chaff ejected
TY1-1697(FS Str.Super/Loki)	87.10.15 12:14:00	95.7	Success
MAC-E-C3/SL(Viper 3A)	87.10.15 13:08:00	113.5-87.9	Success
MAC-E-C 4/L(Str.Super/Loki)	87.10.15 13:32:00	83.9-69.3	Success

Test Flight 1:

<u>Rocket Designation:</u>	<u>Launch Time:</u> UT	<u>Height:</u> km	<u>Comments:</u>
MAC-E-C5/SL (Viper 3A)	87.10.17 11:38:00	106.4-85.1	Success

Night Salvo A:

<u>Rocket Designation:</u>	<u>Launch Time:</u> UT	<u>Height:</u> km	<u>Comments:</u>
MAC-E-F2 (Viper 3A)	87.10.21 21:28:00	112.5	Success
MAC-E-T2 (Iomas)	87.10.21 21:33:00	126	Partial success
MAC-E-T3 (Bugatti)	87.10.21 21:33:20	125.6	Partial success
TY2-1694 31.066 GE(Exert)	87.10.21 21:33:40	122.1	Success
TY1-1688 30.036 UE(MAE)	87.10.21 21:34:00	89	Success
TY2-1692 31.064 UE (NEFS)	87.10.21 21:34:20	179.2	Success
MAC-E-C6/SL (Viper 3A)	87.10.21 21:46:00	101.2	Partial success
TY1-1698(FS Str.Super/Loki)	87.10.21 22:08:00	89.5	Success
TY1-1699(FS Str.Super/Loki)	87.10.21 22:28:00	90.5	Success
MAC-E-C7/L (Str.Super/Loki)	87.10.21 22:37:00	82	Success
MAC-E-C8/SL (Viper 3A)	87.10.21 23:21:00	102.3	Success

Night Salvo A1:

<u>Rocket Designation:</u>	<u>Launch Time:</u> UT	<u>Height:</u> km	<u>Comments:</u>
TY1-1700(FS Str.Super/Loki)	87.10.28 00:11:00	92	Success
TY2-1695 31.067 GE (Exert)	87.10.28 00:21:00	119.2	Success
TY1-1701 (FS Str.Super/Loki)	87.10.28 00:31:00	90.7	Success

Test Flight 2:

<u>Rocket Designation:</u>	<u>Launch Time:</u> UT	<u>Height:</u> km	<u>Comments:</u>
MAC-E-C9/L (Str.Super/Loki)	87.11.01 14:30:00	82	Success

Night Salvo B:

<u>Rocket Designation:</u>	<u>Launch Time:</u> UT	<u>Height:</u> km	<u>Comments:</u>
MAC-E-F3 (Viper 3A)	87.11.11 23:58:00	106.8	Failure
MAC-E-F4 (Viper 3A)	87.11.12 00:16:00	105.2	Success
MAC-E-T4 (Iomas)	87.11.12 00:21:00	126	Success
MAC-E-T5 (Bugatti)	87.11.12 00:21:20	124.2	Partial success
TY1-1689 30.037 UE (MAE)	87.11.12 00:21:43	87.3	Success
TY2-1693 31.065 UE (NEFS)	87.11.12 00:22:00	181.4	Success
TY1-1702 (FS Str.Super/Loki)	87.11.12 00:41:00	95.4	Success
TY1-1703 (FS Str.Super/Loki)	87.11.12 01:01:00	89.8	Success

3.3 Rocket Launches in the USSR

HEISS ISLAND	VOLGOGRAD
	08 Oct
12 Oct	
14 Oct	14 Oct
16 Oct	16 Oct
19 Oct	19 Oct
21 Oct	
23 Oct	23 Oct
26 Oct	26 Oct
28 Oct	28 Oct
30 Oct	30 Oct
02 Nov	02 Nov
04 Nov	04 Nov
06 Nov	06 Nov
09 Nov	09 Nov
11 Nov	11 Nov
13 Nov	13 Nov
16 Nov	16 Nov
18 Nov	18 Nov
20 Nov	20 Nov

Parameters Measured: Profiles of temperature, wind, electron concentration all to 80-85 km.
At Volgograd also turbulent energy dissipation rate at 75-80 km.

3.4 Reports on Ground-Based Measurements

Experiment: PRE (Ramfjordmoen): Success: Yes
Periods of Successful Operation:
Approximate Date When First Results are Available: 1988
In What Form: REMAR-Plots

Experiment: PRE 9MF0 Radar (Ramfjordmoen): Success: Yes
Periods of Successful Operation: 12-15 Oct, 17 Oct - 9 Nov, 11-12 Nov, 19-22 Nov
Approximate Date When First Results are Available: January 1988
In What Form: Magnetic tapes with 5 min profiles, or 1-h profiles, or tidal characteristics (1D and 4D fits). All with 3 km resolution. Tabulations or time series plots, or vector plots available for any intervals upon request.

Experiment: 2.2 MHz Partial Reflection (Volgograd): Success: Yes
Periods of Successful Operation:
Approximate Date When First Results are Available:

In What Form:

Experiment: SOUSY: Success: Yes

Periods of Successful Operation:

Approximate Date When First Results are Available: 1988

In What Form:

Experiment: EISCAT: Success: Yes

Periods of Successful Operation: 15 Oct 0910-2300 UT

29 Oct 0100-0700 UT

16 Oct 1600-2300

29 Oct 2324-2400

18 Oct 1600-2300

30 Oct 0000-0400

19 Oct 1800-2400

30 Oct 2132-2400

21 Oct 2130-2255

03 Nov 0100-0200

23 Oct 1800-2400

03 Nov 0219-0700

25 Oct 1800-2400

04 Nov 0100-0700

26 Oct 1800-2400

05 Nov 0100-0700

27 Oct 1800-2400

Approximate Date When First Results are Available: Feb 1988

In What Form: Color plots or other (on request).

Experiment: MF-Radar (Saskatoon): Success: Yes

Periods of Successful Operation: 1 June - 1 December

Approximate Date When First Results are Available: Today

In What Form: Magnetic tapes with 5 min profiles, or 1-hour profiles, or tidal characteristics (1D and 4D fits). All with 3 km resolution. Tabulations or time series plots, or vector plots, available for any intervals upon request.

Experiment: <u>Riometers</u> at	- Hornsund	77° 00'N	15° 36'E
	- Kevo	69 45	27 01
	- Kilpisjärvi	69 03	20 47
	- Ivalo	68 36	27 25
	- Sodankylä	67 25	26 24
	- Apukka	66 34	26 01
	- Oulu	65 06	25 59
	- Höytiä	62 24	25 22
	- Nurmijärvi	60 31	24 39
	- Vidsel	65 80	20 62
	- Abisko	68 21	18 50
	- Ramfjord	69 43	19 23
	- Andoya	69 18	16 10
	- Siglufjörður	66 09	18 55

Success: Yes

Periods of Successful Campaign period (Continuous)

Approximate Date When First Results are Available: Today

In What Form: Listings of absorption at the first minute of each hour and of maximum absorption during each hour. Paper recordings at 60 mm/h from Kilpisjärvi and Sodankylä also digital recordings with 1 s resolution.

Experiment: Riometer (Kiruna): Success: Yes

Periods of Successful Operation: Campaign period

Approximate Date When First Results are Available: Today

In What Form: Paper recordings, tape.

Experiment: Radio Wave Absorption (Volgograd): Success: Yes

Periods of Successful Operation:

Approximate Date When First Results are Available:

In What Form:

Experiment: Wind in Meteor Zone (Volgograd): Success: Yes

Periods of Successful Operation:

Approximate Date When First Results are Available:

In What Form:

Experiment: HF-Circuit: Success: Yes

Periods of Successful Operation: 07-15 Oct, 23 Oct - 15 Nov

Approximate Date When First Results are Available:

In What Form:

Experiment: Ionosonde (Andenes): Success: Yes

Periods of Successful Operation: Campaign period

Approximate Date When First Results are Available: Feb 1988

In What Form:

Experiment: Ionosonde (Ramfjordmoen): Success: Yes

Periods of Successful Operation: Campaign period, every 20 or 10 minutes

Approximate Date When First Results are Available:

In What Form:

Experiment: A3-Absorption at 6090 and 1539 kHz (CSSR): Success: Yes

Periods of Successful Operation: Campaign period (Continuous)

Approximate Date When First Results are Available: Today

In What Form: Tables or half-hour averages.

Experiment: A3-Absorption at 272 kHz (CSSR): Success: Yes

Periods of Successful Operation: Campaign period (Continuous)

Approximate Date When First Results are Available: Will be evaluated on request only

In What Form:

Experiment: SID-Monitoring (CSSR): Success: Yes

Periods of Successful Operation: Campaign period

Approximate Date When First Results are Available:

In What Form:

Experiment: Riometer (Andenes): Success: Yes

Periods of Successful Operation: Campaign period

Approximate Date When First Results are Available: Feb 1988

In What Form: Listings or plots (on request)

Experiment: Riometer (Ramfjordmoen): Success: Yes

Periods of Successful Operation: Campaign period

Approximate Date When First Results are Available:

In What Form:

Experiment: Magnetometer (Andenes): Success: Yes

Periods of Successful Operation: Campaign period

Approximate Date When First Results are Available: Feb 1988

In What Form: Listings or plots (on request)

Experiment: Magnetometer (Ramfjordmoen): Success: Yes

Periods of Successful Operation: Campaign period

Approximate Date When First Results are Available:

In What Form:

Experiment: OH*-Temperatures (Wuppertal): Success: Yes

Periods of Successful Operation: Good quality: 26 July-8 Aug, 13-22 Aug (with gaps) 1 Sep-6 Oct, 11-31 Oct Varying quality with several gaps: 1 Nov - 13 Dec

Approximate Date When First Results are Available: Today

In What Form: Lists of preliminary nightly mean temperatures

Experiment: Sodium LIDAR (University of Bonn): Success: Yes

Periods of Successful Operation:	14 Oct 1915-2400 UT	25 Oct 1600-2200
	15 Oct 0000-0730	27 Oct 1945-2400
	15 Oct 1050-1330	28 Oct 0000-0050
	19 Oct 0515-1000	30 Oct 1310-1630
	19 Oct 1600-1900	10 Nov 0100-0115
	21 Oct 1300-2400	10 Nov 1730-1800
	22 Oct 0000-2220	12 Nov 1500-2400
	23 Oct 1850-2400	13 Nov 0000-0800
	24 Oct 0000-0140	

Approximate Date When First Results are Available: 15 Jan 1988: List of sudden sodium layers
15 Feb 1988: Plots of initial NA-density profiles
15 Mar 1988: Plots of initial temperature profiles

In What Form: See above.

Experiment: ULIDAR: Success: Yes

Periods of Successful Operation:	31 Oct 1601-1615 UT	08 Nov 0000-2400
	04 Nov 1341-2400	09 Nov 0000-2233
	05 Nov 0000-2400	11 Nov 1854-2316
	06 Nov 0000-2400	13 Nov 0800-0934
	07 Nov 0000-2400	

Approximate Date When First Results are Available: Today

In What Form:

Experiment: Photometer (ARR): Success: Yes

Periods of Successful Operation: Night salvo A, Exert Salvo

Approximate Date When First Results are Available:

In What Form:

Experiment: All-Sky 35 mm Camera (ARR): Success: Yes

Periods of Successful Operation: Night salvo A

Approximate Date When First Results are Available:

In What Form:

Experiment: All-Sky Video Camera (ARR): Success: Yes

Periods of Successful Operation: Night salvo A, Night salvo A1

Approximate Date When First Results are Available:

In What Form:

Experiment: Stereo OH TV: Success: Partial

Periods of Successful Operation:

Approximate Date When First Results are Available:

In What Form:

3.5 CONCLUSION

Considering the complexity of the campaign and the launch criteria, we must conclude that the results are very satisfactory. We have achieved our main goal, to bring home a unique

set of scientific data which we hope will bring us a significant step further in our studies of the middle atmosphere.

A joint analysis of the data will be organized by the project scientist and the campaign participants. The first of a series of data meetings was held in Oslo on 25-26 February 1988. Some preliminary results will be presented in a half-day session in COSPAR Symposium 6 "The Middle Atmosphere After MAP" to be held in Helsinki 18-23 July 1988.

Appendix 6

MIDDLE ATMOSPHERE ELECTRODYNAMICS (MAE)

R. A. Goldberg, Coordinator

MAE has shown remarkable progress in the last two years, considering that most critical measurements must be accomplished with *in situ* probes aboard balloons and rockets. This restriction severely limits the amount of available data that can be acquired which in turn, retards the rate of progress toward new findings. However, by careful selection of geophysical conditions under which to make soundings, by coordination with ground based and satellite observatories, and by employment of new techniques such as long duration balloons, many obstacles have been overcome to permit important advances in the field.

The apparent large (V/m) electric fields observed intermittently in the lower mesosphere have been a principal driver for MAE during the entire MAP era, but are still considered to be controversial. Recently, a new theory [Curtis, 1987] has offered a mechanism to explain the horizontal V/m fields by invoking wind-induced drag effects on charged aerosols, which helps lend credence to their reality. A new rocket program, NLC-90, is in the planning stage for Kiruna in the summer of 1990; this will test the Curtis theory as one of its goals by observing winds, electric fields, and aerosols simultaneously in a noctilucent cloud (NLC) environment. Goldberg [1988] has already reported electric field perturbations within an NLC measured during MAED, a program conducted in Kiruna during July, 1986.

Horizontal electric fields within the stratosphere and mesosphere are normally thought to map down from the magnetosphere, based on early balloon measurements by Mozer [1971] and later measurements by Ogawa et al. [1975]. Now Holzworth [1987], using long duration balloons in the southern hemisphere, has reported that the stratospheric horizontal electric field was observed to rotate with a period expected for quasi-inertial waves in the neutral atmosphere, implying that some of the horizontal electric field properties are governed by local neutral atmospheric control. Other balloon measurements have observed strong vertical electric field reversals above "non-electrical" storm systems [Barcus et al., 1987], similar to those reversals observed earlier above thunderstorms [Holzworth, 1981].

Rocket measurements of MAE parameters above thunderstorms have also been actively pursued in the last two years. No less than three independent rocket programs have been conducted from Wallops Island, VA, with emphasis on the influence of VLF waves caused by lightning on magnetospheric electron precipitation. The most concerted effort was the WIPP Program, conducted in July, 1987. Results reported at the Fall AGU meeting in December, 1987 (San Francisco), imply that individual electron bursts are usually too weak to be observed on a regular basis, but do occur at a low level for most lightning strokes.

Balloons have also been used extensively to monitor changes in electrical conductivity [Gupta and Narayan, 1987; Byrne et al., 1988]. Byrne et al. have observed wide variations of ion conductivity in the lower stratosphere which cannot be accounted for by variations in cosmic ray flux, and attribute such changes to variations in local aerosol population. New studies of satellite data [Baker et al., 1987] now imply the existence of highly relativistic electron precipitation events following solar maximum, which would be another source for severe modulation of MAE parameters [Hale, 1987]. A rocket experiment (MAC-REP) to study such events is currently being planned for launch from Poker Flat, Alaska in 1979.

Turbulence in the mesosphere caused by gravity waves of tropospheric origin has been a question of active interest [e.g., Thrane et al., 1987]. From MAE-3, conducted at Poker Flat, Alaska, in March, 1985, new results show the characteristics of both the fine scale turbulence [Blood et al., 1988] and the large scale waves [Goldberg et al., 1988] caused by gravity waves. MAC/Epsilon, conducted in Andøya, Norway during October-November, 1987, has provided a more sophisticated study of these problems, thereby continuing to demonstrate how the middle atmospheric plasma environment interacts with the neutral environment, and how the plasma can be used to track neutral dynamics within this region.

Preliminary results from MAC/Epsilon are to be presented at the COSPAR XXVII MAP Symposium.

Finally, much activity has revolved around the need and definition for a geoelectric index, which is one topic of concern voiced by the IAGA Working Group IIA on MAE. The American Geophysical Union (AGU), through its Committee on Atmospheric and Space Electricity (CASE) sponsored a special session on this subject during the Fall AGU Meeting in San Francisco in 1986. The AGU publication EOS also featured an article on this topic by Holzworth and Volland [1986]. One promising approach to this problem could be through the monitoring of global lightning by measurement of Schumann resonances in ELF radio waves within the Earth-ionosphere cavity [Sentman, 1983]. New results now indicate that Schumann resonance line widths are also responsive to magnetospheric relativistic electron populations [Sentman and Baker, 1987].

The above listed progress demonstrates that MAE is now expanding, as new discoveries, results, and theories enhance its progress. Hopefully, both the planned and as yet, unplanned programs of the future will permit this momentum to continue.

References:

- Baker, D. N., J. B. Blake, D. J. Gorney, P. R. Higbie, R. W. Klebesadel, and J. H. King, *Geophys. Res. Lett.*, **14**, 1027, 1987.
- Barcus, J. R., I. Iversen, and P. Stauning, *J. Geophys. Res.*, **91**, 9881, 1986.
- Blood, S. P., J. D. Mitchell, C. L. Croskey, T. D. Raymund, E. V. Thrane, T. A. Blix, U. P. Hoppe, D. C. Fritts, and F. J. Schmidlin, *J. Atmos. Terr. Phys.*, **50**, (In Press), 1988.
- Byrne, G. J., J. R. Benbrook, E. A. Bering, D. Oro, C. O. Seubert, and W. R. Sheldon, *J. Geophys. Res.*, **93**, 3879, 1988.
- Curtis, S. A., *IAGA Abstracts, IUGG XIX General Assembly*, Vancouver, B. C. Canada, August, 1987.
- Goldberg, R. A., *J. Geophys. Res.*, **93**, (In Press), 1988.
- Goldberg, R. A., D. C. Fritts, H. -G. Chou, J. R. Barcus, and F. S. Schmidlin, *J. Atmos. Terr. Phys.*, **50**, (In Press), 1988.
- Gupta, S. P., and A. Narayan, *Planet. Space Sci.*, **35**, 439, 1987.
- Hale, L. C., *IAMAP Abstracts, IUGG XIX General Assembly*, Vancouver, B. C. Canada, August, 1987.
- Holzworth, R. H., *J. Atmos. Terr. Phys.*, **43**, 1115, 1981.
- Holzworth, R. H., *IAGA Abstracts, IUGG XIX General Assembly*, Vancouver, B. C., Canada, August, 1987.
- Holzworth, R. H., and H. Volland, *EOS Trans. AGU*, **67**, 545, 1986.
- Mozer, F. S., *Pageoph.*, **84**, 32, 1971.
- Ogawa, T., Y. Tanaka, A. Hutzita, and M. Yasuhara, *Planet. Space Sci.*, **23**, 825, 1975.
- Sentman, D. D., *J. Atmos. Terr. Phys.*, **45**, 55, 1983.
- Sentman, D. D. and D. N. Baker, *Abstracts IUGG XIX General Assembly*, p. 523, Vancouver, B. C., Canada, August, 1987.
- Thrane, E. V., T. A. Blix, C. Hall, T. L. Hansen, U. von Zahn, W. Medyer, P. Czechowsky, G. Schmidt, H. -U. Widdel, and I. A. Neumann, *J. Atmos. Terr. Phys.*, **49**, 751, 1987.

Appendix 7

REPORT ON PROGRESS WITH MASH PROJECT

A. O'Neill

(1) A report on the findings of the Williamsburg 1986 workshop, edited by W. L. Grose and A. O'Neill, on the intercomparison of data and derived quantities for the middle atmosphere of the Southern Hemisphere is in preparation. Expected completion date is October 1988.

(2) Proceedings of the MASH Meeting, held in Adelaide, Australia, 18-20 May 1987, are in the press for a special issue of the Journal of Pure and Applied Geophysics, which will also contain papers from the GRATMAP Meeting held at the same venue.

(3) The next meeting in furtherance of the MASH project will be held from 17 through 19 April 1989, probably at Lake Arrowhead, California (a resort owned by the University of California, Los Angeles). It will immediately follow the Middle Atmosphere Meeting, in San Francisco, organized by the American Meteorological Society. The MASH Meeting is being organized around a series of in-depth, invited talks to be given by many of the leading experts in the field. Funds to support the meeting (mainly for graduate students) are being sought from NASA and NATO. Dr. A. O'Neill, Meteorological Office, London Road, Bracknell, RG12 2SZ, UK, is the Coordinator and Prof. C. R. Mechoso, Dept. of Atmospheric Sciences, University of California, Los Angeles, CA 90024, is the Local Organizer.

Appendix 8

NEW INTERNATIONAL EQUATORIAL OBSERVATORY (NIEO)

S. Kato

- 1. Survey
 - a. July 21 - August 4, 1987
S. Kato, S. Fukao, A. Sumi, T. Tsuda, T. Sato
 - b. Soil property, electrical noise temperature variation, metal erosion
 - c. Electrical power supply
 - d. Logistics
- 2. Antenna Design
RASC, universities, industry
- 3. Administrative Business
 - a. Interview with Indonesian Minister of Research and Technology, Prof. Dr. Habibie for promoting our NIEO plan (see following writeup which appeared in The Jakarta Post, May 14, 1988).
 - b. Invitation by RASC and LAPAN to Indonesian university people concerned with organizing a group for studying radar atmospheric physics at the equator.

"Habibie approves radar station in Pontianak

Jakarta (Antara): Minister of Research and Technology B. J. Habibie has approved the installation of a radar station for the observation of the equatorial atmosphere at the Sinatan Hulu village in Pontianak, West Kalimantan.

The construction and the operation of the radar station will be handled by the Indonesian National Aeronautic and Space Agency (LAPAN) in cooperation with the Atmosphere Radio Scientific Center of the Kyoto University, Japan, LAPAN Head Ir. J. Soegiyo said here Wednesday.

The approval given by Habibie constitutes a moral support which is expected by the Kyoto University to foster the Japanese Government to pay greater attention to the proposal for the construction of the radar station, according to Soegiyo.

The atmosphere observation radar, which is estimated to be completed at a cost of over Rp 100 billion, will have 2,536 antennae that can monitor equatorial atmosphere up to an altitude of 1000 km. The radar station will operate 24 hours a day.

An atmosphere observation radar which is found in Kyoto, Japan, has 457 antennae and can be used to monitor atmosphere up to an altitude of 400 km. Similar radar stations are found in Chung Li (Taiwan) and Adelaide (Australia).

A number of LAPAN experts are now in Japan to study everything concerning atmosphere as part of preparations for the installation and operation of the radar station at West Kalimantan."

Appendix 9

SUPER CAMP

E. Kopp

The main objective of Super CAMP was a study of the cold arctic mesopause in the region of the occurrence of polar mesospheric clouds (PMC) by using *in situ* measurements with sounding rockets combined with ground-based instrumentation and satellite observation. The selected and proposed sounding rocket payloads to NASA for Thule AB, Greenland, were not accepted in their 1990 program. The earliest year for a possible support of rocket launchings from the remote rocket launching place, Thule, by NASA would be summer 1992.

After this decision taken by NASA in late 1987, the scientists involved have discussed a new project NLC-90 for summer 1990 with the launchings of a smaller number of sounding rockets from Esrange in July/August 1990. The NLC-90 project differs from Super CAMP. Its objective is mainly to investigate the electrodynamical properties in the presence of a NLC and the possible relationships to the transport, waves, and turbulent structures of the summer high latitude mesopause. NLC-90 has to be supported by ground-based radars (EISCAT, MWR, etc.), by lidar and microwave measurements near the rocket range and by NLC-observation on an airplane south of Kiruna. A possible coordination with other rocket campaigns in summer 1990 from ranges at high latitudes (Andenes, Heiss Island) will be investigated at the second NLC-90 project meetings in Espoo, July 25, 1988, and in Tallin at the NLC-Workshop July 27-31, 1988.

Appendix 10

GLOBUS NO_x

J. P. Pommereau

The objective of the program was a coordinated observation of nitrogen oxides and related species in the atmosphere by independent and complementary instruments. The field campaign which was held in September 1985 above Southern France, involved 39 experiments distributed among 7 balloons, 5 satellites and 5 observatories on the ground. As a first step, the measurements have been analyzed and compared in order to better understand the performances of the various instruments or methods. As a result, several causes of systematic errors have been identified and reduced. Final uncertainties have been assessed and a self-consistent data set of nitrogen oxides, related species like ozone and atmospheric parameters required for further interpretation, has been issued. The data base now available for photochemical investigations, will be completed in the near future with the few missing results which require still further treatment or checks at the laboratory.

The photochemical analysis of the data is conducted by comparison between experimental results and model predictions. As examples, the ratio between NO and NO₂ in the stratosphere appears larger than that expected; the observed diurnal variation of NO in the late afternoon would require a progressive reduction of NO₂, the photolysis rate of NO₂, which might originate in the multiple scattering of the solar photons by the lower atmosphere at large zenith angle; the NO_x concentration defined as the sum of NO and NO₂, is found in the upper troposphere ten times larger than predicted. A source, tentatively identified as emission from aircrafts, is required. The analysis will be further followed and the data will be made available upon request to scientific groups interested in the interpretation.

Publications

Measurements of Stratospheric Ozone During the MAP/GLOBUS NO_x Campaign, D.Robbins, P.Aimédiu, J.Pelon, J.P.Pommereau, F.Goutail, N.Iwagami, K.Shibasaki, T.Ogawa, M.Koike, P.Marché, J.P.Naudet, P.Rigaud, D.Huguenin, J.Lenoble, G.Maddrea Jr, Submitted J.Gephys.Res, 1988

Comparison of Stratospheric and Mesospheric Ozone Profiles Obtained by Groun-Based and Satellite Observations, J.de La Noe, M.Koike, T.Ogawa, P.Marché, Submitted Quad. Ozone Symp, 1988

Intercomparison of NO Column Measurements During MAP/GLOBUS 1985, R.L.McKenzie, W.A.Matthews, Y.Kondo, R.Zander, P. Demoulin, P.Fabian, D.G.Murcray, F.J.Murcray, O.Lado-Bordowsky, C.Camy-Peyret, H.K.Roscoe, J.A.Pyle, R.D.McPeters, Submitted to J.Atmos.Chemistry, 1988

A NO_x Source in the Upper Troposphere ?, J.P.Pommereau, F.Goutail, Y.Kondo, W.A.Matthews, M.Helten, Submitted to Quad.Ozone Symp., 1988

Nitric Oxide Profiles Measured In Situ During the GLOBUS 85 Campaign, W.A.Matthews, Y.Kondo, P.Fabian, and B.C.Kruger, Submitted to J. Atmos. Chemistry, 1988

Diurnal Variation of Nitric Oxide at 32 km: Measurements and Interpretation, Y.Kondo, W.A.Matthews, P.Aimédiu, D.E.Robbins, J. Geophys.Res. in Press, 1988

Diurnal Variation of Stratospheric NO and NO₂ from MAP/GLOBUS 1985,
J.P.Naudet, M.Pirre, R.Ramaroson, P.Rigaud, P.Fabian, M.Helten, N.Iwagami,
K.Shibasaki, T.Ogawa, Y.Kondo, W.A.Matthews, J.P.Pommereau, F.Goutail,
P.C.Simon, W.Peetermans, Submitted to Quad.Ozone Symp, 1988

**SAGE 2 Nitrogen Dioxide Data Comparison With Infra-Red and Visible
Balloon Remote Sensing Measurements During GLOBUS NOX, J.Lenoble,**
W.P.Chu, D.G.Murcray, O.Lado-Bordowski, C.Camy-Perret, A.Perrin, J.P.Pommereau,
F.Goutail, K.Shibasaki, N.Iwagami, and P.C.Simon, Submitted to Quad.Ozone Symp.,
1988

**Balloon Observations of Nitrogen Dioxide by Visible Occultation During
GLOBUS NOX, J.P.Pommereau, F.Goutail, N.Iwagami, K.Shibasaki, P.C.Simon,**
W.Petermans, J.P.Naudet, P.Rigaud, D.Huguenin, Submitted to J.Atmos.Chemistry, 1988

**Measurements of Column Abundances of Nitrogen Dioxide, NO₂, from the
Ground during the GLOBUS NOX Campaign, R.Zander, P.Demoulin, G.Roland,**
W.A.Matthews, P.V.Johnston, J.P.Pommereau, N.Iwagami, K.Shibasaki, Submitted to
Quad. Ozone Symp, 1988

Appendix 11

PUBLICATIONS WITH RESULTS OF THE PROJECT MAP/WINE

U. von Zahn

- Belikovitch, V. V., E. A. Benediktov, N. P. Goncharov, L. V. Grishkevich, and V. D. Vyakhirev, A study of the winter-time D-region using the partial reflection technique, *J. Atmos. Terr. Phys.*, **48**, 1241-1245, 1986.
- Blix, T. A., E. V. Thrane, and O. Andreassen, Spectral characteristics of positive ion-current fluctuations measured by ion-probes, Proc. 7th ESA Symp. on European Rocket and Balloon Programmes and Related Research, *ESA SP-229*, 271-273, 1985a.
- Blix, T. A., E. V. Thrane, and O. Andreassen, Middle atmosphere turbulence as determined by ion-probes, Proc. 7th ESA Symp. on European Rocket and Balloon Programmes and Related Research, *ESA SP-229*, 371-375, 1985b.
- Brückelmann, H. G., K. U. Grossmann, and D. Offermann, Rocket-borne measurements of atmospheric infrared emissions by spectrometric techniques, *Adv. Space Res.*, **7**(10), 43-46, 1987.
- Bugajeva, I. W., D. A. Tarasenko, and L. A. Rjasanova, Large scale processes and energetic characteristics of the stratosphere during the MAP/WINE experiment, *Meteorol. Hydrologol.* **6**, 21-25, 1986.
- Czechowsky, P., and R. Rüster, Power spectra of mesospheric velocities in polar regions, *Handbook for MAP*, **18**, 207-211, 1985.
- Czechowsky, P., R. Rüster, and G. Schmidt, First results of VHF-radar measurements during the MAP/WINE Campaign, *Adv. Space Res.*, **4**(4), 47-50, 1984.
- Dickinson, P. H. G., G. Witt, A. Zuber, D. Murtagh, K. U. Grossmann, H. G. Brückelmann, P. Schwabbauer, K. D. Baker, J. C. Ulwick, and R. J. Thomas, Measurements of odd oxygen in the polar region on 10 February 1984 during MAP/WINE, *J. Atmos. Terr. Phys.*, **49**, 843-854, 1987.
- Ebel, A., H. J. Jakobs, and P. Speth, Turbulent heating and cooling of the mesopause region and their parameterization, *Ann. Geophysicae*, **1**, 359-370, 1983.
- Fricke, K. H., and U. von Zahn, Mesopause temperatures derived from probing the hyperfine structure of the D₂ resonance line of sodium by LIDAR, *J. Atmos. Terr. Phys.*, **47**, 499-512, 1985.
- Gärtner, V., and M. Memmesheimer, Computation of the zonally averaged circulation driven by heating due to radiation and turbulence, *J. Atmos. Terr. Phys.*, **46**, 755-765, 1984.
- Gärtner, V., and M. Memmesheimer, connection between mesopause temperature, circulation and noctilucent clouds, *Handbook for MAP*, **18**, 35-41, 1985.
- Gärtner, V., M. Memmesheimer, and P. W. Blum, A zonal-averaged dynamical model for the middle atmosphere including gravity wave mean flow interaction: Solstice conditions, *Planet. Space Sci.*, **31**, 1465-1478, 1983.
- Gerndt, R., and D. Offermann, Upper mesospheric temperatures over Europe - Seasonal and latitudinal variations, Proc. 14th Ann. Meet. on Upper Atmos. Studies by Optical Methods, Brit. Antarctic Survey, Cambridge, 1986.
- Gerndt, R., D. Offermann, and T. Blix, Upper atmosphere temperatures obtained by infrared spectroscopy, Proc. 13th Ann. Meet. on Upper Atmosphere Studies by Optical Methods, edited by K. Maseide, *Rep. 86-28*, Dept. Physics, Univ. Oslo, Norway, 1986.
- Grossmann, K. U., Middle infrared emission studies in the upper atmosphere by rocket techniques, Proc. 12th Ann. Meet. on Atmos. Studies by Optical Methods, G. Witt, Ed., Univ. Stockholm AP-23, Stockholm, Sweden, 1985.
- Grossmann, K. U., Recent measurements of trace constituents from rocket and balloon probes, *Adv. Space Res.*, in print, 1987.
- Grossmann, K. U., H. G. Brückelmann, and P. Schwabbauer, Measurements of minor constituents infrared emissions in the middle atmosphere during MAP/WINE campaign, Proc. 7th ESA Symp. on European Rocket and Balloon Programmes and Related Research, *ESA SP-229*, 285-290, 1985.

- Grossmann, K. U., H. G. Brückelmann, D. Offermann, P. Schwabbauer, R. Gyger, K. Künzi, G. K. Hartmann, C. A. Barth, R. Thomas, A. F. Chijov, S. P. Perov, V. A. Yushkov, P. Glöde, and K. H. Grasnick, Middle atmosphere abundances of water vapor and ozone during MAP/WINE, *J. Atmos. Terr. Phys.*, **49**, 827-841, 1987.
- Hall, C., T. A. Blix, A. Brekke, M. Friedrich, T. Hansen, S. Kirkwood, J. Röttger, and E. Thrane, MAP/WINE electron density profiles in the D- and E-regions: a comparison of EISCAT, PRE and rocket data, Proc. 7th ESA Symp. on European Rocket and Balloon Programmes and Related Research, *ESA SP-229*, 279-284, 1985.
- Hass, H., Untersuchungen von Scales dynamischer Prozesse als Beitrag zur Parametrisierung des Eddy transports in der mittleren Atmosphäre, Mitteilungen aus dem Institut für Geophysik und Meteorologie der Universität zu Köln, FRG, *Heft 51*, 1986.
- Hass, H., and A. Ebel, Space and time scales of large scale variations in the upper stratosphere and mesosphere as deduced from the PRM of Nimbus 7, *J. Atmos. Terr. Phys.*, **48**, 1073-1083, 1986.
- Hass, H., and W. Meyer, Gravity wave fields above Andoya, *J. Atmos. Terr. Phys.*, **49**, 705-721, 1987.
- Hauchecorne, A., T. Blix, R. Gerndt, G. A. Kokin, W. Meyer, and N. N. Shefov, Large scale coherence of the mesospheric and upper stratospheric temperature fluctuations, *J. Atmos. Terr. Phys.*, **49**, 649-654, 1987.
- Jakobs, H. J., Untersuchungen von Schwerwelleneffekten mit Hilfe eines 3-D Zirkulationsmodells der mittleren Atmosphäre, Mitteilung aus dem Institut für Geophysik und Meteorologie der Universität zu Köln, FRG, *Heft 50*, 1986.
- Jakobs, J. H., and H. Hass, Normal modes as simulated in a three-dimensional circulation model of the middle atmosphere including regional gravity wave activity, *Ann. Geophysicae*, **4A**, 103-114, 1987.
- Jakobs, H. J., M. Bischof, A. Ebel, and P. Speth, Simulation of gravity wave effects under solstice conditions using a 3-D circulation model of the atmosphere, *J. Atmos. Terr. Phys.*, **48**, 1203-1223, 1986.
- Klein, V., and U.-P. Hoppe, the sodium layer above Andoya, Norway, as observed by LIDAR from January through April 1984, Proc. 7th ESA Symp. on European Rocket and Balloon Programmes and Related Research, *ESA SP-229*, 291-295, 1985.
- Kokin, G. A., Experimental studies data on MAP in 1983-84 winter, Central Aerological Observatory Rep., 183 pages, State Committee of the USSR for Hydrometeorology and Control of Natural Environment, Moscow, 1984.
- Kokin, G. A., and S. V. Pachomov, Complex investigations of the middle atmosphere during the winter 1983-84, *Meteorol. Hydrolol.*, **7**, 107-108, 1985.
- Kokin, G. A., and S. V. Pachomov, Turbulent conditions in the D layer during the winter 1983-84, *Geomagn. Aeron.* **26**, 714-717, 1986.
- Kokin, G. A., I. V. Bugajeva, L. A. Rjasanova, D. A. Tarasenko, and A. I. Butko, Preliminary analysis of processes in the middle atmosphere during the experiment "Winter in Northern Europe" (1983/84), *Meteorol. Hydrolol.*, **6**, 38-43, 1985.
- Krankowsky, D., and U. von Zahn, The project "Winter in Northern Europe" of the Middle Atmosphere Program (MAP/WINE), *Handbook for MAP*, **2**, ed. S. K. Avery, Univ. IL, 481-482, 1981.
- Krankowsky, D., P. Lämmerzahl, a. Götzelmann, M. Friedrich, and K. M. Torkar, Positive ion composition in the lower ionosphere at high latitudes during MAP/WINE, *J. Atmos. Terr. Phys.*, **49**, 809-818, 1987.
- Labitzke, K., A. H. Manson, H. G. Mueller, Z. Rapoport, and E. R. Williams, Hemispheric synoptic analysis of 95 km winds during the winter of 1983/84 and comparison with stratospheric parameters, *J. Atmos. Terr. Phys.*, **49**, 6390648, 1987.
- Labitzke, K. < B. Naujokat, R. Lenschow, K. Petzoldt, and A. O'Neill, The second winter of MAP/DYNAMICS, 1983/84, The winter of MAP/WINE, Beilage zur Berliner Wetterkarte **S0 15/84**, 1984.
- Larsen, S. H. H., Ozone measurements during MAP/WINE, Proc. 7th ESA Symp. on European Rocket and Balloon Programmes and Related Research, *ESA SP-229*, 69-72, 1985.

- Lastovicka, J., and K. Svoboda, On the correlation of the midlatitude lower ionosphere with solar and meteorological parameters during the MAP/WINE winter of 1983/84, *Physica Scripta*, in print, 1987.
- Lastovicka, J., and B. A. de La Morena, The response of the lower ionosphere in central and southern Europe to anomalous stratospheric conditions, *Physica Scripta*, in print, 1987.
- Lübken, F.-J., Ch. Pütz, and U. von Zahn, Turbulent parameters of the lower thermosphere as determined by mass spectrometer during the MAP/WINE campaign, Proc. 7th ESA Symp. on European Rocket and Balloon Programmes and Related Research, *ESA SP-229*, 259-265, 1985.
- Lübken, F.-J., U. von Zahn, E. V. Thrane, T. Blix, G. A. Kokin, and S. V. Pachomov, In-situ measurements of turbulent energy dissipation rates and eddy coefficients during MAP/WINE, *J. Atmos. Terr. Phys.*, **49**, 763-775, 1987.
- Matveeva, O. A., and A. I. Semenov, The results of hydroxyl emission observations during MAP/WINE period; stratospheric warming (February 1984), Newsletter, Middle Atmosphere Program, New Delhi, Aruna Printing Press, **3**, 4-6, 1986.
- Matveeva, O. A., and A. I. Semenov, Temperature variations in mesopause during stratospheric warming, *Geomagn. Aeron.*, USSR, **26**, 331-333, 1986.
- Memmesheimer, M., and P. W. Blum, Seasonal and latitudinal changes in atmospheric conditions favouring the formation of polar mesospheric clouds, *Physics Scripta*, in print, 1987.
- Memmesheimer, M., V. Gärtner, and P. W. Blum, Seasonal transitions and possible polar mesospheric cloud regions calculated by a zonally averaged model of the atmosphere, *J. Atmos. Terr. Phys.*, **48**, 1185-1196, 1986.
- Memmesheimer, M., V. Gärtner, P. W. Blum, and K. G. Schuchardt, Model calculations of middle atmospheric wind and temperature fields, *Adv. Space Res.*, **3**, 33-36, 1983.
- Memmesheimer, M., V. Gärtner, G. E. Thomas, and C. P. McKay, The role of horizontally averaged nonlinear transport in zonally averaged models of the middle atmosphere, *Ann Geophys.*, **3**, 187-194, 1985.
- Meyer, W., Intercomparisons of wind measurements performed with metrockets, Proc. 7th ESA Symp. on European Rocket and Balloon Programmes and Related Research, *ESA SP-229*, 55-60, 1985.
- Meyer, W., R. Gerndt, C. R. Philbrick, and F. J. Schmidlin, The middle atmosphere above Andoya, Norway during the winter 1983/84 as derived from metrockets and OH nightglow observations, Proc. 7th ESA Symp. on European Rocket and Balloon Programmes and Related Research, *ESA SP-229*, 41-47, 1985.
- Meyer, W., C. R. Philbrick, J. Röttger, R. Rüster, H. -U. Widdel, and F. J. Schmidlin, Mean state of winds in the winter middle atmosphere above northern Scandinavia, *J. Atmos. Terr. Phys.*, **49**, 675-687, 1987.
- Nestorov, G. Chr., Spasov, M. Todorov, W. Sachariev, L. Milenkova, and L. A. Rjasanova, Disturbances in stratospheric circulation in late December 1984 and their influence on the lower ionosphere, *Bulg. Geophys. Spis.*, **12**, 1986.
- Offermann, D., and R. Gerndt, Upper mesosphere temperatures from OH* emissions, contribution to CIRA 1987, in print, 1987.
- Offermann, D., R. Gerndt, and R. Kuchler, Middle atmosphere temperature measurements as compared to atmospheric models, *Adv. Space Res.*, **7**(10), 97-104, 1987.
- Offermann, D., R. Gerndt, R. Kuchler, K. Baker, W. R. Pendleton, W. Meyer, U. von Zahn, C. R. Philbrick, and F. J. Schmidlin, Mean state and long term variations of temperature in the winter middle atmosphere above northern Scandinavia, *J. Atmos. Terr. Phys.*, **49**, 655-674, 1987.
- Pachomov, S. V., Z. Ts. Rapoport, V. M. Sinelnikov, G. Entzian, G. von Cossart, W. Singer, D. Samardjiyev, and G. Nestorov, On the relationship between processes in the lower ionosphere and the dynamical processes in the neutral atmosphere during the MAP/WINE experiment, *Bulg. Geophys. Spis.*, **12**, 40-48, 1986.
- Petzoldt, K., Large-scale structure of the middle atmosphere during the winter 1983/84, Proc. 7th ESA Symp. on European Rocket and Balloon Programmes and Related Research, *ESA SP-229*, 33-39, 1985.

- Petzoldt, K., R. Lenschow, A. Hauchecorne, G. A. Kokin, W. Meyer, A. O'Neill, C. R. Philbrick, F. Schmidlin, and R. Thomas, large-scale structure of the stratosphere and the lower mesosphere (20 to 60 km) over the Northern Hemisphere during the MAP/WINE campaign, *J. Atmos. Terr. Phys.*, 49, 621-637, 1987.
- Rapoport, Z. Tz., Measurements of middle atmosphere parameters in the USSR under the MAP/WINE project: Data directory, Soviet Geophysical Committee, Academy of Sciences of the USSR, Moscow, 1984.
- Reid, I. M., R. Rüster, and G. Schmidt, VHF radar observations of cat's-eye-like structures at mesospheric heights, *Nature*, 327, 43-45, 1987.
- Röttger, J., and W. Meyer, Tidal wind observations with incoherent scatter radar and meteorological rockets during MAP/WINE, *J. Atmos. Terr. Phys.*, 49, 689-703, 1987.
- R. Rüster, Winds and waves in the middle atmosphere as observed by ground-based radars, *Adv. Space Res.*, 4(4), 3-18, 1984.
- Rüster, R., and J. Klostermeyer, Instabilities and turbulence at mesospheric heights as observed by VHF radar, *Handbook for MAP*, 18, 216-219, 1985.
- Rüster, R., and J. Klostermeyer, Propagation of turbulence structures detected by VHF radar, *J. Atmos. Terr. Phys.*, 49, 743-750, 1987.
- Sachariev, W., M. Martinov, L. Milenkova, and L. A. Rjasanova, Characteristic processes above southeastern Europe in the winter of 1983/84, *Problems of Meteorology and Hydrology*, Nr. 6, Publ. BAN, Sofia, 1986.
- Schlegel, K., and J. Röttger, Thermodynamics and electrodynamics of the auroral E-region during the D salvo of the MAP/WINE campaign, *J. Atmos. Terr. Phys.*, 49, 819-826, 1987.
- Schmidlin, F. J., and W. R. Michel, The importance of precision radar tracking data for the determination of density and winds from the high-altitude inflatable sphere, *Proc. 7th ESA Symp. on European Rocket and Balloon Programmes and Related Research*, *ESA SP-229*, 49-54, 1985.
- Schuchardt, K. G. H., P. W. Blum, V. Gärtner, and M. Memmesheimer, Seasonal transport and turbulence in the lower thermosphere, *Adv. Space Res.*, 3, 109-111, 1983.
- Thrane, E. V., T. A. Blix, C. Hall, T. L. Hansen, U. von Zahn, W. Meyer, P. Czechowsky, G. Schmidt, H.-U. Widdel, and A. Neumann, Small scale structure and turbulence in the mesosphere and lower thermosphere at high latitudes in winter, *J. Atmos. Terr. Phys.*, 49, 751-762, 1987.
- Ulwick, J. C., K. D. Baker, D. J. Baker, A. J. Steed, W. R. Pendleton, Jr., K. U. Grossmann, and H. G. Brückelmann, Mesospheric minor species determinations from rocket and ground-based i.r. measurements, *J. Atmos. Terr. Phys.*, 49, 855-862, 1987.
- Widdel, H.-U., Vertical movements in the middle atmosphere derived from foil cloud experiments, *J. Atmos. Terr. Phys.*, 49, 723-741, 1987.
- Williams, E. R., G. W. Watkins, T. A. Blix, E. V. Thrane, G. Entzian, G. von Cossart, K. M. Greisiger, W. Singer, J. Taubenheim, M. Friedrich, C. M. Hall, J. R. Katan, J. Lastovicka, B. A. de La Moreno, S. V. Pakhomov, H. Ranta, Z. Ts. Rapoport, V. M. Sinelnikov, D. Samardjiev, G. Nestorov, H. H. Sauer, and P. Stauning, The ionosphere: morphology, development and coupling, *J. Atmos. Terr. Phys.*, 49, 777-808, 1987.
- von Zahn, U., The research project "Winter in Northern Europe (WINE)" of the international "Middle Atmosphere Program (MAP)", 6th ESA Symp. on European Rocket and Balloon Programmes and Related Research, *ESA SP-183*, 147-159, 1983.
- von Zahn, U. (Editor), Campaign Handbook for the Project MAP/WINE, Univ. Bonn Rep. *BONN-EP-83-1*, 207 pages, 1983.
- von Zahn, U., The project MAP/WINE: an overview, *J. Atmos. Terr. Phys.*, 49, 607-620, 1987.
- von Zahn, U., The University of Bonn LIDAR experiment at the Andoya island, *Proc. 13th Ann. Meet. on Upper Atmosphere Studies by Optical Methods*, Ed. K. Maseide, *Rep. 86-28*, Dept. Physics, Univ. Oslo, Norway, 1986.
- von Zahn, U., and Ch. Pütz, On the comparison of turbulent parameters and eddy coefficients in the lower thermosphere, *Proc. 7th ESA Symp. on European Rocket and Balloon Programmes and Related Research*, *ESA SP-229*, 267-270, 1985.

- von Zahn, U., and H.-U. Widdel, Wind corners in the winter mesosphere, *Geophys. Res. Lett.*, **12**, 673-676, 1985.
- von Zahn, U., W. Meyer, and H.-U. Widdel, Wind corners and wind strata in the mesosphere, Proc. 7th ESA Symp. on European Rocket and Balloon Programmes and Related Research, *ESA SP-229*, 61-68, 1985.
- von Zahn, U., K. H. Fricke, R. Gerndt, and T. Blix, Mesospheric temperatures and the OH layer height as derived from ground-based LIDAR and OH* spectrometry, *J. Atmos. Terr. Phys.*, **49**, 863-869, 1987.
- Zimmerman, S. P., T. J. Keneshea, R. Echardt, and U. von Zahn, Analysis of the BUGATTI data for turbulent parameters, *Adv. Space Res.*, **7**(10), 353-357, 1987.

Additional information about MAP/WINE results is available in the form of numerous Ph.D. theses and oral conference contributions, neither of which are not listed here.

Appendix 12

MAP ACTIVITIES - USSR

E. S. Kazimirovsky

The USSR scientific institutions continued to participate in the MAC projects, e.g.:

I. Lower thermosphere and ionosphere

- In situ experiments in the lower ionosphere during MAC-SINCE, MAC-Epsilon, SuperCAMP.
- Analysis of atmospheric turbulence -- MAC-SINE, MAC-Epsilon.
- Ground-based wind measurements in accordance with campaigns MAC-SINE, SuperCAMP, DYNAMICS, ATMAP, GRATMAP, GLOBMET.
- Noctilucent clouds (experimental and theoretical investigations) - SuperCAMP.
- Correlation between electron concentration and radio wave absorption in the ionospheric D region and meteorological and dynamical parameters of the middle atmosphere. Empirical and theoretical models of these relationships - MAC-SINE, SuperCAMP, DYNAMICS.

II. Dynamics of the stratosphere and mesosphere

- In situ rocket experiments - MAC-SINE, MAC-Epsilon, SuperCAMP.
- Seasonal variations of tides in wind field of the middle atmosphere for different latitudes and longitudes, synoptical structure of tides - ATMAP.
- The determination of climatic features of thermodynamical parameters and wind in the middle atmosphere, theoretical models - MASH, CLIMAT, DYNAMICS.
- Theoretical modeling of tides - ATMAP.
- Development of radar methods, constructing of ST radar in Kharkov - MSTRAC.
- Rocket and ground-based measurements of electrical fields in the middle atmosphere -MAE.

III. Minor constituents in the stratosphere and mesosphere - CLIMAT, DYNAMICS, MAC-SINE, GLOBUS, GOSSA.

IV. Ozone investigations in the middle and high latitudes - OZMAP, AMA.

V. Soviet National Program of GLOBMET.

VI. Preparation of databases of the middle atmosphere parameters and change of data and publications via the WDC.

As for the future of middle atmosphere investigations in the USSR there is intention to maintain the Soviet Commission and to continue the international cooperation in this field. We understand that the middle atmosphere is at first the complex system with its own internal interactions and at second the intermediate region in the transfer of energy from the sun to the earth. So we will have the connection with COSPAR, IAGA, and IAMAP and simultaneously serve as a Working Group of the National STEP Committee. In accordance with the STEP Program, the main directions of future investigations are:

1. The energetic budget, chemistry and dynamics of the middle atmosphere and interactions from above (ionosphere, magnetosphere) and below (troposphere) regions.
2. The global effects of magnetospheric effects in the lower thermosphere and mesosphere.
3. The role of electric fields of magnetospheric, ionospheric and thunderstorm origin in the dynamical and chemical processes in the middle atmosphere.
4. The effects of solar and magnetic activity on the chemistry and dynamics in the middle atmosphere.

Appendix 13

MAP ACTIVITIES 1981-1988 - FEDERAL REPUBLIC OF GERMANY

U. von Zahn

Participation of scientists from the FRG in the international Middle Atmosphere Program (MAP) and the Middle Atmosphere Cooperation (MAC) has been supported and funded through special grants by the deutsche Forschungsgemeinschaft (DFG) and the Bundesministerium für Forschung und Technologie (BMFT), Bonn. This institutional and dedicated support of our efforts within MAP and MAC started April 1, 1981 and it will end March 31, 1989.

In the area of major field campaigns scientists from the FRG have initiated and heavily participated in the MAP projects "Global Budget of Stratospheric Trace Constituents 1983" (GLOBUS 1983) and "Winter in Northern Europe" (WINE). A large collection of scientific papers describing results obtained from these projects have been published in *Planet. Space Sci.*, 35, No. 5 (1987) and *J. Atmos. Terr. Phys.*, 49, No. 7/8 (1987), respectively. Experiments from the FRG were also contributed to the campaign GLOBUS NO_x (1985). After completion of MAP and during MAC scientists from the FRG concentrated their efforts on the field campaigns "Summer in Northern Europe" (SINE) and "Epsilon", both of which took place in 1987.

A number of research groups of the FRG are involved in modeling the structure and the processes acting in the middle atmosphere. The opportunities offered by MAP and MAC were used quite successfully by these groups not only to further their own scientific aims and interests, but also to considerably intensify the cooperation among the various groups on a national level.

The dedicated MAP grants by DFG have also supported laboratory studies of selected chemical/photochemical reactions of importance to stratospheric trace gases as well as the development of improved measurement techniques for reactive trace species of the stratosphere.

Outlook: MAP has given middle atmosphere aeronomy a big boost. For the future it seems likely that of the manpower, instrumentation, and know-how available for middle atmosphere research in the FRG, a considerable part will be directed towards exploring the Arctic stratosphere in greater detail than done before.

Appendix 14

MAP ACTIVITIES - BRAZIL

B. R. Clemesha

The main center for middle atmosphere research in Brazil is the Space Research Institute (INPE), although some work is also carried out at other research centers and universities. Work is in progress in the following areas: tropospheric and stratospheric ozone, tropospheric CO, stratospheric aerosols, atmospheric tides and gravity waves, minor constituents in the middle atmosphere and D-region ionization.

1. Research in Progress

Total ozone measurements are made at Cachoeira Paulista and Natal by Dobson spectrophotometers, and surface ozone is measured at Natal and Cuiaba. Stratospheric ozone profiles are measured regularly at Natal, using ECC sondes, and were also obtained in the Amazon rain forest during the 1987 GTE-ABLE experiment. The occurrence of significantly lower surface ozone concentrations in the Amazon region, as compared with Natal, a coastal site, is attributed to increased loss of ozone by reactions with NO. Surface CO is measured regularly at Sao Jose dos Campos, Natal and Fortaleza.

The stratospheric aerosol scattering profile is measured by laser radar at Sao Jose dos Campos, and the same equipment is used to measure the vertical distribution of atmospheric sodium. These measurements are used to study atmospheric dynamics and chemistry in conjunction with airglow observations. The airglow measurements of relevance to the middle atmosphere, made in Cachoeira Paulista and Fortaleza, include the OI 5577 Å, OH (8,3), O₂ atmospheric band 8645 Å and NaD 5890 Å emissions. The O₂ and OH measurements are used to determine rotational temperature, and a long sequence of observations has made it possible to obtain a mean annual variation for this parameter in the emission region of 85 to 95 km. An all-sky imaging photometer, installed at Cachoeira Paulista, has been used to look for spatial variations in the sodium emission.

The rocket sounding program has continued with one launch in 1986. This experiment included photometers to measure the OI 5577 Å and 6300 Å emissions simultaneously with electron density and electron temperature to an apogee of 444 km. Wide-band photometers were included in the payload to study the vehicle glow which was observed in an earlier flight of a similar payload. All the experiments worked well and good profiles were obtained for all the parameters. Of course, only the lowest part of the electron density profile and the E-region component of the 5577 Å emission are of relevance to the Middle Atmosphere Program. Three experiments originally planned for 1987/1988 have been postponed till 1989 because of delays in the new launch site being built at Alcantara. One of these payloads will include 10 photometers to look at emissions such as hydroxyl, sodium, atomic oxygen and molecular oxygen, and another will measure the O₂(¹Δ) emission, from which the mesospheric ozone profile can be derived.

In the field of atmospheric electricity, balloon measurements have been made of electric fields and conductivity over electrified clouds. The results of such experiments have lead to estimates of charges of a few coulombs for electrified convective clouds in the absence of thunderstorm activity.

Studies of the ionized middle atmosphere are mainly concerned with the aeronomic effects of particle precipitation in the South Atlantic Anomaly. In this context, VLF oblique sounding has been used to study ionization and recombination effects in the D region, and transpolar VLF propagation measurements are used to investigate PCA events.

2. Ground-Based Experimental Facilities

1. Sao Jose dos Campos (23°S, 46°W): Laser radar for stratospheric aerosol and atmospheric sodium studies, atmospheric chemistry laboratory, VLF phase-track receiver.
2. Cachoeira Paulista (23°S, 45°W): Airglow observatory, Dobson ozone spectrophotometer.

3. Natal (6°S, 35°W): Dobson ozone spectrophotometer, surface ozone and carbon monoxide monitors.
4. Fortaleza (4°S, 38°W): Multichannel airglow photometer, surfaced carbon monoxide monitoring.
5. Cuiaba (16°S, 56°W): Surface O₃ and CO measurements.
6. Comandante Ferraz, Antarctica (62°S, 58°W): Surface O₃ and CO monitoring.
7. Atibaia (23°S, 47°W): VLF phase track receiver.

3. Balloon and Rocket Launching Facilities

The main launch facilities for stratospheric balloons are at Cachoeira Paulista, but launches are often performed from airstrips in the interiors of the country, depending on the stratospheric winds. Until now, rocket launches have been from the Barreira de Inferno Launch Centre (CLBI) at Natal, but future launches will be from the new launch base under construction at Alcantara.

Appendix 15

MAC ACTIVITIES -- CZECHOSLOVAKIA

J. Lastovicka

The Czechoslovak national MAC program consists of six scientific subprograms:

1. "Disturbances of the atmosphere at heights of 120 to 40 km by penetration of meteoroids of meter and decimeter dimensions" - Dr. Cepelcha (Astronomical Institute, Czechoslovak Academy of Science, Ondrejov):

Systematic photographic observations of fireballs were performed at 17 stations in Czechoslovakia, 21 stations in the FRG, 8 stations in the GDR and 4 stations in The Netherlands. They yielded multistation records of 45 fireballs during this period. Results of the most significant four fireballs have already been published in the SEAN Bulletin. Three fireballs penetrated the whole middle atmosphere, two of them down to the earth's surface, and all were used to derive the instantaneous air-density profiles at heights 80 - 20 km.

2. "Meteor radar observations" - Dr. Simek (Astronomical Institute, Czechoslovak Academy of Science, Ondrejov):

The dynamics and development of the structure of five selected meteor showers was studied by Simek (*Bull. Astron. Inst. Czech.*, 38, 80, 1987) on the basis of long-period radar observations at Ondrejov. The structure of the Giacobini 1985 meteor shower from radar observations at Ondrejov and Dushanbe is described by Chebotarev and Simek (*Bull. Astron. Inst. Czech.*, 38, 362, 1987). The absence of the Giacobinid 1986 activity was proven by Simek (*Bull. Astron. Czech.*, 38, 317, 1987). Porubcan and Simek (*Bull. Astron. Inst. Czech.*, 39, No. 2, 1988) analyzed the mass distribution of meteoric particles in the Lyrid meteoric shower.

3. "Winter anomaly" - Dr. Lastovicka (Geophysical Institute, Czechoslovak Academy Science, Prague):

The ionospheric radio wave absorption in central Europe reflected surprisingly weakly the very early major stratospheric warming of November/December 1987. The rapid breakdown of the winter anomaly at the end of February and early in March 1988 is considered to be of stratospheric origin.

4. "Aeronomic studies with the use of ground-based measurements of radio wave propagation" - Dr. Boska (Geophysical Institute, Czechoslovak. Academy of Science, Prague):

Two ranges of periods of dominant fluctuations were found in the daytime and nighttime LF radio wave absorption in central and southern Europe -- 3.5-5 and 10.5-12 days. They were proven to be consistent with periods observed in winds (90-100 km), but not in solar ionizing radiation, i.e., they are real meteorological planetary waves.

5. "The interplanetary magnetic field effects in the ionosphere and atmosphere" - Dr. Lastovicka (Geophysical Institute, Czechoslovak. Academy of Science, Prague):

The IMF sector structure effects in the ozone mass mixing ratio in the upper stratosphere between 10-0.4 hPa and 40° - 60° N (Europe, Asia) were found not to exist in a measurable form by using winter data over the period December 1979-December 1982. An effect was found to exist in the total ozone in midlatitude Europe for proton sector boundaries, but not for common sector boundaries.

6. "The dynamics of penetration of convective clouds into the stratosphere" - Dr. Podhorsky (Slovak Hydrometeorological Institute, Bratislava):

Based on a successful verification of computations of advective-convective tendencies of cloudiness (according to primary data from the Meteosat geostationary satellite) and on the prediction according to the temperature on the upper boundary of cumulonimbus clouds, an algorithm was elaborated for the selection and development of signatures to determine the classification of selected classes of clouds and phenomena. A prediction model was simultaneously developed. Eight case studies of cumulonimbus penetration into the stratosphere allow us to conclude:

(a) The classification of cumulonimbus clouds penetrating through the tropopause is successful.

- (b) The developed model enables predictions of intensive development of cumulonimbus for 60 minutes.

Appendix 16

MAP ACTIVITIES -- UNITED KINGDOM

L. Thomas

(a) MST radar

An MST radar system operating at 46.5 MHz is being established jointly by the Department of Physics, University College of Wales, and the Rutherford Appleton Laboratory at a site about four miles from the Department. The first phase of the system, based on 64 Yagi antennas and two transmitters giving in excess of 50 kW peak power, is currently being tested. Subject to the outcome of these tests, the system is to be developed, firstly by extending the antenna array to 400 antenna units and secondly by incorporating three more transmitters. It is hoped that the final system will be operational within about two years.

(b) Lidar

The present program of measurements is directed towards studies of stratospheric and mesospheric temperatures based on observations of Rayleigh scattering and of the characteristics and nucleation of ice crystals in high altitude clouds. The latter studies make use of a scanning system which incorporates polarization measurements and measurements of the mixing ratio of water vapor up to the tropopause. The overall program is based on a Nd/Yag laser but plans are in hand to acquire a XeF excimer laser. It is intended that the lidar experiments will be co-located with the MST radar.

(c) Transport of minor constituents

Daily global maps of the total ozone content measured by the TOMS instrument on the NIMBUS-7 satellite are being examined as part of a study of transport of ozone from the stratosphere to the troposphere. Synoptic scale features in the maps are being examined in conjunction with radiosonde temperature measurements and numerical forecast model assimilation fields.

Appendix 17

MAP ACTIVITIES -- HUNGARY

P. Bencze

In this report only those programs are discussed in which new results are obtained.

1. Changes of solar and meteorological origin in the mesosphere and lower thermosphere.

The effect of solar-terrestrial events in the middle atmosphere has been studied in the Geodetical and Geophysical Research Institute, Sopron, Hungarian Academy of Sciences. Using for this purpose data of the level of atmospheric radio noise, it has been found that in the ELF range the effect of Forbush decreases (a reduction of the level) is increasing with frequency (to the cutoff frequency of the earth-ionosphere waveguide). Thus, the behavior of the propagation of radio waves related to Forbush decreases is demonstrated and proven by the waveguide theory not only above, but also below the cutoff frequency.

Investigating the connection between the post-storm effect in the ionospheric absorption of radio waves, it has been found that the post-storm effect depends not only on the maximum velocity of high speed plasma streams in the interplanetary space, but also on its duration and maximum velocity increase, especially in case of plasma streams associated with solar flares. Both the high peak velocities and large velocity increases can support the magnetospheric processes resulting in post-storm effects.

2. Turbulence

The method developed for the determination of turbulent parameters in the lower thermosphere based on sporadic E parameters, on ionospheric and upper atmospheric models in the Geodetical and Geophysical Research Institute, Sopron, Hungarian Academy of Sciences, has been supplemented. Including the basic relation of the wind shear theory referring to electrons, the vertical shears of both horizontal wind components can be determined. In addition, the recombination coefficient outside the Es layer is computed by means of ionospheric models in each case. The recombination coefficient inside the Es layer is calculated from the basic equations using measured values of the wind shear.

The turbulent diffusion coefficient obtained by the method has been studied following stratospheric warmings, during days of the anomalous winter anomaly and as a function of the geomagnetic activity, and a parallelism between the changes of the turbulent diffusion coefficient and that of the ionospheric absorption has been found. A consistent interpretation of these phenomena has emerged, which hints at the role of the turbulent diffusion in the vertical transport of easily ionizable constituents and indicates a possible reaction to the mean zonal momentum dissipation.

APPENDIX 18

Attendees at MAPSC Meeting, July 18, 1988, Espoo, Finland

S. A. Bowhill	A. O'Neill
A. D. Danilov	H. Ranta
D. C. Fritts	P. C. Simon
S. Fukao	J. Soegij
R. A. Goldberg	S.-. Su
G. M. Grechko	J. Taubenheim
I. Hirota	E. V. Thrane
S. Kato	T. E. VanZandt
E. S. Kazimirovsky	R. A. Vincent
E. Kopp	U. von Zahn
K. Labitzke	G. Witt
C. H. Liu	M. Yamamoto
A. H. Manson	

APPENDIX 19

MAP STEERING COMMITTEE, July 18, 1988, Espoo, Finland

AGENDA

1. Welcome and Introductory Remarks - Bowhill
2. Approval of Agenda
3. Minutes of 1987 Meeting, Vancouver
4. Committee Reports:
 - Data Management - Hirota
 - Status of MAP Data Catalogue
 - Publications
 - Status of MAP Summary Document - Vincent
5. MSG Reports
6. Project Reports:

<ul style="list-style-type: none"> AMA, Hirasawa ATMAP, Forbes DYNAMICS, Labitzke GLOBMET, Roper GLOBUS, Pommereau GOSSA, McCormick GRATMAP, Fritts 	<ul style="list-style-type: none"> MAC-Epsilon/MAC-SINE, Thrane MAE, Goldberg MASH, O'Neill NIEO, Kato OZMAP, Heath SSIM, Simon SUPER CAMP, Kopp
--	---
7. Workshops/Symposia:
 - SUPER CAMP, March 1988
 - GLOBMET, July 1988
 - MAP Symposium, July 1988
 - MAC-Epsilon/MAC-SINE, October 1988
 - MST Radar, November/December 1988
 - MAC Symposium in USSR 1989
8. Coordination with STEP
9. Regional Consultative Group Report
10. Reports from Representatives of the Countries
11. Other Business
12. Next Meeting

INTERNATIONAL WORKSHOP ON NOCTILUCENT CLOUDS

Tallinn, Estonia, USSR

July 27-31, 1988

O. A. Avaste

Department of Geophysics, Tartu State University
202400 Tartu, Estonia, USSR

G. E. Thomas

LASP/University of Colorado
Campus Box 392, Boulder, CO 80309-0392

The International Workshop on Noctilucent Clouds was held in Tallinn, USSR from 27-31 July 1988. The NLC Workshop was sponsored by the NLC Working Group of the Commission on the Meteorology of the Upper Atmosphere and the hosts were the Tartu State University and the Institute of Astrophysics and Atmospheric Physics of the Estonian Academy of Sciences. Thirty scientists from eight countries participated in the Workshop. The main topics of the Workshop were new data on the climatology and physics of NLC, especially problems connected with rocket soundings of the mesopause. Twenty papers were presented and a concluding discussion was carried out. Many of the papers will be published in a forthcoming report.

Co-Chairman of the International Working Group on Noctilucent Clouds, G. E. Thomas (USA), gave a review of the previous NLC Workshop in Boulder, Colorado, March 16-18, 1988. He analyzed the main trends and open questions in ion-chemistry versus NLC physics, dynamics of the mesopause, microstructure of NLC, electrodynamics of the mesopause as well as climatology and morphology of NLC.

To the electrodynamics of the mesopause were dedicated two more papers: A. M. Zadorozhny presented results of the measurements of a vertical component of electric field and a nitric oxide vertical distribution in the middle atmosphere by rocket measurements at Heiss Island (81°N, 58°E) and Volgograd (48°N, 46°E). These measurements showed that in a quiet electromagnetic period the electric field strength is significantly less in the high-latitude mesosphere than in the middle latitudes. With strong disturbances, the E-layer profile becomes similar to the midlatitudinal one. At Volgograd the dependence of electric field on geomagnetic disturbance appears to be weaker. R. A. Goldberg (USA) gave a review on the problems of electrodynamics of the high latitude mesosphere. He pointed out that the discovery of apparently large (V/m) electric fields within the mesosphere suggests that this region is more active electrically than previously suspected. New measurements show the influence of NLC on electric fields mapping downward from the ionosphere. Future projects are planned to study the mesospheric cloud influences on the local electrical environment. Electrical parameters can be used to track neutral air turbulence and wave structure at high latitudes, thereby providing a powerful tool for the study of mesospheric neutral dynamics and its relationship to the problems of electrodynamics.

Problems of the effects of gravity waves on the temperature field near the mesopause were discussed in the paper by A. Ebel (FRG). He demonstrated the results deduced from a 3-D model of the global circulation. The depth of the temperature minimum, as simulated by the model, clearly depends on the intensity of gravity wave activity. He analyzed the inter-relation of gravity wave breaking and NLC formation. E. Kopp (Switzerland) investigated the ion composition in the presence of NLC. The proton hydrate ions of the cold arctic mesopause regions are candidates for nucleation cores of the ice particles that form noctilucent and polar mesospheric clouds (especially when the mesopause temperature is lower than 150 K). Ion composition can also give important information on the thermal structure and the composition of neutral minor species, such as H₂O, H₂O₂, NO and O. He analyzed three rocket measurements above Kiruna (July 30 and August 13, 1978; August 3, 1982) in the presence of

NLC. At the transition height, where the dominant proton hydrates change into molecular ions, the observed cutoff of proton hydrates is much sharper than the model would predict, a situation which indicates a sudden change of eddy transport.

M. I. Taylor (UK) [co-authors R. P. Lowe (Canada), P. I. Baker and J. Ulwick (USA)] presented a paper on the association of NLC with the OH nightglow emission. Michelson interferometer measurements, carried out on several consecutive nights from Poker Flat Research Range, Alaska (65.1°N, 147.5°W) during August 1986, as well as NLC observations from Gulkana Airport (62.2°N, 145.5°W), demonstrated that a study of the OH intensity and temperature should provide information on the atmospheric conditions in the vicinity of the mesopause during NLC displays. P. Rothwell and P. N. Smith (UK) presented information of a CCD imaging system capable of studying the wave structure in NLC and OH airglow, possibly at the same time. This system has undergone a satisfactory initial test.

NLC climatology from Earth surface observations was reviewed by N. P. Fast and W. H. Fast (USSR). O. B. Vasilyev et al. (USSR) presented a review on several hypotheses of NLC genesis, composition and structure of their particles.

G. E. Thomas (USA) [co-authors E. J. Jensen, O. B. Toon (USA)] analyzed the apparent discrepancy in the comparison of photometric data for NLC and polar mesospheric clouds (PMC). In the latitude range (50° - 65°) NLC brightness can be ten or more times higher than the atmospheric Rayleigh background. However PMC brightness, measured by satellite limb sensor, indicates very weak clouds (relative to background). Thomas also presented a time-dependent model, which considers small tidal variations of temperature and dynamics at mesopause height. This model showed that cloud brightness maximizes at about 23 hours local time. This peak occurs primarily as the result of a burst of nucleation of new particles at the time of temperature minimum (at about 19 hours LT), but also from an increased condensation growth of the pre-existing particles. A simple 1-D model of NLC formation was given by J. L. Langebraun (USSR). She demonstrated that the lifetime of cubic and hexagonal ice particles in NLC cloud layer is higher than that of other forms, which fall out before they have grown to visible sizes.

A. Roddy (Ireland) pointed out the importance of laboratory studies of ice nucleation at low temperatures, relevant to noctilucent clouds. G. Witt (Sweden) presented the results of optical and rocket studies of the summertime mesopause. N. Wilhelm (Sweden) described a compact scattered-light photometer for rocket-borne NLC experimentation.

Observations of NLC were reported in the paper by M. Gadsden (Scotland) and W. Schröder (FRG). They presented a review on the climatological study of NLC in northwest Europe. They pointed out the importance of the comparison of meteor train drift data with the night-to-night occurrence of noctilucent clouds, the study of the morphology of wave-like patterns seen in noctilucent clouds, including the presence of gravity wave breaking; systematic measurements of the heights of noctilucent clouds by triangulation (parallactic photography from widely separated sites).

The paper by A. I. Lazarev, O. A. Avaste, and T. A. Damynova (USSR) was dedicated to the analysis of the inter-relations of NLC occurrences and volcanic eruptions. They proposed a hypothesis that the low-latitude NLC layers, seen by Soviet cosmonauts, are caused by the particles and gases transported to the mesopause when large volcanic eruptions occur.

U. von Zahn and W. Meyer (FRG) presented new data on the mesopause temperature, derived from the rocket campaign in Andoya Rocket Range (June 10-July 19, 1987) during the MAC/SINE period. A total of 26 passive falling spheres were tracked precisely by radar systems, and temperature profiles were calculated from the atmospheric drag information. The average mesopause height was at an altitude 88 ± 1 km, and its temperature was 128 ± 5 K. They pointed out that water vapor condensation may occur at the mesopause altitudes not only in the regions in which temperatures are locally depressed by the passage of atmospheric waves, but also under undisturbed (= mean) conditions.

In his second paper U. von Zahn discussed the temperature profiles of the mesopause, derived from measurements of the Doppler-width of the laser excited Na D₂ resonance lines. This technique allows us to determine from ground-based lidar measurements neutral gas temperatures between 80 and 110 km. During nighttime, temperature profiles were collected

over 10 min integration periods, 1 km altitude bins with an accuracy of ± 5 K. It was shown that from two winter soundings (1985/86, 1986/87) from December through February the mesopause temperature was found close to 193 K at an altitude of 100 km. C. R. Philbrick (USA) presented climatological mean values of rocket soundings. The mean conditions of the high latitude summer mesopause exhibit a temperature minimum near 125 K near 90 km. The summer season is strikingly different from the winter, not only in the mean profile, but in the character, frequency and content of the wave structure. The summer profiles show very little wave activity below 70 km; however waves of large amplitude can grow between 80 and 100 km. The sources of waves from below are limited in the summer and thus, nearly monochromatic waves are frequently observed. The waves observed are important in the formation of noctilucent clouds and other small condensation nuclei because of the even lower temperatures reached at the minima of the wave. Temperatures as low as 110 K are probably not uncommon.

The participants of the Workshop had a sightseeing tour in Tallinn. They visited the Tartu State University and the Institute of Astrophysics and Atmospheric Physics in Tõravere. The next meeting on the subject of NLF climatology, physics of nucleation, and monitoring from space, will be carried out within the framework of the IAMAP General Assembly in Reading, United Kingdom, where a half-day (morning) session on NLC will be held on August 2, 1989. The current issues to be addressed are: 1) characteristic sizes and shapes of NLC and PMC particles; 2) modes of nucleation and growth; 3) influence of waves, particularly breaking waves; 4) large-scale behavior; 5) possible alteration of their chemical, ionic and electrical environment.

For further information, please contact Dr. M. J. Taylor, Department of Physics, The University of Southampton, SO9 5NH, United Kingdom.

INTERNATIONAL WORKSHOP ON NOCTILUCENT CLOUDS

Tallinn, Estonia, USSR July 28-31, 1988

PROGRAM

Registration July 27, 9:00 AM - 7:00 PM Hotel Olympia
 July 28, 9:00 AM - 10:00 AM Tallinn Club of
 Engineers, To'nisma"gi str.7.

July 28

<u>Speaker</u>	<u>Topic</u>	<u>Time</u>
H. Peremees Vice-Chairman of the Committee of Education of the Estonian SSR	Welcoming Remarks	10:00 - 10:10
O. Avaste	Information	10:10 - 10:15

CONVENOR: A.D. POVZNER

G.E. Thomas, G.B. Bjarnasson, E. J. Jensen, D. Siskind and A. Stern (USA)	International workshop on noctilucent clouds Boulder, Colorado, March 16-18, 1988	10:15 - 10:45
A. Ebel, H.J. Jakobs and M. Dameris (FRG)	The effect of gravity waves on the temperature minimum near the mesopause - a model study	10:45 - 11:15
	<u>Coffee Break</u>	11:15 - 11:30
A.M. Zadorozhny G.A. Tuckov, and A.A. Tyutin (USSR)	<i>In situ</i> measurements of electric field strength and nitric oxide distribution in the middle atmosphere during MAP/MAC period.	11:30 - 12:00
E. Kopp (Switzerland)	Positive ion composition in the presence of noctilucent clouds	12:00 - 12:30
	<u>Lunch</u>	12:30 - 2:30
M.J. Taylor (UK), R.P. Lowe (Canada) D.J. Baker and J. Ulvick (USA)	Simultaneous hydroxyl airglow intensity and temperature measurements	2:30 - 3:00

	and noctilucous cloud observations	
P. Rothwell and P.N. Smith (UK)	A computer controlled, Peltier cooled, integrating CCD TV camera system for the study of wave structure in NLC and OH airglow	3:00 - 3:30
	<u>Coffee Break</u>	3:30 - 3:50
N.P. Fast and W.H. Fast (USSR)	The Climatology of noctilucous clouds	3:50 - 4:20
O.B. Vasilyev, Ch.I. Willmann, L.S. Ivlev, A.I. Lazarev and S.H. Rosenfeld (USSR)	On the nature of noctilucous clouds	4:20 - 5:30
	<u>Group Discussion</u>	4:50 - 5:30
Sightseeing tour in Tallinn		6:15 - 8:00
Reception in Restaurant "Pirita"		8:00 - 9:00

July 29

CONVENOR: O.B. VASILYEV

G.E. Thomas, E.J. Jensen and O.B. Toon (USA)	Modelling of the diurnal variability of noctilucous clouds	9:00 - 9:30
M. Gadsden (UK) and W. Schröder (FRG)	The nature of noctilucous clouds	9:30 - 10:00
A Roddy (Ireland)	Ice nucleation measurements relevant to noctilucous clouds	10:00 - 10:30
G. Witt (Sweden)	Optical and other studies of NLC and the summertime mesopause.	10:30 - 11:00
	<u>Coffee Break</u>	11:00 - 11:20
O. Avaste, A.I. Lazarev and T.A. Danyanova (USSR)	On the genesis of noctilucous clouds	11:20 - 11:50
J.L. Langebraun (USSR)	On the formation mechanism of noctilucous clouds	11:50 - 12:20

Lunch

12:30 - 2:30

CONVENOR: M. GADSDEN

P. Kalv (USSR)	Noctilucent cloud display in Tallinn on the night 27/28 July 1988.	2:30 - 3:00
----------------	--	-------------

U. von Zahn and W. Meyer (FRG)	Mesopause temperatures in polar summer, derived from passive falling sphere experiments	3:00 - 3:30
-----------------------------------	---	-------------

U. von Zahn (FRG)	Temperature profiles from measurements of the Doppler width of the laser-excited NaD ₂ resonance lines	3:30 - 4:00
-------------------	--	-------------

Coffee Break

4:00 - 4:20

C.R. Philbrick (USA)	Structure of the high latitude summer mesosphere	4:20 - 4:50
----------------------	---	-------------

R.A. Goldberg (USA)	Electrodynamics of the high latitude mesosphere	4:50 - 5:20
---------------------	--	-------------

N. Wilhelm (USA)	Small-size scattered light photometers for NLC experiment	5:20 - 5:50
------------------	--	-------------

Group Discussion

5:50 - 6:30

July 30

Excursion to Tartu State University and To'ravere	9:00 AM - 9:00 PM
--	-------------------

Lunch in Tartu "Gunpowder Cellar"	2:00 PM - 3:00 PM
-----------------------------------	-------------------

Refreshments in ADAVERE WINDMILL	7:00 PM - 9:00 PM
----------------------------------	-------------------

July 31

Future Projects Discussion	9:00 - 11:20
----------------------------	--------------

E. Kopp (Switzerland) Overview of NLC Campaigns, Past and Future	11:00 - 11:30
---	---------------

Concluding Remarks	11:30 - 12:00
--------------------	---------------

Adjourn

CUMULATIVE LISTING FOR THE MAP HANDBOOK

<u>Volume</u>	<u>Contents</u>	<u>Publication Date</u>
1	National Plans, PMP-1, PMP-2, PMP-3 Reports, Approved MAP Projects	June 1981
2	Symposium on Middle Atmosphere Dynamics and Transport	June 1981
3	PMP-5, MSG-1, MSG-2, MSG-3 Reports, Antarctic Middle Atmosphere Project (AMA), EXOS-C Scientific Observations, WMO Report No. 5., Updated Chapter 2 of MAP Planning Document, Condensed Minutes of MAPSC Meetings	November 1981
4	Proceedings of MAP Assembly, Edinburgh, August 1981 Condensed Minutes of MAPSC Meetings, Edinburgh, Proceedings of MAP Open Meeting, Hamburg, August 1981,	April 1982
5	A Catalogue of Dynamic Parameters Describing the Variability of the Middle Stratosphere during the Northern Winters	May 1982
6	MAP Directory	November 1982
7	Acronyms, Condensed Minutes of MAPSC Meetings, Ottawa, May 1982, MAP Projects, National Reports, Committee, PMP, MSG, Workshop Reports, Announcements, Corrigendum	December 1982
8	MAP Project Reports: DYNAMICS, GLOBUS, and SSIM, MSG-7 Report, National Reports: Czechoslovakia, USA	July 1983
9	URSI/SCOSTEP Workshop on Technical Aspects of MST Radar, Urbana, May 1983	December 1983
10	International Symposium on Ground-Based Studies of the Middle Atmosphere, Schwerin, May 1983	May 1984
11	Condensed Minutes of MAPSC Meetings, Hamburg, 1983, Research Recommendations for Increased US Participation in the Middle Atmosphere Program, GRATMAP and MSG-7 Reports	June 1984
12	Coordinated Study of the Behavior of the Middle Atmosphere in Winter (PMP-1) Workshops	July 1984
13	Ground-Based Techniques	November 1984
14	URSI/SCOSTEP Workshop on Technical Aspects of MST Radar, Urbana, May 1984	December 1984
15	Balloon Techniques	June 1985
16	Atmospheric Structure and its Variation in the Region 20 to 120 km: Draft of a New Reference Middle Atmosphere	July 1985
17	Condensed Minutes of MAPSC Meeting, Condensed Minutes of MAP Assembly, MAP Project, MSG, and National Reports	August 1985
18	MAP Symposium, Kyoto, November 1984	December 1985
19	Rocket Techniques	March 1986
20	URSI/SCOSTEP Workshop on Technical and Scientific Aspects of MST Radar, Aguiadilla, October 1985	June 1986
21	MAPSC Minutes, ATMAP Workshop, Atmospheric Tides Workshop, MAP/WINE Experimenters Meetings, National Reports: Co-ordinated Study of the Behavior of the Middle Atmosphere in Winter	July 1986
22	Middle Atmosphere Composition Revealed by Satellite Observations	September 1986
23	Condensed Minutes of MAPSC Meetings, Toulouse, June/July 1986	December 1986
24	MAP Directory	May 1987
25	First GLOBMET Symposium, Dushanbe, August 1985	August 1987
26	MAPSC Minutes, Abstracts and Report of Workshop on Noctilucent Clouds, Boulder, October 1985	June 1988
27	COSPAR Symposium 6, The Middle Atmosphere After MAP, Espoo, July 1988, MAPSC Minutes, Espoo, July 1988; Workshop on Noctilucent Clouds, Tallinn, July 1988	April 1989